

ADVANCED TWO- AND THREE-DIMENSIONAL TSUNAMI MODELS:
BENCHMARKING AND VALIDATION

A THESIS SUBMITTED TO
THE GRADUATE SCHOOL OF NATURAL AND APPLIED SCIENCES
OF
MIDDLE EAST TECHNICAL UNIVERSITY

BY

DENİZ VELİOĞLU

IN PARTIAL FULFILLMENT OF THE REQUIREMENTS
FOR
THE DEGREE OF DOCTOR OF PHILOSOPHY
IN
CIVIL ENGINEERING

JUNE 2017

Approval of the thesis:

**ADVANCED TWO- AND THREE-DIMENSIONAL TSUNAMI MODELS:
BENCHMARKING AND VALIDATION**

submitted by **DENİZ VELİOĞLU** in partial fulfillment of the requirements for the degree of **Doctor of Philosophy in Civil Engineering Department, Middle East Technical University** by,

Prof. Dr. Gülbin Dural Ünver
Dean, Graduate School of **Natural and Applied Sciences**

Prof. Dr. İsmail Özgür Yaman
Head of Department, **Civil Engineering**

Prof. Dr. Ahmet Cevdet Yalçiner
Supervisor, **Civil Engineering Dept., METU**

Examining Committee Members

Prof. Dr. Ayşe Burcu Altan Sakarya
Civil Engineering Dept., METU

Prof. Dr. Ahmet Cevdet Yalçiner
Civil Engineering Dept., METU

Prof. Dr. Yalçın Yüksel
Civil Engineering Dept., Yıldız Teknik University

Assoc. Prof. Dr. Utku Kanoğlu
Aerospace Engineering Dept., METU

Assoc. Prof. Dr. Yakup Darama
Civil Engineering Dept., Atılım University

Date: 15 June 2017

I hereby declare that all information in this document has been obtained and presented in accordance with academic rules and ethical conduct. I also declare that, as required by these rules and conduct, I have fully cited and referenced all material and results that are not original to this work.

Name, Last name : Deniz, Velioğlu

Signature :

ABSTRACT

ADVANCED TWO- AND THREE-DIMENSIONAL TSUNAMI MODELS: BENCHMARKING AND VALIDATION

VELİÖĞLU, Deniz

Ph. D., Department of Civil Engineering

Supervisor: Prof. Dr. Ahmet Cevdet Yalçiner

June 2017, 380 pages

Field observations provide valuable data regarding the nearshore tsunami impact, yet only in inundation areas where tsunami waves have already flooded. Therefore, tsunami modeling is essential in order to understand tsunami behavior and prepare for tsunami inundation. Analytical and numerical methods are widely applied to predict tsunami motion and inundation characteristics. On the other hand, the data obtained from field surveys and laboratory experiments are generally used for validation and performance assessment of numerical models. Nonlinear forms of two-dimensional depth-averaged shallow water equations are the most common tools that are used to estimate tsunami wave transformation and inundation. However, they may not suffice when three-dimensional flow characteristics, such as strong turbulent motion, develop in shallow water zones due to various nearshore conditions. In this respect, the performance of numerical codes that are capable of predicting tsunami motion in shallow water zones gains more importance. There are numerous numerical codes to be used for simulating tsunami motion and inundation. In this study, two numerical codes, NAMI DANCE and FLOW-3D[®], are selected for validation and performance comparison. NAMI DANCE solves nonlinear forms of two-dimensional depth-averaged shallow water (2D-NSW) equations in long wave problems, specifically tsunamis. FLOW-3D[®] simulates linear and nonlinear propagating surface waves as well as long waves by solving three-dimensional Reynolds-averaged Navier-Stokes (3D-RANS) equations. The codes are validated

and their performances are compared via analytical benchmarking, experimental benchmarking and field benchmarking. The results are assessed according to the accuracy and run time of the solutions. The variations between the numerical solutions of two- and three-dimensional models are evaluated through statistical error analysis. By referring to the validity range determined by these comparisons, recommendations pertinent to applying relevant models to various tsunami problems are made.

Keywords: Tsunami, inundation, solitary wave, long wave, shallow water, benchmarking, 2D-NSW, 3D-RANS, NAMI DANCE, FLOW-3D[®]

ÖZ

GELİŞMİŞ İKİ VE ÜÇ BOYUTLU TSUNAMİ MODELLERİ: KIYASLAMA VE DOĞRULAMA

VELİOĞLU, Deniz

Doktora, İnşaat Mühendisliği Bölümü

Tez Danışmanı: Prof. Dr. Ahmet Cevdet Yalçiner

Haziran 2017, 380 sayfa

Saha gözlemleri, tsunaminin yakın kıyıdaki etkisine dair değerli verilerin toplanmasına olanak sunmaktadır ancak bu bilgiler sadece daha önce tsunami su baskını yaşanan alanlarda elde edilebilmektedir. Bu nedenle tsunami davranışını anlamak ve tsunami su baskınına karşı önlem alabilmek için tsunami modellemesi yapmak gereklidir. Analitik ve sayısal metotlar, tsunami hareketi ve tsunami su baskın karakterlerini tahmin edebilmek için yaygın olarak uygulanmaktadır. Öte yandan, arazi çalışmaları ve laboratuvar deneylerinden elde edilen veriler genellikle sayısal modellerin doğrulanması ve performans değerlendirmesi için kullanılmaktadır. İki boyutlu derinliğe göre ortalaması alınmış sığ su denklemlerinin doğrusal olmayan formları, tsunami dalga dönüşümünü ve su baskını tahmin etmek için kullanılan en yaygın araçlardır. Ancak, bu araçlar güçlü türbülans hareketleri gibi üç boyutlu akım özelliklerinin olduğu sığ su bölgelerinde yeterli olmayabilir. Bu bakımdan sığ sulardaki tsunami hareketini tahmin edebilen sayısal modellerin performansı daha da önem kazanmaktadır. Tsunami hareketinin ve tsunami su baskınının benzetimi yapan bir çok sayısal model vardır. Bu çalışmada, doğrulama ve performans karşılaştırması için iki sayısal kod, NAMI DANCE ve FLOW-3D[®], seçilmiştir. NAMI DANCE, uzun dalga – özellikle tsunami – problemlerinin benzetiminde, iki boyutlu derinliğe göre ortalaması alınmış doğrusal olmayan sığ su (2D-NSW) denklemlerini kullanmaktadır. FLOW-3D[®] ise doğrusal ve doğrusal olmayan yüzey dalgaları ile uzun dalga ilerlemesini, üç boyutlu Reynolds ortalamalı

Navier-Stokes (3D-RANS) denklemlerini çözerek benzetimlemektedir. Kodlar analitik kıstas problemler, deneysel kıstas problemler ve alansal kıstas problemlere uygulanarak doğrulanmış ve performansları karşılaştırılmıştır. Sonuçlar, çözümlerin hassasiyeti ve benzetimlerin tamamlanma zamanına göre incelenmiştir. İki ve üç boyutlu modellerin sayısal çözümleri arasındaki farklılıklar istatistiksel hata analizi uygulanarak değerlendirilmiştir. Bütün bu karşılaştırmaların sonunda saptanan geçerlilik sınırları göz önüne alınarak, çeşitli tsunami problemlerine uygulanacak ilgili modeller hakkında önerilerde bulunulmuştur.

Anahtar Kelimeler: Tsunami, baskın, soliter dalga, uzun dalga, sığ su, kıyaslama, 2D-NSW, 3D-RANS, NAMI DANCE, FLOW-3D®

*“I dedicate this dissertation to
my precious family and my husband Erdinç.
You are all dear to me.”*

ACKNOWLEDGMENTS

I would like to express my gratitude to my thesis advisor *Professor Ahmet Cevdet Yalçiner*, who supervised this study with his invaluable guidance and encouragement. Without his support, this dissertation would never have materialised. I would also like to thank *Professor Ayşen Ergin* for her motivation, enthusiasm, and immense knowledge. She made great contributions to my coastal engineering education and her guidance helped me considerably throughout my study. I am also very grateful to *Dr. Işıkhhan Güler* for his endless support and joyful personality. I would like to express my gratitude to *Assistant Professor Gülizar Özyurt Tarakçıoğlu* and *Assistant Professor Cüneyt Baykal* for informing me of the proper research techniques to be adopted and leading me in the right direction while preparing this dissertation.

I especially would like to thank *Professor Ayşe Burcu Altan Sakarya* and *Associate Professor Utku Kanoğlu* of my thesis committee who gave me valuable guidance.

My thanks extend to the Faculty of Engineering, Department of Civil Engineering at the Middle East Technical University, of which I am proud to be a member of staff, for making the realisation of this dissertation possible.

I would also like to thank the faculty staff of Coastal Engineering and Water Resources Laboratories of the Middle East Technical University for their understanding and compassion towards me during this study.

The best outcome of these past several years of many academic and personal challenges is that I got to know *Erdoğan Söğüt*, my husband, who gave me lots of courage and love and patiently stood by me to help me persist in my efforts. Being a coastal engineer himself, he made undeniable contributions to this study and I am truly indebted to him.

Special thanks to *Gonca Ünal*, my precious friend and sister, for her moral support and enjoyable moments she has always given me. She was always there for me at the most difficult times, as she has been for the past 12 years. I am certainly grateful to *Rozita Kian*, my lovely companion, who guided me through this study with her invaluable advice. She still continues to walk by my side even from overseas. I really appreciate the assistance and support of my dearest friends *Mustafa Akçelik* and *Cihan Sadık Yürek* who took most of the burden of work off my shoulders.

I want to thank the technical support staff of Turkish branch of Flow Sciences, Inc. for their invaluable assistance. My special thanks extend to *Ömer Faruk Korkmaz*, who patiently answered all my questions about FLOW-3D®. I also appreciate *Ayhan Karadeniz*, *Arif Kayışlı* and *Yusuf Korkut* for their moral support and encouragement.

My deepest thought goes to my beloved ones; my mother *Zuhal Velioğlu* and my father *Mustafa Serdar Velioğlu*, who are also a part of the coastal engineering family in the Middle East Technical University, Ocean Engineering Research Center. I am very thankful to my aunt, *Aysun Velioğlu*, who greatly helped with the writing of this dissertation. My family shared with me all the joys and hardships of the experience of conducting this study with great love and patience.

Finally, I thank *Mustafa Kemal ATATÜRK*, who is a fearless soldier, a farsighted statesman and the father of all Turks. I will always follow his way and cherish his guidance: *Turkish Youth! Your first duty is to preserve and to defend Turkish Independence and the Turkish Republic forever.*

TABLE OF CONTENTS

ABSTRACT	v
ÖZ.....	vii
ACKNOWLEDGMENTS.....	x
TABLE OF CONTENTS	xii
LIST OF TABLES	xvi
LIST OF FIGURES.....	xviii
LIST OF SYMBOLS AND ABBREVIATIONS.....	xxx
CHAPTERS	
1. INTRODUCTION.....	1
1.1. General Description.....	1
1.2. Base of the Study.....	7
1.3. Objective of the Study	10
1.4. Contents of Chapters	11
2. LITERATURE REVIEW.....	13
2.1. Analytical and Experimental Approaches	14
2.2. Numerical Modeling.....	24
2.3. NAMI DANCE Applications	37
2.4. FLOW-3D® Applications	44
3. THEORETICAL FRAMEWORK OF THE NUMERICAL MODELS	49
3.1. NAMI DANCE.....	50
3.1.1. Model Background.....	50
3.1.2. Numerical Scheme	52
3.1.3. Solution Technique	61
3.1.4. Initial Conditions.....	64
3.1.5. Boundary Conditions.....	64
3.1.6. Stability	66
3.1.7. Methodology	67
3.2. FLOW-3D®	68

3.2.1.	Model Background.....	68
3.2.2.	Numerical Scheme	77
3.2.2.1.	Periodic Linear Waves.....	84
3.2.2.2.	Stokes' Wave	86
3.2.2.3.	Cnoidal Wave.....	89
3.2.2.4.	Random Wave.....	94
3.2.2.5.	Solitary Wave.....	96
3.2.3.	Solution Technique	98
3.2.4.	Initial Conditions.....	102
3.2.5.	Boundary Conditions	103
3.2.6.	Stability	109
3.2.7.	Methodology	110
4.	BENCHMARKING	113
4.1.	BMP 1: Solitary Wave Runup on a Simple Beach.....	119
4.1.1.	Problem Description.....	119
4.1.2.	NAMI DANCE Model.....	127
4.1.2.1.	Spatial Discretization	129
4.1.2.2.	Friction.....	131
4.1.3.	FLOW-3D [®] Model	133
4.1.3.1.	Spatial Discretization	134
4.1.3.2.	Friction.....	136
4.1.4.	Simulation Results	138
4.2.	BMP 2: Solitary Wave on a Conical Island	154
4.2.1.	Problem Description.....	154
4.2.2.	NAMI DANCE Model.....	167
4.2.2.1.	Spatial Discretization	170
4.2.2.2.	Friction.....	171
4.2.3.	FLOW-3D [®] Model	173
4.2.3.1.	Spatial Discretization	174
4.2.3.2.	Friction.....	175
4.2.4.	Simulation Results	177

4.3. BMP 3: Solitary Wave Propagation over a Complex Shelf	197
4.3.1. Problem Description.....	197
4.3.2. NAMI DANCE Model	204
4.3.2.1. Spatial Discretization	206
4.3.2.2. Friction	207
4.3.3. FLOW-3D® Model	209
4.3.3.1. Spatial Discretization	210
4.3.3.2. Friction	212
4.3.4. Simulation Results.....	214
4.4. BMP 4: Tsunami Runup onto a Complex 3D Beach: Monai Valley	227
4.4.1. Problem Description.....	227
4.4.2. NAMI DANCE Model	239
4.4.2.1. Spatial Discretization	241
4.4.2.2. Friction	242
4.4.3. FLOW-3D® Model	243
4.4.3.1. Spatial Discretization	245
4.4.3.2. Friction	246
4.4.4. Simulation Results.....	247
4.5. BMP 5: Tsunami Inundation in Constructed Environments	256
4.5.1. Problem Description.....	256
4.5.2. NAMI DANCE Model	268
4.5.2.1. Spatial Discretization	270
4.5.2.2. Friction	270
4.5.3. FLOW-3D® Model	274
4.5.3.1. Spatial Discretization	277
4.5.3.2. Friction	277
4.5.4. Simulation Results.....	281
4.6. BMP 6: 2011 Tōhoku Tsunami in Hilo Harbor, Hawaii	291
4.6.1. Problem Description.....	291
4.6.2. NAMI DANCE Model	299
4.6.2.1. Spatial Discretization	301

4.6.2.2. Friction	303
4.6.3. FLOW-3D [®] Model	305
4.6.3.1. Spatial Discretization	306
4.6.3.2. Friction	308
4.6.4. Simulation Results	310
5. SUMMARY AND CONCLUSIONS	321
REFERENCES.....	333
APPENDICES	361
A. GOVERNING EQUATIONS OF FLUID DYNAMICS	361
A.1. Derivation of Flow Equations	364
A.1.1 Equation of Continuity	364
A.1.2 Equations of Motion	366
A.2. Leibniz Integral Rule	371
CURRICULUM VITAE	373

LIST OF TABLES

TABLES

Table 3.1 Values of Manning's roughness coefficient, n , for certain types of sea bottom (Imamura et al., 2006).....	56
Table 3.2 Classification of waves with respect to d/λ	82
Table 4.1 Allowable error limits for model validation/verification according to OAR-PMEL-135 standard (Synolakis et al., 2007)	117
Table 4.2 NAMI DANCE: Maximum runup values for different Δx values ($n = 0.01$)	129
Table 4.3 FLOW-3D [®] : Maximum runup values for different Δx values ($n = 0.01$)	134
Table 4.4 The predicted maximum vertical and horizontal velocity components of a fluid particle <i>at the free surface</i> for the case where $H/d = 0.0185$	147
Table 4.5 The predicted maximum vertical and horizontal velocity components of a fluid particle <i>at the free surface</i> for the case where $H/d = 0.3$	147
Table 4.6 NRMSE and MAX errors for the case where $H/d = 0.0185$	149
Table 4.7 NRMSE and MAX errors for the case where $H/d = 0.3$	150
Table 4.8 NRMSE and MAX errors for the water level dynamics at two locations, $x/d = 0.25$ and $x/d = 9.95$, for the case where $H/d = 0.0185$	151
Table 4.9 BMP 2 wave gauge locations (Briggs et al., 1995).....	164
Table 4.10 NAMI DANCE: Predicted runup values at Gauge 9 for different Δx values ($n = 0.01$).....	170
Table 4.11 FLOW-3D [®] : Predicted runup values at Gauge 9 for different Δx values ($n = 0.01$).....	175
Table 4.12 The predicted maximum horizontal and vertical velocity components of a fluid particle <i>at the free surface</i> for Case A, where $H/d = 0.045$	188
Table 4.13 The predicted maximum horizontal and vertical velocity components of a fluid particle <i>at the free surface</i> for Case C, where $H/d = 0.181$	188
Table 4.14 NRMSE and MAX errors for Case A, where $H/d = 0.045$	191
Table 4.15 NRMSE and MAX errors for Case B, where $H/d = 0.091$	192

Table 4.16 NRMSE and MAX errors for Case C, where $H/d = 0.181$	193
Table 4.17 BMP 3 gauge locations (NTHMP, 2011).....	203
Table 4.18 NRMSE and MAX errors for the free surface profiles	221
Table 4.19 NRMSE and MAX errors for the velocity components.....	222
Table 4.20 Fault parameters of DRC-17a (Takahashi et al., 1995)	230
Table 4.21 Recorded runup for the six trials (Matsuyama and Tanaka, 2001).....	236
Table 4.22 NAMI DANCE: Predicted runup values on the pocket beach for different Δx values ($n = 0.012$).....	241
Table 4.23 NAMI DANCE: Predicted runup values on the pocket beach for different Manning's roughness coefficients.....	242
Table 4.24 FLOW-3D [®] : Predicted runup values on the pocket beach for different Δx values ($n = 0.012$)	245
Table 4.25 FLOW-3D [®] : Predicted runup values on the pocket beach for different Manning's roughness coefficients.....	246
Table 4.26 NRMSE and MAX errors for BMP 4	253
Table 4.27 The coordinates of the measurement locations for BMP 5 (Park et al., 2013).....	263
Table 4.28 The identifications and depths of current meters at observation stations (Arcos and LeVeque, 2014)	294
Table 4.29 NRMSE and MAX errors for BMP 6	315
Table 5.1 Mesh properties and process time for all BMPs	330

LIST OF FIGURES

FIGURES

Figure 1.1. Tsunami wave generation mechanisms: (a) earthquakes; (b) volcanic eruptions; (c) landslides; (d) meteorite strikes (Switzer, 2005)	2
Figure 1.2. (a) A devastated city, Banda Aceh, located on the island of Sumatra after the 2004 Indian Ocean tsunami (Credit: DigitalGlobe); (b) another view of Banda Aceh, the most devastated region in Indonesia, struck by the 2004 Indian Ocean tsunami (Credit: U.S. Navy); (c) a yacht washed ashore by the 2011 Great East Japan tsunami sits on top of a building in Otsuchi, Japan (Credit: Yomiuri Shimbun); (d) soil-liquefaction at Shinkiba after the 2011 Great East Japan tsunami (Credit: Morio); (e) tsunami wave hitting Miyako City located in Iwate Prefecture after the 2011 Great East Japan earthquake (Credit: REUTERS/Mainichi Shimbun); (f) Sendai Airport swept by the 2011 Great East Japan tsunami (Credit: REUTERS/Kyodo)	3
Figure 1.3. A descriptive scheme for the tsunami parameters	4
Figure 1.4. Kalutara Beach, Sri Lanka – 2004 Indian Ocean earthquake: (a) before tsunami, January 1, 2004; (b) drawback occurring few minutes before tsunami, December 26, 2004; (c) during tsunami, December 26, 2004 (Credit: Satellite Imaging Corporation)	6
Figure 3.1 Point schematics of staggered leapfrog scheme in (a) space and (b) time (Imamura et al., 2006)	63
Figure 3.2 Methodology of modeling via NAMI DANCE	67
Figure 3.3 The level set function (Maguire, 2011)	69
Figure 3.4 Details of the VOF technique: (a) surface in one-dimensional column of elements; (b) surface in two-dimensional grid of elements (Flow Science, 2002)	70
Figure 3.5 FLOW-3D [®] meshing techniques: (a) linked mesh; (b) conforming mesh, (c) nested mesh; (d) partially overlapping mesh (Flow Science, 2002) ..	73

Figure 3.6 Progressive wave types: (a) periodic linear waves; (b) Stokes' wave; (c) cnoidal wave; (d) solitary wave	81
Figure 3.7 Applicability ranges of various wave theories.....	82
Figure 3.8 Linear waves coming from a flat bottom reservoir into the computational domain (Flow Science, 2002).....	84
Figure 3.9 Stokes' waves coming from a flat bottom reservoir into the computational domain (Flow Science, 2002).....	86
Figure 3.10 Cnoidal waves coming from a flat bottom reservoir into the computational domain (Flow Science, 2002)	89
Figure 3.11 Solitary wave coming from a flat bottom reservoir into the computational domain (Flow Science, 2002).....	96
Figure 3.12 Location of variables in a mesh cell (Flow Science, 2002)	99
Figure 3.13 Methodology of modeling via FLOW-3D [®]	112
Figure 4.1 The procedure of testing a numerical model via benchmarking.....	118
Figure 4.2 Scientists gathered at Heriot-Watt University successfully recreated a solitary wave having smaller dimensions than the one observed by Russell (Hereman, 2013)	119
Figure 4.3 Russell's (1845) observation of the evolution of a solitary wave in a wave tank (reproduced from the original drawing) (Miles, 1980)	120
Figure 4.4 Dimensionless solitary wave profile indicating effective wavelength (not to scale)	122
Figure 4.5 A sketch of the canonical beach, i.e. sloping beach connected to a constant depth region (distorted scale) (Horrillo et al., 2015)	123
Figure 4.6 Wave tank used in the experiments (not to scale): (a) schematic side view; (b) schematic typical cross section; (c) a photograph before an experiment (Synolakis, 1986)	125
Figure 4.7 NAMI DANCE model: a typical computational domain and the orientation of the coordinate system (top view)	127
Figure 4.8 Solitary wave profiles of two experimental runs	127
Figure 4.9 NAMI DANCE computational domain constructed for the case where $H/d = 0.633$: (a) 2D top view; (b) 3D view	128

Figure 4.10 NAMI DANCE convergence test for the case where $H/d = 0.0185$ at: (a) $t^* = 60$ – the time of maximum runup; (b) $t^* = 70$ – the time of maximum rundown	130
Figure 4.11 NAMI DANCE model results for different Manning's roughness coefficients	132
Figure 4.12 FLOW-3D [®] computational domain constructed for the case where $H/d = 0.005$: (a) meshing; (b) boundary conditions; (c) after using FAVOR [™]	133
Figure 4.13 FLOW-3D [®] convergence test for the case where $H/d = 0.0185$ at: (a) $t^* = 60$ – the time of maximum runup; (b) $t^* = 70$ – the time of maximum rundown	135
Figure 4.14 FLOW-3D [®] model results for different Manning's roughness coefficients	137
Figure 4.15 Non-dimensional free surface profiles for the case where $H/d = 0.0185$: (a) $t^* = 30$; (b) $t^* = 40$; (c) $t^* = 50$; (d) $t^* = 60$; (e) $t^* = 70$	139
Figure 4.16 Non-dimensional free surface profiles for the case where $H/d = 0.3$: (a) $t^* = 15$; (b) $t^* = 20$; (c) $t^* = 25$; (d) $t^* = 30$	140
Figure 4.17 The water level dynamics at two locations: (a) $x/d = 0.25$; (b) $x/d =$ 9.95	142
Figure 4.18 Maximum runup values on 1:19.85 slope when $n = 0.01$	143
Figure 4.19 Maximum runup values on different slopes when $n = 0.01$	144
Figure 4.20 Evolution of vertical velocity component, w , for the case where $H/d =$ 0.3.....	145
Figure 4.21 Velocity time histories for: (a) $H/d = 0.0185$; (b) $H/d = 0.3$	146
Figure 4.22 Error bars for the case where $H/d = 0.0185$: (a) % NRMSE; (b) % MAX error	149
Figure 4.23 Error bars for the case where $H/d = 0.3$: (a) % NRMSE; (b) % MAX error	150
Figure 4.24 Tsunami attack site in Riangkroko (Credit: Harry Yeh) (Yeh et al., 1994)	154

Figure 4.25 (a) Map of the Indonesian region; (b) Map of Flores Island (Yeh et al., 1994)	155
Figure 4.26 Tsunami runup heights from sea level at the time of the tsunami attack. (Yeh et al., 1994)	156
Figure 4.27 (a) Babi Island; (b) catastrophe on the back side of Babi Island (Yeh et al., 1994)	157
Figure 4.28 Basin geometry, coordinate system and location of gauges (not to scale) (Credit: Frank Gonzalez) (Horrillo et al., 2015)	159
Figure 4.29 Definition sketch for the conical island (not to scale)	160
Figure 4.30 A view of the conical island and the directional spectral wave generator from the back side of the island (Briggs et al., 1995)	161
Figure 4.31 An overhead photograph of the wave runup on the lee side of the island	161
Figure 4.32 Schematic showing the gauge locations around the conical island (not to scale).....	163
Figure 4.33 The free surface elevation time series recorded at Gauge 2 for: (a) Case A; (b) Case B; (c) Case C (Briggs et al., 1995)	166
Figure 4.34 NAMI DANCE model: a typical computational domain and the orientation of the coordinate system (top view)	168
Figure 4.35 NAMI DANCE computational domain and gauge locations for BMP 2: (a) 3D top view; (b) side view	169
Figure 4.36 NAMI DANCE runup predictions according to different Manning's roughness coefficients for: (a) Case A; (b) Case B; (c) Case C.....	172
Figure 4.37 FLOW-3D [®] computational domain constructed for BMP 2: (a) meshing (enlarged for clarity); (b) boundary conditions and gauge locations; (c) after using FAVOR [™]	173
Figure 4.38 FLOW-3D [®] runup predictions according to different Manning's roughness coefficients for: (a) Case A; (b) Case B; (c) Case C.....	176
Figure 4.39 The wave transformation around the conical island for Case A, where $H/d = 0.045$ at: (a) Gauge 6; (b) Gauge 9; (c) Gauge 16; (d) Gauge 22	178

Figure 4.40 The wave transformation around the conical island for Case B, where $H/d = 0.091$ at: (a) Gauge 6; (b) Gauge 9; (c) Gauge 16; (d) Gauge 22	179
Figure 4.41 The wave transformation around the conical island for Case C, where $H/d = 0.181$ at: (a) Gauge 6; (b) Gauge 9; (c) Gauge 16; (d) Gauge 22	180
Figure 4.42 Inundation around the perimeter of the conical island for Case A, where $H/d = 0.045$	182
Figure 4.43 Inundation around the perimeter of the conical island for Case B, where $H/d = 0.091$	183
Figure 4.44 Inundation around the perimeter of the conical island for Case C, where $H/d = 0.181$	184
Figure 4.45 Evolution of vertical velocity component, w , around the conical island for Case C, where $H/d = 0.181$ at: (a) $t = 10.7$ sec; (b) $t = 13.0$ sec; (c) $t = 13.6$ sec; (d) $t = 14.5$ sec (not to scale).....	186
Figure 4.46 Velocity time histories for Case C at: (a) constant depth region; (b) Gauge 9; (c) Gauge 22	187
Figure 4.47 NAMI DANCE model: wave transformation around the conical island for Case C, where $H/d = 0.181$	189
Figure 4.48 Error bars for Case A, where $H/d = 0.045$: (a) % NRMSE; (b) % MAX error	191
Figure 4.49 Error bars for Case B, where $H/d = 0.091$: (a) % NRMSE; (b) % MAX error	192
Figure 4.50 Error bars for Case C, where $H/d = 0.181$: (a) % NRMSE; (b) % MAX error	193
Figure 4.51 BMP 1 discussed in the ISEC 2009 workshop: (a) schematic sketch of the experimental setup; (b) wave gauge and ADV locations; (c) a photograph of the complex shelf (NTHMP, 2011)	198
Figure 4.52 BMP 2 discussed in the ISEC 2009 workshop: (a) schematic sketch of the experimental setup; (b) wave gauge and ADV locations; (c) a photograph of the experimental setup (NTHMP, 2011).....	198

Figure 4.53 3D representation of the bathymetry of BMP 3 including the coordinate system (Velioglu et al., 2016)	201
Figure 4.54 Screenshots from the experiment at OSU, available at URL1 (Lynett, 2015)	202
Figure 4.55 Screenshots from the dye study at OSU, available at URL2 (Lynett, 2015)	202
Figure 4.56 The free surface elevation time series recorded at Gauge 1 (NTHMP, 2015).....	203
Figure 4.57 NAMI DANCE model: computational domain and the orientation of the coordinate system (top view)	205
Figure 4.58 3D top view of NAMI DANCE computational domain for BMP 3.....	205
Figure 4.59 NAMI DANCE convergence test at: (a) Gauge 2; (b) Gauge 3; (c) Gauge 7	206
Figure 4.60 NAMI DANCE results according to different Manning's roughness coefficients: (a) leading wave profile at Gauge 2; (b) leading wave profile at Gauge 3; (c) leading wave profile at Gauge 7; (d) horizontal velocity component at Gauge 2; (e) horizontal velocity component at Gauge 3	208
Figure 4.61 FLOW-3D [®] computational domain constructed for BMP 3: (a) meshing (enlarged for clarity); (b) boundary conditions and gauge locations; (c) after using FAVOR [™]	209
Figure 4.62 FLOW-3D [®] convergence test at: (a) Gauge 2; (b) Gauge 3; (c) Gauge 7	211
Figure 4.63 FLOW-3D [®] results according to different Manning's roughness coefficients: (a) leading wave profile at Gauge 2; (b) leading wave profile at Gauge 3; (c) leading wave profile at Gauge 7; (d) horizontal velocity component at Gauge 2; (e) horizontal velocity component at Gauge 3	213
Figure 4.64 The predicted and measured free surface profiles at: (a) Gauge 2; (b) Gauge 3; (c) Gauge 7; (d) Gauge 4; (e) Gauge 5; (f) Gauge 6; (g) Gauge 8; (h) Gauge 9	215

Figure 4.65 The predicted and measured velocity components at Gauge 2: $x, y, z =$ (13 m, 0 m, 0.75 m)	216
Figure 4.66 The predicted and measured velocity components at Gauge 3: $x, y, z =$ (21 m, 0 m, 0.77 m)	217
Figure 4.67 The predicted and measured velocity components at Gauge 10: $x, y, z =$ (21 m, -5 m, 0.77 m)	218
Figure 4.68 NAMI DANCE model simulations for BMP 3 (not to scale).....	220
Figure 4.69 FLOW-3D [®] model simulations for BMP 3 (not to scale)	220
Figure 4.70 Error bars for the free surface profiles: (a) % NRMSE; (b) % MAX error	221
Figure 4.71 Error bars for the velocity components: (a) % NRMSE; (b) % MAX error	222
Figure 4.72 1993 southwest-off Hokkaidō earthquake (Credit: Wikipedia).....	227
Figure 4.73 Bathymetry and topography of the region affected by the 1993 Hokkaidō Nansei- Oki tsunami. The red dot represents the earthquake epicenter (NTHMP, 2011)	228
Figure 4.74 The distribution of runup heights around Monai (Shuto, 1994)	229
Figure 4.75 (a) Waves overtopped roadway, west coast of Okushiri Island; (b) Monai after the tsunami with debris in the foreground, including a broken steel reinforced concrete utility pole. This small valley leading to the ocean experienced a spectacular runup of 31.7 m; (c) damage at Monai; (d) debris line at Monai (Credit: NOAA/NGDC, Commander Dennis J. Sigrist. International Tsunami Information Center)	229
Figure 4.76 CRIEPI wave flume: (a) photographs taken at site (Credit: Central Research Institute for Electric Power Industry); (b) schematic drawing (Matsuyama and Tanaka, 2001)	231
Figure 4.77 Google Earth image of the area around Monai (Matsuyama and Tanaka, 2001)	232
Figure 4.78 (a) the bathymetry of the whole model area and the detailed topography of the area where the maximum runup was observed; (b) the scaled offshore profile of the model (Matsuyama and Tanaka, 2001)	233

Figure 4.79 The partly-shown topographic profile of the 1:400 scale model around Monai (Matsuyama and Tanaka, 2001).....	234
Figure 4.80 General view of the model: (a) before tsunami; (b) just before the wave reaches the highest point. The partly-shown topographic profile of the 1:400 scale model around Monai: (c) before runup; (d) during the flooding of the pocket beach; (e) during the flooding of the south valley; (f) during the highest runup; (g) a closer snapshot of the highest runup (Matsuyama and Tanaka, 2001)	235
Figure 4.81 Recorded runup for the six trials (Matsuyama and Tanaka, 2001).....	236
Figure 4.82 The computational domain: (a) top view (Synolakis et al., 2008); (b) 3D view (ISEC, 2004)	237
Figure 4.83 Incident wave profile of BMP 4	238
Figure 4.84 NAMI DANCE model: computational domain and the coordinate system	240
Figure 4.85 3D top view of NAMI DANCE computational domain for BMP 4.....	240
Figure 4.86 FLOW-3D [®] computational domain constructed for BMP 4: (a) meshing (enlarged for clarity); (b) boundary conditions and gauge locations; (c) after using FAVOR [™]	244
Figure 4.87 The predicted and measured free surface profiles at: (a) Gauge 5; (b) Gauge 7; (c) Gauge 9	248
Figure 4.88 (a) Frames 10, 25, 40, 55, and 70 from the overhead movie of the laboratory experiment (Liu et al., 2008; NTHMP, 2011); (b) snapshots of the NAMI DANCE simulation at the time intervals corresponding to the movie frames; (c) snapshots of the FLOW-3D [®] simulation at the time intervals corresponding to the movie frames	250
Figure 4.89 Runup and inundation comparisons: (a) runup; (b) inundation	251
Figure 4.90 Evolution of vertical velocity component, w , at: (a) $t = 15.5$ sec; (b) $t = 16.5$ sec; (c) $t = 17.0$ sec (not to scale)	252
Figure 4.91 Error bars for BMP 4: (a) % NRMSE; (b) % MAX error	253
Figure 4.92 Seaside, Oregon: 1:50 physical model region, macro-roughness region and tsunami inundation line (Park et al., 2013)	259

Figure 4.93 Photograph of 1:50 scale model of the town of Seaside, Oregon constructed in the Tsunami Wave Basin at OSU (Cox et al., 2008; Rueben et al., 2011)	260
Figure 4.94 Plan and elevation view of the physical model in the Tsunami Wave Basin (Park et al., 2013)	260
Figure 4.95 Detailed plan view of macro-roughness elements of the physical model, annotated with measurement locations (Park et al., 2013)	262
Figure 4.96 (a) Rectified, merged, and cropped image from the Argus cameras; (b) difference image taken at $t = 24.06$ sec during wave breaking; (c) difference image taken at $t = 27.26$ sec during inundation (Rueben et al., 2011)	264
Figure 4.97 (a) Image taken at $t = 26.3$ sec during inundation; (b) image taken at $t = 28.7$ sec during inundation (Rueben et al., 2011)	265
Figure 4.98 Computational domain for BMP 5 (NTHMP, 2015)	266
Figure 4.99 (a) Wavemaker displacement time series – real data, which can be used to drive a moving wall boundary condition; (b) incident-only wave time series at $x = 5$ m – simulated data, which can be used to drive a stationary input wave boundary condition at $x = 5$ m (NTHMP, 2015)	267
Figure 4.100 NAMI DANCE model: computational domain and the coordinate system	268
Figure 4.101 3D top view of NAMI DANCE computational domain for BMP 5 ...	268
Figure 4.102 Comparison of computed and recorded free surface elevation at the control point, WG3	269
Figure 4.103 Comparison of predicted and measured overland flow depth for locations B1, B4, B6 and B9, respectively	271
Figure 4.104 Comparison of predicted and measured cross-shore velocity for locations B1, B4, B6 and B9, respectively	272
Figure 4.105 Comparison of predicted and measured cross-shore momentum flux for locations B1, B4, B6 and B9, respectively	273

Figure 4.106 FLOW-3D [®] computational domain constructed for BMP 5: (a) meshing (enlarged for clarity); (b) boundary conditions and gauge locations; (c) after using FAVOR [™]	275
Figure 4.107 Comparison of computed and recorded free surface elevation at the control point, WG3	276
Figure 4.108 Comparison of predicted and measured overland flow depth for locations B1, B4, B6 and B9, respectively	278
Figure 4.109 Comparison of predicted and measured cross-shore velocity for locations B1, B4, B6 and B9, respectively	279
Figure 4.110 Comparison of predicted and measured cross-shore momentum flux for locations B1, B4, B6 and B9, respectively	280
Figure 4.111 Comparison of predicted and measured overland flow depth for locations B1, B4, B6 and B9, respectively	283
Figure 4.112 Comparison of predicted and measured cross-shore velocity for locations B1, B4, B6 and B9, respectively	284
Figure 4.113 Comparison of predicted and measured cross-shore momentum flux for locations B1, B4, B6 and B9, respectively	285
Figure 4.114 NRMSE of (a) NAMI DANCE; (b) FLOW-3D [®] predictions along lines A, B, C, and D	287
Figure 4.115 Snapshots of (a) NAMI DANCE; (b) FLOW-3D [®] simulations at time $t = 30$ sec	288
Figure 4.116 (a) The epicenter of 2011 Tōhoku earthquake; (b) contours of maximum wave amplitudes, detailing tsunami energy propagation (Credit: NOAA); (c) the maximum tsunami heights observed after 2011 Tōhoku earthquake (Credit: Wikipedia)	292
Figure 4.117 Location of current velocity meter stations deployed around Hawaii, including the two stations at Hilo Harbor, which are used in BMP 6 (Cheung et al., 2013; Arcos and LeVeque, 2014)	293
Figure 4.118 Hilo Bay and the town of Hilo in 1929, the year when the breakwater was completed (Credit: Wikipedia)	295
Figure 4.119 Google Earth images of Hawaiian Islands and Hilo Harbor	296

Figure 4.120 The bathymetry of Hilo Harbor	297
Figure 4.121 The incident wave of BMP 6: time series of ocean surface elevation at Control Point (NTHMP, 2015)	298
Figure 4.122 NAMI DANCE computational domain for BMP 6	300
Figure 4.123 3D top view of NAMI DANCE computational domain for BMP 6 ..	300
Figure 4.124 NAMI DANCE convergence test for BMP 6 at: (a) Hilo tide station; (b) HA1125; (c) HA1126	302
Figure 4.125 NAMI DANCE results according to different Manning's roughness coefficients at: (a) Hilo tide station; (b) HA1125; (c) HA1126	304
Figure 4.126 FLOW-3D [®] computational domain constructed for BMP 6: (a) meshing (enlarged for clarity); (b) boundary conditions and gauge locations; (c) after using FAVOR [™]	305
Figure 4.127 FLOW-3D [®] convergence test for BMP 6 at: (a) Hilo tide station; (b) HA1125; (c) HA1126	307
Figure 4.128 FLOW-3D [®] results according to different Manning's roughness coefficients at: (a) Hilo tide station; (b) HA1125; (c) HA1126	309
Figure 4.129 Comparison of the free surface elevation time series at Hilo tide station	311
Figure 4.130 Comparison of velocity components in E – W and N – S directions at HA1125, located at the entrance of the Hilo Harbour and at HA1126, located inside the Hilo Harbour	312
Figure 4.131 The distribution of the computed maximum current speed during the entire duration of the NAMI DANCE simulation	313
Figure 4.132 The distribution of the computed maximum current speed during the entire duration of the FLOW-3D [®] simulation	314
Figure 4.133 Error bars for BMP 6: (a) % NRMSE; (b) % MAX error	315
Figure A.1 Approaches for the continuum fluid: (a) fluid passing through a finite control volume fixed in space; (b) finite control volume moving with the fluid; (c) fluid passing through an infinitesimal cubical element fixed in space; (d) an infinitesimal cubical element moving with the fluid (Anderson, 2009)	362

Figure A.2 Fluid passing through an infinitesimal cubical element	364
Figure A.3 Stress components acting on the surface of the fluid element: <i>(a)</i> shear stress; <i>(b)</i> normal stress on xy plane	367
Figure A.4 Surface forces in x direction exerted on the fluid element	368

LIST OF SYMBOLS AND ABBREVIATIONS

A	Cross-sectional area of flow
A_x, A_y, A_z	Fractional areas in x, y, z directions, respectively
\acute{A}	Eddy viscosity
\mathcal{A}	Coefficient used in the higher-order finite difference method
a	Wave amplitude
a	Acceleration (change in velocity with time)
b	Flow loss across porous media
c	Wave celerity (speed)
c_0	Wave speed in still water
c	Local phase speed of the wavelike flow
C	Non-dimensional phase speed
C	Courant number
C	A constant used in the derivation of cnoidal wave equations
D	Total water depth
D	Total derivative
\mathcal{D}	Dissipation
D_h	Hydraulic diameter
d	Undisturbed flow depth
E	Wave energy spectrum
f	Friction coefficient

f	Viscous acceleration
$f(x_i)$	Observed data
F	Fluid fraction
F	Fetch length
\mathcal{F}	Volume-of-Fluid function
F_x	Net force in x direction
g	Gravitational acceleration
\vec{g}	Body force due to gravitational acceleration
G	Body acceleration
\hbar	Local solitary wave height
h	Elevation of the ground
H	Wave height
I	Internal energy
i	Increment in x direction
in	Number of grids in x direction
j	Increment in y direction
jn	Number of grids in y direction
k	Angular wave number
k	Increment in time
\acute{k}	Turbulent kinetic energy
k_s	Nikuradse equivalent surface roughness
L	Effective wavelength of a solitary wave

L^*	Non-dimensional effective wavelength of a solitary wave
m	Mass
M	Discharge flux in horizontal plane along x coordinate
\mathcal{M}	Parameter in McCowan's (1891) expansion
N	Discharge flux in horizontal plane along y coordinate
N	Finite integer
\mathcal{N}	Parameter in McCowan's (1891) expansion
n	Number of data points
n	Manning's roughness coefficient
\vec{n}	Outward vector normal to the surface
O	Truncation error
P	Pressure
\bar{P}	Wetted perimeter
q	Turbulence quantity for energy
q	Value of some quantity
Q	Volume flow rate
\mathcal{Q}	A dependent physical quantity
R	Earth's radius
R	Wave runup
R_h	Hydraulic radius
R_{DIF}	Turbulent diffusion term
R_{SOR}	Mass source term

\mathcal{R}	Coefficient depending on the coordinate system
r	Radial direction in the cylindrical coordinate system
r_m	Fixed reference radius
S	Control surface
S_c	Schmidt number
T	Wave period
t	Time
t^*	Non-dimensional time
U	Uniform current in the direction of wave propagation
U	Water particle velocity in X direction
\bar{U}	Uniform current in X direction
U_r	Ursell number
U_{10}	Wind speed 10 m above sea level
u	Water particle velocity in x direction
u^*	Non-dimensional water particle velocity in x direction
u_b	Horizontal velocity component in x direction at $z = -d$
u_s, v_s, w_s	Fluid velocity relative to the source in x, y, z directions, respectively
u_w, v_w, w_w	Velocity of the source component in x, y, z directions, respectively
V	Control volume
V_F	Fractional volume
\vec{V}	Velocity vector
v	Water particle velocity in y direction

w	Angular wave frequency
w	Water particle velocity in z direction
w^*	Non-dimensional water particle velocity in z direction
w_p	Angular frequency at the spectrum peak
W	Water particle velocity in Z direction
x	Horizontal x axis in the Cartesian coordinate system
x	Dimensionless horizontal coordinate
X_0	Dimensionless x location where the toe of beach slope is defined
X_1	Dimensionless x location where height of solitary wave is defined
X	x axis in a moving reference system that travels with wave speed
X	The distance travelled by a solitary wave
y	Horizontal y axis in the Cartesian coordinate system
y_i	Predicted data
z	Vertical z axis in the Cartesian coordinate system
Z	z axis in a moving reference system that travels with wave speed
dV	Differential volume
M_w	Moment magnitude scale
$\Delta x, \Delta y, \Delta z$	Grid sizes in x, y, z directions, respectively
Δt	Time step
Δw	Angular wave frequency interval
ΔV	Volume of a fluid element
τ	Shear stress

∂	Partial derivative
\emptyset	Function with two variables, space x and time t
α	Beach slope
ε	Wave height over undisturbed water depth ratio
ε	Turbulence dissipation rate
ϵ	Wave steepness
ϕ	Phase shift angle
ϕ	Latitude (corresponds to y axis in the Cartesian coordinate system)
λ	Longitude (corresponds to x axis in the Cartesian coordinate system)
λ	Wavelength
ω	Angular speed of Earth's rotation
μ	Dynamic viscosity
ϑ_ρ	Mass diffusivity coefficient
γ	Dimensionless wave frequency
γ	Peak enhancement factor – JONSWAP spectrum
Θ	Factor depending on angular wave frequency – JONSWAP spectrum
η	Free surface elevation
η^*	Non-dimensional free surface profile
ρ	Fluid density
σ	Dimensionless wave number
δ	Scaling parameter for wave energy spectrums
θ	Azimuthal coordinate

φ	Velocity potential
ψ	Dispersion coefficient
Ψ	Stream function
ξ	Coordinate conversion coefficient
1D, 2D, 3D	One-dimensional, Two-dimensional, Three-dimensional
ADCP	Acoustic Doppler Current Profiler
ADV	Acoustic-Doppler Velocimeters
AF	Area Fraction
AIAA	American Institute of Aeronautics and Astronautics
AWI	Alfred Wegener Institute
BEM	Boundary Element Method
BIEM	Boundary Integral Equation Method
BMP	Benchmark Problem
CAD	Computer-Aided Design
CFD	Computational Fluid Dynamics
CFL	Courant-Friedrichs-Lewy
CPU	Central Processing Units
CRIEPI	Central Research Institute for Electric Power Industry
DART	Deep-ocean Assessment and Reporting of Tsunamis
DCRC	Disaster Control Research Center
DHI	Danish Hydrological Institute
DoF	Degrees of Freedom
DSWG	Directional Spectral Wave Generator

E, N, S, W	East, North, South, West
EDFT	Early Detection and Forecast of Tsunami
ENO	Essentially Non-Oscillatory
ERCOTAC	European Research Community on Flow, Turbulence and Combustion
FAVOR TM	Fractional Area/Volume Obstacle Representation
FDM	Finite Difference Method
FEMA	Federal Emergency Management Agency
FVM	Finite Volume Method
GEBCO	General Bathymetric Chart of the Oceans
GIS	Geographic Information System
GITEWS	German–Indonesian Tsunami Early Warning System
GMO	General Moving Object
GMT	Greenwich Mean Time
GO	Grid Overlay
GUI	Graphical User Interface
HP	Horse Power
HWRL	Hinsdale Wave Research Laboratory
ISEC	Inundation Science & Engineering Cooperative
JCR	European Commission Joint Research Center
JMA	Japan Meteorological Agency
KdV	Korteweg deVries
KOERI	Kandilli Observatory and Earthquake Research Institute
LBM	Lattice Boltzmann Method

LDN	Leading-depression
LEN	Leading-elevation
LIDAR	Light Detection and Ranging
MAC	Marker-and-Cell Method
MAX	Maximum
MCDA	Multi-Criteria Decision Analysis
METU	Middle East Technical University
NEES	Network for Earthquake Engineering Simulation
NGDC	National Geophysical Data Center
NOAA	National Oceanic and Atmospheric Administration
NSF	National Science Foundation
NSW	Nonlinear shallow water
NTHMP	National Tsunami Hazard Mitigation Program
OAR-PMEL	Oceanic and Atmospheric Research-Pacific Marine Environmental Lab.
OSU	Oregon State University
PDE	Partial-Differential Equations
P-M	Pierson-Moskowitz
RANS	Reynolds-averaged Navier-Stokes
SL-VOF	Segment Lagrangian Volume-of-Fluid
SPH	Smoothed Particle Hydrodynamics
SRTM	Shuttle Radar Topography Mission
STL	STereoLithography
SWL	Still Water Level

TIME	Tsunami Inundation Modeling Exchange
TruVOF [®]	Improved Volume-of-Fluid
UCLA	University of California – Los Angeles
UNESCO	United Nations Educational, Scientific and Cultural Organization
U.S.	United States
USACE	United States Army Corps of Engineers
USAID	United States Agency for International Development
USGS	United States Geological Survey
UTM	Universal Transverse Mercator coordinate system
usWG	Ultra-Sonic Wave Gauge
VF	Volume Fraction
VOF	Volume-of-Fluid
WEC	Wave Energy Converter
WENO	Weighted Essentially Non-Oscillatory
WES	U.S. Army Engineer Waterways Experiment Station
WG	Wave Gauge

CHAPTER 1

INTRODUCTION

“The fishermen know that the sea is dangerous and the storm terrible, but they have never found these dangers sufficient reason for remaining ashore.”

Vincent Van Gogh

1.1. General Description

Coastal regions have always been attractive settling grounds for human populations since they have provided a great deal of marine resources and opportunities for transportation and trade. This has led to high population densities and high levels of development in many coastal regions. Today, a large part of the world's population inhabits coastal areas and the population density on these regions is still growing rapidly. However, coastal environments are dynamic natural systems and they pose a great challenge to human habitation since they are prone to water related hazards such as floods, storms and tsunamis, tsunamis being one of the most devastating hazards related to these dynamics.

The term *tsunami* originates from Japanese and it stands for *harbor wave*. Tsunamis were referred to as harbor waves before the Great Sanriku earthquake, which occurred in Japan in 1896. Nearly 27,000 people were killed and over 10,000 buildings were destroyed after the tsunami triggered by the earthquake. It was then that the term *tsunami* came into use in other languages with its new definition as *seismic sea waves*.

A tsunami is an extremely long wave or a series of waves that are generated by the displacement of a substantial volume of water or perturbation of the sea. There are a number of factors that lead to the generation of large displacements in a body of

water, namely disturbances which are known to be primarily triggered by earthquakes that occur below or near the ocean floor, landslides, volcanic eruptions, atmospheric pressure changes, underwater explosions, glacier calvings or more rarely meteorite strikes and nuclear tests. Figure 1.1 shows several generation mechanisms of a tsunami. Any large body of water can lead to the occurrence of a tsunami. Even in inland lakes, a tsunami may take place due to landslides or glacier calving. Very small tsunamis occur frequently as a result of minor earthquakes and other events. These are not considered to be destructive and they can not be detected without specialized equipment.

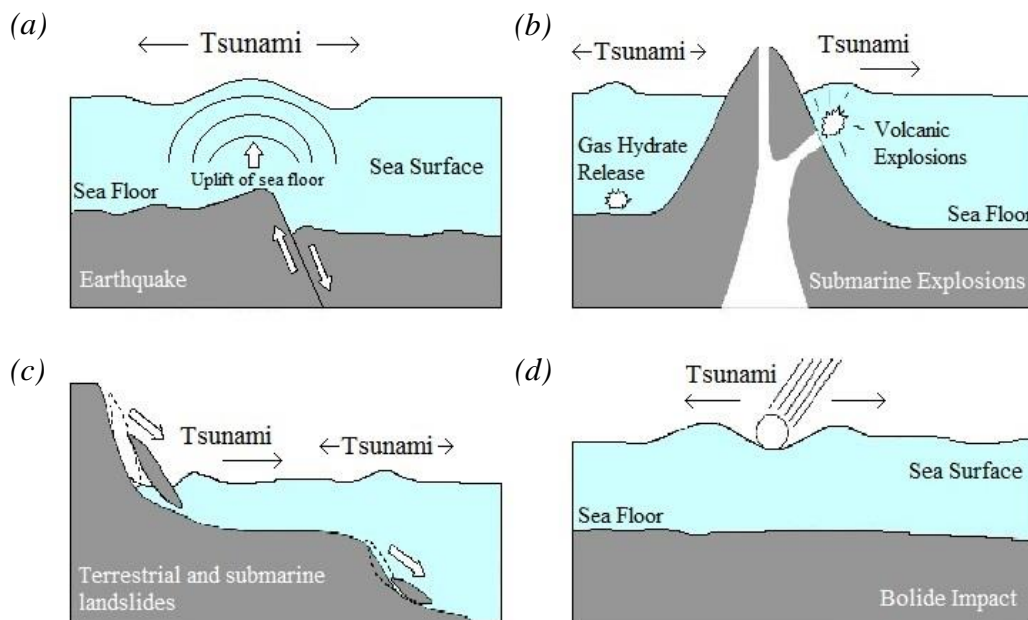


Figure 1.1. Tsunami wave generation mechanisms: (a) earthquakes; (b) volcanic eruptions; (c) landslides; (d) meteorite strikes (Switzer, 2005)

Since 1850s, 440,000 lives have been lost and the damage to coastal structures and habitats amounts to billions of dollars as a consequence of tsunamis. The most recent and destructive tsunamis occurred as a result of 2004 Indian Ocean earthquake and 2011 Great East Japan earthquake. The devastating impact was created by the occurrence of strong tsunami-induced currents and massive flow depths in inundation zones. Figure 1.2 portrays the effects of 2004 Indian Ocean Tsunami on Sumatra Island and the effects of 2011 Great East Japan Tsunami along the east coasts of Japan.



Figure 1.2. (a) A devastated city, Banda Aceh, located on the island of Sumatra after the 2004 Indian Ocean tsunami (Credit: DigitalGlobe); (b) another view of Banda Aceh, the most devastated region in Indonesia, struck by the 2004 Indian Ocean tsunami (Credit: U.S. Navy); (c) a yacht washed ashore by the 2011 Great East Japan tsunami sits on top of a building in Otsuchi, Japan (Credit: Yomiuri Shimbun); (d) soil-liquefaction at Shinkiba after the 2011 Great East Japan tsunami (Credit: Morio); (e) tsunami wave hitting Miyako City located in Iwate Prefecture after the 2011 Great East Japan earthquake (Credit: REUTERS/Mainichi Shimbun); (f) Sendai Airport swept by the 2011 Great East Japan tsunami (Credit: REUTERS/Kyodo)

Tsunami waves have small wave heights and long wavelengths – up to hundreds of kilometers long – offshore. As the waves move towards nearshore, they undergo changes depending on the nearshore bathymetry; their celerity is reduced considerably and they become significantly higher. When they reach the shoreline, the waves generated climb up the shore and travel relatively large distances inland. Thus, it is inevitable that tsunamis are a source of extensive damage to coastal and marine structures, as well as causing loss of many lives and creating a substantial financial burden. The damage caused by tsunamis even leads to the destruction of whole settlements because they can drag huge objects and carry them into buildings, scour the foundations of buildings, collapse the shoreline due to liquefaction and overflow tsunami defense structures (Borrero et al., 2003).

With the exception of the largest tsunamis, the approaching wave gets onshore as a rapidly rising turbulent surge of water carrying debris, without breaking. Tsunami wave height, runup height and inundation distance are the hydrodynamic parameters that are effective in the determination of the damage level inland (Figure 1.3). *Tsunami wave height* is the maximum height of the wave above the mean sea level. *Runup* is a measurement of the maximum vertical height onshore above the sea level that is reached by a tsunami. *Inundation distance* is a horizontal measurement of the path of the tsunami and is the maximum distance from the shoreline at the time of a tsunami.

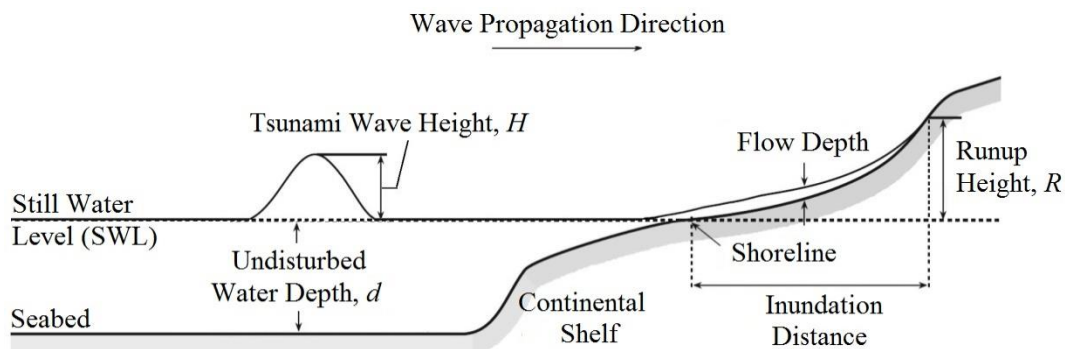


Figure 1.3. A descriptive scheme for the tsunami parameters

All waves have a positive and negative peak, called the *ridge* and the *trough*, respectively. During a tsunami, if the ridge is the first part to arrive, there will be a massive breaking wave or sudden flooding on land. However, if the first part to arrive is the trough, the shoreline will recede dramatically and expose areas that are normally submerged (Figure 1.4). In other words, a drawback will occur, giving a brief warning of the approaching tsunami.

The frequency of occurrence of tsunamis varies greatly from region to region. The highest frequency of tsunamis is observed in the Pacific Ocean with the rate of 25.4% due to the seismic and volcanic activity taking place along the Pacific Ring of Fire. Next is the East Indian Ocean with 20.3%. The frequency of tsunami events on the coasts of Japan-Russia is 18.6%, it is 13.8% in the Caribbean, 10.1% in the Mediterranean, 8.9% in the Pacific East Coast, 1.6% in the Atlantic East coast, 0.8% in the Bay of Bengal and 0.4% in the Atlantic West Coast (Bryant, 2008).



Figure 1.4. Kalutara Beach, Sri Lanka – 2004 Indian Ocean earthquake: (a) before tsunami, January 1, 2004; (b) drawback occurring few minutes before tsunami, December 26, 2004; (c) during tsunami, December 26, 2004 (Credit: Satellite Imaging Corporation)

1.2. Base of the Study

Tsunami generation and the parameters that may play a role in its properties need to be researched more carefully and quantitatively so that the devastating impact of tsunamis on coastal areas can be fully understood. To achieve this, the collaborative work of different scientific and engineering disciplines is required, whereby existing earthquake and tsunami data can be enhanced and exchanged, topographic and bathymetric data developed in sufficient resolution, potential or credible tsunami scenarios selected, and available computational tools utilized (Pamuk, 2014).

The mechanisms which are involved in tsunami evolution and propagation are generally understood. The shallow water theory is regarded as a key instrument in analytical modeling of evolution and propagation of long waves such as tsunamis (Aydin and Kanoglu, 2012). However, the effective prediction of the tsunami motion at coastlines still represents a formidable challenge due to the complexities of coastline formations and the presence of numerous coastal structures that interact and alter the flow. Theoretical approaches taken towards the nearshore tsunami motion are difficult to apply due to strong nonlinearities of equations that govern tsunami behaviors, the three-dimensionality of the flow, and the turbulence that develops due to shoaling effects. Thus, the theoretical analysis of nearshore hydrodynamics presents considerable difficulties.

The main part of tsunami research comprises physical models and laboratory experiments since they have the qualities of observability, measurability, repeatability, input control, process control, reasonable cost and robustness. In fact, physical modeling of long waves in laboratories is still a valuable and trustworthy option to study long wave propagation and runup, nearshore dynamics and complex nonlinear interactions of approaching wave and macro-roughness elements on the shore (Goseberg et al., 2013).

On the other hand, with the rapid development of computing technology, a large number of models that can be employed in coastal hydrodynamic problems have become available. The numerical techniques can be based on the finite element method, finite difference method, boundary element method, finite volume method or Eulerian-Lagrangian method. The time stepping algorithm can be implicit, semi-implicit, explicit or characteristic-based. The shape function can be of the first order, second order or a higher order. The modeling can be simplified into different spatial dimensions; a one-dimensional model, a two-dimensional depth-averaged model, a two-dimensional lateral-integrated model, a two-dimensional layered model or a three-dimensional model (Chau, 2010). Open boundary conditions, model parameters and numerical scheme determine the accuracy of the prediction.

Numerical modeling has proved to be an accurate and useful method of modeling tsunami inundations on a coastline. However, it is necessary that all numerical models used in tsunami emergency planning be validated and verified. Validation/verification of a numerical code must never cease; even proven models must be tested continuously as new knowledge and data are acquired (Synolakis et al., 2008). Careful and explicit validation/verification of tsunami models through the comparison of their predictions with benchmark analytical solutions, laboratory experiments and field measurements has helped them evolve in the last two decades. A numerical code that has performed well in all benchmark tests will not necessarily make realistic inundation predictions in every instance. However, in the results of validated/verified codes, the level of uncertainty is largely reduced to the uncertainty in the geophysical initial conditions. Furthermore, when validated/verified codes and real-time free-field tsunami measurements from tsunameters are employed together, they are the only option to be able to realistically forecast tsunami inundation (Synolakis et al., 2008).

According to the theory of long waves, the pressure distribution is not affected by the vertical motion of water particles. The equations of mass conservation and momentum are reduced to two-dimensional depth-averaged equations on the basis of

this approximation and by neglecting vertical acceleration. Until recently, two-dimensional depth-averaged numerical models solving linear/nonlinear shallow water or Boussinesq equations were employed to predict wave transformation over complex bathymetries and interaction with coastal structures, while the use of three-dimensional Navier-Stokes models was restricted to research studies (Watanabe et al., 2005; Christensen, 2006). Although two-dimensional depth-averaged models have been developed enough to be fast, relatively accurate and reliable, they have limited accuracy in the prediction of wave breaking, runup and wave loading because they use simplified assumptions to describe the variation of flow along depth in the surf and swash zone. Therefore, nearshore tsunami behavior can not be predicted accurately by means of depth-averaged techniques, including Boussinesq models (Lynett et al., 2002). With the progress of computer technology, the computational cost associated with performing and post-processing three-dimensional simulations has become affordable for engineering related problems. Moreover, recent advances in computational fluid dynamics (CFD) have made it possible to use CFD techniques for the investigation of nearshore tsunami motion. The development of open source computational fluid dynamics software with advanced meshing and computational capabilities has also promoted the use of fully three-dimensional CFD models for engineering applications (Dimakopoulos et al., 2014).

1.3. Objective of the Study

This study aims to investigate the sufficiency of nonlinear forms of two-dimensional depth-averaged shallow water equations in tsunami wave evolution, propagation, amplification and inundation. Moreover, the variations between the numerical solutions of two- and three-dimensional models are determined. The study focuses on two numerical tools; NAMI DANCE and FLOW-3D[®]. NAMI DANCE solves nonlinear forms of two-dimensional depth-averaged shallow water (2D-NSW) equations in long wave problems, specifically tsunamis. FLOW-3D[®] simulates linear and nonlinear propagating surface waves as well as long waves by solving three-dimensional Reynolds-averaged Navier-Stokes (3D-RANS) equations. The codes are applied to analytical, experimental and field benchmark problems for validation and performance comparison.

The benchmark problems are selected with great care. Each problem is capable of identifying the shortcomings of numerical models in terms of tsunami motion and inundation parameters such as water surface elevation, current velocity and runup. A total of six benchmark problems are considered in this study.

The first benchmark problem (BMP 1) covers both analytical and experimental investigations. The problem analyzes the evolution, propagation and runup of a single solitary wave climbing up a plane beach having a slope of 1:19.85. BMP 1 has been widely used for validation of many numerical codes.

After the 1992 Flores tsunami, an unexpectedly large tsunami runup height was observed in the lee side of conical Babi Island. Benchmark problem 2 (BMP 2) is composed of physical model studies which were carried out in the coastal hydraulic laboratory of Engineering Research and Development Center, U.S. Army Corps of Engineers so that a better understanding of the physical phenomena could be provided.

Benchmark problem 3 (BMP 3) describes a series of experiments that analyze the transformation of a single solitary wave as it propagates up a triangular shaped shelf with an island feature located at the offshore point of the shelf. The currents that are formed in the vicinity of the island are also investigated in the experiments. This problem is Benchmark Problem 5 of the 2015 National Tsunami Hazard Mitigation Program (NTHMP) workshop, which was held in Portland, U.S.

An extreme runup height of 31.7 m was measured near the village of Monai, in Okushiri Island after the 1993 Okushiri tsunami. Benchmark problem 4 (BMP 4) provides the data of a 1:400 scale laboratory experiment of the Monai runup, conducted at Central Research Institute for Electric Power Industry (CRIEPI) in Abiko, Japan.

Benchmark problem 5 (BMP 5) covers a series of experiments having a single long period wave that propagates up a piecewise linear slope and onto a small-scale model of the town of Seaside, Oregon. This problem is Benchmark Problem 4 of the 2015 National Tsunami Hazard Mitigation Program (NTHMP) workshop held in Portland, U.S.

The last benchmark problem, Benchmark problem 6 (BMP 6), is a field data set of the Japan 2011 tsunami recorded in Hilo Harbor, Hawaii. This problem is Benchmark Problem 2 of the 2015 National Tsunami Hazard Mitigation Program (NTHMP) workshop, which was held in Portland, U.S.

1.4. Contents of Chapters

Chapter 2 covers a review of the literature pertinent to this study. It gives the details of different approaches to the calculation of the parameters related to tsunami motion and inundation. It also gives information about previous numerical applications that use two- or three-dimensional tsunami models.

In Chapter 3, the numerical backgrounds of the codes solving two-dimensional depth-averaged shallow water equations (NAMI DANCE) and three-dimensional Reynolds-averaged Navier-Stokes equations (FLOW-3D[®]) are explained in detail.

In Chapter 4, all the benchmark problems discussed in this study and the results of the two- and three-dimensional numerical simulations based on them are explained in detail. The codes are validated and the numerical results are compared through the application of these benchmark problems. The statistical evaluations of the results are also given in this chapter for each benchmark problem.

Chapter 5 provides a summary and general evaluation and discussion of the results. Moreover, suggestions for further studies are given in the light of the conclusions and discussions.

To summarize, this dissertation questions the sufficiency of 2D-NSW equations in determining tsunami behavior in shallow water zones where fully three-dimensional flow characteristics develop, and emphasizes the variations between the 2D-NSW and 3D-RANS equations. In addition, based on the results of the analyses, a validity range is determined regarding the use of two- and three-dimensional numerical models and recommendations related to applying relevant models to various tsunami problems are made. As a result, the study is expected to contribute to the available knowledge concerning the two- and three-dimensional numerical modeling of tsunami motion and inundation as well as tsunami currents and to support the findings of the previous investigations.

CHAPTER 2

LITERATURE REVIEW

In Section 2.1, theoretical approaches that analyze the offshore and nearshore long wave behavior (i.e. evolution, propagation, amplification and runup) are summarized. The improvements in analytical techniques employed to solve shallow water equations are given. Several analytical and experimental studies which establish the milestone of benchmark problems used for the validation/verification of tsunami numerical models are also presented.

There are numerous studies on the application of tsunami numerical models using different processing and computational techniques, which makes it impossible to summarize all of them in this dissertation. A great deal of information about the most recent studies regarding the development, validation/verification and application of two- and three-dimensional tsunami numerical models is presented in Section 2.2.

NAMI DANCE is a well-known tsunami simulation model applied in many studies. Section 2.3 presents an overview of the most prominent and recent studies which are conducted using NAMI DANCE.

FLOW-3D[®] specializes in the solutions of time-dependent free surface problems in one, two and three dimensions. FLOW-3D[®] is a common modeling tool among hydraulic engineers as well as environmental engineers, while it is not employed widely to coastal engineering problems. There are a handful of studies in literature that utilizes FLOW-3D[®] to solve three-dimensional long wave motion. Section 2.4 summarizes the most remarkable ones.

2.1. Analytical and Experimental Approaches

There is a significant amount of research on analytical solutions to explain nearshore tsunami behavior and runup, and thus, on the use of nonlinear shallow water equations or Boussinesq approximations. Most of these solutions are tested and compared with the results of laboratory experiments. Some of the resulting studies are summarized in this section.

Airy (1845) gave a linearized description of the propagating gravity waves on the surface of a homogeneous fluid layer with a uniform mean depth and an inviscid, incompressible and irrotational flow in his theory known as *Airy Wave Theory* or *Linear Wave Theory*. He also found out that the fluid particle orbits were circular in deep water and ellipsoidal in finite depth. Equation [2.1] represents the well-known linear wave theory:

$$\eta(x, t) = a \cos(kx - wt) \quad [2.1]$$

where η is the free surface elevation, a is the wave amplitude, k is the angular wave number in radian/m and given by $k = 2\pi/\lambda$, w is the angular wave frequency in radian/sec and given by $w = 2\pi/T$, λ is wavelength, T is wave period, x is the horizontal x axis in the Cartesian coordinate system and t is time.

Stokes (1847) developed Airy's (1845) linear theory further and extended it to cover nonlinear wave motion using a perturbation series approach, called *Stokes' Wave Theory*. This theory is used for waves on intermediate and deep water and its applicability is limited to small amplitude long waves.

Saint-Venant's (1871) equations, also known as *shallow water flow equations*, were derived from Reynolds depth-averaged forms of the Navier-Stokes equations. Saint-Venant maintained that if the horizontal length scale was much greater than the vertical length scale, then the vertical velocity of the fluid was small according to the

law of conservation of mass. He also employed the momentum equation to prove that vertical pressure gradients were nearly hydrostatic, and thus the horizontal velocity field was constant throughout the depth of the fluid. After these evaluations, he vertically integrated the Navier-Stokes equations, deriving the shallow water equations. One-dimensional (1D) Saint-Venant equations describing the incompressible flow in an open channel of arbitrary cross-section in x direction are given by Equations [2.2] and [2.3]:

$$\frac{\partial A}{\partial t} + \frac{\partial(Au)}{\partial x} = 0 \quad [2.2]$$

$$\frac{\partial u}{\partial t} + u \frac{\partial u}{\partial x} + g \frac{\partial \eta}{\partial x} = -\frac{\bar{P}}{A} \tau \quad [2.3]$$

where $A(x, t)$ is the cross-sectional area of the flow at location x , u is the velocity of water particles in x direction, $\tau(x, t)$ is the wall shear stress along the wetted perimeter, $\bar{P}(x, t)$, of the cross section, ρ is fluid density and g is gravitational acceleration.

Boussinesq (1872) derived a set of equations for finite amplitude long waves. They were valid for one-dimensional and constant water depth problems. The terms weak dispersion and weak nonlinearity were accounted for in these equations. The total pressure under the wave had both a hydrostatic and a dynamic component. Equations [2.4] and [2.5] are reduced to shallow water equations when the right-hand sides are set to zero.

$$\frac{\partial \eta}{\partial t} + \frac{\partial}{\partial x} [(d + \eta)u_b] = \frac{1}{6}d^3 \frac{\partial^3 u_b}{\partial x^3} \quad [2.4]$$

$$\frac{\partial u_b}{\partial t} + u_b \frac{\partial u_b}{\partial x} + g \frac{\partial \eta}{\partial t} = \frac{1}{2}d^2 \frac{\partial^3 u_b}{\partial t \partial x^2} \quad [2.5]$$

Equations [2.4] and [2.5] can be also reduced to Equation [2.6]; a single partial differential equation for the free surface elevation, η :

$$\frac{\partial \eta}{\partial t} - gd \frac{\partial^2 \eta}{\partial x^2} - gd \frac{\partial^2}{\partial x^2} \left(\frac{3}{2} \frac{\eta^2}{d} + \frac{1}{3} d^2 \frac{\partial^2 \eta}{\partial x^2} \right) = 0 \quad [2.6]$$

where d is the undisturbed flow depth, u_b is the horizontal velocity component in x direction at $z = -d$.

McCowan (1891) presented a higher degree of approximation of Boussinesq solution, in which he represented the structure of solitary waves by a series expansion. However, he estimated only first term of the expansion. The free surface profile according to McCowan's (1891) expansion is given in Equation [2.7]

$$\frac{\eta}{d} = \frac{\mathcal{N}}{\mathcal{M}} \frac{\sin \left[\mathcal{M} \left(1 + \frac{\eta}{d} \right) \right]}{\cos \left[\mathcal{M} \left(1 + \frac{\eta}{d} \right) \right] + \cosh \left(\mathcal{M} \frac{x}{d} \right)} \quad [2.7]$$

\mathcal{N} and \mathcal{M} are parameters depending on η/d and given by Equations [2.8] and [2.9]:

$$\frac{H}{d} = \frac{\mathcal{N}}{\mathcal{M}} \tan^{1/2} \left[\mathcal{M} \left(1 + \frac{H}{d} \right) \right] \quad [2.8]$$

$$\mathcal{N} = \frac{2}{3} \sin^2 \left[\mathcal{M} \left(1 + \frac{2}{3} \frac{H}{d} \right) \right] \quad [2.9]$$

where H is wave height.

McCowan (1891) accepted $\mathcal{M} = \sqrt{3H/d}$ and $\mathcal{N} = 2H/d$ as a first approximation.

Korteweg and deVries' (1895) proposal was a nonlinear partial differential equation whose solutions could be exactly and precisely specified. The KdV equation is a nonlinear, dispersive partial differential equation and is given by Equation [2.10]:

$$\partial_t \phi + \partial_x^3 \phi + 6\phi \partial_x \phi = 0 \quad [2.10]$$

where ∂_x and ∂_t are partial derivatives with respect to x and t and ϕ is a function with two variables, space x and time t .

Munk (1949) published a study which was a part of a project carried out during World War II to extend wave forecasting into the surf zone. In his study, he gave a summary of useful relationships derived by means of solitary wave theory and reviewed various studies, field and laboratory observations and theoretical studies. He recommended the expansions given by McCowan (1891) and stated that for most applications, McCowan's (1891) first approximation was adequate.

Ursell (1953) developed a dimensionless parameter which indicated the nonlinearity of long surface gravity waves on a fluid layer. The parameter, called *Ursell number*, was given by $U_r = H\lambda^2/d^3$ where H is wave height, λ is wavelength and d is undisturbed water depth. Ursell (1953) emphasized the importance of wave height, wavelength and water depth relation in the determination of the mathematical treatment of wave motion. Ursell (1953) stated that for small $H\lambda^2/d^3$ values, linear wave theory was valid; however, a nonlinear wave theory such as Boussinesq equations should be used for waves with large $H\lambda^2/d^3$ values (i.e. solitary waves).

Stoker (1957) is believed to have presented the first numerical solution of the shallow water equations using the method of characteristics for a sloping beach. The path of the shoreline during runup and rundown was a characteristic line and this led to efficient and direct computation of the shoreline path. Very accurate results were obtained for simple cases with this method. The method of characteristics is now practically out of use.

Carrier and Greenspan (1958) proposed a method to transform the nonlinear shallow water equations into a set of linear equations. They used this theory to investigate the runup of periodic waves with several different initial shapes on a plane slope.

Carrier (1966) hypothesized that nonlinear effects became considerably small far from the shoreline; therefore, the linear form of the transformation equations were applicable there. He conducted a theoretical study of tsunami runup. He considered long slightly dispersive plane waves of height, H propagating in water depth of d and having a runup R on a gentle slope α , after travelling a dimensionless distance x/d .

$$\frac{R}{H} \approx 2.1\alpha^{-1/2} \left(\frac{x}{d}\right)^{-1/6} \quad [2.11]$$

Van Dorn (1966) described a theoretical and experimental investigation of wave mechanism in shoaling water up to the point of maximum runup on beaches of arbitrary slope, considering only the case of wave propagation normal to the shore. He regarded the study as an attempt to bridge the gap between the small amplitude runup theory and the results of numerous experiments with waves of finite amplitude. He first carried out a series of experiments with small amplitude waves and then reinterpreted the previous large amplitude experimental results in terms of small amplitude theory with appropriate corrections. His runup formula for a wave propagating from deep water to a region of constant depth is given by Equation [2.12]:

$$\frac{R}{H} = \frac{2\pi d^{1/2}}{H} \left(\frac{\alpha}{\gamma}\right) \left[\tanh \sigma \left(1 + \frac{2\sigma}{\sinh 2\sigma}\right) \right]^{1/4} \quad [2.12]$$

where R is the maximum runup, α is the beach slope, γ is the dimensionless wave frequency given by $2\pi\sqrt{(g/d)}/T$ and σ is the dimensionless wave number given by $2\pi d/\lambda$.

Peregrine (1967) numerically calculated solutions to the Boussinesq equation for a wave approaching a straight beach of constant slope. In addition, Peregrine (1967) obtained analytical solutions for a wave reflected off the slope by using linear theory.

Madsen and Mei (1969) solved the Boussinesq equations numerically for the case of a solitary wave ascending a straight ramp. They were able to experimentally confirm the disintegration of the solitary wave on the shelf into two or more solitary waves.

Fenton (1972) formulated an exact operator equation in order to determine numerical coefficients for an assumed form of solution to the solitary wave, which were calculated to the ninth order. He used the ninth-order solution to obtain a solitary wave with amplitude of 0.85 m and to obtain approximations to physical quantities associated with the solitary wave, such as the surface profile and wave speed.

Tuck and Hwang (1972) worked on the Carrier and Greenspan (1958) transformation and further used it to solve long wave runup also under prescribed initial water-surface configurations. Tuck and Hwang (1972) investigated the problem of the generation of waves on a slope created by a bottom disturbance.

Spielvogel (1976) also extended the Carrier and Greenspan (1958) transformation and used it inversely to determine the long wave runup assuming a logarithmic initial surface profile on the slope at the maximum runup position.

Goring's (1978) theory for the laboratory generation of long waves of permanent form such as solitary and cnoidal waves was applied to the wave generators which had a vertical plate moving horizontally. The results of his experiments corresponded to the generation theory. Even though accurate results are obtained from Goring's method only for small amplitude solitary waves, it has remained the most commonly employed method for decades.

Hibbert and Peregrine (1979) suggested solving the shallow water equations by using the Lax-Wendroff scheme (Richtmyer and Morton, 1967) in order to make a possible calculation of wave breaking. The researchers managed to calculate the evolution of a uniform bore up a sloping beach.

Thacker (1981) introduced a number of exact solutions to the nonlinear shallow water equations. The exact solutions corresponded to time dependent motions in parabolic basins and it was assumed that the shoreline moved freely. He viewed the exact solutions as a valuable comparison test and a more practical way for numerical models since the numerical integration of nonlinear shallow water equations and the other assumptions required were not easy.

Pedersen and Gjevik (1983) used a Lagrangian description to develop a finite difference scheme for the Boussinesq equations that could predict the runup process and also the possibility of wave breaking during rundown.

Freilich and Guza (1984) designed two one-dimensional nonlinear models for the evolution of wind waves advancing shoreward over impermeable, slowly changing topography. Afterwards, they conducted a field experiment to measure wave parameters of sea surface elevation, pressure and horizontal velocity in Torrey Pines Beach, California in 1980. They primarily aimed to determine the operational validity of the two nonlinear shoaling models they had developed. They discovered that both nonlinear models were good predictors of the wave field in the shoaling region for all data sets.

Synolakis (1986, 1987) simplified the Carrier and Greenspan (1958) transformation and applied it to the problem of a solitary wave propagating in a fixed water depth and climbing up a simple plane beach. Having introduced an approximate theory for non-breaking waves, he derived an asymptotic result for the maximum runup of solitary waves. He conducted a series of laboratory experiments to support the theory. He concluded that the linear theory predicted the maximum runup

satisfactorily, and also described the runup of solitary waves equally well. He also discovered different runup regimes for the runup of breaking and non-breaking solitary waves. His study is currently being used to explain some of the existing empirical runup relationships and functions as a benchmark problem for validation/verification of tsunami numerical models.

Shuto (1991) discussed the effects of dispersion on tsunami propagation after comparing the numerical results of linear Boussinesq, Boussinesq and linear long wave theories in deep water. He concluded that the linear Boussinesq and Boussinesq equations were nearly the same as the true solution that was given by linear surface wave theory and suggested that the nonlinear term was not important in deep water propagation of tsunamis.

Madsen et al. (1991) extended the standard Boussinesq equations to obtain improved linear dispersive properties in deep water. They added higher order terms to these equations and stated that this addition increased the accuracy of the computed phase speed in deeper water, enabling the application of the model in deeper water without significant loss of accuracy.

Madsen and Sorensen (1992) extended the equations of Madsen et al. (1991) to include the effects of bottom slope. Based on the assumption of a slowly varying bottom slope, they neglected higher order spatial derivative of the water depth, and obtained a new set of Boussinesq equations. The equations served to provide an improved accuracy of both linear dispersion and shoaling properties.

Tadepalli and Synolakis (1994) used a first-order theory and derived asymptotic results for the maximum runup. They observed a class of N-shaped waves with very interesting behavior, which was regarded as a new phenomenon for tsunami runup studies. Similar trends emerged in the maximum runup results.

Liu (1994) and Wei et al. (1995) offered a set of highly nonlinear Boussinesq-type equations that could be applied to intermediate water depth and were capable of simulating wave propagation with strong nonlinear interaction. They also developed a high-order numerical scheme to solve these equations. They successfully improved the usage of Boussinesq-type equation model so that long wave evolution from relatively deep water to the breaking point could be accurately estimated.

Briggs et al. (1995) and Liu et al. (1995) investigated runup of solitary waves on a circular island in a series of laboratory experiments. Maximum vertical runup measurements were made around the perimeter of the island. They observed that runup on the back side of the island was higher than that on the front side. Their data are still in use for the benchmarking of tsunami numerical models.

Zhang (1996) investigated the runup associated with a solitary wave moving to a plane beach at an angle and found a linear solution for the three-dimensional runup using Fourier synthesis.

Tadepalli and Synolakis (1995, 1996) demonstrated that a coastal tidal wave was *N-wave like* and proved that the runup of a leading-depression (LDN) wave was higher than that of a leading-elevation (LEN) wave. Their formulations were based on the depth-averaged linear and nonlinear shallow water equations.

Kanoglu and Synolakis (1998), who investigated long wave runup on piecewise linear topographies, developed a general solution method to determine amplification factors for different ocean topographies that consisted of linearly varying and constant-depth segments. They studied the evolution of solitary waves by using their results.

Li and Raichlen (2001) conducted experiments on the runup of solitary waves on a uniform plane beach. They presented a nonlinear solution to the classical shallow water equation analytically, for which they used a hodograph transformation. They

compared the water surface elevation results with the results of the approximate nonlinear theory presented by Synolakis (1987) and with the experimental data. They came to the conclusion that the vertical velocity was smaller than 20% of horizontal velocity for all locations, which supported the assumption that the effects of nonlinearities could be neglected near and offshore of the toe of the slope. The results showed that the assumptions made by Synolakis (1987) could be satisfactorily applied to especially gentle slopes where the breaking wave height was significantly smaller than that of the steep slopes.

Carrier et al. (2003) analyzed tsunami runup and drawdown motions on a uniformly sloping beach based on fully nonlinear shallow water theory. Having transformed the nonlinear equations of mass conservation and linear momentum to a single linear hyperbolic equation, they applied the Fourier–Bessel transform to solve the equation with arbitrary initial conditions. They discovered that the direction of both the maximum flow velocity and the maximum momentum flux depended on the initial waveform.

Kanoglu (2004) analytically solved the initial value problem of the nonlinear evolution and shoreline motion of long waves that climbed up sloping beaches for different initial wave forms. He introduced a simplified equation for the calculation of runup/rundown motion of the shoreline and then applied this approach to Gaussian and leading depression N-wave initial forms presented by Carrier et al. (2003). When the results were compared, Kanoglu (2004) concluded that his solution was simpler and produced identical results. He also suggested that the method he proposed could be efficient in the assessment of the impact of long waves generated by seafloor displacements and in the validation of tsunami numerical models.

Liu et al. (2005) conducted a series of three-dimensional laboratory experiments at Oregon State University, in which a solid wedge was used in a large wave tank to represent underwater landslide induced tsunami waves. The data obtained from the experiments are still being used for the benchmarking of tsunami numerical models.

Synolakis et al. (2008) discussed analytical, experimental and field benchmark tests that could be employed to validate and verify tsunami numerical models. The benchmark tests and their expected solutions were described in detail. A scientific and operational evaluation of numerical models was offered and the necessity of continuous validation and verification processes was stressed.

2.2. Numerical Modeling

Numerical computation techniques that are employed to solve various problems regarding water waves have gained popularity since the 1960s (Goda, 2010). Many different tsunami generation and propagation models have been developed over the past few decades, based on different classes of governing equations, numerical methods, spatial and temporal discretization techniques and wetting-drying algorithms. Depth-averaged, hydrostatic or non-hydrostatic long wave equations act as the basis of the majority of the current tsunami models (Horrillo et al., 2015). The development and description of several tsunami models are given in this section.

Hansen (1956) formulated an approach to hydrodynamic modeling. He used a suitably stable finite difference approximation for the time derivative and the dependent fields were stepped forward in time. He carried out numerical computations of a heavy storm surge that struck the coasts of Holland, in the North Sea in 1953. He also presented numerical solutions of nonlinear tidal propagation for the Ems River, Germany.

Fischer (1959) developed a finite difference method to determine water heights and movements in adjacent seas and transformed the vertically integrated equations of motion and the continuity equation into an explicit system of equations. These equations were solved stepwise in time with an electronic computer. He also examined the effects of a smoothing technique and the mesh size of the grid on the results. Moreover, he studied storm surges and tides in the North Sea and compared the results in selected cases with the results of other methods or with observations.

Leendertse (1967) utilized the finite difference method to develop a two-dimensional vertically-averaged hydrodynamic model, in which the effects of the earth's rotation and bottom roughness were included, in order to solve the differential equations of long wave propagation. The input to the numerical scheme was water depths at certain points. Leendertse (1967) is also known for his significant contributions in the area of numerical stability and accuracy. He and subsequently Liu built a three-dimensional model (Leendertse et al., 1973, Leendertse and Liu, 1975) and afterwards included realistic turbulent exchange processes (Leendertse and Liu, 1978). The model was tested and applied to tides, wind and density driven motion and transport of pollutants.

Abbott and Ionescu (1967) constructed an implicit finite difference scheme in order to solve the continuity and momentum equations and, in particular, to solve any form of the Saint Venant equations (i.e. kinematic, diffusive, or dynamic). This scheme has become the basis of the widely-known MIKE modeling systems. The Danish Hydraulic Institute (DHI) modeling team that Abbott initiated in 1962 has been improving MIKE software. MIKE 21 and MIKE 3 are general hydrodynamic flow modeling systems which are aimed at applications within oceanographic, coastal and estuarine environments. MIKE 21 solves two-dimensional depth-averaged equations whereas MIKE 3 deals with three-dimensional hydrostatic equations. These model systems can be used while working with single grids, multiple grids and flexible mesh.

Hwang et al. (1972) developed a numerical model through which they analyzed the generation and propagation of tsunami waves. The model was based on hydrodynamic equations in a spherical coordinate system to account for the spherical nature of the Earth. They employed a multi-step finite difference procedure to solve the equations of motion and continuity equation. The model was verified by hindcasting the wave behavior following the Alaskan earthquake of 1964. When compared with a runup record at Cape Yakatage and transoceanic propagation of the tsunami wave, it was found that the model was consistent with the wave behavior.

Arakawa and Lamb (1977), who developed a 12-layer UCLA general circulation model, discussed the selection of the finite difference schemes for homogeneous incompressible flow and nonlinear two-dimensional nondivergent flow. They also introduced the *Arakawa Grid System*, which serves to represent and compute orthogonal velocity and mass related quantities on rectangular grids.

Longuet-Higgins and Cokelet (1976) asserted that the existing theories were only valid for symmetric progressive waves; therefore, they developed a numerical technique to solve periodic, two-dimensional, deep water breaking wave problems. In their method, the only independent variables were the coordinates and velocity potential of marked particles at the free surface. The researchers tested the method on a free, steady finite amplitude wave and found that it was in excellent agreement with the independent calculations based on Stokes's series.

Vinje and Brevick (1981) offered a method similar to the Longuet-Higgins and Cokelet's (1976) numerical one, claiming that the latter was based on potential theory. The exceptions were that the problem was solved in the physical plane and finite depth was introduced.

Hirt and Nichols (1981) developed a simple method based on the concept of a fractional volume of fluid, and they approximated free boundaries via the finite difference scheme. They used an incompressible hydrodynamics code that used the Volume-of-Fluid (VOF) technique to track free fluid surfaces. The new code demonstrated the flexibility and efficiency of the method and proved to be efficient for a wide range of complex problems.

Kim et al. (1983) developed the Boundary Integral Equation Method (BIEM) as a tool to analyze two-dimensional, nonlinear water wave problems such as wave generation, wave propagation and wave runup on steep slopes. Nonlinear free surface boundary conditions were included in the numerical formulation. Examples for either a solitary wave or two successive solitary waves were provided.

Dold and Peregrine (1986) dealt with the numerical computations of the evolution of small amplitude modulations on a uniform wave train. They based their method of computation on Boundary Element Method (BEM) solutions of the two-dimensional potential flow approximation of the canonical problem. They concluded that the computations were able to clearly indicate when breaking occurred.

Kobayashi et al. (1987) designed a numerical flow model to predict the flow characteristics of a normally incident wave train during the uprush and downrush on a rough slope. They used an explicit dissipative Lax-Wendroff finite difference method to solve the finite-amplitude shallow water equations including the effects of bottom friction numerically in the time domain. They observed that the computed results were in agreement with the available data on wave runup, reflection, and rundown. They concluded that more detailed flow measurements needed to be made to improve and calibrate the numerical model.

Grilli and Svendsen (1989a) presented a computational model for highly nonlinear two-dimensional water waves, by means of which they investigated the problems of wave generation and absorption. In this model, a high order Boundary Element Method (BEM) was coupled with a high order explicit time stepping technique for the temporal evolution of the waves. Grilli and Svendsen (1990) further investigated BEM by analyzing the transformation of solitary waves above a mild slope, from intermediate to shallow water and the interaction of these waves with coastal structures located in the shallow area. Computations included wave runup, overturning and reflection from steep slopes or a vertical wall, and from a combination of a slope and a submerged breakwater. Upon comparison of the results with other numerical, analytical and experimental data, it was found that when solitary waves having steepness up to 0.50 climbed up on a relatively steep slope, there would be significant differences between the velocity profiles and the depth uniform velocity.

Zelt and Raichlen (1990) developed a Lagrangian finite-element Boussinesq wave model and studied non-breaking solitary wave runup on two- and three-dimensional bathymetries. Zelt (1991) further investigated the runup of non-breaking and breaking solitary waves on plane impermeable beaches by using this model. The comparisons with the laboratory data indicated that, for the steep slope, excellent agreement was obtained with the laboratory data. For the gradual slope, wave shoaling, breaking, and subsequent collapse at the shoreline were successfully predicted, although the breaking algorithm did not attempt to model the details of the turbulent flow in the breaking region. In addition, Zelt (1991) analysed the landward inundation of non-breaking solitary waves which climb up a nonplanar slope.

Grilli et al. (1989, 1994) and Subramanya and Grilli (1994) proposed a very efficient method for the calculation of the runup of solitary waves whose initial height was close to the limiting wave height. Their findings were in good agreement with laboratory data and no calibration was needed. However, although they took breaking waves into consideration, they only calculated their evolution up to the breaking point.

LeVeque (1994) released the first version of CLAWPACK, a software package designed to solve nonlinear hyperbolic partial differential equations using high-resolution finite volume methods based on Riemann solvers and limiters. A Fortran code was used for solving problems on a single, uniform Cartesian grid in one or two space dimensions, together with some Matlab scripts for plotting solutions. Berger and LeVeque (1998) extended the code to employ the high-resolution wave propagation algorithms in a more general framework. Langseth and LeVeque (2000) implemented three-dimensional versions of the wave propagation algorithm. CLAWPACK has been developed further as an open source project and many CLAWPACK software repositories have been put into use; GeoClaw is among them. GeoClaw is widely used to solve two-dimensional depth-averaged shallow water equations over topography for modeling tsunami generation, propagation, and inundation at present (Mandli et al., 2016).

Liu et al. (1994, 1998) aimed to simulate tsunami wave propagation and runup, and developed a nested multi-grid finite difference model in Fortran, called COMCOT (Cornell Multi-grid Coupled Tsunami model), which could use either linear or nonlinear forms of shallow water equations with different types of coordinate systems (i.e. Cartesian or spherical). The linear and nonlinear shallow water equations were both discretized with the explicit leapfrog finite difference scheme. The model was applied to several numerical examples and analytical solutions and good agreements were observed.

Imamura et al. (1995) developed TUNAMI, a tsunami propagation model, in the framework of Tsunami Inundation Modeling Exchange (TIME) program taking place in Disaster Control Research Center (DCRC) of Sendai, Japan. Developed in Fortran and based on nonlinear shallow water equations, the model used the second-order explicit leapfrog finite difference scheme for computations. TUNAMI code is widely used at present. TUNAMI-N1 (Tōhoku University's Numerical Analysis Model for Investigation of Near field tsunamis, No.1) uses linear theory with constant grids; TUNAMI-N2 (Tōhoku University's Numerical Analysis Model for Investigation of Near field tsunamis, No.2) employs linear theory in deep water, shallow water theory in shallow water and runup on land with constant grids; TUNAMI-N3 (Tōhoku University's Numerical Analysis Model for Investigation of Near field tsunamis, No.3) solves linear theory with varying grids; TUNAMI-F1 (Tōhoku University's Numerical Analysis Model for Investigation of Far field tsunamis, No.1) employs linear theory for propagation of long waves in deep ocean in spherical coordinates and TUNAMI-F2 (Tōhoku University's Numerical Analysis Model for Investigation of Far field tsunamis, No.2) employs linear theory for the propagation of long waves in deep ocean and coastal waters.

Imamura and Imteaz (1995) developed a linear numerical model called TWO LAYER, using the staggered leapfrog scheme for computation of water level and discharge in one-dimensional propagation. They used the Fourier transform to solve the linearized equations for two-layers analytically. They validated the numerical

model by comparing the results with the analytical solutions for different boundary conditions. Imteaz and Imamura (2001) extended the linear model to a nonlinear model to predict the propagation of a unidirectional two-layered tsunami wave. Four governing equations, two for each layer, were derived from Euler's equations of motion and continuity, assuming a long wave approximation, negligible friction and no interfacial mixing. The developed nonlinear model was compared with the existing validated linear model for different non-dimensional wave amplitudes.

Titov and Synolakis (1995) presented a model called VTCS-2, which is a variable grid finite difference formulation of the shallow water equations that allows the calculation of breaking and non-breaking wave evolution on sloping beaches. Upon comparing the computational results with analytical solutions, other numerical computations and laboratory data for breaking and non-breaking solitary waves, the researchers found that the model accurately predicted the evolution and runup of non-breaking waves. Titov and Synolakis (1998) implemented a shoreline algorithm which was the generalization of the earlier algorithm employed in the code VTCS-2. Large-scale laboratory data from solitary wave experiments attacking a conical island were used in the validation process. The modeling of the 1993 Okushiri, Japan, the 1994 Kuril Islands, Russia, and the 1996 Chimbote, Peru tsunamis was done by applying this method. It was concluded that the model served well in the prediction of overland flow and extreme events such as the 30-m runup and the 20-m/s inundation velocities measured during field surveys.

Sato (1996) modeled the energy dissipation occurring at the tsunami wave front due to breaking by using a numerical model based on the Boussinesq equation, which included the effects of frequency dispersion. After the validity of the model was tested with the existing laboratory data of dispersive wave trains breaking on a slope, the model was applied to the simulation of the 1993 Southwest Hokkaidō earthquake tsunami around the southern part of Okushiri Island.

Zhang (1996) designed a finite difference scheme for the shallow water equations and the Boussinesq equations, which is used to model the runup by remapping the grid points at the surface according to the instant shoreline position.

Grilli and Subramanya (1996) aimed to study wave breaking caused by shoaling over a gentle plane slope and wave breaking induced by a moving lateral boundary. For this, they improved and validated several numerical aspects of an existing model for fully nonlinear waves. The model was based on the fully nonlinear potential flow theory and combined a higher order Boundary Element Method (BEM) to solve Laplace's equation at a given time and Lagrangian Taylor expansions to update the time of the free surface position and potential. Both the resolution and extent of computations were greatly improved through the use of the new methods.

Grilli et al. (1997) developed a fully nonlinear potential flow scheme by employing boundary element techniques and used it to calculate various characteristics of solitary wave propagation and breaking. The scheme provided detailed information about wave breaking including the shape of the plunging jet generated by the breaking process. However, it was not able to predict maximum runup because the computation terminated when the plunging jet struck the free surface.

Titov and Gonzalez (1997) implemented and tested a set of numerical simulation codes, known as the MOST (Method of Splitting Tsunami) model. Introduced as a part of the Early Detection and Forecast of Tsunami (EDFT) project, the model was capable of simulating the processes of tsunami evolution such as generation by an earthquake, transoceanic propagation, and inundation of dry land. Simulation of the generation process in the MOST model was based on elastic deformation theory (Gusiakov, 1978; Okada, 1985) and the method of computing inundation was a derivative of the VTCS-2 model (Titov, 1997; Titov and Synolakis, 1995, 1996, 1997). Generation and propagation capabilities were tested against the deep ocean bottom pressure recorder data recorded during the 1996 Andreanov tsunami. The inundation computations were compared with the field measurements of maximum

runup on Okushiri Island, which were gathered shortly after the 1993 Hokkaidō Nansei-Oki tsunami. The results of the simulations were consistent with the observations. The MOST model is widely used at present.

Kirby et al. (1998) designed a finite difference model called FUNWAVE that can be used to solve a free surface wave problem using the fully nonlinear, extended or standard Boussinesq equations or the nonlinear shallow water equations. Given the initial conditions and bathymetry, the program dealt with free surface elevations and horizontal velocities on a rectilinear non-staggered grid.

Lin et al. (1999) developed a numerical model to solve the Reynolds equations for the mean flow field and the \bar{k} - ϵ equations for the turbulent kinetic energy, \bar{k} , and the turbulence dissipation rate, ϵ . Then they applied the model to wave breaking and runup. The free surface locations and movement were tracked by the Volume-of-Fluid (VOF) technique. The researchers observed that the numerical results agreed fairly well with the experimental results in terms of the wave profile and velocities, but were unable to provide jet and splash up information.

Yoon (2002) proposed a two-dimensional finite difference numerical scheme in order to simulate transoceanic propagation of tsunamis over gradually varying topography. This scheme solved the shallow water equations on a uniform grid system. The dispersion effect of waves was considered in the computation by utilizing the numerical dispersion error arising from the leapfrog scheme. Having tested the model for several cases, Yoon (2002) concluded that the numerical model was less accurate for short waves than the original Boussinesq equation model; however, it was computationally more efficient. Thus, the model was regarded as superior to that of the conventional finite difference models.

Lynett et al. (2002) developed a Boussinesq-type wave model, COULWAVE (Cornell University Long and Intermediate Wave Modeling Package), which was used for coastal and ocean wave propagation. They used a high-order finite

difference scheme in order to solve highly nonlinear and weakly dispersive equations, in addition to an eddy viscosity model which they used to investigate breaking wave runup. They were able to validate both the wave breaking parameterization and the moving boundary technique since they accurately predicted non-breaking and breaking solitary wave runup. The results of their investigation into two-dimensional wave runup in a parabolic basin and around a conical island were in excellent agreement with the published data.

Stelling and Zijlema (2003) introduced a numerical technique for the approximation of vertical gradient of the non-hydrostatic pressure arising in the Reynolds-averaged Navier–Stokes equations for simulating non-hydrostatic freesurface flows. The proposed technique was stated to be capable of simulating relatively short wave propagation, in which both frequency dispersion and nonlinear effects played an important role. The results indicated that the technique was able to capture the essential wave phenomena, such as shoaling, dispersion, refraction and diffraction and was expected to be computationally competitive with the extended Boussinesq-type wave models.

Biausser et al. (2003) referred to the study of Guignard et al. (1999, 2001), who efficiently and accurately computed wave breaking on sloping beaches combining the segment Lagrangian Volume-of-Fluid (SL-VOF) and Boundary Element Method (BEM) for two-dimensional flows. Biausser et al. (2003) extended this methodology to three-dimensional flows and verified it on two simple applications. The three-dimensional Boundary Element Method (3D BEM) produced similar results for the case of a solitary wave shoaling and breaking on a sloping beach.

Watts et al. (2005) developed four separate sources for the December 26, 2004 tsunami, which were based on differences in seafloor morphology along a 1200 km long rupture zone. A numerical simulation of the tsunami performed with a higher-order Boussinesq model led them to conclude that the numerical results and a few observed runup values were in reasonable agreement.

Koh et al. (2005) from University of Malaysia developed an in-house tsunami model, TUNA, which was made up of two parts: TUNA-M2 which predicted tsunami generation and propagation and TUNA-RP which estimated tsunami runup and inundation. TUNA model used the Okada equation for tsunami sources generation due to an earthquake. The explicit finite difference method and staggered scheme were employed so that linear shallow water equations were discretized and tsunami propagation could be predicted. However, nonlinear shallow water equations were applied for the cases of tsunami runup and inundation.

Synolakis and Bernard (2006) collected and summarized the approaches towards tsunami numerical calculations in their extensive study on tsunami numerical modeling. They focused on the improvements in tsunami simulations by numerical modeling after the destructive 2004 Sumatra tsunami. The developments in tsunami inundation modeling tools were explained in detail in terms of hydrodynamics.

Dao and Tkalich (2007) carried out research into the sensitivity of the modified version of the numerical model TUNAMI-N2 in terms of astronomic tide, sea bottom friction, dispersion, coriolis force, and spherical curvature by modeling the 2004 Sumatra event as the tsunami scenario. A modified version of the code, TUNAMI-N2-NUS, was introduced later. The code used nonlinear shallow water equations; however, it solved Boussinesq Equations when the dispersion effect was considered.

Zhang and Baptista (2008) developed a new finite-element model, SELFIE, for cross-scale ocean modeling. It was a semi implicit Eulerian–Lagrangian finite element model based on the three-dimensional Navier Stokes equations. It employed an unstructured grid in horizontal dimension for the adjustment of complex coastal topographic features and coastal structures. The researchers conducted a field application to the Columbia River estuary and plume to assess the performance of SELFIE.

Harig et al. (2008) designed a tsunami simulation model, TsunAWI, as part of the German aid contribution in the framework of the German–Indonesian Tsunami Early Warning System (GITEWS) at Alfred Wegener Institute for Polar and Marine Research (AWI). Based on an unstructured grid approach, the model used the finite element method to solve the governing shallow water equations, as this allowed a flexible discretization of the model domain.

Franchello and Krausmann (2008) developed HyFlux2 in order to solve the shallow water equations within the framework of European Commission Joint Research Center's (JRC) MAHB-NEDIES project. The model was used to predict both tsunami surges on coastal plains and dam-break waves in flood plains. HyFlux2 was capable of capturing local discontinuities (i.e. shock waves) and reducing numerical diffusion and unphysical viscosity effects dominating in all finite difference methods with the help of its basic ingredient, which was a 2D finite volume Approximate Riemann Solver, with a high-resolution Flux Vector Splitting technique and implicit treatment of the source terms.

Yamazaki et al. (2009) formulated, verified and validated a numerical model, NEOWAVE (Non-hydrostatic Evolution of Ocean WAVEs). This depth-integrated, non-hydrostatic model had a semi-implicit, finite difference scheme, whose formulation built on the nonlinear shallow water equations and utilized a non-hydrostatic pressure term in order to describe weakly dispersive waves. Good agreement with the available laboratory data for wave propagation, transformation, breaking, and runup was observed. Yamazaki et al. (2011a) managed to apply NEOWAVE to recent tsunami case studies.

Abadie et al. (2010) designed a multiple fluid Navier Stokes model, THETIS, for waves generated by idealized slide geometries or deforming slides. Analytical solutions and several laboratory experiments from previous studies, including the three-dimensional landslide experiment described in Liu et al. (2005) and Synolakis

et al. (2007), were used to validate this model, which accepted all computational domain regions as Newtonian fluids.

Horrillo et al. (2010, 2013) developed and validated a simplified three-dimensional Navier-Stokes model, TSUNAMI3D (Tsunami Solution Using Navier-Stokes Algorithm with Multiple Interfaces). The model employed the Volume of Fluid (VOF) method to track the fluid interface and the surfaces were obtained by integrating the fluxes of each individual fluid cell along the water column. In the momentum equation, the pressure term was divided into hydrostatic and non-hydrostatic components. The viscosity coefficient was adjusted to solve the internal friction in a simplified manner.

Dutykh et al. (2011) developed a tsunami numerical model, VOLNA, aiming to introduce a tool for tsunami wave modeling which covered the whole spectrum from generation to inundation. Because the model algorithm worked on unstructured triangular meshes, it could be run in arbitrary complex domains. It solved nonlinear shallow water equations with the finite volume scheme. The researchers partially validated their algorithm through several realistic test cases that they presented.

Titov et al. (2011) described a web-based community tsunami model for inundation modeling called Community Modeling Interface for Tsunamis (ComMIT), which was initially developed for Indian Ocean countries and supported by the United Nations Educational, Scientific and Cultural Organization (UNESCO), the United States Agency for International Development (USAID), and the National Oceanic and Atmospheric Administration (NOAA). ComMIT, which is currently being widely used, uses initial conditions taken from a precomputed propagation database and also allows incorporation of other tsunami models such as TsunAWI (Harig et al., 2008) or TUNAMI (Imamura, 1995). ComMIT supplies an interface which makes the selection of model input data (initial condition, bathymetry grids, etc.) possible. In addition, a platform to display model output through a graphical user interface (GUI) is available.

Kaiser et al. (2011) carried out detailed inundation simulations which aimed to support damage analysis and risk assessment regarding the 2004 tsunami in Phang Nga and Phuket, Thailand. The numerical models ComMIT, developed by the National Oceanic and Atmospheric Administration (NOAA) Center for Tsunami Research, and Mike 21 FM, a depth-averaged and hydrostatic wave evolution model designed by the Danish Hydrological Institute (DHI), were employed to gain an understanding of the observed tsunami inundation and to draw conclusions on the effect of land cover on inundation patterns.

Roeber and Cheung (2012) developed a Boussinesq Model for Ocean and Surf Zones (BOSZ). The model combined the weakly dispersive properties of the Boussinesq approximation with the conservative form of the nonlinear shallow water equations up to fifth-order in Cartesian coordinates.

2.3. NAMI DANCE Applications

NAMI DANCE is a tsunami numerical model developed by Middle East Technical University (METU), Turkey and Laboratory of Special Research Bureau for Automation of Marine Research, Far Eastern Branch of Russian Academy of Sciences, Russia. NAMI DANCE gained importance and popularity in a short span of time in the area of coastal modeling and was recommended by the United Nations Educational, Scientific and Cultural Organization (UNESCO) to be used in the simulations of possible tsunami scenarios.

Yalciner et al. (2005) issued a report about the field survey results concerning runup, arrival time and damages of the 2004 Indian Ocean tsunami. They carried out the field survey between January 21-31, 2005 at the north coasts of Sumatra Island in Medan and Meulaboh cities and in Simeulue Island. In addition, they simulated the 2004 Indian Ocean tsunami using NAMI DANCE and compared the numerical results with the observed field data of other tsunami survey teams at Sumatra, Thailand, Sri Lanka, India and Maldives.

Yalciner et al. (2007a) applied NAMI DANCE to five different tsunami scenarios which were likely to be generated in the Eastern Mediterranean. The available data of earthquake epicenters and magnitudes measured in the last century and subduction zone properties of Hellenic Arc were used in their simulations, whose results showed that the south of Crete and Peloponnesus, the north of Libya and Egypt were all vulnerable to tsunami waves.

Zaitsev et al. (2009) presented the data of the instrumental registration of the tsunami on Sakhalin and Hokkaidō islands as well as performing numerical simulations of the tsunami propagation in the Tatar Strait using NAMI DANCE software. They found that the numerical results were in satisfactory agreement with the observed data.

Dilmen (2009) employed NAMI DANCE to study the possible tsunami scenarios for the Gulf of Fethiye in Turkey and for the coasts Kyparissia, Zakynthos and Pylos in Greece. GIS based tsunami inundation maps were prepared and it was found that when the superstructure was taken into account in the formation of the topographical data, there was a reduction in the tsunami inundation.

Insel (2009) studied the effects of landslide parameters, density and thickness of the slid material on tsunami wave generation in Yalova in the Sea of Marmara. The generation of the landslide generated tsunamis were modeled using TWO-LAYER and the propagation and coastal amplification of the landslide generated waves were simulated via NAMI DANCE. In the study, it was concluded that higher densities and thicknesses of slide material caused higher water surface elevations.

Yalciner et al. (2010) performed numerical simulations for a selected tsunami scenario in Caribbean Sea using the numerical models TUNAMI N3 and NAMI DANCE and presented the numerical results of potential tsunamis generated in the region.

Zaitsev and Pelinovsky (2011) discussed forecasting of tsunami wave heights at the Russian coast of the Black Sea. The calculations of the tsunami wave characteristics were made using NAMI DANCE. The results of the numerical modeling of the historical events (in 1939 and 1966) were compared with the available observed data.

Onat (2011) generated a database of various seismic sources and applied it to Eastern Mediterranean by using NAMI DANCE. The difficulties in defining seismic source parameters and the effects of dip and rake (slip) angle on seismic generated tsunamis were also evaluated. Simulations were performed in nested domains for Bodrum, Kas and Iskenderun, which were presented as case studies. It was evident that the north-west and the south-west of Turkey were more vulnerable to tsunami than the other regions.

Ozer and Yalciner (2011) described the term *hydrodynamic demand* as a parameter used to represent the potential for tsunami drag force related damage to structures along coastlines. While performing analyses using NAMI DANCE in two altered regular-shaped basins with different bottom slopes, they implemented the simulations using a single sinusoidal wave with particular initial conditions, such as leading elevation wave and leading depression wave profiles with different wave periods.

Ozel et al. (2011) aimed at having a better understanding of the tsunami potential of the coasts of Turkey; therefore, they investigated the historically and instrumentally recorded tsunamis in the region. The modeling results of NAMI DANCE from selected tsunamigenic regions, Rhodes and the southwest of Turkey were included in the study. It was also stated that Kandilli Observatory and Earthquake Research Institute (KOERI) had started to install 5 sea floor observation systems in the Sea of Marmara to increase the observational capabilities and reduce the early warning time in case of a tsunami. The researchers emphasized the short arrival times in the Marmara and Aegean Seas and explained why it is utmost importance to establish a tsunami warning center in Turkey.

Ayca (2012) developed a Web based Geographic Information System (GIS) to serve tsunami inundation maps through the web. The four main stages of the research methodology were: (i) simulating tsunamis based on six different scenarios using NAMI DANCE; (ii) processing simulation data by means of a GIS application; (iii) development of web interfaces and implementation of the developed model for Web-GIS application; (iv) validation of the created model for Marmara Sea Region.

Onat and Yalciner (2013), upon creating 38 possible scenarios in the Eastern Mediterranean by employing NAMI DANCE, carried out simulations in nested domains for the towns of Iskenderun and Kas as case studies. They also analysed the uncertainties in defining seismic source parameters. The north-west and the south-west coasts of Turkey were found to be more vulnerable to tsunami waves than the other coasts.

Dilmen et al. (2014) prepared a tsunami inundation map for the Gulf of Fethiye by using NAMI DANCE based on their tsunami simulation and inundation assessment for the region. They used a high resolution bathymetry and topography data set for 14 probable tsunami scenarios and found that lowland nearshore regions with lowland topography were prone to a considerable level of inundation. Dilmen et al. (2014) also claimed that, although the presence of Sovalye Island located in front of the bay partly prevented the entrance of the tsunami waves, it created more agitation in the area.

Yalciner et al. (2014a) modeled a hypothetical landslide tsunami at Nile Delta in the Eastern Mediterranean Sea in order to study the risks it would pose to the region. The generation and propagation of a realistic landslide scenario was simulated numerically, which was the basis of the methodology used, and two different models, TWO LAYER and NAMI DANCE were selected for the simulations. The researchers discovered that there were wave reflections because of the semi-enclosed nature of the eastern Mediterranean, which resulted in several wave trains arriving at every coastal site. They recommended that deepwater pressure gauges be used so that

any landslide-generated tsunamis in the Eastern Mediterranean could be detected and early warning would be possible.

Yalciner et al. (2014b) conducted a numerical modeling study, whose main focus was the western part of Peloponnese in Greece, in the framework of European Union funded project, SEAHELLARC. In the study, simulations of possible tsunami source scenarios for the Pylos, Kyparissia, Filiatra and Zakynthos regions, located at the western part of Greece, were carried out by using NAMI DANCE to estimate extreme but possible tsunami wave effects in these regions. Finally, the tsunami arrival times and maximum positive and negative amplitudes were computed, plotted and compared.

Necmioglu and Ozel (2014) studied the sensitivity of earthquake source parameters in tsunami generation and propagation, focusing on the Eastern Mediterranean, using NAMI DANCE. They concluded that tsunami hazard studies should analyse a range of parameters, and that the *maximum* generated tsunami should be taken into consideration. Where this was not possible owing to computational limitations, at least sensitivity studies should be carried out and, in the selection of parameters, it was important that those that would result in maximum tsunami generation be favoured.

Ozdemir (2014) performed a series of simulations via NAMI DANCE by inputting previously determined seismic sources in the Sea of Marmara in order to develop a simple high-speed informative tsunami warning system for Marmara coasts. The results indicated that the maximum expected tsunami wave height at a gauge selected near Haydarpasa Port in the Sea of Marmara was around 1 to 2 m.

Pamuk's (2014) research into the influence of buildings and roughness coefficient on tsunami motion in an inundation zone was based on the comparison of 5 different simulations performed for the Belek region in Antalya using NAMI DANCE. In the study, the results showed that high resolution bathymetry and topography were

necessary for tsunami analysis for residential areas in order to obtain accurate velocities and inundation depths. It was stated that when friction was included, the inundation distances and discharge fluxes observed in the selected region were reduced. To identify possible morphological changes caused by a tsunami attack, the use of a non-dimensional parameter, the Rouse number, was also highlighted in the study.

Sozdinler et al. (2014) employed NAMI DANCE to analyse a tsunami parameter, namely hydrodynamic demand, which expressed the relative value of the drag force (i.e. damage level) of tsunami waves in inundation zones. The maximum values of inundation depth and current velocity are investigated as well as those of the water elevation and discharge flux that took place during several tsunami inundation scenarios. The simulations were conducted considering various orientations of regular shaped basins. The results of the analyses provided information about the damage levels in residential areas and the efficiency of coastal protection structures.

Aytore (2015) assessed the tsunami resilience of Haydarpasa Port in Istanbul according to the most effective submarine earthquake by carrying out numerical simulations with NAMI DANCE. Having analysed the possible effects of increasing data and model resolution to a higher level and including existing structures as elevation data, Aytore (2015) concluded that the highest model and data resolution produced more accurate results in tsunami modeling studies.

Sozdinler et al. (2015) calculated the damage inflicted by tsunami waves on structures and coastlines in Kamaishi Bay in terms of the square of the Froude number, Fr^2 , by conducting a numerical modeling study. The analyses were performed via NAMI DANCE with nested domains at a higher resolution and the effect of the Kamaishi breakwater on the tsunami inundation distance was tested. Also, the coastal damage was evaluated using the conditions with breakwater, without breakwater and damaged breakwater.

Kian et al. (2015a) used NAMI DANCE to investigate the resonance oscillations, periods of free oscillations and flow patterns of long waves in Haydarpasa Port, Istanbul. The possible effects of long wave amplification and resonance oscillations on Haydarpasa Port were discussed.

Kian et al. (2015b) investigated the response and behavior of water motions inside the enclosed basins under long wave conditions by using NAMI DANCE. The spatial and temporal changes of main tsunami parameters and their adverse effects on harbor performance were analysed by monitoring the wave and current amplifications and consequent variation of sediment motion in terms of the Rouse number. Several case studies for the possible effects of tsunamis or long waves on Belek, Antalya and on Haydarpasa Port, Istanbul were conducted.

Patel et al. (2016) modeled the Makran 1945 tsunami using NAMI DANCE for the coasts of Pakistan, Iran, India and Oman. The epicenter was 25.15N - 63.48E, the fault line was 200 km long and 100 km wide, focal depth was 15 km and strike, dip and rake angles were 2460, 70 and 900, respectively. The bathymetry data were obtained from General Bathymetric Chart of the Oceans (GEBCO) and land topography data from Shuttle Radar Topography Mission (SRTM) The results were consistent with the available reports and published data.

Cankaya et al. (2016) worked on a new methodology for tsunami vulnerability assessment for areas prone to tsunami. In their proposal, the Yenikapı region was selected as a case study and available data sets from the Istanbul Metropolitan Municipality and Turkish Navy were used as inputs for high-resolution GIS-based multi-criteria decision analysis (MCDA) evaluation of tsunami risk in that region. Earthquake worst case scenarios were considered in the deterministic computation of the tsunami hazard using NAMI DANCE.

2.4. FLOW-3D[®] Applications

FLOW-3D[®] is a general purpose computational fluid dynamics model (CFD), which is a direct descendant of the work on the volume of fluid method (VOF) carried out at the Los Alamos National Laboratory (Hirt and Nichols, 1981). FLOW-3D[®] solves Navier–Stokes equations via the finite difference method (FDM) and utilizes the VOF method for computing free surface motion.

Choi et al. (2007) employed FLOW-3D[®] to simulate wave runup on a conical island, based on the unexpectedly large tsunami runup elevations which had been observed in the circular Babi Island in the 1992 Flores tsunami and in the pear shaped Okushiri Island in the 1993 Okushiri tsunami. They maintained that the results obtained using two- and three-dimensional models were in good agreement with each other as well as the laboratory data of the physical model studies conducted earlier in the Coastal Hydraulic Laboratory, Engineering Research and Development Center, U.S. Army Corps of Engineers by Briggs et al. in 1994. They also closely examined the three-dimensional velocity distribution around the conical island and found that the velocity distribution along the vertical coordinate was not uniform.

Choi et al. (2008) conducted an analytical and numerical analysis of the runup of a solitary wave on a non-plane beach. Before carrying out the numerical analyses using FLOW-3D[®], they applied nonlinear shallow water theory to obtain an analytical solution for a simplified bottom geometry, such as an inclined channel with a parabolic cross-slope shape. After parameters such as water displacement, velocity field and energy dissipation were analysed, it was proven that the existence of a parabolic cross-slope channel on the plane beach led to runup intensification, a phenomenon commonly observed in post-tsunami field surveys.

Bhinder et al. (2009) studied experimental and numerical modeling of a surging point absorber wave energy converter (WEC). After simulating single degree-of-freedom motion of the WEC using FLOW-3D[®], they compared the numerical results with the experimental data. They also tested the ability of the code to simulate free surface linear waves and wave-structure interaction. They concluded that the solver of FLOW-3D[®] was quite sound and efficient in wave modeling.

Basu et al. (2009) assessed the impulse waves generated by the subaerial landslide at Lituya Bay, Alaska by conducting numerical simulations. FLOW-3D[®] software was used in order to track the free surface and shoreline movements. The simulation results were compared with the experimental ones obtained in a physical model of a real case and they were found to be in good agreement with the measured data. It was concluded that the model captured the basic flow properties which were associated with the time-dependent evolution of the flowfield as the landslide interacts with the bay.

Das et al. (2009) studied the tsunami wave generation by submarine and aerial landslides. They used two different numerical tools to simulate the time histories of fluid motion, free surface deformation, shoreline movement and wave runup: FLOW-3D[®] and SPH (Smoothed Particle Hydrodynamics), the latter employing a fully Lagrangian approach. The landslide and subsequent wave generations were modeled with a freely falling wedge in the simulations. The numerical results obtained from both models were compared with the experimental data and good agreement was observed.

Parambath (2010) employed FLOW-3D[®] to quantify the forces acting on an existing wind power unit due to a tsunami bore impact. The applicability of FLOW-3D[®] to these types of problems was evaluated by comparing the results obtained from the numerical simulations with those determined by the small scale laboratory experiments.

Lai et al. (2010) conducted experimental and numerical analyses of wave propagation over a coarse grained sloping beach, in which the wave profile and velocity field were simulated via FLOW-3D[®]. When the numerical results were compared with the experimental ones to examine the validity of the model, it was discovered that wave propagation over a coarse grained sloping beach affected the breaker types in shallow water.

Kim (2012) carried out laboratory scale experiments of tsunami generation by subaerial landslide and integrated them with the numerical simulations. His work focused on the numerical validation of two three-dimensional Navier-Stokes models, namely FLOW-3D[®] and TSUNAMI3D. Three large-scale landslide scenarios were selected from a set of laboratory experiments done by a tsunami research team in Georgia Institute of Technology. The numerical results obtained by both models were found to be reliable, as they had lower error than the allowable errors indicated by the National Tsunami Hazard Mitigation Program.

Chen (2012) employed FLOW-3D[®] to simulate internal solitary wave motion in a density stratified fluid, in which the upper layer is fresh water whereas the lower layer is brine water. Chen (2012) concluded that if FLOW-3D[®] was applied using a very fine grid, the results would provide a better understanding of the internal wave characteristics compared to those of the physical laboratory experiments.

Choi et al. (2012) aimed at quantifying an equivalent resistance coefficient that included the effect of drag caused by buildings and the bottom friction by means of a series of laboratory experiments and three-dimensional numerical simulations with FLOW-3D[®]. A semi-analytical formula for the equivalent resistance coefficient was also developed via momentum analysis. The equivalent resistance coefficient values resulting from the experimental data, the numerical data, and the semi-analytical formula were in good agreement with each other.

Ko et al. (2011) devised the internal wave generation method by applying a mass source, which was proposed by Lin and Liu (1999), into FLOW-3D[®] code. They found that, in comparison to the existing wave-maker scheme, the generated wave profiles of the internal wave-maker were in better agreement with the analytical solutions even though the nonlinearity of wave was increased.

Pelinovsky et al. (2013) cited both the highest wave runup which was recorded at Lhok Nga Twin Peaks after the 2004 Sumatra-Andaman earthquake and the 2011 earthquake, which generated extremely destructive tsunami waves up to 37.9 m in height at the tiny fishery port Koborinai situated north of Miyako City in the Iwate Prefecture. Upon successfully reproducing these extremely large runups of tsunami waves in both cases via FLOW-3D[®], the researchers discovered that the water flow that climbed the coast featured a strong vertical velocity component.

Kim et al. (2013) analysed the coastal behavior of the tsunami at the Lhok Nga Twin Peaks within the framework of fully nonlinear dispersive Reynolds-averaged Navier–Stokes equations via FLOW-3D[®]. The extreme characteristics of the tsunami in the studied coastal area, including the observed overflow through the saddleback between the twin peaks, were reproduced successfully. Thus, it was recommended that three-dimensional non-hydrostatic numerical models be used in order to predict tsunami characteristics on steep coasts and to estimate tsunami risk for such areas.

Kim et al. (2013) worked on the simulation of the extreme runup height of 37.49 m which was observed at the Koborinai Port due to the 2011 East Japan earthquake tsunami. The Princeton Ocean Model was used in the first stage of tsunami propagation (i.e. from the source to the coast) and the wave runup at the Koborinai Port was modeled via FLOW-3D[®]. The researchers recommended that non-hydrostatic numerical models be used in the prediction of tsunami characteristics on steep coasts.

Kim et al. (2015) reproduced the dynamics of extreme runup height, which was measured as 31.7 m at Monai Valley as a result of the 1993 Hokkaidō Nansei-Oki tsunami. They used FLOW-3D[®] in order to investigate the role of diffraction in the extreme runup. The results revealed that the shape and layout of the coast line as well as the diffraction of tsunami waves by the two islands located in front of the valley had led tsunami waves to converge, leading to the extreme runup height.

Wu et al. (2016) focused on the generation of solitary waves in a wave flume using a piston-type wavemaker. They made experimental observations in order to evaluate the stability of the generated solitary waves, defining stability as the generated solitary wave travelling a longer distance without an apparent decay. They discovered that the solitary wave heights were greatly deteriorated owing to the imperfect fitness of wave paddle to the flume. They carried out numerical simulations using FLOW-3D[®] to support their experimental results.

In the light of these studies in the literature, the benchmarking and validation of two- and three-dimensional numerical modeling tools, namely NAMI DANCE and FLOW-3D[®], are carried out and the strengths and weaknesses of these numerical models in the prediction of nearshore long wave behavior are determined. The details are given in the following sections.

CHAPTER 3

THEORETICAL FRAMEWORK OF THE NUMERICAL MODELS

The shallow water equations describe the evolution of *incompressible flow*, neglecting density change along depth. They can be applied to cases where the horizontal scale of the flow is much bigger than the depth of the fluid. Tsunami waves, which have long wave periods and wavelengths, are categorized as shallow water waves, with wavelengths much larger than the water depth. Therefore, tsunami wave motion can be estimated by shallow water models.

The propagation of tsunami waves offshore can be adequately described by linear long wave theory as:

$$\frac{\partial \eta}{\partial t} + \frac{\partial M}{\partial x} + \frac{\partial N}{\partial y} = 0 \quad [3.1]$$

$$\frac{\partial M}{\partial t} + gD \frac{\partial \eta}{\partial x} = 0 \quad [3.2]$$

$$\frac{\partial N}{\partial t} + gD \frac{\partial \eta}{\partial y} = 0 \quad [3.3]$$

where x and y are the horizontal x and y axes in the Cartesian coordinate system, respectively, t is time, η is the free surface elevation, g is gravitational acceleration, M and N are the discharge fluxes on horizontal plane along x and y axes, respectively and D is the total water depth given by $D = d + \eta$.

Linear shallow water equations, which are the simplest form of equations used in tsunami motion prediction, do not contain the nonlinear convective terms. As numerical simulations based on linear theory necessitate a relatively small amount of

computation, they are preferred for the prediction of tsunami wave propagation in deep water. On the other hand, the linear long wave theory is no longer dependable due to the nonlinear conditions in shallower regions because, as tsunami waves approach shallower regions (i.e. to the shoreline), nonlinear effects gain significance. Thus, nonlinear shallow water equations, which include the effects of bottom friction on tsunami wave propagation, are employed to describe tsunami motion in shallow water zones inspite of the difficulties inherent in them. There is ample evidence that the bottom friction term exerts considerable influence on the propagation of tsunami waves in shallow water (Liu et al., 2008) and therefore the nonlinear shallow water theory is regarded as the proper tool to predict nearshore motion of tsunami waves.

3.1. NAMI DANCE

The numerical scheme of NAMI DANCE is given and its capabilities and limitations are explained in detail in the following subsections.

3.1.1. Model Background

Among the many numerical models that have been developed to predict tsunami motion both offshore and nearshore either for academic or operational purposes, one of the TUNAMI models, the tsunami propagation model known as TUNAMI-N2 (Tōhoku University's Numerical Analysis Model for Investigation of Near field tsunamis, No.2) has become prominent. Its source code was developed in the framework of UNESCO Tsunami Inundation Modeling Exchange (TIME) program which has been held in Disaster Control Research Center (DCRC) of Sendai, Japan since 1995. TUNAMI-N2 employs linear theory in deep water, long wave theory in shallow water and runup on land with constant grids (Imamura, 1995). To solve nearshore tsunami motion, TUNAMI-N2 uses the second-order explicit leapfrog finite difference scheme, which supplies a stable solution and shorter computation time in reasonable error limits. In this model, the initial wave development is based on the Okada (1985) calculations for co-seismic tsunamis. The shape of the initial wave and the dynamic inputs of the wave at a specified location in the study domain

can be controlled by the user. The model is developed in Fortran and is used in Windows operating system with Visual Studio interface. TUNAMI-N2 was later modified, improved and registered in U.S., and copyright was granted to Professors Imamura, Yalciner and Synolakis in 2000 (Yalciner et al., 2001; Yalciner et al., 2002; Zaitsev et al., 2002; Yalciner et al., 2003; Kurkin et al., 2003; Zahibo et al., 2003; Yalciner et al., 2004; Yalciner and Pelinovsky, 2007).

NAMI DANCE is a numerical model which serves to simulate tsunami evolution, propagation and inundation. It has been developed by the collaboration of Ocean Engineering Research Center, Middle East Technical University, Turkey, and Special Research Bureau for Automation of Marine Researches, Russia, by scientists Andrey Zaytsev, Ahmet Cevdet Yalciner, Anton Chernov, Efim Pelinovsky and Andrey Kurkin. NAMI DANCE uses C++ programming language and is based on the computational procedures of TUNAMI-N2. The nonlinear forms of long wave equations are solved based on a rectangular structured mesh via NAMI DANCE with respect to related initial and boundary conditions. The solution procedure is a staggered leapfrog scheme. In general, the explicit numerical solution of nonlinear shallow water equations is favoured since the amount of computer time and memory it consumes is reasonable and the results are in acceptable error limits (Velioglu et al., 2016).

NAMI DANCE, which is an improved form of TUNAMI-N2, provides direct simulations in nested domains, allowing the user to select from two coordinate systems (i.e. Cartesian or spherical) and two equation types (i.e. linear or nonlinear shallow water equations) in multiprocessor environments. NAMI DANCE computes maximum and minimum water surface elevations, velocities and directions of wave currents, momentum fluxes and their directions, flow depths, the Froude number and the Rouse number in the study domain. As opposed to TUNAMI-N2, NAMI DANCE has the capability to create the initial wave by using both tsunamigenic rupture parameters of an earthquake and user defined shapes of the initial water surface disturbance. The calculations can be made by using either a static source

inputted as an initial wave or a dynamic source (time history of water surface fluctuation) inputted from an arbitrary location. The model also has the capacity of preparing three-dimensional plots of sea state at selected time intervals by arranging different camera and light positions monitored by the user, and animating the tsunami propagation and inundation in the study domain. The code was modified in order to make the calculations in a multi-processor pattern. In other words, NAMI DANCE performs the numerical calculations by using all the processors of the executed computer in order to increase the simulation speed while reducing the process time.

NAMI DANCE has been subjected to testing via specific benchmark problems commonly used by coastal scientists and it has proved to be reliable and functional. Some of these benchmark problems were introduced in *International Workshops on Long-Wave Runup Models*, which were held on Catalina Island, U.S. in 1991, 1995 and 2004 and funded by National Science Foundation (NSF) (Synolakis, 1991, Synolakis et al., 1995, 2004; Liu et al., 2008). Several tsunami events have been modeled by applying NAMI DANCE in more than 10 institutes worldwide (Zaitsev et al., 2008; Yalciner et al., 2010, 2012).

3.1.2. Numerical Scheme

Navier-Stokes Equations, which are the governing equations in the prediction of fluid motion, form the basis of long wave/shallow water theory (Vreugdenhil, 1994). The tsunami motion computations are mainly based on the shallow water theory (Shuto 1991), in which the vertical motion of water particles is not taken into consideration because of its negligible effect on the pressure distribution. Therefore, the pressure distribution is accepted to be hydrostatic. Given this approximation, necessary dynamic and kinematic conditions are used and the bottom friction terms (for nonlinearity) are included so that the fundamental equations of NAMI DANCE are obtained and are discretized by means of the staggered leapfrog scheme (Velioglu et al., 2016).

Neglecting the vertical motion of water particles, the equations of continuity (conservation of mass) and momentum are given by the following set of equations (Imamura et al., 2006):

The Continuity Equation:

$$\frac{\partial \eta}{\partial t} + \frac{\partial u}{\partial x} + \frac{\partial v}{\partial y} + \frac{\partial w}{\partial z} = 0 \quad [3.4]$$

The Momentum Equations in x , y and z directions:

$$\frac{\partial u}{\partial t} + u \frac{\partial u}{\partial x} + v \frac{\partial u}{\partial y} + w \frac{\partial u}{\partial z} + \frac{1}{\rho} \frac{\partial P}{\partial x} + \frac{1}{\rho} \left(\frac{\partial \tau_{xx}}{\partial x} + \frac{\partial \tau_{xy}}{\partial y} + \frac{\partial \tau_{xz}}{\partial z} \right) = 0 \quad [3.5]$$

$$\frac{\partial v}{\partial t} + u \frac{\partial v}{\partial x} + v \frac{\partial v}{\partial y} + w \frac{\partial v}{\partial z} + \frac{1}{\rho} \frac{\partial P}{\partial y} + \frac{1}{\rho} \left(\frac{\partial \tau_{xy}}{\partial x} + \frac{\partial \tau_{yy}}{\partial y} + \frac{\partial \tau_{yz}}{\partial z} \right) = 0 \quad [3.6]$$

$$g + \frac{1}{\rho} \frac{\partial P}{\partial z} = 0 \quad [3.7]$$

where z is the vertical axis in the Cartesian coordinate system, ρ is the fluid density, P is the pressure, u , v and w are the water particle velocities in x , y and z directions, τ_{ij} is the normal or tangential shear stress in i direction on the j normal plane.

The surface tension force between air-water interface is neglected, which leads to the *dynamic boundary condition at the free surface* given by Equation [3.8]:

$$P = 0 \quad \text{at} \quad z = \eta \quad [3.8]$$

It is accepted that a water particle which is once at the free surface remains at the free surface throughout the motion. This gives the *kinematic boundary condition at the free surface* which is given by Equation [3.9]:

$$w = \frac{\partial \eta}{\partial t} + u \frac{\partial \eta}{\partial x} + v \frac{\partial \eta}{\partial y} \quad \text{at} \quad z = \eta \quad [3.9]$$

The *kinematic boundary condition at the impermeable sea bottom* is given by Equation [3.10]:

$$w = -u \frac{\partial d}{\partial x} - v \frac{\partial d}{\partial y} \quad \text{at} \quad z = -d(x, y) \quad [3.10]$$

where d is water depth. Equation [3.10] equals to zero in case of a flat sea bottom.

When the dynamic boundary condition at the free surface is applied to the equation of momentum in z direction, the hydrostatic pressure distribution is obtained:

$$P = \rho g(\eta - z) \quad [3.11]$$

After integrating Equations [3.4] – [3.7] from sea bed, $-d$, to the free surface, η , using the Leibniz integral rule and applying boundary conditions at the free surface and at the sea bottom, the *two-dimensional* depth-averaged nonlinear shallow water equations including the discharge fluxes are obtained (Imamura et al., 2006):

$$\frac{\partial \eta}{\partial t} + \frac{\partial M}{\partial x} + \frac{\partial N}{\partial y} = 0 \quad [3.12]$$

$$\frac{\partial M}{\partial t} + \frac{\partial}{\partial x} \left(\frac{M^2}{D} \right) + \frac{\partial}{\partial y} \left(\frac{MN}{D} \right) + gD \frac{\partial \eta}{\partial x} + \frac{\tau_x}{\rho} = \dot{A} \left(\frac{\partial^2 M}{\partial x^2} + \frac{\partial^2 M}{\partial y^2} \right) \quad [3.13]$$

$$\frac{\partial N}{\partial t} + \frac{\partial}{\partial x} \left(\frac{MN}{D} \right) + \frac{\partial}{\partial y} \left(\frac{N^2}{D} \right) + gD \frac{\partial \eta}{\partial y} + \frac{\tau_y}{\rho} = \dot{A} \left(\frac{\partial^2 N}{\partial x^2} + \frac{\partial^2 N}{\partial y^2} \right) \quad [3.14]$$

where τ_x and τ_y are the shear stresses in x and y directions, respectively and \dot{A} is the eddy viscosity which is assumed to be constant in space.

In the case of long waves, the horizontal eddy viscosity, \bar{A} , is neglected since its effect is negligible compared to the effect of bottom friction.

The discharge fluxes M and N are defined by:

$$M = \int_{-d}^{\eta} u dz = u(d + \eta) = uD \quad [3.15]$$

$$N = \int_{-d}^{\eta} v dz = v(d + \eta) = vD \quad [3.16]$$

The shear stresses in x and y directions, τ_x and τ_y , for the uniform flow with bottom friction are defined as:

$$\frac{\tau_x}{\rho} = \frac{1}{2g} \frac{f}{D^2} M \sqrt{M^2 + N^2} \quad [3.17]$$

$$\frac{\tau_y}{\rho} = \frac{1}{2g} \frac{f}{D^2} N \sqrt{M^2 + N^2} \quad [3.18]$$

where f is the friction coefficient.

For the bed resistance to flow in open channels, the Manning's roughness coefficient, n , is preferred to be used rather than the friction coefficient, f , in most engineering problems. The use of n has also been adapted to shallow water models. The formula for the relationship between the Manning's roughness coefficient and the friction coefficient is given as:

$$n = \sqrt{\frac{f D^{1/3}}{2g}} \quad [3.19]$$

By substituting Equation [3.19] in Equations [3.17] and [3.18], the shear stress terms are redefined as:

$$\frac{\tau_x}{\rho} = \frac{n^2}{D^{7/3}} M \sqrt{M^2 + N^2} \quad [3.20]$$

$$\frac{\tau_y}{\rho} = \frac{n^2}{D^{7/3}} N \sqrt{M^2 + N^2} \quad [3.21]$$

Equations [3.20] and [3.21] suggest that the bottom friction increases with the fluxes, and is inversely proportional to total depth, causing wave energy to dissipate faster as the wave propagates in shallow water areas.

The values of Manning's roughness coefficient are categorized in Arcement and Schneider (1989) and Chow (1959). Imamura et al. (2006) also propose values for n , given in Table 3.1, for certain types of sea bottom.

Table 3.1 Values of Manning's roughness coefficient, n , for certain types of sea bottom (Imamura et al., 2006)

Bed Material	n
Neat cement, smooth metal	0.010
Rubble masonry	0.017
Smooth earth	0.018
Natural channels in good condition	0.025
Natural channels with stones/weeds/etc.	0.035
Natural channels in poor condition	0.060

However, according to Ven Te Chow (1959), selecting an appropriate n value from those tables is not something tangible: “*To veteran engineers, this means the exercise of sound engineering judgment and experience; for beginners, it can be no more than a guess, and different individuals will obtain different results*”.

The alternative is to determine the value of n from in-situ measurements as explained in French (1985). It must be remembered that either of these methods can pose problems.

Manning's roughness coefficient is entered manually in NAMI DANCE and is chosen as constant for a given condition of sea bottom.

After all the assumptions and substitutions are employed, the nonlinear shallow water equations, which are the fundamental equations of NAMI DANCE, are obtained and given in Equations [3.22] – [3.34] (Imamura et al., 2006):

$$\frac{\partial \eta}{\partial t} + \frac{\partial M}{\partial x} + \frac{\partial N}{\partial y} = 0 \quad [3.22]$$

$$\frac{\partial M}{\partial t} + \frac{\partial}{\partial x} \left(\frac{M^2}{D} \right) + \frac{\partial}{\partial y} \left(\frac{MN}{D} \right) + gD \frac{\partial \eta}{\partial x} + \frac{n^2}{D^{7/3}} M \sqrt{M^2 + N^2} = 0 \quad [3.23]$$

$$\frac{\partial N}{\partial t} + \frac{\partial}{\partial x} \left(\frac{MN}{D} \right) + \frac{\partial}{\partial y} \left(\frac{N^2}{D} \right) + gD \frac{\partial \eta}{\partial y} + \frac{n^2}{D^{7/3}} N \sqrt{M^2 + N^2} = 0 \quad [3.24]$$

NAMI DANCE predicts tsunami wave motion by solving Equations [3.22] – [3.24] simultaneously and by applying proper boundary conditions. Here, it is important to note that Equations [3.22] – [3.24] are *non-dispersive* and valid only in the *Cartesian coordinate* system (i.e. x, y, z).

Equations [3.22] – [3.24] are not the only governing equations of NAMI DANCE. NAMI DANCE also solves *linear shallow water equations*, Equations [3.1] – [3.3], offshore up to 50 meters depth when the simulation area is considerably large, i.e. an entire ocean basin.

NAMI DANCE solves the *non-dispersive linear and nonlinear shallow water equations*. With the *dispersion* term included in Equations [3.22] – [3.24], the nonlinear dispersive shallow water equations – known as the Boussinesq Model – are obtained (Peregrine, 1972). The nonlinear dispersive shallow water equations are given in Equations [3.25] – [3.27]:

$$\frac{\partial \eta}{\partial t} + \frac{\partial M}{\partial x} + \frac{\partial N}{\partial y} = 0 \quad [3.25]$$

$$\frac{\partial M}{\partial t} + \frac{\partial}{\partial x} \left(\frac{M^2}{D} \right) + \frac{\partial}{\partial y} \left(\frac{MN}{D} \right) + gD \frac{\partial \eta}{\partial x} + \frac{\tau_x}{\rho} = \frac{\partial \psi}{\partial x} \quad [3.26]$$

$$\frac{\partial N}{\partial t} + \frac{\partial}{\partial x} \left(\frac{MN}{D} \right) + \frac{\partial}{\partial y} \left(\frac{N^2}{D} \right) + gD \frac{\partial \eta}{\partial y} + \frac{\tau_y}{\rho} = \frac{\partial \psi}{\partial y} \quad [3.27]$$

where ψ is the dispersion potential function defined by (Horrillo et al., 2006):

$$\psi = \frac{d^2}{3} \left(\frac{\partial^2 u}{\partial x \partial t} + \frac{\partial^2 v}{\partial y \partial t} \right) \quad [3.28]$$

Dispersion (i.e. frequency dispersion) is the spreading of energy in the direction of wave advance owing to different wave celerities for wave modes of different lengths. Dispersion tends to be considered negligible for tsunamis, especially if they are earthquake-induced. However, when the tsunami source is narrow or non-seismic, the generated tsunami waves may be short and the dispersion effect can play an important role in the transformation of tsunami waves (Løvholt et al., 2012b). The dispersion of the 2004 Indian Ocean tsunami was significant in the Bengal Bay and Andaman Sea (Ioualalen et al., 2007; Horrillo et al., 2006) and it became more distinct at the transoceanic distances (Glimsdal et al., 2006). Similarly, the dispersion for the long-distance propagation of the 2011 Tōhoku tsunami was apparent (Løvholt et al., 2012b; Grilli et al., 2012). For smaller earthquakes involving shorter length

scales, dispersion is expected to be prominent at shorter wave propagation distances, of which the 2009 Samoa tsunami is a case in point (Zhou et al., 2012).

For transoceanic propagation of tsunamis, the nonlinearity of waves can be neglected because the free surface displacement is much smaller compared to the water depth. However, the dispersion effect should be definitely taken into account (Kim, 2010) since, rather than nonlinear or bottom friction effects, the dispersion effect dominates the transformation of teletsunamis (also called far-field tsunami, trans-ocean tsunami, distant-source tsunami or ocean-wide tsunami). For teletsunamis, the linear Boussinesq equations, which neglect nonlinear effects but include the dispersion effect, can be used as a governing equation. On the other hand, nonlinear and bottom friction effects become more important for the transformation of tsunamis in the near-field (i.e. shallow water) and near coastal areas. In shoaling water, the length-to-depth ratio of a tsunami wave increases and the dispersive effect decreases; meanwhile the amplitude of the wave grows and nonlinear effects dominate. However, nonlinearity leads to the front of the tsunami wave to steepen and, as a result, breaking may occur or dispersive effects may reappear (i.e. development of undular bores) (Glimsdal et al., 2013).

The shallow water theory can be considered as the best option for most aspects of tsunami modeling because of its efficiency, software implementation and good performance. Yet, sometimes a dispersive wave model may be needed. Tsunamis generated by non-seismic sources are often too short to be adequately described by the shallow water theory. Also, a global propagation analysis may require dispersive models even for earthquake generated tsunamis (Løvholt et al., 2010).

In short, the dispersion term gains importance when a wave amplifies near the shore or when waves propagate considerably long distances on the water body.

NAMI DANCE is also capable of predicting tsunami motion in the *spherical coordinate* system (i.e. λ , ϕ , z) by taking into account Earth's curvature and Coriolis force that stems from Earth's rotation. Coriolis force affects the wave amplitude and the arrival time of the first wave in the case of considerably long propagation distances. Therefore, it is more convenient to formulate the nonlinear shallow water equations in the spherical coordinate system for teletsunamis. The *nonlinear dispersive shallow water equations in the spherical coordinate system* are:

$$\frac{\partial \eta}{\partial t} + \frac{1}{R \cos \phi} \left[\frac{\partial M}{\partial \lambda} + \frac{\partial (N \cos \phi)}{\partial \phi} \right] = 0 \quad [3.29]$$

$$\begin{aligned} \frac{\partial M}{\partial t} + \frac{1}{R \cos \phi} \frac{\partial}{\partial \lambda} \left(\frac{M^2}{D} \right) + \frac{1}{R} \frac{\partial}{\partial \phi} \left(\frac{MN}{D} \right) + \frac{gD}{R \cos \phi} \frac{\partial \eta}{\partial \lambda} + \frac{\tau_x}{\rho} = \\ (2\omega \sin \phi)N + \frac{gD}{R \cos \phi} \frac{\partial d}{\partial \lambda} + \frac{1}{R \cos \phi} \frac{\partial D \psi}{\partial \lambda} \end{aligned} \quad [3.30]$$

$$\begin{aligned} \frac{\partial N}{\partial t} + \frac{1}{R \cos \phi} \frac{\partial}{\partial \lambda} \left(\frac{MN}{D} \right) + \frac{1}{R} \frac{\partial}{\partial \phi} \left(\frac{N^2}{D} \right) + \frac{gD}{R} \frac{\partial \eta}{\partial \phi} + \frac{\tau_y}{\rho} = \\ -(2\omega \sin \phi)M + \frac{gD}{R} \frac{\partial d}{\partial \phi} + \frac{1}{R} \frac{\partial D \psi}{\partial \phi} \end{aligned} \quad [3.31]$$

where λ is longitude, ϕ is latitude, z is the vertical axis, R is the Earth radius taken as 6378 km and ω is the angular speed of Earth's rotation taken as 7.27×10^{-5} rad/s.

3.1.3. Solution Technique

The differential equations must be transformed into algebraic form in order to solve them numerically. This transformation is most commonly achieved via the finite difference method. The continuous variables are represented by their values at a finite set of points, and derivatives are approximated by the differences between their values at adjacent points. The study domain is partitioned into several discrete horizontal layers, each of which is divided up into grid cells. Then the variables are evaluated at the center of each cell. In the same way, the time interval under consideration is divided into a finite number of discrete time steps.

NAMI DANCE employs the explicit leapfrog finite difference scheme to solve the nonlinear shallow water equations. Imamura and Goto (1988), in their investigation of different schemes for long wave simulations, showed that the staggered leapfrog scheme is better in terms of numerical accuracy. For the sake of clarity, the numerical scheme is applied to the linear one-dimensional shallow water equations, where dispersion and bottom friction effects are excluded:

$$\frac{\partial \eta}{\partial t} + \frac{\partial M}{\partial x} = 0 \quad [3.32]$$

$$\frac{\partial M}{\partial t} + gD \frac{\partial \eta}{\partial x} = 0 \quad [3.33]$$

The finite difference method based on the Taylor expansion series is as follows:

$$\eta(x, t + \Delta t) = \eta(x, t) + \Delta t \frac{\partial \eta(x, t)}{\partial t} + \frac{\Delta t^2}{2} \frac{\partial^2 \eta(x, t)}{\partial t^2} + \frac{\Delta t^3}{3!} \frac{\partial^3 \eta(x, t)}{\partial t^3} + \dots \quad [3.34]$$

where Δt is the temporal grid interval (or time step).

The *forward* difference scheme is obtained by rearranging Equation [3.34]:

$$\frac{\partial \eta(x, t)}{\partial t} = \frac{\eta(x, t + \Delta t) - \eta(x, t)}{\Delta t} + O(\Delta t) \quad [3.35]$$

where $O(\Delta t)$ is the truncation error in the order of Δt . The truncation error is the difference between the partial derivative and its finite difference representation.

If Δt is replaced by $\Delta t/2$ and $-\Delta t/2$, then the *central* difference scheme with the second order of truncation error is obtained:

$$\frac{\partial \eta(x, t)}{\partial t} = \frac{\eta\left(x, t + \frac{\Delta t}{2}\right) - \eta\left(x, t - \frac{\Delta t}{2}\right)}{\Delta t} + O(\Delta t^2) \quad [3.36]$$

The central difference approximation is superior to the forward difference approximation in terms of truncation error; therefore, the *staggered leapfrog scheme* is applied using the central difference method. The leapfrog scheme provides more accurate results because it increases the calculation points and decreases the truncation error. By applying the staggered leapfrog scheme, Equations [3.32] and [3.33] are discretized as:

$$\frac{1}{\Delta t} (\eta_i^{k+1} - \eta_i^k) + \frac{1}{\Delta x} \left(M_{i+\frac{1}{2}}^{k+\frac{1}{2}} - M_{i-\frac{1}{2}}^{k+\frac{1}{2}} \right) + O(\Delta x^2) = 0 \quad [3.37]$$

$$\frac{1}{\Delta t} \left(M_{i+\frac{1}{2}}^{k+\frac{1}{2}} - M_{i+\frac{1}{2}}^{k-\frac{1}{2}} \right) + g \frac{(D_{i+1}^k - D_i^k)}{2} \frac{1}{\Delta x} (\eta_{i+1}^k - \eta_i^k) + O(\Delta x^2) = 0 \quad [3.38]$$

where Δx is grid size in x direction, Δt is the time step, i is the increment in x direction, and k is the increment in time. The notation $\eta(x, t)$ indicates η_i^k and the notation $M(x, t)$ represents $M_{i+\frac{1}{2}}^{k+\frac{1}{2}}$ in the staggered leapfrog scheme, which is applied using the central difference method. Moreover, the numerical scheme of the total water depth, D , is given as $D_i^k = \eta_i^k + d_i^k$.

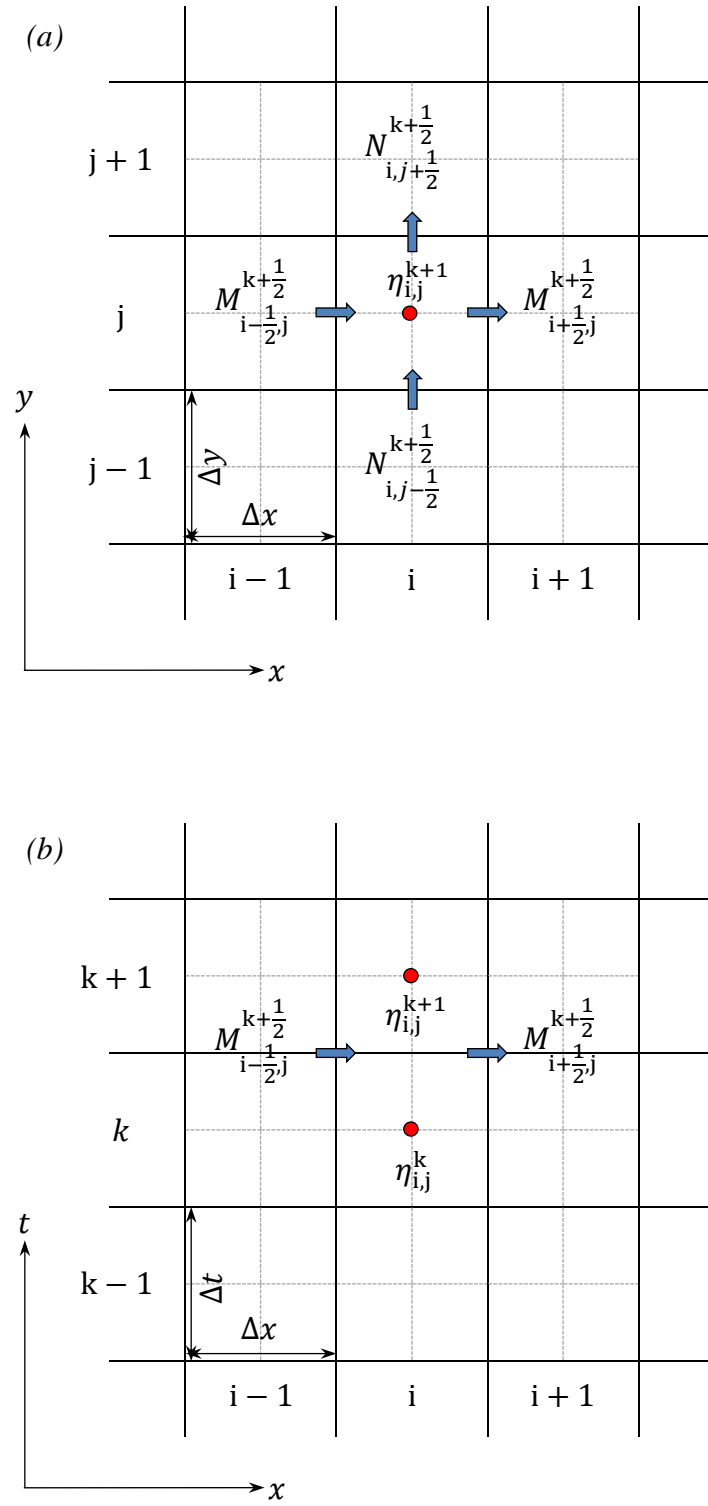


Figure 3.1 Point schematics of staggered leapfrog scheme in (a) space and (b) time (Imamura et al., 2006)

The water elevation, η , is calculated at different grids than the fluxes, M and N , in space and time. For more accurate results, NAMI DANCE calculates the fluxes, M and N , in the half-time and half-space whereas η is computed in one-time and one-space (Figure 3.1).

3.1.4. Initial Conditions

An initial condition is a requirement for the initiation of the iterations in the numerical scheme. NAMI DANCE assumes *no motion* up to time $k - 1$ as an initial condition in the sea:

$$\eta_{i,j}^{k-1} = M_{i+\frac{1}{2},j}^{k-\frac{1}{2}} = N_{i,j+\frac{1}{2}}^{k-\frac{1}{2}} = 0 \quad [3.39]$$

NAMI DANCE accepts the initial water level, η , as equal to the elevation of the ground, h , up to time $k - 1$ as an initial condition for runup computations on land:

$$\eta_{i,j}^{k-1} = -h_{i,j} \quad [3.40]$$

The ground elevation values take a negative sign on land.

3.1.5. Boundary Conditions

The pure sinusoidal motion at the offshore boundary leads to a forced oscillation and reflected waves are not allowed to pass, causing additional water elevations and unreliable predictions. Therefore, the open boundary conditions are used in order to allow reflected waves to pass freely through the boundary.

The total derivative of water surface elevation is constant and given as:

$$\frac{D\eta}{Dt} = \frac{\partial\eta}{\partial t} + u \frac{\partial\eta}{\partial x} + v \frac{\partial\eta}{\partial y} \quad [3.41]$$

When Equation [3.41] is equal to 0 (zero), the boundary is outgoing (open) boundary and when Equation [3.41] is equal to 1.0 (one), it is reflective boundary. For the sake of simplicity, the values of u and v are both accepted as \sqrt{gd} at the boundary. The numerical scheme for the open boundaries is defined as:

$$\frac{\eta_{i,j}^{k+1} - \eta_{i,j}^k}{\Delta t} + \sqrt{gd_{i,j}^k} \frac{\eta_{i+1,j}^k - \eta_{i,j}^k}{\Delta x} + \sqrt{gd_{i,j}^k} \frac{\eta_{i,j+1}^k - \eta_{i,j}^k}{\Delta y} = 0 \quad [3.42]$$

$$\eta_{i,j}^{k+1} = \eta_{i,j}^k - \sqrt{gd_{i,j}^k} (\eta_{i+1,j}^k - \eta_{i,j}^k) \frac{\Delta t}{\Delta x} - \sqrt{gd_{i,j}^k} (\eta_{i,j+1}^k - \eta_{i,j}^k) \frac{\Delta t}{\Delta y} \quad [3.43]$$

The velocity in x direction, u , is omitted at the top and bottom boundaries of the computational domain:

$$\eta_{i,j=1}^{k+1} = \eta_{i,j=jn}^{k+1} = \eta_{i,j}^k - \sqrt{gd_{i,j}^k} (\eta_{i,j+1}^k - \eta_{i,j}^k) \frac{\Delta t}{\Delta y} \quad [3.44]$$

where jn is the number of grids in y direction.

The velocity in y direction, v , is omitted at the top and bottom boundaries of the computational domain:

$$\eta_{i=1,j}^{k+1} = \eta_{i=in,j}^{k+1} = \eta_{i,j}^k - \sqrt{gd_{i,j}^k} (\eta_{i+1,j}^k - \eta_{i,j}^k) \frac{\Delta t}{\Delta x} \quad [3.45]$$

where in is the number of grids in x direction.

Wave runup calculations are carried out by using nonlinear shallow water equations since linearity is not allowed in shallow water zones. The wave front condition is kept under control by defining the condition of each cell in each time step; i.e. the cell is submerged or dry. The flow depth at an arbitrary cell is evaluated as:

$$\begin{aligned}
\text{If } D = d + \eta > 0 & : \text{ the cell is submerged} \\
\text{If } D = d + \eta \leq 0 & : \text{ the cell is dry}
\end{aligned}
\tag{3.46}$$

NAMI DANCE places the wave front between submerged and dry cells. The condition of each cell is determined at half-grids, i.e. at $j + 1/2$ in the staggered leapfrog scheme. Defining the moving boundary conditions on land is difficult. In inundation calculations, when the water level of a cell is higher than the following one, the water moves into the next cell. Otherwise, the discharge is accepted as zero.

3.1.6. Stability

An unexpected divergence in the numerical solution may occur because the selected grid size and/or time step may lead to an instability in numerical simulations. To achieve a stable numerical scheme, errors from various sources (round-off, truncation, etc.) must be prevented from increasing in the sequence of numerical procedures as the calculation proceeds from one marching step to the next. The stability is ensured by employing the Courant-Friedrichs-Lewy (CFL) condition in NAMI DANCE. The numerical speed of the wave, $\Delta x/\Delta t$, has to be equal to or greater than the actual speed passing through each grid at each time step. CFL condition is given as:

$$\frac{\Delta x}{\Delta t} \geq c
\tag{3.47}$$

where c is the wave celerity and $c = \sqrt{gD}$.

NAMI DANCE calculates the largest time step that satisfies the stability condition, Equation [3.47], provided that the bathymetry data of the study domain is inputted. This guarantees stable calculations because it allows the user to select smaller time step values than the suggested one.

3.1.7. Methodology

Study Area

- The study area is determined according to:
 - earthquake and tsunami potential
 - social and economic importance
 - superstructure and infrastructure

Data Acquisition and Processing

- The raw satellite data of the study area is collected from the available sources
- The collected data is analysed and eliminated
- The data is processed and digitized

Bathymetry and Gauge Files

- The required resolution of the study area is determined
- Bathymetric and topographic maps are created in *.xyz format and are converted to *.grd format via available tools
- Gauge file is created in *.txt format

Source File

- Possible tsunami sources are determined based on historical earthquakes
- The most effective source is determined
- The source file is created by implementing:
 - Rupture source input (fault length, fault width, dip angle, etc.)
 - Border source input (time series of water surface fluctuation in *.grd)

Simulation

- Simulation duration, output file time interval and friction coefficient are all inputted in this step
- Initial and boundary conditions are applied; discharge fluxes, wave arrival times and max./min. free surface levels are computed

Post-processing

- Results are visualized: Summary of results, 1D, 2D graphs, inundation mapping, 3D animations, etc.

Figure 3.2 Methodology of modeling via NAMI DANCE

3.2. FLOW-3D®

The following subsections discuss the numerical scheme of FLOW-3D® in detail and explain its capabilities and limitations.

3.2.1. Model Background

FLOW-3D®, which was developed and commercialized by Flow Sciences, Inc., is a general purpose computational fluid dynamics (CFD) software. Flow Sciences, Inc. was founded in Santa Fe, New Mexico U.S. in 1980 by Dr. C. W. (Tony) Hirt. Dr. Hirt was one of the scientists who pioneered in the design of the Volume-of-Fluid (VOF) technique, which was first reported in Nichols and Hirt (1975), and more completely in Hirt and Nichols (1981), during their work at the Los Alamos National Laboratory. FLOW-3D® is a direct descendant of this work.

In the marine environment, the free surface, which represents the interface between the water and the air, particularly interests engineers using CFD to analyse hydrodynamic flows. Simply defined, the free surface is where there is a sharp change at the interface, such as still water. A more complex definition can be made if breaking waves with air entrainment are considered. The fact that the shape and position of the free surface is only known at the initial time, and that its location at later times has to be determined as part of the solution presents the main difficulty in dealing with free surfaces. The methods employed in CFD to resolve the free surface are mostly categorized into two groups: (i) interface tracking and (ii) interface capturing (Maguire, 2011). In the first method, a sharp interface is maintained by following its motion. As the mesh is adapted to the position of the free surface at each time step, one of the boundaries is, by default, the free surface where the boundary conditions are applied. The second method is implemented on a predetermined fixed grid. The three main techniques in this category are Marker-and-Cell (MAC) technique, Level set technique and VOF technique. There are other methods used for tracking the free surface, some of which are Lattice Boltzmann (LBM) method, simple Front tracking and Shock capturing methods.

Harlow and Welch (1965) proposed the Marker-and-Cell (MAC) technique, in which there are massless tracer particles at the free surface and these are tracked throughout the calculation. This technique can resolve nonlinearities. However, especially in three-dimensions, computational high cost is a downside. The level set technique, which is presented by Osher and Sethian (1988), is conceptually simple. The level set function is initially defined in each cell as the distance from the free surface, positive in one direction, negative in the other and zero at the free surface (Figure 3.3). The level set function is easily tracked due to its smooth change across the interface. The implementation of level set technique is relatively easy and accurate under certain conditions. However, in the flow regimes that have high vorticity or significantly deformed interface, it is possible to encounter problems such as loss of mass and/or volume. The third interface tracking technique, which is more efficient than the MAC and level set schemes, is the Volume-of-Fluid (VOF) approach. The VOF technique is implemented in FLOW-3D[®] and can be applied to complex free surfaces and breaking waves (Ferziger and Peric, 1999).

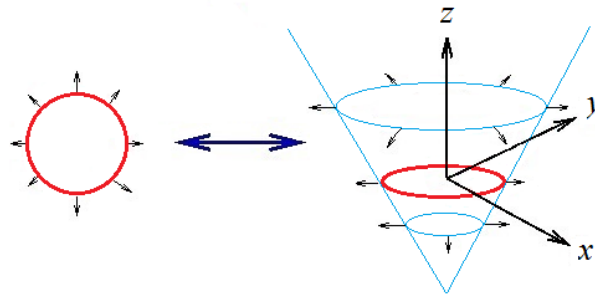


Figure 3.3 The level set function: red line represents the zero level set which is the collection of points that are at height zero (Maguire, 2011).

The VOF technique is made up of three ingredients: a scheme to locate the surface, an algorithm to track the surface, and a means of applying boundary conditions at the surface. This technique works on the principle of recording the fractional portion of the cell volume that is occupied by liquid in each grid cell. The fractional volume is typically represented by a VOF function, $\mathcal{F}(x, y, z, t)$, which has a value between 0 and 1 and satisfies Equation [3.48] in the Cartesian coordinate system:

$$\frac{\partial \mathcal{F}}{\partial t} + \frac{1}{V_F} \left[\frac{\partial}{\partial x} (\mathcal{F} A_x u) + \frac{\partial}{\partial y} (\mathcal{F} A_y v) + \frac{\partial}{\partial z} (\mathcal{F} A_z w) \right] = 0 \quad [3.48]$$

where V_F is the fractional volume open to flow, A_x , A_y and A_z are the fractional areas open to flow in x , y and z directions, respectively.

$\mathcal{F} = 1$ represents the regions full of liquid whereas $\mathcal{F} = 0$ indicates the liquid-free regions (Figure 3.4). There is a free surface where \mathcal{F} changes from 0 to 1, implying that any element with an \mathcal{F} value lying between 0 and 1 has a surface. The VOF method does not directly define a free surface, but rather defines the location of bulk fluid. Therefore, when fluid regions merge or break up, they do not cause computational difficulties.

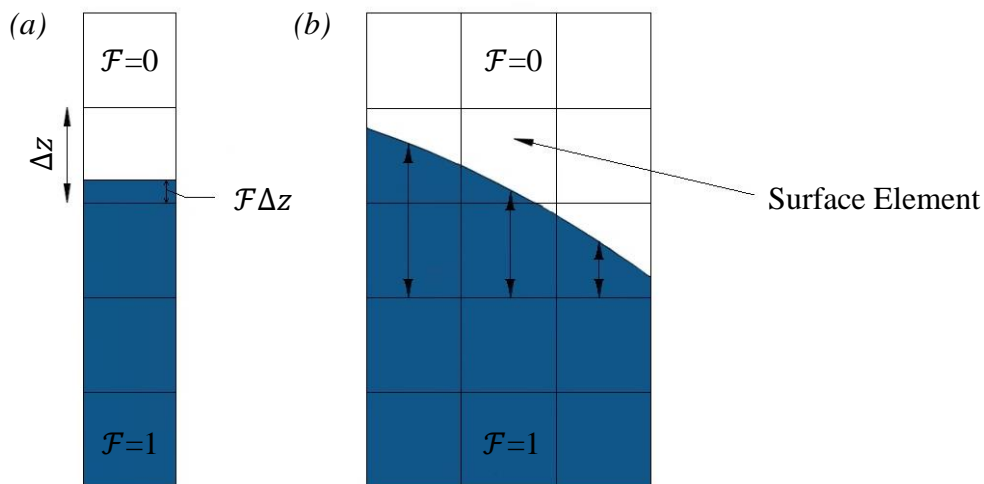


Figure 3.4 Details of the VOF technique: (a) surface in one-dimensional column of elements; (b) surface in two-dimensional grid of elements (Flow Science, 2002)

In recent years, such major improvements beyond the original VOF method have been made in FLOW-3D[®] that the dynamics in void or air regions are not computed, and thus the speed and accuracy of tracking distinct liquid or gas interfaces are increased. The improved form of the original VOF implementation is known as TruVOF[®] method.

FLOW-3D[®] serves to compute free surface motion by means of TruVOF[®] method whereas Fractional Area/Volume Obstacle Representation (FAVOR[™]) technique is used to model complex geometric regions (Hirt and Sicilian, 1985). FAVOR[™] is a unique technique which is used to describe geometric objects in a computational domain within the *rectangular grid*. It works well with complex geometries since it is based on the concept of Area Fraction (AF) and Volume Fraction (VF) methods (Hirt and Sicilian, 1985). Despite being a powerful method, FAVOR[™] is affected by the resolution of the computational grid, like all discrete methods. The geometrical representation is improved with increasing mesh resolution (i.e. decreasing cell size).

FAVOR[™] technique has contributed to the development of the general moving object (GMO) model. In FLOW-3D[®], the GMO model is perceived as a rigid body with any kind of motion that is either user-prescribed or dynamically coupled with fluid flow. It can have six-degrees-of-freedom or be subject to motion constraints such as a fixed axis or fixed point. The GMO model involves multiple rigid bodies under independent motion types as well as rigid body interactions including collisions and continuous contact.

In FLOW-3D[®], the STereoLithography (STL) format is used to represent complex geometries, regardless of the application area – micro fluids, metal casting, water and environmental, aerospace, etc. The STL files are produced using various types of Computer-aided Design (CAD) software. It is also possible to convert small scale bathymetry and/or topography data to STL via online converter tools. The STL format is commonly used by many industries to represent and share 3D; however, in the water and environmental industries surface-driven representations of the environment are favoured. The raster file format known as ESRI ASCII is employed to import the terrain data directly to FLOW-3D[®]. All GIS software packages are able to export the *.asc format.

Surface roughness is a crucial parameter in modeling of flood waves, tsunami inundation, etc. In FLOW-3D[®], with a uniformly rough surface, it is possible to

adopt a constant roughness value; however, with a non-uniform surface, an equivalent roughness value that will supply accurate results must be selected. A local, spatially-varying surface roughness is another choice for modeling surface roughness. This is done by transferring the surface roughness coefficients into FLOW-3D[®] in ESRI ASCII raster format.

When an equivalent roughness value is required, the Manning's roughness coefficient, n , can be converted to the friction coefficient of FLOW-3D[®], f , by:

$$f \cong 3.72067 D_h \exp \left(\frac{-0.103252 D_h^{1/6}}{n} \right) \quad [3.49]$$

where $D_h = 4R_h$ is the hydraulic diameter and R_h is the hydraulic radius and:

$$R_h = \frac{A}{\bar{P}} \quad [3.50]$$

where A is the cross-sectional area of the fluid and \bar{P} is the wetted perimeter.

FLOW-3D[®] defines surface roughness as the average height of uniformly distributed roughness elements and uses Nikuradse equivalent surface roughness, k_s . Nikuradse (1933) measured the velocity profile and pressure drop in smooth and rough pipes and related the friction factor to mean flow velocity and the Reynolds number. It is possible to convert the Nikuradse equivalent surface roughness, k_s , to n using the relation derived by Yen (1991) for wide open channels of impervious rigid boundary:

$$k_s = \left(\frac{n}{0.0389} \right)^6 \quad [3.51]$$

The relation given in Equation [3.51] is a practical tool and used in this dissertation in order to convert the Manning's roughness coefficient values to k_s .

FLOW-3D[®] has a variety of meshing techniques. The simplicity of meshing is attributed to the *structured mesh* that is used by FLOW-3D[®], whereas various features enabled by multi-block meshing provide the efficiency and robustness. Owing to the use of multiple mesh blocks, local refinement in the areas of interest is possible and there is significant reduction in computational resources required for a given simulation. There are several multi-block meshing capabilities such as linked, conforming, nested and/or partially overlapping mesh blocks (Figure 3.5). These can be used to accurately resolve small obstacles, complex geometries and thin channels that are smaller than the overall domain size. Linked mesh blocks serve only to mesh the areas of interest and limit the total number of computational cells. Nested mesh blocks enhance the resolution around an area of interest. Conforming and partially overlapping mesh blocks are employed to resolve irregularly shaped features with sharp changes in scale. These meshing techniques provide users with the flexibility to create simple yet efficient meshes. In this way, solver performance is improved and process time is reduced.

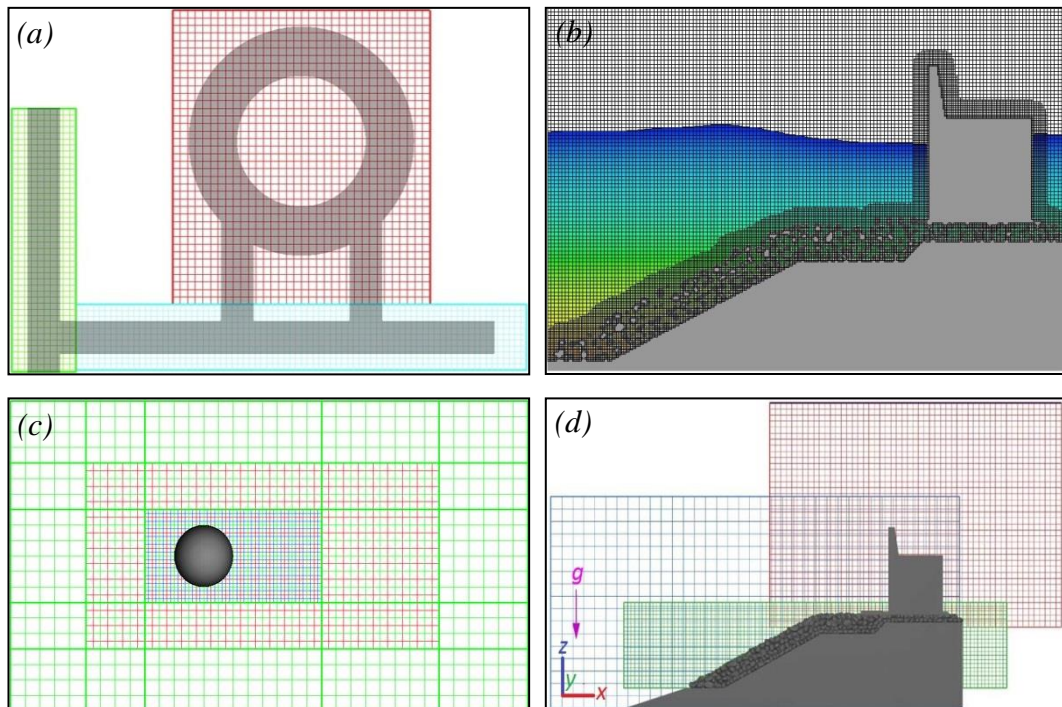


Figure 3.5 FLOW-3D[®] meshing techniques: (a) linked mesh; (b) conforming mesh, (c) nested mesh; (d) partially overlapping mesh (Flow Science, 2002)

FLOW-3D[®] offers a unique hybrid shallow water/3D flow model through which standard shallow water or 3D equations are selected and employed in the computational domain. In other words, FLOW-3D[®] is capable of simulating both 2D shallow water models and 3D models.

With the capacity to simulate multiphysics including fluid-structure interaction, 6-DoF moving objects, and multiphase flow, the FLOW-3D[®] software also simulates incompressible and compressible flows as well as laminar and turbulent flows. A variety of physics models are offered for sediment scour and transport, density stratification and mixing, bubbles and cavitation (i.e. air entrainment), evaporation and phase change, chemical fate and transport and porous media. Municipal hydraulics, river planning and restoration, dam safety, hydroelectric and spillway operations, design, and optimization, reservoir maintenance and planning, and coastal and estuary engineering are among the many applications of FLOW-3D[®], which is currently used in commercial, academic, and government fields.

FlowSight[™] is an advanced visualization tool based on the EnSight[®] post-processor, which is used to post-process and visualize FLOW-3D[®] output data. The tool has capabilities such as analyzing and comparing multiple simulation results simultaneously, volume rendering, defining new variables such as time averages, integrated values, dimensionless parameters, etc., creating multiple, time-varying 2D and 3D animated plots and visualizing the streamlines with moving arrows or cones. Moreover, FlowSight[™] offers an integrated graphing tool which brings an advanced level of analytical ability to general history, diagnostics, and mesh dependent data, as it shows different simulation data comparatively.

FLOW-3D[®], being a CFD model, should be approached cautiously since, like any numerical analysis, CFD is liable to error and uncertainty. The majority of fluid flow processes are satisfactorily described by the Navier-Stokes equations. To obtain a solution in CFD, the governing continuous equations must be replaced with a discrete representation and numerical solutions to these approximate equations will

be available through the use of a computer. Errors are likely to arise in this discretisation process. There will also be errors if the chosen governing equations do not adequately represent the fluid flow of interest. Moreover, the user is bound to make mistakes in the definition of the problem or the analysis and interpretation of the results.

According to the European Research Community on Flow, Turbulence and Combustion (ERCOFTAC, 2002), errors and uncertainty can be caused by seven different sources (Maguire, 2011):

- (i) *Model error and uncertainty*: Defined as being the difference between the real flow and the exact solution of the model equations, modeling errors and uncertainty are caused by solving the wrong equations.
- (ii) *Discretisation or numerical error*: This type of error is defined as the difference between the exact solution of the modeled equations and the numerical solution on a mesh of finite grid points, owing to the use of finite differences to represent exact derivatives. As the number of grid points is increased, the likelihood of this error will decrease and will tend to zero at a rate determined by the order of the numerical method employed.
- (iii) *Iteration or convergence error*: The difference between a fully converged solution on a finite number grid points and a solution that is not fully converged leads to this type of error (MARNET, 2002). These errors could only be avoided if the iterative process was allowed to continue indefinitely, which is not possible since modelers have time constraints and convergence limits are set to tolerances on accuracies.
- (iv) *Round-off error*: This type of error is the difference between the calculated approximation of a number and its exact mathematical value. It is caused by the fact that computers can store a given value only through a limited number of digits, namely 16, 32 and 64 bits.

- (v) *Application uncertainties*: When the problem is complex and can not be defined accurately, these errors may arise. These uncertainties include, but are not limited to, geometry definition, boundary conditions or whether the flow is steady or unsteady.
- (vi) *User errors*: At any stage of the user's interaction with the code (i.e. geometry generation, meshing, pre-processing or post-processing) errors can be made. The more experienced the user, the fewer errors there will be.
- (vii) *Code errors*: Often known as programming errors or bugs, these are unintentional programming errors in the implementation of models or compiler errors on the computer hardware. They can primarily be detected through verification and validation of the code, which often proves to be difficult.

It is obvious that any numerical analysis, particularly CFD, will always be subject to error and uncertainty. Therefore, it is necessary that errors and uncertainty be quantified and error bounds be placed upon the results so as to make sure that the results presented using a numerical model can be trusted.

3.2.2. Numerical Scheme

FLOW-3D[®] solves the fully three-dimensional mass continuity and momentum (Navier–Stokes) equations via the finite difference or finite volume method in the Cartesian coordinate system (x, y, z) to describe fluid motion. For cylindrical coordinates, (r, θ, z) , x -coordinate is interpreted as the radial direction, r , y -coordinate is transformed to the azimuthal coordinate, θ , and z is the axial coordinate. FLOW-3D[®] adds additional terms to Cartesian equations of motion for cylindrical geometry. These terms are included with a coefficient, ξ , such that $\xi = 0$ corresponds to Cartesian geometry, while $\xi = 1$ corresponds to cylindrical geometry.

All equations are formulated with area and volume porosity functions, FAVOR[™] (i.e. obstacles are defined by zero-volume porosity regions). Area and volume fractions are time independent in FLOW-3D[®]. However, these quantities vary with time when the GMO is employed.

The general *mass continuity equation* is given by (Flow Science, 2002):

$$V_F \frac{\partial \rho}{\partial t} + \frac{\partial}{\partial x}(\rho u A_x) + \mathcal{R} \frac{\partial}{\partial y}(\rho v A_y) + \frac{\partial}{\partial z}(\rho w A_z) + \xi \frac{\rho u A_x}{x} = R_{DIF} + R_{SOR} \quad [3.52]$$

where R_{DIF} is a turbulent diffusion term and R_{SOR} is a mass source.

The velocity components (u, v, w) are defined in (x, y, z) or (r, θ, z) coordinate systems. The coefficient \mathcal{R} depends on the coordinate system such that when cylindrical coordinates are used, y derivatives are converted to azimuthal derivatives:

$$\mathcal{R} \frac{\partial}{\partial y} = \frac{1}{r} \frac{\partial}{\partial \theta} \quad [3.53]$$

where $\mathcal{R} = r_m/r$, $y = r_m \theta$ and r_m is a fixed reference radius. In the Cartesian coordinate system, \mathcal{R} is unity and $\xi = 0$.

The turbulent diffusion term, R_{DIF} , is effective for turbulent mixing processes in fluids that have a non-uniform density and is defined as:

$$R_{DIF} = \frac{\partial}{\partial x} \left(\vartheta_\rho A_x \frac{\partial \rho}{\partial x} \right) + \mathcal{R} \frac{\partial}{\partial y} \left(\vartheta_\rho A_y \mathcal{R} \frac{\partial \rho}{\partial y} \right) + \frac{\partial}{\partial z} \left(\vartheta_\rho A_z \frac{\partial \rho}{\partial z} \right) + \xi \frac{\vartheta_\rho A_x}{x} \frac{\partial \rho}{\partial x} \quad [3.54]$$

where ϑ_ρ is a coefficient and $\vartheta_\rho = S_c \mu / \rho$, in which μ is dynamic viscosity and S_c is referred to as the turbulent Schmidt number.

The density source term, R_{SOR} , is commonly employed to model mass injection through porous obstacle surfaces.

Compressible flow problems necessitate the solution of the full density transport equation as stated in Equation [3.52]. For incompressible fluids, ρ is constant and Equation [3.52] reduces to:

$$\frac{\partial}{\partial x} (u A_x) + \mathcal{R} \frac{\partial}{\partial y} (v A_y) + \frac{\partial}{\partial z} (w A_z) + \xi \frac{u A_x}{x} = \frac{R_{SOR}}{\rho} \quad [3.55]$$

The *equations of motion* for the fluid velocity components (u, v, w) in x, y and z directions are the Navier-Stokes equations with some additional terms (Flow Science, 2002):

$$\begin{aligned} \frac{\partial u}{\partial t} + \frac{1}{V_F} \left\{ u A_x \frac{\partial u}{\partial x} + v A_y \mathcal{R} \frac{\partial u}{\partial y} + w A_z \frac{\partial u}{\partial z} \right\} - \xi \frac{A_y v^2}{x V_F} \\ = -\frac{1}{\rho} \frac{\partial P}{\partial x} + G_x + f_x - b_x - \frac{R_{SOR}}{\rho V_F} (u - u_w - \Delta u_s) \end{aligned} \quad [3.56]$$

$$\begin{aligned} \frac{\partial v}{\partial t} + \frac{1}{V_F} \left\{ u A_x \frac{\partial v}{\partial x} + v A_y \mathcal{R} \frac{\partial v}{\partial y} + w A_z \frac{\partial v}{\partial z} \right\} + \xi \frac{A_y u v}{x V_F} \\ = -\frac{1}{\rho} \left(\mathcal{R} \frac{\partial P}{\partial y} \right) + G_y + f_y - b_y - \frac{R_{SOR}}{\rho V_F} (v - v_w - \Delta v_s) \end{aligned} \quad [3.57]$$

$$\begin{aligned} \frac{\partial w}{\partial t} + \frac{1}{V_F} \left\{ u A_x \frac{\partial w}{\partial x} + v A_y \mathcal{R} \frac{\partial w}{\partial y} + w A_z \frac{\partial w}{\partial z} \right\} \\ = -\frac{1}{\rho} \frac{\partial P}{\partial z} + G_z + f_z - b_z - \frac{R_{SOR}}{\rho V_F} (w - w_w - \Delta w_s) \end{aligned} \quad [3.58]$$

where G_x , G_y and G_z are body accelerations, f_x , f_y and f_z are viscous accelerations and b_x , b_y and b_z are the flow losses across porous media in x , y and z directions, respectively. The last terms account for the injection of mass at a source.

The viscous accelerations for a variable dynamic viscosity, μ , are given as:

$$\rho V_F f_x = w_{s_x} - \left\{ \frac{\partial}{\partial x} (A_x \tau_{xx}) + \mathcal{R} \frac{\partial}{\partial y} (A_y \tau_{xy}) + \frac{\partial}{\partial z} (A_z \tau_{xz}) + \frac{\xi}{x} (A_x \tau_{xx} - A_y \tau_{yy}) \right\} \quad [3.59]$$

$$\rho V_F f_y = w_{s_y} - \left\{ \frac{\partial}{\partial x} (A_x \tau_{xy}) + \mathcal{R} \frac{\partial}{\partial y} (A_y \tau_{yy}) + \frac{\partial}{\partial z} (A_z \tau_{yz}) + \frac{\xi}{x} (A_x + A_y \tau_{xy}) \right\} \quad [3.60]$$

$$\rho V_F f_z = w_{s_z} - \left\{ \frac{\partial}{\partial x} (A_x \tau_{xz}) + \mathcal{R} \frac{\partial}{\partial y} (A_y \tau_{yz}) + \frac{\partial}{\partial z} (A_z \tau_{zz}) + \frac{\xi}{x} (A_x \tau_{xz}) \right\} \quad [3.61]$$

where

$$\tau_{xx} = -2\mu \left\{ \frac{\partial u}{\partial x} - \frac{1}{3} \left(\frac{\partial u}{\partial x} + \mathcal{R} \frac{\partial v}{\partial y} + \frac{\partial w}{\partial z} + \frac{\xi u}{x} \right) \right\} \quad [3.62]$$

$$\tau_{yy} = -2\mu \left\{ \mathcal{R} \frac{\partial v}{\partial y} - \frac{1}{3} \left(\frac{\partial u}{\partial x} + \mathcal{R} \frac{\partial v}{\partial y} + \frac{\partial w}{\partial z} + \frac{\xi u}{x} \right) \right\} \quad [3.63]$$

$$\tau_{zz} = -2\mu \left\{ \frac{\partial w}{\partial z} - \frac{1}{3} \left(\frac{\partial u}{\partial x} + \mathcal{R} \frac{\partial v}{\partial y} + \frac{\partial w}{\partial z} + \frac{\xi u}{x} \right) \right\} \quad [3.64]$$

$$\tau_{xy} = -\mu \left\{ \frac{\partial v}{\partial x} + \mathcal{R} \frac{\partial u}{\partial y} - \frac{\xi v}{x} \right\} \quad [3.65]$$

$$\tau_{xz} = -\mu \left\{ \frac{\partial u}{\partial z} + \frac{\partial w}{\partial x} \right\} \quad [3.66]$$

$$\tau_{yz} = -\mu \left\{ \frac{\partial v}{\partial z} + \mathcal{R} \frac{\partial w}{\partial y} \right\} \quad [3.67]$$

The parameters u_w , v_w and w_w represent the velocity of the source component, which is non-zero for a mass source in the GMO model.

The parameters u_s , v_s and w_s represent the fluid velocities at the surface of the source relative to the source itself. $U_s = (u_s, v_s, w_s)$ and it is computed in each control volume as:

$$U_s = \frac{dQ}{\rho Q dA} \vec{n} \quad [3.68]$$

where dQ is the mass flow rate, ρQ is the fluid source density, dA is the area of the source surface in the cell and \vec{n} is the outward vector normal to the surface.

At a *stagnation pressure source*, fluid is assumed to enter the domain at zero velocity. A deflating balloon or fluid that emerges at the end of a rocket are some examples of the stagnation pressure source. At a *static pressure source*, fluid velocity is computed from the mass flow rate and the surface area of the source, which can be illustrated by fluid coming out of a long straight pipe.

Applied to a wide range of fluid flow and heat transfer phenomena, FLOW-3D[®] employs highly specialized numerical techniques to solve the equations of motion for fluids to obtain transient, three-dimensional solutions to multi-scale, multi-physics flow problems.

FLOW-3D[®] is equipped with various types of boundary conditions (i.e. slip/no-slip wall boundary conditions, open boundary conditions, moving solid boundary conditions, incident wave boundary conditions, etc.). This dissertation focuses solely on wave hydrodynamics; thus, in the following sections only the numerical schemes of the wave generation module of FLOW-3D[®] are described.

The wave generation module is used to generate a certain type of wave in the area of interest as an incident wave boundary condition. FLOW-3D[®] is capable of generating periodic linear waves and nonlinear waves such as cnoidal wave, Stokes' wave and solitary wave through its wave generation module (Figure 3.6). It is also possible to integrate the time history of water surface fluctuation data, which is defined by the user, into FLOW-3D[®] as an initial wave profile at the boundary.

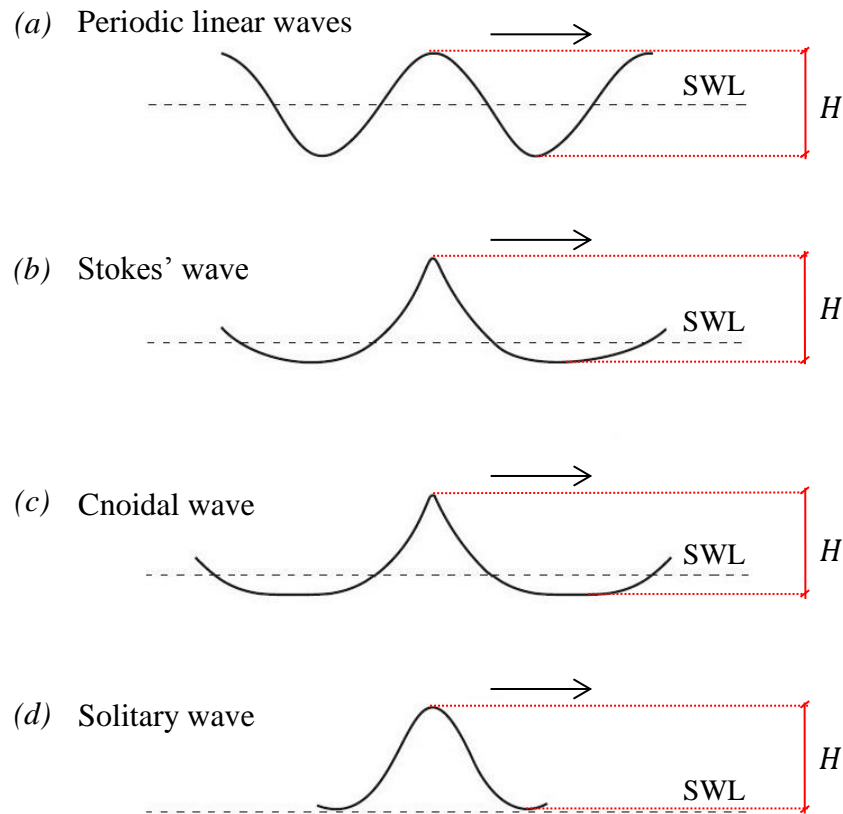


Figure 3.6 Progressive wave types: (a) periodic linear waves; (b) Stokes' wave; (c) cnoidal wave; (d) solitary wave (The vertical dimension is exaggerated.)

In FLOW-3D[®] waves are classified as deep water, intermediate water or shallow water waves according to the water depth and wavelength ratio, d/λ , values which are given in Table 3.2. The applicability ranges for linear wave, Stokes wave and other wave theories are given in Figure 3.7.

Table 3.2 Classification of waves with respect to d/λ

Region	d/λ
Deep Water	$0.50 - \infty$
Intermediate Water	$0.05 - 0.50$
Shallow Water	$0.00 - 0.05$

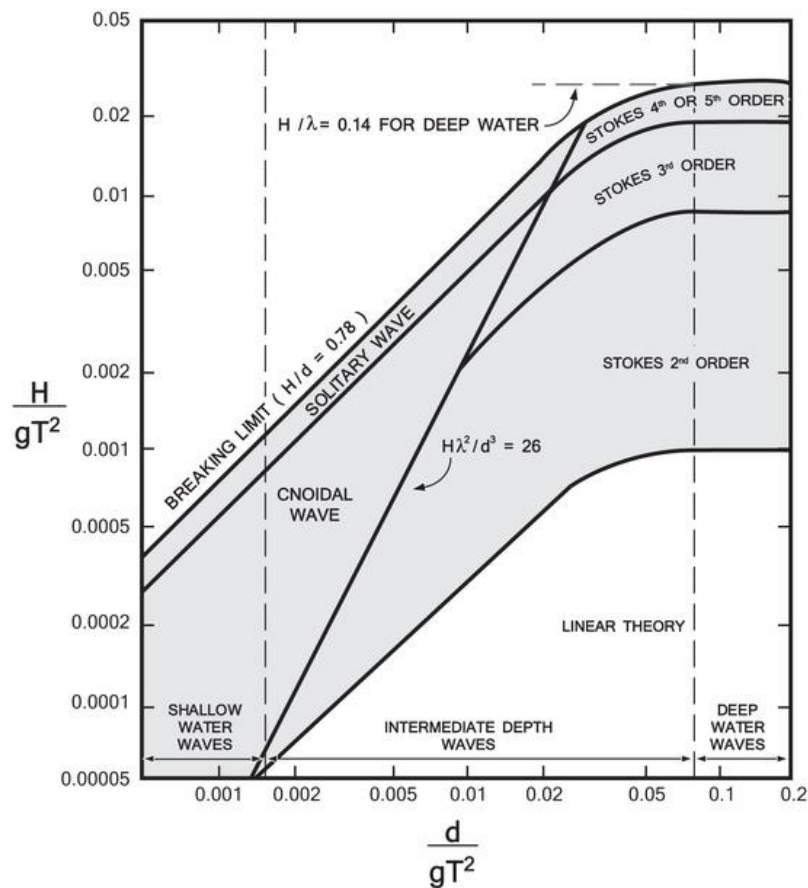


Figure 3.7 Applicability ranges of various wave theories
(U.S. Army Corps of Engineers, 2006)

Waves in FLOW-3D[®] are generated at mesh boundaries. Once a wave enters the computational domain, it is supposed to transform into any type of wave with or without breaking, the bottom does not need to be flat any longer, and flow can be inviscid, laminar or turbulent. The wave may also break inside the computational domain.

The numerical schemes of FLOW-3D[®] that are used to generate linear and nonlinear waves are given in detail in the following subsections.

3.2.2.1. Periodic Linear Waves

The surface profile of a linear wave is sinusoidal, and the amplitude is small compared to the wavelength and fluid depth. A linear wave is characterized by the parameters: (i) wave amplitude, a , (ii) wavelength, λ , (iii) wave period, T , (vi) angular wave frequency, $\omega = 2\pi/T$, and (v) wave number, $k = 2\pi/\lambda$.

The linear wave model of FLOW-3D[®] is based on Airy's (1845) linear wave theory:

$$\eta(x, t) = a \sin(\omega t + \phi) \quad [3.69]$$

where ϕ is the phase shift angle in degrees. The default phase shift is zero, which means at time $t = 0$ the wave elevation is zero and is on the rise.

It is assumed that the linear wave comes from an infinite reservoir which has a flat bottom and assumed to exist outside the computational domain, immediately adjacent to the mesh boundary (Figure 3.8). The generation of the wave at the mesh boundary is based on this assumption.

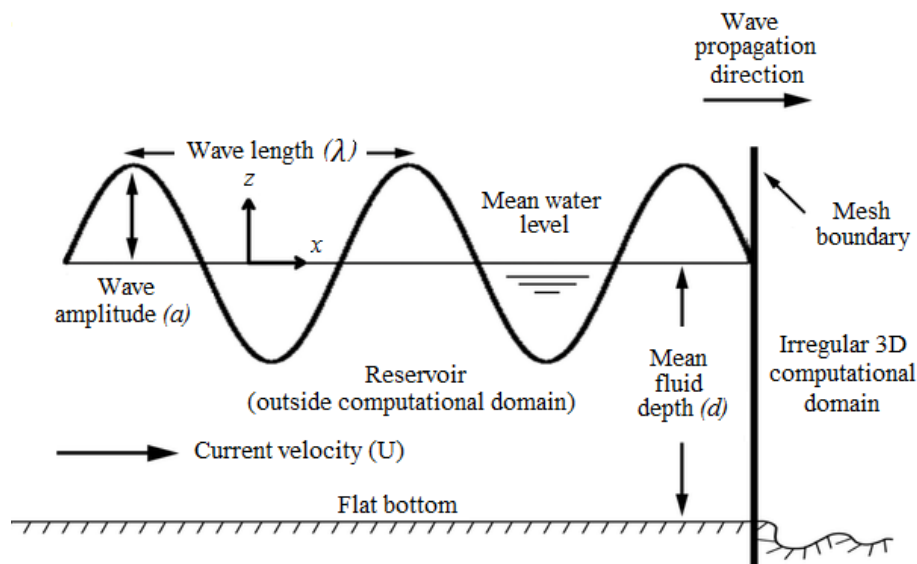


Figure 3.8 Linear waves coming from a flat bottom reservoir into the computational domain (Flow Science, 2002)

FLOW-3D[®] makes the existence of a constant net current, U , (inflow or outflow) in any horizontal direction possible. However, the linear wave solution is valid as long as the current velocity, U , is slower than the wave speed, c . The current is assumed to be uniform across the boundary.

The linear wave theory is based on the following assumptions:

- (i) fluid is incompressible, inviscid and irrotational.
- (ii) flow is two-dimensional.
- (iii) the wave amplitude, a , is small compared to the undisturbed water depth, d , and wavelength λ .

Accordingly, the velocity potential, $\phi(x, z, t)$, and velocity components in x and z directions, $u(x, z, t)$ and $w(x, z, t)$ are obtained as:

$$\phi(x, z, t) = xU + \frac{aw \cosh[k(z + d)] \sin(kx - wt + \phi)}{k \sinh(kd)} \quad [3.70]$$

$$u(x, z, t) = U + \frac{aw \cosh[k(z + d)] \cos(kx - wt + \phi)}{\sinh(kd)} \quad [3.71]$$

$$w(x, z, t) = \frac{aw \cosh[k(z + d)] \sin(kx - wt + \phi)}{\sinh(kd)} \quad [3.72]$$

The dispersion equation in FLOW-3D[®] is given in terms of wave speed, $c = w/k$.

$$(c - U)^2 = \frac{g}{k} \tanh(kd) \quad [3.73]$$

Equation [3.73] indicates that the wave frequency and wavelength are interdependent; given either the wave frequency or wavelength, the other quantity is calculated by the dispersion equation.

3.2.2.2. Stokes' Wave

A Stokes' wave is a nonlinear wave with sharper crests and flatter troughs than a linear wave. FLOW-3D[®] uses either Fenton's Fourier series method or the fifth-order Stokes' wave theory developed by Fenton (1985) to generate Stokes' waves. The former is the favoured Stokes' wave generator due to the higher order accuracy it provides. Unlike the linear wave theory (Airy's theory), the Stokes' wave theory is a nonlinear theory for finite-amplitude progressive surface waves.

Similar to the linear wave, the Stokes' wave is assumed to come from an infinite reservoir with a flat bottom, which is outside the computational domain and immediately adjacent to the mesh boundary (Figure 3.9).

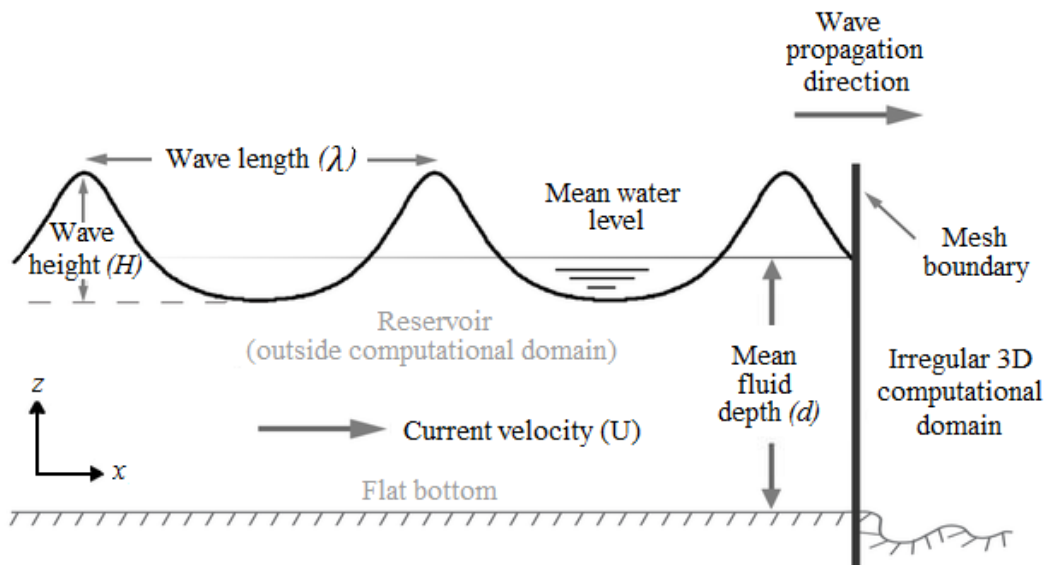


Figure 3.9 Stokes' waves coming from a flat bottom reservoir into the computational domain (Flow Science, 2002)

A Stokes' wave is characterized by: (i) wave height, H , (ii) wavelength, λ and (iii) wave period, T . The free surface elevation, η , is time dependent and measured along z direction from the bottom to the water surface. A constant net current, U , (inflow or outflow) in any horizontal direction is allowed.

The Stokes' wave theory assumes potential flow, namely the fluid flow is incompressible and irrotational. Therefore, the stream function, Ψ , exists and satisfies the Laplace equation:

$$\nabla^2 \Psi = 0 \quad [3.74]$$

The fluid velocity components in x and z directions are given by:

$$u = \frac{\partial \Psi}{\partial x} \quad \text{and} \quad w = -\frac{\partial \Psi}{\partial z} \quad [3.75]$$

With the further assumption that wave crest occurs at $x = 0$ when $t = 0$, and employing the boundary conditions at the free surface and at the sea bed, the Laplace equation for Ψ is solved using a perturbation method. The perturbation parameter is the wave steepness, $\epsilon = kH/2$. The solution for the water elevation and velocity with fifth-order accuracy with respect to ϵ is given as:

$$\begin{aligned} \eta(x, t) = & d + \frac{\epsilon}{k} \cos kX + \frac{\epsilon^2}{k} B_{22} \cos 2kX + \frac{\epsilon^3}{k} B_{31} (\cos kX - \cos 3kX) \\ & + \frac{\epsilon^4}{k} (B_{42} \cos 2kX + B_{44} \cos 4kX) \\ & + \frac{\epsilon^5}{k} [-(B_{53} + B_{55}) \cos kX + B_{53} \cos 3kX + B_{55} \cos 5kX] \end{aligned} \quad [3.76]$$

$$u(x, z, t) = U + C_0 \left(\frac{g}{k^3} \right)^{1/2} \sum_{i=1}^5 \epsilon^i \sum_{j=1}^i A_{ij} jk \cosh jkz \cos jkX \quad [3.77]$$

$$w(x, z, t) = C_0 \left(\frac{g}{k^3} \right)^{1/2} \sum_{i=1}^5 \epsilon^i \sum_{j=1}^i A_{ij} jk \sinh jkz \sin jkX \quad [3.78]$$

where $X = x - ct$ and $kX = kx - wt$. The coefficients A_{ij} , B_{ij} , and C_0 are nonlinear functions of kd presented by Fenton (1985).

The wave number and wave frequency are dependent parameters and satisfy the nonlinear equation:

$$\left(\frac{k}{g}\right)^{1/2} U - \frac{w}{(gk)^{1/2}} + C_0 + \left(\frac{kH}{2}\right)^{1/2} C_2 + \left(\frac{kH}{2}\right)^4 C_4 = 0 \quad [3.79]$$

where C_0 , C_2 and C_4 are nonlinear functions of kd presented by Fenton (1985).

It is not possible to input both wavelength and wave period simultaneously when a wave is generated at the mesh boundary. If the wavelength is given, then the wave period is obtained from Equation [3.79]. If wave period is known, the wavelength is calculated from Equation [3.79] iteratively. The first approximation of k is:

$$k = \frac{\alpha + \beta^2 \operatorname{sech}^2 \beta}{(\tanh \beta + \beta \operatorname{sech}^2 \beta) d} \quad [3.80]$$

where $\alpha = w^2 d / g$ and $\beta = \alpha \sqrt{\coth \alpha}$.

The fifth-order Stokes' wave theory can be applied to waves in both deep and shallow water if: (i) wave steepness is small, (ii) waves do not break, (iii) wavelength is short compared to water depth. The upper limit for wavelength is $(T g / d)^{1/2} \approx \lambda / d \approx 10$ (Fenton, 1985). Beyond this limit, Fenton's Fourier series method is a more reliable way to generate Stokes' waves.

3.2.2.3. Cnoidal Wave

A cnoidal wave is a nonlinear oscillatory wave in shallow water, which has sharper crests and flatter troughs than a Stokes' wave. Fenton's Fourier series method (Fenton, 1999) is employed to generate cnoidal waves in FLOW-3D®.

A steady-state wave train is assumed to exist in a flat-bottom reservoir outside the computational domain, and it propagates into the computational domain through a mesh boundary (Figure 3.10).

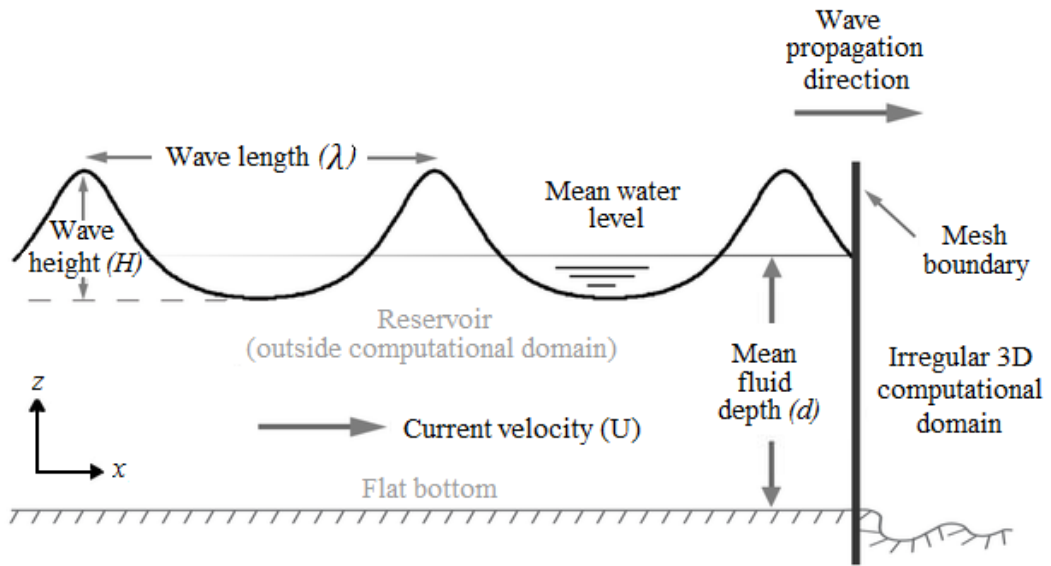


Figure 3.10 Cnoidal waves coming from a flat bottom reservoir into the computational domain (Flow Science, 2002)

A Cnoidal wave is characterized by: (i) wave height, H , (ii) undisturbed water depth, d , (iii) wavelength, λ and (vi) wave period, T . The wavelength, λ and wave period, T are dependent parameters and thus are not inputted at the same time. A constant net current, U , (inflow or outflow) in any horizontal direction may also exist.

At first, the *non-transient* solution of a cnoidal wave is obtained in a *moving reference system* (X, Z) that travels with the wave speed, c . Afterwards, the *transient* solution of the wave in the *stationary system* (x, z) is found through a coordinate transformation. The transformation equations are given as:

$$\text{Coordinate } x = X + ct \text{ and } Z = z \quad [3.81]$$

$$\text{Water velocity } u = U + c \text{ and } w = W \quad [3.82]$$

where u and w denote the x and z components of water velocity in the stationary system (x, z) , respectively; U and W denote the particle velocities in the moving reference system (X, Z) , respectively.

The transformation of constant net current in x direction between the two systems is:

$$U = \bar{U} + c \quad [3.83]$$

where \bar{U} is the constant net current in (X, Z) system.

It is assumed that the flow is incompressible and irrotational. Therefore, the stream function, $\Psi(X, Z)$, exists in (X, Z) system and satisfies the Laplace equation:

$$\nabla^2 \Psi(X, Z) = 0 \quad [3.84]$$

U and W are related to $\Psi(X, Z)$ as:

$$U = \frac{\partial \Psi}{\partial X} \quad \text{and} \quad W = -\frac{\partial \Psi}{\partial Z} \quad [3.85]$$

Two kinematic boundary conditions exist for Equation [3.84]:

$$\Psi(X, 0) = 0 \quad \text{at the sea bed} \quad [3.86]$$

$$\Psi(X, \eta(X)) = Q \quad \text{at the free surface } (Z=\eta(X)) \quad [3.87]$$

where Q is the volume flow rate in X direction per unit length in Y .

The Bernoulli equation at the free surface provides the third and last boundary condition, which is a dynamic boundary condition:

$$\frac{1}{2} \left[\left(\frac{\partial \Psi}{\partial X} \right)^2 + \left(\frac{\partial \Psi}{\partial Z} \right)^2 \right] + |g|\eta = \mathcal{C} \quad \text{at the free surface (Z}=\eta(X)) \quad [3.88]$$

where \mathcal{C} is a constant.

The crest and trough of the wave are assumed to occur at $X = 0$ and $X = \lambda/2$, respectively, and the Fourier series method is applied to represent $\Psi(X, Z)$:

$$\Psi(X, Z) = \bar{U}Z + \sqrt{\frac{g}{k^3}} \sum_{j=1}^N B_j \frac{\sinh jkZ}{\cosh jkd} \cosh jkX \quad [3.89]$$

where B_j ($j = 1, 2, 3, \dots, N$) is a dimensionless coefficient and N is a finite integer.

Equation [3.89] automatically satisfies the Equations [3.84] and [3.86]. Equations [3.87] and [3.88] are solved simultaneously to determine the coefficient B_j . The numerical scheme to solve the problem is described below.

The wave is first divided from $X = 0$ to $X = \lambda/2$ into N equal intervals; having $j = 1, 2, 3, \dots, N + 1$ denote the discrete points. The X coordinate of point n is $X_n = (n - 1)\lambda/(2\lambda)$, which gives $kX_n = (n - 1)\pi/N$. Equation [3.89] is substituted into Equations [3.87] and [3.88] at point n , yielding:

$$\bar{U} \sqrt{\frac{k}{g}} k\eta_n + \sum_{j=1}^N B_j \frac{\sinh jk\eta_n}{\cosh jkd} \cosh jkX_n - Q \sqrt{\frac{k^3}{g}} = 0 \quad [3.90]$$

and

$$\begin{aligned} & \frac{1}{2} \left(U \sqrt{\frac{k}{g}} + \sum_{j=1}^N j B_j \frac{\cosh j k \eta_n}{\cosh j k d} \cosh j k X_n \right)^2 \\ & + \frac{1}{2} \left(\sum_{j=1}^N j B_j \frac{\sinh j k \eta_n}{\cosh j k d} \sinh j k X_n \right)^2 + k \eta_n - \mathcal{C} \frac{k}{g} = 0 \end{aligned} \quad [3.91]$$

Equations [3.90] and [3.91] provide $2N + 2$ nonlinear equations with $2N + 5$ dimensionless variables for $N + 1$ points: (i) $k \eta_n$ for $n = 1, 2, 3, \dots, N + 1$; (ii) B_j for $j = 1, 2, 3, \dots, N$; (iii) $\bar{U} \sqrt{k/g}$; (iv) kd and (v) $\mathcal{C}k/g$.

Three more equations are required to obtain a closed-form solution. The first one employs the trapezoidal rule of integration for the undisturbed water depth, d :

$$\frac{1}{2N} (k \eta_1 + k \eta_{N+1}) + \frac{1}{N} \sum_{n=2}^N k \eta_n - kd = 0 \quad [3.92]$$

The second equation relates the wave height, H and free surface elevation, η :

$$k \eta_1 - k \eta_{N+1} - kd \frac{H}{d} = 0 \quad [3.93]$$

The third and last equation is applicable if the wavelength, λ , is known:

$$kd - 2\pi \frac{d}{\lambda} = 0 \quad [3.94]$$

When the wavelength is unknown, but the wave period, T , is known, Equation [3.94] is replaced by Equation [3.95]:

$$-\sqrt{kd} \bar{U} \sqrt{k/g} + kd \frac{U}{\sqrt{gd}} - \frac{2\pi}{T \sqrt{gd}} = 0 \quad [3.95]$$

The known variables are H , d , U and either λ or T . There are $2N + 5$ unknown dimensionless variables for $2N + 5$ nonlinear equations, providing a closed-form solution. The nonlinear equations are iteratively solved using Newton's method. The transient fluid velocity in the stationary system (x, z) is calculated via Equations [3.96] – [3.99] after the unknown variables are determined.

$$u(x, z, t) = U + \sqrt{\frac{g}{k}} \sum_{j=1}^N jB_j \frac{\cosh jkz}{\cosh jkd} \cosh jk(x - ct) \quad [3.96]$$

$$w(x, z, t) = \sqrt{\frac{g}{k}} \sum_{j=1}^N jB_j \frac{\sinh jkz}{\cosh jkd} \sinh jk(x - ct) \quad [3.97]$$

$$\eta(x, t) = \frac{E_1}{2} + \sum_{j=2}^{N+1} E_j \cos[(j - 1)k(x - ct)] \quad [3.98]$$

E_j is calculated by numerical integration for $j = 1, 2, 3, \dots, N + 1$:

$$E_j = \frac{2}{N} \prod_{n=1}^{N+1} \eta_n \cos \frac{(j - 1)(n - 1)\pi}{N} \quad [3.99]$$

where \prod represents a trapezoidal-type summation.

3.2.2.4. Random Wave

FLOW-3D[®] treats a random wave as the superposition of many linear component waves of different amplitudes, periods and initial phases. The wave amplitudes are calculated using wave energy spectrum. FLOW-3D[®] is equipped with two internally defined energy spectra: *Pierson-Moskowitz (P-M) spectrum* (Pierson and Moskowitz, 1964) and *JONSWAP spectrum* (Hasselmann et al., 1973). The wind speed 10 m above the sea level has to be provided for both spectrums. The *fetch length* and *peak enhancement factor* are necessary parameters to be defined for JONSWAP spectrum. The default value of the peak enhancement factor is 3.3. The wave energy spectrum can also be defined using an external data file.

The wave components initially exist in a flat-bottom reservoir and propagate simultaneously into the computational domain through the mesh boundary. Their water elevations and velocities at the mesh boundary are summed up respectively whereby the boundary condition for the random wave simulation is obtained. Water elevation of the random wave is expressed as:

$$\eta = \sum_{j=1}^N a_j \cos(k_j x - w_j t + \phi_j) \quad [3.100]$$

The wave energy spectrum, $E(w)$, is used to calculate the parameters of the component waves. The range of the angular frequency, w , is divided equally into N intervals, each of which represents a linear wave component and w_j is the mid-point value of w in the j^{th} interval. a_j is calculated as:

$$a_j = 2E(w_j)\Delta w \quad [3.101]$$

for $j = 1, 2, 3, \dots, N$ where Δw is the w interval.

k_j is calculated using the dispersion equation for linear waves because it is a function of ϕ_i and d and the component waves are linear. ϕ_i is a real number which is randomly selected between 0 and $2/\pi$.

FLOW-3D[®] automatically generates 1000 linear component waves at the wave boundary for a random wave simulation (i.e. $N = 1000$) The wave periods are evenly distributed between 0.2 sec. and 2.0 sec.

The *Pierson-Moskowitz (P-M) spectrum* can be applied in fully developed sea conditions with a sufficiently large fetch length and sufficiently long wind duration. The only necessary parameter is the wind speed. The P-M spectrum is given by:

$$E(w) = \frac{\delta g^2}{w^5} \exp \left[-\frac{5}{4} \left(\frac{w_p}{w} \right)^4 \right] \quad [3.102]$$

where $w_p = 0.855g/U_{10}$ is the angular frequency at the spectrum peak, U_{10} is the wind speed 10 m above the sea level and $\delta = 0.0081$ is the scaling parameter.

The *JONSWAP spectrum* is applicable for fetch-limited conditions. It is given by:

$$E(w) = \frac{\delta g^2}{w^5} \exp \left[-\frac{5}{4} \left(\frac{w_p}{w} \right)^4 \right] \gamma^{\exp \left[-\frac{(w-w_p)^2}{2\Theta^2 w_p^2} \right]} \quad [3.103]$$

where $w_p = 22[g^2/(U_{10} F)]^{1/3}$, F is the fetch length, $\delta = 0.076[U_{10}^2/(Fg)]^{0.22}$, γ is the peak enhancement factor and $1 \leq \gamma \leq 7$, $\Theta = 0.07$ for $w \leq w_p$ and $\Theta = 0.09$ for $w \geq w_p$.

3.2.2.5. Solitary Wave

A solitary wave is a nonlinear non-oscillatory wave which has a single crest and no trough and is completely above the undisturbed water level. A tsunami wave is often defined by a solitary wave in numerical simulations. FLOW-3D® attributes the solitary wave solution to McCowan's theory (McCowan, 1891), which has a higher order accuracy than Boussinesq's theory (Boussinesq, 1871) and is recommended by Munk (Munk, 1949).

The solitary wave solution is derived for an infinite reservoir with a flat bottom, which is assumed to exist outside the computational domain and immediately adjacent to the mesh boundary. The solitary wave is initially located outside the computational domain. By default, *the initial distance from the crest to the wave boundary is one half of the wavelength* (Figure 3.11). FLOW-3D® defines the wavelength of a solitary wave as the extent of the wave in its propagation direction, which is measured between two points at opposite sides of the crest where the surface displacement is 1% of the wave height.

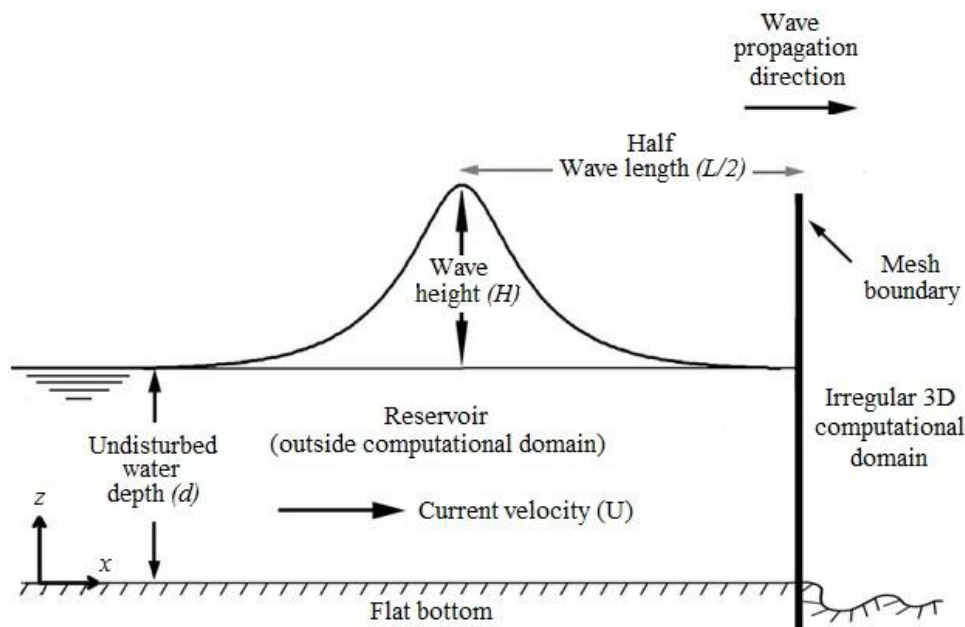


Figure 3.11 Solitary wave coming from a flat bottom reservoir into the computational domain (Flow Science, 2002)

In the solitary wave model, a constant net current, U , can exist in any horizontal direction at the wave boundary if the current is slower than the speed of the solitary wave. U is accepted to be uniform across the boundary.

The equations to determine water elevation, η , x -velocity, u , z -velocity, w , and wave speed, c are (Munk ,1949):

$$\frac{\eta}{d} = \frac{\mathcal{N}}{\mathcal{M}} \frac{\sin \left[\mathcal{M} \left(1 + \frac{\eta}{d} \right) \right]}{\cos \left[\mathcal{M} \left(1 + \frac{\eta}{d} \right) \right] + \cosh \left(\mathcal{M} \frac{X}{d} \right)} \quad [3.104]$$

$$\frac{u(x, z, t) - U}{c_0} = \mathcal{N} \frac{1 + \cos \left(\frac{\mathcal{M}z}{d} \right) \cosh \left(\frac{\mathcal{M}X}{d} \right)}{\left[\cos \left(\frac{\mathcal{M}z}{d} \right) \cosh \left(\frac{\mathcal{M}X}{d} \right) \right]^2} \quad [3.105]$$

$$\frac{w(x, z, t)}{c_0} = \mathcal{N} \frac{\sin \left(\frac{\mathcal{M}z}{d} \right) \sinh \left(\frac{\mathcal{M}X}{d} \right)}{\left[\cos \left(\frac{\mathcal{M}z}{d} \right) \cosh \left(\frac{\mathcal{M}X}{d} \right) \right]^2} \quad [3.106]$$

where $c_0 = \sqrt{g(d + H)}$ is the wave speed in still water, $c = c_0 + U$ and $X = x - ct$.

\mathcal{M} and \mathcal{N} satisfy:

$$\varepsilon = \frac{\mathcal{N}}{\mathcal{M}} \tan \left[\frac{1}{2} \mathcal{M} (1 + \varepsilon) \right] \quad [3.107]$$

$$\mathcal{N} = \frac{2}{3} \sin^2 \left[\mathcal{M} \left(1 + \frac{2}{3} \varepsilon \right) \right] \quad [3.108]$$

where $\varepsilon = H/d$.

Equations [3.104] – [3.108] are nonlinear and are solved via Newton-Raphson method. The initial estimates of \mathcal{M} and \mathcal{N} are $\mathcal{M} = \sqrt{3\varepsilon}$ and $\mathcal{N} = 2\varepsilon$. The initial estimate of η is the Boussinesq's solution for solitary waves:

$$\frac{\eta}{d} = \varepsilon \operatorname{sech}^2 \left(\sqrt{\frac{3\varepsilon X}{4d}} \right) \quad [3.109]$$

3.2.3. Solution Technique

The fluid flow takes place over a continuous region or continuum, where the fluid equations of motion, Navier-Stokes equations, apply. However, continuous governing partial differential equations can not be solved by computers. Therefore, the continuum has to be discretised into finite spatial and temporal elements. There are various techniques used to discretise the governing equations but they all aim to turn a calculus problem into an algebraic one. Some of the methods employed to discretise the spatial volumes are: (i) finite difference, (ii) finite volume and (iii) finite element. The discretisation methods involve a variety of schemes such as: (i) central schemes, (ii) flux vector splitting scheme, (iii) flux difference splitting scheme, (iv) upwind scheme, (v) Essentially Non-Oscillatory (ENO) scheme and (vi) Weighted ENO (WENO) scheme. The equations are discretised upon: (i) a structured and/or (ii) an unstructured mesh.

A computational mesh is the numerical space that replaces the physical one and it forms the basis of a numerical model. It serves to define the flow parameters at discrete locations, set boundary conditions and develop numerical approximations for the fluid motion equations. A computational mesh is composed of a number of interconnected elements, or cells. The cells subdivide the physical space into small volumes with several nodes that are used to store values of the unknowns, such as pressure, temperature and/or velocity.

In FLOW-3D[®], the flow domain is divided into a grid of rectangular cells, called brick elements. The computational cells are numbered in a consecutive manner using three indices: i in x -direction, j in y -direction and k in z -direction.

The finite difference and finite volume methods, which are the core methods of FLOW-3D[®], are used to deal with the numerical approaches. The finite difference method (FDM) is based on the properties of the Taylor expansion, which is one of the oldest methods used to solve differential equations. Euler (1768) is believed to have developed the first application of the Taylor expansion; a first-order numerical procedure for solving ordinary differential equations with a given initial value. On the other hand, as the finite volume method (FVM) is derived directly from the *integral form* of the conservation laws for fluid motion, it already possesses the conservation properties. In brief, in FDM, the partial derivatives of the governing equations are replaced with a Taylor expansion representation following each node, whereas in FVM, the governing equations are integrated over a volume (i.e. cells).

Fluid velocities and pressures are located at staggered mesh locations: u and A_x are located at the centers of cell faces normal to x -direction, v and A_y are located at the centers of cell faces normal to y -direction and w and A_z are located at the centers of cell faces normal to z -direction. Pressures, P , fluid fractions, F , fractional volumes, V_F , densities, ρ , internal energy, I , turbulence quantities for energy, q , dissipation, \mathcal{D} , and viscosity, μ , are all located at cell centers (Figure 3.12).

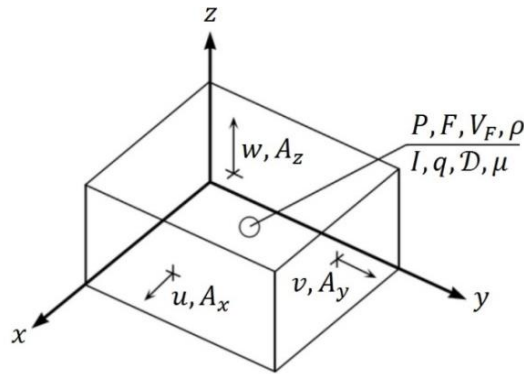


Figure 3.12 Location of variables in a mesh cell (Flow Science, 2002)

A solution is advanced through one increment in time, Δt , in three steps:

- (i) The initial values of the new time-level velocities are computed via explicit approximations of the momentum equations, Equations [3.56] – [3.58].
- (ii) The pressures are iteratively adjusted in each cell to satisfy the continuity equation, Equation [3.52] or Equation [3.55], and the velocity changes induced by each pressure change are added to the velocities computed in Step (1).
- (iii) When there is a free-surface or fluid interface, it is updated using the VOF function so that the new fluid configuration is determined. For compressible fluid problems, density and energy are updated in order to reflect advective, diffusive, and source processes. Turbulence quantities and wall temperatures are also updated.

A solution can be advanced through any desired time interval by repeating these steps. At each step, of course, suitable boundary conditions have to be imposed at all mesh, obstacle, and free-boundary surfaces.

The general forms for the finite difference approximation of momentum equations are given below:

$$u_{i,j,k}^{n+1} = u_{i,j,k}^n + \Delta t^{n+1} \left[-\frac{P_{i+1,j,k}^{n+1} - P_{i,j,k}^{n+1}}{(\rho\Delta x)_{i+\frac{1}{2},j,k}^n} + G_x - FUX - FUY - FUZ \right. \\ \left. + VISX - BX - WSHX \right] \quad [3.110]$$

$$v_{i,j,k}^{n+1} = v_{i,j,k}^n + \Delta t^{n+1} \left[-\frac{P_{i,j,k+1}^{n+1} - P_{i,j,k}^{n+1}}{(\rho\Delta y)_{i,j,k+\frac{1}{2}}^n} \mathcal{R}_{i+\frac{1}{2}} + G_y - FVX - FVY - FVZ \right. \\ \left. + VISY - BY - WSHY \right] \quad [3.111]$$

$$w_{i,j,k}^{n+1} = w_{i,j,k}^n + \Delta t^{n+1} \left[-\frac{P_{i,j,k+1}^{n+1} - p_{i,j,k}^{n+1}}{(\rho\Delta z)_{i,j,k+\frac{1}{2}}^n} + G_z - FWX - FWY - FWZ \right. \\ \left. + VISZ - BZ - WSHZ \right] \quad [3.112]$$

where FUX , FUY and FUZ are the advective fluxes of u , v and w , $VISX$, $VISY$ and $VISZ$ are the x , y and z components of viscous acceleration, BX , BY and BZ are the flow loss for a baffle normal to x , y and z directions and $WSHX$, $WSHY$ and $WSHZ$ are the viscous wall accelerations in x , y and z directions. G_x , G_y and G_z terms include gravitational, rotational, and general non-inertial accelerations in x , y and z directions, respectively and

$$(\rho\Delta x)_{i+\frac{1}{2},j,k}^n = \frac{\rho_{i,j,k}^n\Delta x_i + \rho_{i+1,j,k}^n\Delta x_{i+1}}{2}$$

and

$$\mathcal{R}_{i+\frac{1}{2}} = \begin{cases} 1.0 & \text{Cartesian coordinate system} \\ \frac{x_{max}}{\frac{1}{2}(x_i + x_{i+1})} & \text{cylindrical coordinates} \end{cases}$$

The simplest finite difference approximation that FLOW-3D[®] uses is the *first-order* centered difference scheme, which is simple and computationally stable.

In some cases; however, the cost of using the mesh resolution necessary for an accurate first-order solution can be too high. This can be avoided by employing a *second-order* accurate approximation for the advective and viscous accelerations. This algorithm is the most CPU intensive.

The other *higher order* finite difference scheme is a second-order, monotonicity-preserving upwind-difference method (Van Leer, 1977). This scheme is derived by using second-order polynomial approximations of the advected quantity in each of the coordinate directions (Bronisz and Hirt, 1991).

To illustrate the higher-order method, the flux passing through a cell-face for a variable Q advected in x direction, Q^* , is given:

$$Q^* = Q_i + \frac{1}{2} \mathcal{A}(1 - 2C)\Delta x_i \quad [3.113]$$

where Q_i is the cell-centered value, C is the Courant number and Δx_i is cell size. Coefficient \mathcal{A} is computed from two neighboring first derivatives using linear interpolation, provided the derivatives are second-order accurate. Equation [3.114] is the second-order accurate first derivative of Q at the point between Q_i and Q_{i+1} :

$$\frac{dQ}{dx_{i+\frac{1}{2}}} = 2 \frac{Q_{i+1} - Q_i}{\Delta x_{i+1} + \Delta x_i} \quad [3.114]$$

To ensure monotonicity (Van Leer, 1977):

$$\mathcal{A} \leq 2 \min \left(\frac{dQ}{dx_i}, \frac{dQ}{dx_{i+1}} \right) \quad [3.115]$$

If the two centered derivatives appearing in Equation [3.115] are of opposite sign, then \mathcal{A} is set to zero and the first-order finite difference approximation is used.

3.2.4. Initial Conditions

The initial state of the solution (i.e. at time $t = 0$) for transient fluid flow problems has to be known in order to obtain a solution. The accuracy of the initial conditions is not as important as that of the boundary conditions because their effect is diminished as time progresses. Due to this effect, it can be assumed that the pressure and velocity fields are uniform. This typically produces good results within a relatively short time where the solution is affected by physical initial conditions. Initial conditions in FLOW-3D[®] are defined at a global scale or in more localized regions.

Each problem that is modeled using FLOW-3D[®] has different solution techniques and thus various initial conditions. The solitary wave motion is the primary focus here, since solitary waves are the numerical representations of tsunami waves. The initial conditions used to solve the solitary wave motion, Equations [3.104] – [3.108], are given in Section 3.2.2.5. Furthermore, it is also possible to define wave motion as an initial condition. The wave is allowed to initially exist throughout the computational domain in order to shorten the computation time to reach steady wave motion. To achieve this, the initial wave elevation and/or fluid velocity are generated by using external data.

3.2.5. Boundary Conditions

The equations that govern the motion of fluid flow are in the category of initial and boundary value problems, which means that the solution at the boundaries has to be known at the initial time in order to solve the problem. The solution of the governing partial differential equations inside the domain are based on the initial and boundary conditions, which implies that the solution of the problem is fundamentally defined by what is assumed at the boundaries.

In FLOW-3D[®], the appropriate boundary condition(s) are automatically applied to components depending on the component type and active physical model(s). However, the boundary conditions on the faces of the mesh block (i.e. x_{\min} , x_{\max} , y_{\min} , y_{\max} , z_{\min} and z_{\max}) have to be set manually for each mesh block. It is possible to set a variety of conditions using the layer of fictitious cells surrounding the mesh (i.e. the boundary separating the $i=1$ and $i=2$ layer of cells). The $i=1$ cells are regarded as fictitious because variable values are set, not calculated, in these cells to satisfy the boundary conditions. FLOW-3D[®] has ten different boundary conditions:

Wall Boundary Condition: When a boundary condition is to reflect the properties of a rigid wall, the normal velocity is taken as zero and the tangential velocity is set to any value for a no-slip type of wall. The wall boundary conditions are:

$$\begin{aligned}
u_{1,j,k} &= 0 \\
P_{1,j,k} &= P_{2,j,k} \\
\rho_{1,j,k} &= \rho_{2,j,k}
\end{aligned}
\tag{3.116}$$

Continuative Boundary Condition: A continuative boundary condition is made up of zero normal derivatives at the boundary for all quantities. The zero derivative condition represents a smooth continuation of the flow through the boundary. The continuative boundary condition does not have a physical basis. It is a mathematical statement that may or may not provide the desired flow behavior, especially for low speed or incompressible flows. As a general rule, it is essential that a physically meaningful boundary condition (i.e. a specified pressure condition) be used at outflow boundaries whenever possible. When a continuative condition is used, it should be placed as far as possible from the main flow region so that the adverse effects on the main flow are reduced.

The continuative boundary conditions used at the $i = 1$ layer are the vanishing *normal derivatives of*:

$$\begin{aligned}
u_{1,j,k} &= u_{2,j,k} \\
v_{1,j,k} &= v_{2,j,k} \\
w_{1,j,k} &= w_{2,j,k} \\
P_{1,j,k} &= P_{2,j,k} \\
\rho_{1,j,k} &= \rho_{2,j,k}
\end{aligned}
\tag{3.117}$$

When the direction of the flow is *out of* the computational domain, the conditions given in Equation [3.117] are valid. If the flow direction is *into* the computational domain, then all the conditions given by Equation [3.117] are applied except for the normal velocity component, which is set to zero to make the inward flow more difficult.

Outflow Boundary Condition: A boundary condition that allows outgoing waves to smoothly leave the computational mesh with minimum reflection must be employed for wave propagation problems. FLOW-3D[®] uses the radiation boundary condition, which was originally proposed by Sommerfeld (1912) for mathematical physics, later revised by Orlanski (1976) for hydraulic flow and implemented in FLOW-3D[®] by Hirt (1999). The Sommerfeld radiation boundary condition is a simple mathematical continuation that has the form of outgoing waves (Hirt, 1999):

$$\frac{\partial Q}{\partial t} + c \frac{\partial Q}{\partial x} = 0 \quad [3.118]$$

where Q is a dependent physical quantity, $+x$ points out of the boundary and c is the local phase speed of the assumed wavelike flow.

Equation [3.118] states that any flow quantity, Q , at the boundary translates across the boundary with speed, c . When there is no time variation, Equation [3.118] is reduced to *continuative boundary condition* of zero normal derivative.

The second-order difference approximation (i.e. in space and time) of Equation [3.118] is given below in terms of x_{\max} (maximum x boundary) of the computational region (Hirt, 1999):

$$\frac{1}{2}(q_i^{n+1} - q_i^n) + \frac{1}{2}(q_{i-1}^{n+1} - q_{i-1}^n) + \frac{c\Delta t}{\Delta x} \left[\frac{1}{2}(q_i^{n+1} - q_{i-1}^{n+1}) + \frac{1}{2}(q_i^n - q_{i-1}^n) \right] = 0 \quad [3.119]$$

where i is the index of the spatial location on the boundary where a value of some quantity q is required. The first two terms of Equation [3.119] are the time derivatives centered about $n + 1/2$. One term is at location i and the other at $i - 1$, so their average is centered about $x = i - 1/2$. The last term contains an average of two x derivatives centered about $i - 1/2$ at times n and $n + 1$. This term is also centered about $i - 1/2$ and $n + 1/2$. It should be noted that the grid spacing, Δx , and time interval, Δt are assumed to be constant. Rearranging Equation [3.119]:

$$q_i^{n+1} = q_{i-1}^n + \frac{1-C}{1+C} (q_i^n - q_{i-1}^{n+1}) \quad [3.120]$$

where $C = c\Delta t/\Delta x$ is the non-dimensional phase speed.

The i index is shifted one node to the left to solve for C :

$$\frac{1-C}{1+C} = \frac{q_{i-1}^{n+1} - q_{i-2}^n}{q_{i-1}^n - q_{i-2}^{n+1}} \quad [3.121]$$

Substituting Equation [3.121] into Equation [3.120] gives the needed boundary value for q_i^{n+1} (Hirt, 1999).

There are two cases that limit the use of Equation [3.121]: (i) the value of C has to be positive since only the outgoing waves are considered and the incoming flow has to be suppressed, and (ii) the value of C has to be less than or equal to unity to ensure the computational stability (i.e. $0 \leq C \leq 1$).

Symmetry Boundary Condition: A symmetry boundary condition imposes free-slip conditions by setting all velocity derivatives to zero (zero-gradient condition) at the boundary. Moreover, the velocity normal to the boundary is taken as zero.

Specified Pressure Boundary Condition: FLOW-3D[®] has the capability of specifying a pressure condition at one or more boundaries of a computational region. In general, a pressure condition does not apply in the case of a boundary where velocities are also specified since velocities are influenced by pressure gradients.

The two types of pressure conditions are *static* or *stagnation pressure conditions*. When the pressure is static, it is continuous across the boundary and the velocity at the boundary is assigned a value based on a zero normal-derivative condition. However, if a stagnation pressure condition exists outside the boundary, the upstream

velocity at the boundary is zero and the pressure drops across the boundary for the flow to enter the computational region. The stagnation pressure condition is generally more physical and yields more specific results than the static pressure condition; therefore, it is recommended for most applications.

The case of the flow of a fluid in a pipe section illustrates the differences between these two conditions clearly. If the upstream end of the computational region corresponds to the physical entrance to the pipe, it is necessary to use a stagnation condition to approximate the conditions of a large reservoir of stationary fluid. On the other hand, if the upstream boundary of the computing region is inside the pipe, and away from the entrance, then the static pressure condition would be a more reasonable representation.

Volume Flow Rate Boundary Condition: At a specified volume flow rate boundary, the flow rate at the boundary has to be indicated.

Specified Velocity Boundary Condition: At a fixed velocity boundary, the normal velocity and the tangential velocities (i.e. u , v and w) at the boundary have to be specified. It should be noted that scalar quantities are defined at the centers of the boundary cells which are half a cell away from the actual mesh boundary location, and this affects the gradients of the tangential velocities at all open mesh boundaries. The normal boundary velocities are always set at the edge of the boundary.

Periodic Boundary Condition: Periodic boundaries are applied in pairs and, in each pair, any fluid that leaves through one boundary is reintroduced through the other boundary. That is, the conditions at both $i = 1$ and $i = IMAX$ layers have to be set to reflect the periodicity. The conditions for periodic flow in the x direction at $i = 1$ for all j , k are:

$$\begin{aligned}
u_{1,j,k} &= u_{IM2,j,k} \\
v_{1,j,k} &= v_{IM2,j,k} \\
w_{1,j,k} &= w_{IM2,j,k} \\
\rho_{1,j,k} &= \rho_{IM2,j,k}
\end{aligned}
\tag{3.122}$$

for all j, k:

$$\begin{aligned}
u_{IM1,j,k} &= u_{2,j,k} \\
v_{IM1,j,k} &= v_{2,j,k} \\
w_{IM1,j,k} &= w_{2,j,k} \\
P_{IM1,j,k} &= P_{2,j,k} \\
v_{IMAX,j,k} &= v_{3,j,k} \\
w_{IMAX,j,k} &= w_{3,j,k} \\
\rho_{IMAX,j,k} &= \rho_{3,j,k}
\end{aligned}
\tag{3.123}$$

where $IM1 = IMAX - 1$ and $IM2 = IMAX - 2$.

Wave Boundary Condition: The wave boundary condition is applied at the boundary in order to create the velocity field associated with the requested wave type. It collaborates with the wave generator module of FLOW-3D[®], which is given in detail in the subsections of Section 3.2.2.

Grid Overlay Boundary Condition: The function of the Grid Overlay (GO) boundary condition is to apply restart data from the source simulation to set flow parameters at the boundary. The boundary flow, which is fixed throughout the restart simulation, serves to determine the flow parameters.

3.2.6. Stability

Numerical stability can be maintained by observing the restrictions on the time step size in FLOW-3D®. The time step size is automatically adjusted so that it is as large as possible without exceeding any of the stability limits, affecting accuracy, or unnecessarily increasing the effort required to enforce the continuity condition. The time step size is also reduced when pressure and/or temperature iterations are greater than the corresponding nominal values depending on the iteration options. The automatic time step selection should be favoured whenever possible to achieve optimum results.

Time steps can also be specified manually. However, in this case, time steps satisfying the basic stability condition given in Equation [3.124] have to be selected.

$$\Delta t < CON * \min \left(\frac{V_F \Delta x_i}{A_x u}, \frac{V_F \Delta y_j}{\mathcal{R}_i A_y v}, \frac{V_F \Delta z_k}{A_z w} \right) \quad [3.124]$$

where CON is the stability factor. $CON = 0.45$ is typically used to account for a simplified stability analysis. For compressible flow applications, the factor is reduced to $CON = 0.25$.

The time step size stability condition regarding the propagation of surface waves is that these waves should not propagate more than one cell in one time step. If z is the normal direction to the surface and G_z is the acceleration in z direction, then:

$$\Delta t < \frac{\sqrt{V_F}}{2G_z \Delta z_k \left(\frac{A_x}{x_i^2} \max \left(1, \frac{\Delta x_i}{\Delta z_k} \right) + \frac{A_y \mathcal{R}_i^2}{y_j^2} \max \left(1, \frac{\Delta y_j}{\mathcal{R}_i \Delta z_k} \right) \right)} \quad [3.125]$$

Similar limits have to be imposed in x and y directions for each cell that contains a free-surface.

In the case of shallow water flows, the time step stability limit is controlled by the surface wave speed, which is readily evaluated from the depth of the fluid, $F\Delta z$, where F is the fluid fraction in the cell.

$$\Delta t < 0.5 \frac{\min \left\{ \Delta x_i, \frac{\Delta y_j}{\mathcal{R}_i} \right\}}{\sqrt{F\Delta z_k G_z}} \quad [3.126]$$

3.2.7. Methodology

FLOW-3D[®] is a Computational Fluid Dynamics (CFD) software. The governing equations for fluid flows (the conservation of mass, momentum, and energy) that are subject to the prescribed initial and boundary conditions in up to three dimensions are most commonly solved through CFD modeling.

If a CFD model fails to represent the actual phenomenon accurately, the results will be biased and unrealistic. Therefore, it essential that the actual physical situation and the capabilities of the CFD model be assessed carefully by taking the following issues into consideration (Maguire, 2011):

- Information/data required from the calculation
- The scale and the mesh design needed to capture important phenomena
- The boundary condition(s) that best represent the actual physical situation
- The kinds of fluids to be used
- The fluid properties which are important for the problem
- Important physical phenomena
- The initial fluid state
- The system of units to be used

Evaluating the strengths and weaknesses of CFD is also crucial. CFD is an excellent analysis option when:

- Standard engineering calculations do not suffice because of the complexity of the geometry, physics, or the required level of detail.
- Physical experiments are costly.
- Information about the flow that can be gathered from an experiment is insufficient.
- Accurate experimental measurements are difficult to obtain owing to dangerous or hostile conditions, processes that do not scale well, etc.

CFD is less effective when:

- The variations in the scales of interest are unmanagable because solutions require:
 - (i) significant computational resources
 - (ii) assumptions to reduce the domain size
 - (iii) semi-empirical models to account for unresolved physical phenomena.
- The important physical phenomena are unknown.
- The physical phenomena are poorly understood or extremely complex because the governing equations tend to be semi-empirical or have limited ranges of applicability.

Domain Selection and Data Acquisition/Processing

- The study area is determined according to the purpose of the model
- The physical features of the study domain are reviewed
- Satellite data is collected from the available sources
- The collected data are analysed and eliminated
- The eliminated data is digitized

Bathymetric and Topographic Map Preparation

- Bathymetric and topographic maps in required resolution(s) are created in *.xyz format after digitization
- The map data is converted from *.xyz format to *.STL or *.asc format using the available tools

Model Setup

- A workspace is created in FLOW-3D[®]
- The relevant physical mechanisms (i.e. shallow water, turbulence, gravity, viscosity, surface tension, etc.) are defined according to the type of the problem so that additional terms are substituted into the governing equations during the simulation
- Fluid properties such as density, temperature, etc. are defined
- The map geometry file (STL and/or ASC) is inputted as a component
- Component properties are defined if needed; i.e. porosity, surface roughness, thermal conductivity, etc.
- The mesh is created and mesh properties are adjusted
- Boundary conditions are applied at each face of the mesh block
- Initial conditions for the fluid are determined, i.e. the initial fluid elevation, temperature, velocities, pressure distribution, etc.

Post-processing

- The output data is selected: Restart Data (the default FLOW-3D[®] output data set) or Selected Data (the user-defined output data set)
- The results are visualized using FlowSight[™]: 1D, 2D, 3D plots, probe polts, animations, text outputs, graphs, etc.

Figure 3.13 Methodology of modeling via FLOW-3D[®]

CHAPTER 4

BENCHMARKING

According to many researchers, verification and validation are the two phases of analysis that a numerical code should be subjected to in assessing the quality of a CFD model. (Roache, 1998; AIAA, 1998; Ferziger and Peric, 1999; Freitas, 2002; MARNET, 2002; Celik et al., 2008; Oberkampf and Roy, 2010; Maguire, 2011). These two terms are synonyms in common use, yet they have quite different meanings in the field of numerical modeling. The shorthand reference to these two terms is V&V.

Broadly defined (AIAA, 1998):

Verification is the process of determining that a model implementation accurately represents the developer's conceptual description of the model and its solution.

Validation is the process of determining the degree to which a model is an accurate representation of the real world from the perspective of the intended model use.

Blottner (1989) defines the terms as follows:

Verification is the process of solving the equations right.

Validation is the process of solving the right equations.

Synolakis et al. (2007) define *validation* as the process of ensuring that the model solves the parent equations of motion accurately, and *verification* as the process of assuring that the model represents geophysical reality appropriately.

The aim of verification is not to endorse the physical or mathematical model, but to identify and quantify the errors in the model implementation and the solution as it is only concerned with mathematics. Validation, on the other hand, deals with the deviations of the numerical model predictions from the physical reality. Its objective

is to make sure that the governing mathematical equations represent the physical reality accurately.

For the prediction of tsunami currents, forces and runup on coastal structures, and inundation of coastlines, the numerical computation of the evolution of a tsunami wave from the deep ocean to its target has to be conducted (Synolakis et al., 2007). In the development of a numerical model, validation and verification processes are the most essential parts. In order to conduct the process of verification and validation, the numerical model is subjected to a series of benchmark tests which are regarded to be valid by the scientific community. There are three categories of benchmarking of numerical models: (i) analytical benchmarking, (ii) experimental benchmarking and (iii) field benchmarking.

Analytical benchmarking: Analytical solutions are practical and useful because complex numerical models used in realistic applications can be validated via exact solutions and, more importantly, the dependence of desired results (i.e. runup) on the problem parameters (i.e. deep water wave height, beach slope, depth variation, etc.) can be identified efficiently by means of analytical benchmarking. Systematic errors can be identified through comparisons of numerical predictions with analytical solutions, as when friction factors or dissipative terms are used to supplement the idealized equations of motion.

Laboratory benchmarking: Before numerical codes were available, small scale physical models were employed to visualize wave phenomena in the laboratory to make predictions, which were then scaled to the prototype. Currently, the function of scale model tests is to confirm different flow details and validate the numerical models used in the analysis. The scale differences are considered to be insignificant for the validation of tsunami inundation models. If predictions from a numerical code agree well with the measurements from small scale laboratory experiments, it is expected that the code will also model geophysical scale tsunamis well.

The bottom friction characteristics of scale models are not generally similar to those of ocean floors or sandy beaches, but this is not considered as a severe limitation. In tsunami modeling, friction gains importance only in cases of extreme inundation; however, the predictions may not be sensitive to the first order even with numerical codes that use friction factors within reasonable limits (Synolakis et al., 2007).

Field benchmarking: Verification of a model using the real world data is essential for model validation, especially for operational models. Analytical and laboratory data comparisons can not guarantee robust model performance in the operational environment; however, test comparisons with the real world data can, which is an important step in the validation process.

Testing a tsunami model against real world events poses a challenge because it is difficult to overcome the uncertainties of the tsunami source. In a controlled laboratory setup, the source is deterministic and can be reproduced precisely, whereas in the numerical computation of a prototype tsunami, the initialization is less constrained (Synolakis et al., 2008). A better agreement between the model predictions and observations can be obtained by introducing ad hoc amplification factors in standard source solutions (Okada, 1985). Yet, at present, as more DART (Deep-ocean Assessment and Reporting of Tsunamis) buoys, namely tsunamographs, are being deployed, such methods are becoming obsolete. The most accurate (unambiguous) data quantifying the source of a tsunami are obtained from deep ocean measurements (Bernard et al., 2006). This has been illustrated by Wei et al. (2008).

It is not possible to obtain numerical results that exactly match the benchmark data owing to the approximations incorporated during the formulation of the numerical scheme. Particularly for field benchmarking, additional issues arise due to the uncertainties in the tsunami source and in the topography where wave runup and inundation are observed. Therefore, relating the numerical results and benchmark data within a statistical framework is a reasonable way to assess the capability of

numerical models. National Oceanic and Atmospheric Administration (NOAA) introduces different types of statistical errors to determine the correlation between the calculated values, y_i , and observed (analytical/experimental/field) values, $f(x_i)$. The most common two statistical errors are: (i) the Normalized Root Mean Square Error (NRMSE) and (ii) the error of the maximum value (MAX).

NRMSE is a tool used to assess the overall model performance, which is the accuracy of a numerical model in predicting the entire set of observed data. NRMSE is valid when applied within a space segment or time period to all observed data points. The interval of numerical and observed data sets has to be the same in the selected time or space segment.

The NRMSE approach is based on the assumption that the error is normally distributed with no bias; therefore, it is not an indicator of under-prediction or over-prediction.

NRMSE is formulated as:

$$\text{NRMSE} = \frac{1}{f(x_i)_{\max} - f(x_i)_{\min}} \sqrt{\frac{\sum (f(x_i) - y_i)^2}{n}} \quad [4.1]$$

where $f(x_i)$ and y_i represent the observed and predicted data, respectively and the difference between the maximum and minimum values of the observed data is used for normalization.

The highest wave in a tsunami wave train is usually the first or second one, and n is the number of the observed points obtained within an arbitrary space segment or time period. Therefore, NRMSE is time or space dependent and sensitive to phase lags in the predicted values and it mainly serves to assess the overall model performance.

MAX error, which is a relative error based on the maximum magnitude of the observed values, is employed to quantify the predictive accuracy of a numerical model for the maximum value regardless of time or location:

$$\text{MAX} = \frac{|f(x_i)_{\max} - y_{i\max}|}{f(x_i)_{\max}} \quad [4.2]$$

The NOAA Technical Memorandum OAR-PMEL-135 standard introduces the most recent allowable error limits (Synolakis et al., 2007) (Table 4.1). The selected benchmark problems in this dissertation represent all the categories of the reference data used to assess the numerical models: (i) analytical solutions, (ii) laboratory experiments and (iii) field measurements. The allowable errors vary according to the types of reference data and the tested parameter (i.e. wave amplitude, current velocity, runup, etc.). These threshold values may be subject to change and it may be necessary to update them according to future studies.

Table 4.1 Allowable error limits for model validation/verification according to OAR-PMEL-135 standard (Synolakis et al., 2007)

Category	Tested Parameter		OAR PMEL-135 Allowable Error	
	NRMSE	MAX	% NRMSE	% MAX
Analytical Solutions	Water level time history/water level in the selected data segment	Runup or max./min. free surface elevation	10	5
Laboratory Experiments	Water level time history/water level in the selected data segment	Runup or max./min. free surface elevation	15	10
Field Measurements	Water level time history/water level in the selected data segment	Runup or max./min. free surface elevation	25	20
Analytical Solutions	Velocity time history/velocity in the selected data segment	Max./min velocity	10	25
Laboratory Experiments	Velocity time history/velocity in the selected data segment	Max./min velocity	15	25

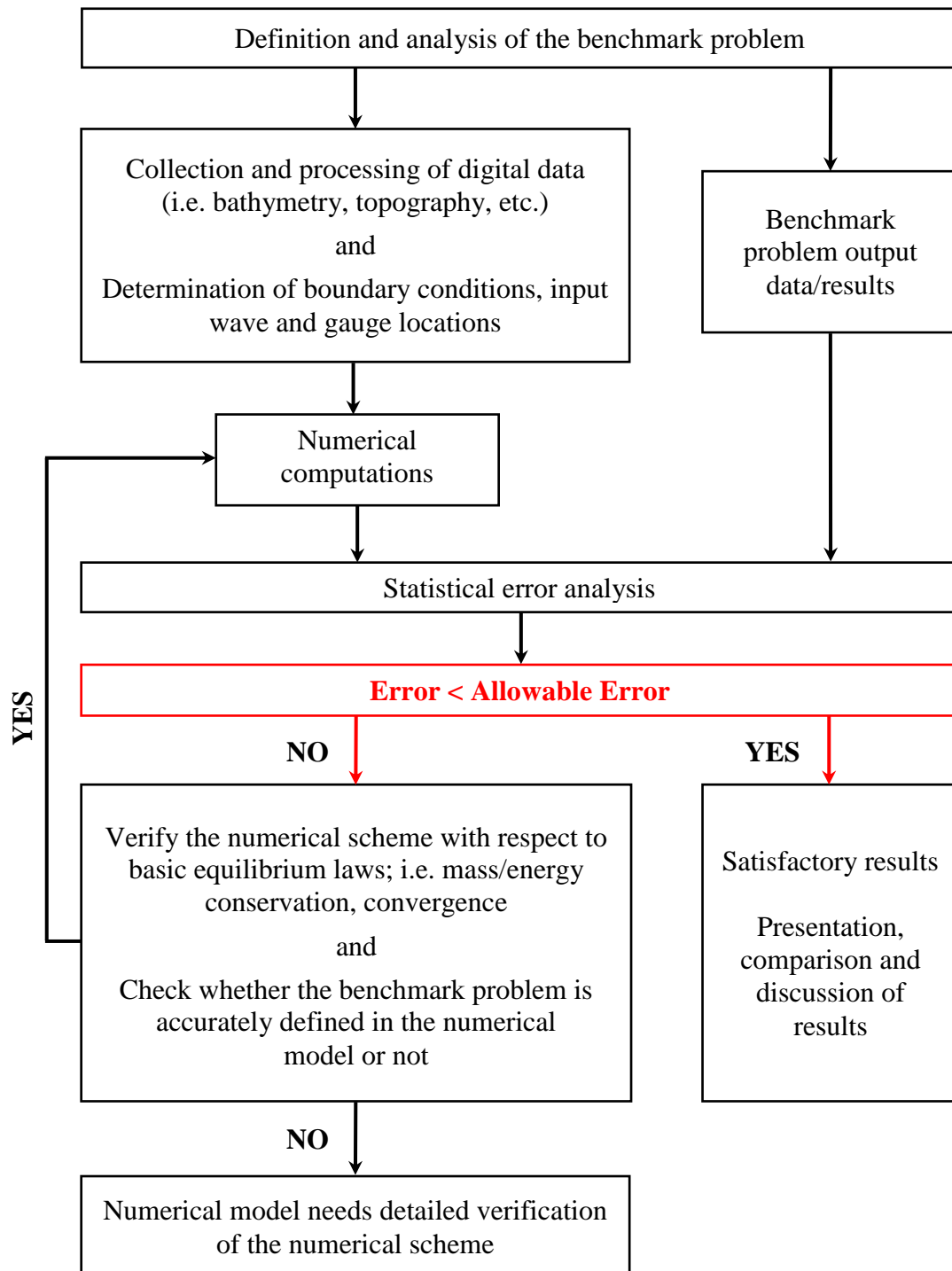


Figure 4.1 The procedure of testing a numerical model via benchmarking

4.1. BMP 1: Solitary Wave Runup on a Simple Beach

4.1.1. Problem Description

A solitary wave is a localized gravity wave that maintains its integrity through nonlinear hydrodynamics. Solitary waves have finite amplitude and propagate with constant speed and shape. They are commonly used to model tsunamis, especially in experimental and mathematical studies (Madsen et al., 2008). They also comprise a good model for extreme design waves of coastal structures because they have the largest energy, impulse, and runup (Grilli et al., 1994).

John Scott Russell, a Scottish engineer and a naval architect, was the first person to observe a solitary wave in shallow water. Russell (1845) saw a form of a large solitary elevation, a rounded, smooth and well-defined heap of water, in a narrow channel, when a boat rapidly drawn along this channel by a pair of horses was abruptly stopped. The solitary elevation did not change its form or speed during its course along the channel (Figure 4.2). Russell described this wave, which he called *Wave of Translation*, in the British Association Report in 1845 (Rayleigh, 1876). He further studied the properties of this wave by building a water tank to replicate the phenomenon (Emmerson, 1977).



Figure 4.2 Scientists gathered at Heriot-Watt University successfully recreated a solitary wave having smaller dimensions than the one observed by Russell (Hereman, 2013).

Russell either released an impounded elevation of water or dropped a weight at one end of the laboratory channel to produce solitary waves (Figure 4.3).

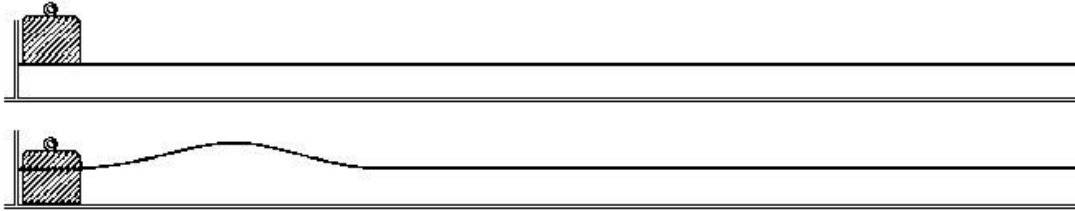


Figure 4.3 Russell's (1845) observation of the evolution of a solitary wave in a wave tank (reproduced from the original drawing) (Miles, 1980)

Russell's conclusion from his experiments was that: the volume of the wave is equal to that of the initial displacement and a wave of amplitude H in water of depth d advances with the speed:

$$c = \sqrt{g(d + H)} \quad [4.3]$$

Another conclusion was that breaking occurs when $H \approx d$. Equation [4.3] was confirmed by Bazin (1865), who repeated Russell's experiments and found that breaking occurs for H somewhat less than d (Miles, 1980).

A conflict arose between Russell's observations and Airy's (1845) wave theory as Russell described the wave as a solitary elevation of finite amplitude and permanent form, whereas, according to Airy, a wave of finite amplitude can not propagate without change of form. This stimulated considerable scientific interest at the time and later in the nineteenth century (Miles, 1980). Boussinesq (1872) and Rayleigh (1876) resolved this conflict independently of each other. They showed that appropriate allowance for vertical acceleration – which is ultimately responsible for dispersion but is neglected in the shallow water theory – leads to the solution of the solitary wave.

Boussinesq (1872), Rayleigh (1876) and later McCowan (1891) formulated the first sound approximate theory that is able to predict the wave phenomena observed by Russell. The free surface displacement of a solitary wave is given by (Boussinesq, 1872; Rayleigh, 1876; Munk, 1949; Laitone, 1960; Wiegel, 1964; Goring, 1978; Sorensen, 1993; Dean and Dalrymple, 1984; Dingemans, 1994; Choi et al., 2007; Madsen et al., 2008; McCormick, 2010; Goseberg et al., 2013):

$$\eta(x, t) = H \operatorname{sech}^2 \left[\sqrt{\frac{3H}{4d^3}} (x - ct) \right] \quad [4.4]$$

where wave celerity, c , is:

$$c = \sqrt{gd} \left(1 + \frac{H}{2d} \right) \approx \sqrt{g(d + H)} \quad [4.5]$$

In theory, there is only a single crest in space and time, (x, t) , in the solitary wave solution, corresponding to an infinite wave period and an infinite wavelength. However, an effective (i.e. characteristic) length is defined and considered for engineering purposes, because an infinitely long wave has no value in practice. The effective wavelength of a solitary wave is the distance between the points of the wave profile for which the local wave height, h , is a small fraction of the maximum wave height, H (i.e. between points with $h = H/100$). In other words, the effective wavelength of a solitary wave is the distance between the front and the tail of the wave, where the local height is 1% of the maximum (Figure 4.4). The effective wavelength of a solitary wave is (Madsen et al., 2008; Chan and Liu, 2012):

$$L = \frac{2\pi}{\sqrt{\frac{3H}{4d^3}}} \quad [4.6]$$

where L is the effective wavelength of a solitary wave.

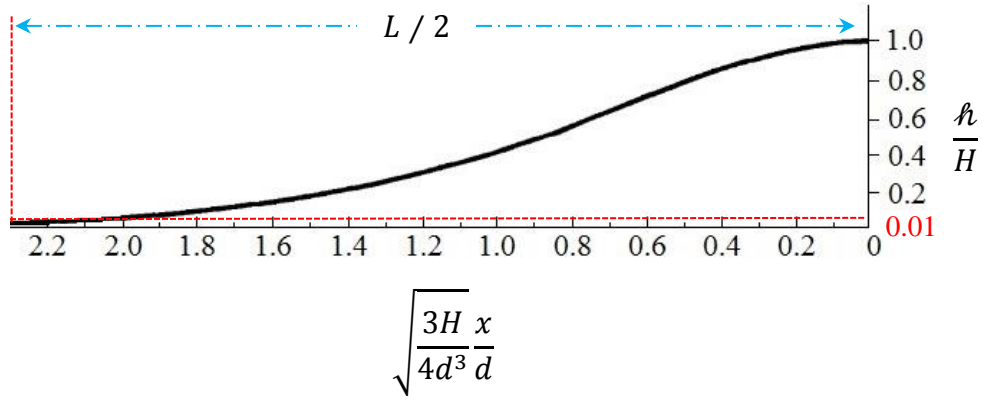


Figure 4.4 Dimensionless solitary wave profile indicating effective wavelength (not to scale)

Synolakis (1986, 1987) conducted analytical and experimental research on the problem of a solitary wave propagating in a constant water depth and climbing up a simple plane beach. His study depicted Benchmark Problem 1 and Benchmark Problem 4 (BMP 1 and BMP 4) of the 2011 National Tsunami Hazard Mitigation Program (NTHMP) workshop held in Portland, U.S. (NTHMP, 2011). BMP 1 is an analytical benchmark problem whereas BMP 4, which is the laboratory counterpart of BMP 1, requires comparison of the model predictions with laboratory measurements.

Having established the differences between breaking and non-breaking waves by using solitary waves as a long wave model, Synolakis (1986) was able to evaluate the relevance of the nonlinear theory in the wave runup process and maintain that this theory predicts the maximum runup of solitary waves on sloping bathymetry as accurately as the linear theory. He derived an asymptotic result for the calculation of non-breaking solitary wave runup on plane beaches. Another discovery Synolakis (1986) made was that there were different runup regimes for breaking and non-breaking solitary waves. Synolakis (1986) introduced an approximate theory for the runup of breaking solitary waves on plane beaches, which he verified by conducting a series of laboratory experiments. His runup formula was modified and improved by Li and Raichlen (2001). This modification provided a maximum 10 % improvement in accuracy, which confirmed that Synolakis's (1986) assumptions in his nonlinear theory were satisfactory for most engineering applications (Li and Raichlen, 2001).

Synolakis (1986) states that a solitary wave centered at $x = X_1$ at time $t = 0$ (Figure 4.5) has the following non-dimensional surface profile, η^* :

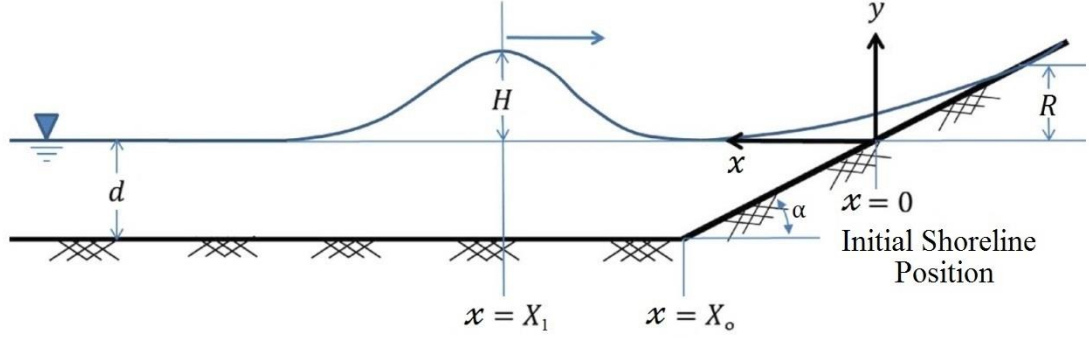


Figure 4.5 A sketch of the canonical beach, i.e. sloping beach connected to a constant depth region (distorted scale) (Horrillo et al., 2015)

$$\eta^*(x, 0) = \frac{H}{d} \operatorname{sech}^2 \left[\sqrt{\frac{3H}{4d}} (x - X_1) \right] \quad [4.7]$$

where x is the dimensionless horizontal coordinate and increases monotonically seaward and X_1 is the dimensionless x location where the offshore height of a solitary wave is defined. Also, $x = 0$ and $x = X_0 = d \cot(\alpha)$ define the positions of the initial shoreline and the toe of the beach, respectively.

The non-dimensional effective wavelength, L^* , is given by (Synolakis, 1986):

$$L^* = \frac{2}{\sqrt{\frac{3H}{4d}}} \cosh^{-1} \left(\sqrt{\frac{1}{0.05}} \right) \quad [4.8]$$

Synolakis (1986) accepted the effective wavelength as the distance between the front and the tail of the wave where the local height is 5% of the maximum so that a reasonable scaling in the laboratory conditions could be obtained.

Synolakis (1986) derived the following expression, which is normalized by the constant offshore depth, for the maximum runup of non-breaking solitary waves on a plane beach having a slope of α :

$$\frac{R}{d} = 2.831\sqrt{\cot\alpha}\left(\frac{H}{d}\right)^{5/4} \quad [4.9]$$

Synolakis (1986) stated that the shoreline usually took a parabolic shape at the time of maximum runup. After recording the minimum and average positions of the shoreline at that time, he discovered that the relation between the H/d ratios and the runup distances was similar to that defined for the maximum position of the shoreline. Synolakis (1986) expressed the dependence of maximum runup on the maximum position of the shoreline for breaking solitary waves as:

$$\frac{R}{d} = 1.109\left(\frac{H}{d}\right)^{0.582} \quad [4.10]$$

Synolakis (1986) also carried out a series of experiments in the California Institute of Technology (Caltech), Pasadena, California in order to support his theories. The wave tank used in the experiments was 31.73 m long, 60.96 cm deep and 39.37 cm wide, consisting of 12 identical sections. The sidewalls of each section were made of 1.52 m long, 63.50 cm high and 1.27 cm thick glass panels. The bottom of each section consisted of 2.54 cm thick painted stainless steel plates (Figure 4.6). A ramp was installed at one end of the wave tank in order to model the bathymetry, which consisted of a sloping beach joined to a channel of constant depth. The ramp had a slope of 1:19.85 (i.e. $\alpha = \cot^{-1}(19.85) = 2.88^\circ$) and was constructed out of four 6.35 mm thick aluminum plates with a width of 38.1 cm. The toe of the ramp was 14.95 m away from the rest position of the piston that was used to generate waves (i.e. wave plate) (Figure 4.6). Detailed information about the hydraulic system used in the experiments can be found in Goring (1978) and Synolakis (1986). All wave gauges were calibrated before and after the experiments.

Figure 4.6 Wave tank used in the experiments (not to scale): (a) schematic side view; (b) schematic typical cross section; (c) a photograph before an experiment (Synolakis, 1986).

In laboratory conditions, solitary waves can dissipate. When the wave height is measured far offshore and used as an initial condition for non-dissipative numerical models, the comparisons will be less meaningful due to the slight change that occurs in the solitary wave as it propagates along the wave tank. Meaningful comparisons can be obtained by keeping the same relative offshore distance to define the initial condition. Synolakis (1986) identified the initial solitary waves at an offshore location, which is $L/2$ away from the toe of the beach, i.e. $X_1 = X_0 + L/2$. In other words, the wave height is centered at $x = X_1$ at $t = 0$.

Synolakis (1986) performed more than 40 experiments involving solitary waves of varying heights. The water depths ranged from 6.25 cm to 38.32 cm. The wave height-to-water depth ratio, H/d , ranged from 0.005 to 0.633. Synolakis (1986) measured the water level profiles of solitary waves with $H/d = 0.0185$ and $H/d = 0.3$ at several non-dimensional times, $t^* = t\sqrt{g/d}$. He also analytically solved the wave dynamics at two locations, $x/d = 0.25$ and $x/d = 9.95$, for the case where $H/d = 0.0185$. Synolakis (1986) discovered distinct runup regimes for non-breaking and breaking solitary waves, where he defined non-breaking solitary waves as *waves that did not break during runup process*. According to observations of Synolakis (1986), solitary waves break when $H/d \geq 0.044$ for the particular beach slope of 1:19.85. Therefore, the experimental wave with $H/d = 0.0185$ is a non-breaking solitary wave and it is possible to describe its surface profile analytically, whereas the surface profile of the breaking solitary wave with $H/d = 0.3$ is only represented by the experimental data.

By means of this benchmark problem, the predicted water surface profiles are compared with the analytical and experimental ones at certain given non-dimensional times for the case of non-breaking solitary wave, $H/d = 0.0185$. The differences between the numerical model results and laboratory data are also analysed for the case of breaking solitary wave, $H/d = 0.3$. Moreover, the maximum runup values obtained from Equation [4.9] and the laboratory measurements are compared.

4.1.2. NAMI DANCE Model

The same set of physical experiments is reproduced in a 2D domain using NAMI DANCE. The fluid is inviscid and the flow is incompressible. Fluid density is taken constant throughout the fluid domain. The Cartesian coordinate system is used so that positive x increases seaward and positive y direction is perpendicular to the direction of the flow. The gravitational force, g , is in the downward direction (Figure 4.7).

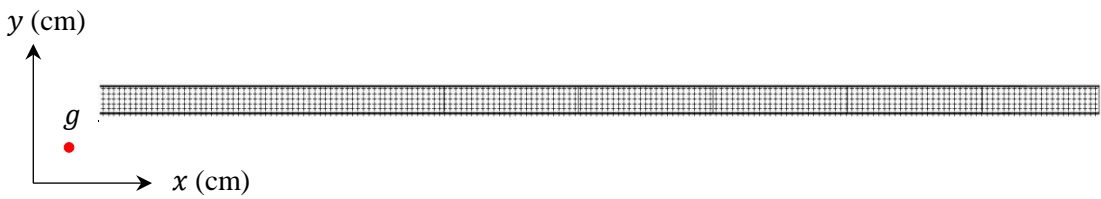


Figure 4.7 NAMI DANCE model: a typical computational domain and the orientation of the coordinate system (top view)

The water surface elevation time series (i.e. solitary wave profile) for each experimental run is reproduced using the d versus H/d data set provided by Synolakis (1986) and using Equation [4.4] (Figure 4.8).

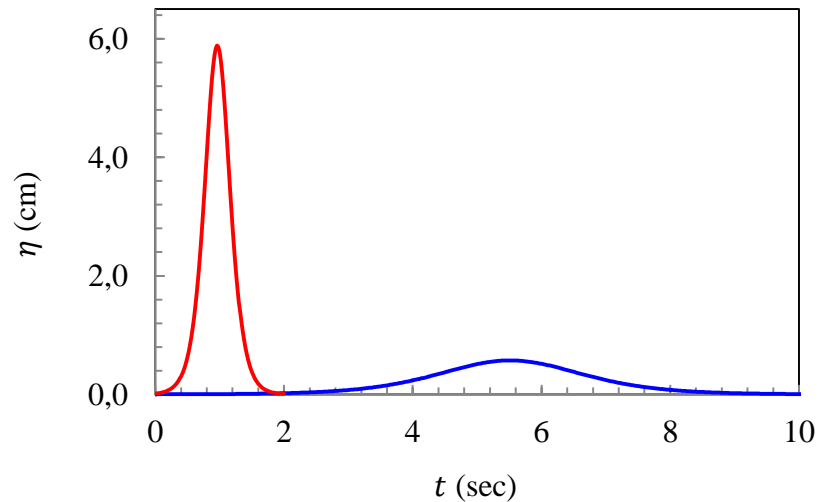


Figure 4.8 Solitary wave profiles of two experimental runs. The blue line represents the water surface elevation time series for the first case where $H/d = 0.0185$; the red line represents the water surface elevation time series for the second case where $H/d = 0.3$.

The gauge points are placed in the middle of the basin (i.e. $y = 20$ cm) and at every 2 cm along x direction. Figure 4.9 illustrates the NAMI DANCE computational domain constructed for the case where $H/d = 0.633$, including the dimensions, gauge points and wave direction.

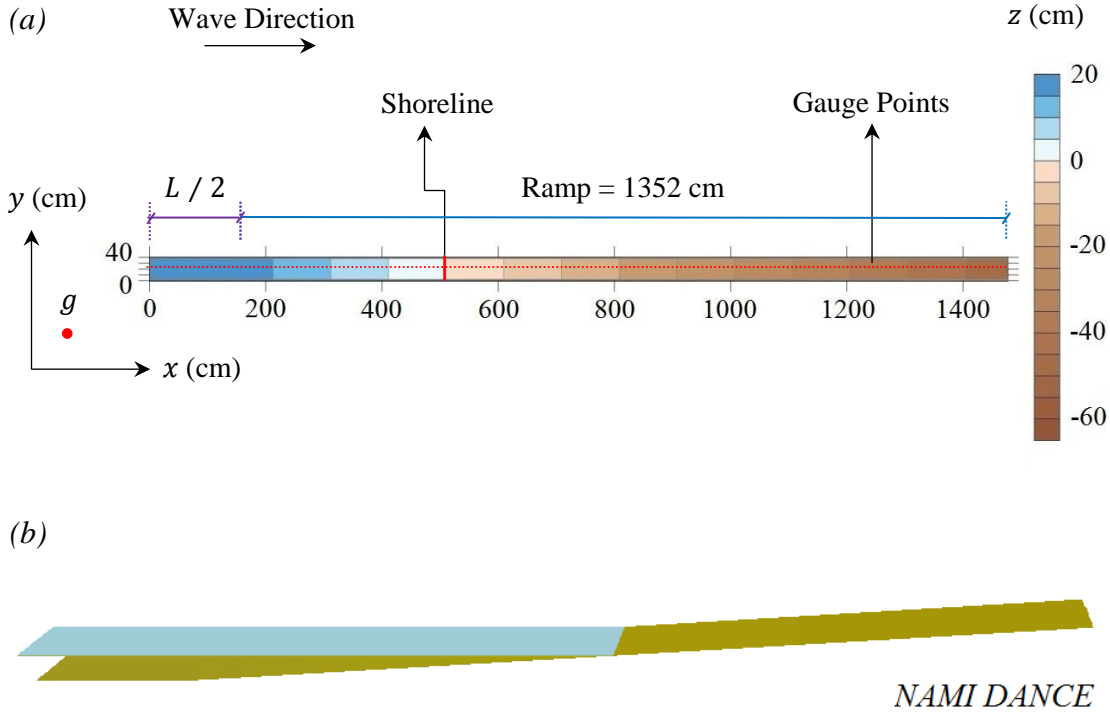


Figure 4.9 NAMI DANCE computational domain constructed for the case where $H/d = 0.633$: (a) 2D top view; (b) 3D view

The water surface elevation time series is inputted at the upstream end of the computational domain (i.e. minimum x boundary), which is located $L/2$ distance away from the toe of the slope. This enables the initial wave profile to adjust the governing equations before it reaches the slope. The maximum x boundary has a rigid wall boundary condition, which defines the downstream end of the wave tank. The minimum and maximum y boundaries are also defined as rigid walls in order to prevent outflow from the computational domain.

4.1.2.1. Spatial Discretization

The computational domain, represented by a structured mesh (i.e. rectangular cells), covers the entire length of the flume with grid sizes, Δx and Δy , which are uniform throughout the mesh.

It is important to note that reducing the cell size does not necessarily guarantee a better result from a practical perspective since it may lead to unstable results and unnecessarily abundant computational resources and time. The previous numerical model validations that used BMP 1 (NTHMP, 2011) are taken into account in the determination of the grid size. It is found that in the recent studies either $\Delta x = d/20$ (Alaska Tsunami Model and Alaska Tsunami Forecast Model), or $\Delta x = 1$ cm (FUNWAVE-TVD, MOST, NEOWAVE and SELFE) is used (NTHMP, 2011). After a careful analysis, the grid size is selected as 1 cm; i.e. $\Delta x = \Delta y = 1$ cm.

It has been suggested in the literature that the convergence of a tsunami modeling algorithm be assessed by simulating the extreme positions of the shoreline – the maximum runup and rundown. Thus, of the four cases where the effect of Δx is investigated, in the first two, the minimum and maximum H/d values are analysed, and the third and the fourth cases are the ones where $H/d = 0.0185$ and $H/d = 0.3$, respectively (Table 4.2).

Table 4.2 NAMI DANCE: Maximum runup values for different Δx values ($n = 0.01$)

Grid Size Δx (cm)	Maximum Dimensionless Runup (R/d)			
	$H/d = 0.005$	$H/d = 0.633$	$H/d = 0.0185$	$H/d = 0.3$
0.125	0.019	0.626	0.084	0.414
0.25	0.019	0.626	0.084	0.414
0.5	0.018	0.625	0.084	0.412
1.0	0.018	0.623	0.083	0.403
2.0	0.014	0.612	0.078	0.391
5.0	0.011	0.588	0.072	0.343

The results for the two non-breaking wave cases, where $H/d = 0.005$ and $H/d = 0.0185$, indicate that the numerical predictions converge to the exact solution after the spatial discretization is refined (i.e. finer grids).

The non-dimensional free surface profiles at $t^* = 60$ and $t^* = 70$ are recomputed with grid resolutions of $\Delta x = 0.125$ cm, $\Delta x = 0.25$ cm, $\Delta x = 0.5$ cm, $\Delta x = 1.0$ cm, $\Delta x = 2.0$ cm and $\Delta x = 5.0$ cm in order to test the grid convergence for the case where $H/d = 0.0185$ (Figure 4.10).

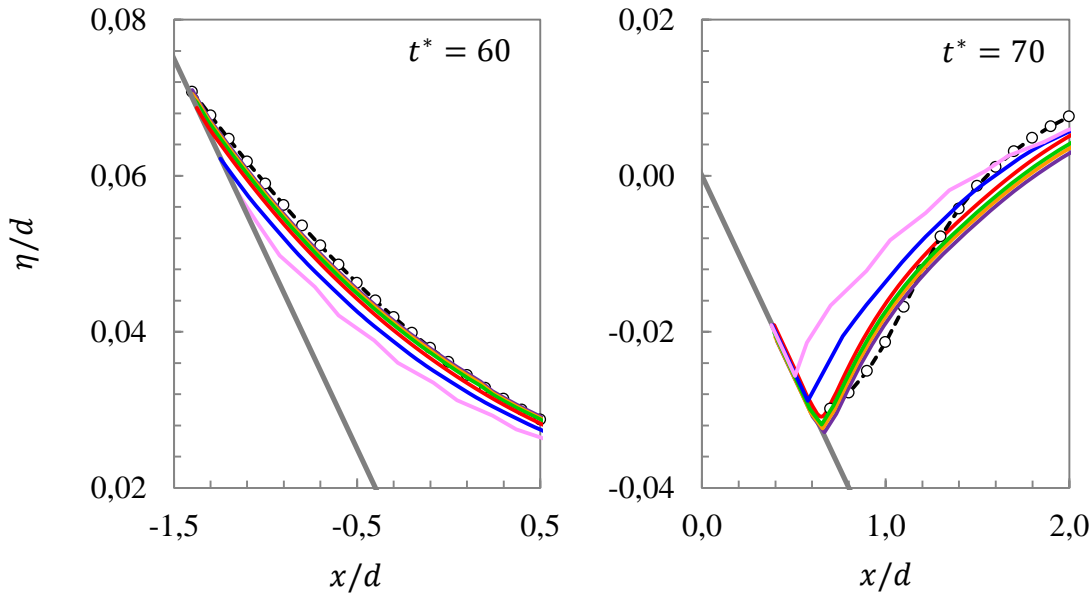


Figure 4.10 NAMI DANCE convergence test for the case where $H/d = 0.0185$ at: (a) $t^* = 60$ – the time of maximum runup; (b) $t^* = 70$ – the time of maximum rundown. The circles and dashed black line represent the analytical solution; the purple line: $\Delta x = 0.125$ cm; the orange line: $\Delta x = 0.25$ cm; the green line: $\Delta x = 0.5$ cm; the red line: $\Delta x = 1.0$ cm; the blue line: $\Delta x = 2.0$ cm; the pink line: $\Delta x = 5.0$ cm

The analyses are conducted for a frictionless bottom in order to be consistent with the assumptions made in the derivation of the analytical solutions of the maximum runup and free surface profiles. It is seen that the finer the grid size, the closer are the predicted results to the exact solutions. In fact, no considerable change is observed after $\Delta x = 1.0$ cm. The analytically and numerically computed maximum runup values and free surface profiles differ by less than 1% for $\Delta x \leq 1.0$ cm.

The maximum time step size that fulfills the CFL stability criteria is calculated automatically by NAMI DANCE for each run, depending on the bathymetry. According to this limitation, time step, Δt , is selected as 0.02 second for all runs.

4.1.2.2. Friction

Manning's roughness coefficients used to assess the effect of friction on the maximum runup values are:

- (i) $n = 0$ (i.e. frictionless bottom)
- (ii) $n = 0.01$ (i.e. neat cement/concrete/smooth glass beach)
- (iii) $n = 0.03$ (i.e. fine particles along the channel bottom)

In order to be consistent with the assumptions made by Synolakis (1986) in the analytical solution of the 1D solitary wave runup, the results of the analyses for a frictionless bottom are regarded as the basis of the comparison of the predicted solitary wave profiles with the analytical ones. On the other hand, n is taken as 0.01 in order to reflect real laboratory conditions while comparing the predicted maximum runup data and the extreme wave profiles (i.e. $H/d = 0.3$) with the laboratory measurements.

The results reveal that the predicted maximum runup values do not depend on n for small non-breaking waves, $H/d \leq 0.01$. The computed runup heights are found to be slightly affected by the bottom friction when $0.01 < H/d < 0.044$. In the case of breaking solitary waves, $H/d \geq 0.044$, the maximum runup strongly depends on n . It is expected that the predicted maximum runup values for a frictionless bottom will be larger than those measured and that the predicted and measured data will be in good agreement when $n = 0.01$. However, the maximum runup values of *breaking solitary waves* are found to be approximately 9 %, 17 % and 30 % less than the laboratory measurements for $n = 0$, $n = 0.01$ and $n = 0.03$, respectively (Figure 4.11). This shows that the solutions of depth-averaged NSW equations can not fully reflect the real life situation due to the existence of the strong wave breaking process.

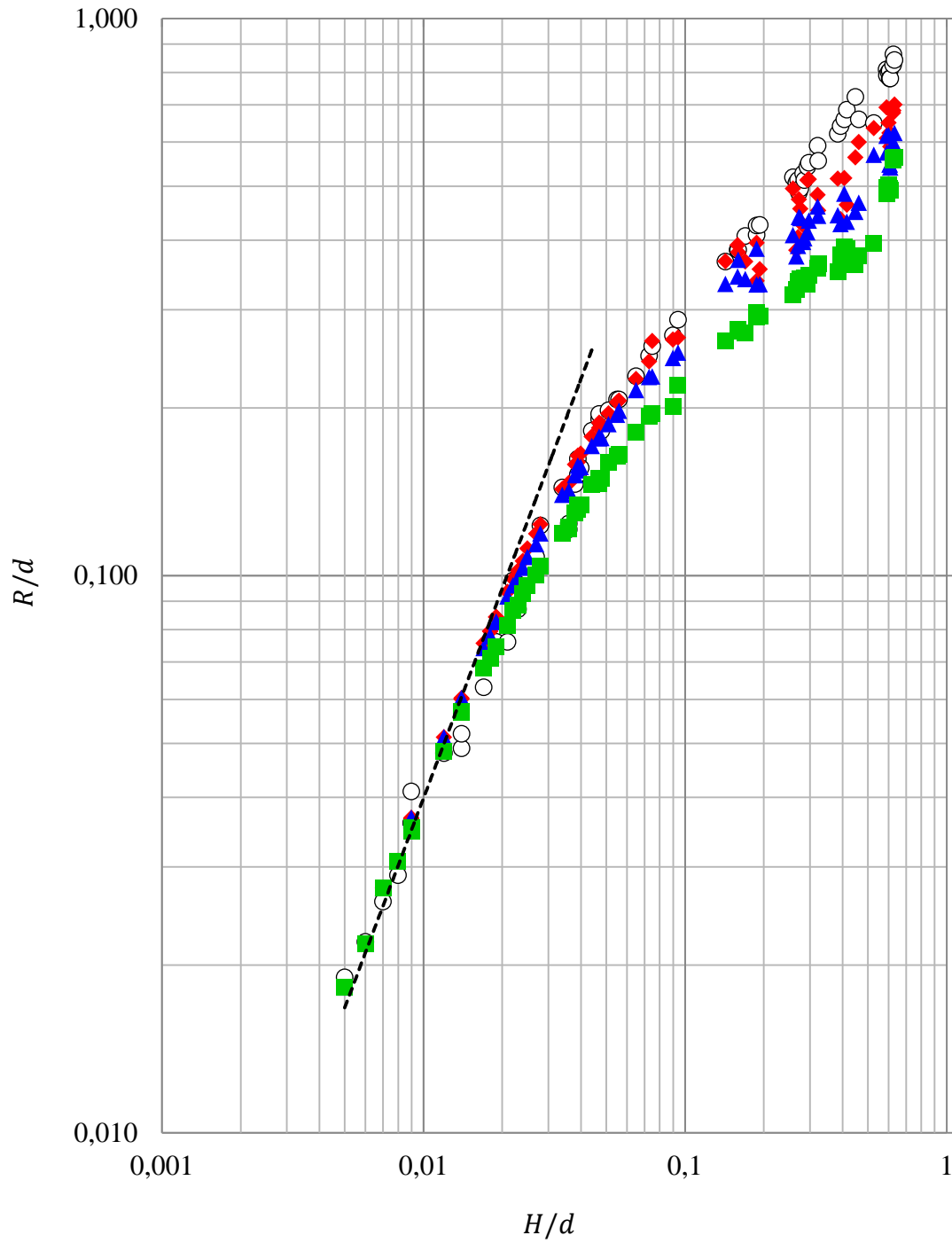


Figure 4.11 NAMI DANCE model results for different Manning's roughness coefficients. The dashed black line and circles represent the runup law and experimental data of Synolakis (1986), respectively, the red diamonds represent the results when $n = 0$; the blue triangles represent the results when $n = 0.01$; the green squares represent the results when $n = 0.03$.

4.1.3.FLOW-3D® Model

The same set of physical experiments is reproduced using FLOW-3D® in a 3D domain, throughout which the fluid is inviscid, the flow is incompressible and the fluid density is constant. The effects of surface tension and air entrainment at the surface of the flow are neglected.

The numerical model is constructed using the Cartesian coordinate system, where the positive x direction is oriented along the fluid flow into the domain and the positive y direction is perpendicular to the direction of the flow. The gravitational acceleration, g , is in the downward direction (i.e. $-z$ direction). Figure 4.12 illustrates the FLOW-3D® computational domain constructed for the case where $H/d = 0.005$.

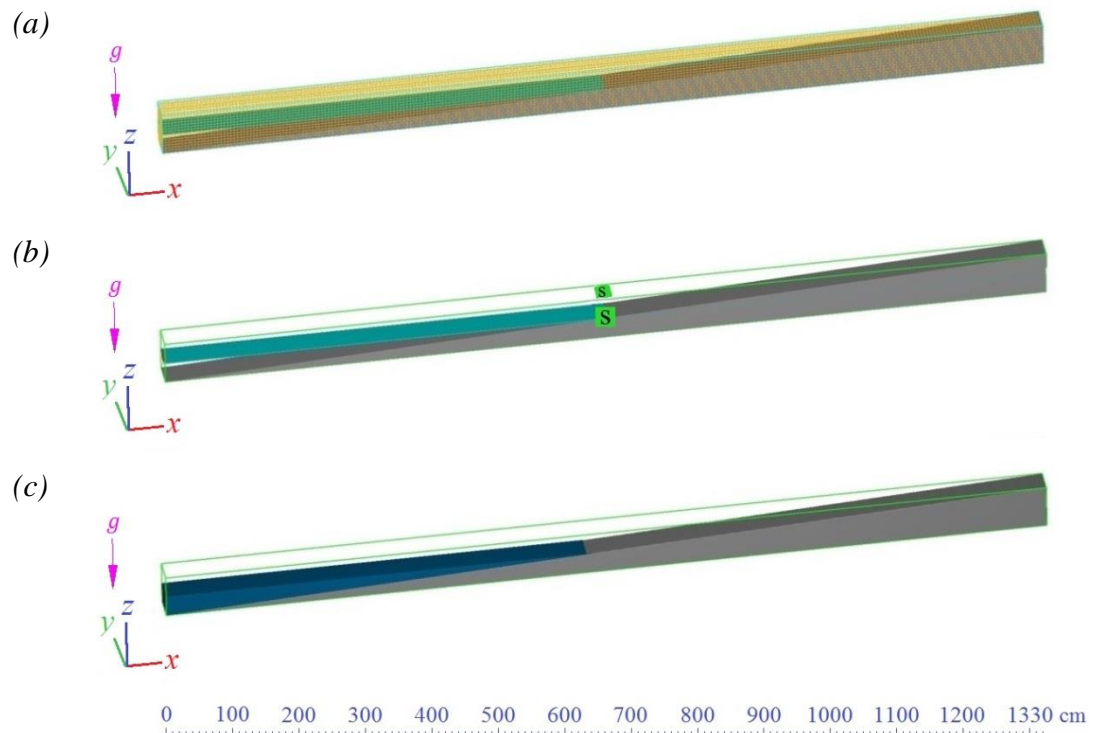


Figure 4.12 FLOW-3D® computational domain constructed for the case where $H/d = 0.005$: (a) meshing; (b) boundary conditions; (c) after using FAVOR™

For the water surface elevation time series (i.e. the solitary wave profile) in each experimental run to be reproduced by the solitary wave generator module of FLOW-3D[®], the d and H values provided by Synolakis (1986) are used.

The minimum x boundary is defined as the wave boundary where solitary waves are reproduced. It is important to note that FLOW-3D[®] initiates the motion of solitary waves at a distance, expressed as $L/2$, from the mesh boundary as default. Therefore, the FLOW-3D[®] computational domain is only composed of a ramp. The wall boundary condition is applied at the maximum x boundary in order to define the downstream end of the wave tank. The minimum and maximum y boundaries as well as the maximum z boundary feature the symmetrical boundary condition where all the velocity derivatives and velocity components normal to the boundaries are set to zero. The wall boundary condition is also valid for the minimum z boundary where the bottom of the wave flume is defined.

4.1.3.1. Spatial Discretization

The computational domain is represented by an isotropic grid with $\Delta x = \Delta y = \Delta z$ where the grid size is selected as 1 cm (Please refer to the explanations in Section 4.1.2.1). BMP 1 is modeled via FLOW-3D[®] for different Δx values in order to test the grid dependency.

Table 4.3 FLOW-3D[®]: Maximum runup values for different Δx values ($n = 0.01$)

Grid Size Δx (cm)	Maximum Dimensionless Runup (R/d)			
	$H/d = 0.005$	$H/d = 0.633$	$H/d = 0.0185$	$H/d = 0.3$
0.125	0.019	0.839	0.084	0.511
0.25	0.019	0.839	0.084	0.511
0.5	0.018	0.839	0.084	0.511
1.0	0.018	0.839	0.084	0.510
2.0	0.017	0.831	0.081	0.507
5.0	0.013	0.813	0.078	0.498

The results for the two non-breaking wave cases, where $H/d = 0.005$ and $H/d = 0.0185$, indicate that the numerical predictions converge to the exact solution at finer resolutions.

The non-dimensional free surface profiles at $t^* = 60$ and $t^* = 70$ are recomputed with grid resolutions of $\Delta x = 0.125$ cm, $\Delta x = 0.25$ cm, $\Delta x = 0.5$ cm, $\Delta x = 1.0$ cm, $\Delta x = 2.0$ cm and $\Delta x = 5.0$ cm in order to test the grid convergence for the case where $H/d = 0.0185$ (Figure 4.13).

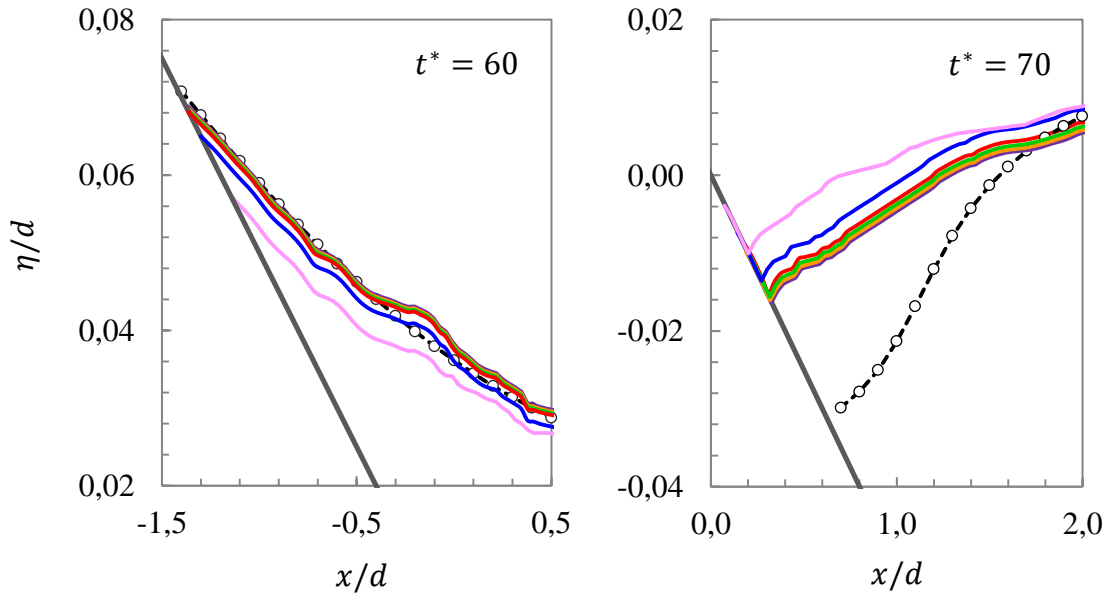


Figure 4.13 FLOW-3D[®] convergence test for the case where $H/d = 0.0185$ at:
 (a) $t^* = 60$ – the time of maximum runup; (b) $t^* = 70$ – the time of maximum rundown. The circles and dashed black line represent the analytical solution; the purple line: $\Delta x = 0.125$ cm; the orange line: $\Delta x = 0.25$ cm; the green line: $\Delta x = 0.5$ cm; the red line: $\Delta x = 1.0$ cm; the blue line: $\Delta x = 2.0$ cm; the pink line: $\Delta x = 5.0$ cm

The analyses are conducted for a frictionless bottom in order to be consistent with the assumptions made in the derivation of the analytical solutions of the maximum runup and free surface profiles. It is seen that the finer the grid size, the closer are the predicted results to the exact solutions. In fact, no considerable change is observed after $\Delta x = 1.0$ cm. The analytically and numerically computed maximum runup values and free surface profiles differ by less than 0.8% for $\Delta x \leq 1.0$ cm.

It is also necessary to analyse the effect of the vertical grid size, Δz , on the runup values and free surface profiles in a three-dimensional model. The predictions get close to the analytical solution for the non-breaking solitary wave case when a fine vertical grid size (i.e. $\Delta z \leq 1.0$ cm) is used, with Δx kept constant. No considerable change is observed after $\Delta z = 1.0$ cm.

The time step, Δt , is selected as 0.02 second to be consistent with the simulations conducted using NAMI DANCE. When variable time stepping is employed in order to assess the effect of the time step size, no significant effect is observed.

4.1.3.2. Friction

In order to assess the effect of friction on the maximum runup values, different Manning's roughness coefficients are considered: $n = 0$ (i.e. frictionless bottom), $n = 0.01$ (i.e. neat cement/concrete/smooth glass beach) and $n = 0.03$ (i.e. fine particles along the channel bottom). Please refer to Section 4.1.2.2 for the comparison criteria.

The results indicate that the predicted maximum runup values are not dependent on n for small non-breaking waves, $H/d \leq 0.01$. The computed runup heights are slightly affected by the bottom friction when $0.01 < H/d < 0.044$. In the case of breaking solitary waves, $H/d \geq 0.044$, the maximum runup strongly depends on n . It is expected that the predicted maximum runup values for a frictionless bottom will be larger than those measured and that the predicted and measured data will be in good agreement when $n = 0.01$. The predicted maximum runup values of breaking solitary waves are found to be approximately 8% larger than the measured ones for a frictionless bottom. The results are in fairly good agreement, with a 4% difference, for steep solitary waves when $n = 0.01$. The predicted maximum runup values are found to be approximately 20% less than the measured ones when $n = 0.03$. It is seen that the results are in good agreement with the expectations, implying that the three-dimensional model reflects real life situations satisfactorily (Figure 4.14).

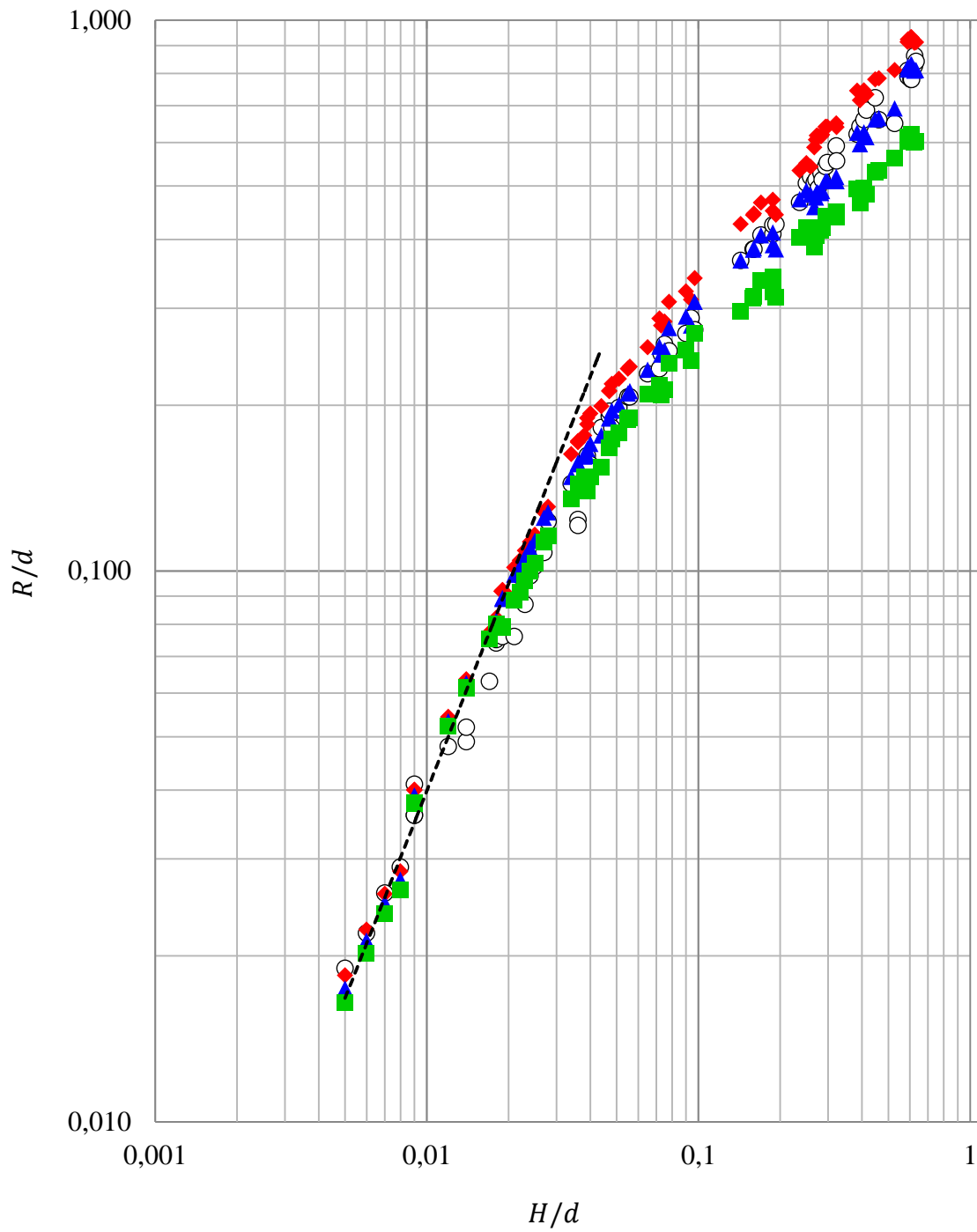


Figure 4.14 FLOW-3D[®] model results for different Manning's roughness coefficients. The dashed black line and circles represent the runup law and experimental data of Synolakis (1986), respectively, the red diamonds represent the results when $n = 0$; the blue triangles represent the results when $n = 0.01$; the green squares represent the results when $n = 0.03$.

4.1.4. Simulation Results

The solitary wave runup on a plane slope is an intensively studied benchmark problem in long wave modeling. Synolakis's (1986) laboratory experiments have supplied frequently used data for validation of wave breaking and runup models.

Synolakis's (1986) theoretical study is based on the analytical solution of the non-dispersive nonlinear shallow water (NSW) equations. BMP 1 poses a challenging case for non-dispersive NSW models. Due to the existence of strong wave breaking, the solutions of the NSW equations do not fully agree with the laboratory measurements. For instance, hydrostatic numerical models predict that the leading front of the solitary wave will steepen and become singular shortly after the initiation of the computations. The numerical singularity moves towards the beach until it meets the shoreline where it dissipates. As the numerical dispersion can compensate for the absence of physical dispersion in hydrostatic numerical models, a better agreement with the reference data is possible. This topic is still being actively researched in the field of shallow water modeling (Horrillo et al., 2015).

The simulation time, the time required for the simulation of the complete real case, is 60 seconds for BMP 1. The process time indicates the time taken by the processors in order to simulate the case, read the input files and generate the output files. The process time of the simulations that are performed via NAMI DANCE is approximately 10 minutes whereas it takes 4 hours to complete the simulations using FLOW-3D[®].

Figure 4.15 illustrates the evolution and propagation of the non-breaking (i. e. small amplitude) solitary wave over the ramp. NAMI DANCE and FLOW-3D[®] compute the wave motion with considerable accuracy. Figure 4.16 illustrates the evolution and propagation of the large amplitude solitary wave for non-dimensional times, $t^* = 15$, $t^* = 20$, $t^* = 25$ and $t^* = 30$. The results reveal that FLOW-3D[®] provides better results for this extreme wave case.

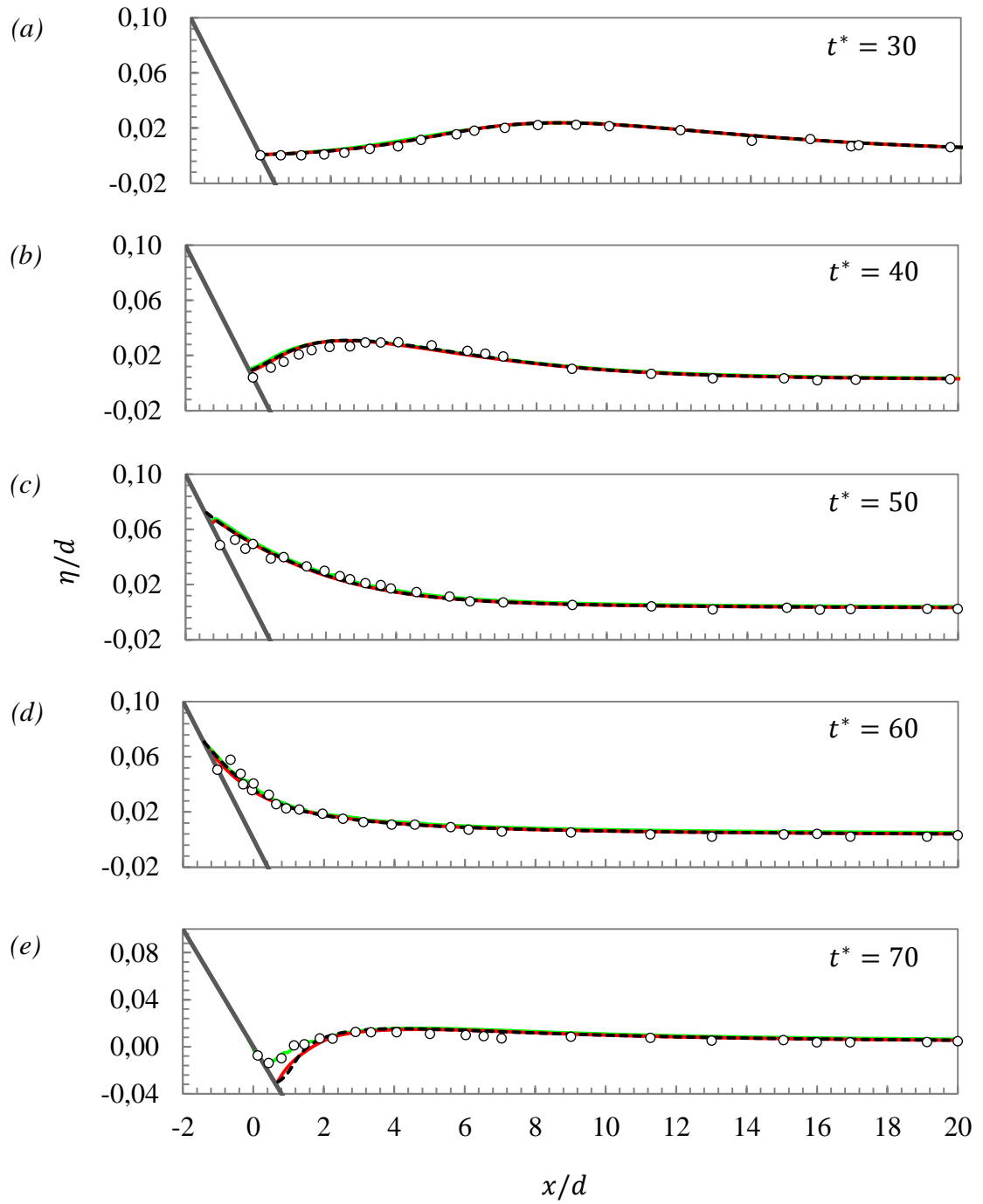


Figure 4.15 Non-dimensional free surface profiles for the case where $H/d = 0.0185$:
(a) $t^* = 30$; (b) $t^* = 40$; (c) $t^* = 50$; (d) $t^* = 60$; (e) $t^* = 70$. The black line and the circles represent the analytical solution and experimental results of Synolakis (1986), respectively; the red line represents NAMI DANCE results; the green line represents FLOW-3D[®] results.

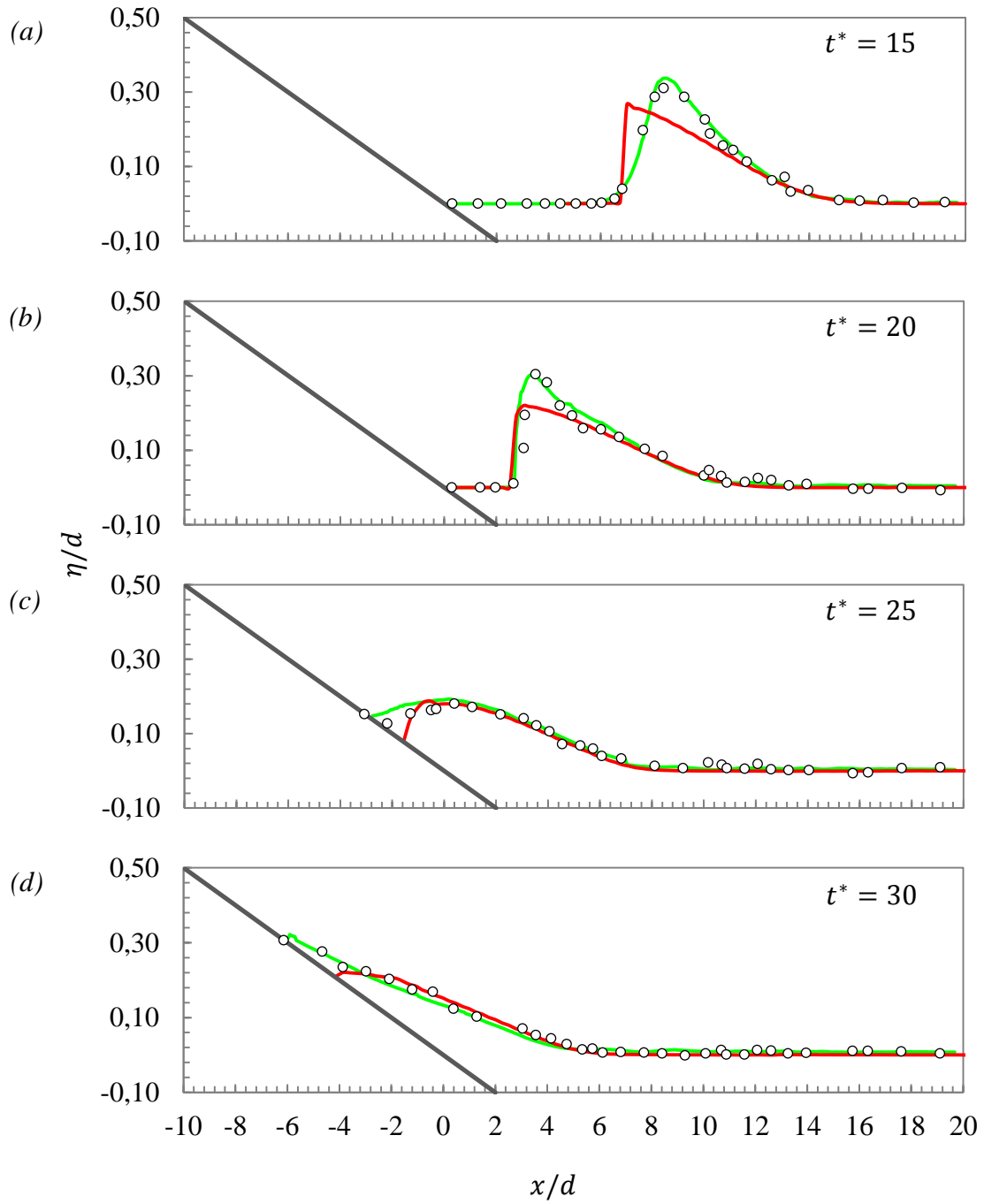


Figure 4.16 Non-dimensional free surface profiles for the case where $H/d = 0.3$:
 (a) $t^* = 15$; (b) $t^* = 20$; (c) $t^* = 25$; (d) $t^* = 30$. The circles represent the experimental results of Synolakis (1986); the red line represents the NAMI DANCE results; the green line represents the FLOW-3D[®] results.

The existence of strong wave breaking hinders the agreement of the predicted values with the laboratory measurements for the two-dimensional depth-averaged model, NAMI DANCE. Due to the fact that the experimental parameters violate the shallow water wave assumption, the predicted wave amplitude is smaller and steeper than that of the measured wave amplitude. Consequently, when wave amplitudes are large, the predicted and observed wave height and runup values do not agree as well as those in cases with amplitudes for which shallow water wave assumptions are valid. On the other hand, the predicted wave profiles obtained via the three-dimensional model, FLOW-3D[®], are in astoundingly good agreement with the laboratory data, indicating that the strong nonlinearities and wave energy transfers can be simulated efficiently via the three-dimensional model. This exemplifies the effect of the vertical velocity component, which is a crucial parameter and should not be ignored in cases where strong wave breaking is dominant.

Additional plots of the predicted and analytically computed sea surface elevation during propagation and reflection of the solitary wave are displayed in Figure 4.17 for the case where $H/d = 0.0185$, at two positions:

- (i) $x / d = 0.25$ – near the initial shoreline
- (ii) $x / d = 9.95$ – between the beach toe and the initial wave crest.

During rundown, both the numerical and analytical solutions show that the water retreats between $t^* = 67$ and $t^* = 82$, and the point $x / d = 0.25$ temporarily becomes dry – hence the data gap occurring between $67 < t^* < 82$. On the other hand, point $x / d = 9.95$ remains wet throughout the entire experiment.

When the analytical and numerical solutions at these two points are compared, it is found that there is good agreement between the two solutions at $x / d = 0.25$ and $x / d = 9.95$ during the propagation and reflection of the wave.

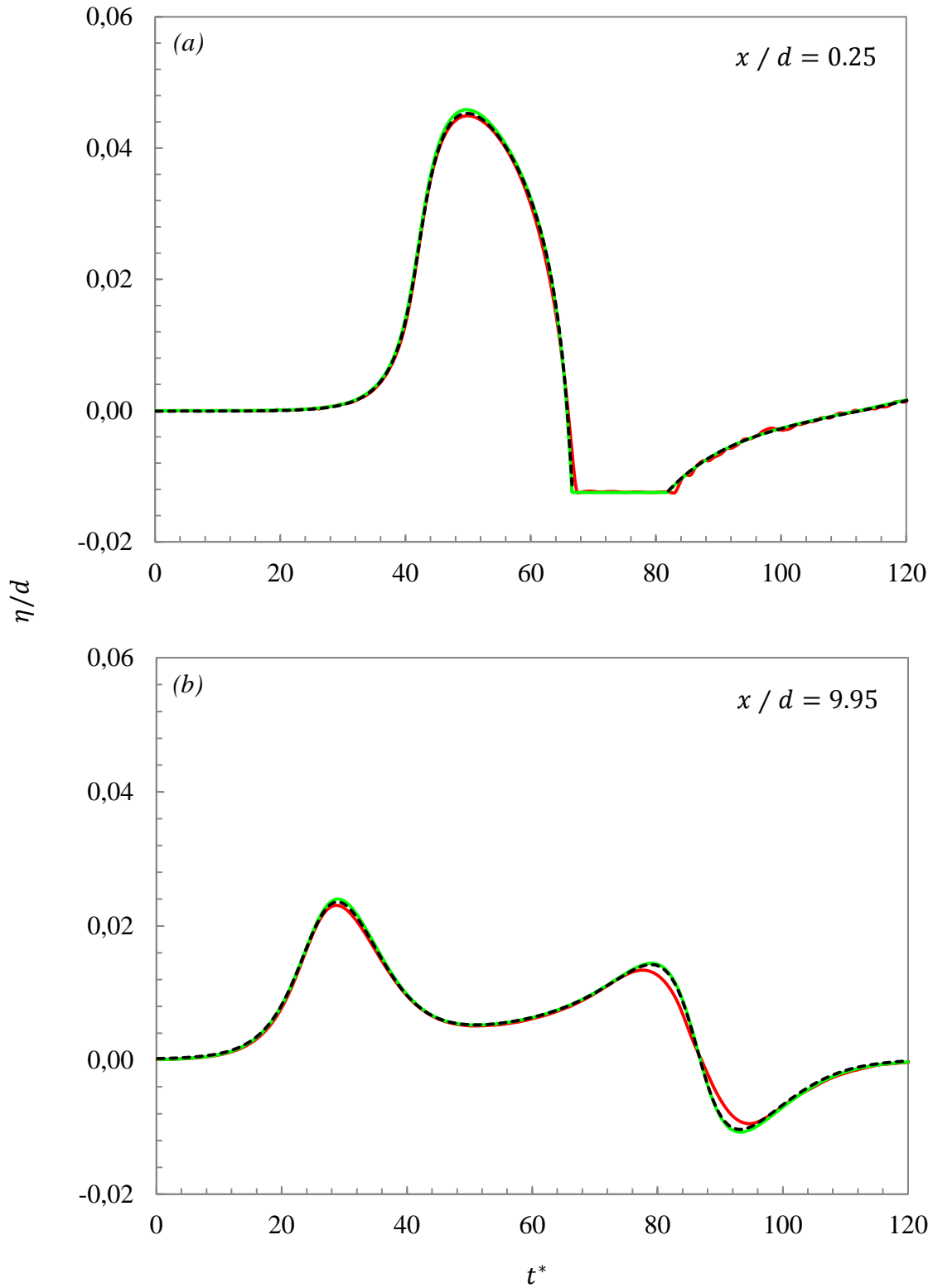


Figure 4.17 The water level dynamics at two locations: (a) $x/d = 0.25$; (b) $x/d = 9.95$. The dashed black line represents the analytical solution of Synolakis (1986); the red line represents the NAMI DANCE results; the green line represents the FLOW-3D[®] results.

The inundation of the 1:19.85 sloped beach by solitary waves with different H/d ratios is simulated in several series of numerical model runs. In each series, the bottom friction is parameterized by Manning's roughness coefficient, $n = 0.01$.

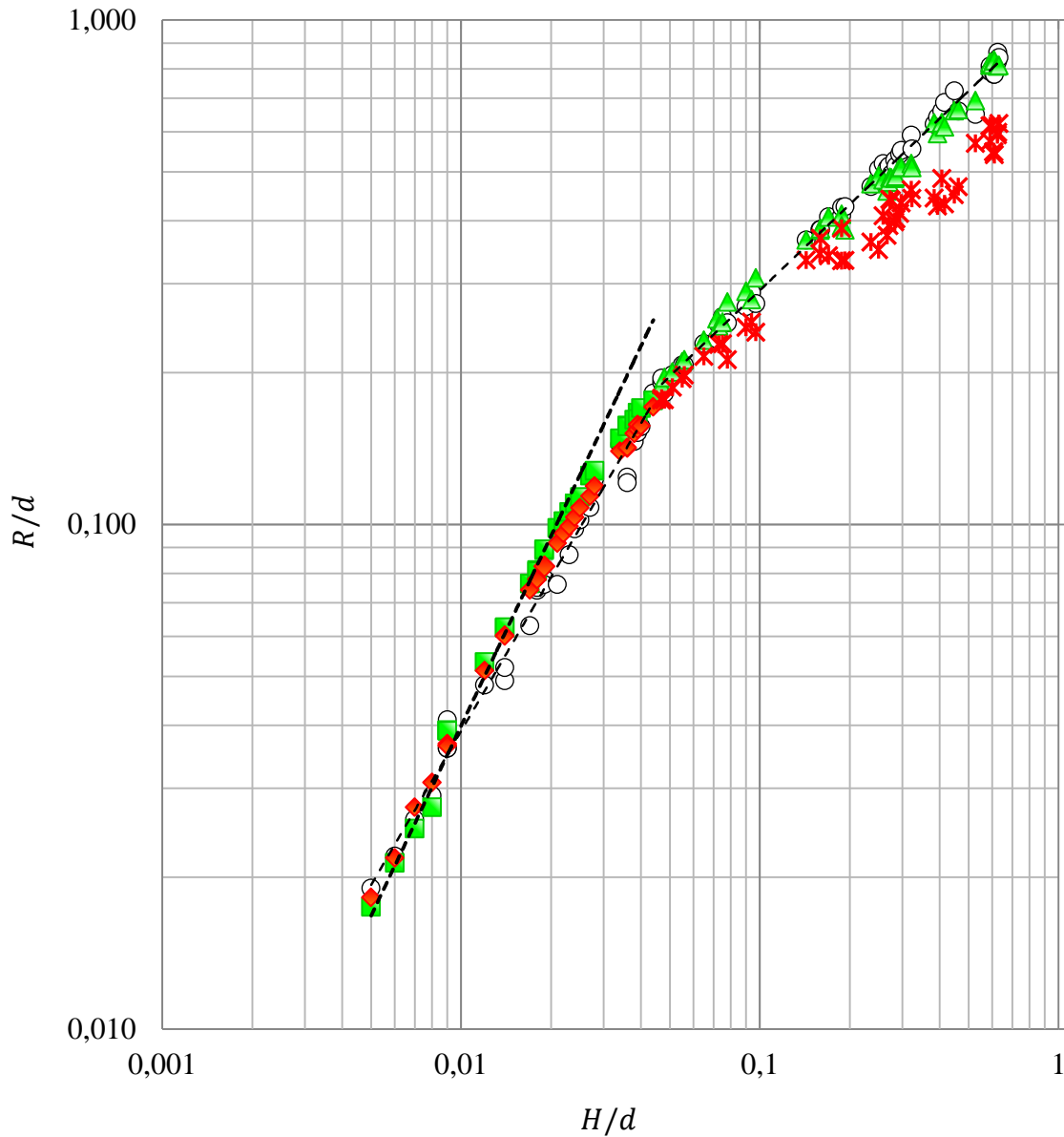


Figure 4.18 Maximum runup values on 1:19.85 slope when $n = 0.01$: The dashed black line represents the runup law (Synolakis, 1986); the circles represent the experimental results of non-breaking and breaking solitary waves (Synolakis, 1986); the red diamonds and crosses represent the NAMI DANCE results for non-breaking and breaking solitary waves, respectively; green squares and triangles represent the FLOW-3D[®] results for non-breaking and breaking solitary waves, respectively.

The maximum runup of solitary waves climbing up different slopes is analysed in order to test the validity of the runup law derived by Synolakis (1986) (Figure 4.19).

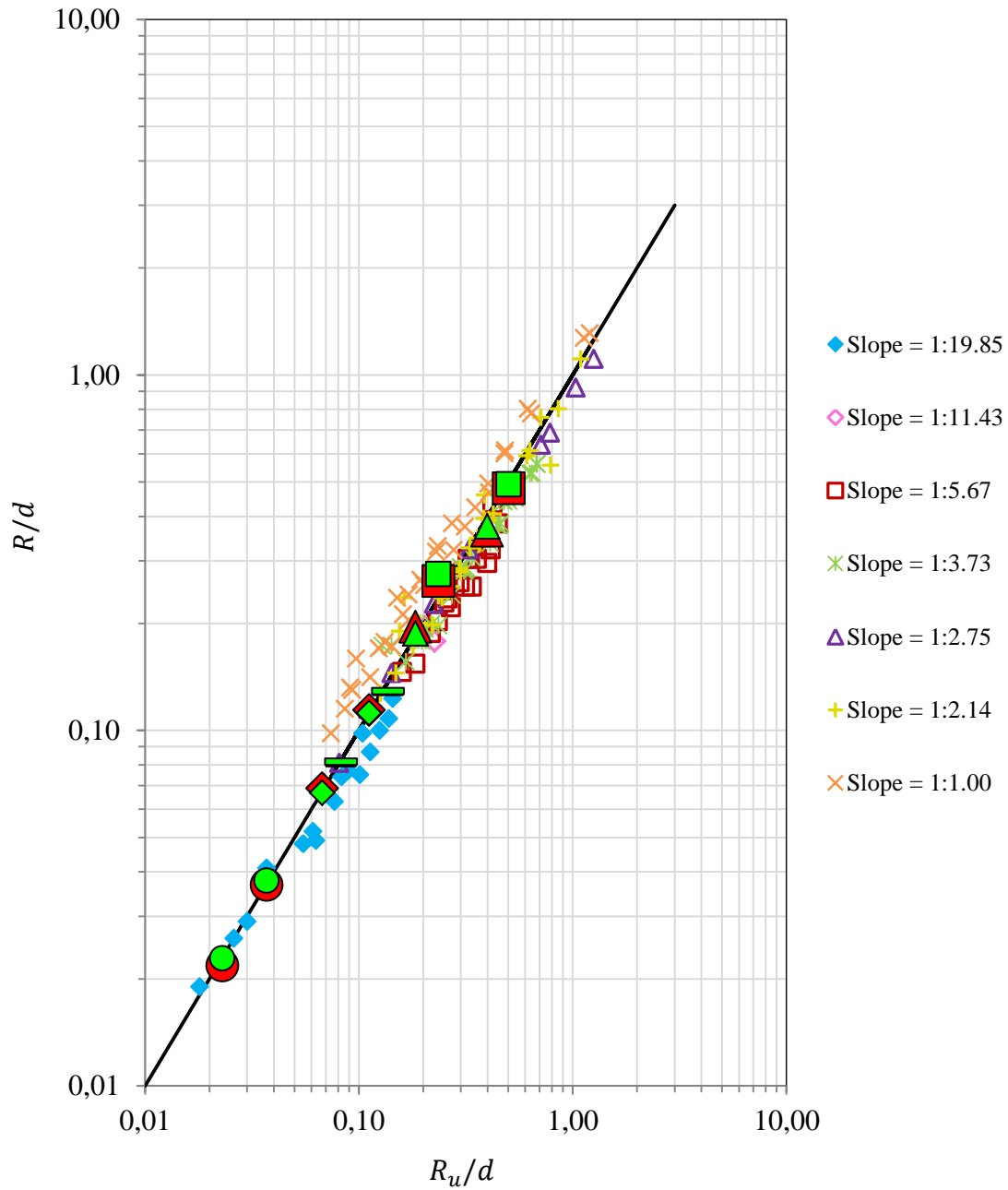


Figure 4.19 Maximum runup values on different slopes when $n = 0.01$: The black line represents the runup law (Synolakis, 1986); the red circles, diamonds, dashes, triangles and squares represent the NAMI DANCE results for 1:20, 1:15, 1:10, 1:6 and 1:4 slopes, respectively; the green circles, diamonds, dashes, triangles and squares represent the FLOW-3D[®] results for 1:20, 1:15, 1:10, 1:6 and 1:4 slopes, respectively.

The evolution of vertical velocity component, w , along the ramp is also analysed via FLOW-3D[®] for the extreme case where $H/d = 0.3$.

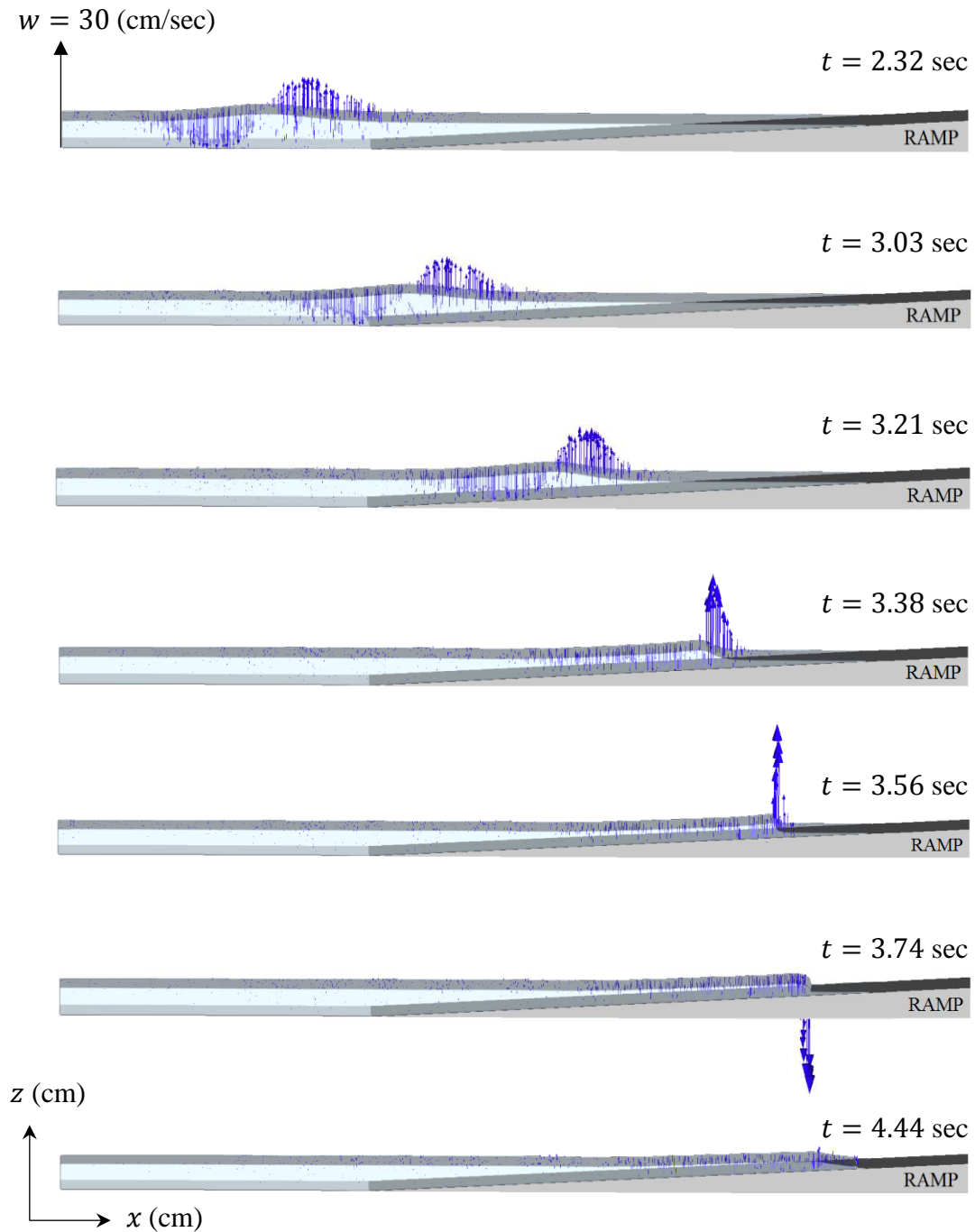


Figure 4.20 Evolution of vertical velocity component, w , for the case where $H/d = 0.3$ (not to scale)

NAMI DANCE is a depth-averaged model; therefore, the vertical velocity component is neglected in the simulations. On the other hand, FLOW-3D® accounts for the effects of w . The velocity time histories at the free surface for the constant depth region (i.e. $d = 30.97$ cm for $H/d = 0.0185$ and $d = 19.62$ cm for $H/d = 0.3$) and the shallower region (i.e. nearshore) are given in Figure 4.20 in terms of non-dimensional horizontal and vertical velocity components, $u^* = u/\sqrt{gd(1 + H/d)}$ and $w^* = w/\sqrt{gd(1 + H/d)}$ for both cases where $H/d = 0.0185$ and $H/d = 0.3$.

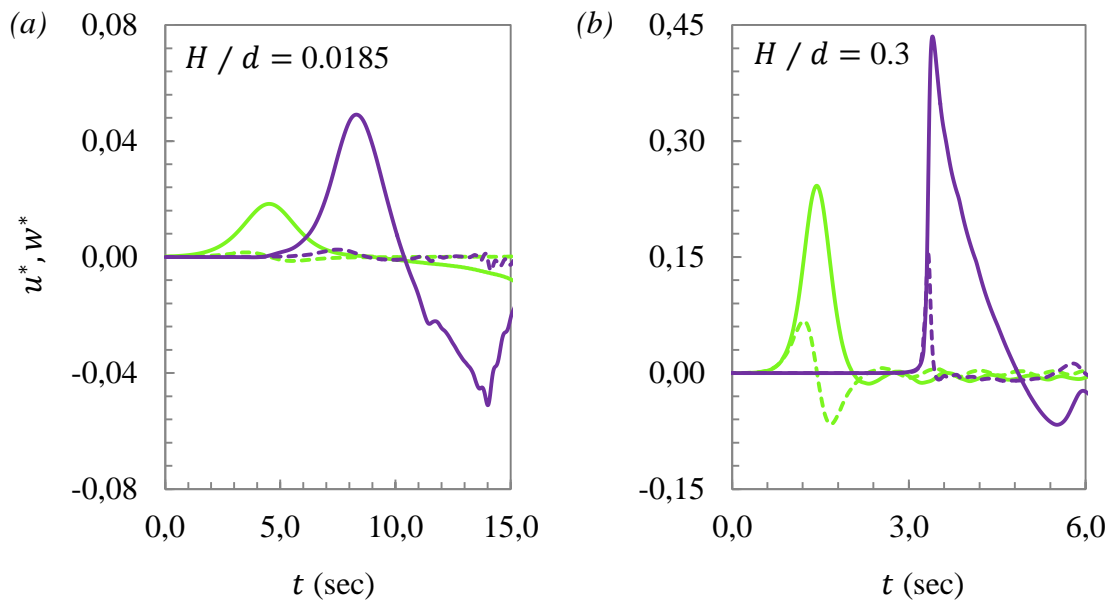


Figure 4.21 Velocity time histories for: (a) $H/d = 0.0185$; (b) $H/d = 0.3$. The solid and dashed green lines represent the predicted horizontal and vertical velocity components at the constant depth region, respectively; the solid and dashed purple lines represent the predicted horizontal and vertical velocity components near the shoreline (i. e. $d = 4.5$ cm), respectively.

The results reveal that, for the non-breaking wave case, there is negligible change in the vertical velocity component as the wave propagates towards the shoreline. In fact, the vertical velocity component is considerably small compared to the horizontal one throughout the simulation. On the other hand, in the extreme case, the vertical velocity component rapidly increases just before breaking and it becomes as large as the half of the horizontal velocity component (i.e. $d = 4.5$ cm).

Tables 4.4 and 4.5 summarize the predicted maximum values of the horizontal and vertical velocity components of a fluid particle for several water depths. Since NAMI DANCE is a depth-averaged model, it does not provide vertical velocity components and horizontal velocity components are constant along depth. On the other hand, being a three-dimensional model, FLOW-3D[®] calculates vertical velocity components, which change along depth, having the maximum values at the *free surface*.

Table 4.4 The predicted maximum horizontal and vertical velocity components of a fluid particle *at the free surface* for the case where $H/d = 0.0185$

d (cm)	NAMI DANCE	FLOW-3D [®]	
	u (cm/sec)	u (cm/sec)	w (cm/sec)
30.97	3.75	3.20	0.20
15.00	5.00	4.90	0.30
10.00	6.30	6.00	0.35
4.50	9.90	9.60	0.40

Table 4.5 The predicted maximum horizontal and vertical velocity components of a fluid particle *at the free surface* for the case where $H/d = 0.3$

d (cm)	NAMI DANCE	FLOW-3D [®]	
	u (cm/sec)	u (cm/sec)	w (cm/sec)
19.62	38.90	38.30	10.65
15.00	44.00	43.70	11.10
10.00	55.00	53.30	13.70
4.50	61.50	60.90	28.30

NAMI DANCE displays a uniform distribution of u along the vertical direction, without any significant deviation, as expected. The FLOW-3D[®] model produces similar results. In both models, the horizontal velocity component decays to zero at the sea bottom. On the other hand, the vertical velocity component, w , changes along the vertical direction, having the largest value at the free surface and reaching zero at the sea bottom. The results indicate that the maximum w increases by 30% just

before reaching the shoreline in the non-breaking wave case. The maximum w is 6%, 6%, 6% and 4% of the maximum u at the constant depth region and at water depths of 15 cm, 10 cm and 4.5 cm, respectively. In the case of the large amplitude solitary wave, the value of w increases as the wave propagates towards the shallower regions and reaches its peak before breaking. In fact, the value of maximum w increases by 130% just before the wave breaks; getting as large as approximately half of the maximum u . For this extreme case, maximum w is 28%, 25%, 25% and 50% of maximum u at the constant depth region and at water depths of 15 cm, 10 cm and 4.5 cm, respectively. All these results imply that, for the evolution of large amplitude waves and/or for very shallow regions, w should not be neglected. It is obvious that 3D numerical modeling should be used in cases where extreme wave heights and/or nonlinearities (i.e. wave breaking) are involved.

Before elaborating on the results of the error analyses of BMP 1, it is crucial to emphasize the method proposed for the calculation of statistical errors, NRMSE and MAX. A segment of time or space, in which the maximum and, on a number of occasions, minimum water level/velocity values are included, is determined beforehand in order to provide consistency in the statistical error analyses of all BMPs in this dissertation. In addition, this method helps eliminate potential disturbances in the data, which may cause the value of NMRSE to increase unnecessarily. Each segment starts when 0.01% of the maximum amplitude/velocity of the first/leading wave occurs. If there is a minimum wave, upon its completion, the end point of the segment is taken as 0.01% of its amplitude/velocity. Moreover, if there is a time shift, it is neglected while calculating the MAX error.

The allowable error thresholds vary according to the reference data types. The data types that BMP 1 provides are analytical solutions and laboratory measurements, for which the allowable NRMSE limits are 10% and 15%, respectively. Moreover, Synolakis et al. (2007) maintain that any well-benchmarked code should produce results within 5% and 10% of the maximum value obtained from analytical solutions and laboratory measurements, respectively.

The NRMSE and MAX errors for the non-breaking solitary wave solution are given in Table 4.6 and Figure 4.22.

Table 4.6 NRMSE and MAX errors for the case where $H/d = 0.0185$

t^*	NAMI DANCE		FLOW-3D [®]	
	% NRMSE	% MAX	% NRMSE	% MAX
30	0.3	0.2	2.3	0.3
40	1.2	0.8	1.7	0.5
50	0.8	5.0	1.5	4.0
60	0.8	1.7	1.7	0.1
70	2.0	4.2	6.5	2.3

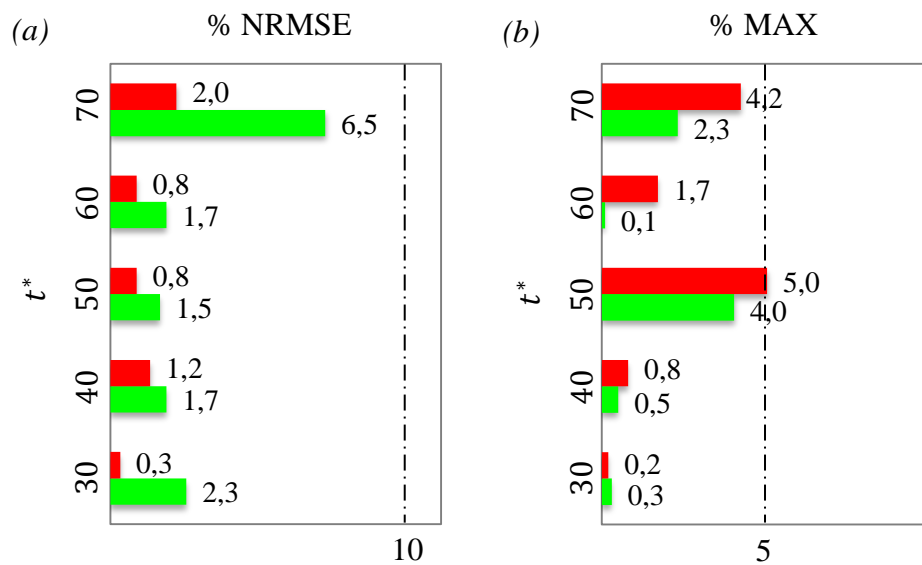


Figure 4.22 Error bars for the case where $H/d = 0.0185$: (a) % NRMSE; (b) % MAX error. The red and green bars represent the errors of NAMI DANCE and FLOW-3D[®] results, respectively.

The NRMSE of the NAMI DANCE results is between 0.3% and 2% while the MAX error ranges from 0.2% to 5%. FLOW-3D[®] results have an NRMSE range between 1.5% and 6.5% and a MAX error range between 0.1% and 4%. The errors are within the OAR PMEL-135 standard analytical error range. Both models predict the evolution and propagation of the non-breaking solitary wave considerably well.

The NRMSE and MAX errors for the large amplitude solitary wave case are given in Table 4.7 and Figure 4.23.

Table 4.7 NRMSE and MAX errors for the case where $H/d = 0.3$

t^*	NAMI DANCE		FLOW-3D [®]	
	% NRMSE	% MAX	% NRMSE	% MAX
15	11.0	19.9	1.5	5.0
20	9.5	20.0	5.0	3.5
25	6.3	4.5	3.5	1.0
30	4.0	17.0	4.4	4.2

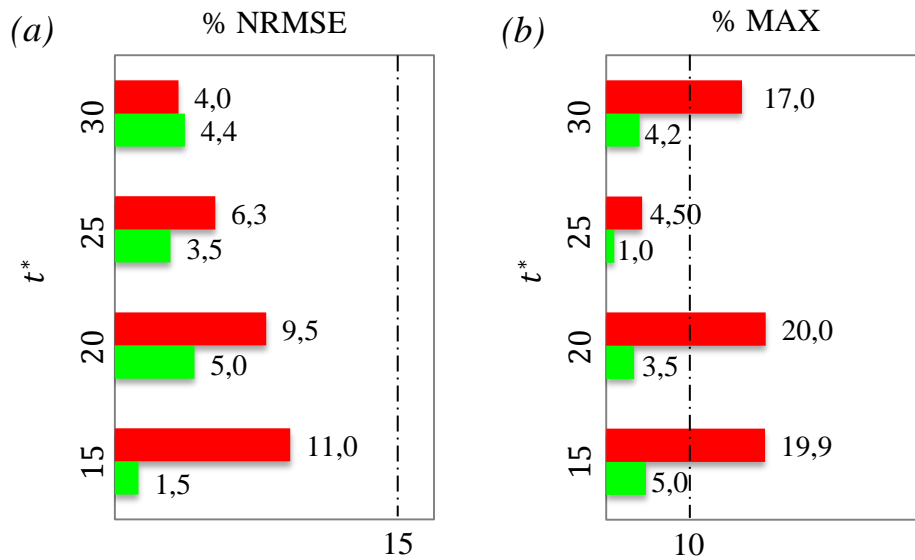


Figure 4.23 Error bars for the case where $H/d = 0.3$: (a) % NRMSE; (b) % MAX error. The red and green bars represent the errors of NAMI DANCE and FLOW-3D[®] results, respectively.

NAMI DANCE results have an NRMSE range between 4% and 11% and a MAX error range between 4.5% and 20%. The NRMSE of FLOW-3D[®] results; however, is between 1.5% and 5% while the MAX error ranges from 1% to 5%. Although the MAX error of NAMI DANCE results is larger than the OAR PMEL-135 standard error for laboratory measurements, it is concluded that these errors are more than acceptable, considering the difficulty in reproducing this benchmark test, which features breaking waves. In fact, the allowable error limit is raised from 10% to 20%

when conducting challenging laboratory experiments, such as those involving breaking waves (Horrillo et al., 2015).

The NRMSE and MAX error for the water level dynamics at two locations $x/d = 0.25$ and $x/d = 9.95$ are given in Table 4.8 for the case where $H/d = 0.0185$

Table 4.8 NRMSE and MAX errors for the water level dynamics at two locations, $x / d = 0.25$ and $x / d = 9.95$, for the case where $H/d = 0.0185$

x / d	NAMI DANCE		FLOW-3D [®]	
	% NRMSE	% MAX	% NRMSE	% MAX
0.25	0.4	1.2	0.5	1.1
9.95	3.3	5.4	1.1	0.6

To sum up, the two- and three-dimensional models, NAMI DANCE and FLOW-3D[®], are first tested against the analytical solutions of one-dimensional (1D), hydrostatic shallow water equations defining the runup of solitary waves on plane beaches where the bottom friction is neglected. 1D models are the first step in the testing and validation of tsunami models despite the fact that they are not completely reliable for tasks such as tsunami inundation mapping. In addition to the analytical solution, the numerical predictions are compared by a set of laboratory measurements that has been widely used for many code validations. The data sets for the non-breaking and breaking solitary waves, which feature $H/d = 0.0185$ and $H/d = 0.3$ respectively, are the most frequently used and appropriate ones for tsunami code validation.

When all the results are assessed, it is seen that the bottom friction is an important parameter in tsunami inundation and should be included in the simulations in order to reach reliable results. It is discovered that smaller friction leads to larger runup values. Furthermore, the runup distance of large amplitude solitary waves is found to be more friction sensitive as a wave becomes a thin layer of liquid traveling up the slope after breaking and the friction is inversely proportional to the water depth. On

the other hand, for non-breaking solitary waves with $H/d \leq 0.01$, the predicted maximum runup values are independent of n . The reason for this may be that small amplitude waves do not travel very large distances on land and thus are slightly affected by the surface roughness. Similar results were reported by Lynett et al. (2002). When Manning's roughness coefficient, n , is 0.01, NAMI DANCE predicted the maximum runup values with an NRMSE of 13%, whereas FLOW-3D[®] results have an NRMSE of 4% (Figure 4.18).

NAMI DANCE, which is a 2D depth-averaged model, can not accurately describe the nonlinearity of large amplitude solitary waves. As seen in the model results, the wave crest steepens, which is typical of any hydrostatic model, owing to lack of energy dissipation. Since NAMI DANCE fails to capture the strong nonlinearities existing in the wave breaking process, the predicted wave heights are smaller than the laboratory measurements. This leads to the underestimation of the runup distances of large amplitude solitary waves, by approximately 20%. However, the model is able to reasonably simulate the runup process following the occurrence of wave breaking. Both models reproduce the overall pattern of wave arrival quite well without any shift in the wave arrival times. Local disagreements observed in the wave profiles might be caused by a combination of instrumentation and model errors since the computed results agree with the measured data toward the end.

The effect of the vertical velocity component, w , is negligible both at the constant depth region and in the shallower regions in the case of small amplitude solitary waves since the value of w is very small compared to the horizontal velocity component, u , when it reaches the shoreline. On the other hand, in the case of large amplitude solitary waves, the vertical velocity component rapidly increases and its maximum becomes as large as the half of the maximum horizontal velocity component just before the wave reaches the shoreline and breaks.

Thus, it is concluded that, both models give satisfactory results and can be used for plane beaches where there is no complex topographical element and the turbulence effect is negligible. However, three-dimensional models should be preferred when large amplitude waves and/or shallower regions are studied.

It is important to note that the trend towards modeling of tsunamis using solitary waves has lost popularity in recent years. Synolakis et al. (2007) stated that, even though some of the basic physics of tsunamis can be captured through the use of solitary waves in numerical models, the physical manifestation of tsunamis in nature can not be sufficiently modeled owing to the fact that tsunamis are always N-wave like with a leading-depression wave followed by an elevation wave.

4.2. BMP 2: Solitary Wave on a Conical Island

4.2.1. Problem Description

The eastern region of Flores Island, a volcanic island located at the transition between the Sunda and Banda Island arc systems in Indonesia was struck by an earthquake with a magnitude of 7.8 M_w on December 12, 1992 (Figures 4.24 and 4.25). The earthquake was followed by 25-meter-high tsunami waves that hit the town of Maumere, resulting in substantial casualties and property damage. Four days after the incident, Japanese television channels reported that 1000 people had been killed in Maumere and two-thirds of the population of Babi Island had been annihilated by the tsunamis. In the end, the number of deaths was reported as 2080, and there were 2144 injured people. Approximately 50% of the total toll was caused by the tsunami waves.



Figure 4.24 Tsunami attack site in Riangkroko (Credit: Harry Yeh) (Yeh et al., 1994)

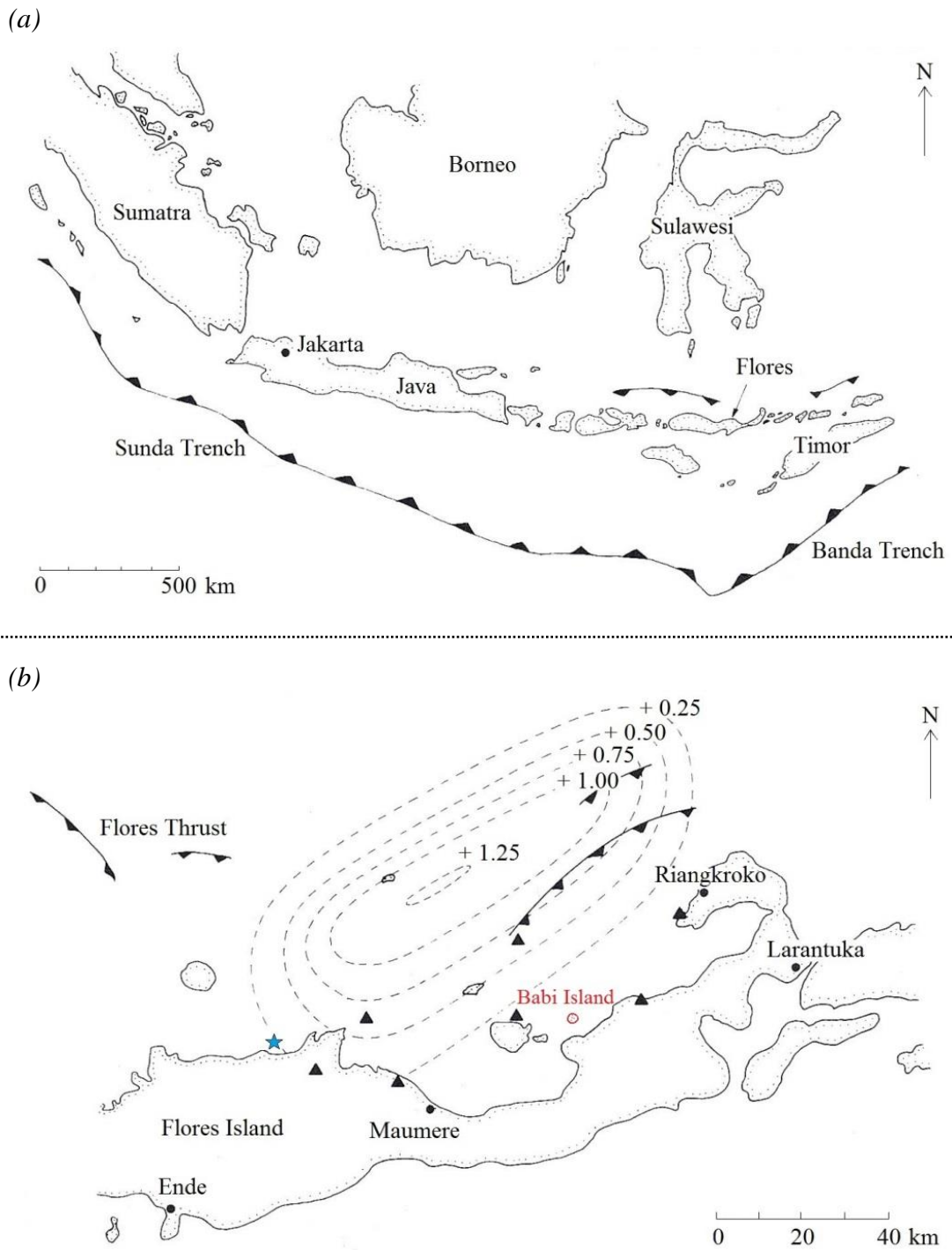


Figure 4.25 (a) Map of the Indonesian region; (b) Map of Flores Island. The star represents the epicenter of the main shock; the triangles show the aftershock locations; the dashed contour lines indicate the predicted vertical seafloor displacement in meters, which is directly translated to the initial tsunami condition (Yeh et al., 1994).

The tsunami survey plan, which was started 3 days after the catastrophe, consisted of a ground survey including measurements of maximum tsunami runup heights and distances, average runup heights and areas of inundation, flow patterns of runup and rundown, eyewitness accounts, observations of subsidence, uplift and landslides, and a helicopter aerial survey (Yeh et al., 1994). The water marks on the structures and/or ground, breakage of tree limbs, scratch marks on the trees or structures caused by water borne objects, and/or the location of water borne debris were analysed to determine the maximum tsunami runup height (Yeh et al., 1994).

At Riangkroko, an extremely large tsunami runup was measured to be approximately 26 meters. Based on four different tsunami marks, the average height was found to be 19.8 m (Figure 4.26) and the runup inundation distance from the shoreline to be approximately 600 m.

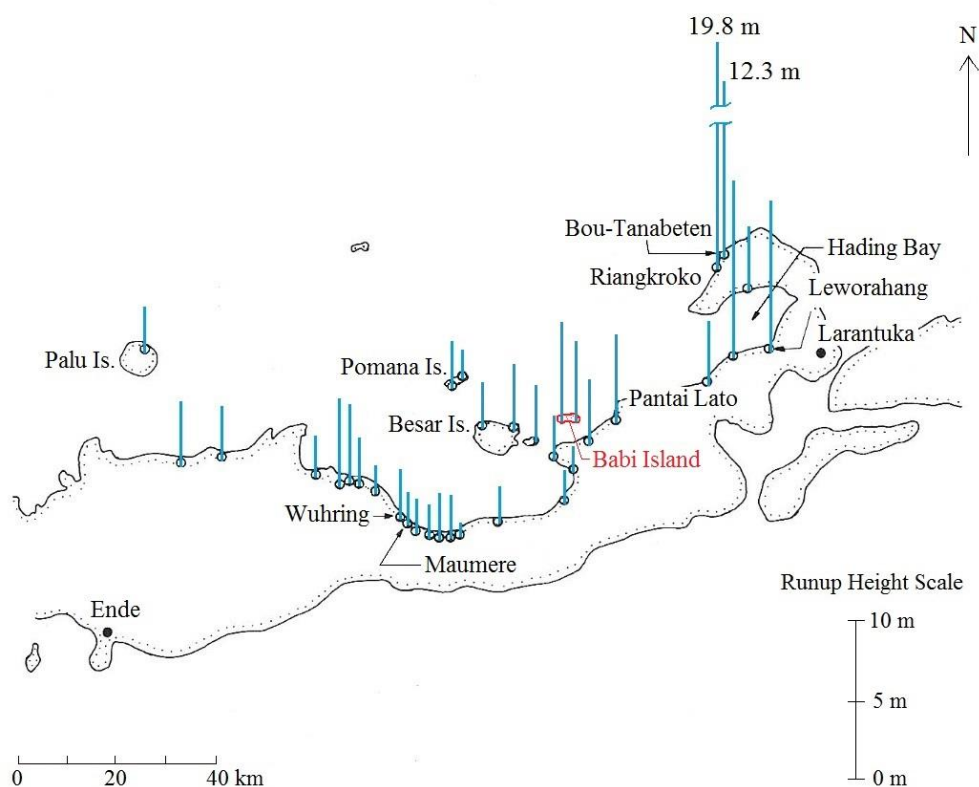


Figure 4.26 Tsunami runup heights from sea level at the time of the tsunami attack. The values were measured at each location and averaged from multiple measurements by the tsunami survey team (Yeh et al., 1994).

Babi Island, which is about 5 km offshore from Flores, was also severely affected by the tsunamis. Out of a population of 1093, 263 people were killed due to the strong earthquake motions and tsunamis. Babi Island has a conical shape, with a summit elevation of 351 m and a diameter of approximately 2 km. The water around Babi Island is quite deep despite its proximity to the main island. There is a wide coral reef on the north shore, which faces the Flores Sea. On the south shore, where the villages were located, there is a much narrower coral reef. There was a Moslem village, Kampungbaru, on the west-side and a Christian village, Pagaraman, on the east side, separated by a small tidal flat near the middle of the south shore. These two villages were totally devastated by the tsunamis and nothing was left of the Christian village (Yeh et al., 1994) (Figure 4.27).



Figure 4.27 (a) Babi Island; (b) catastrophe on the back side of Babi Island (Yeh et al., 1994)

The wave conditions on the south side of Babi Island are usually calm even when there are strong wind waves and swells of the Flores Sea attacking from the north. The reason for this is that most of the incoming wave energy is dissipated on the wide coral reef on the north side. However, the south shore was prone to the 1992 tsunami attack, although it was usually protected from wind waves and swells. According to Yeh et al. (1994) the tsunami disaster at the south side can be attributed to the shape of the island and wave reflection. The reflection of tsunamis in the deep sea between Babi Island and the opposite shore of Flores Island could potentially create a wave resonance phenomenon. If this was the case, this phenomenon may have been partially responsible for the catastrophe on Babi Island (Yeh et al., 1994). The maximum tsunami runup heights were 5.6 m in the Christian village and 4.6 m

in the Moslem village. The maximum runup height, which was measured on the steep slope on the west side of the island, was 7.3 m. The directions of tree falls and debris accumulations helped estimate the tsunami runup and rundown directions, which showed that the villages were attacked by the tsunami generated flow from all directions (Yeh et al., 1994).

The fact that the tsunami attacked the conically shaped Babi Island from the north, but an extremely high inundation was observed in the south (back or lee side of the island), suggests that there is a need for a better understanding of the important physical parameters involved in a three-dimensional tsunami runup.

Approaching an island from deep water, a tsunami wave goes through refraction, diffraction and breaking, as do short waves. The height and steepness of a tsunami wave increase with complicated currents and multiple wave trains. The number of tsunami waves and their amplitudes around the perimeter of the island may be affected by reflections from adjacent shorelines (Briggs et al., 1995). When the tsunami damage on Babi Island was investigated, it was found that there were unexpectedly large runup heights, especially on the back or lee side of the island. A surprising finding was that the results of the numerical simulations carried out by various international teams were substantially different from those of the field measurements, often by factors of ten.

A three-year study was initiated in 1992 by the National Science Foundation in order to develop large-scale experimental databases for verification and modification of numerical models and to analyse the parameters involved in three-dimensional tsunami runup. The participants were from Cornell University, Harvard University, University of Washington, University of Southern California and the U.S. Army Engineer Waterways Experiment Station (WES). The reason why a conical island was selected for the study was its mathematical simplicity and realistic geometry compared to actual islands (i.e. Babi Island, Okushiri Island, and Hawaiian Islands) (Briggs et al., 1995). The large-scale experiments were conducted at WES during

1993 and 1994. A 30-m-wide by 25-m-long flat bottom wave tank was installed at the US Army Engineer Waterways Experimental Station (WES), Vicksburg, Mississippi, in the center of which a model of the conical island was constructed (Briggs et al., 1995; Liu et al., 1995) to understand the cause of the observed high inundation at the opposite side of the island. The basin wall dimensions were 29.3 m x 30 m (Figure 4.28). An absorbing material, 5-cm-thick synthetic horsehair, was rolled into cylinders approximately 0.9 m in diameter, and characterized by a reflection coefficient that varied slightly with wave frequency (NTHMP, 2011). The surface of the basin and the conical island were made of smooth concrete.

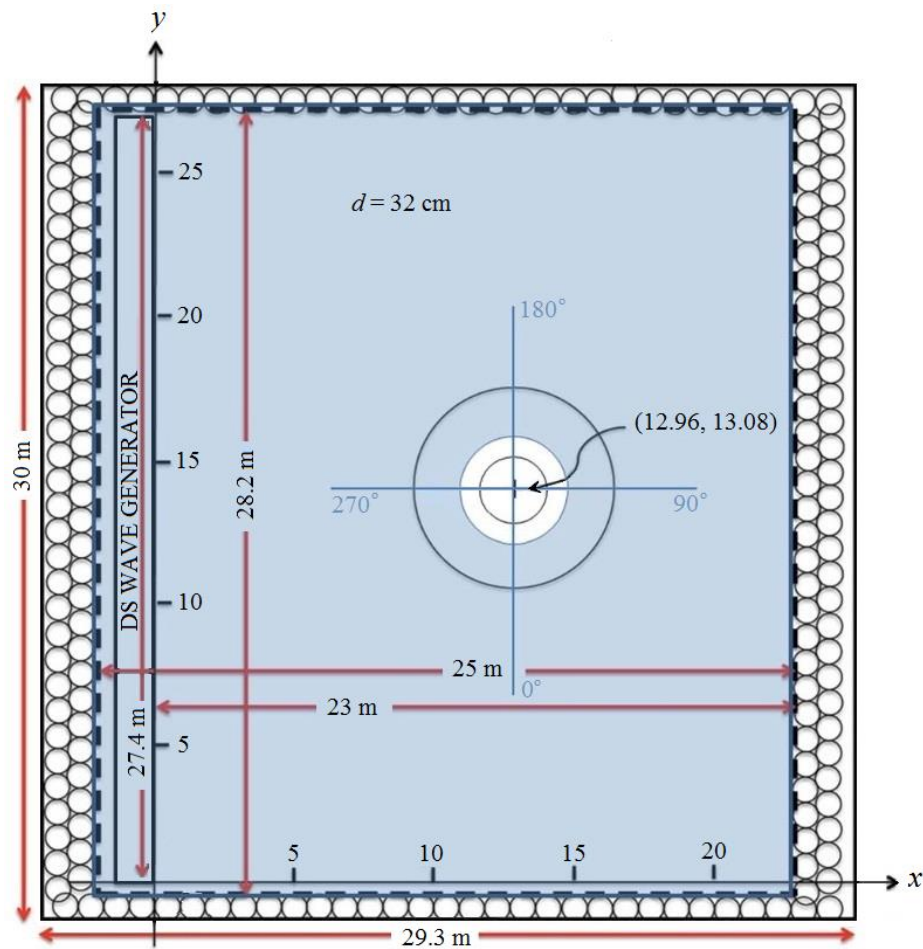


Figure 4.28 Basin geometry, coordinate system and location of gauges. The circles along the walls and the dashed lines represent wave absorbing material (not to scale) (Credit: Frank Gonzalez) (Horrillo et al., 2015).

The island was shaped like a truncated, right circular cone with diameters of 7.2 m at the toe and 2.2 m at the crest. The vertical height of the island was approximately 0.625 m, with 1V:4H beach face (i.e., $\beta = 14^\circ$) (Figure 4.29). The water depth in the basin was set at 0.32 m. A Directional Spectral Wave Generator (DSWG), located at $x = 12.96$ m from the island, generated waves with an initial solitary wave-like profile with H/d ratios ranging from 0.05 to 0.20.

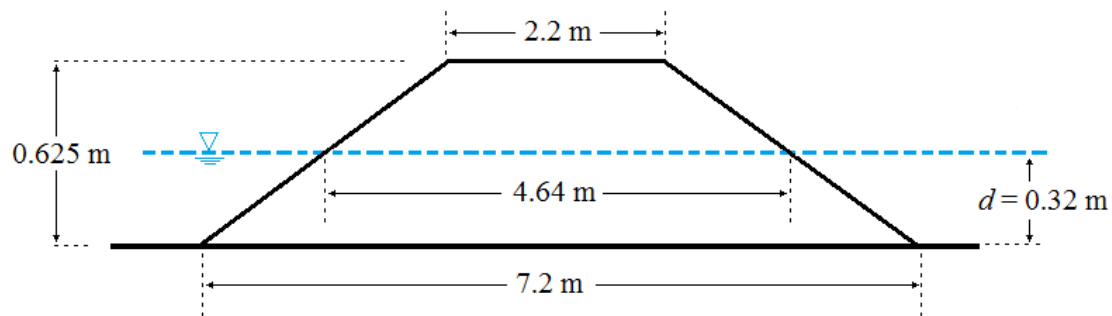


Figure 4.29 Definition sketch for the conical island (not to scale)

Figure 4.30 shows refracting waves around the island with the DSWG in the background and an overhead view of the wave runup is given in Figure 4.31. The electronically controlled DSWG was 27.4 m long and consisted of 60 paddles, which were 46 cm wide and 76 cm high. A 3/4 HP closed-loop servomotor was used to independently drive each of the 61 paddle joints in piston mode. The maximum stroke of the DSWG was 30.5 cm (Briggs et al., 1995).

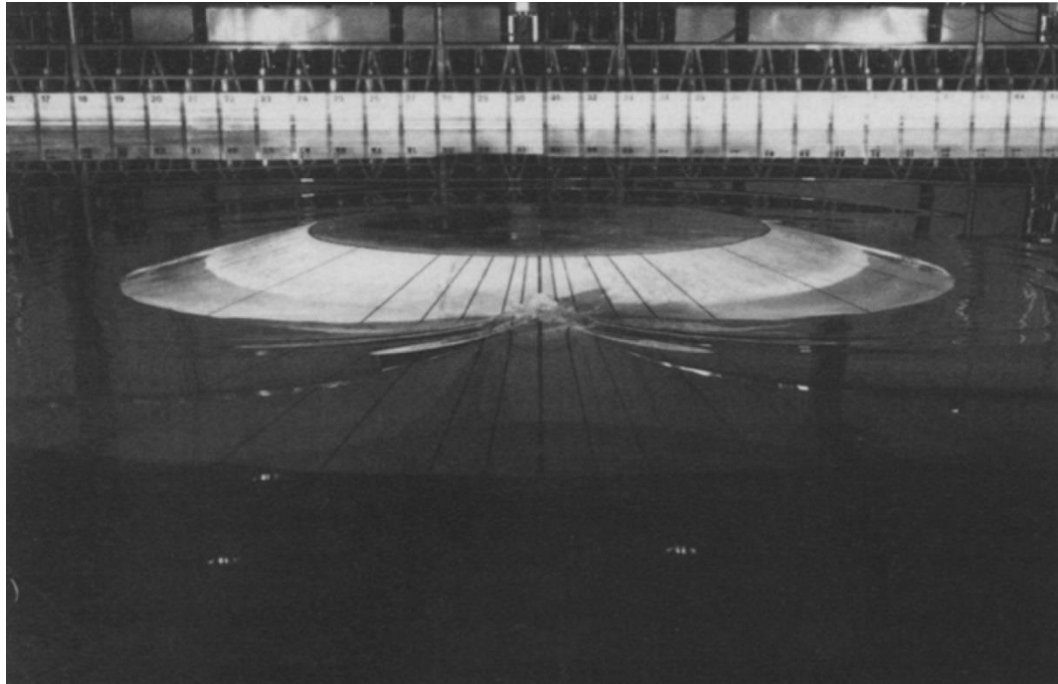


Figure 4.30 A view of the conical island and the directional spectral wave generator from the back side of the island (Briggs et al., 1995)

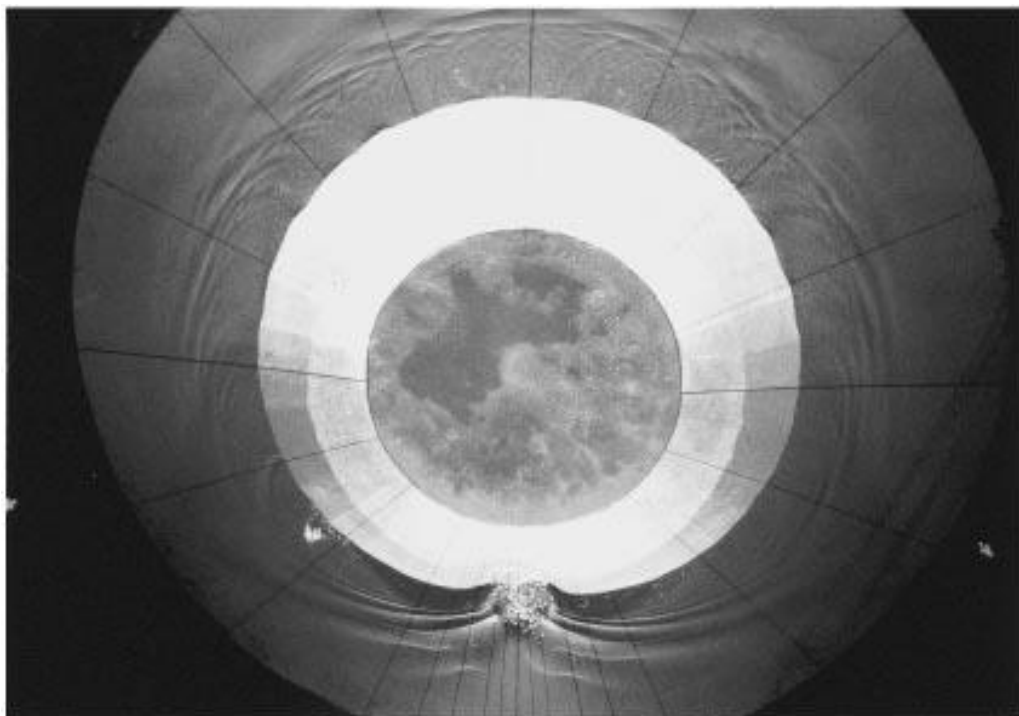


Figure 4.31 An overhead photograph of the wave runup on the lee side of the island (Briggs et al., 1995)

In order to measure the free surface elevations, twenty seven capacitance wave gauges were used, the first four of which were situated parallel to the wavemaker to measure incident wave conditions. Before each run, the distance of these four gauges from the toe of the island was calculated as half of the wavelength, $L/2$, of the wave that would be generated. Thus, it was possible to measure the tsunami wave always at the same relative stage of evolution. A circular measurement grid of six concentric circles, covering a maximum distance of 2.5 m beyond the toe of the island, was defined. The remaining gauges were located at the intersection of these concentric circles and the 90° radial lines (i.e. 0° , 90° , 180° and 270° transects around the perimeter of the island) (Figure 4.32). The maximum vertical runup measurements were carried out at twenty locations around the perimeter of the island by using rod and transit. In addition, in order to record runup time series on the back/lee side of the island, a digital runup gauge was used.

The experimental setup is also described in varying detail in Briggs et al. (1994), Liu et al. (1994), Briggs et al. (1995), Liu et al. (1995), Briggs et al. (1996), Kanoglu (1998), Kanoglu and Synolakis (1998), Fujima et al. (2000), Synolakis et al. (2007).

The locations of the 27 wave gauges are listed in Table 4.9. The first four gauges are placed according to the characteristics of the initial wave (i.e. $L/2$). In other words, they are replaced for each run having different H/d ratios.

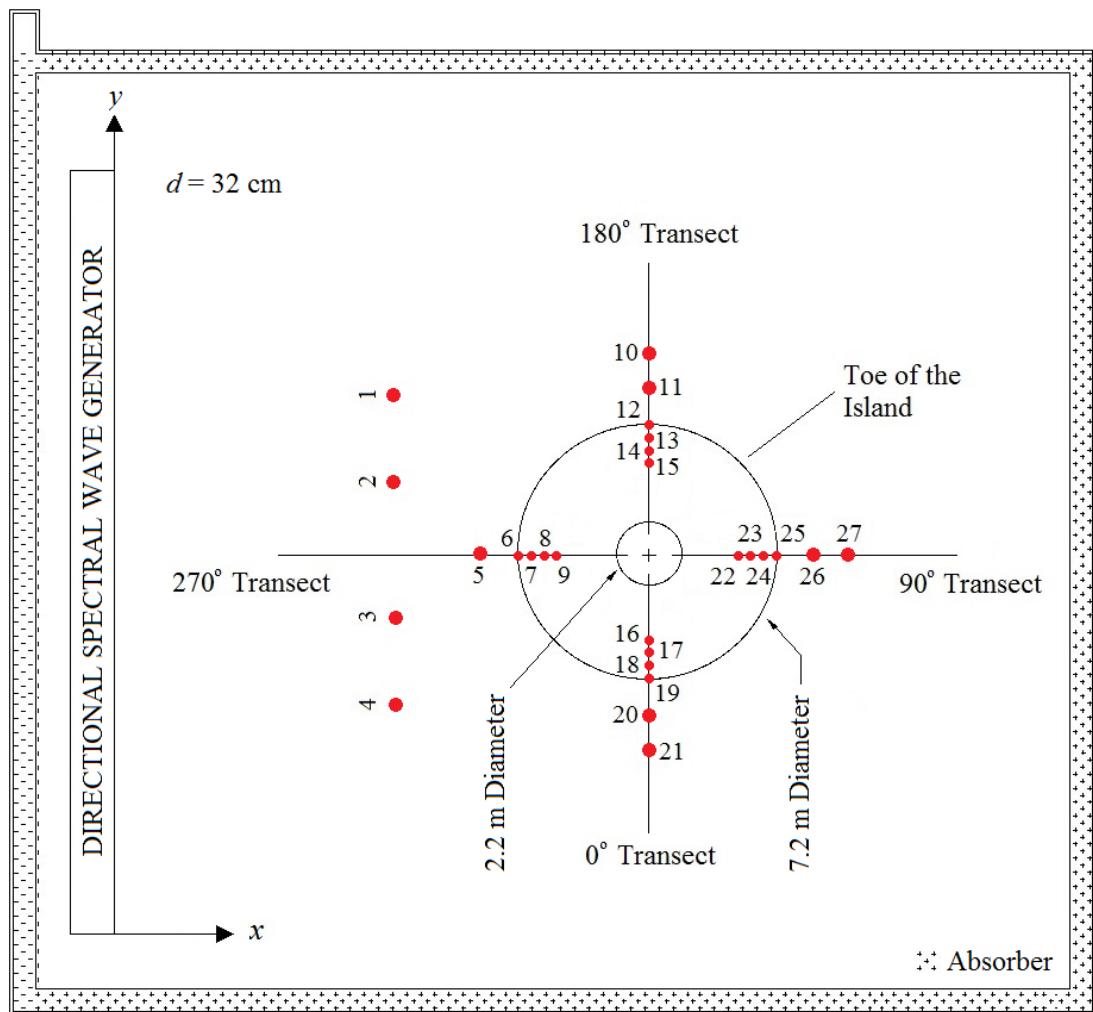


Figure 4.32 Schematic showing the gauge locations around the conical island (not to scale)

Table 4.9 BMP 2 wave gauge locations (Briggs et al., 1995)

Gauge ID	x (m)	y (m)	z (m)	Comments
1	$f(L/2)$	16.05	32.0	Incident Gauge
2	$f(L/2)$	14.55	32.0	Incident Gauge
3	$f(L/2)$	13.05	32.0	Incident Gauge
4	$f(L/2)$	11.55	32.0	Incident Gauge
5	8.36	13.80	32.0	270° transect
6	9.36	13.80	31.7	270° transect
7	9.76	13.80	22.5	270° transect
8	10.08	13.80	14.7	270° transect
9	10.36	13.80	8.2	270° transect
10	12.96	19.93	32.0	180° transect
11	12.96	18.43	32.0	180° transect
12	12.96	17.43	31.5	180° transect
13	12.96	17.00	22.5	180° transect
14	12.96	16.68	14.6	180° transect
15	12.96	16.40	7.9	180° transect
16	12.96	11.22	7.9	0° transect
17	12.96	10.92	15.2	0° transect
18	12.96	10.60	21.9	0° transect
19	12.96	10.25	30.1	0° transect
20	12.96	9.17	32.0	0° transect
21	12.96	7.67	32.0	0° transect
22	15.56	13.80	8.3	90° transect
23	15.84	13.80	15.7	90° transect
24	16.16	13.80	22.8	90° transect
25	16.59	13.80	31.7	90° transect
26	17.59	13.80	32.0	90° transect
27	19.09	13.80	32.0	90° transect

As some of the coastal effects of tsunamis can be modeled efficiently and in a reliable way in the laboratory by using solitary waves, the initial waves that were generated had a solitary wave like profile. The surface profile of a solitary wave centered at $x = X_1$ at time t is given by Equation [4.4] (Synolakis, 1986) and the effective wavelength is calculated as:

$$L = \frac{2d}{\sqrt{\frac{3H}{4d}}} \cosh^{-1} \left(\sqrt{\frac{1}{0.05}} \right) \quad [4.11]$$

so that it is equal to the distance between the two end points in the symmetric profile where the height is 5 percent of the height at the crest H (Briggs et al., 1995).

Three different cases are selected from the laboratory experiments to validate the numerical models, namely Case A, Case B and Case C, where the initial H/d ratios are equal to 0.045, 0.091 and 0.181 at 32 cm water depth, respectively.

The free surface conditions at the minimum x boundary are set according to measurements at Gauge 2 (Figure 4.33), which is located offshore, for both models, instead of modeling the action of the generator paddles in order to simulate the incident waves. In this way, consistency with the analyses is achieved.

The experiments of Briggs et al. (1995) were used as benchmark tests for validating 2+1 numerical codes in the 1995 Friday Harbor, Seattle, Washington Long-Wave Runup Models Workshop (Yeh et al., 1996) and have become a standard for validation of runup models (Liu et al., 1995a; Titov and Synolakis, 1998; Chen et al., 2000; Lynett et al., 2002; Wei et al., 2006 and Yamazaki et al., 2009). The waves are generated at one side of the tank and overtake the island as they travel toward the opposite side. The tests provide runup observations for validating numerical models and supplement comparisons with analytical results (Kanoglu and Synolakis, 1998).

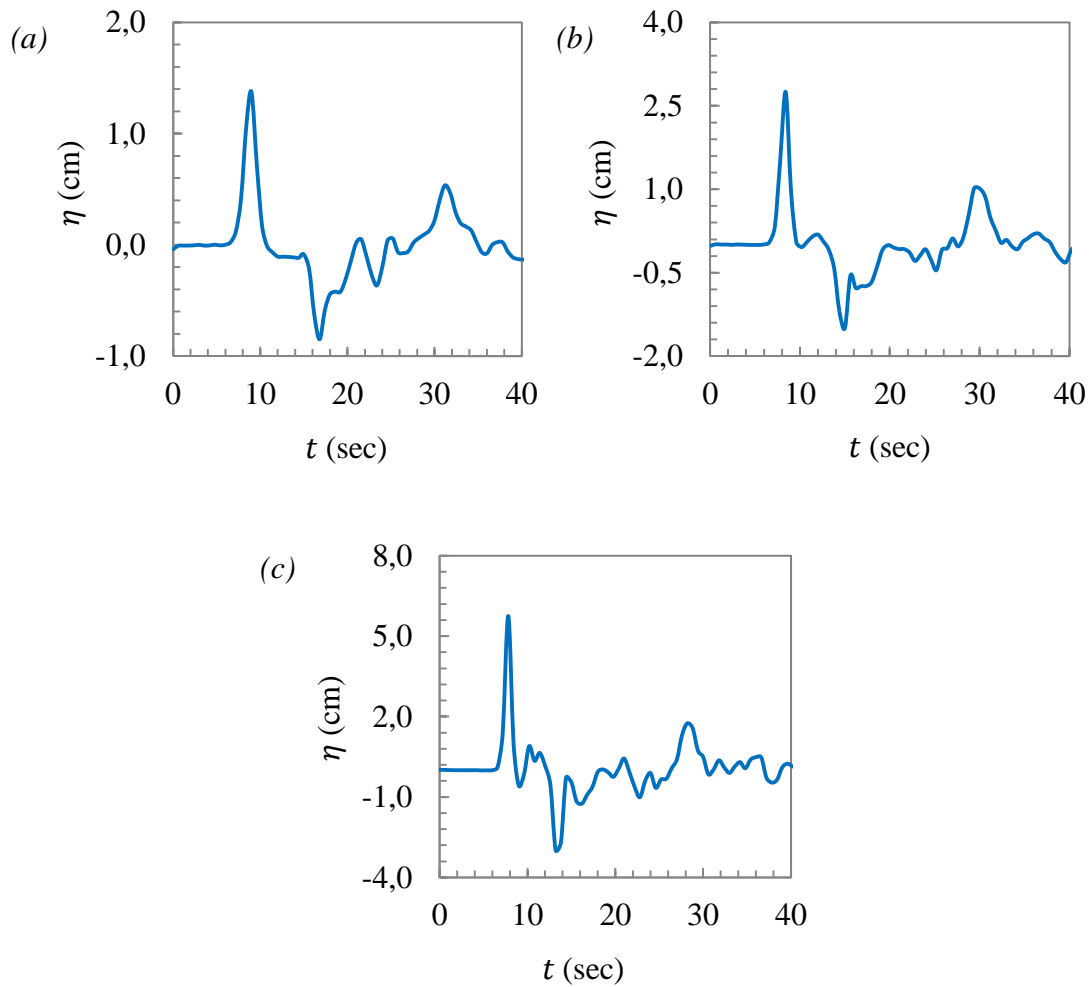


Figure 4.33 The free surface elevation time series recorded at Gauge 2 for: (a) Case A; (b) Case B; (c) Case C (Briggs et al., 1995).

To perform BMP 2, it is necessary to demonstrate that the modeled wave fronts split in front of the island and collide behind it (as edge waves) producing an extreme localized runup. Moreover, the computed water levels at the four gauges around the island; namely, Gauges 6 – in the front of the island at the toe, 9, 16 and 22 – closest to the shoreline located at the 0° , 90° , and 180° radial lines, are replicated and the angular distribution of runup is compared with the laboratory data for the various cases of incident waves. These gauges provide sufficient coverage of the wave conditions that are crucial to the experiment.

4.2.2. NAMI DANCE Model

The same set of experiments is reproduced in a 2D domain using NAMI DANCE. The fluid is inviscid and the flow is incompressible. Fluid density is taken constant throughout the fluid domain.

The x axis of the Cartesian coordinate system is perpendicular to the wavemaker and the y axis is parallel to the wavemaker (Figure 4.34). The origin is located at the end of the wavemaker, in line with the front surface of all paddles at their rest position. The center of the island is located at $x = 12.96$ m and $y = 13.80$ m. A local coordinate system, where polar convention is used, is located at the center of the island (Figure 4.35). Figure 4.35 also illustrates the 3D view of NAMI DANCE computational domain and location of gauge points. The gravitational force, g , is in the downward direction.

The water surface elevation time series recorded at Gauge point 2 is inputted at the upstream end of the computational domain (i.e. minimum x boundary), which is located $L/2$ distance away from the toe of the slope. The maximum x boundary has a rigid wall boundary condition, which defines the downstream end of the wave tank. The minimum and maximum y boundaries are also defined as rigid walls in order to prevent outflow from the computational domain.

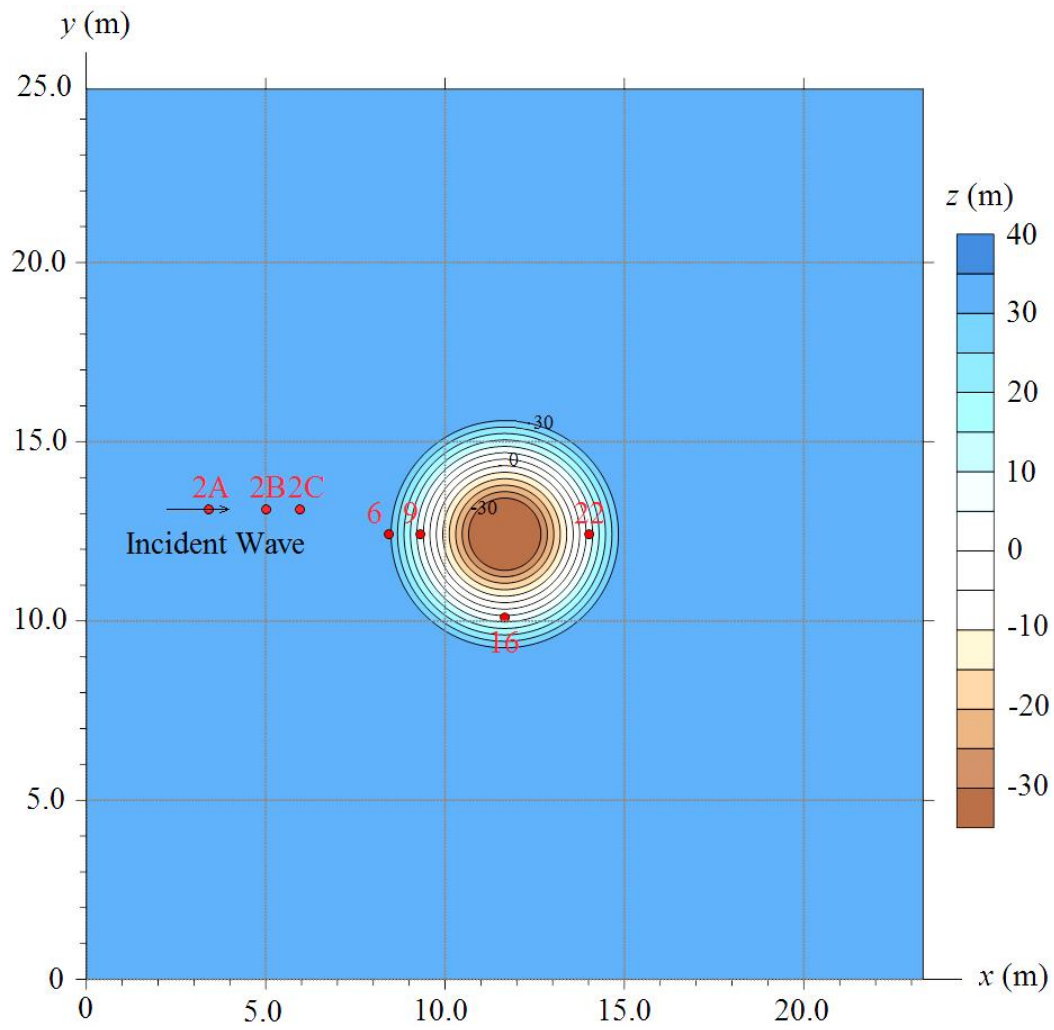


Figure 4.34 NAMI DANCE model: a typical computational domain and the orientation of the coordinate system (top view)

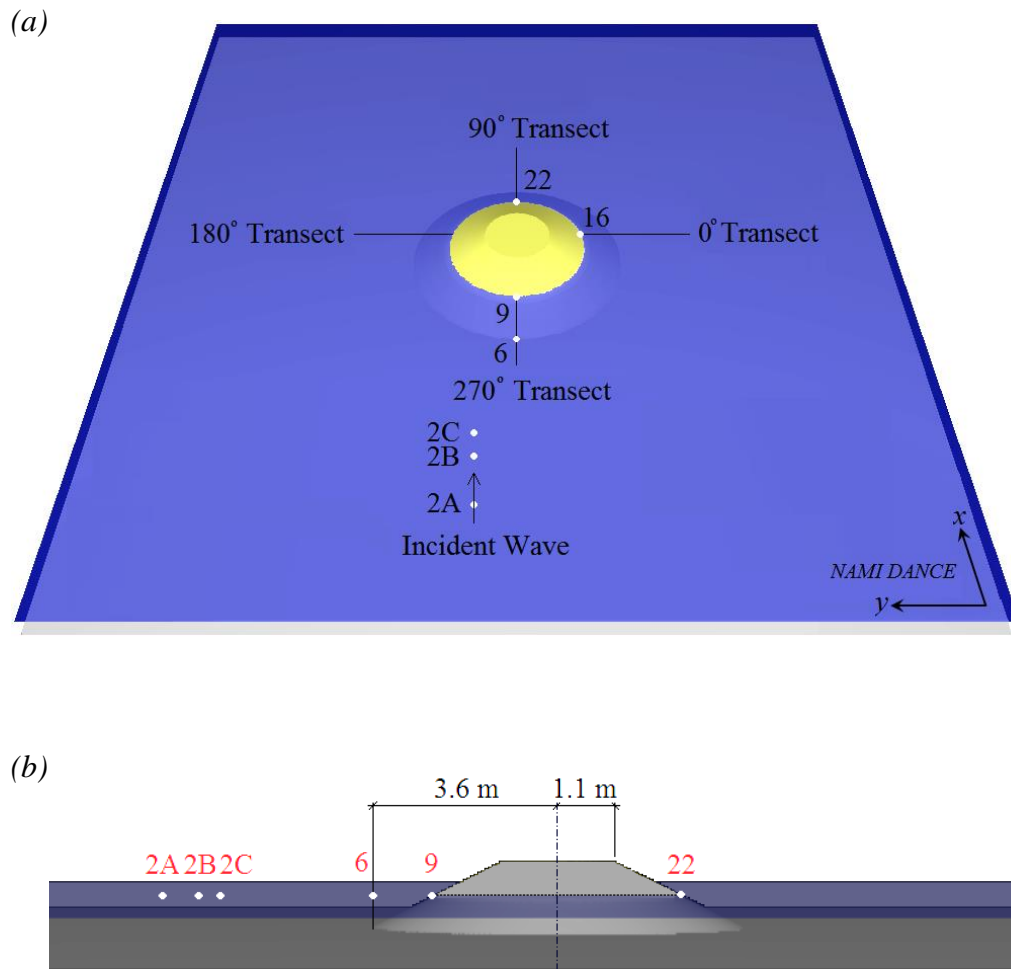


Figure 4.35 NAMI DANCE computational domain and gauge locations for BMP 2: (a) 3D top view; (b) side view

4.2.2.1. Spatial Discretization

The computational domain, represented by a structured mesh (i.e. rectangular cells), covers the entire length of the flume with grid sizes, Δx and Δy , which are uniform throughout the mesh.

It is important to note that reducing the cell size does not necessarily guarantee a better result from a practical perspective since it may lead to unstable results and unnecessarily abundant computational resources and time. The previous numerical model validations that used BMP 2 (NTHMP, 2011) are taken into account in the determination of the grid size. It is found that in the recent studies the grid size used in the vicinity of the island is either $\Delta x = 0.01$ m (Alaska Tsunami Model, Alaska Tsunami Forecast Model and SELFE), or $\Delta x = 0.05$ m (MOST, NEOWAVE and BOSZ) (NTHMP, 2011). After a careful analysis, the grid size is selected as 5 cm; i.e. $\Delta x = \Delta y = 0.05$ m.

It has been suggested in the literature that the convergence of tsunami modeling algorithms be assessed by simulating the extreme positions of the shoreline – the maximum runup and rundown. The convergence of NAMI DANCE is tested by comparing the predicted runup values at Gauge 9, for Cases A, B and C, respectively (Table 4.10).

Table 4.10 NAMI DANCE: Predicted runup values at Gauge 9 for different Δx values ($n = 0.01$)

Grid Size Δx (m)	Maximum Runup (cm)		
	$H/d = 0.045$	$H/d = 0.091$	$H/d = 0.181$
0.01	2.28	5.44	8.80
0.05	2.28	5.44	8.80
0.1	2.25	5.41	8.77
0.5	2.21	5.40	8.75
1.0	2.18	5.37	8.67

The match between the predicted data and laboratory measurements increases as the computational grid resolution is decreased from 1.0 m to 0.01 m. The most obvious manifestation of this convergence is the improved form of the first wave. In fact, no considerable change is observed after $\Delta x = 0.5$ m. The predicted runup values differ by less than 1% for $\Delta x \leq 0.5$ m.

The maximum time step size that fulfills the CFL stability criteria is calculated automatically by NAMI DANCE for each run, depending on the bathymetry. According to this limitation, time step, Δt , is selected as 0.02 second for all runs.

4.2.2.2. Friction

Manning's roughness coefficients used to assess the effect of friction on the maximum runup values are:

- (i) $n = 0$ (i.e. frictionless bottom)
- (ii) $n = 0.01$ (i.e. neat cement/concrete/smooth glass beach)
- (iii) $n = 0.03$ (i.e. fine particles along the channel bottom)

The results reveal that the effect of friction varies spatially over the computational domain since the friction term is a function of water depth. Introduction of the friction coefficient improves the numerical predictions. It is seen that, around the perimeter of the conical island, the predicted and measured runup values match when $n = 0.01$, including the extreme runup behind the conical island. Accordingly, the predicted inundation level on the frictionless surface is higher than the measured one, whereas the predicted runup values are smaller than the measured ones with increased friction coefficients. These situations are most spotted in Cases B and C, where $H/d = 0.091$ and $H/d = 0.181$, respectively. The predicted runup values are not significantly affected by n for Case A, where $H/d = 0.045$ (Figure 4.36).

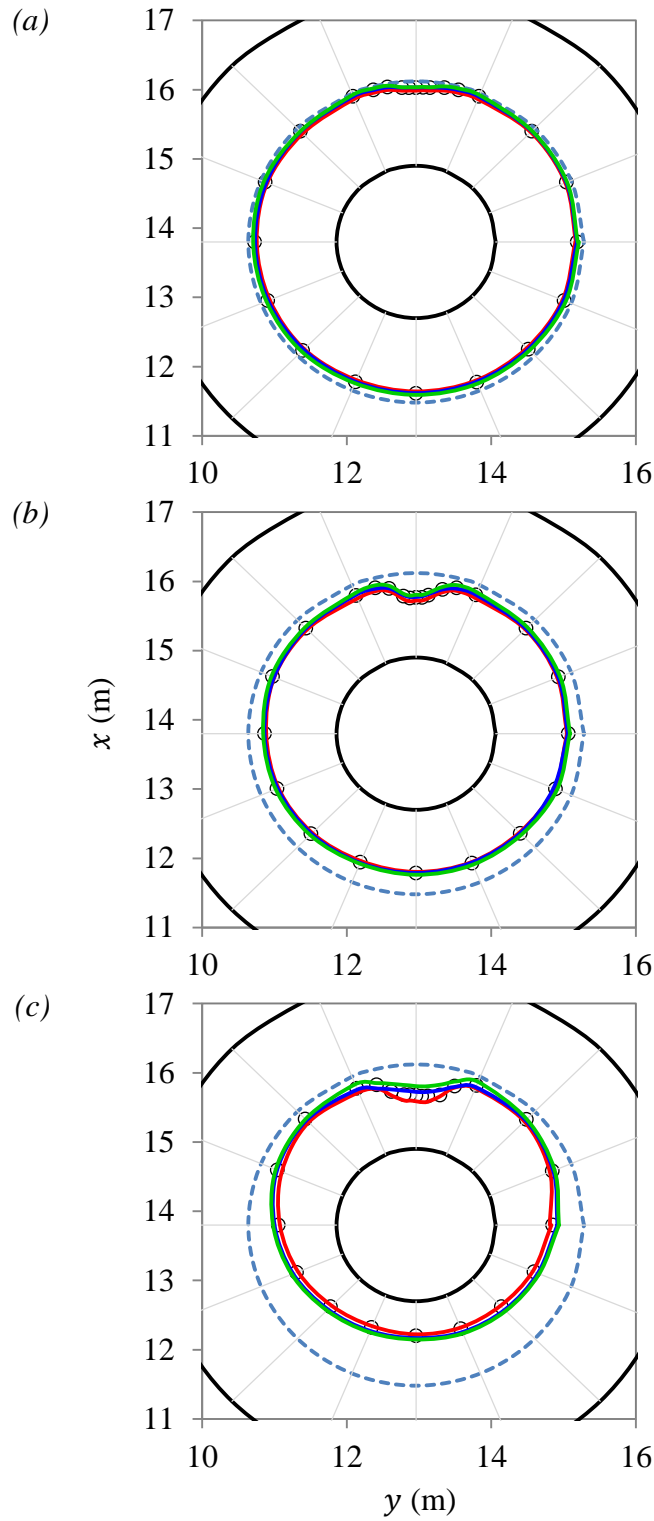


Figure 4.36 NAMI DANCE runup predictions according to different Manning's roughness coefficients for: (a) Case A; (b) Case B; (c) Case C. The dashed blue line represents the initial shoreline; the red line represents the results when $n = 0$; the blue line represents the results when $n = 0.01$; the green line represents the results when $n = 0.03$.

4.2.3.FLOW-3D® Model

The same set of physical experiments is reproduced using FLOW-3D® (Figure 4.37):

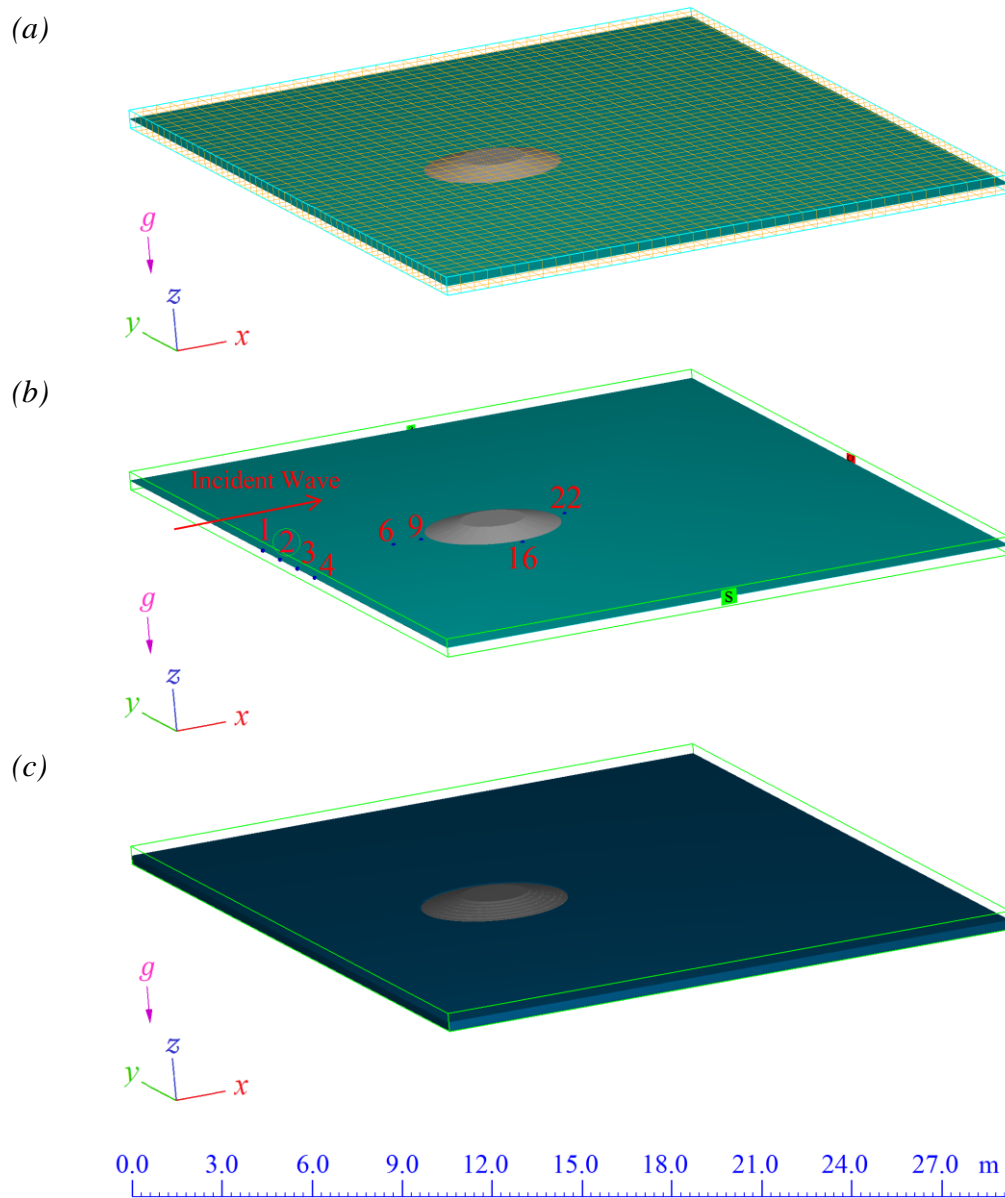


Figure 4.37 FLOW-3D® computational domain constructed for BMP 2: (a) meshing (enlarged for clarity); (b) boundary conditions and gauge locations; (c) after using FAVOR™

The fluid is inviscid, the flow is incompressible and the fluid density is constant. The effects of surface tension and air entrainment at the surface of the flow are neglected. The numerical model is constructed using the Cartesian coordinate system, where the positive x direction is oriented along the fluid flow into the domain and the positive y direction is perpendicular to the direction of the flow (Figure 4.37). The gravitational acceleration, g , is in the downward direction (i.e. $-z$ direction).

The pressure boundary condition is employed at the minimum x boundary. This boundary condition allows the user to enter the input data manually, which is the free surface elevation time series recorded at Gauge 2 in this case. The maximum x boundary has the outflow boundary condition so that the wave reflection from the boundary is minimized as much as possible. The minimum and maximum y boundaries as well as the maximum z boundary feature the symmetrical boundary condition where all the velocity derivatives and velocity components normal to the boundaries are set to zero. The minimum and maximum y boundaries are sufficiently far away from the conical island so that the wave reflection from those boundaries does not have an adverse effect on the simulations. The wall boundary condition is applied at the minimum z boundary where the bottom of the wave flume is defined.

4.2.3.1. Spatial Discretization

The computational domain is represented by an isotropic grid with $\Delta x = \Delta y = \Delta z$ where the grid size is selected as 5 cm (Please refer to the explanations in Section 4.2.2.1). BMP 2 is modeled via FLOW-3D[®] for different Δx values in order to test the grid dependency. Table 4.11 summarizes the predicted runup values at Gauge 9 for different Δx values, for Cases A, B and C, respectively. The agreement between the predicted data and laboratory measurements improves as the computational grid resolution is decreased from 1.0 m to 0.01 m. No considerable change is observed after $\Delta x = 0.5$ m.

Table 4.11 FLOW-3D[®]: Predicted runup values at Gauge 9 for different Δx values ($n = 0.01$)

Grid Size Δx (m)	Maximum Runup		
	$H/d = 0.045$	$H/d = 0.091$	$H/d = 0.181$
0.01	2.28	5.64	9.60
0.05	2.28	5.64	9.60
0.1	2.27	5.63	9.58
0.5	2.23	5.60	9.55
1.0	2.20	5.57	9.47

It is also necessary to analyse the effect of the vertical grid size, Δz , on runup values in a three-dimensional model. Changing the vertical grid size is effective in the vicinity of the island. In fact, a fine vertical grid size (i.e. $\Delta z \leq 0.5$ m) gives results closer to the measured values, with Δx kept constant. No considerable change is observed after $\Delta z = 0.5$ m.

The time step, Δt , is selected as 0.02 second in order to be consistent with the simulations conducted using NAMI DANCE. When variable time stepping is employed in order to assess the effect of the time step size, no significant effect is observed.

4.2.3.2. Friction

In order to assess the effect of friction on the maximum runup values, different Manning's roughness coefficients are considered: $n = 0$ (i.e. frictionless bottom), $n = 0.01$ (i.e. neat cement/concrete/smooth glass beach) and $n = 0.03$ (i.e. fine particles along the channel bottom). (Please refer to Section 4.2.2.2 for the comparison criteria).

The results obtained via FLOW-3D[®] are similar to those obtained using NAMI DANCE. The effect of friction is not felt in Cases A and B, whereas the runup values appear to be dependent on n in the extreme case, Case C, where $H/d = 0.181$. Lower inundation levels are obtained with a higher friction coefficient (Figure 4.38).

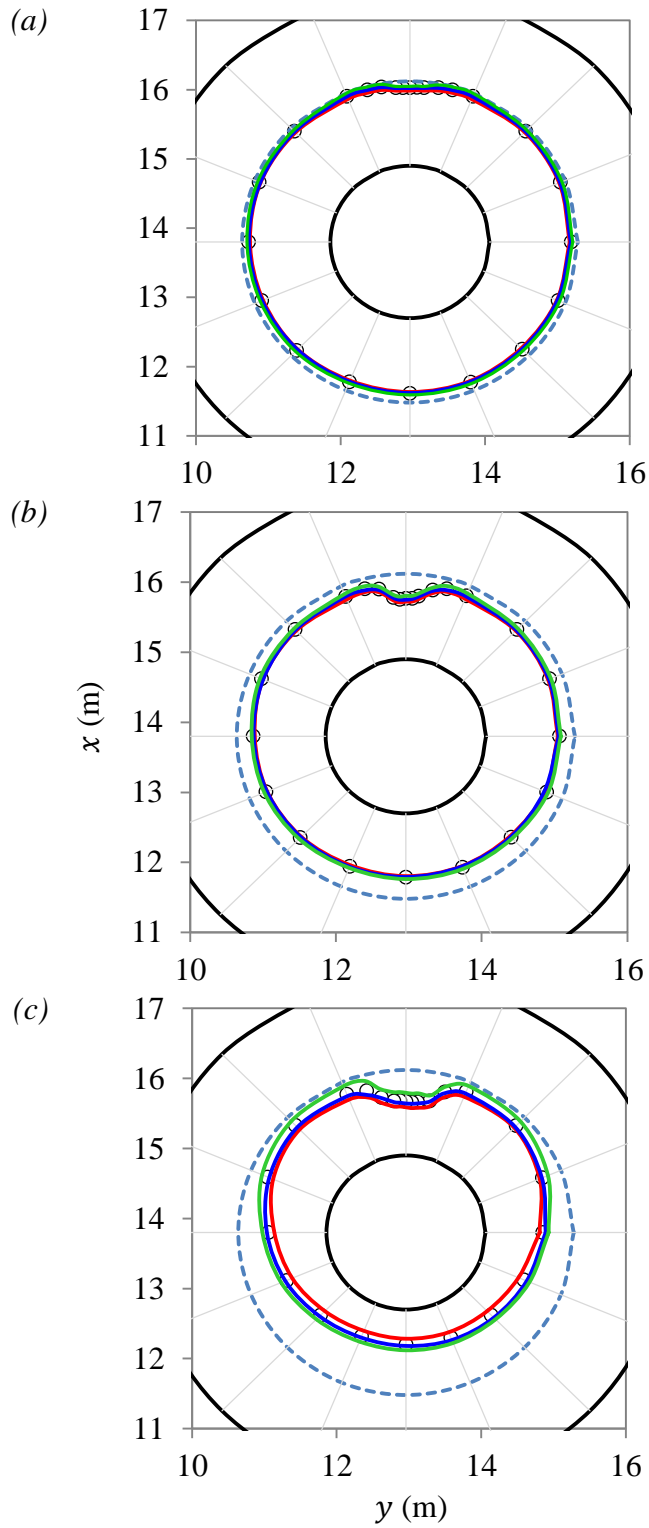


Figure 4.38 FLOW-3D[®] runup predictions according to different Manning's roughness coefficients for: (a) Case A; (b) Case B; (c) Case C. The dashed blue line represents the initial shoreline; the red line represents the results when $n = 0$; the blue line represents the results when $n = 0.01$; the green line represents the results when $n = 0.03$.

4.2.4. Simulation Results

BMP 2 is a challenging test case because it is a difficult task to reproduce the wave that splits at the front side of the island, refracts and wraps around both sides, and then recombines at the lee side of the island to produce a runup spike. The three test cases of BMP 2 illustrate the important fact that the runup and inundation levels on the sheltered back side of an island can exceed those on the exposed front side, due to trapping of the wave fronts that propagate around the island circumference.

The numerical simulations are conducted using a computer with 16-core central processing units (CPUs). The computations are terminated after the first reflection of the wave from the island, which is 40 seconds. The simulations that are performed via NAMI DANCE are completed in approximately 40 minutes whereas it takes 6 hours to complete the simulations using FLOW-3D[®].

The wave evolution around the conical island is assessed by using the free surface time series recorded at four gauges; namely Gauges 6, 9, 16 and 22. The comparison of NAMI DANCE and FLOW-3D[®] results with the laboratory measurements are given in the following graphs.

NAMI DANCE and FLOW-3D[®] predict the wave transformation around the conical island considerably well for Case A and B, where $H/d = 0.045$ and $H/d = 0.091$, respectively (Figures 4.39 and 4.40). NAMI DANCE computes the wave transformation around the conical island satisfactorily and FLOW-3D[®] model produces accurate predictions for Case C, where $H/d = 0.181$ (Figure 4.41).

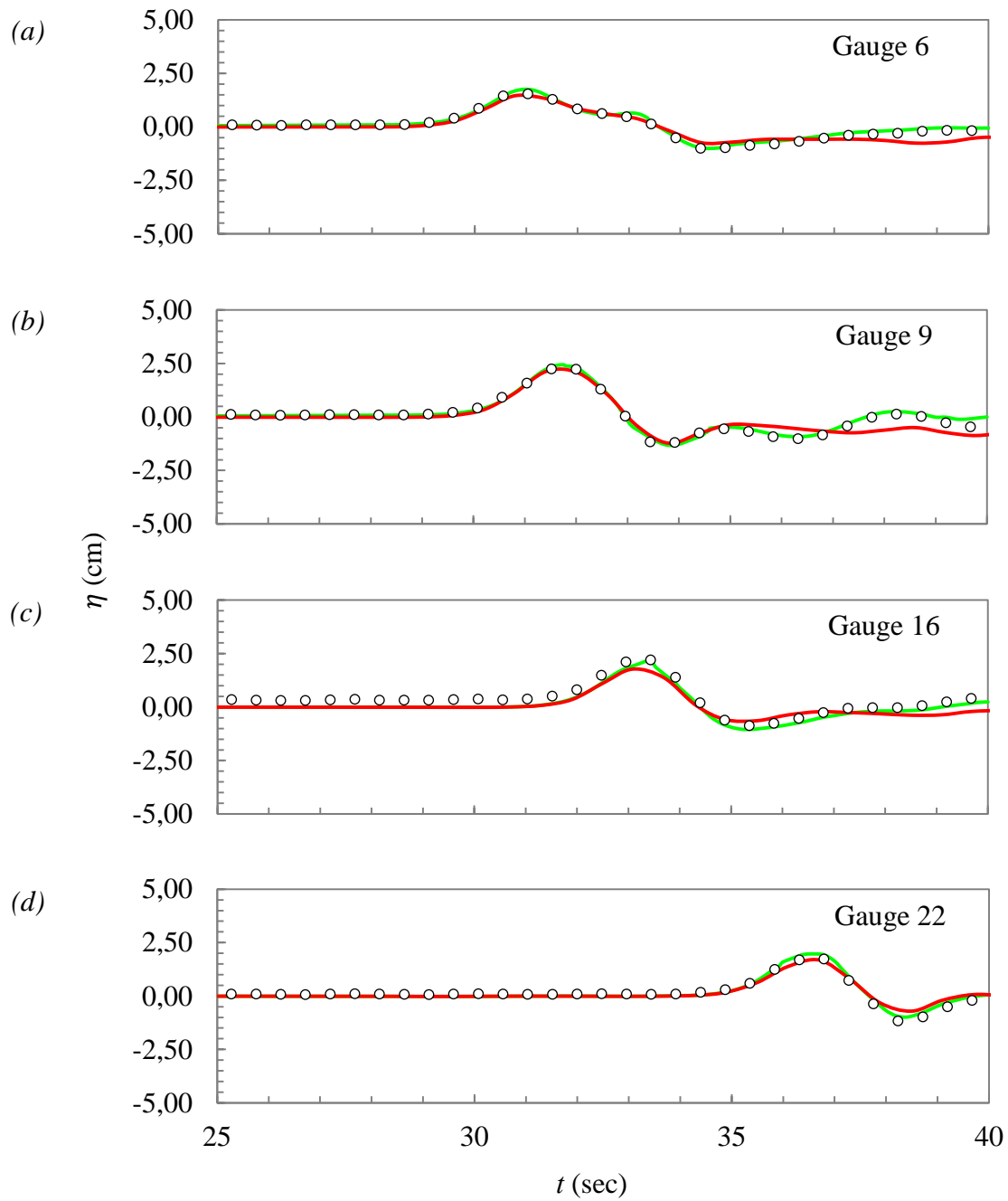


Figure 4.39 The wave transformation around the conical island for Case A, where $H/d = 0.045$ at: (a) Gauge 6; (b) Gauge 9; (c) Gauge 16; (d) Gauge 22. The circles represent the laboratory measurements; the red line represents the NAMI DANCE results; the green line represents the FLOW-3D[®] results.

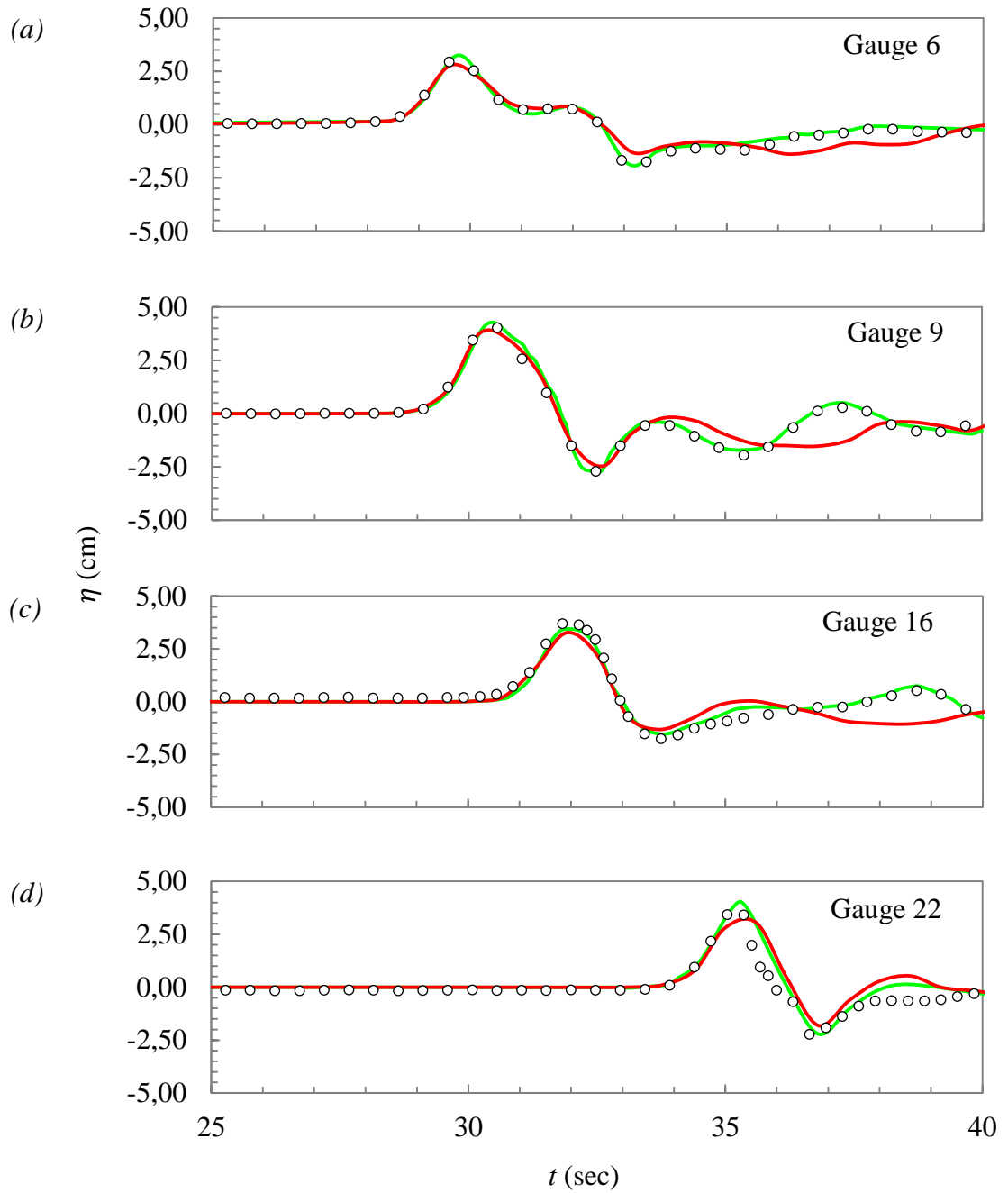


Figure 4.40 The wave transformation around the conical island for Case B, where $H/d = 0.091$ at: (a) Gauge 6; (b) Gauge 9; (c) Gauge 16; (d) Gauge 22. The circles represent the laboratory measurements; the red line represents the NAMI DANCE results; the green line represents the FLOW-3D[®] results.

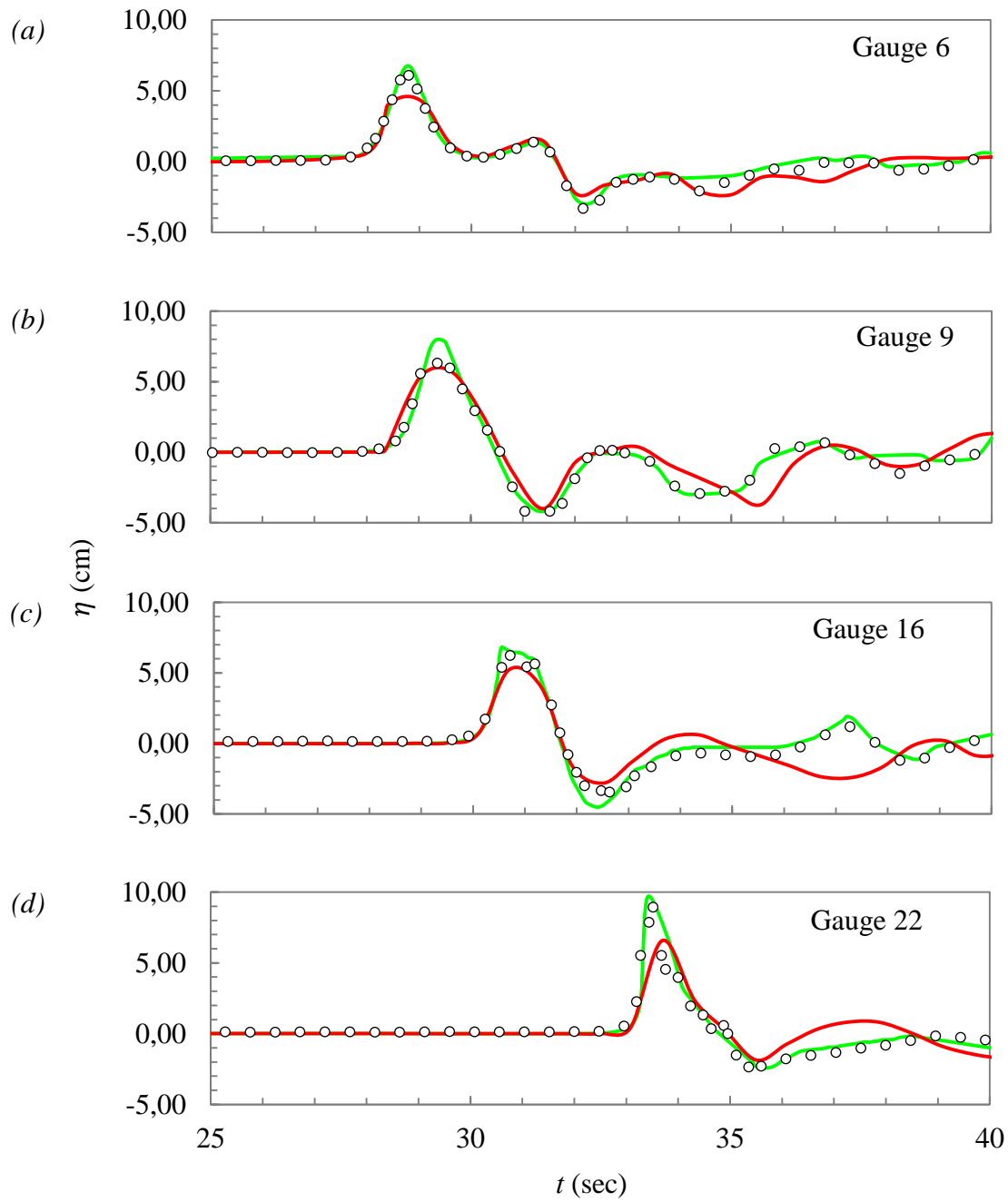


Figure 4.41 The wave transformation around the conical island for Case C, where $H/d = 0.181$ at: (a) Gauge 6; (b) Gauge 9; (c) Gauge 16; (d) Gauge 22. The circles represent the laboratory measurements; the red line represents the NAMI DANCE results; the green line represents the FLOW-3D® results.

The maximum vertical runup is recorded at twenty four locations around the perimeter of the island. Sixteen of the gauges are evenly spaced at every 22.5° around the perimeter. The other eight gauges, which are more narrowly spaced, are located at the lee side of the island, so that the resolution at this critical area is improved.

Most of the previous studies did not take friction into consideration in this numerical experiment (Liu et al., 1995a; Titov and Synolakis, 1998; Chen et al., 2000 and Lynett et al., 2002). In this study, in order to reflect the real laboratory conditions as much as possible, the runup predictions are made for a Manning's roughness coefficient $n = 0.01$, which is used for smooth concrete. (For detailed friction analysis please refer to Sections 4.2.2.2 and 4.2.3.2).

In order to investigate the changes in the runup shape and magnitude, the initial wave height is altered. Figures 4.41 – 4.43 illustrate the polar distribution of maximum vertical runup at 32 cm water depth for Cases A, B and C, respectively. The crest and toe of the conical island and the initial shoreline are shown for reference.

It is seen from Figure 4.42 that there is a fairly uniform inundation around the perimeter of the island for Case A, where $H/d = 0.045$. This ratio corresponds to an initial wave with a height of 1.44 cm. The predictions of both models are in good agreement with the measured water level dynamics at the given locations. No distinctive difference between the model results and the measured data is observed in the maximum runup values. The runup is largest on the island quadrant between 180° and 360° , where it is closest to the source. In other words, the runup on the front side of the island is larger than that on the back side. Figure 4.43 illustrates the inundation predictions for Case B, where $H/d = 0.091$. This ratio corresponds to an initial wave with a height of 2.92 cm. The runup is largest on the island quadrant between 67.5° and 112.5° . Figure 4.44 illustrates the inundation predictions for Case C, where $H/d = 0.181$ – an initial wave with a height of 5.79 cm. Case C is a formidable test case because the modeled wave is steeper than most realistic tsunamis.

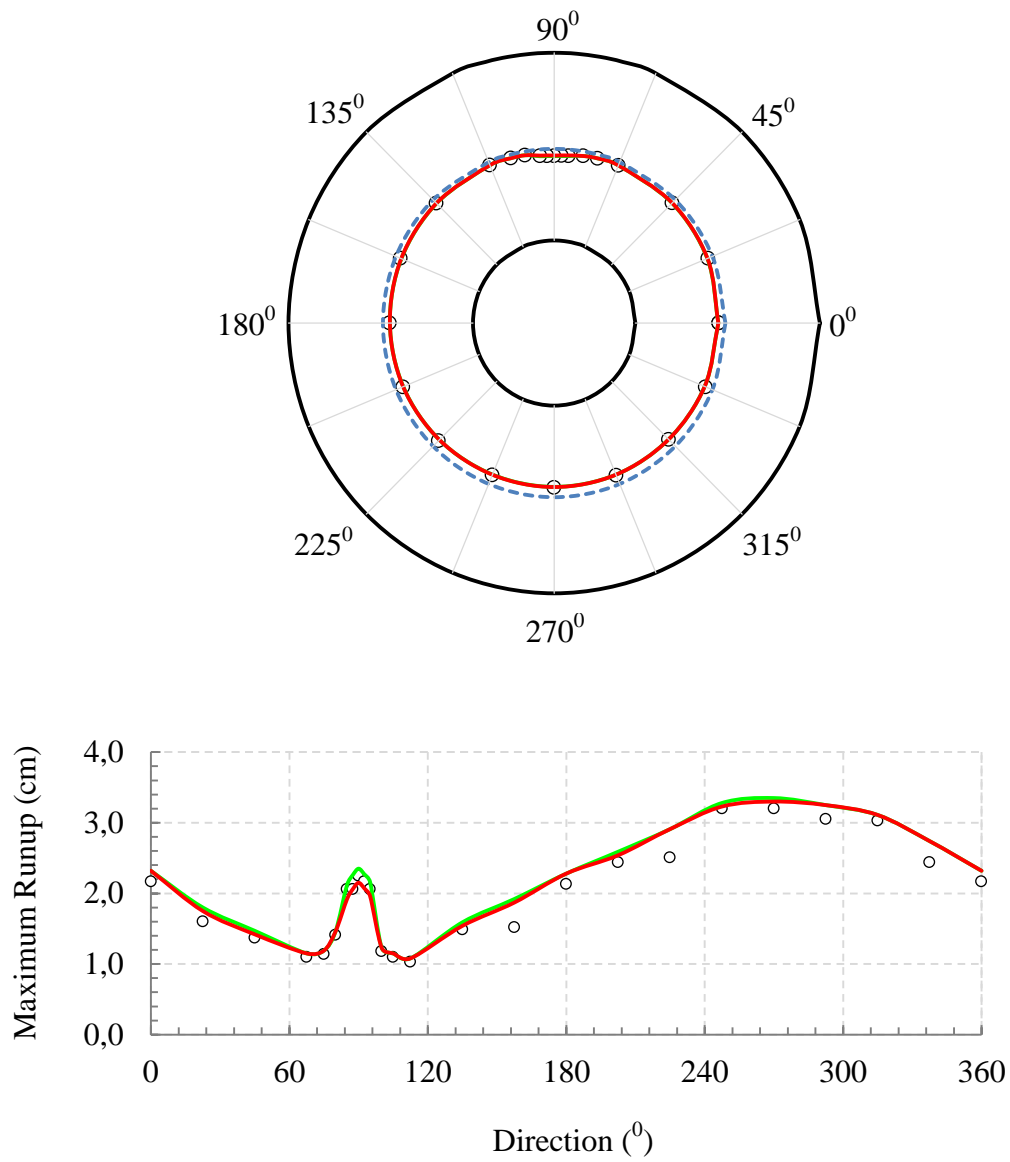


Figure 4.42 Inundation around the perimeter of the conical island for Case A, where $H/d = 0.045$. The circles represent the laboratory measurements; the dashed blue line represents the initial shoreline; the red line represents the NAMI DANCE results; the green line represents the FLOW-3D[®] results.

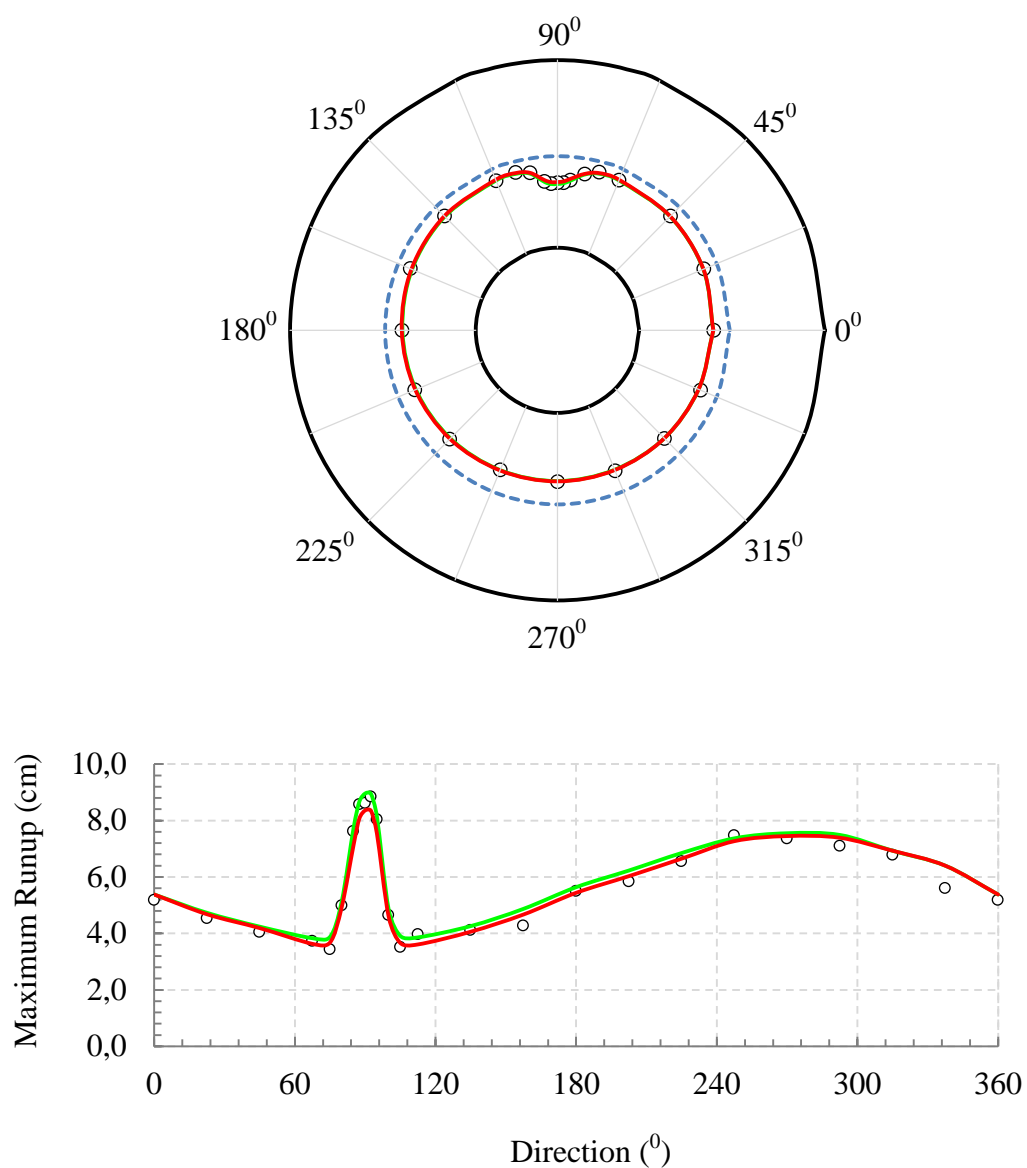


Figure 4.43 Inundation around the perimeter of the conical island for Case B, where $H/d = 0.091$. The circles represent the laboratory measurements; the dashed blue line represents the initial shoreline; the red line represents the NAMI DANCE results; the green line represents the FLOW-3D[®] results.

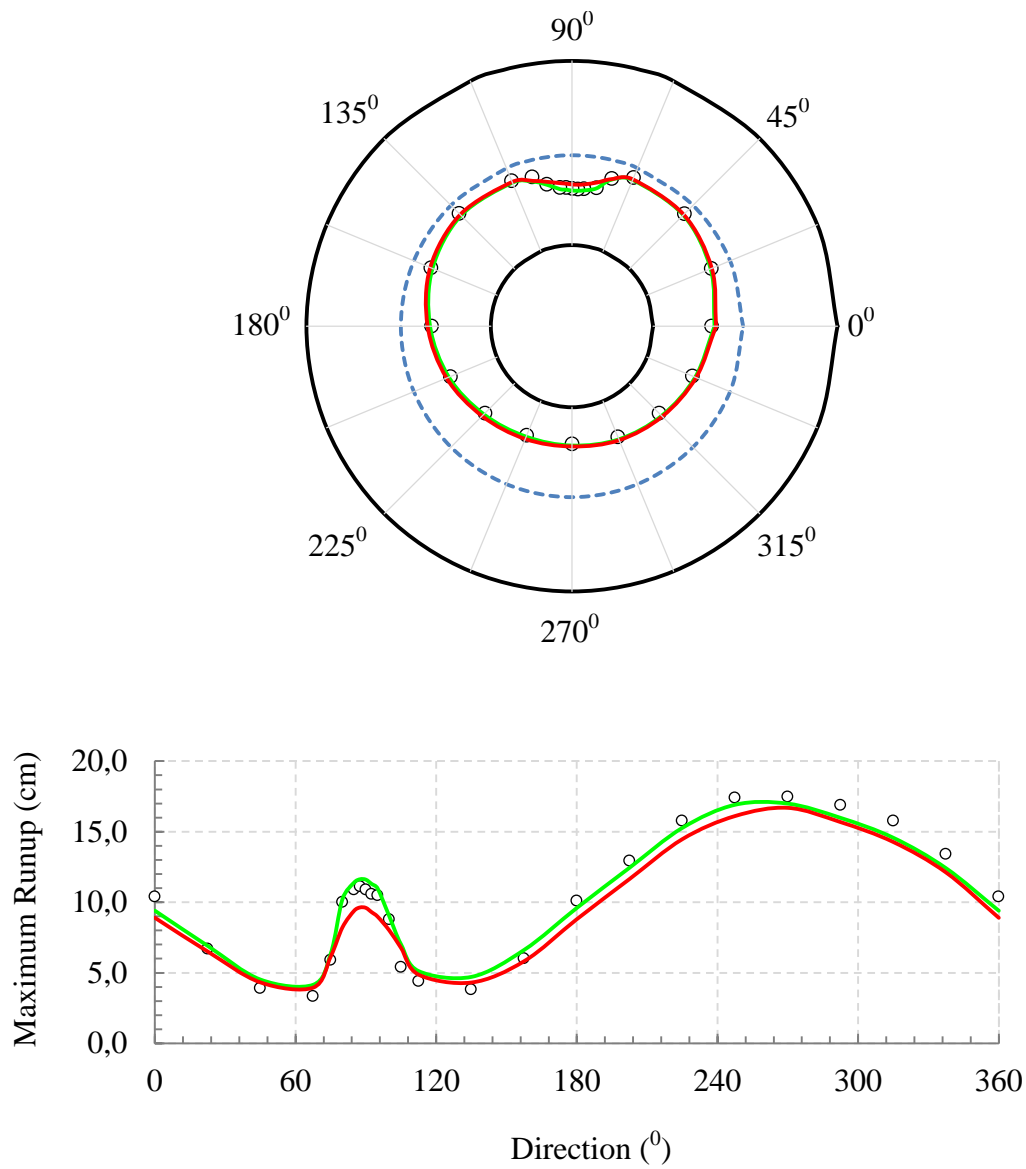


Figure 4.44 Inundation around the perimeter of the conical island for Case C, where $H/d = 0.181$. The circles represent the laboratory measurements; the dashed blue line represents the initial shoreline; the red line represents the NAMI DANCE results; the green line represents the FLOW-3D[®] results.

Case C is an extreme case, in which a distinctive pattern of runup emerges because of the edge waves that propagate around the island. The runup on the back side of the island is almost as large as that on the front side. NAMI DANCE predicts the runup on the back of the island approximately 20% less than the measured value. FLOW-3D[®], however, satisfactorily predicts the runup around the perimeter of the island.

NAMI DANCE is a depth-averaged model; therefore, the vertical velocity component, w , is neglected in the simulations. On the other hand, FLOW-3D[®] accounts for the effects of w . The vertical velocity component in the vicinity of the island needs to be analysed in order to assess its effect in complex extreme cases (i.e. turbulence, wave reflection, edge waves). The analysis is conducted via FLOW-3D[®] for the extreme case, Case C, where $H/d = 0.181$.

Figure 4.45 illustrates the evolution of the vertical velocity component around the conical island and Figure 4.46 shows the velocity time histories for the constant depth region and the shallower region (i.e. at Gauges 9 and 22).

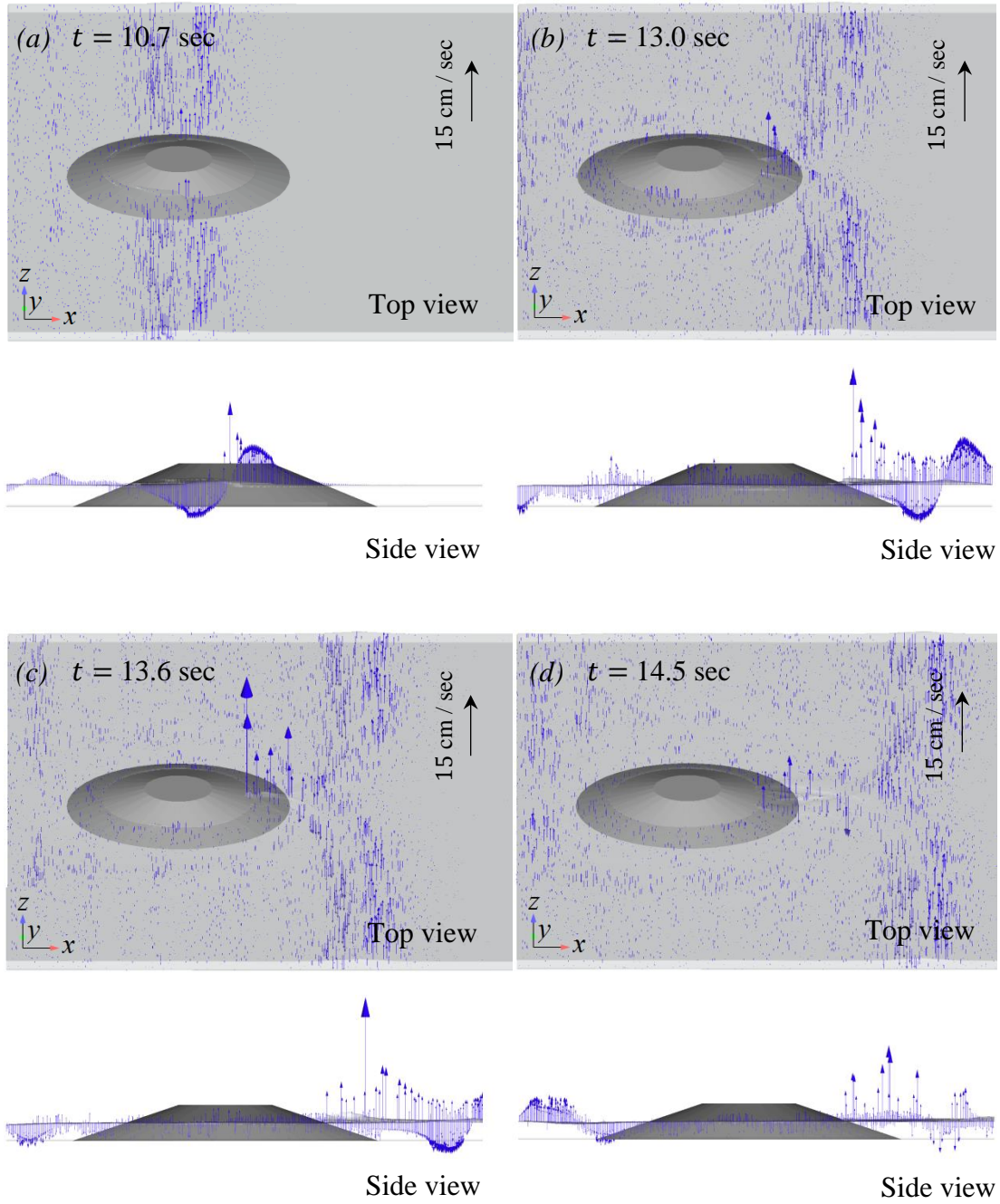


Figure 4.45 Evolution of vertical velocity component, w , around the conical island for Case C, where $H/d = 0.181$ at: (a) $t = 10.7$ sec; (b) $t = 13.0$ sec; (c) $t = 13.6$ sec; (d) $t = 14.5$ sec (not to scale)

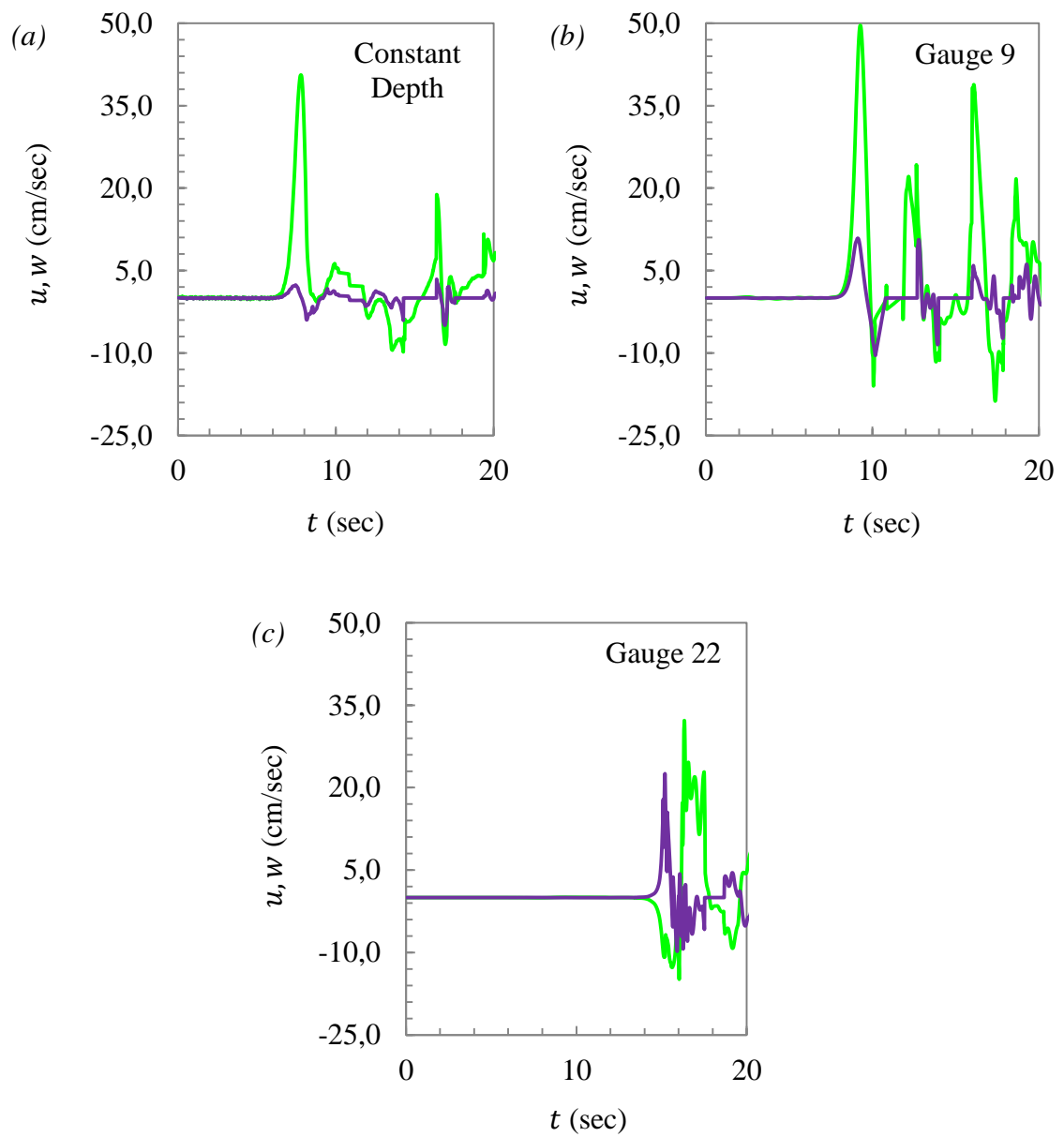


Figure 4.46 Velocity time histories for Case C at: (a) constant depth region; (b) Gauge 9; (c) Gauge 22. The green line represents the predicted horizontal velocity component; the purple line represents the predicted vertical velocity component.

The results reveal that, in the extreme case, there is a considerable increase in the vertical velocity as the wave propagates towards the island. The maximum vertical velocity component is only 6% of the maximum horizontal velocity component at the constant depth region; however, it gets as large as one third of the maximum horizontal velocity component at the front side of the island just before breaking. At the back side of the island, the maximum w becomes nearly as large as the maximum horizontal velocity component the moment the two waves that are splitted earlier meet.

Tables 4.12 and 4.13 summarize the maximum values of the horizontal and vertical velocity components of a fluid particle computed at the constant depth region and at Gauges 6, 9 and 22 for Cases A and C. NAMI DANCE does not provide vertical velocity components and horizontal velocity components are constant along depth. On the other hand, FLOW-3D[®] calculates vertical velocity components, which change along depth, having the maximum values at the *free surface*.

Table 4.12 The predicted maximum vertical and horizontal velocity components of a fluid particle *at the free surface* for Case A, where $H/d = 0.045$

Location	NAMI DANCE	FLOW-3D [®]	
	u (cm/sec)	u (cm/sec)	w (cm/sec)
Constant Depth Region	9.00	8.90	0.55
Gauge 6	7.00	6.80	1.90
Gauge 9	19.50	19.00	2.10
Gauge 22	16.00	15.70	1.50

Table 4.13 The predicted maximum vertical and horizontal velocity components of a fluid particle *at the free surface* for Case C, where $H/d = 0.181$

Location	NAMI DANCE	FLOW-3D [®]	
	u (cm/sec)	u (cm/sec)	w (cm/sec)
Constant Depth Region	41.20	40.70	2.70
Gauge 6	35.00	32.40	9.70
Gauge 9	52.00	49.90	11.70
Gauge 22	35.00	32.30	23.80

The NAMI DANCE simulation for Case C (Figure 4.47):

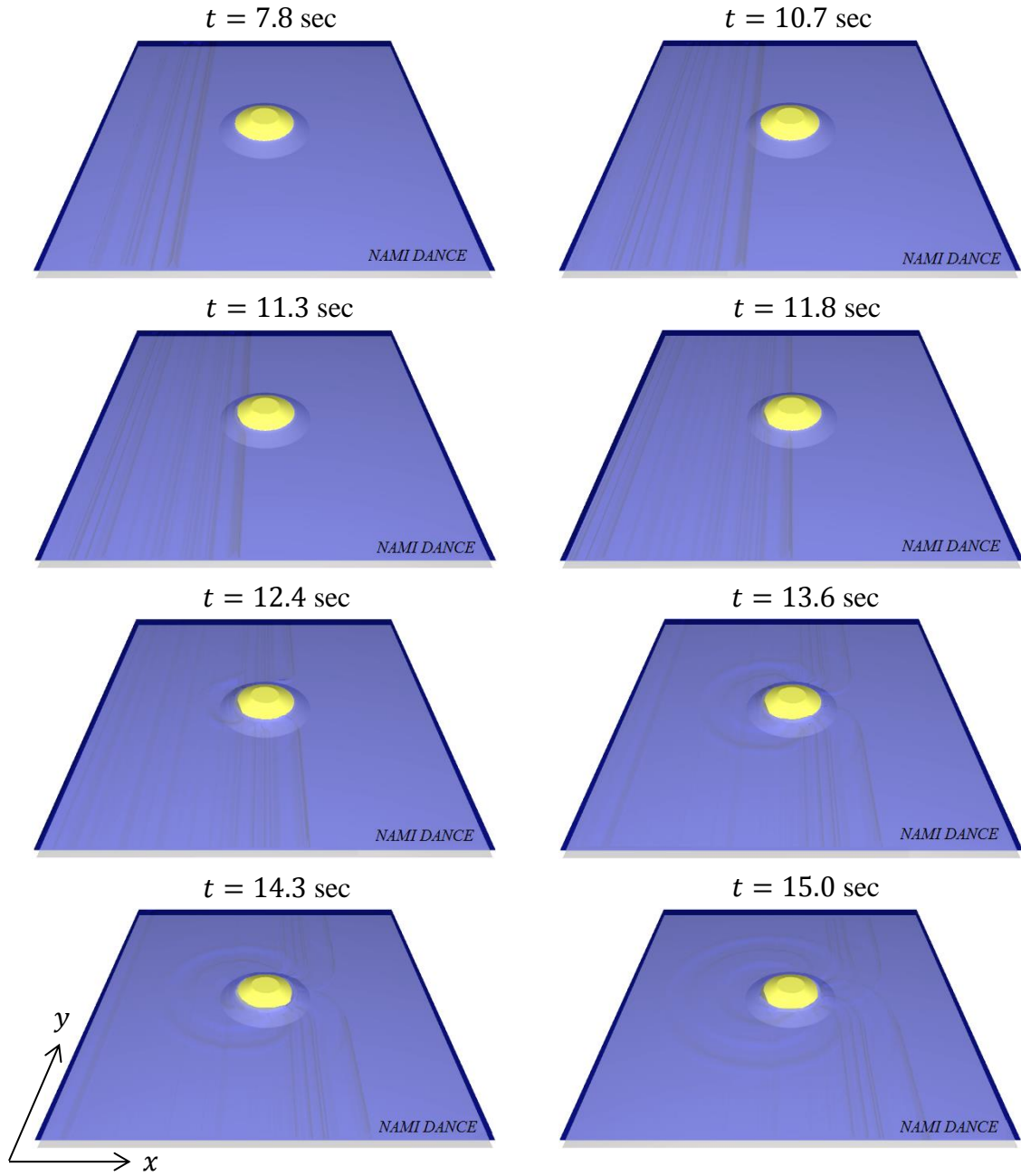


Figure 4.47 NAMI DANCE model: wave transformation around the conical island for Case C, where $H/d = 0.181$

The initial wave evolution and its split into two wave fronts can be observed in Figure 4.47.

NAMI DANCE and FLOW-3D[®] produce similar values of the predicted horizontal velocity components. NAMI DANCE, which solves depth-averaged NSW equations, displays a uniform distribution of u along the vertical direction, without any significant deviation, as expected. In both models, the horizontal velocity component decays to zero at the sea bottom. On the other hand, the vertical velocity component, w , changes along the vertical direction, having the largest value at the free surface and reaching zero at the sea bottom. The results indicate that the vertical velocity component gains importance when the initial wave height is considerably large (i.e. extreme case). In fact, the maximum w is only 10% of the maximum u just before reaching the shoreline on the front side of the island for Case A, where H/d ratio is relatively small. Moreover, at the back side of the island, it is found that the effect of the vertical velocity component is minimal. On the other hand, for the extreme wave case, Case C, the maximum vertical velocity component increases to 25% of the maximum horizontal velocity component at Gauge 9, which is located at the front side of the island. At the lee side of the island, however, it is surprising to see that the maximum w is nearly 80% of the maximum u . All these results imply that, w should not be neglected when evolution of large amplitude waves are analysed upon circular/conical bathymetries.

The allowable error thresholds vary according to the reference data types. The data type that BMP 2 provides is laboratory measurements, for which the allowable NRMSE and MAX limits are 15% and 10%, respectively. (Please refer to Section 4.1.4 for the method proposed for the calculation of statistical errors, NRMSE and MAX).

The NRMSE and MAX errors for Case A are given in Table 4.14 and Figure 4.48.

Table 4.14 NRMSE and MAX errors for Case A, where $H/d = 0.045$

Gauge	NAMI DANCE		FLOW-3D [®]	
	% NRMSE	% MAX	% NRMSE	% MAX
6	7.3	7.1	3.4	7.2
9	7.9	7.8	4.1	5.8
16	8.3	10.0	3.5	5.6
22	7.0	7.3	4.7	7.1

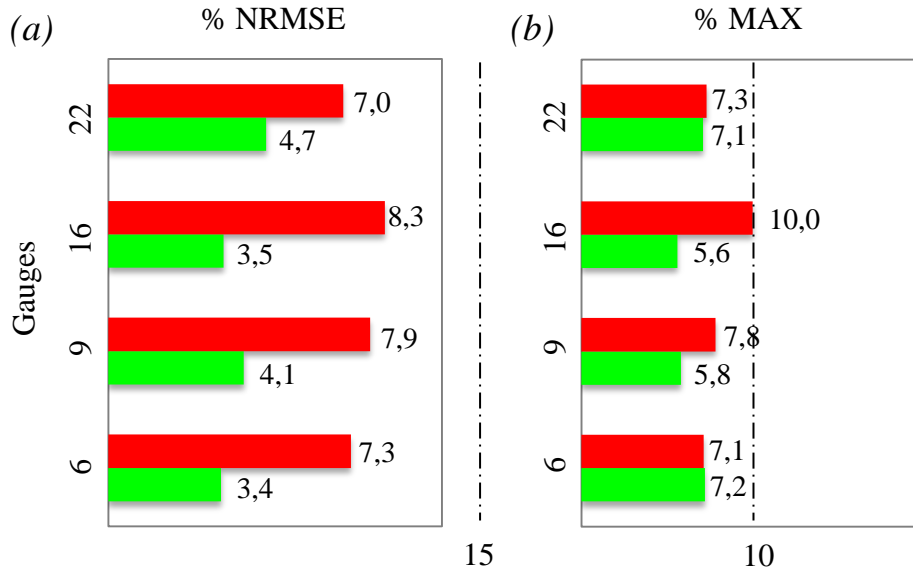


Figure 4.48 Error bars for Case A, where $H/d = 0.045$: (a) % NRMSE; (b) % MAX error. The red and green bars represent the errors of NAMI DANCE and FLOW-3D[®] results, respectively.

The NRMSE of the NAMI DANCE results is between 7% and 8% while the MAX error ranges from 7% to 10%. FLOW-3D[®] results have an NRMSE range between 3% and 4% and a MAX error range between 5% and 7%. The errors are within the OAR PMEL-135 standard error range. In Case A, the initial wave is a small amplitude wave. Both models predict the wave transformation around the island equally well. This indicates that for small amplitude waves, 3D-RANS equations have no significant advantage over the 2D-NSW equations.

The NRMSE and MAX errors for Case B are given in Table 4.15 and Figure 4.49.

Table 4.15 NRMSE and MAX errors for Case B, where $H/d = 0.091$

Gauge	NAMI DANCE		FLOW-3D [®]	
	% NRMSE	% MAX	% NRMSE	% MAX
6	8.2	10.6	3.0	2.2
9	8.7	7.6	3.8	4.2
16	11.5	10.7	5.5	3.3
22	8.7	10.7	6.1	0.9

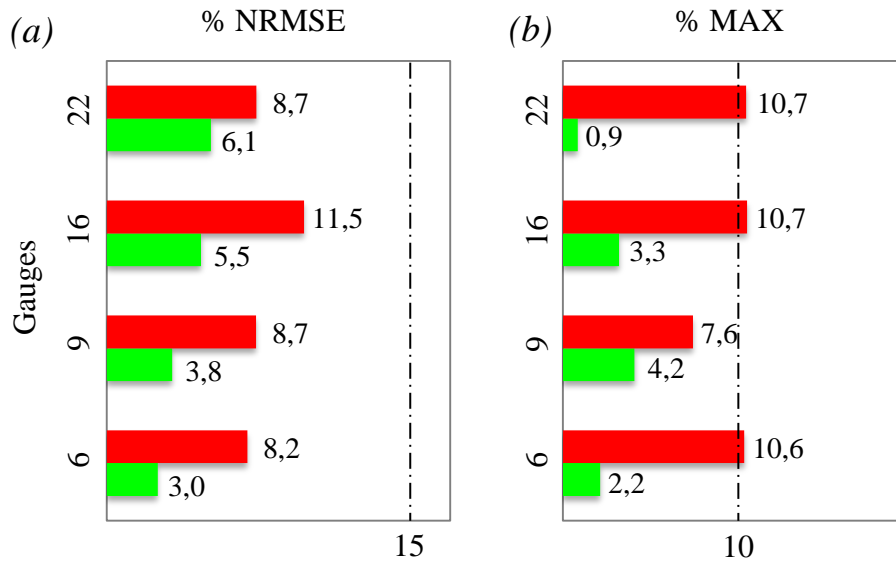


Figure 4.49 Error bars for Case B, where $H/d = 0.091$: (a) % NRMSE; (b) % MAX error. The red and green bars represent the errors of NAMI DANCE and FLOW-3D[®] results, respectively.

NAMI DANCE results have an NRMSE range between 8% and 11% and a MAX error range between 8% and 10%. The NRMSE of FLOW-3D[®] results, however, is between 3% and 6% while the MAX error ranges from 1% to 4%. In Case B, the initial wave is fairly high. The results indicate that even though 2D-NSW equations predict the wave evolution and transformation around the island satisfactorily, 3D-RANS equations provide more improved results. It is seen that especially on one side and back of the island (i.e. Gauges 16 and 22), there is considerable agreement between the three-dimensional model predictions and laboratory measurements.

The NRMSE and MAX errors for Case C are given in Table 4.16 and Figure 4.50.

Table 4.16 NRMSE and MAX errors for Case C, where $H/d = 0.181$

Gauge	NAMI DANCE		FLOW-3D [®]	
	% NRMSE	% MAX	% NRMSE	% MAX
6	7.0	19.1	3.9	5.9
9	9.3	7.8	5.3	9.8
16	12.2	14.3	5.3	8.4
22	10.5	17.9	5.9	6.1

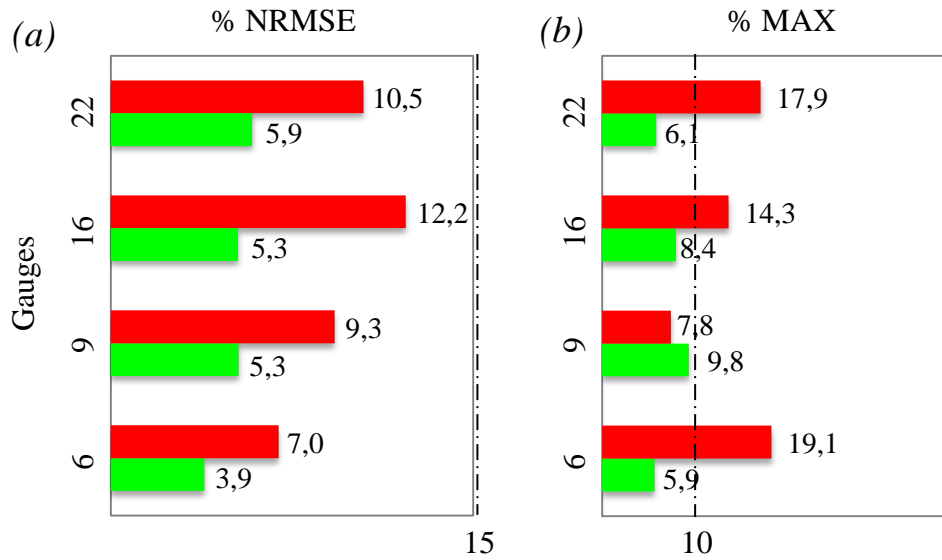


Figure 4.50 Error bars for Case C, where $H/d = 0.181$: (a) % NRMSE; (b) % MAX error. The red and green bars represent the errors of NAMI DANCE and FLOW-3D[®] results, respectively.

NAMI DANCE results have an NRMSE range between 7% and 12% and a MAX error range between 8% and 19%. Although the MAX error of NAMI DANCE results exceeds the threshold for laboratory measurements, the results are accepted as reliable, considering the difficulty in reproducing Case C, where the initial wave is extremely high. The NRMSE of FLOW-3D[®] results is between 4% and 5% while the MAX error ranges from 6% to 10%. The results indicate that 2D-NSW equations can not predict the wave evolution and transformation around the island accurately,

especially on one side and back of the island (i.e. Gauges 16 and 22), whereas 3D-RANS equations provide very close results to the laboratory measurements.

The NRMSE of NAMI DANCE and FLOW-3D[®] results regarding the maximum runup around the perimeter of the island are below the threshold value given by OAR PMEL-135 standard. The NRMSE of NAMI DANCE results is 4%, 6% and 8% for Cases A, B, and C, respectively. The NRMSE of FLOW-3D[®] results is 4%, 5% and 5% for Cases A, B, and C, respectively.

To sum up, the two- and three-dimensional models, NAMI DANCE and FLOW-3D[®], are tested against a set of laboratory measurements that include tsunami wave transformation, reflection and edge waves forming around a conical island. Three data sets with $H/d = 0.045$, $H/d = 0.091$ and $H/d = 0.181$ are used in order to assess the effect of initial tsunami wave height on inundation on a conical island. The reasons for the extreme runup on the back side of the island are investigated.

The initial wave splits into two wave fronts in front of the island, before it superposes and breaks symmetrically behind the island as if it is a standing wave. Good agreement is seen overall and, in particular, between predicted and measured time series for the first wave. The agreement for the later wave details becomes progressively worse, as multiple reflections and refraction occur at the basin boundaries, the wavemaker face, and the island. Therefore, only the first maximum and minimum waves are considered for all comparisons in the analyses.

The computed results are symmetric about the wave propagation direction despite the use of a Cartesian grid to describe curved surfaces. Especially the inundation on the lee side of the island is captured satisfactorily by both models. Increasing the grid spacing from $\Delta x = 0.01$ m to $\Delta x = 0.5$ m hardly affects the quality of the results. However, the maximum runup outline appears less detailed due to the coarser grid.

Most of the previous studies neglected friction in BMP 2 (Liu et al., 1995a; Titov and Synolakis, 1998; Chen et al., 2000 and Lynett et al., 2002). Liu et al. (1995a) pointed out that the computed results are not sensitive to the surface roughness coefficient due to the steep 1:4 slope of the conical island. When all the results are assessed, it is seen that the bottom friction does not play an important role in the runup distances of small and/or medium amplitude waves and can be neglected in the simulations for this particular benchmark problem. However, for large amplitude waves, the friction coefficient is fairly effective on the runup values. In other words, smaller friction leads to larger runup distances. Similar results were reported by several researchers who took part in the 2011 NTHMP Model Benchmarking Workshop (NTHMP, 2011). For Case C, when Manning's roughness coefficient, n , is 0.01, NAMI DANCE predicted the maximum runup values with an NRMSE of 8%, whereas FLOW-3D[®] results have an NRMSE of 5%. The NRMSE of both model predictions are below 10%, which is within the proposed threshold values (Synolakis et al., 2008).

When NAMI DANCE results for Case C are assessed, it is seen that the simulated runup does not exactly match the measured runup on the lee side; in fact, it is 20% less than the measured one. The reason for this is that the 2D depth-averaged NSW equations that NAMI DANCE solves are hydrostatic and the computed wave height is smaller than the one measured in the laboratory. Therefore, with higher nonlinearity, the crest of the solitary wave is narrower and the reflection is more distinct. This leads to the underestimation of the runup distance of the large amplitude wave. In fact, when previous studies are examined, it is seen that for all NSW models, such as ALASKA, GEOCLAW and MOST, the simulated waves steepen more rapidly than those measured in the laboratory experiments for large amplitude waves, which is a well-known effect of the shallow water approximation (NTHMP, 2011). Moreover, previous studies reveal that non-hydrostatic models, such as BOSZ, FUNWAVE, NEOWAVE and SELFE, capture the water level dynamics slightly better than the hydrostatic ones (NTHMP, 2011). In Case C, it is obvious that 3D-RANS equations show an appreciable improvement over the 2D

depth-averaged NSW equations. This can be deduced from Table 4.14, 4.15 and 4.16, where the NRMSE of NAMI DANCE results for Cases A, B and C have a wide range of variation, i.e., between 7% and 12%, while FLOW-3D[®] results have a narrow NRMSE range, which is between 3% and 5%. For the maximum wave amplitude, regardless of the location where the maxima occurred, the errors of NAMI DANCE results range between 7% and 19%, whereas the error range is between 1% and 6% for FLOW-3D[®] results. It is seen that the 3D model performs slightly better than the 2D model for the extreme case; therefore, 3D-RANS equations are required to adequately resolve the initial wavelength and to prevent the wave front from steepening prior to the island impact.

The vertical velocity component, w , is fairly effective on the back side of the island for the large amplitude case. It rapidly increases and its maximum becomes nearly as large as the maximum horizontal velocity component the moment the two splitting waves converge behind the island. The wave bends around the island as edge waves due to refraction and diffraction. The island and the source being modeled as symmetric, the wave wraps evenly around the island. Therefore, the vertical velocities are very high, causing a relatively large runup on the back side. This shows that, contrary to what many people think, the back side of an island may not be safer than the front side. In fact, for Case C, the results reveal that the runup on the back side of the island is almost as high as that on the front side.

It is concluded that both models give satisfactory results regarding the maximum runup values since the NRMSE of the numerical predictions is less than 20%. No significant time shift is observed at the gauge points. Even though NSW equations are capable of estimating the major features of propagation, refraction, and runup observed in the laboratory experiments for small and/or medium amplitude waves, three-dimensional models should be preferred when large amplitude waves are studied in the areas featuring strong nonlinearities.

4.3. BMP 3: Solitary Wave Propagation over a Complex Shelf

4.3.1. Problem Description

In the summer of 2009, a summer workshop, whose main focus was the understanding of nearshore wave dynamics via large-scale laboratory experiments and numerical modeling, was co-sponsored by the Inundation Science & Engineering Cooperative (ISEC) and the Network for Earthquake Engineering Simulation (NEES) Tsunami Research Facility at the O.H. Hinsdale Wave Research Laboratory (HWRL), Oregon State University (OSU). Aiming to find out how to expand the modeling and experimental capabilities and how to propose and plan an experiment, the researchers worked on a variety of topics. In the first stage of the workshop, the 3D wavemaker in the tsunami wave basin and the 2D wavemaker in the large wave flume were introduced and ways of testing structural specimens and validating analytical and numerical models were discussed. The second part of the workshop concentrated on the development and application of numerical models.

Two nearshore wave benchmark problems were discussed in the workshop. The first one involved overtopping of a solitary wave on a complex reef shelf whose empirical data had been gathered during large-scale tests at the HWRL one year before the workshop. The second problem, which is BMP 3 discussed in this dissertation, was more challenging as it included an island feature located at the offshore point of the complex shelf (Figures 4.51 and 4.52). The tests of this benchmark were conducted just prior to the workshop.

BMP 3 serves to investigate the three-dimensional kinematic properties associated with a breaking solitary wave as it propagates, evolves and breaks over an irregular shallow water bathymetry. It also deals with currents induced by breaking and overtopping of a solitary wave on a circular island and a complex shelf.

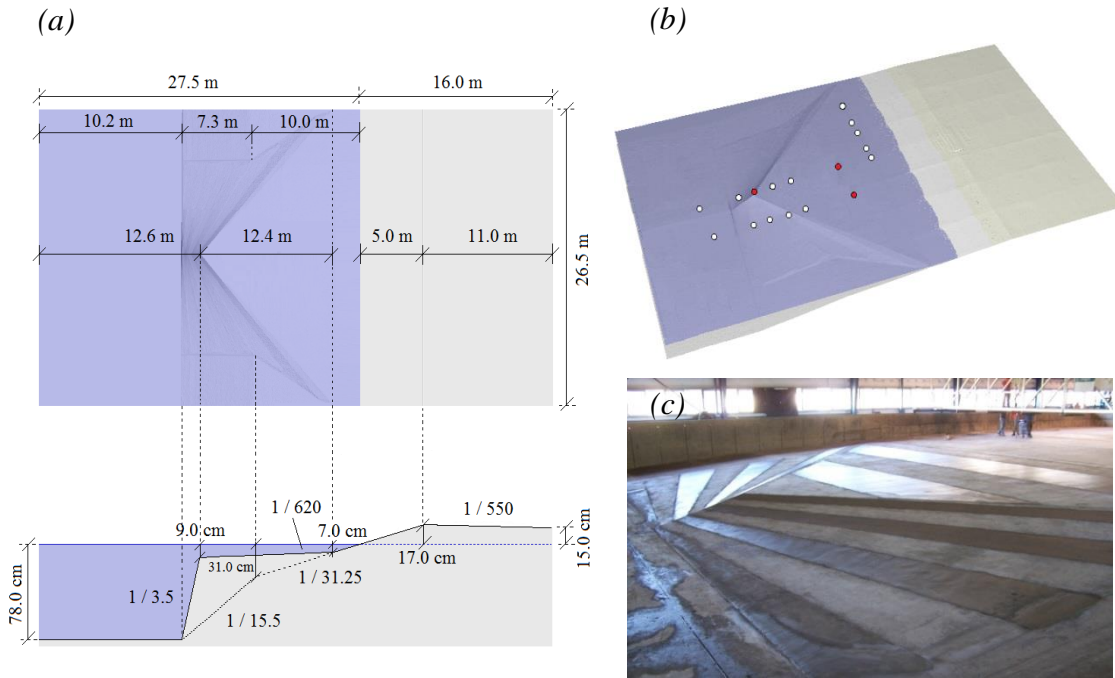


Figure 4.51 BMP 1 discussed in the ISEC 2009 workshop: (a) schematic sketch of the experimental setup; (b) wave gauge and ADV locations - the white and red circles represent usWGs and ADVs, respectively; (c) a photograph of the complex shelf (NTHMP, 2011)

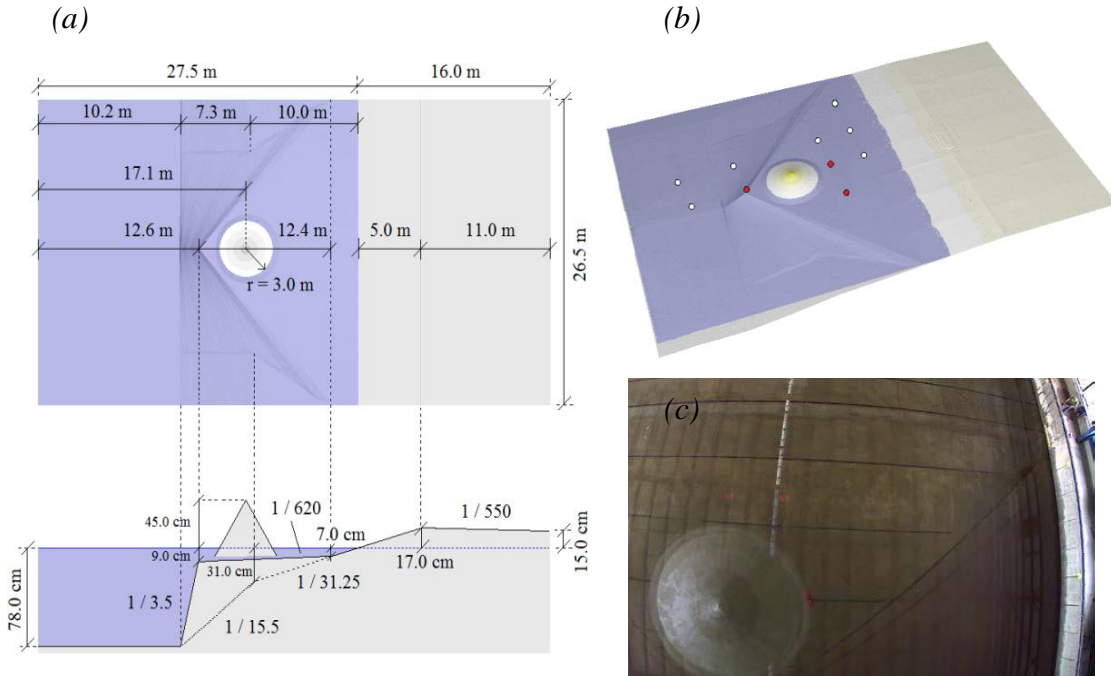


Figure 4.52 BMP 2 discussed in the ISEC 2009 workshop: (a) schematic sketch of the experimental setup; (b) wave gauge and ADV locations - the white and red circles represent usWGs and ADVs, respectively; (c) a photograph of the experimental setup (NTHMP, 2011)

The kinematic properties associated with a breaking wave are of particular importance when trying to predict wave forces on structures, nearshore mixing and circulations, sediment transport, and ultimately coastal morphology (Swigler, 2009). In fact, if the physics behind the evolution of breaking waves and the development of currents near the surf zone is understood better, the prediction of the transport of sediment can be more accurate. It has been shown that the flow fields associated with breaking waves are particularly important since they greatly affect the dynamic equilibrium of beaches (Dalrymple, 1992). There have been extensive experimental and numerical studies that focused on increasing the knowledge of wave dynamics that develops as waves interact with an underlying bathymetry and break.

The physics that governs the evolution of waves as they approach a shoreline has been the subject of many extensive experimental studies, which have provided insight to specific phenomena that are known to occur such as shoaling, refraction and breaking. Beginning offshore where the water depth is sufficiently deep and constant, waves are found to be symmetric with respect to the wave crest (Hsiao et al., 2008) before they began to deform due to interactions with the bathymetry. Over a sloping bottom, waves begin to become more asymmetric resulting in a steeper front face and an increase in wave height with a decrease in water depth. This phenomenon is known as shoaling and is directly related to bottom slope where on a gentler slope shoaling is greater as compared to a sufficiently steep slope (Grilli et al., 1994). At a point when the slope becomes sufficiently steep, Grilli et al. (1994) found that the amount of reflection experienced by the incident wave increased causing the increase in wave height to be less noticeable. Due to shoaling, the asymmetry of the wave reaches a point where it becomes unstable and breaking occurs.

Models which attempted to predict the flow dynamics resulting from breaking waves have been adapted and significantly improved over time. By understanding the physics of near shore wave motion, the accuracy and reliability of models have evolved, but calibration and verification of models still need to be done via laboratory studies.

The experiments of BMP 3 were conducted in the large wave basin of Oregon State University's O.H. Hinsdale Wave Research Laboratory in 2009. The wave basin was 48.8 m long, 26.5 m wide, and 2.1 m deep and was equipped with a piston-type wavemaker, which had a waveboard consisting of 29 independently functioning paddles capable of producing both linear and nonlinear waves up to 0.8 m in height (Swigler, 2009). The walls and underlying bathymetry of the basin were made of finished concrete.

In accordance with the Cartesian coordinate system used in the study, $x = 0$ at the wavemaker and increased positively in the direction of wave propagation. At the centerline of the basin, $y = 0$ and y -axis was parallel to the wavemaker. Finally, $z = 0$ at the basin floor in the constant depth portion of the basin near the wavemaker and it was positive upwards.

Opposite the wavemaker, a complex shallow water bathymetry was built to force the generated wave to break symmetrically about the centerline of the basin. The area between $x = 0$ m and $x = 10.2$ m was determined as the flat backshore area. A 1:30 slope planar beach was constructed which began at $x = 10.2$ m and extended to $x = 32.5$ m with a height of 0.95 m before becoming level and extending to the back wall of the basin. Beginning at the toe of the planar beach, a three dimensional triangular shallow water shelf with steep drop-offs was built (Swigler, 2009). The top of the shelf was located at an elevation of $z = 0.71$ m with the apex located at $x = 12.6$ m. The still water shoreline intersected the planar beach at $x = 27.5$ m and the water level was maintained at a depth of 0.78 m ($z = 0.78$ m) measured from the constant depth portion of the basin. A 0.45 m high cone with a 3 meter-radius was placed on the shelf to enhance vortex formation. The center of the cone was at $x = 17.1$ m. All these details are illustrated in Figure 4.52. Also, the 3D representation of the bathymetry is given in Figure 4.53.

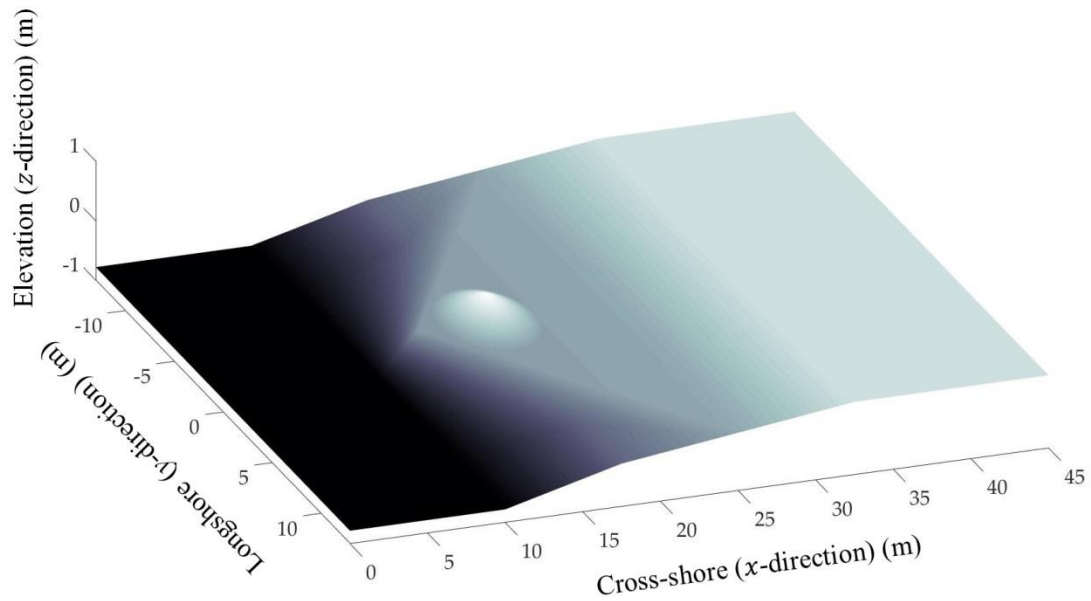


Figure 4.53 3D representation of the bathymetry of BMP 3 including the coordinate system (Velioglu et al., 2016)

The free surface elevations were measured using two types of wave gauges; the resistance-type, wire wave gauges, which were used offshore of the still water shoreline, and ultra sonic wave gauges, which were used onshore of the still water shoreline. Once the breaking wave reached the still water shoreline, the usWGs were used to track the runup on the planar beach. The fluid velocity components, u , v and w , were recorded via three-dimensional Acoustic-Doppler Velocimeters (ADV). The locations of the gauges are listed in Table 4.17.

An initial solitary wave of 0.39 m amplitude propagates over a uniform water depth of 0.78 m before transforming over the shelf system and inundating the backshore area. Both the incident and receding waves wrap around the cone and the subsequent opposing flows provide a vortex generation mechanism. The images in Figures 4.54 and 4.55 provide a visual explanation of the experiment, which is vital to understanding the mechanism of BMP 3.

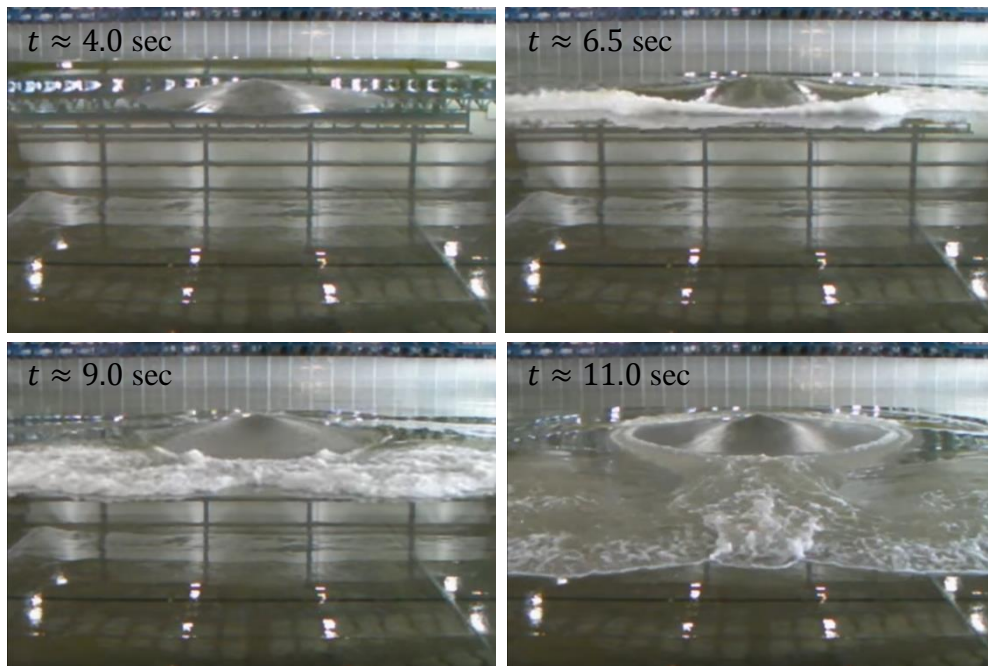


Figure 4.54 Screenshots from the experiment at OSU, available at URL1 (Lynett, 2015)

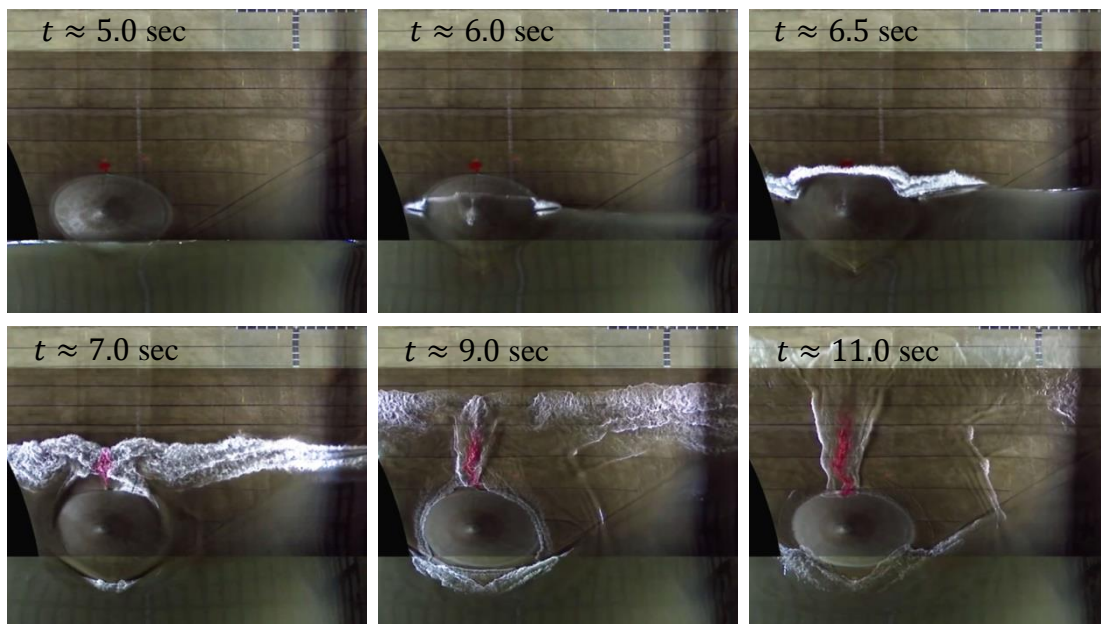
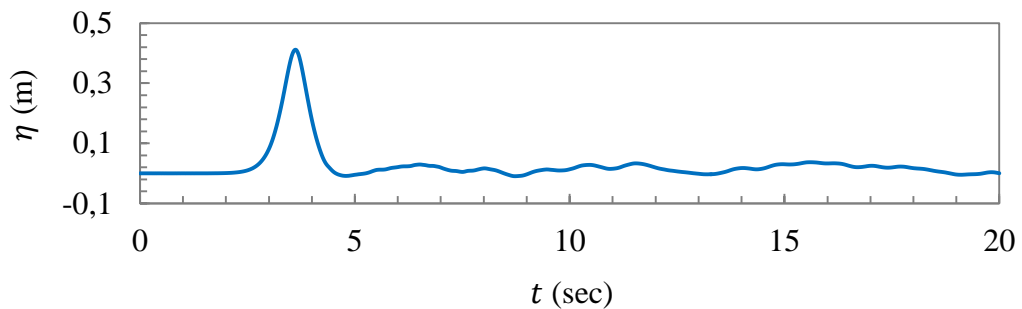


Figure 4.55 Screenshots from the dye study at OSU, available at URL2 (Lynett, 2015)

Table 4.17 BMP 3 gauge locations (NTHMP, 2011)

Gauge ID	x (m)	y (m)	z (m)	Comments
1	7.5	0	–	Wave Gauge
2	13	0	–	Wave Gauge
2*	13	0	0.75	ADV – 3 cm below SWL
3	21	0	–	Wave Gauge
3*	21	0	0.77	ADV – 1 cm below SWL
4	7.5	5	–	Wave Gauge
5	13	5	–	Wave Gauge
6	21	5	–	Wave Gauge
7	25	0	–	Wave Gauge
8	25	5	–	Wave Gauge
9	25	10	–	Wave Gauge
10	21	-5	0.77	ADV – 1 cm below SWL

Even though FLOW-3D[®] is capable of modeling the action of the generator wave paddles via its GMO module, for the sake of consistency between the two models, the incident wave is inputted manually. The free surface elevation time series recorded at Gauge 1 is defined as the input wave (Figure 4.56).

**Figure 4.56** The free surface elevation time series recorded at Gauge 1 (NTHMP, 2015)

BMP 3 involves energetic wave breaking; therefore, to perform BMP 3, it is necessary to compare the free surface elevations and all velocity components (u , v and w) recorded throughout the tank.

4.3.2. NAMI DANCE Model

The same set of experiments is reproduced in a 2D domain using NAMI DANCE. The fluid is inviscid and the flow is incompressible. Fluid density is taken constant throughout the fluid domain. The x axis of the Cartesian coordinate system is perpendicular to the wavemaker and the y axis is parallel to the wavemaker (Figure 4.57). The origin is located at the wavemaker, in line with the front surface of all paddles at their rest position. The gravitational force, g , is in the downward direction.

Figure 4.58 illustrates the 3D view of NAMI DANCE computational domain.

The incident wave, which is the water surface elevation time series recorded at Gauge 1, is inputted at the upstream end of the computational domain along y -direction (i.e. minimum x boundary) where $x = 7.5$ m. The maximum x boundary has a rigid wall boundary condition, which defines the downstream end of the wave tank. The minimum and maximum y boundaries are also defined as rigid walls in order to prevent outflow from the computational domain.

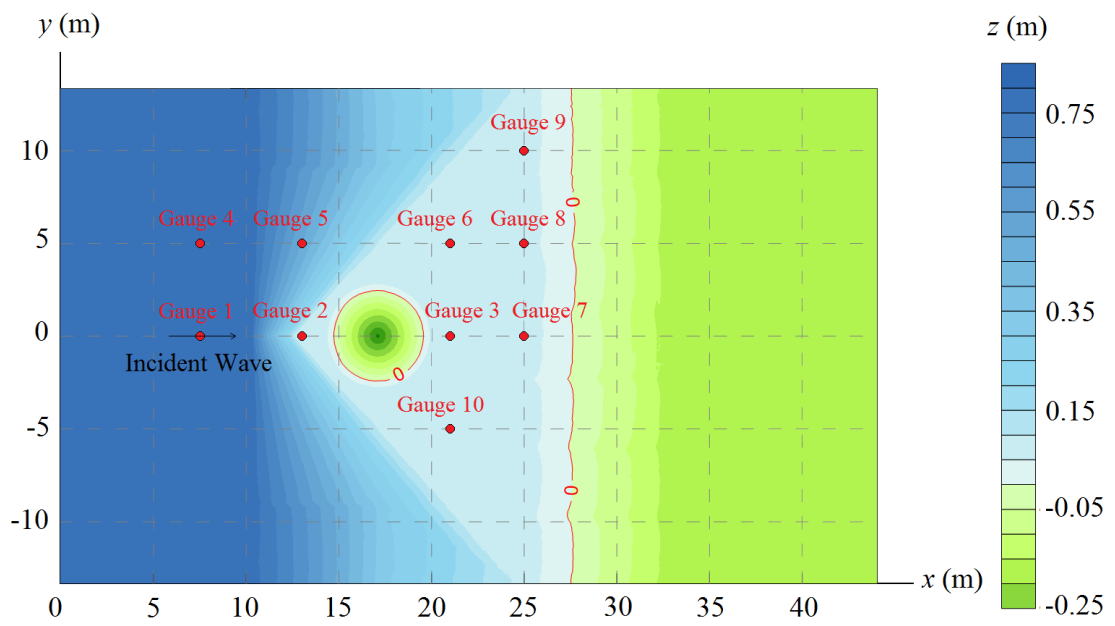


Figure 4.57 NAMI DANCE model: computational domain and the orientation of the coordinate system (top view)

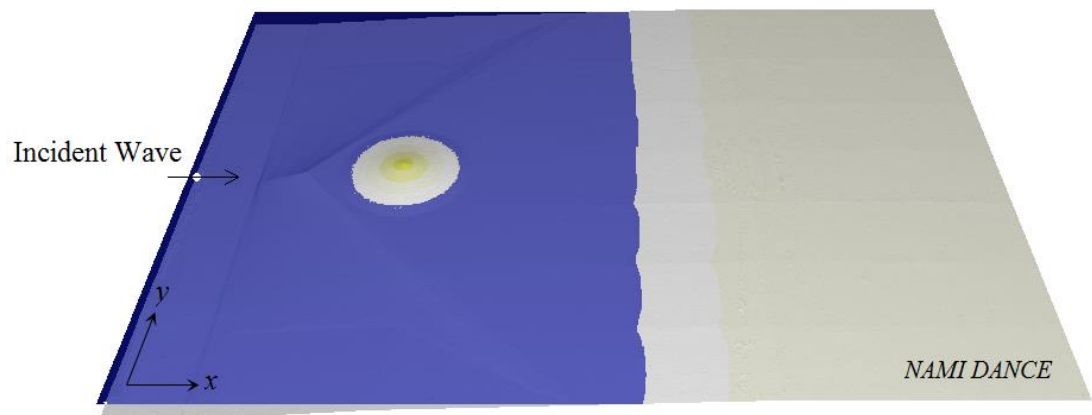


Figure 4.58 3D top view of NAMI DANCE computational domain for BMP 3

4.3.2.1. Spatial Discretization

The computational domain, represented by a structured mesh (i.e. rectangular cells), covers the entire length of the flume with grid sizes, Δx and Δy , which are uniform throughout the mesh. The previous numerical model validations that used BMP 3 (ISEC, 2009; NTHMP, 2011) are taken into account in the determination of the grid size. It is found that in the recent studies $\Delta x = 0.05$ m (Alaska Tsunami Model, Alaska Tsunami Forecast Model and SELFE) (NTHMP, 2011). After a careful analysis, the grid size is selected as 5 cm; i.e. $\Delta x = \Delta y = 0.05$ m.

The convergence of NAMI DANCE is tested by comparing the free surface profiles of the first/leading wave at Gauge 2: $(x, y) = (13 \text{ m}, 0 \text{ m})$, Gauge 3: $(x, y) = (21 \text{ m}, 0 \text{ m})$ and Gauge 7: $(x, y) = (25 \text{ m}, 0 \text{ m})$ for $\Delta x = 0.01$ m, $\Delta x = 0.05$ m, $\Delta x = 0.1$ m and $\Delta x = 0.2$ m (Figure 4.59).

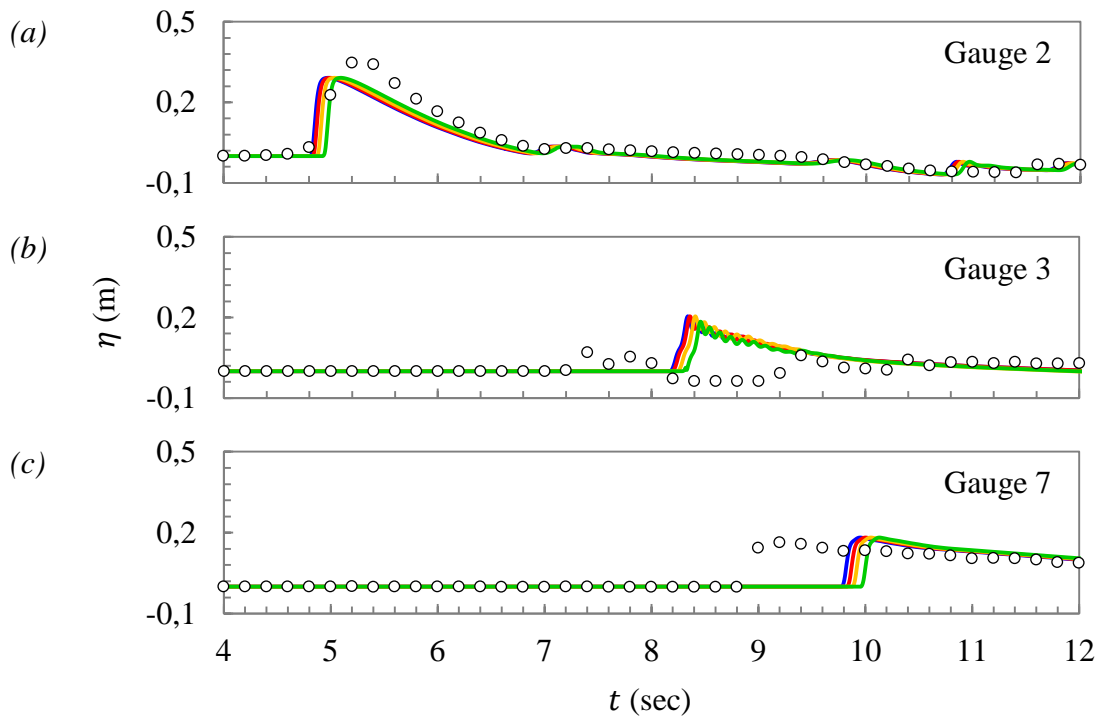


Figure 4.59 NAMI DANCE convergence test at: (a) Gauge 2; (b) Gauge 3; (c) Gauge 7. The circles represent the laboratory measurements; the blue, red, orange and green lines represent NAMI DANCE results for $\Delta x = 0.01$ m, $\Delta x = 0.05$ m, $\Delta x = 0.1$ m and $\Delta x = 0.2$ m; respectively.

The results reveal that the grid size has a minor effect on the predictions for the gauges located behind the island, Gauges 3 and 7, where nonlinearity is dominant (i.e. there is vorticity). On the other hand, for Gauge 2, which is located in front of the island, the effect of spatial resolution is negligible. It can be concluded that since most of the hydraulic processes are fairly hydrostatic, simulations with a coarser grid of up to $\Delta x = 0.2$ m still account for the main flow structure and agree reasonably with the laboratory data, especially for locations in front of the island. Also, the spatial resolution plays a minor role in the flow velocity.

The maximum time step size that fulfills the CFL stability criteria is calculated automatically by NAMI DANCE for each run, depending on the bathymetry. According to this limitation, time step, Δt , is selected as 0.001 second for all runs.

4.3.2.2. Friction

Manning's roughness coefficients that are used to assess the effect of friction are: (i) $n = 0$ (i.e. frictionless bottom), (ii) $n = 0.01$ (i.e. neat cement/concrete/smooth glass beach), (iii) $n = 0.03$ (i.e. fine particles along the channel bottom).

The results reveal that the varying friction is mostly effective at locations behind the obstacle. It is felt more at the gauges located farther behind, where smaller friction produces results closer to the measured data. The shape and amplitude of the signal is well captured and friction has little effect along the line in front of the obstacle (i.e. $x = 13$ m). Along the lines located behind the obstacle (i.e. $x = 21$ m and $x = 25$ m), the results show that the value of friction affects the level of agreement of the predicted values with the observations. Where the flow depth is small, there are significant changes in flow speed due to variations in roughness. It is observed that, in general, frictionless bottom or $n < 0.01$ leads to an overestimation of flow speed and, in turn, to a small mismatch in the wave amplitude and arrival times at the wave gauges. On the other hand, when $n > 0.03$, the flow speed is underestimated (Figure 4.60).

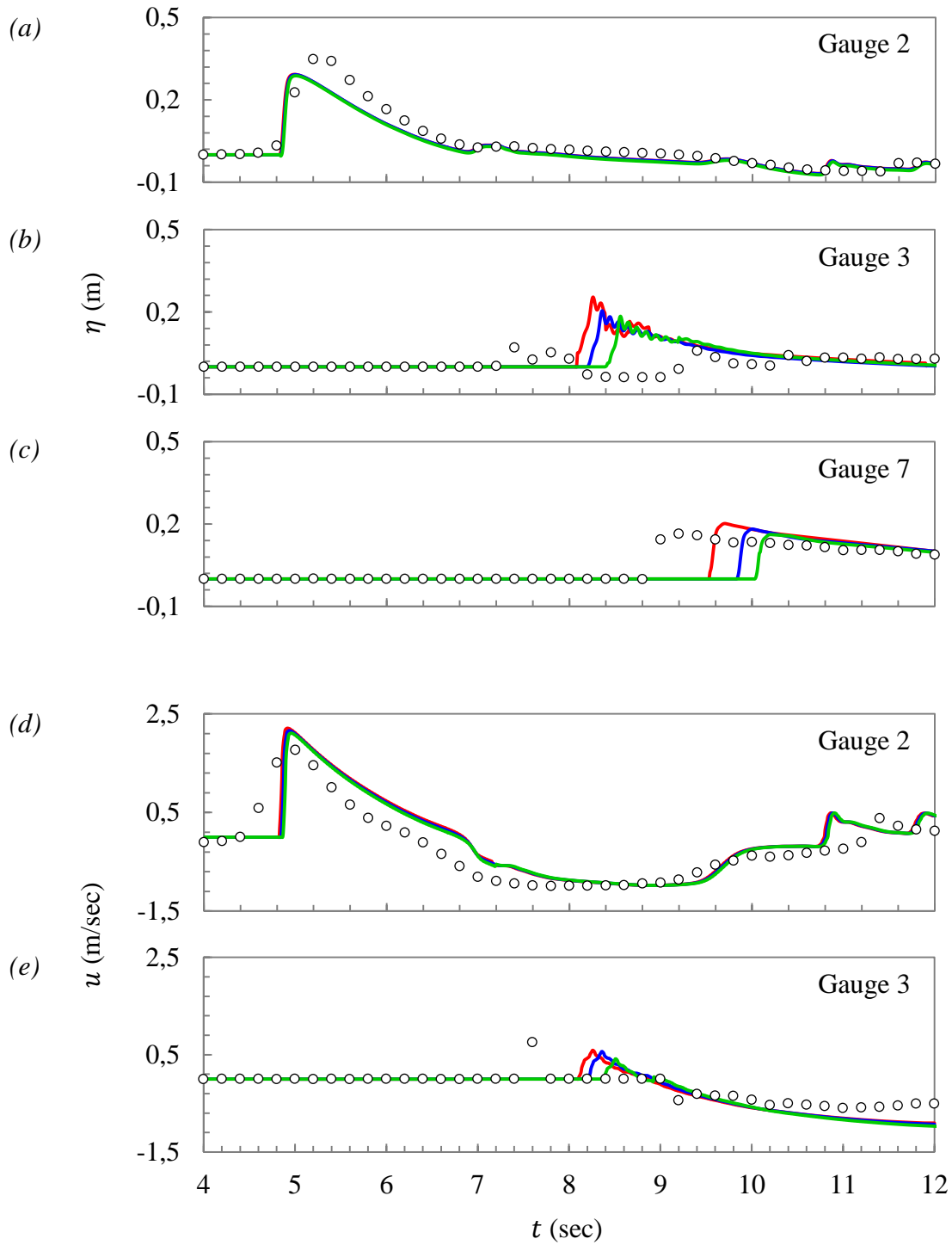


Figure 4.60 NAMI DANCE results according to different Manning's roughness coefficients: (a) leading wave profile at Gauge 2; (b) leading wave profile at Gauge 3; (c) leading wave profile at Gauge 7; (d) horizontal velocity component at Gauge 2; (e) horizontal velocity component at Gauge 3. The circles represent the laboratory measurements; the red line represents the results when $n = 0$; the blue line represents the results when $n = 0.01$; the green line represents the results when $n = 0.03$.

4.3.3.FLOW-3D® Model

The same set of physical experiments is reproduced using FLOW-3D® (Figure 4.61):

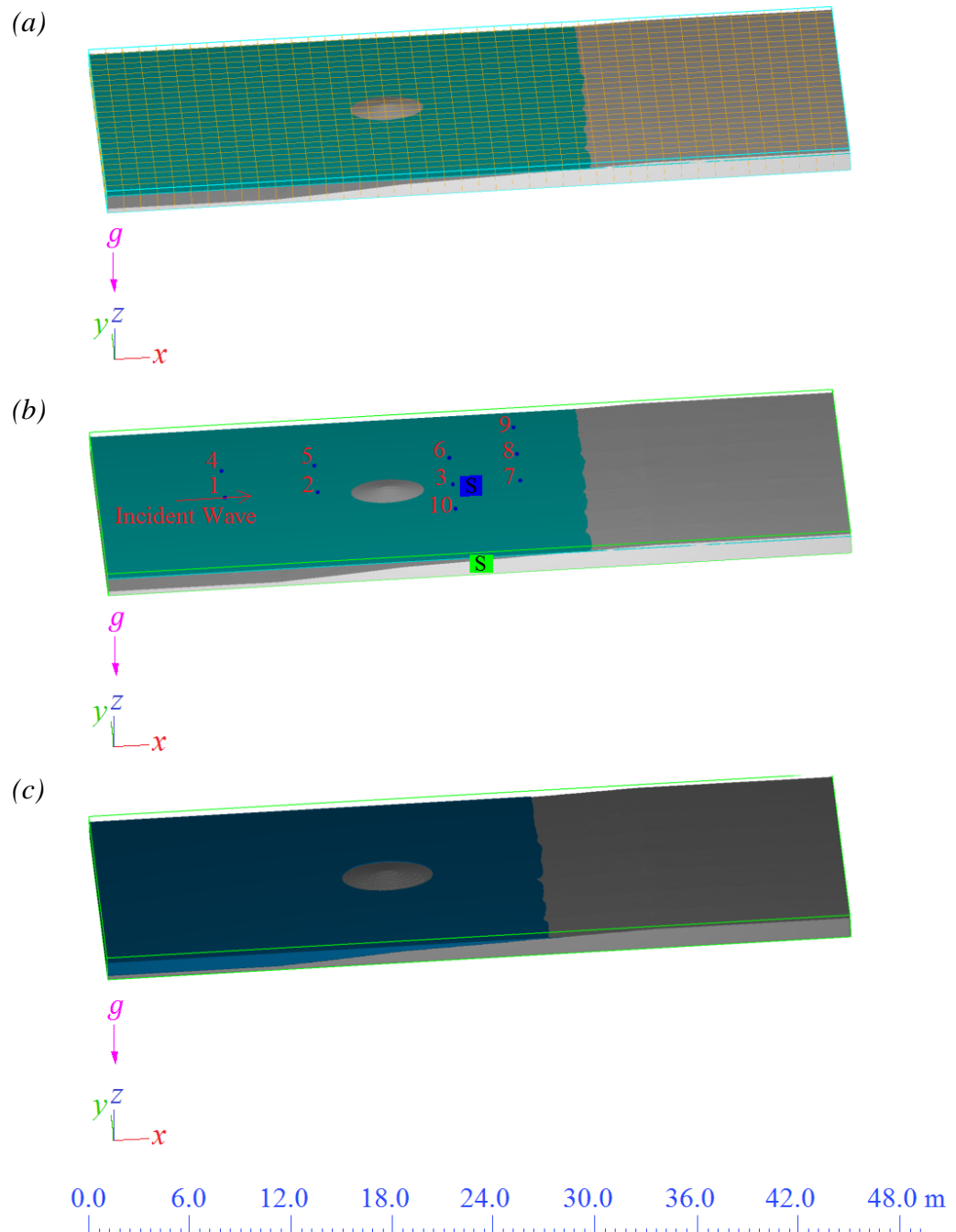


Figure 4.61 FLOW-3D® computational domain constructed for BMP 3: (a) meshing (enlarged for clarity); (b) boundary conditions and gauge locations; (c) after using FAVOR™

The fluid is inviscid, the flow is incompressible and the fluid density is constant. The effects of surface tension and air entrainment at the surface of the flow are neglected. The numerical model is constructed using the Cartesian coordinate system, where the positive x direction is oriented along the fluid flow into the domain and the positive y direction is perpendicular to the direction of the flow, along the wavemaker. The gravitational acceleration, g , is in the downward direction (i.e. $-z$ direction).

The pressure boundary condition is used at the minimum x boundary. This boundary condition allows the user to enter the input data manually, which is the free surface elevation time series recorded at Gauge 1, i.e. $(x, y) = (7.5 \text{ m}, 0 \text{ m})$, in this case. The maximum x boundary has the wall boundary condition so as to define the end of the wave tank. The minimum and maximum y boundaries as well as the maximum z boundary feature the symmetrical boundary condition, where all the velocity derivatives and velocity components normal to the boundaries are set to zero. The wall boundary condition is valid for the minimum z boundary, where the bottom of the wave flume is defined.

4.3.3.1. Spatial Discretization

The computational domain is represented by an isotropic grid with $\Delta x = \Delta y = \Delta z$ where the grid size is selected as 0.05 m (Please refer to the explanations in Section 4.3.2.1). BMP 3 is modeled via FLOW-3D[®] for different Δx values in order to test the grid dependency at Gauges 2, 3 and 7 (Figure 4.62).

The numerical resolution has no evident influence on the free surface profiles, even in the areas with high vorticity concentration (i.e. Gauges 3 and 7). Still, there is a small improvement in the results after $\Delta x = 0.1 \text{ m}$.

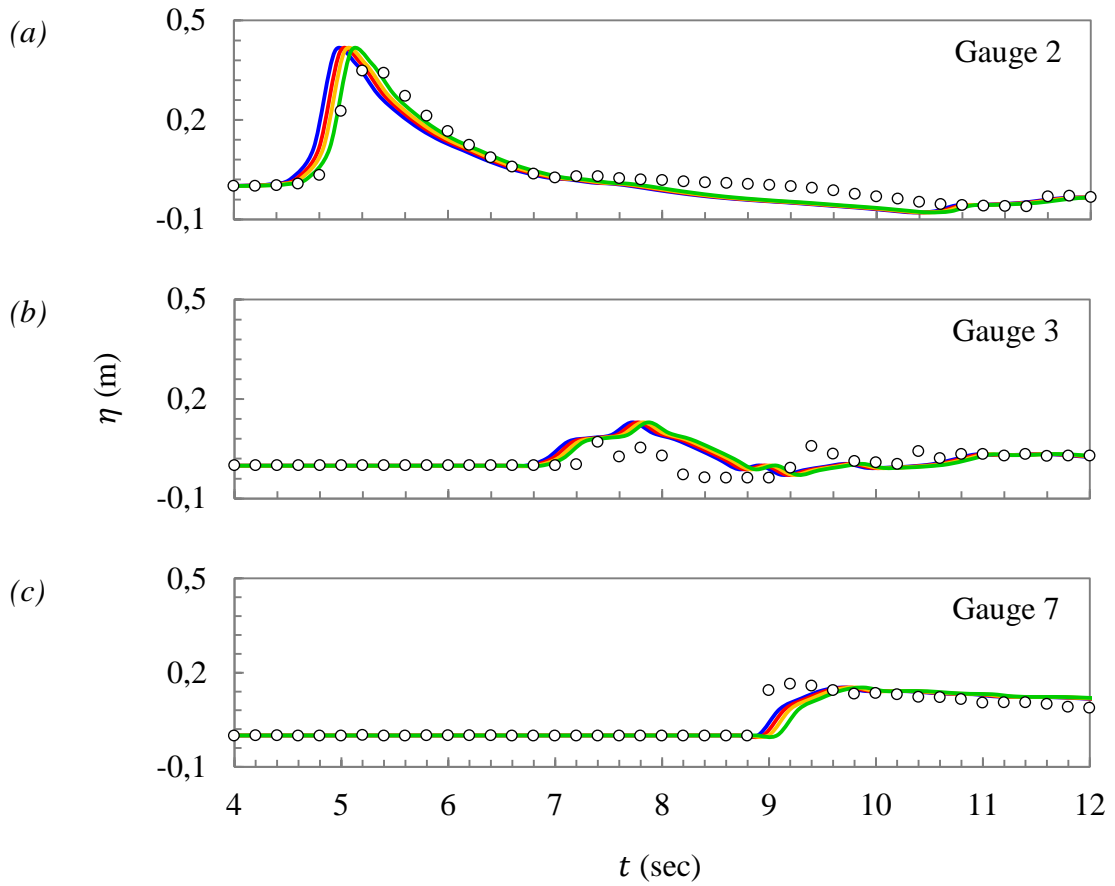


Figure 4.62 FLOW-3D[®] convergence test at: (a) Gauge 2; (b) Gauge 3; (c) Gauge 7. The circles represent the laboratory measurements; the blue, red, orange and green lines represent FLOW-3D[®] results for $\Delta x = 0.01$ m, $\Delta x = 0.05$ m, $\Delta x = 0.1$ m and $\Delta x = 0.2$ m; respectively.

It is also necessary to analyse the effect of the vertical grid size, Δz , on the free surface profiles in a three-dimensional model. Changing the vertical grid size is effective in the very shallow zone and in the vicinity of the island. In fact, a fine vertical grid size (i.e. $\Delta z \leq 0.1$ m) gives results closer to the measured values, with Δx kept constant. No considerable change is observed after $\Delta z = 0.1$ m.

The time step, Δt , is selected as 0.001 second to be consistent with the simulations conducted using NAMI DANCE. When variable time stepping is employed in order to assess the effect of the time step size, no significant effect is observed.

4.3.3.2. Friction

In order to assess the effect of friction on the maximum runup values, different Manning's roughness coefficients are considered:

- (i) $n = 0$ (i.e. frictionless bottom)
- (ii) $n = 0.01$ (i.e. neat cement/concrete/smooth glass beach)
- (iii) $n = 0.03$ (i.e. fine particles along the channel bottom)

Please refer to Section 4.2.2.2 for the comparison criteria.

The results obtained via FLOW-3D[®] are similar to those obtained using NAMI DANCE. The shape and amplitude of the signal is well captured and friction has little effect along the line in front of the obstacle (i.e. $x = 13$ m). Along the lines located behind the obstacle (i.e. $x = 21$ m and $x = 25$ m), the results show that the value of friction affects the level of agreement of the predicted values with the observations (Figure 4.63).

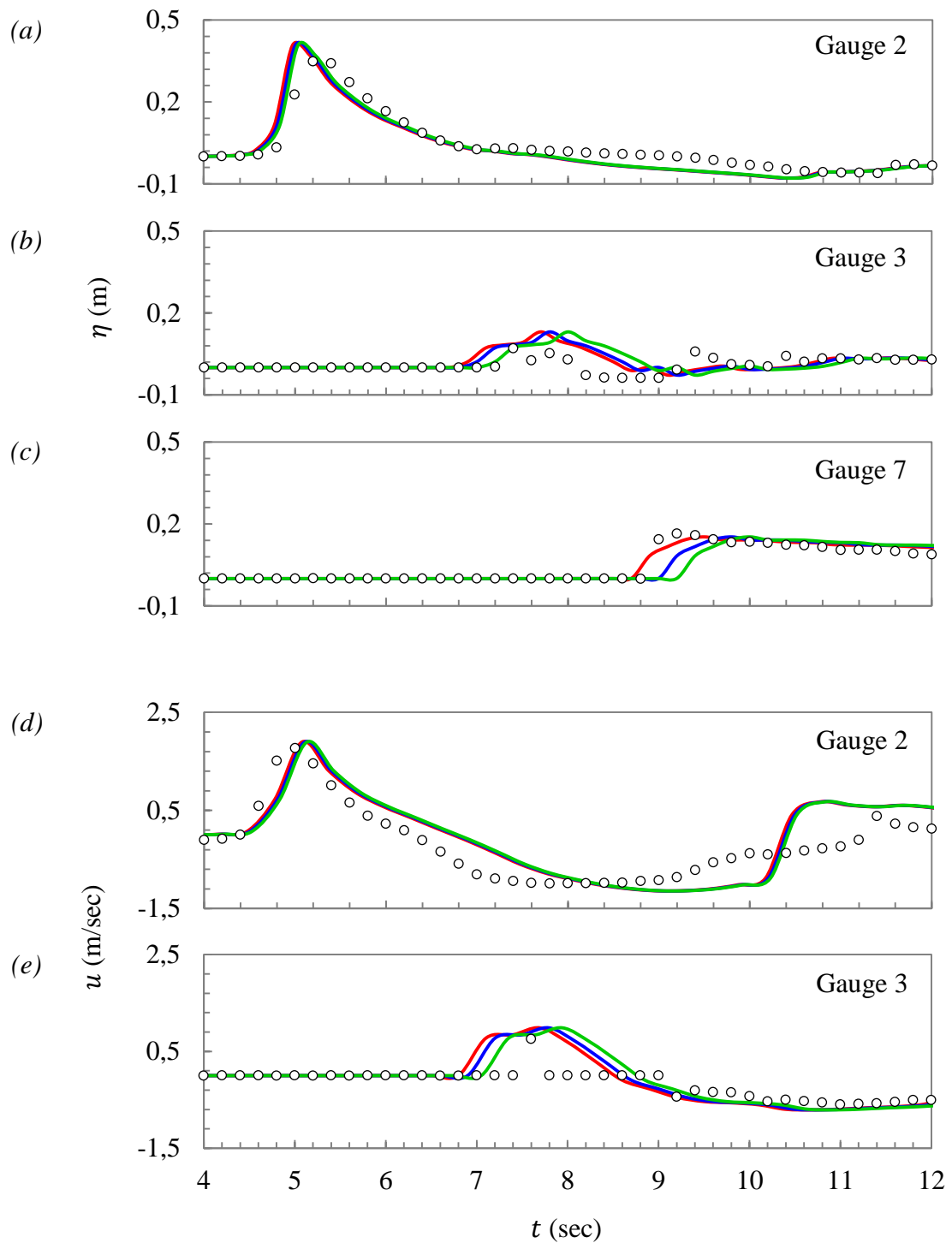
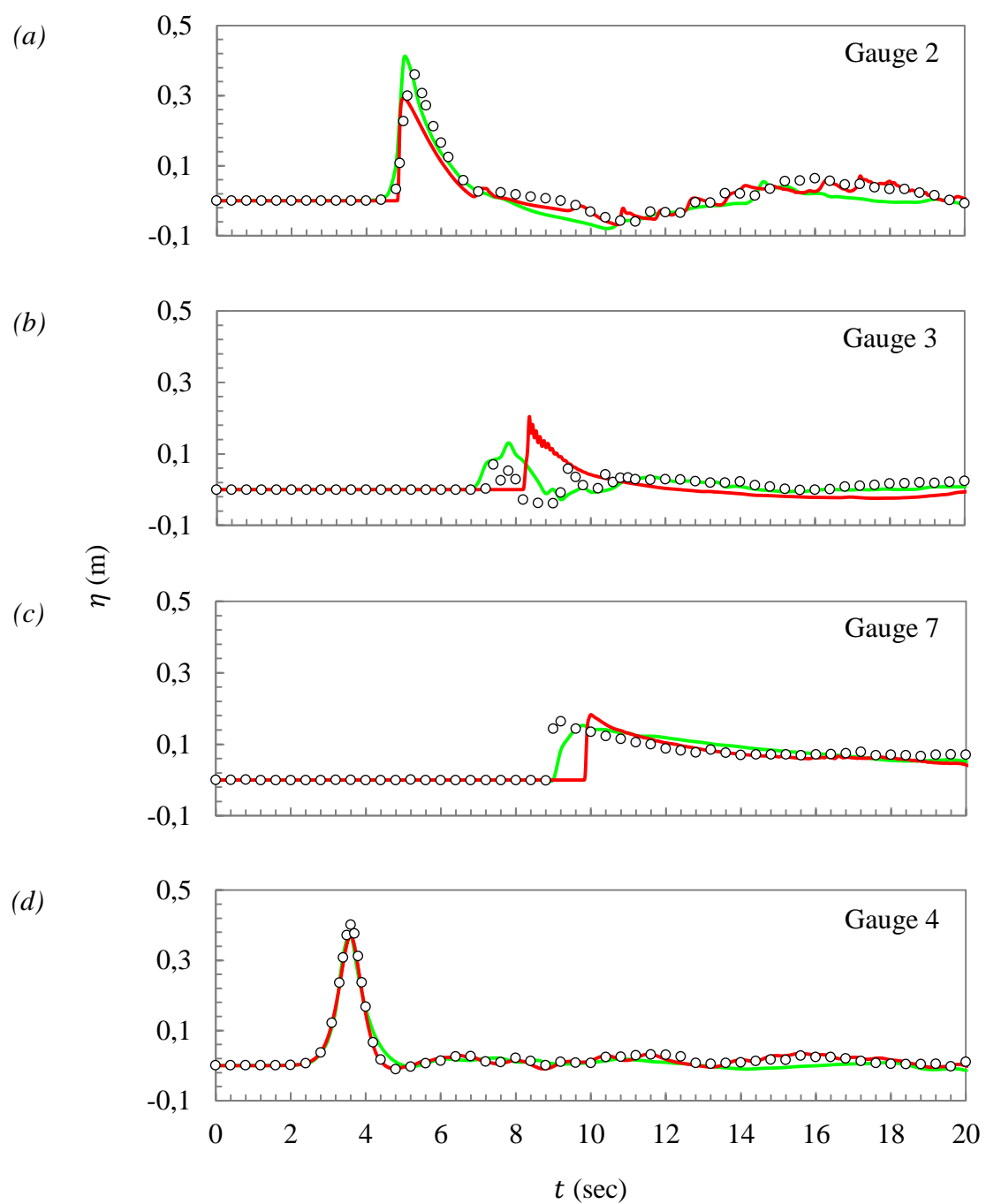


Figure 4.63 FLOW-3D[®] results according to different Manning's roughness coefficients: (a) leading wave profile at Gauge 2; (b) leading wave profile at Gauge 3; (c) leading wave profile at Gauge 7; (d) horizontal velocity component at Gauge 2; (e) horizontal velocity component at Gauge 3. The circles represent the laboratory measurements; the red line represents the results when $n = 0$; the blue line represents the results when $n = 0.01$; the green line represents the results when $n = 0.03$.

4.3.4. Simulation Results

The NAMI DANCE and FLOW-3D[®] results regarding the wave transformation in the shallow zone and in the vicinity of the conical island are given in Figure 4.64.



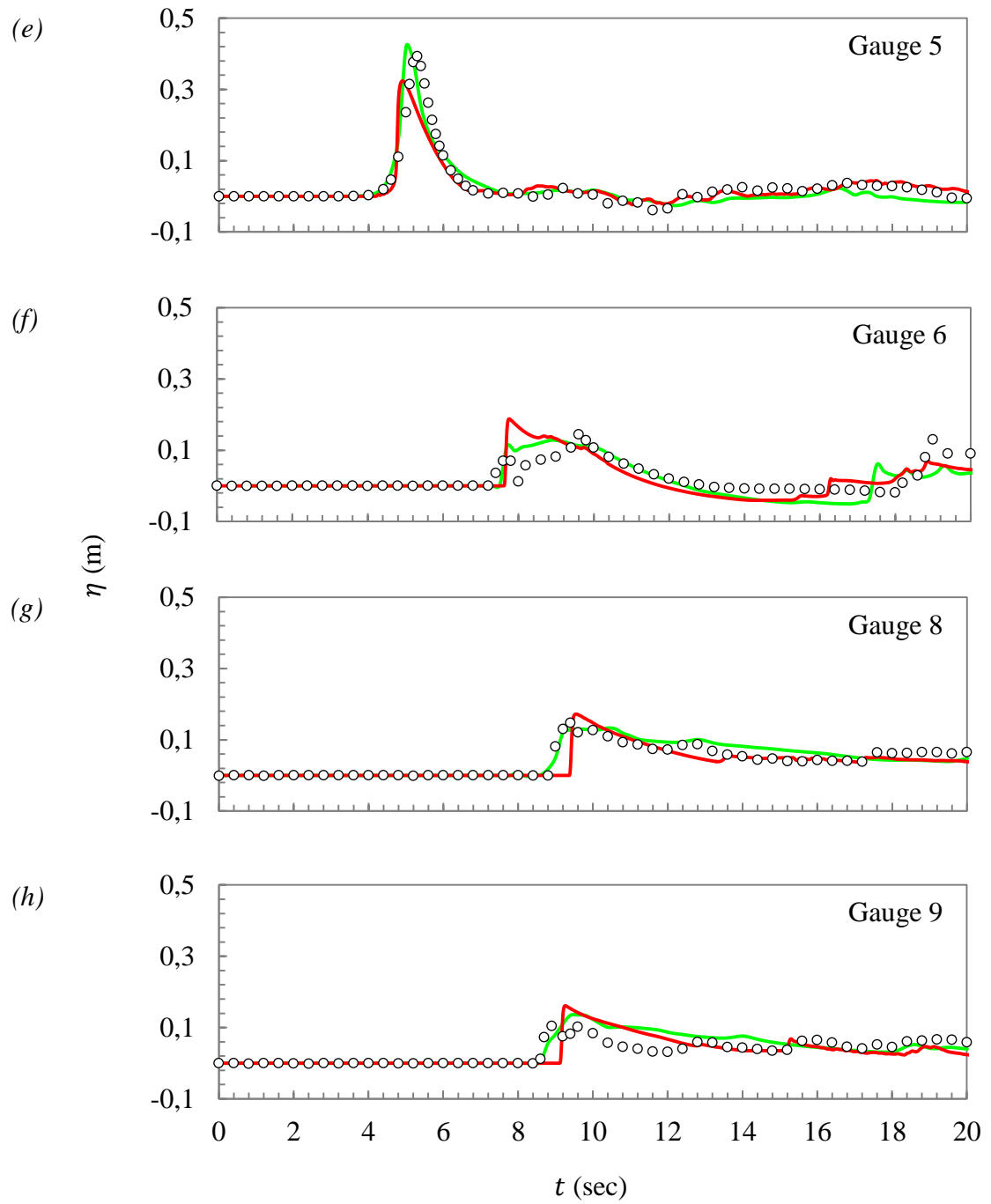


Figure 4.64 The predicted and measured free surface profiles at: (a) Gauge 2; (b) Gauge 3; (c) Gauge 7; (d) Gauge 4; (e) Gauge 5; (f) Gauge 6; (g) Gauge 8; (h) Gauge 9. The circles represent the laboratory measurements; the red line represents the NAMI DANCE results; the green line represents the FLOW-3D[®] results.

The predicted velocity components are given in Figures 4.65 – 4.67.

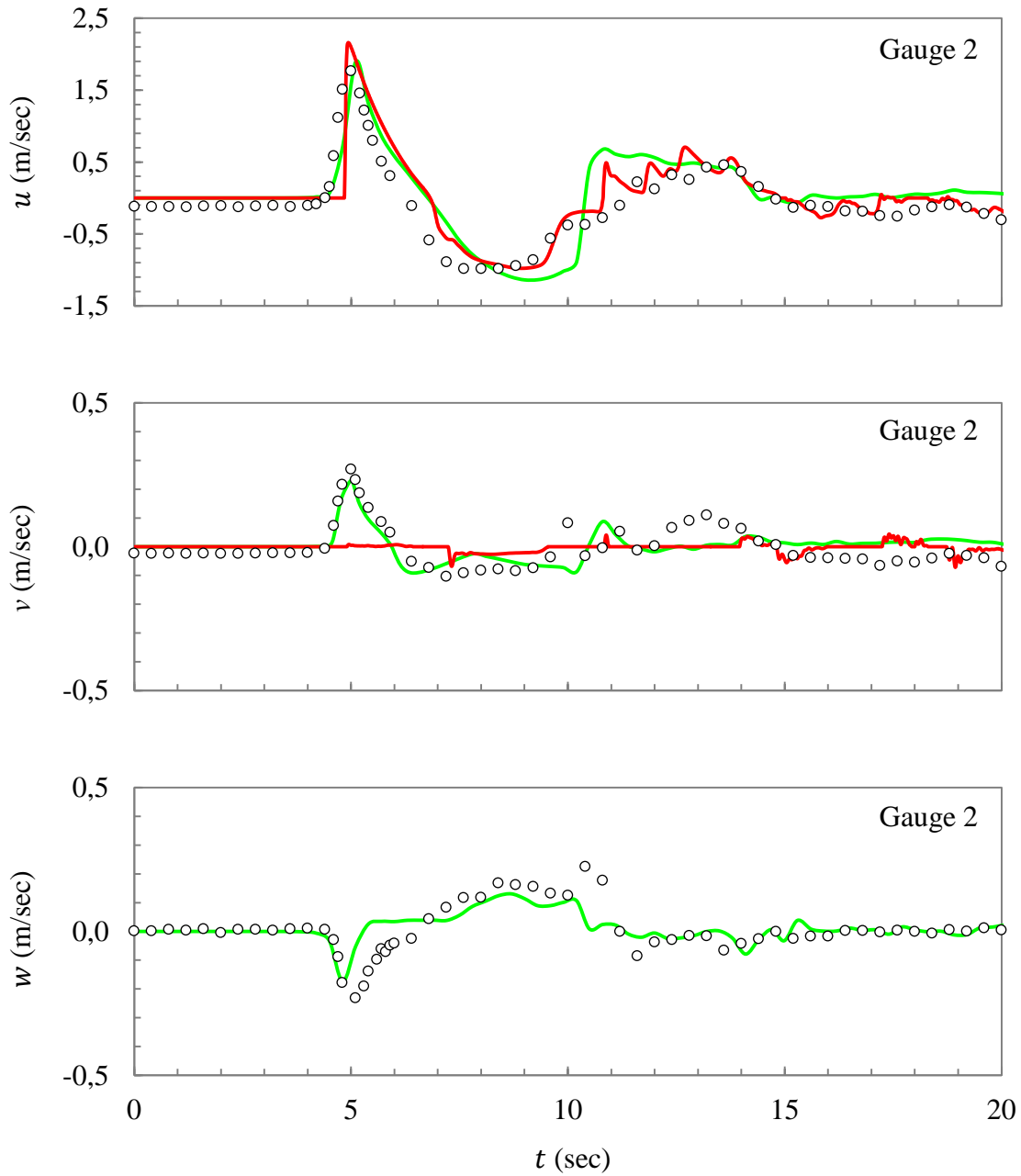


Figure 4.65 The predicted and measured velocity components at Gauge 2: $(x, y, z) = (13 \text{ m}, 0 \text{ m}, 0.75 \text{ m})$. The circles represent the laboratory measurements; the red line represents the NAMI DANCE results; the green line represents the FLOW-3D[®] results.

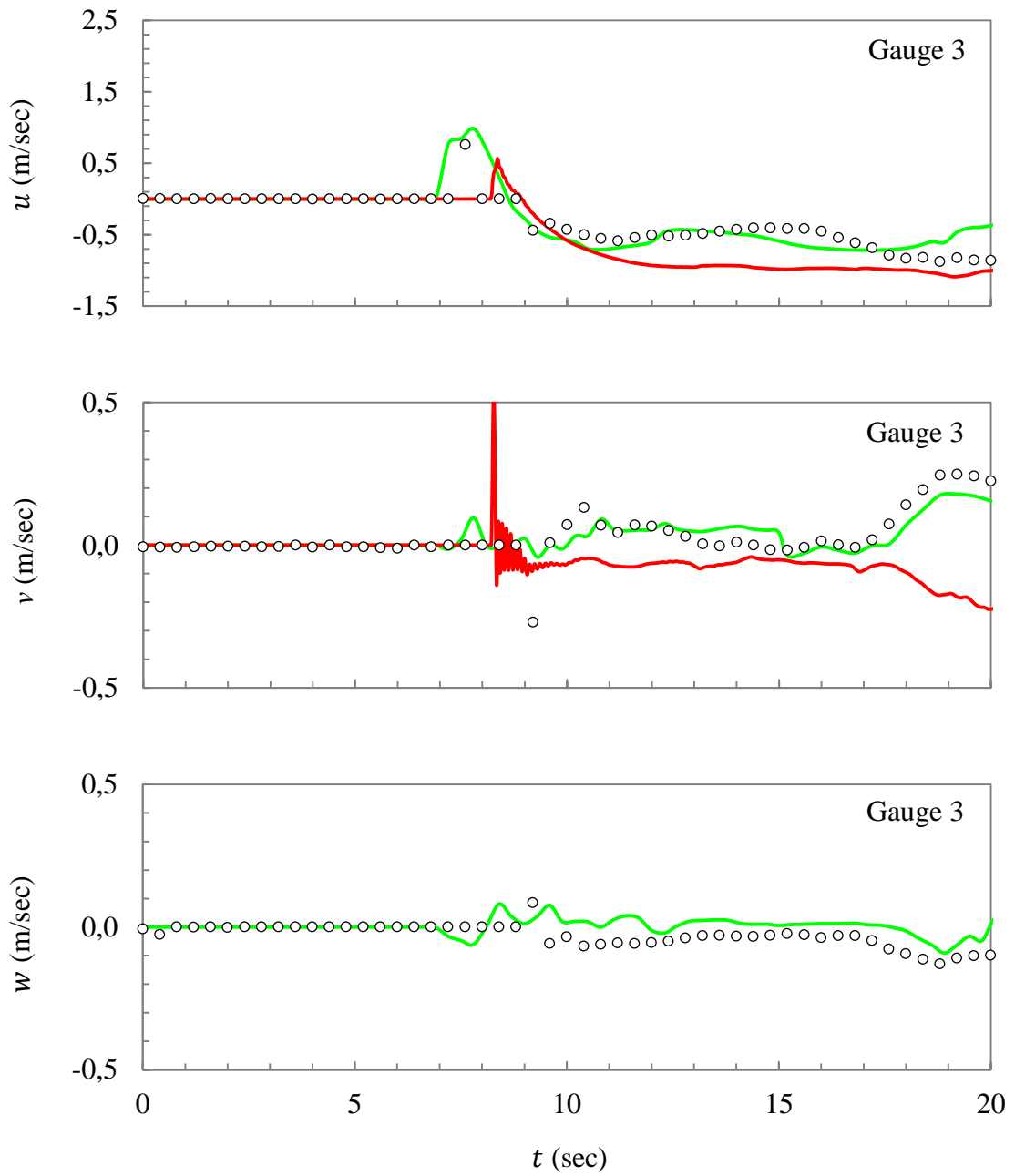


Figure 4.66 The predicted and measured velocity components at Gauge 3: $(x, y, z) = (21 \text{ m}, 0 \text{ m}, 0.77 \text{ m})$. The circles represent the laboratory measurements; the red line represents the NAMI DANCE results; the green line represents the FLOW-3D[®] results.

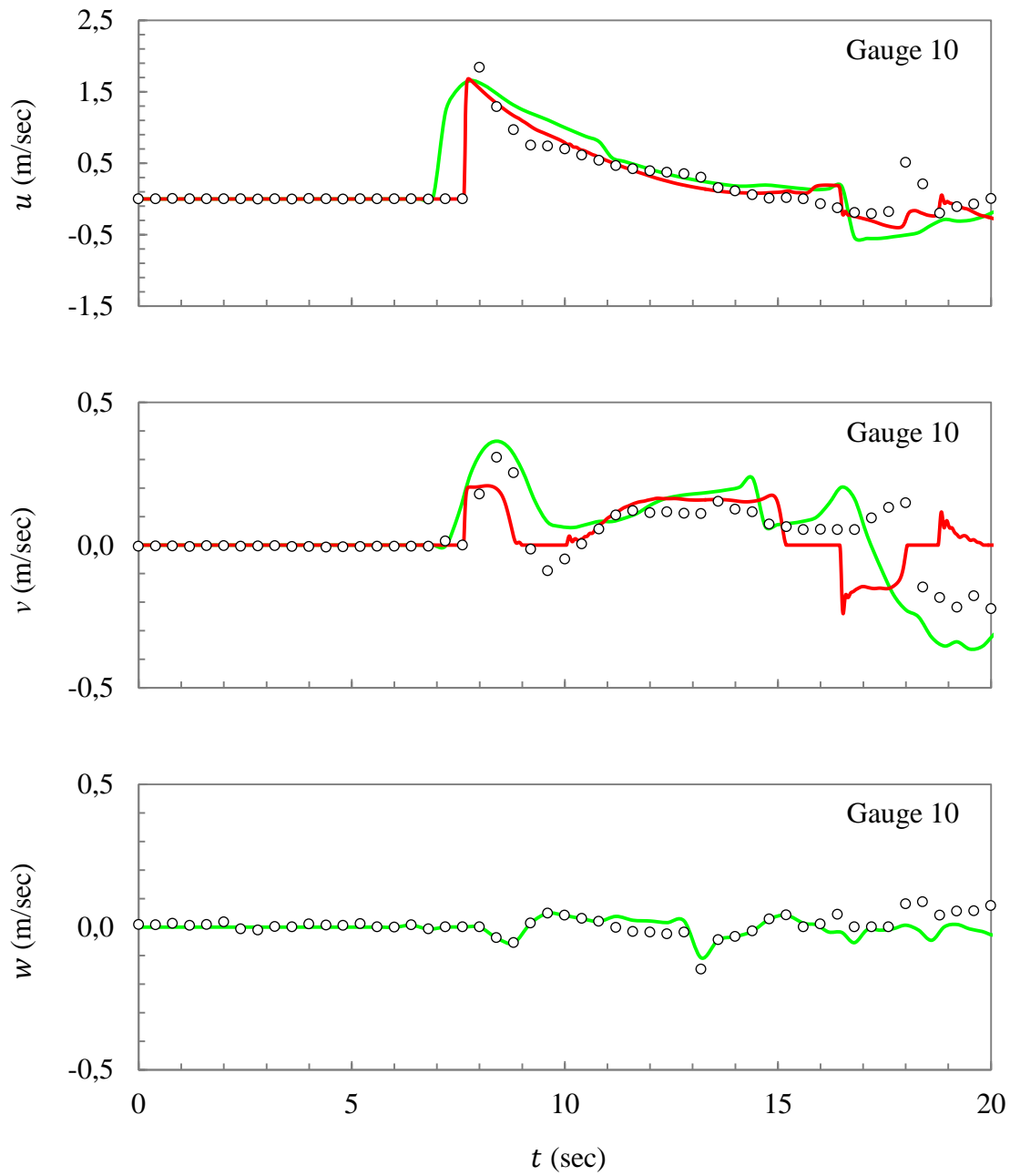


Figure 4.67 The predicted and measured velocity components at Gauge 10: $(x, y, z) = (21 \text{ m}, -5 \text{ m}, 0.77 \text{ m})$. The circles represent the laboratory measurements; the red line represents the NAMI DANCE results; the green line represents the FLOW-3D[®] results.

Please note that since NAMI DANCE is a depth-averaged model, the vertical velocity components are only compared with the FLOW-3D[®] results.

The computations are terminated after the first reflection of the wave from the island, which is 20 seconds. The simulations that are performed via NAMI DANCE are completed in approximately 15 hours whereas it takes 2 days to complete the simulations using FLOW-3D[®].

According to the results given in the above figures, it is found that the free surface profiles are satisfactorily represented via NAMI DANCE, except for Gauges 3 and 7, which are located behind the obstacle. Since NAMI DANCE is a 2D depth-averaged model, it fails to capture the strong nonlinearities occurring just behind and a little farther behind the island because it predicts steep wave fronts. FLOW-3D[®], on the other hand, accurately describes the evolution and transformation of the wave, as well as the complex free surface profiles occurring behind the island.

The maximum cross-shore velocity component, u , is approximately 5 times larger than the maximum longshore velocity component at all three gauges. The reason for this may be the focusing of wave energy at the wake of the island.

The results reveal that for the gauges located far behind the obstacle, little time shifts are observed for the NAMI DANCE results. At the gauges located at the wake of the island, (i.e. $x = 13.0$ m, $y = 0$ m and $x = 21.0$ m, $y = 0$ m), NAMI DANCE provides a good fit for the cross-shore velocity component, u , while the longshore velocity component, v , is not well captured. FLOW-3D[®] captures the maximum and minimum values of all three velocity components. The vertical velocity component is also very well predicted for all the gauges. Moreover, no time shift is observed between the FLOW-3D[®] predictions and the laboratory data.

The illustrations of the simulations which are done via NAMI DANCE and FLOW-3D[®] are given in Figures 4.68 and 4.69, respectively.

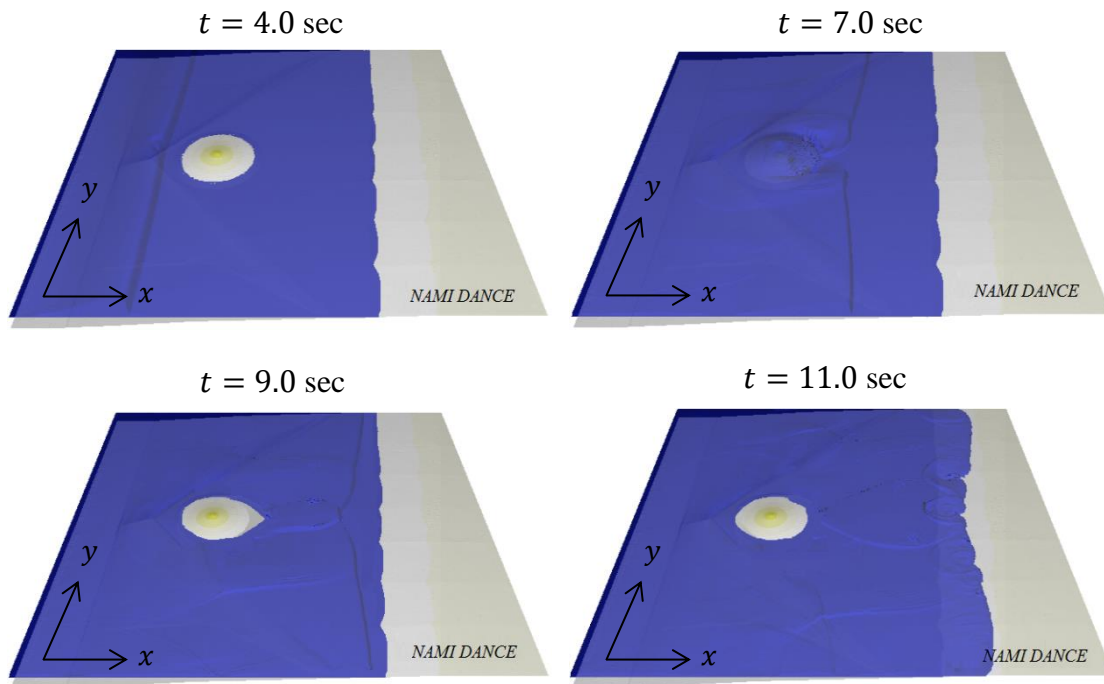


Figure 4.68 NAMI DANCE model simulations for BMP 3 (not to scale)

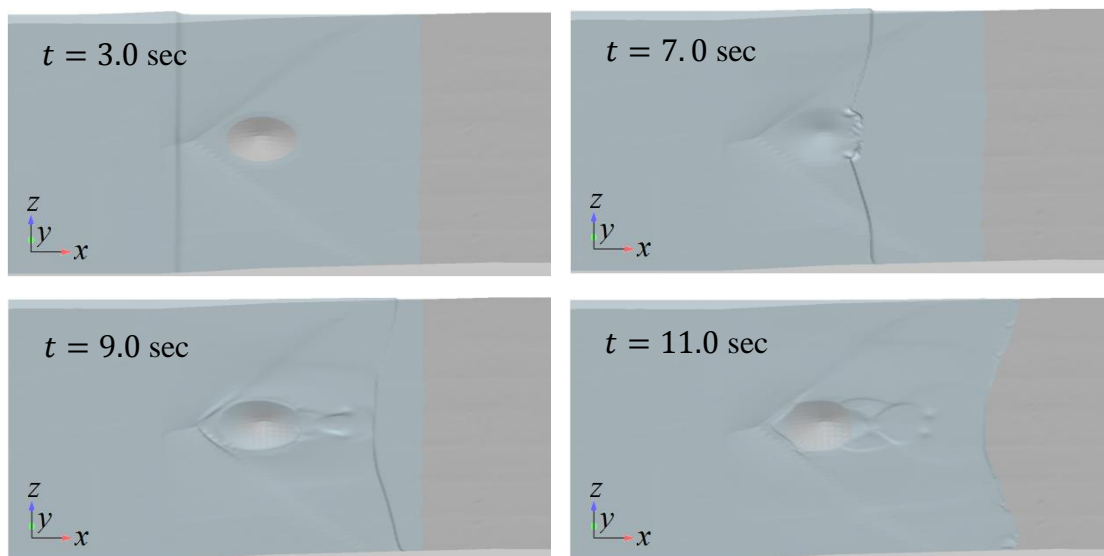


Figure 4.69 FLOW-3D[®] model simulations for BMP 3 (not to scale)

The NRMSE and MAX errors for the free surface profiles are given in Table 4.18 and Figure 4.70.

Table 4.18 NRMSE and MAX errors for the free surface profiles

Gauge	NAMI DANCE		FLOW-3D®	
	% NRMSE	% MAX	% NRMSE	% MAX
2	8.5	9.7	6.2	6.2
3	19.2	17.7	7.5	5.0
4	4.4	7.6	2.8	7.4
5	10.7	13.2	9.1	5.3
6	13.8	9.2	9.1	4.7
7	14.2	9.2	8.6	4.9
8	15.2	11.9	5.1	3.6
9	15.9	12.6	9.8	8.4

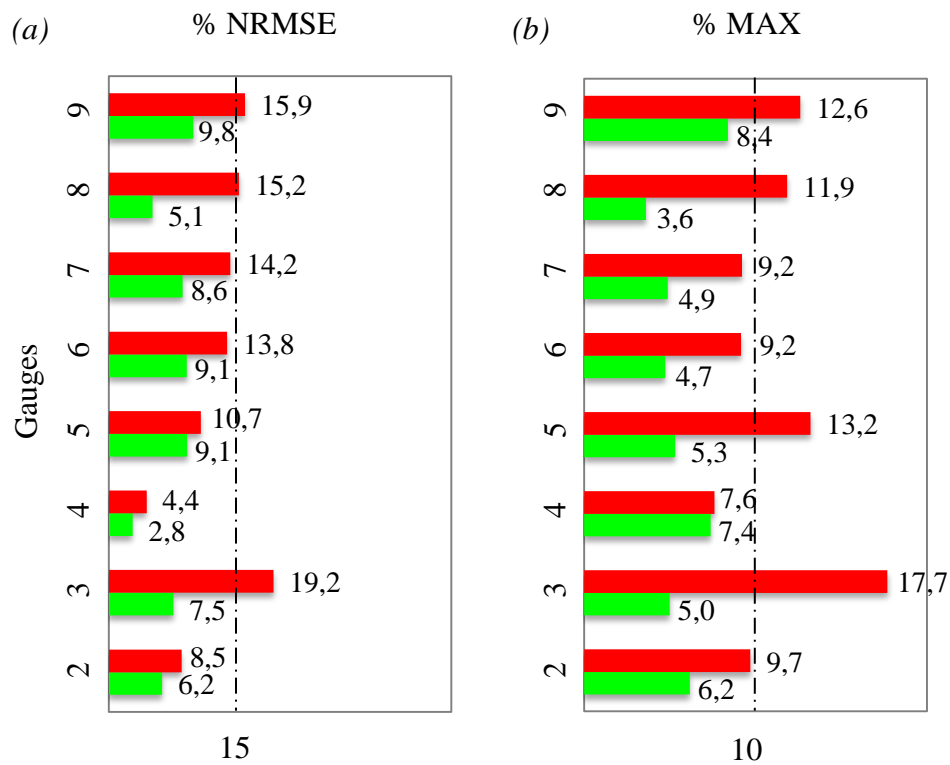


Figure 4.70 Error bars for the free surface profiles: (a) % NRMSE; (b) % MAX error. The red and green bars represent the errors of NAMI DANCE and FLOW-3D® results, respectively.

The NRMSE and MAX errors for the velocity components are given in Table 4.19 and Figure 4.71.

Table 4.19 NRMSE and MAX errors for the velocity components

Gauge	Velocity Component	NAMI DANCE		FLOW-3D [®]	
		% NRMSE	% MAX	% NRMSE	% MAX
2	u	12.0	18.4	9.8	3.3
	v	19.9	34.3	9.7	6.8
	w	NA	NA	11.2	9.6
3	u	19.5	11.9	9.8	7.6
	v	NA	NA	10.7	10.2
	w	NA	NA	8.3	10.1
10	u	8.5	16.1	11.0	9.3
	v	14.1	23.5	10.7	11.2
	w	NA	NA	10.5	9.2

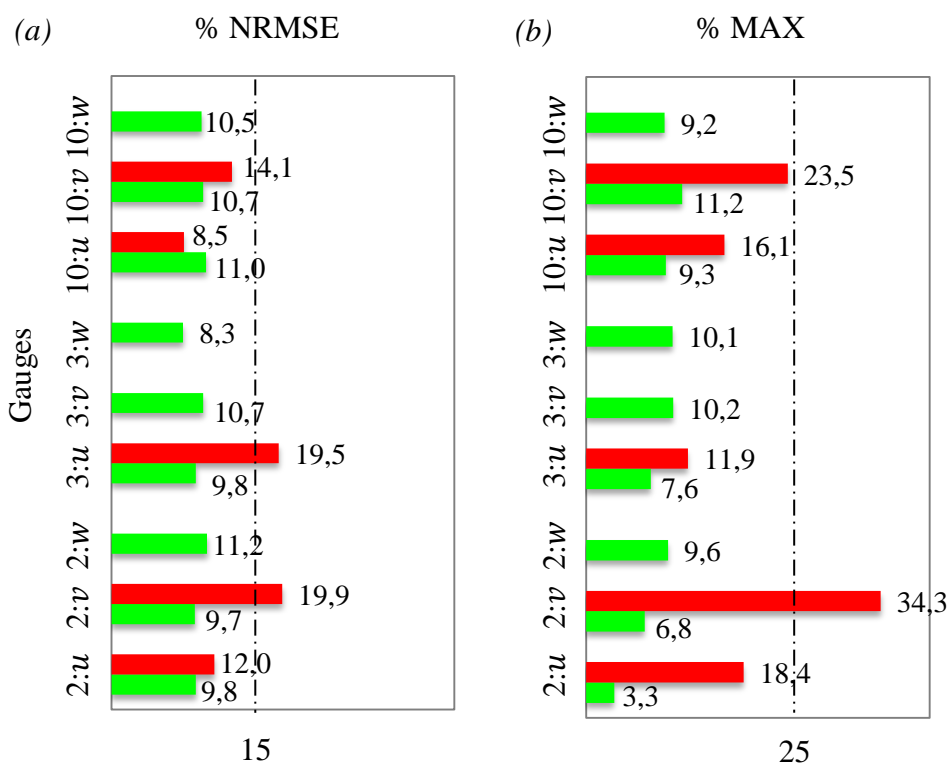


Figure 4.71 Error bars for the velocity components: (a) % NRMSE; (b) % MAX error. The red and green bars represent the errors of NAMI DANCE and FLOW-3D[®] results, respectively.

For the free surface elevation, the NRMSE of the NAMI DANCE results has a wide range, which is between 5% and 19%, while the FLOW-3D[®] results have a much narrower NRMSE range, which is between 3% and 9%. The MAX error of the NAMI DANCE results ranges from 8% to 18% whereas it is between 4% and 8% for the FLOW-3D[®] results.

It is hard to capture exact solutions of the velocity components due to the uncertainty in the nature of the complex flows occurring in shallow shelf zones and in the vicinity of obstacles. This is why the standard MAX error threshold for the velocity components is increased to 25% for laboratory measurements.

For the cross-shore velocity component, the NAMI DANCE results have an NRMSE range between 8% and 12% and a MAX error range between 12% and 18%. The NRMSE of the FLOW-3D[®] results is between 9% and 11% and the MAX error ranges from 3% to 9%. For the longshore velocity component, the NAMI DANCE results have larger NRMSE and MAX error ranges, which are between 14% and 19% and 23% and 34%, respectively. The NRMSE of the FLOW-3D[®] results is between 9% and 11% and the MAX error ranges from 6% to 11%. In addition, FLOW-3D[®] predicts the vertical velocity component, w , fairly well, with an NRMSE between 8% and 11% and a MAX error from 9% to 10%.

The NRMSE and MAX errors of the FLOW-3D[®] results are within the OAR PMEL-135 standard error range both for the free surface elevation time series predictions and velocity component computations. On the other hand, even though NAMI DANCE predicts the evolution of the wave satisfactorily before and immediately after it reaches the shallow water zone, especially for the gauges located behind the obstacle, the errors exceed the threshold values. Multiple borefronts and reflected waves develop on the shelf due to the interaction of flow with the bathymetry; therefore, an NRMSE threshold up to 20% is acceptable for this specific case.

To sum up, BMP 3 investigates the interactions between a breaking solitary wave and a 3D shallow water shelf with a conical island located at the offshore point of the shelf. The two- and three-dimensional models, NAMI DANCE and FLOW-3D[®], are tested against a set of laboratory measurements that include tsunami wave transformation, wave reflection and edge wave formation.

BMP 3 involves energetic breaking waves with overtopping, vortex formation and runup, where the free surface and velocity data measurements are compared with the numerical predictions. In the experiment, the solitary wave breaks at the apex of the reef flat at $t = 5.1$ sec and the resulting surge completely overtops the cone at $t = 6.6$ sec. The refracted waves from the two sides of the cone and the diffracted waves converge in the back at $t = 8.6$ sec. While the refracted waves continue to wrap around as trapped waves, the diffracted waves radiate from the back of the cone. Both models satisfactorily reproduce the recorded surface elevations in front of the cone and the collapse of the bore behind the cone.

The time segment used for the analyses includes the propagation and transformation of the incident wave as well as its overtopping the island. In both models, simulations are forced with the free surface elevation time series measured at Gauge 1 through the left boundary at $x = 7.5$ m for the sake of consistency. For the three-dimensional model predictions, free surface elevation and velocity data show very good agreement at all the gauges with no delay in the arrival times. However, the depth-averaged model, NAMI DANCE, shows small time delays at the gauges located behind the island with some differences. To illustrate, even though Gauges 7 and 8 are located at equal distances from the obstacle, the time delay at Gauge 8 is less than the one observed at Gauge 7, which is closer to the island. The reason for the time delays may be the mislocation of the gauge points in the model due to the gridding method or the nonlinearity of the flow.

In order to analyse the effect of grid size, computations are performed with grid resolutions varying from 0.01 m to 0.2 m, the time increment being 0.001 sec, and the roughness coefficient $n = 0.01$. The results reveal that grid spacing has minimal effect on the overall free surface elevation and flow velocity time series. Both models show little grid sensitivity.

Variations in roughness can lead to significant changes in flow speed over the bathymetries where the flow depth is small. It is found that, in general, $n < 0.01$ leads to a slight overestimation of the flow speed and subsequently to a small mismatch in the wave amplitudes and phase at the wave gauges. With $n \geq 0.03$, the flow speed is underestimated and fairly large lags in the wave arrival times are observed, especially for the gauges located in the wake of and far behind the island.

NAMI DANCE underestimates the propagation speed of the wave and somewhat misrepresents the waveform, especially behind the obstacle, on the centerline. It is important to note that strong turbulence and nonlinearities occur at the wake of the island and the flow condition on the centerline is chaotic. Therefore, no reasonable match can be expected with depth-averaged models regarding the velocity components at this location. Discrepancies occur at the two gauges immediately behind the island because NAMI DANCE can not capture the three-dimensional turbulent flow that occurs due to the overtopping of the island. The modeled flow components at the off-center location agree well with the observations.

Overall, both model results agree well with the observations for the points located in front of the obstacle, including where the process of breaking starts. However, the exact arrival time and shape are not well captured by the depth-averaged model, getting a much better agreement for the three-dimensional model. FLOW-3D[®] predicts the cross-shore velocity components reasonably well with no mismatch in the phase as well as the longshore velocity components, which are an order of magnitude smaller.

The results reveal that the depth-averaged model predicts the wave amplitude nearly 10% less prior to wave breaking. Moreover, even though the cross-shore velocity component, u , is predicted satisfactorily at the tip of the triangular shelf (i.e. Gauge 2) and at the gauge point located far away from the island (i.e. Gauge 10), it is 20% less than the measured one at the gauge located in the wake of the island (i.e. Gauge 3). The 2D depth-averaged NSW equations are not capable of reflecting strong nonlinearities in the flow. Therefore, 3D-RANS equations are required to adequately resolve the initial wavelength and to prevent the wave front from steepening prior to island impact. In other words, even though NSW equations are capable of estimating the major features of propagation, refraction, and runup observed in the laboratory experiments for small and/or medium amplitude waves, three-dimensional models should be preferred when large amplitude waves are studied in the areas featuring strong nonlinearities.

BMP 3 provides both insight into long wave evolution over shallow bathymetry and a unique 3D data set to validate and calibrate numerical models. While extrapolations to geophysical-scale events, such as tsunamis, need to be done with great caution, it is still possible to draw a few relevant conclusions from this experiment. While it is generally accepted that long wave runup is a primary function of the upper beach slope (Synolakis, 1987), shallow offshore bathymetry can also play a major, and possibly counterintuitive, role in inundation. When considering processes dominated by turbulent dynamics, such as mixing and transport, this experiment indicates that the turbulence created through borefronts and spatial velocity gradients is massive compared to that generated through bottom stress (Lynett et al., 2010).

4.4. BMP 4: Tsunami Runup onto a Complex 3D Beach: Monai Valley

4.4.1. Problem Description

A 7.7 M_w earthquake occurred west of Hokkaidō, Japan on July 12, 1993 at 13:17 GMT (Figures 4.72 and 4.73). The massive tsunami it triggered affected Hokkaidō and southeastern Russia, as well as the countries that have coasts on the Sea of Japan. The death toll was 230 and there was substantial physical damage. 165 of the casualties were from the island of Okushiri, which was devastated by the earthquake, the tsunami and a large landslide. The damage caused by the earthquake was not very severe; yet, the tsunami destroyed an entire coastal community on Okushiri Island before it hit the west coast of Hokkaidō. A tsunami warning was issued by the Japan Meteorological Agency (JMA) 5 minutes after the earthquake but it was too late because the tsunami struck Okushiri Island between 2 – 7 minutes after the quake. The total damage became even greater because of the fires in the town of Okushiri. The whole town sank lower by 5 – 80 centimeters.

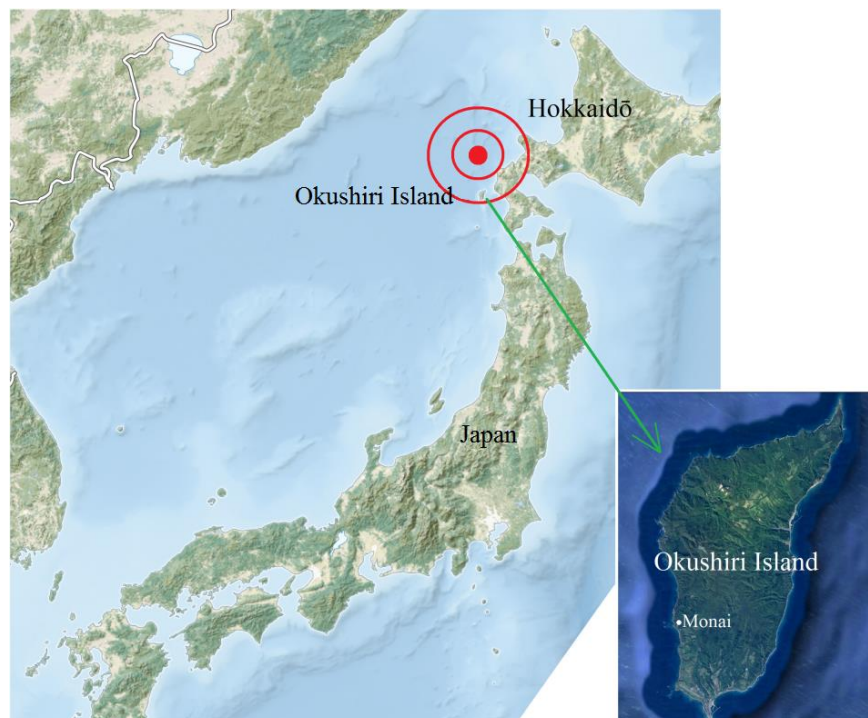


Figure 4.72 1993 southwest-off Hokkaidō earthquake (Credit: Wikipedia)

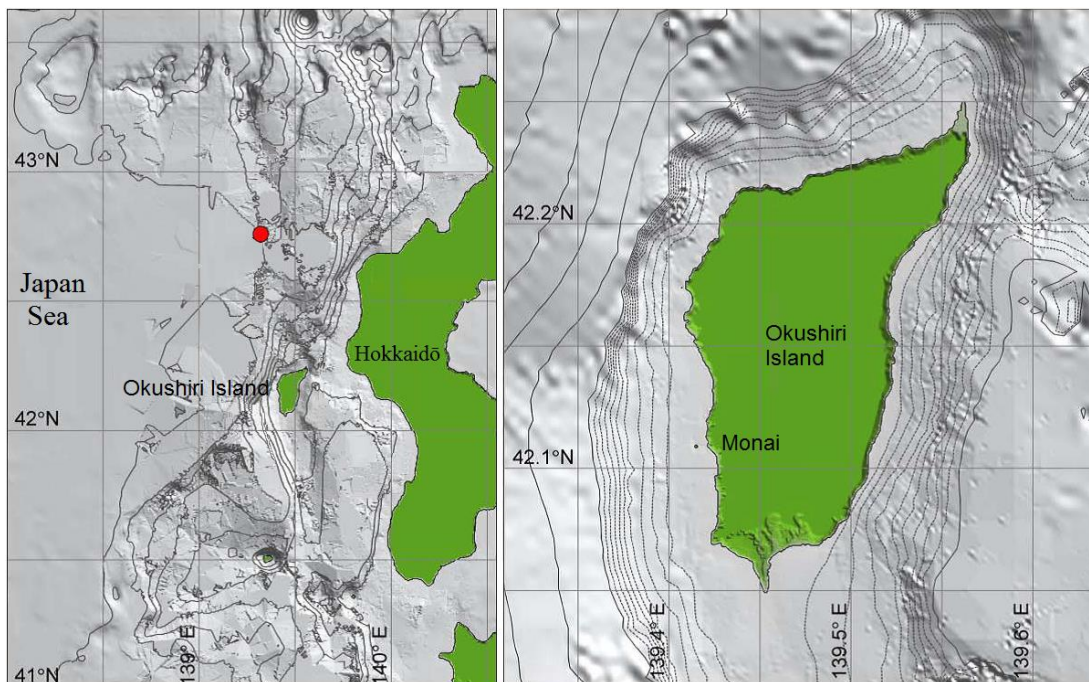


Figure 4.73 Bathymetry and topography of the region affected by the 1993 Hokkaidō Nansei- Oki tsunami. The red dot represents the earthquake epicenter (NTHMP, 2011).

The tsunami defences on Okushiri were overhauled by the destructive power of the tsunami and large parts of the island were inundated.

A maximum runup exceeding 20 meters (Figure 4.74) was measured in a number of locations on the west side of the Okushiri Island, but what made this tsunami remarkable was the maximum runup height of 31.7 m measured at the bottom of the Monai Valley, which opens onto a small pocket beach. It was reported that a large tsunami wave hit the valley after an initial withdrawal of the water, resulting in the extreme runup. The scale of the damage is illustrated in Figure 4.75.

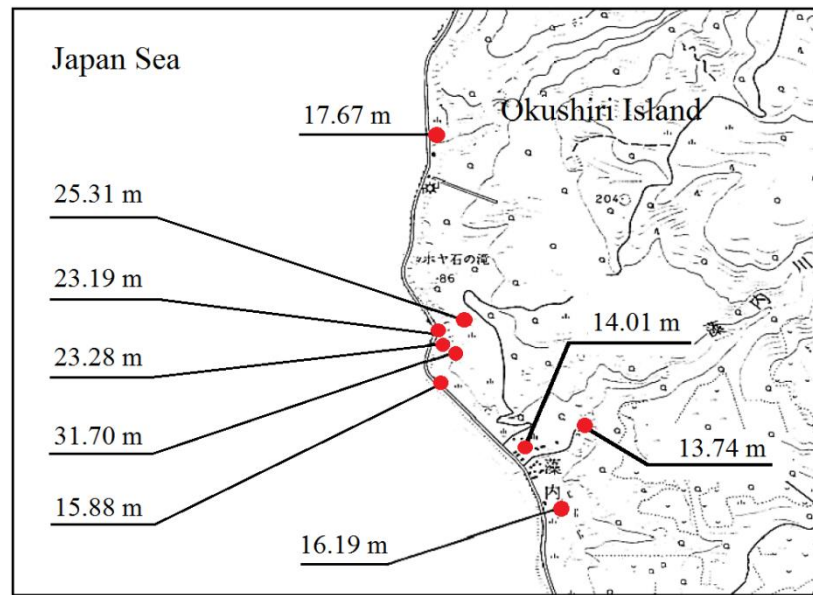


Figure 4.74 The distribution of runup heights around Monai (Shuto, 1994)



Figure 4.75 (a) Waves overtopped roadway, west coast of Okushiri Island; (b) Monai after the tsunami with debris in the foreground, including a broken steel reinforced concrete utility pole. This small valley leading to the ocean experienced a spectacular runup of 31.7 m; (c) damage at Monai; (d) debris line at Monai (Credit: NOAA/NGDC, Commander Dennis J. Sigrist. International Tsunami Information Center)

Shuto and Matsutomi (1995) and Takahashi et al. (1995) conducted a field survey and a numerical model study after the event. The Hokkaidō Tsunami Survey Group (1993) studied the impacts and characteristics of the earthquake and tsunami, including runup, ground deformation, arrival time, and structural damage (Shuto and Matsutomi, 1995). The Disaster Control Research Center (DCRC) in Tōhoku University investigated the focal mechanism and derived a set of fault parameters (DCRC-17a) summarized in Table 4.20 that produces overall good agreement with recorded runup and bottom deformation (Takahashi et al., 1995). DCRC provided the measured runup, recorded tide gauge data, initial deformation, and digitized bathymetry from nautical charts as a field benchmark for tsunami models (Takahashi, 1996).

Table 4.20 Fault parameters of DRC-17a (Takahashi et al., 1995)

No	Length (km)	Width (km)	Strike Angle (°)	Dip Angle (°)	Rake Angle (°)	Slip (m)	Depth (km)	Lat. (°N)	Long. (°E)
1	90	25	188	35	105*	5.71	10	43.13	139.40
2	30	25	175	60	80*	2.50	5	42.34	139.25
3	24.5	25	163	60	80*	12.00	5	42.10	139.30

* Modifications based on the initial deformation profile of Takahashi et al. (1995).

The Hokkaidō Nansei-Oki tsunami of 1993 that struck Okushiri Island, Japan, with an extreme runup height of 31.7 m and currents of the order of 10-18 m/sec was a disaster, but its upside was that it provided high-quality data for tsunami researchers. The extreme tsunami runup mark was discovered at the tip of a very narrow gully within a small cove at Monai. When the high resolution seafloor bathymetry that existed before the event and the bathymetric surveys following the event were coupled, it was possible to make meaningful identification of the seafloor deformation. Thus, a laboratory benchmark based on the characteristics of the Monai Valley and the tsunami wave that struck the region could be designed. The benchmark case was used in the 2004 Catalina Island, Los Angeles, California NSF Long-Wave Runup Models Workshop (Liu et al., 2008).

Matsuyama and Tanaka (2001) carried out a laboratory study at the Central Research Institute for Electric Power Industry (CRIEPI) to investigate the 31.7 m runup in Monai zone during the 1993 Hokkaidō Nansei-Oki earthquake tsunami.

The CRIEPI wave flume is 3.4 m wide, 205 m long and 6 m deep in the 115 m-long generator-side flat section (Figure 4.76). It is equipped with a hydraulic, piston-type wavemaker capable of generating N-waves. The driving system is electro-hydraulic servo actuators.

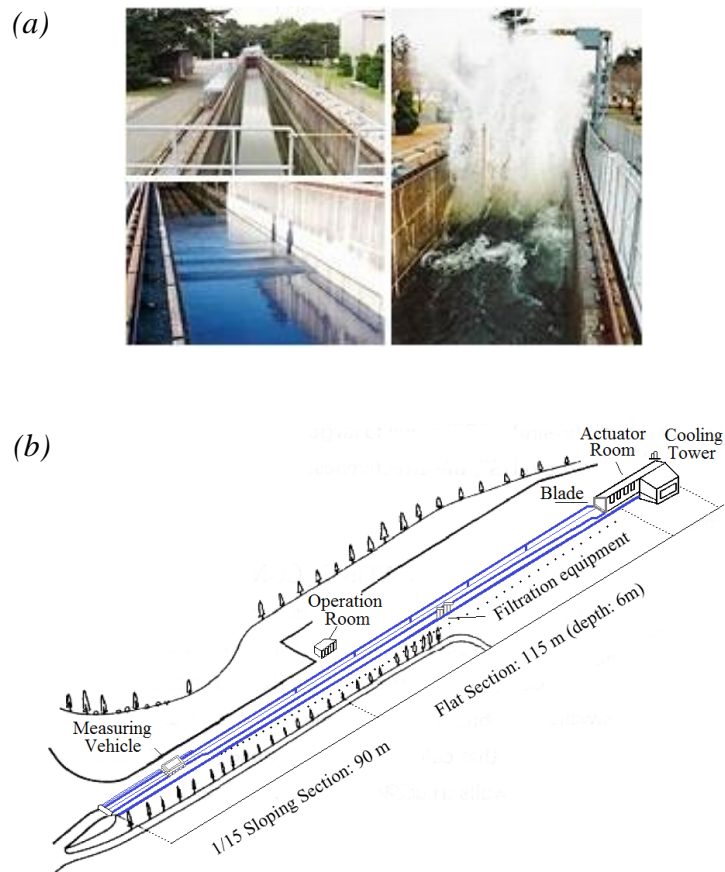


Figure 4.76 CRIEPI wave flume: (a) photographs taken at site (Credit: Central Research Institute for Electric Power Industry); (b) schematic drawing (Matsuyama and Tanaka, 2001)

The area, which was reproduced in the flume, was selected to be a rectangular area enclosed by the red line shown in Figure 4.77.

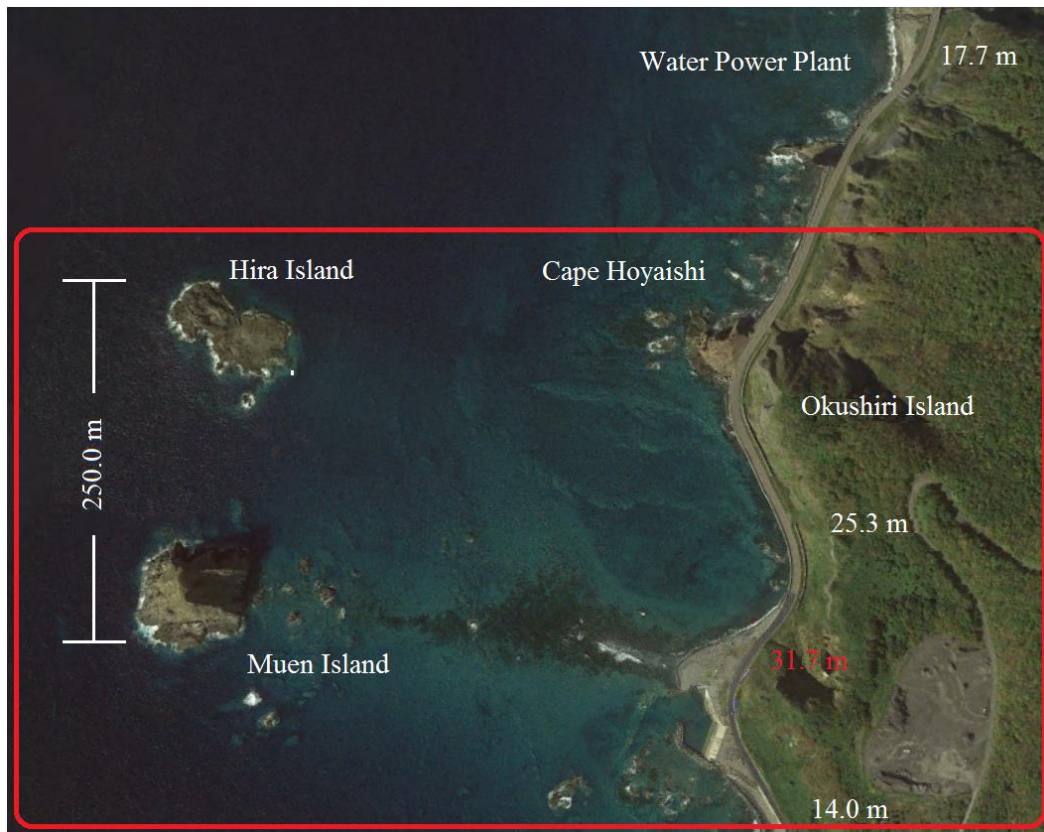


Figure 4.77 Google Earth image of the area around Monai. The region bordered by the red line represents the reproduced area in the CRIEPI wave flume (Matsuyama and Tanaka, 2001).

Based on the high resolution seafloor bathymetry that existed before the event, the 1:400 scale model of Monai zone was set in the flume with no distortion. The model included a small, curved pocket beach, which was 200 m long (Figure 4.78). The two valleys behind the pocket beach were also idealized. The maximum runup height was recorded in the south (right) valley.

Contour lines were drawn at every 3.6 m ground height on the model. Also, in order to check its effect, Muen Island was imitated by a wooden column, which was removable. In the flume, there was no land except Muen Island and the pocket beach. The maximum water depth in the flume was 4.0 m.

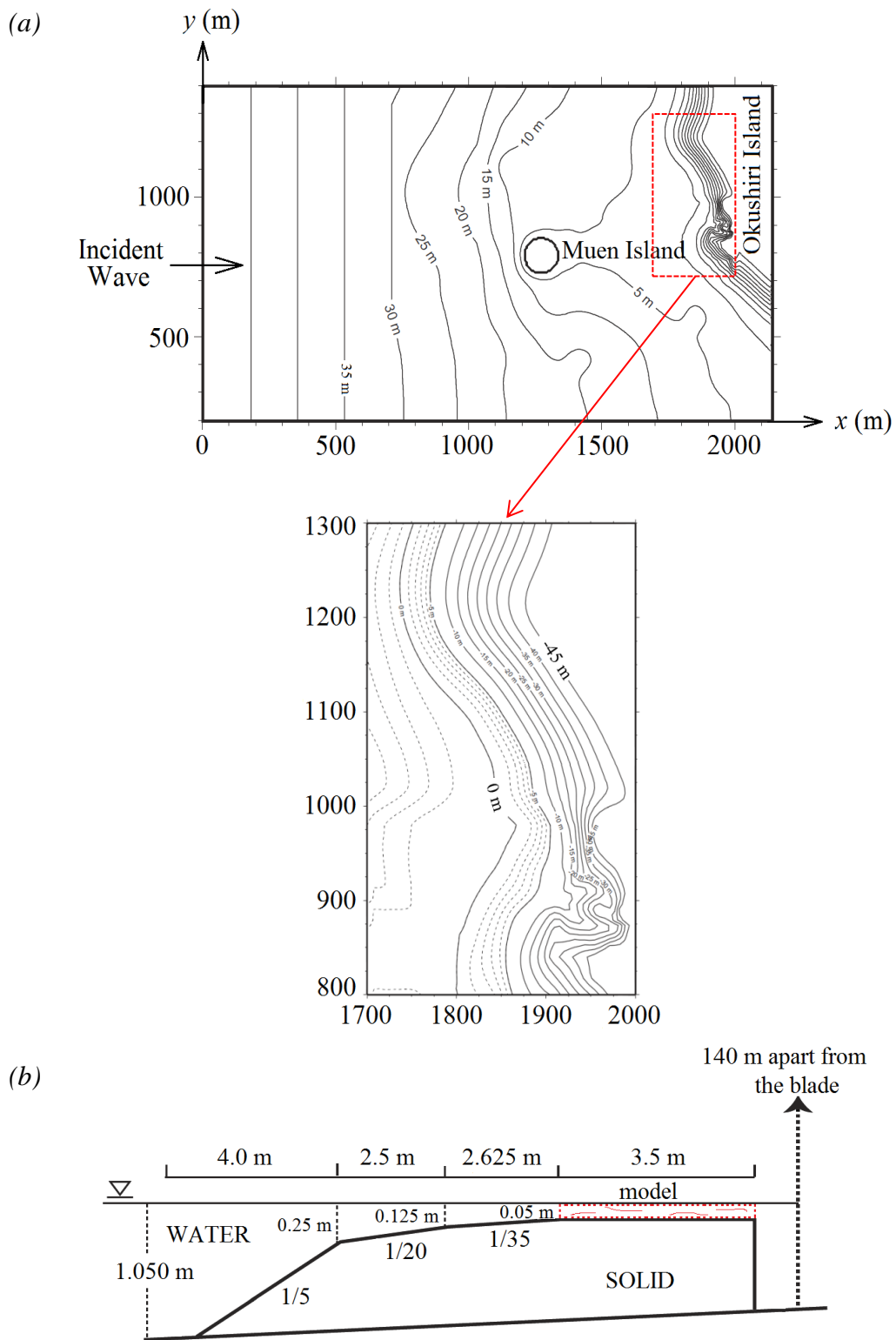


Figure 4.78 (a) the bathymetry of the whole model area and the detailed topography of the area where the maximum runup was observed; (b) the scaled offshore profile of the model (Matsuyama and Tanaka, 2001)

The model was constructed of 9 mm-thick painted plywood and installed approximately 140 m from the wavemaker (Figure 4.79).

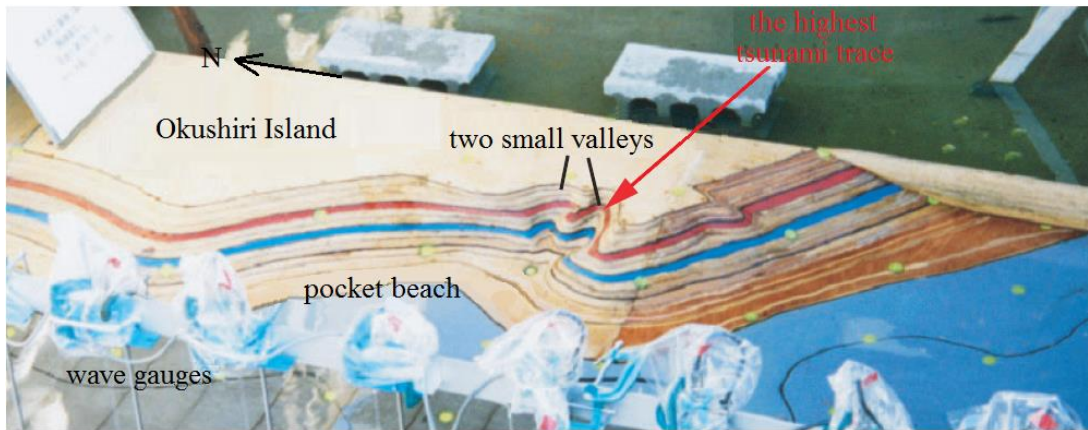


Figure 4.79 The partly-shown topographic profile of the 1:400 scale model around Monai (Matsuyama and Tanaka, 2001)

The incoming wave in the experiment was created by wave paddles located away from the shoreline.

Matsuyama and Tanaka (2001) satisfactorily reproduced the effects of 1993 Hokkaidō Nansei-Oki tsunami on the Monai zone in the CRIEPI wave flume. They succeeded in reproducing the distribution of the tsunami runup heights, including the maximum one (31.7 m), around Monai. They found that Muen Island did not have much influence on the tsunami propagation and runup in the shallow sea (i.e. less than 20 m depth) so it did not serve as a shelter for the waves to diffract.

The induced water level dynamics were measured by capacitance-type wave gauges. At the same time, by using normal and high-speed digital video cameras, recordings were made from several angles (Figure 4.80).

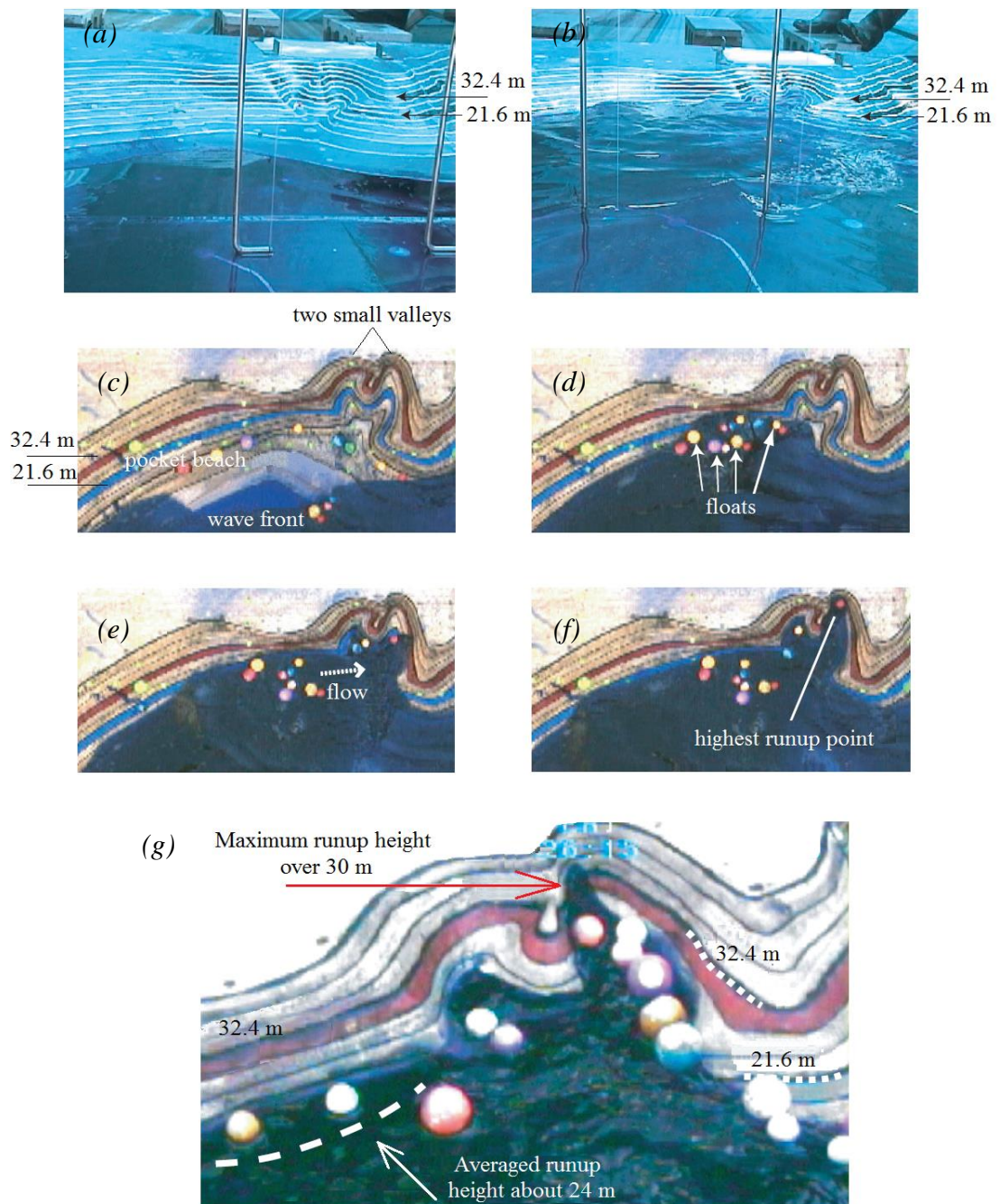


Figure 4.80 General view of the model: (a) before tsunami; (b) just before the wave reaches the highest point. The partly-shown topographic profile of the 1:400 scale model around Monai: (c) before runup; (d) during the flooding of the pocket beach; (e) during the flooding of the south valley; (f) during the highest runup; (g) a closer snapshot of the highest runup (Matsuyama and Tanaka, 2001)

Figure 4.81 and Table 4.21 show the runup measurements along transects at $y = 2.2062$ m, $y = 2.32$ m and $y = 1.88$ m – where the maximum runup value was measured from a series of tests in the laboratory experiment of Matsuyama and Tanaka (2001).

Table 4.21 Recorded runup for the six trials (Matsuyama and Tanaka, 2001)

Trial No.	R_{max} (cm) (Full scale in m)	$y = 2.2062$ m R (cm) (Full scale in m)	$y = 2.32$ m R (cm) (Full scale in m)
209_105	8.75 (35.0)	5.25 (21.0)	5.25 (21.0)
209_106	9.00 (36.0)	5.75 (23.0)	5.50 (22.0)
209_107	8.00 (32.0)	5.50 (22.0)	5.50 (22.0)
209_101	9.00 (36.0)	6.50 (26.0)	5.75 (23.0)
209_102	10.00 (40.0)	6.75 (27.0)	5.75 (23.0)
209_103	9.00 (36.0)	6.50 (26.0)	5.75 (23.0)
Mean	8.97 (35.8)	6.04 (24.2)	5.58 (22.3)

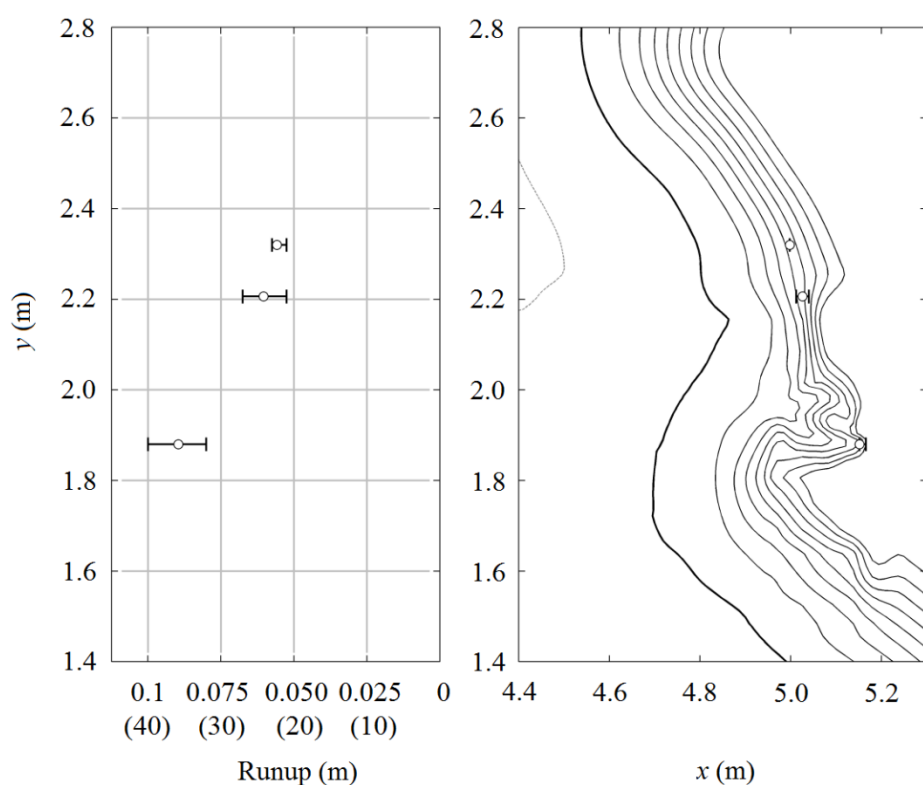


Figure 4.81 Recorded runup for the six trials (Matsuyama and Tanaka, 2001)

As stated previously, the experiment carried out by Matsuyama and Tanaka (2001) has been used as a benchmark problem to validate tsunami models. The features of the numerical design of this experiment are given below.

The computational domain represents a 5.488 m by 3.402 m portion of the wave tank near the shore and is divided into 0.014 m x 0.014 m grid cells. In other words, the recommended grid size for numerical simulations is $\Delta x = 1.4$ cm. Moreover, the recommended time step size, Δt , is 0.05 sec. The boundary conditions along segments $y = 0$ m, $y = 3.4$ m, and $x = 5.5$ m are to be set completely reflective. The complete time histories of the free surface elevations are provided at three locations, Gauges 5, 7 and 9, i.e., $(x, y) = (4.521, 1.196)$, $(4.521, 1.696)$, and $(4.521, 2.196)$ in meters, respectively (Figure 4.82). The measurements are provided with the courtesy of the Third International Workshop on Long-Wave Runup Models (Liu et al., 2008).

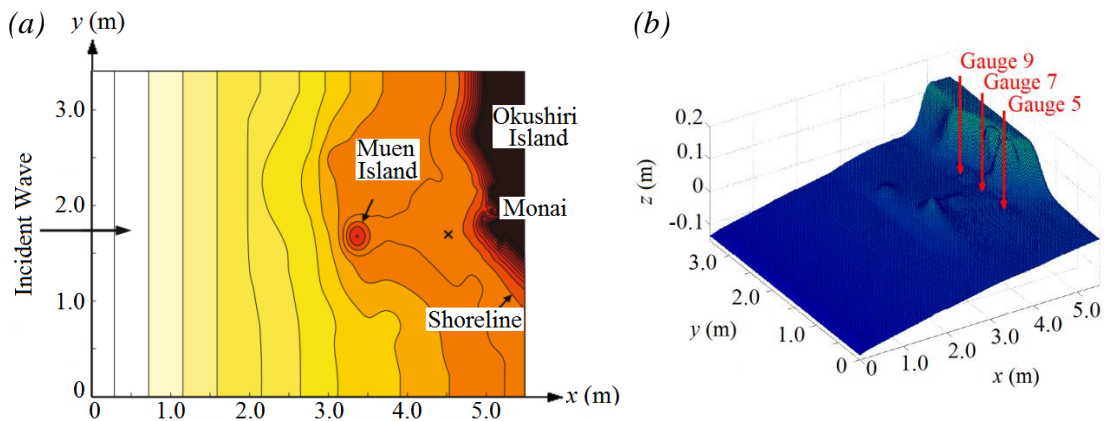


Figure 4.82 The computational domain: (a) top view (Synolakis et al., 2008); (b) 3D view (ISEC, 2004). Locations of the gauges, at which the modeled and measured water level dynamics are compared, are shown by arrows.

The free surface elevation time series of the incident wave at the water depth 13.5 cm is known. The initial wave, which is a LDN wave, has a leading-depression height of 2.5 mm and a crest of 1.6 cm behind it (Figure 4.83). The input data only covers 22.5 seconds.

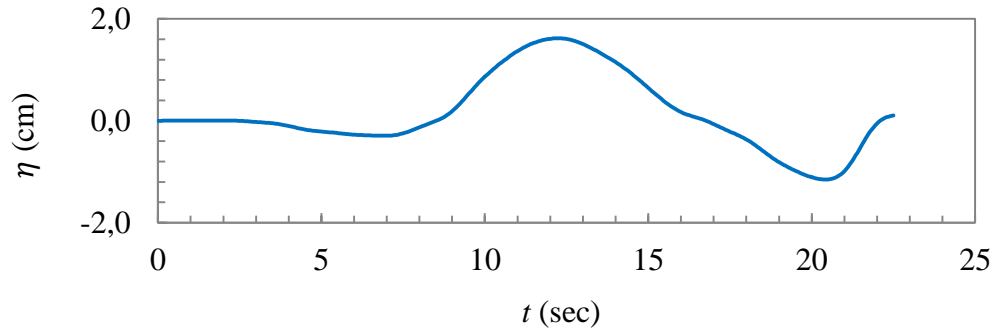


Figure 4.83 Incident wave profile of BMP 4

The primary theme of this benchmark problem is the temporal and spatial variations of the shoreline location, as well as the temporal variations of the free surface at the specified nearshore locations. Matsuyama and Tanaka (2001) installed an overhead video camera that focused on the narrow gully, where the highest runup was observed. The frames obtained from this camera are also used to support the comparison of the numerical and laboratory data. Since the video has the frequency of 30 frames per second, it is possible to select frames that are 0.5 seconds apart. The lateral extent of the video frames approximately correspond to the region $4.7 \leq x \leq 5.2$ and $1.5 \leq y \leq 2.2$ of the computational domain. Frame 10 approximately occurs at 15.3 seconds (LeVeque, 2011).

To accomplish BMP 4, the propagation of the incident and reflective wave in the laboratory is to be compared with the numerical predictions. The numerical and experimental data of the water level dynamics at Gauges 5, 7, and 9 are to be compared. The maximum runup in the narrow valley is also to be computed by the numerical models. Finally, the snapshots of the numerically computed water level at times synchronous with those of the video frames are to be shown. The times of the snapshots that best fit the data should be found (LeVeque, 2011).

4.4.2. NAMI DANCE Model

The experimental setup of Matsuyama and Tanaka (2001) is reproduced in a 2D domain using NAMI DANCE. The fluid is inviscid and the flow is incompressible. Fluid density is taken constant throughout the fluid domain. The x axis of the Cartesian coordinate system is perpendicular to the wavemaker and the y axis is parallel to the wavemaker (Figure 4.84). The gravitational force, g , is in the downward direction. Moreover, the 3D view of NAMI DANCE computational domain is illustrated in Figure 4.85.

The incident wave, which is recorded at a water depth of 13.5 cm, is inputted at the upstream end of the computational domain along y -direction (i.e. minimum x boundary) where $x = 0$ m. The maximum x boundary has a rigid wall boundary condition, which defines the downstream end of the wave tank. The minimum and maximum y boundaries are also defined as rigid walls in order to prevent outflow from the computational domain.

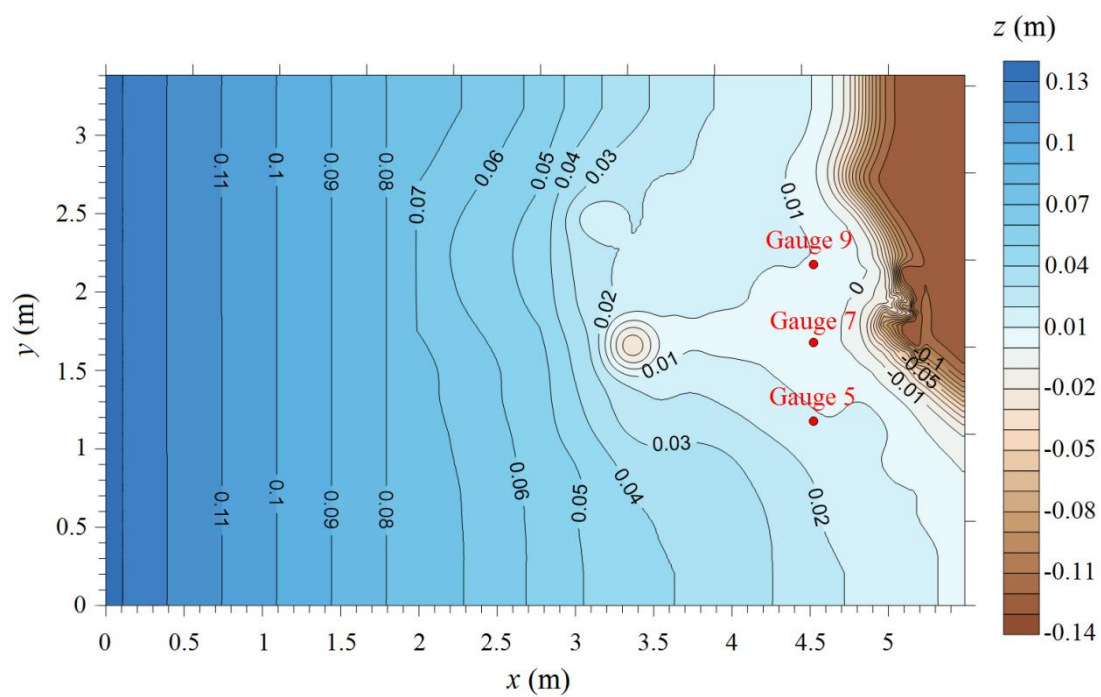


Figure 4.84 NAMI DANCE model: computational domain and the coordinate system

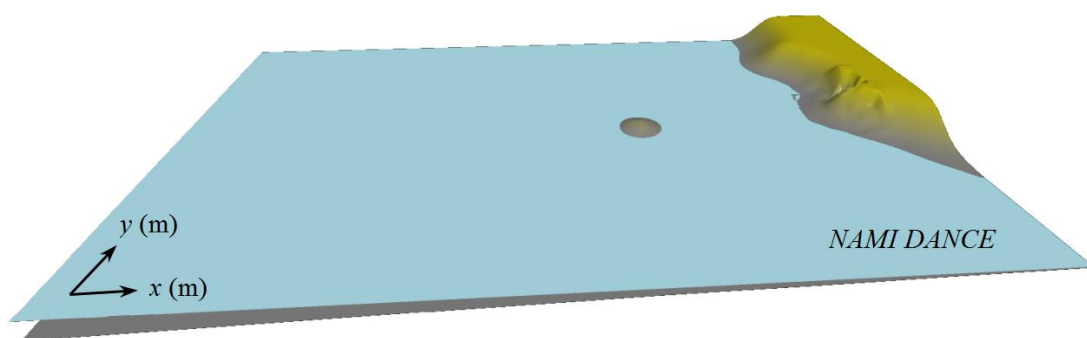


Figure 4.85 3D top view of NAMI DANCE computational domain for BMP 4

4.4.2.1. Spatial Discretization

The computations were performed with a grid of 393 x 244 nodes at 1.4 cm spacing (i.e. $\Delta x = \Delta y = 0.014$ m), covering the region of 5.488 m x 3.402 m as recommended (NTHMP, 2011). However, the convergence of NAMI DANCE is tested in order to see whether there are better resolution options or not. The runup measurements along the transects at $y = 1.88$ m – where the maximum runup was recorded, $y = 2.2062$ m and $y = 2.32$ m are compared for $\Delta x = 0.007$ m, $\Delta x = 0.014$ m, $\Delta x = 0.028$ m and $\Delta x = 0.056$ m (Table 4.22).

Table 4.22 NAMI DANCE: Predicted runup values on the pocket beach for different Δx values ($n = 0.012$)

Grid Size Δx (m)	Maximum Runup (cm)		
	$y = 1.88$ m	$y = 2.2062$ m	$y = 2.32$ m
0.007	8.70	5.10	5.00
0.014	8.70	5.10	5.00
0.028	8.65	5.00	4.95
0.056	8.10	4.70	4.60

The results reveal that the grid size has a negligible effect on the runup predictions up to $\Delta x = 0.028$ m. The model predictions are in good agreement with the laboratory data. Matsuyama and Tanaka (2001) measured the average runup values along the transects $y = 2.2062$ m and $y = 2.32$ m as 6.04 cm and 5.58 cm, respectively. Also, the average maximum runup is measured as 8.97 cm. It is found that a much coarser grid size (i.e. $\Delta x \geq 0.028$ m) may lead to unreasonable runup values.

The time step, Δt , is selected as 0.05 second as recommended for BMP 4. Different time steps are also tested; however, no significant change is observed in the numerical predictions.

4.4.2.2. Friction

The Manning's coefficient $n = 0.012$ indicates the surface roughness of the painted plywood relief model (Chaudhry, 1993). Therefore, in order to reflect real laboratory conditions as much as possible, the Manning's coefficient is selected as 0.012 for the numerical simulations. However, it is still necessary to test the effect of friction in order to assess its importance in inundation. Manning's roughness coefficients used to assess the effect of friction on the maximum runup values are: (i) $n = 0$ (i.e. frictionless bottom), (ii) $n = 0.012$ (i.e. painted plywood), (iii) $n = 0.03$ (i.e. very rough surface) (Table 4.23). The results are compared along the transects at $y = 1.88$ m – where the maximum runup was recorded, $y = 2.2062$ m and $y = 2.32$ m.

Table 4.23 NAMI DANCE: Predicted runup values on the pocket beach for different Manning's roughness coefficients

n	Maximum Runup (cm)		
	$y = 1.88$ m	$y = 2.2062$ m	$y = 2.32$ m
No Friction	8.75	5.25	5.15
0.012	8.70	5.10	5.00
0.030	8.00	4.50	4.45

The results reveal that the effect of varying friction is only felt during the inundation, as expected. It is found that the predicted runup values are slightly larger on a frictionless bottom, whereas when $n = 0.03$, lower runup values are computed, which are approximately 10 – 15% less than the laboratory measurements. These results indicate that friction plays an important role in the predicted runup values and $n = 0.012$ is a good choice for the simulations.

4.4.3. FLOW-3D[®] Model

The same physical experiment is reproduced using FLOW-3D[®] in a 3D domain, throughout which the fluid is inviscid, the flow is incompressible and the fluid density is constant. The effects of surface tension and air entrainment at the surface of the flow are neglected.

The numerical model is constructed using the Cartesian coordinate system, where the positive x direction is oriented along the fluid flow into the domain and the positive y direction is perpendicular to the direction of the flow, along the wavemaker. The gravitational acceleration, g , is in the downward direction (i.e. $-z$ direction).

The pressure boundary condition is defined and applied at the minimum x boundary. This boundary condition allows the user to enter the input data manually, which is the free surface elevation time series recorded at $d = 13.5$ cm. The maximum x boundary has the wall boundary condition so as to define the end of the wave tank. The minimum and maximum y boundaries feature the wall boundary condition since reflective boundaries are needed for this benchmark problem. The wall boundary condition is also valid for the minimum z boundary where the bottom of the wave flume is defined. The symmetrical boundary condition, where all the velocity derivatives and velocity components normal to the boundaries are set to zero, is applied at the maximum z boundary (Figure 4.86).

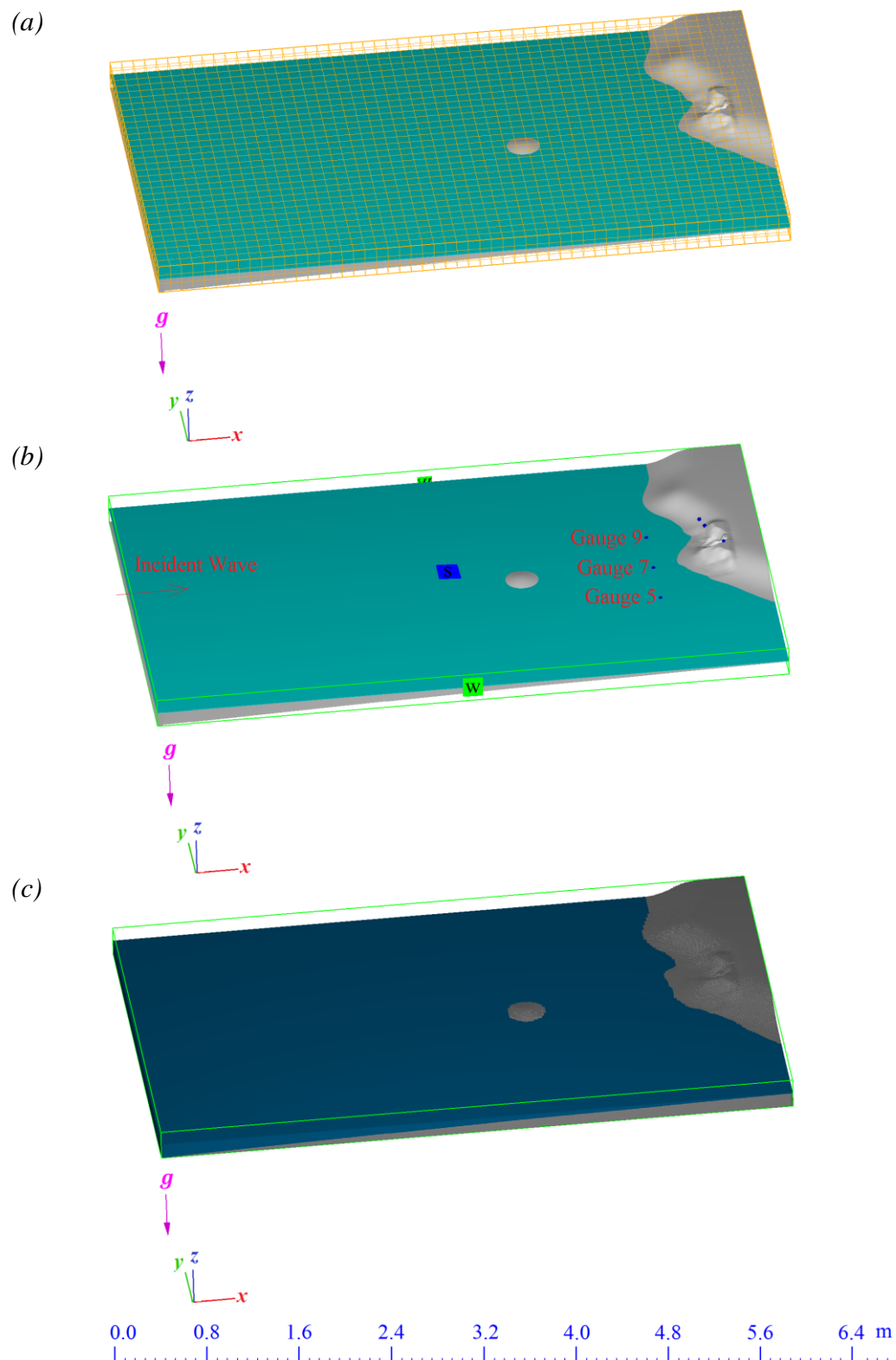


Figure 4.86 FLOW-3D® computational domain constructed for BMP 4: (a) meshing (enlarged for clarity); (b) boundary conditions and gauge locations; (c) after using FAVOR™

4.4.3.1. Spatial Discretization

The computational domain is represented by an isotropic grid with $\Delta x = \Delta y = \Delta z$ where the grid size is selected as 0.014 m (Please refer to the explanations in Section 4.4.2.1). BMP 4 is modeled via FLOW-3D[®] for different Δx values in order to test the grid dependency of the runup values along the transects at $y = 1.88$ m – where the maximum runup was recorded, $y = 2.2062$ m and $y = 2.32$ m are compared (Table 4.24).

Table 4.24 FLOW-3D[®]: Predicted runup values on the pocket beach for different Δx values ($n = 0.012$)

Grid Size Δx (m)	Maximum Runup (cm)		
	$y = 1.88$ m	$y = 2.2062$ m	$y = 2.32$ m
0.007	8.95	5.20	5.10
0.014	8.95	5.20	5.10
0.028	8.90	5.00	5.10
0.056	8.50	4.90	4.85

The numerical resolution is not effective up to $\Delta x = 0.028$ m. There is considerable improvement in the results for $\Delta x \leq 0.028$ m. The model predictions are in good agreement with the laboratory data. Matsuyama and Tanaka (2001) measured the average runup values along the transects $y = 2.2062$ m and $y = 2.32$ m as 6.04 cm and 5.58 cm, respectively. Also, the average maximum runup is measured as 8.97 cm. It is found that unreasonable runup values may be obtained when the grid size is increased.

It is also necessary to analyse the effect of the vertical grid size, Δz , on runup values in a three-dimensional model. It is found that changing the vertical grid size does not have a significant effect on the predicted runup values for $\Delta z \leq 0.028$ m with Δx kept constant. For larger Δz values, unreliable runup values are obtained since the valley geometry can not be defined very well for very coarse Δz values.

The time step, Δt , is selected as 0.05 second as recommended. When variable time stepping is employed in order to assess the effect of the time step size, no significant effect is observed.

4.4.3.2. Friction

In order to assess the effect of friction on the maximum runup values, different Manning's roughness coefficients are considered: (i) $n = 0$ (i.e. frictionless bottom), (ii) $n = 0.012$ (i.e. painted plywood), (iii) $n = 0.03$ (i.e. very rough surface) (Table 4.25). The results are compared along the transects at $y = 1.88$ m – where the maximum runup was recorded, $y = 2.2062$ m and $y = 2.32$ m.

Table 4.25 FLOW-3D[®]: Predicted runup values on the pocket beach for different Manning's roughness coefficients

n	Maximum Runup (cm)		
	$y = 1.88$ m	$y = 2.2062$ m	$y = 2.32$ m
No Friction	8.95	5.25	5.10
0.012	8.95	5.20	5.10
0.030	8.10	4.95	4.85

The results obtained via FLOW-3D[®] are similar to those obtained using NAMI DANCE. The effect of varying friction is only felt during the inundation and the predicted runup values are slightly larger on a frictionless bottom. When $n = 0.03$, the predicted runup values are ~10% less than the laboratory measurements.

4.4.4. Simulation Results

The estimated extreme values of the 10-18 m/sec overland flow velocities and the 31.7 m-high wave runup generated by the 1993 Hokkaidō Nansei-Oki earthquake were the largest recorded in Japan in the 20th century (Shuto and Matsutomi, 1995) and are still in the category of the highest values that have ever been documented for non-landslide generated tsunamis.

BMP 4 is applied to confirm the estimated overland flow velocities and extreme runup measured in the narrow gully in the Monai zone, and it is found that both the 2D depth-averaged NSW model, NAMI DANCE, and the 3D-RANS model, FLOW-3D[®], predict nearshore wave profiles and tsunami inundation levels satisfactorily. Both models have the ability to handle runup processes over complex nearshore bathymetry and topography.

Numerical simulations are conducted using a computer with 16-core central processing units (CPUs). The computations are terminated after the first reflection of the wave from the coast, which is 50 seconds. The simulations that are performed via NAMI DANCE are completed in approximately 3 hours whereas it takes 3 days to complete the simulations using FLOW-3D[®].

The NAMI DANCE and FLOW-3D[®] results regarding the wave transformation in the shallow zone, i.e. at Gauges 5, 7 and 9, where $(x, y) = (4.521 \text{ m}, 1.196 \text{ m})$, $(4.521 \text{ m}, 1.696 \text{ m})$ and $(4.521 \text{ m}, 2.196 \text{ m})$, are given in Figure 4.87.

The predicted free surface elevations are in good agreement with the laboratory measurements at the three gauges located behind the island. The models reproduce the small amplitude waves generated by reflection from the coast. The minor phase lags in the reflected waves are likely due to errors in the laboratory experiment. Similar results are also obtained in the previous applications (ISEC, 2004; NTHMP, 2011).

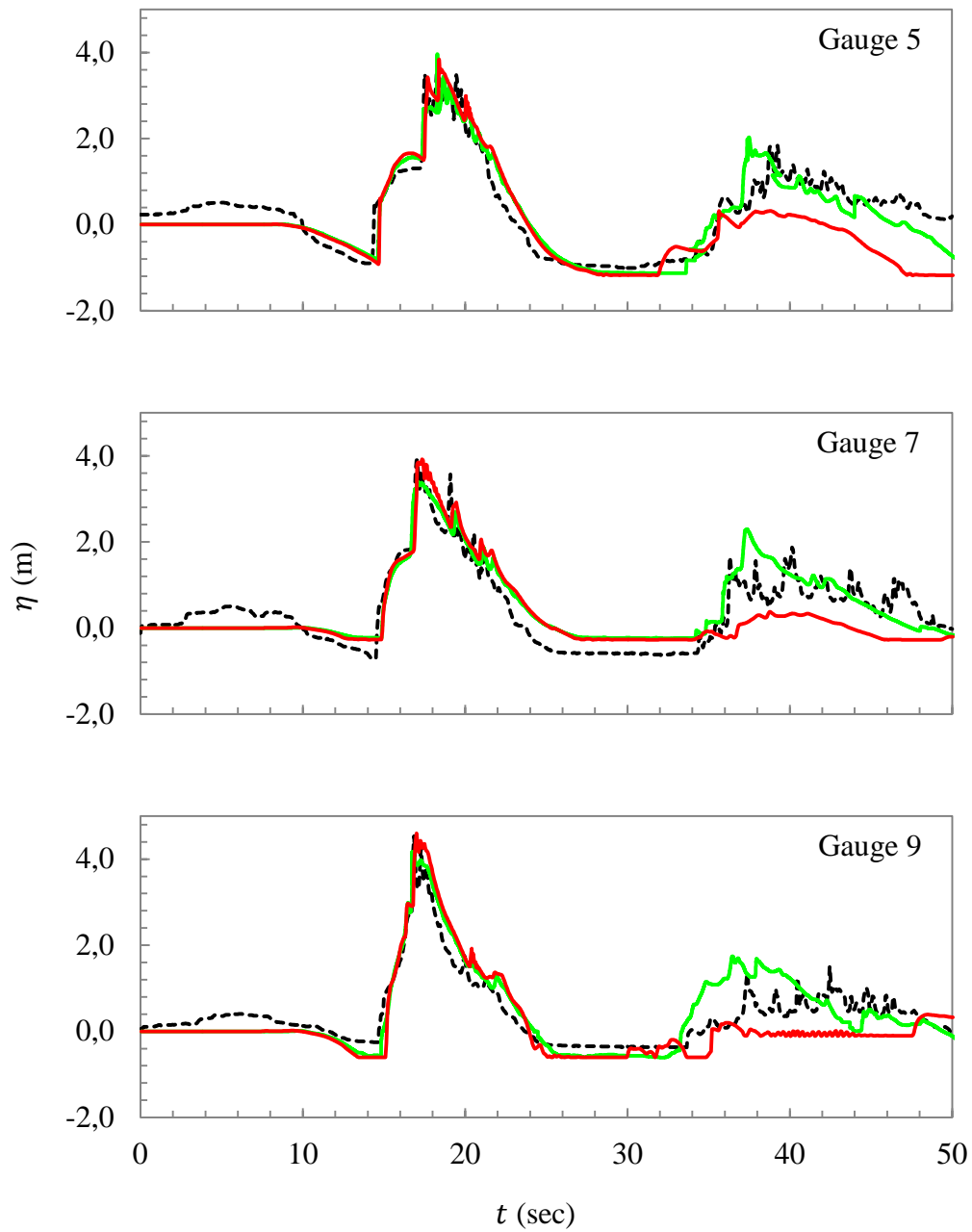


Figure 4.87 The predicted and measured free surface profiles at: (a) Gauge 5; (b) Gauge 7; (c) Gauge 9. The black line represents the laboratory measurements; the red line represents the NAMI DANCE results; the green line represents the FLOW-3D[®] results.

Figure 4.88 compares the movie frames that are extracted from the overhead camera used during the laboratory experiments with the results of numerical simulations. The frames are 0.5 second apart and focused on the narrow gully where the highest runup is observed. The actual shoreline location is ambiguous in the movie. Therefore, the dashed yellow lines on the frames are provided as part of the benchmark specification and show the approximate shoreline (LeVeque, 2011).

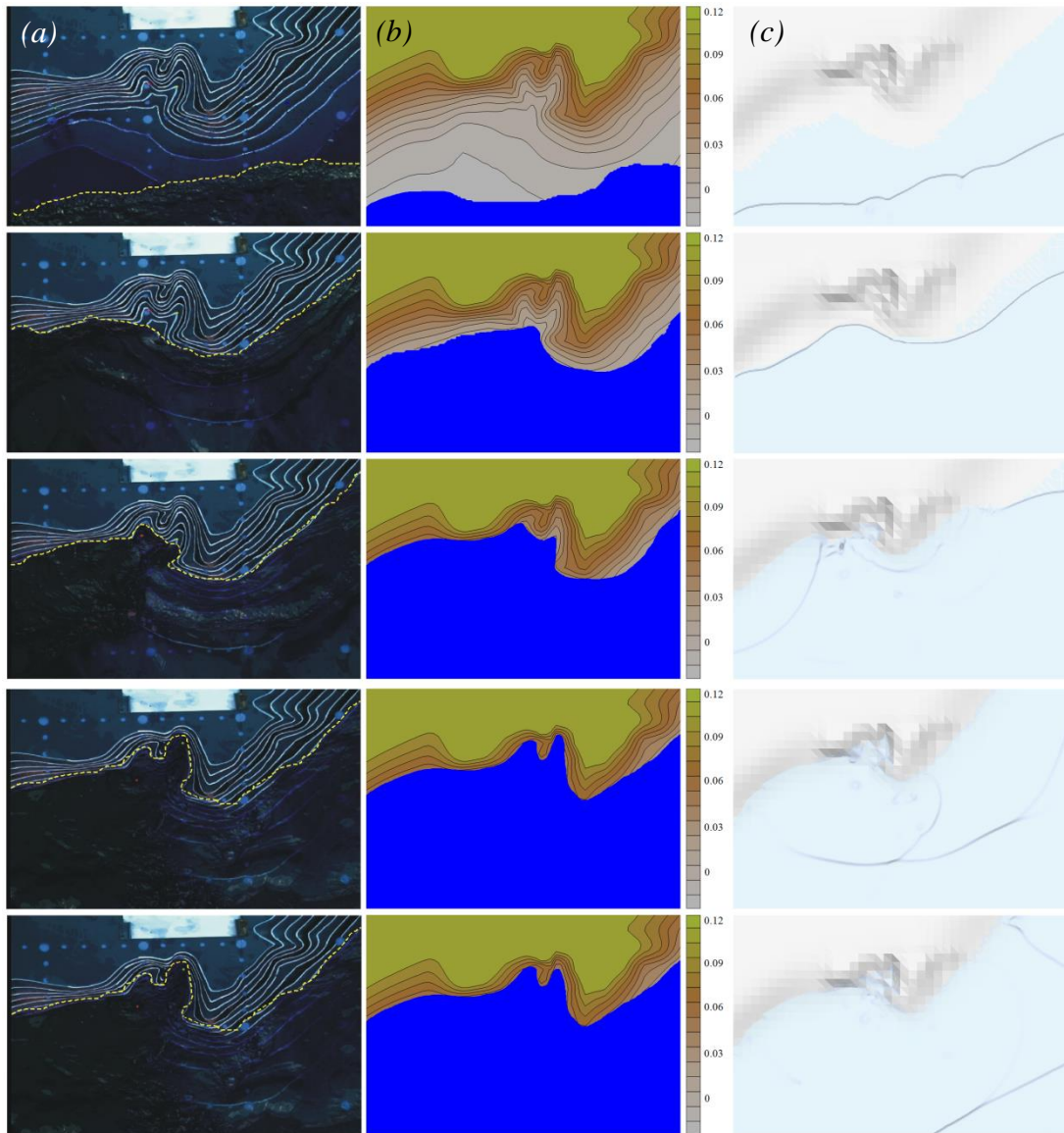


Figure 4.88 (a) Frames 10, 25, 40, 55, and 70 from the overhead movie of the laboratory experiment (Liu et al., 2008; NTHMP, 2011); (b) snapshots of the NAMI DANCE simulation at the time intervals corresponding to the movie frames; (c) snapshots of the FLOW-3D[®] simulation at the time intervals corresponding to the movie frames

Twelve isolines are drawn with a 1 cm interval from the original shoreline to a land elevation of up to 11 cm. The first snapshot, supposedly corresponding to Frame 10 of the video recording, occurs at 15.3 sec (LeVeque, 2011). Reasonably good agreement is found starting at 15.0 seconds for Frame 1 and then taking 0.5 second increments for both models. Side-by-side comparison with the series of frames reveals that both models simulate the case satisfactorily throughout the domain, especially where the maximum runup occurred. The maximum runup height in the narrow gully is computed as 8.70 cm via NAMI DANCE and as 8.95 cm via FLOW-3D[®]. These values are comparable with the laboratory (8.97 cm) and field data (31.7 m).

The runup and inundation comparisons of the NAMI DANCE and FLOW-3D[®] results are shown in Figure 4.89.

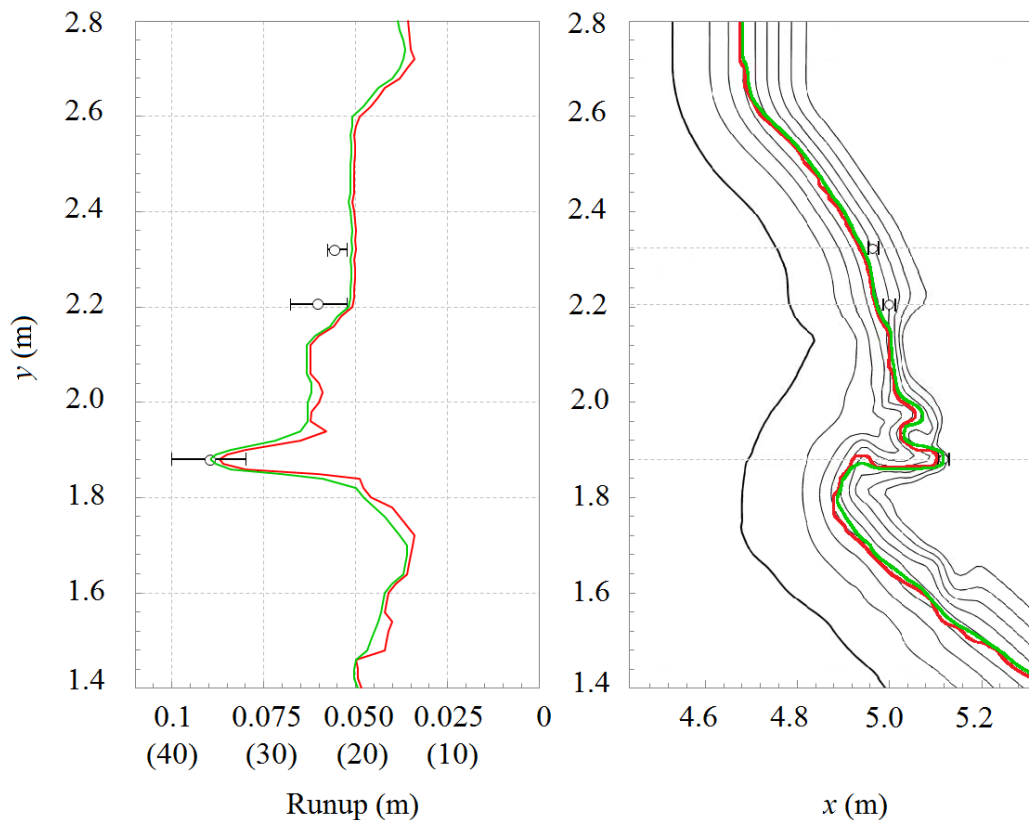


Figure 4.89 Runup and inundation comparisons: (a) runup; (b) inundation. The circles represent the laboratory data of Matsuyama and Tanaka (2001); the red line represents the NAMI DANCE results; the green line represents the FLOW-3D[®] results.

While both models were able to simulate the runup values sufficiently, the extreme runup prediction made by FLOW-3D® was the closest to the laboratory measurements.

The role of the vertical velocity component, w , in the extreme runup is also analysed via FLOW-3D® (Figure 4.90).

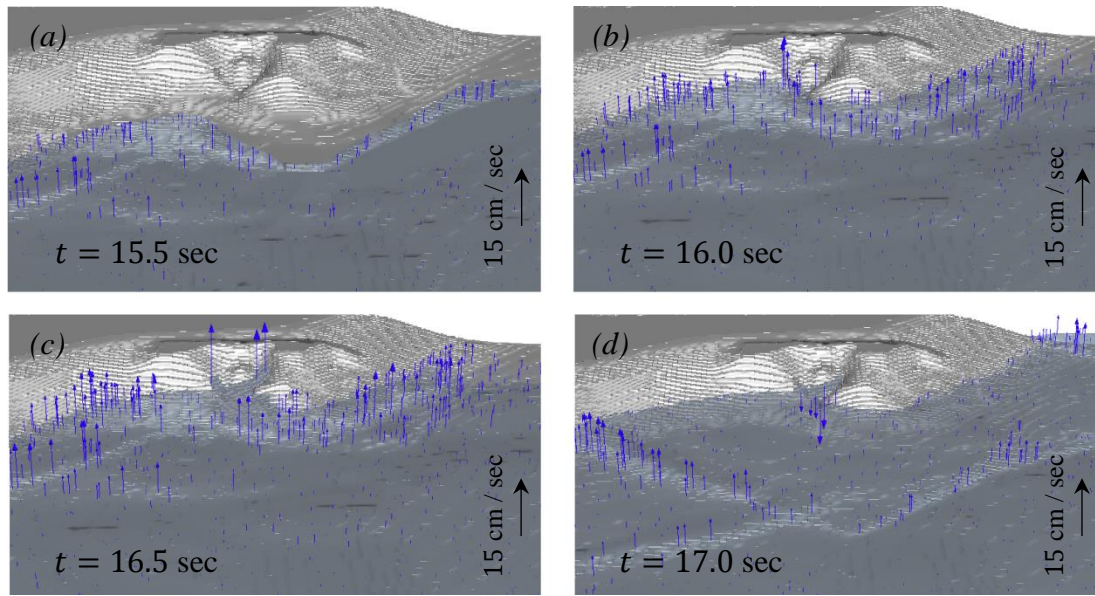


Figure 4.90 Evolution of vertical velocity component, w , at: (a) $t = 15.5$ sec; (b) $t = 16.0$ sec; (c) $t = 16.5$ sec; (d) $t = 17.0$ sec (not to scale)

Figure 4.90 shows that the vertical velocity component gets extremely large, up to 15 cm/sec, on the steep slopes of the Monai Valley in comparison to the horizontal velocity component. This value corresponds to 3 m/sec in the prototype scale. Moreover, previous studies revealed that the vertical velocity of the backwash water gets as large as 10 cm/sec in the laboratory scale (2 m/sec in the prototype scale). This illustrates the significance of vertical velocity component during runup on very steep slopes. In fact, most of the damage is attributed to the large current velocities occurring during the inundation process. Therefore, non-hydrostatic effects should be considered significant, especially for steep coasts.

The NRMSE and MAX errors for the free surface dynamics recorded at three gauges, Gauges 5, 7 and 9, are given in Table 4.26 and Figure 4.91.

Table 4.26 NRMSE and MAX errors for BMP 4

Gauge	NAMI DANCE		FLOW-3D [®]	
	% NRMSE	% MAX	% NRMSE	% MAX
5	7.1	4.2	6.5	2.7
7	7.5	4.3	5.8	1.3
9	7.7	0.7	6.0	0.5

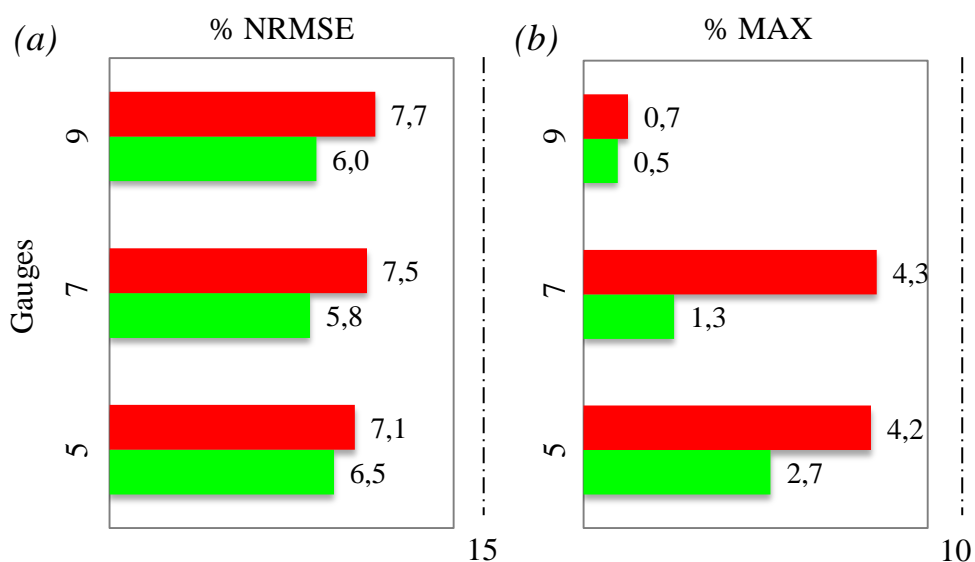


Figure 4.91 Error bars for BMP 4: (a) % NRMSE; (b) % MAX error. The red and green bars represent the errors of NAMI DANCE and FLOW-3D[®] results, respectively.

The NRMSE of the NAMI DANCE results is around 7% while the MAX error ranges from 1% to 4%. The FLOW-3D[®] results have an NRMSE around 6% and a MAX error range between 0.5% and 3%. The errors are within the OAR PMEL-135 standard error range. It can be concluded that both models satisfactorily predict the evolution and transformation of the initial wave.

The percentage difference between the measured and predicted values of the extreme runup is 2% and 0.2% for the NAMI DANCE and FLOW-3D[®] results, respectively.

To sum up, the calculation of three-dimensional tsunami inundation flow is crucial to hazard mitigation planning; however, for giant tsunamis, it is still an extremely challenging task. Yet, large-scale laboratory experiments (Titov and Synolakis, 1993; Yeh et al., 1994; Liu et al., 1995; Briggs et al., 1995) have provided valuable data regarding the validation of tsunami models and understanding the physics behind giant tsunamis. The Hokkaidō Nansei-Oki earthquake of July 12, 1993 was also like a large-scale experiment because it allowed the measurement of high-quality runup data and the inference of fairly unambiguous ground deformation contours. The proximity of the earthquake to seismic instrument arrays in a locale where high-resolution bathymetry and topography data exist made this task possible (Titov and Synolakis, 1997).

BMP 4 is employed to investigate the propagation and inundation of a tsunami wave over a complex 3D beach. It provides data that are fairly well specified, and is able to represent a reasonable physical tsunami problem because it is designed by scaling down a physical problem. Thus, BMP 4 is a good test for tsunami models. It has been commonly used for the validation of tsunami numerical models and many models have been shown to give results that agree quite well with the laboratory measurements (NTHMP, 2011). The two- and three-dimensional models, NAMI DANCE and FLOW-3D[®], are tested against the laboratory measurements that include tsunami wave transformation over the complex bathymetry and wave reflection from the coast. Not only are point-wise comparisons made at the gauges, but also the snapshots of the computed and observed water height of the whole domain are plotted.

The results reveal that the recommended grid size, $\Delta x = 0.014$ m, and time step, $\Delta t = 0.05$ sec, are sufficient to simulate BMP 4. Both NAMI DANCE and FLOW-3D[®] reproduce the overall flow and inundation patterns in fully hydrostatic and non-breaking events considerably well and produce similar results to the previous studies. Both models are able to capture the rapid sequence of runup and rundown. However, NAMI DANCE predicts the amplitude of the waves reflected from the coast 20% -

30% less than the values measured in the laboratory. The reason for this may be that flow conditions are not fully hydrostatic after the wave is reflected from the coast and thus 2D depth-averaged NSW equations are not sufficient to describe all the flow conditions after the reflection. Therefore, even though the results are reassuring with regard to the validity of NSW equations for real tsunamis, for regions where wave characteristics become complex, 3D numerical models seem more reliable.

Both models are able to reproduce the maximum runup in the narrow gully near the village of Monai. It is found that local extreme runup is sensitive to the near shore interpolation of bathymetry and topography as well as the friction coefficient. In fact, Titov and Synolakis (1997) reported that even small local bathymetric structures directly affect the runup and that the resolution of the bathymetric data may be more important than the grid resolution.

As a result, it is possible to reproduce the extreme characteristics of the tsunami in the Monai Valley, including the observed extreme runup value using both models. However, it is also found that vertical velocity component gets extremely large on steep slopes and thus nonlinear effects should not be neglected. In fact, for this specific case, Titov and Synolakis (1997) stated that their results suggest that during overland flow, coastal devastation has a stronger correlation with inundation velocities than inundation heights. This shows that, due to its considerable significance, the vertical velocity component should be correctly predicted. Thus, 3D numerical models may be a better choice for the prediction of tsunami characteristics on steep coasts and for the estimation of tsunami risk for such areas.

4.5. BMP 5: Tsunami Inundation in Constructed Environments

4.5.1. Problem Description

Due to the fact that tsunamis are unpredictable phenomena most commonly resulting from large magnitude earthquakes along coastal plate boundaries, they cause substantial damage to coastal communities near or far from the epicenter. The first tsunami wave often arrives at the shoreline in tens of minutes and can inundate several kilometers inland very quickly. This leaves little or no time for preparation or evacuation and, as a result, hundreds of thousands of people are killed or injured and there is great local and regional devastation (Imamura et al., 2006).

The 2004 Indian Ocean Tsunami field survey emphasized the importance of coastal structures in tsunami hazard mitigation (Dalrymple and Kriebel, 2005; Tomita et al., 2006). The field survey which was conducted after the 2011 Great East Japan Tsunami also highlighted that tsunami damage is strongly dependent on location and environment. Yeh (2006) showed that the hydrodynamic force of the tsunami on structures in the inundation zone is proportional to the momentum flux, which is the inundation depth multiplied by the squared velocity and it can be related to the probability of damage (FEMA, 2008; Koshimura et al., 2009a, 2009b).

It is a fact that, in order to minimize casualties and destruction, further tsunami research should be done, particularly into the complex flows associated with tsunami inundation and return flow over complex bathymetry and around structures. As numerical schemes have more computational power and maturation today, numerical modeling of tsunami inundation has gained importance in tsunami mitigation studies (Lynett, 2007; Park et al., 2013). To model the tsunami hazard for coastal communities accurately, the constructed environment must be incorporated into the numerical model as it strongly influences the flow hydrodynamics. During the last decade, tsunami inundation modeling methods have evolved into sophisticated numerical techniques, capable of simulating tsunami runup for complex, three-dimensional shoreline topography (Rueben et al., 2011). Since the 2004 Indian

Ocean Tsunami, there has been a significant increase in tsunami model research, particularly at the ocean-basin scale. But fewer models are capable of handling complex overland flows (Lynett, 2007) and the flow around groups of buildings (Tomita et al., 2006) remains an active area of research.

It is necessary to test the performance of tsunami inundation models via benchmarking in terms of predicting the free surface elevations and flow velocity components as well as sensitivity to tuning parameters. Several benchmark tests are prevalent as standard verification methods for the numerical modeling of tsunamis such as exact solutions and physical model data of solitary waves on simple sloped beaches (i.e. BMP 1) (Synolakis, 1987) and on compound sloped beaches (Kanoglu and Synolakis, 1998), large scale conical island physical model (i.e. BMP 2) (Briggs et al., 1995), and runup on a complex three-dimensional coast (i.e. BMP 4) (Hokkaidō Tsunami Survey Group, 1993). Even though most casualties and damage from tsunamis are attributed to complex inundation flows, which include wave breaking near the shoreline and interaction with coastal structures, the most advanced numerical models and benchmark tests only provide the maximum runup heights or a time series of free surface elevation. It is difficult to estimate complex flows due to the required computing power. Their validation is also difficult owing to the absence of proper benchmark tests. As a result, most numerical models focus on the estimation of tsunami propagation, and calculation of arrival times and maximum runup heights.

Several studies have been conducted into macro-roughness and tsunami velocity variation. Cox et al. (2008) carried out physical model tests of Seaside, Oregon, which showed that the macro-roughness reduced the tsunami inundation velocity by 40% (Rueben et al., 2011). The reduction in runup elevations and maximum overland velocities due to obstructions have been studied numerically (Lynett, 2007). Other studies on the influence of macro-roughness element arrays compared the free surface elevation of numerical and physical model results (Goseberg and Schlurmann, 2010), and the effect of bed slope and bottom friction on maximum

tsunami runup height and velocity using numerical models (Apotsos et al., 2011). A more recent numerical and field study was carried out by Nandasena et al. (2012), which focused on the importance of artificial and natural structures on tsunami mitigation. BMP 5 is based on the physical model tests of Cox et al. (2008), which investigate the effect of macro-roughness elements on inundation flow depth, cross-shore velocity and momentum flux.

Cox et al. (2008) designed a hydraulic model to study tsunami flow over and around macro-roughness to observe the role of building shape and density on tsunami inundation and to develop a new data set for the evaluation of the next generation of numerical models for complex flows.

Unlike previous hydraulic model studies that focused on the maximum extent of tsunami inundation and were often conducted on a scale of 1:200 or smaller, the experiment of Cox et al. (2008) focused on the initial inundation zone along an urban waterfront in order that the flow among several individual buildings can be observed. The model, constructed at 1:50 scale, was an idealization of the town of Seaside, Oregon, located in the Pacific Northwest of the United States (Figure 4.92) and featured several of the characteristic structures, including a 2 m high (prototype) seawall, large hotels along the water front, and smaller commercial and residential structures.

This location was chosen for several reasons. One reason was that the constructed environment (i.e. the seawall, hotels, residential and commercial buildings) was typical of coastal communities vulnerable to tsunamis with populations concentrated within the first 200 m of shoreline. Second, the bathymetry at Seaside was fairly easy to construct with uniform, shore-parallel contours. Third, the United States Geological Survey (USGS) report (USGS, 2006) provided reasonable guidance for an expected tsunami height triggered by a Cascadia Subduction Zone event.

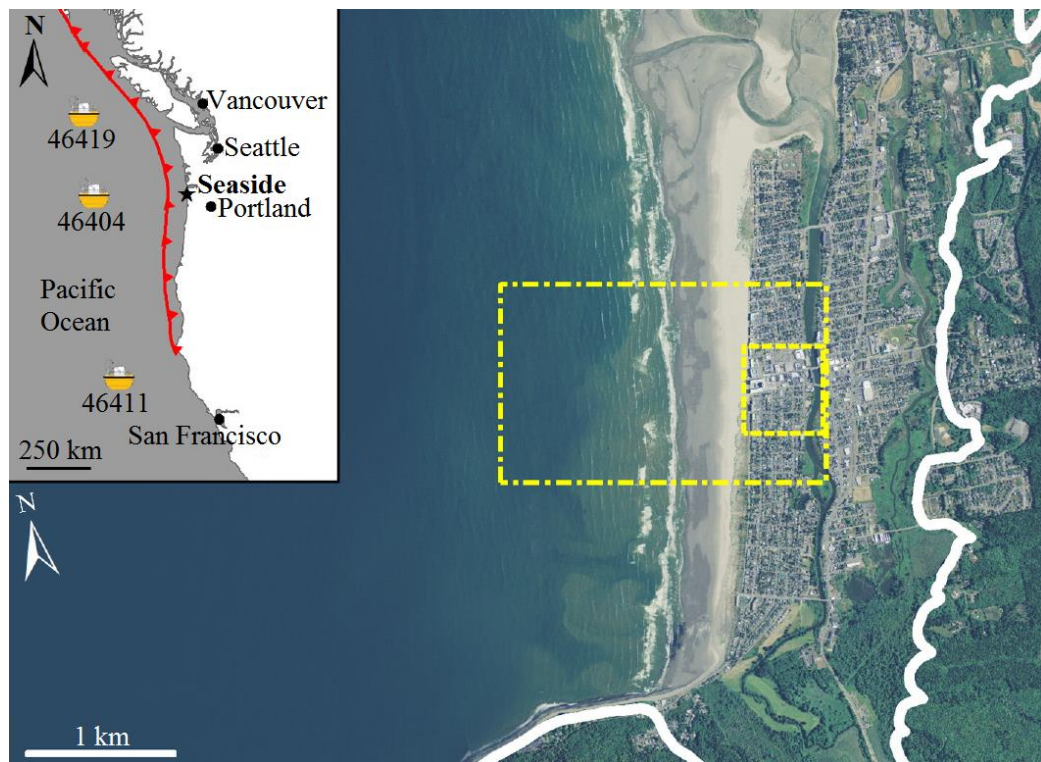


Figure 4.92 Seaside, Oregon: 1:50 physical model region (dashed-dotted yellow line), macro-roughness region (dashed yellow line) and tsunami inundation line (solid white line). Inset map shows regional location of Seaside, location of offshore DART buoys, and proximity to the Cascadia subduction zone (solid red line) (Park et al., 2013).

The idealized bathymetry was composed of a 10 m horizontal section near the wavemaker with a depth of 0.97 m, an 8 m section at a 1:15 slope, a 15 m section at a 1:30 slope, on which the SWL intersected, and another horizontal section 11 m in length which extended to the back wall (Park et al., 2013). In the real town, the hotels along the beach are fronted by an approximately 2 m high seawall in the center, which was idealized in the model as 4 cm high and longshore uniform. The largest structure in the area is a modern, eight storey, U-shaped condominium with a five storey parking garage behind, located in the center of the beachfront. The remaining buildings are other light commercial buildings, idealized as a square, and residential buildings, idealized as a smaller rectangle with a pitched roof. The individual macro-roughness units were color coded with blue for large hotels or commercial buildings, red for smaller commercial buildings, and yellow for residential structures (Park et al., 2013) (Figures 4.93 and 4.94).



Figure 4.93 Photograph of 1:50 scale model of the town of Seaside, Oregon constructed in the Tsunami Wave Basin at OSU (Cox et al., 2008; Rueben et al., 2011).

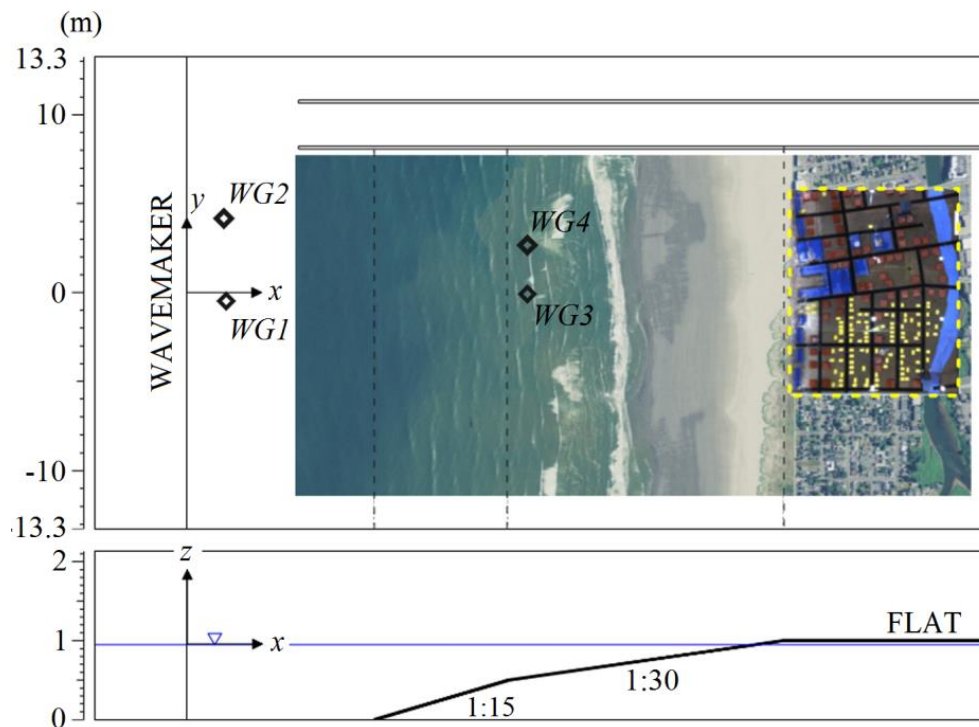


Figure 4.94 Plan and elevation view of the physical model in the Tsunami Wave Basin. The laboratory photo provides the scale of the Seaside, Oregon model (Park et al., 2013).

All the elements were fixed in place so that the experiment could be rerun with the same macro-roughness conditions, and a LIDAR survey was conducted to quantify the location of all the roughness elements (Cox et al., 2008). The Necanicum River, which flows through the center of the city approximately parallel to the beach crest, and the city streets were not modeled for the experiment but their positions were painted on the physical model for reference, the river with a light blue color ($x = 42$ m) and the streets with black (Figure 4.94). The effects of vegetation, small-scale roughness, debris or sediments were not included, either.

The tests were conducted in the Tsunami Wave Basin of the Tsunami Research Facility at the O.H. Hinsdale Wave Research Laboratory (HWRL), Oregon State University (OSU). The basin was a rectangular box, 48.8 m long by 26.5 m wide by 2.1 m high. The coordinate system for this experiment is shown in Figure 4.94, with x positive onshore and $x = 0$ at the rest position of the wavemaker, z is positive up with $z = 0$ at the flat bottom of the basin, and y is positive to the south with $y = 0$ along the centerline of the basin. The basin was equipped with a segmented, piston-type wavemaker with a maximum stroke of 2.1 m and maximum velocity of 2.0 m/sec (Cox et al., 2008).

The idealized bathymetry for the town of Seaside was constructed of smooth concrete with a flat finish and an estimated roughness height of 0.1 – 0.3 mm (Rueben et al., 2011). The design tsunami condition produced by the wavemaker used an error function to maximize the full 2.0 m stroke, and had a duration of 10.0 seconds. The wave height measured at WG1, over the horizontal section of the basin, was approximately 0.20 m. At prototype scale, this wave height is 10 m, which corresponds to the estimated tsunami wave height for the “500-yr” Cascadia Subduction Zone tsunami for this region (Tsunami Pilot Study Working Group, 2006).

The white boxes labeled A to D and 1 through 9, shown in Figure 4.95, represented the measurement locations of the overland flow depth and cross-shore velocity. The measurement locations were divided into 4 lines: A to D. Line A was located on a city street parallel to the primary inundation flow direction and numbered from 1 to 9, as the measurement locations moved inland. Lines B and C were on streets inclined approximately 10° to the flow direction, were flanked by hotels or commercial buildings, and numbered the same as line A. Line D was located mostly behind the buildings and only had 4 measurement locations. In total there were 31 measurement locations (Park et al., 2013).

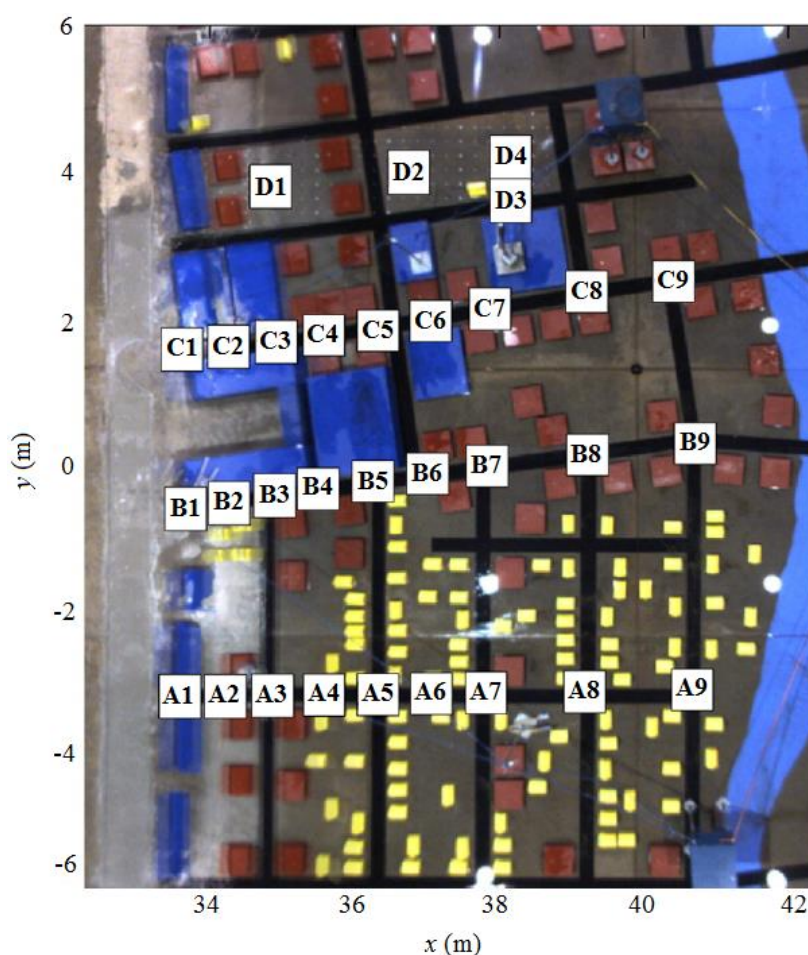


Figure 4.95 Detailed plan view of macro-roughness elements of the physical model, annotated with measurement locations (Park et al., 2013).

Four surface piercing wire resistance wave gauges (WG1 – WG4) were fixed in the basin at the following locations: WG1: $(x, y) = (2.086 \text{ m}, 0.515 \text{ m})$, WG2: $(x, y) = (2.068 \text{ m}, 4.065 \text{ m})$, WG3: $(x, y) = (18.618 \text{ m}, 0.000 \text{ m})$, and WG4: $(x, y) = (18.618 \text{ m}, 2.860 \text{ m})$. Four pairs of co-located ultra-sonic surface wave gauges (usWG, Senix Corporation TS-30S1-IV) and Acoustic-Doppler velocimeter (ADV, Nortec Vectrino) sensors were used to measure the overlaid land flow depth and flow velocity along lines A, B, C, and D, simultaneously (Cox et al., 2008). Table 4.27 lists the coordinates of each measurement location and the total number of trials performed and available (Park et al., 2013).

Table 4.27 The coordinates of the measurement locations for BMP 5 (Park et al., 2013)

Number	<i>Line A</i>		<i>Line A</i>		<i>Line C</i>		<i>Line D</i>	
	$x \text{ (m)}$	$y \text{ (m)}$	$x \text{ (m)}$	$y \text{ (m)}$	$x \text{ (m)}$	$y \text{ (m)}$	$x \text{ (m)}$	$y \text{ (m)}$
1	33.61	-3.19	33.72	-0.59	33.81	1.51	35.12	3.71
2	34.10	-3.19	34.22	-0.53	34.55	1.60	36.68	3.89
3	34.53	-3.18	34.68	-0.47	35.05	1.69	38.09	4.07
4	35.04	-3.18	35.18	-0.41	35.56	1.77	38.14	3.59
5	35.54	-3.19	35.75	-0.32	36.05	1.85	—	—
6	36.35	-3.20	36.64	-0.23	37.05	1.99	—	—
7	37.76	-3.20	37.77	-0.07	38.24	2.19	—	—
8	39.22	-3.20	39.22	0.14	39.21	2.34	—	—
9	40.67	-3.23	40.67	0.27	40.40	2.58	—	—

The need for physical model data raises questions about how to make accurate measurements of the free surface and velocity in complex domains, especially around macro-roughness. Since the location of the advancing inundation front is clearly visible to the human eye, Cox et al. (2008) favoured optical measurement methods and installed two Argus cameras directly over the wave basin. In general, optical measurements from these cameras were accurate to approximately 1 cm for most of the field of view. Cox et al. (2008) converted the frames from RGB color images to intensity images in order to isolate the wave edge. They subtracted a

reference image for which the wave was not present from each video frame, forming a difference image (Figure 4.96).

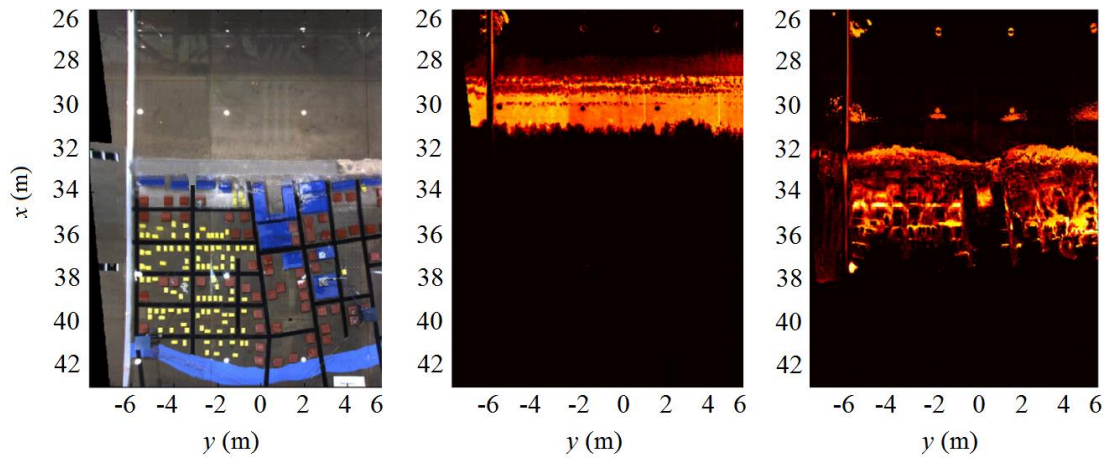


Figure 4.96 (a) Rectified, merged, and cropped image from the Argus cameras; (b) difference image taken at $t = 24.06$ sec during wave breaking; (c) difference image taken at $t = 27.26$ sec during inundation (Rueben et al., 2011).

Figure 4.96 clearly shows that the optical system captured complexities of the flow field around the macro-roughness elements. The measured velocities at the leading edge of the wave were not recorded by the ADV, so the leading velocities were obtained from the optical measurements (Rueben et al., 2011) and velocity fitting curves were constructed via interpolation to calculate the specific momentum flux.

Figure 4.97 illustrates the mean edge wave positions over 21 trials at $t = 26.3$ sec and $t = 27.8$ sec. The macro-roughness along the urban waterfront and in the residential and commercial areas reduced bore propagation speed significantly. In the narrow spacings of the macro-roughness, large hydraulic jumps were formed on the seaward side of the roughness elements with large, turbulent wakes in their lee. Unlike on open streets running parallel to the flow direction, in the areas with macro-roughness the flow was delayed.

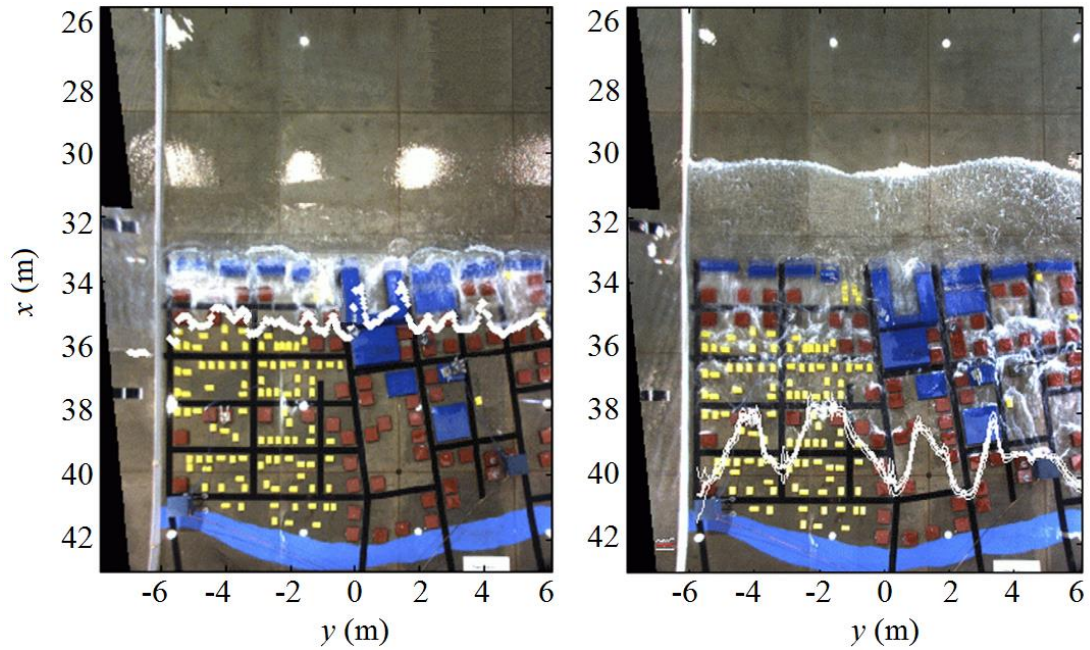


Figure 4.97 (a) Image taken at $t = 26.3$ sec during inundation; (b) image taken at $t = 28.7$ sec during inundation. The white lines represent the mean edge wave position determined over 21 trials (Rueben et al., 2011).

The results of this study (i.e. BMP 5) indicate that the macro-roughness elements have a significant effect on the tsunami inundation process compared to the areas without macro-roughness. The macro-roughness elements lead to 40% reduction in the inundation speed. Moreover, the characteristics of the macro-roughness elements affect the tsunami inundation significantly (Rueben et al., 2011).

As stated previously, the experiment of Cox et al. (2008) provided a great amount of data for laboratory benchmarking of numerical models. The recommended computational domain for the modelers is given in Figure 4.98.

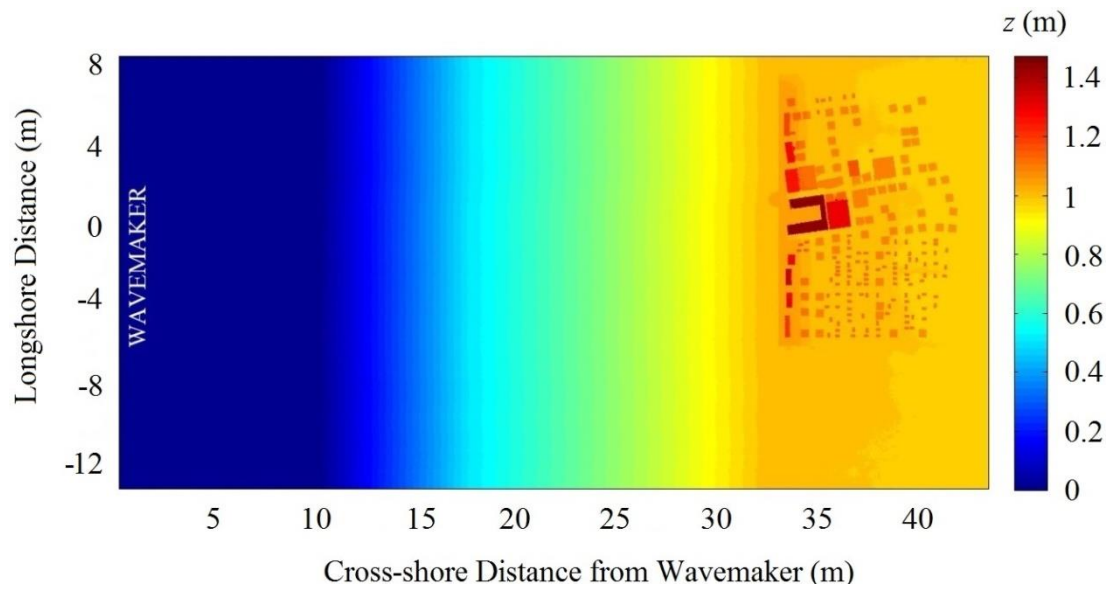


Figure 4.98 Computational domain for BMP 5 (NTHMP, 2015)

In BMP 5, the generated (incident) wave is a long period custom wave, not a solitary wave. Unlike a solitary wave, a custom wave is not permanent.

Numerically, the wave can be generated using two different methods (Figure 4.99): (i) the wavemaker displacement time series can be used if a moving wall boundary condition is available in the numerical model, (ii) a synthetic time series of incident wave elevation at $x = 5$ m can be used to force the numerical model at $x = 5$ m. Even though the wave elevation time series is based on the simulation of a moving wall boundary condition, it is supposed to reproduce the wave very well.

To efficiently run BMP 5, firstly, the free surface elevation comparisons at WG3 have to be made to ensure that the generated waves in the model are correct in terms of amplitude, period, and arrival time. Secondly, the overland flow depth, cross-shore velocity and cross-shore specific momentum flux at four locations, B1, B4, B6 and B9 are compared.

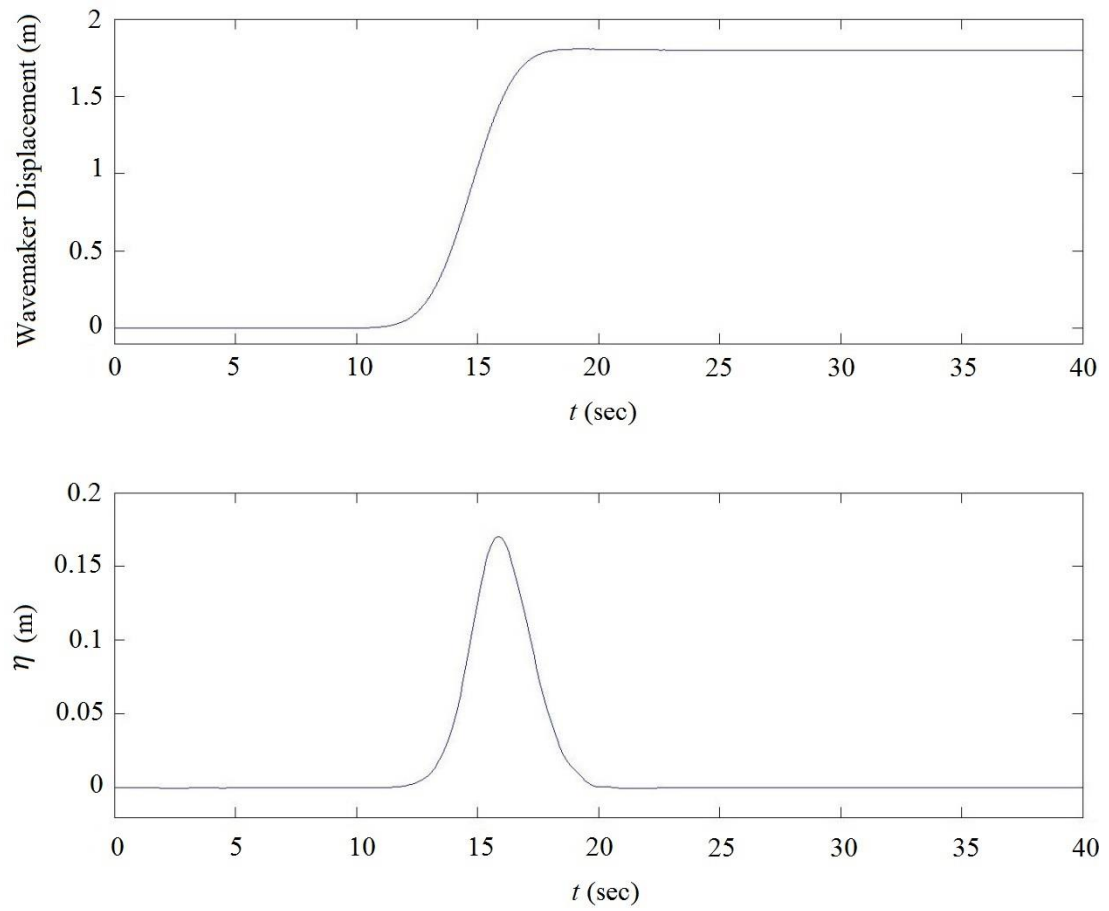


Figure 4.99 (a) Wavemaker displacement time series – real data, which can be used to drive a moving wall boundary condition; (b) incident-only wave time series at $x = 5$ m – simulated data, which can be used to drive a stationary input wave boundary condition at $x = 5$ m (NTHMP, 2015).

4.5.2. NAMI DANCE Model

The physical experiment of Cox et al. (2008) is reproduced in a 2D domain using NAMI DANCE (Figure 4.100).

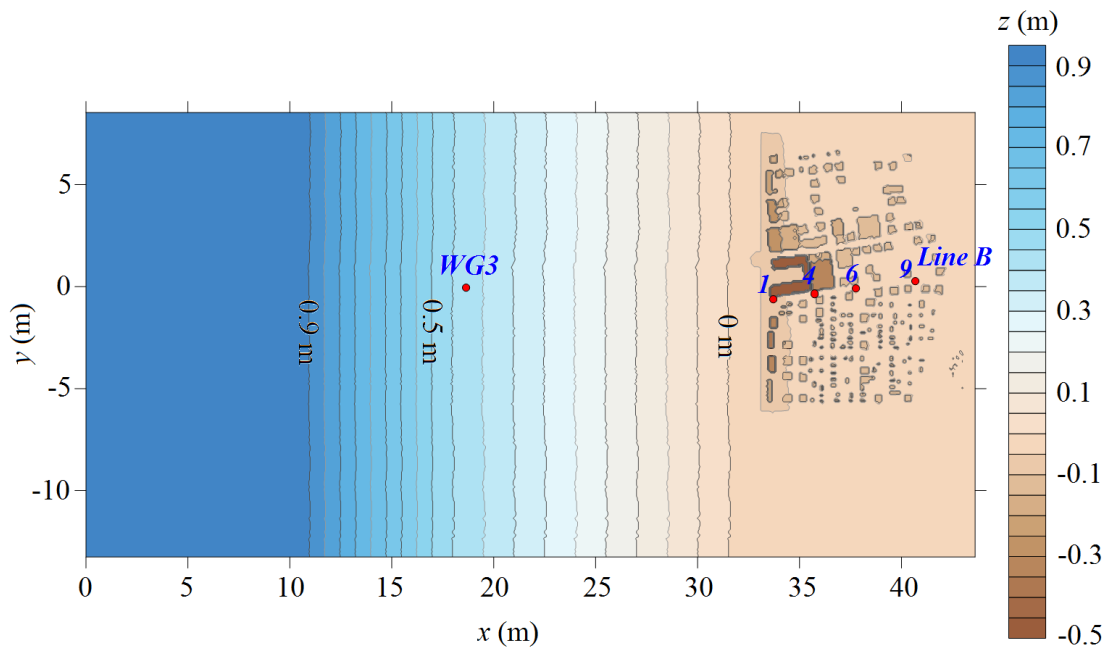


Figure 4.100 NAMI DANCE model: computational domain and the coordinate system

Figure 4.101 illustrates the 3D view of NAMI DANCE computational domain.

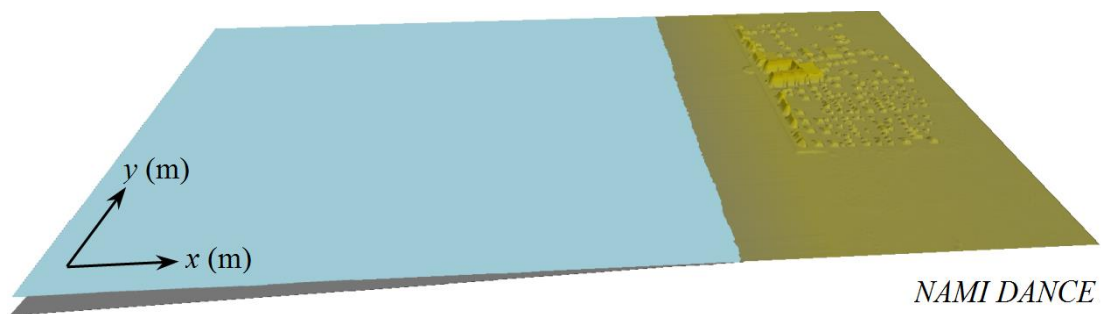


Figure 4.101 3D top view of NAMI DANCE computational domain for BMP 5

The fluid is inviscid, the flow is incompressible and the fluid density is constant. The x axis of the Cartesian coordinate system is perpendicular to the wavemaker and the y axis is parallel to the wavemaker. The incident wave, which is a long period wave, is a synthetic time series, produced from the simulation of a moving wall boundary condition. Since the incident wave signal is recorded at a distance $x = 5$ m in the laboratory setting, the bathymetry is cropped to discard the initial section between $x = 0$ m and $x = 5$ m. This adjustment allows the incoming wave to be introduced into the domain exactly at the location where it is recorded (Figure 4.102).

Excellent agreement between the predicted and recorded wave forms are reached at the control point – WG3 for both the first wave and the reflected wave train. In fact, the predicted maximum incident wave amplitude is only 0.0002 m less than the measured one.

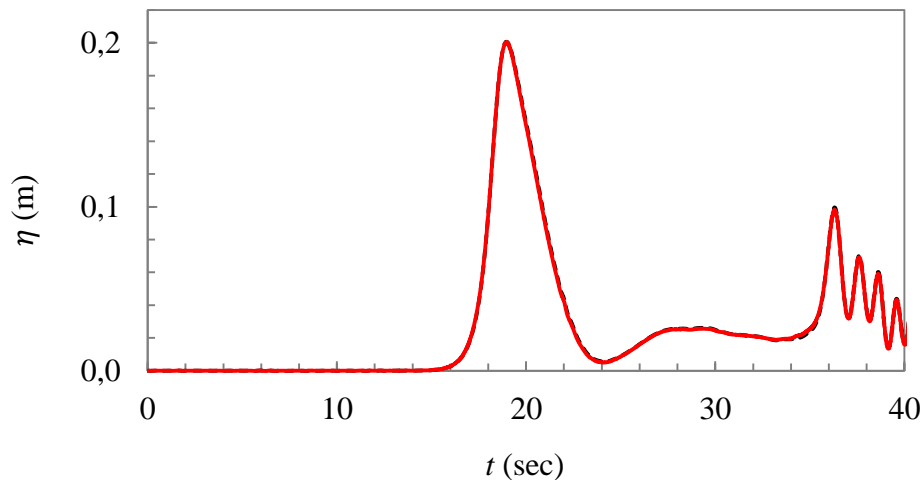


Figure 4.102 Comparison of computed and recorded free surface elevation at the control point, WG3. The red line represents the NAMI DANCE prediction; the black line represents the recorded free surface elevation at WG3.

The maximum x boundary has a rigid wall boundary condition, which defines the downstream end of the wave tank. The minimum and maximum y boundaries are also defined as rigid walls in order to prevent outflow from the computational domain.

4.5.2.1. Spatial Discretization

In order to simulate BMP 5 correctly, it is necessary to model the macro-roughness elements properly. To achieve this, after several trials using different spatial resolutions, it is found that the grid size selected has to be smaller than 0.1 m, i.e. $\Delta x \leq 0.1$ m, since for larger grid resolutions, macro-roughness elements can not be modeled sufficiently.

For $\Delta x = 0.1$ m, the macro-roughness elements can be modeled properly; however, a finer grid size provides a better definition of the Seaside model. For grid resolutions smaller than 0.05 m, there is no visible change in the inundation distance; thus, it is concluded that after $\Delta x = 0.05$ m, the results are insensitive to grid size. Moreover, the effect of grid size is negligible offshore; the free surface elevation comparisons at the control point (i.e. WG3) show that the predicted wave profile is not affected by the grid resolution.

The previous numerical model validations that used BMP 5 recommend the use of adaptive mesh refinement, the coarsest grid having a resolution of approximately 0.1 m and the finest grid, which only covered the town of Seaside model region, having a 0.01 m resolution (NTHMP, 2015). However, the application of such a technique is not possible in NAMI DANCE; therefore, the computational domain is represented by a uniform grid size, Δx and Δy , which is selected as 0.05 m.

The time step, Δt , is selected as 0.001 second, which satisfies the stability condition for NAMI DANCE solutions. Different time steps are also tested; however, no significant change is observed in the numerical predictions.

4.5.2.2. Friction

Manning's roughness coefficients used to assess the effect of friction are: (i) $n = 0$ (i.e. frictionless bottom), (ii) $n = 0.005$, (iii) $n = 0.01$, (iv) $n = 0.02$ and (v) $n = 0.03$ (Figure 4.103 – 4.105).

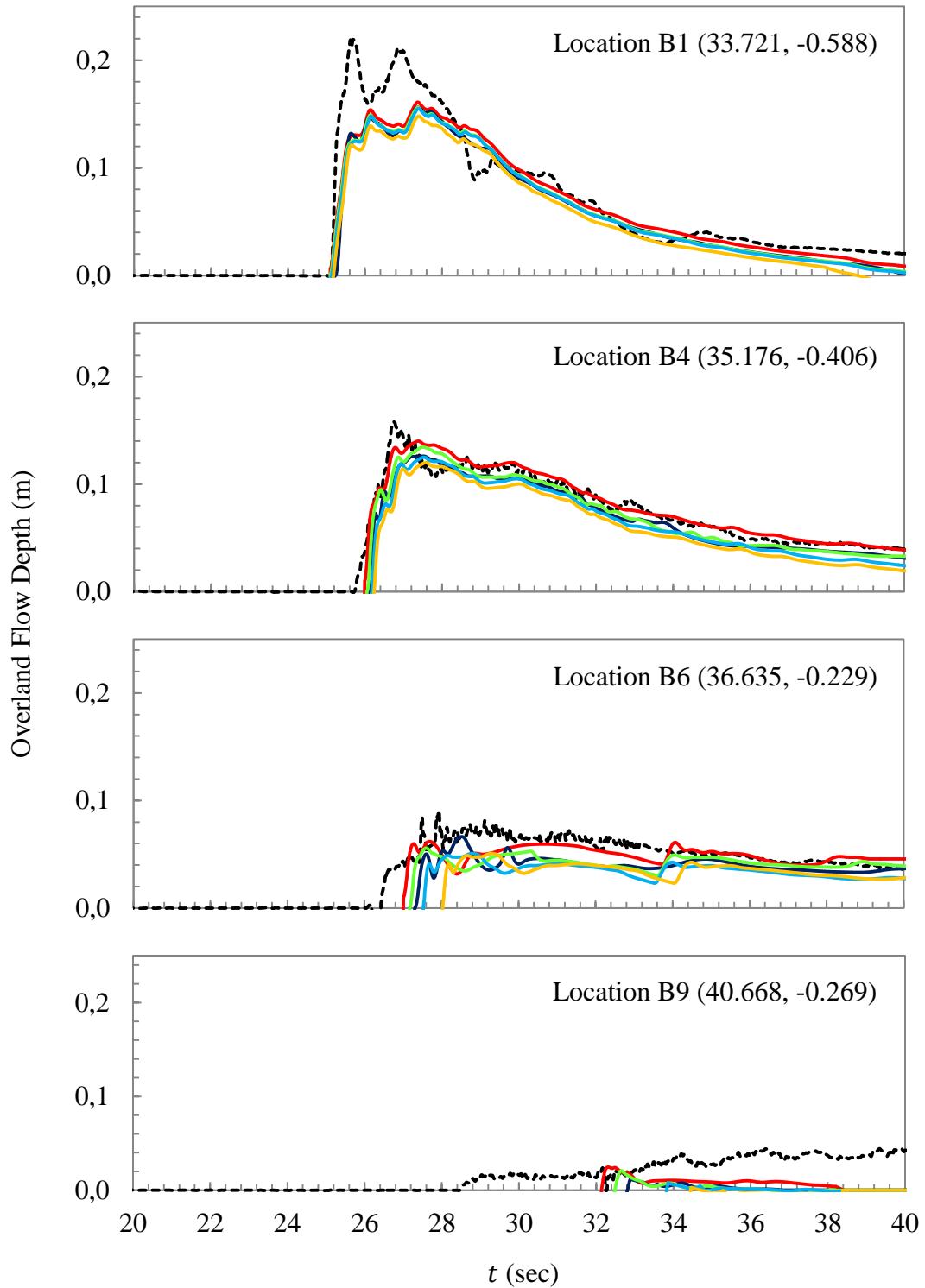


Figure 4.103 Comparison of predicted and measured overland flow depth for locations B1, B4, B6 and B9, respectively. The dashed black line represents the measured data; the red, green, purple, blue and orange lines represent the NAMI DANCE predictions when $n = 0$, $n = 0.005$, $n = 0.01$, $n = 0.02$ and $n = 0.03$, respectively.

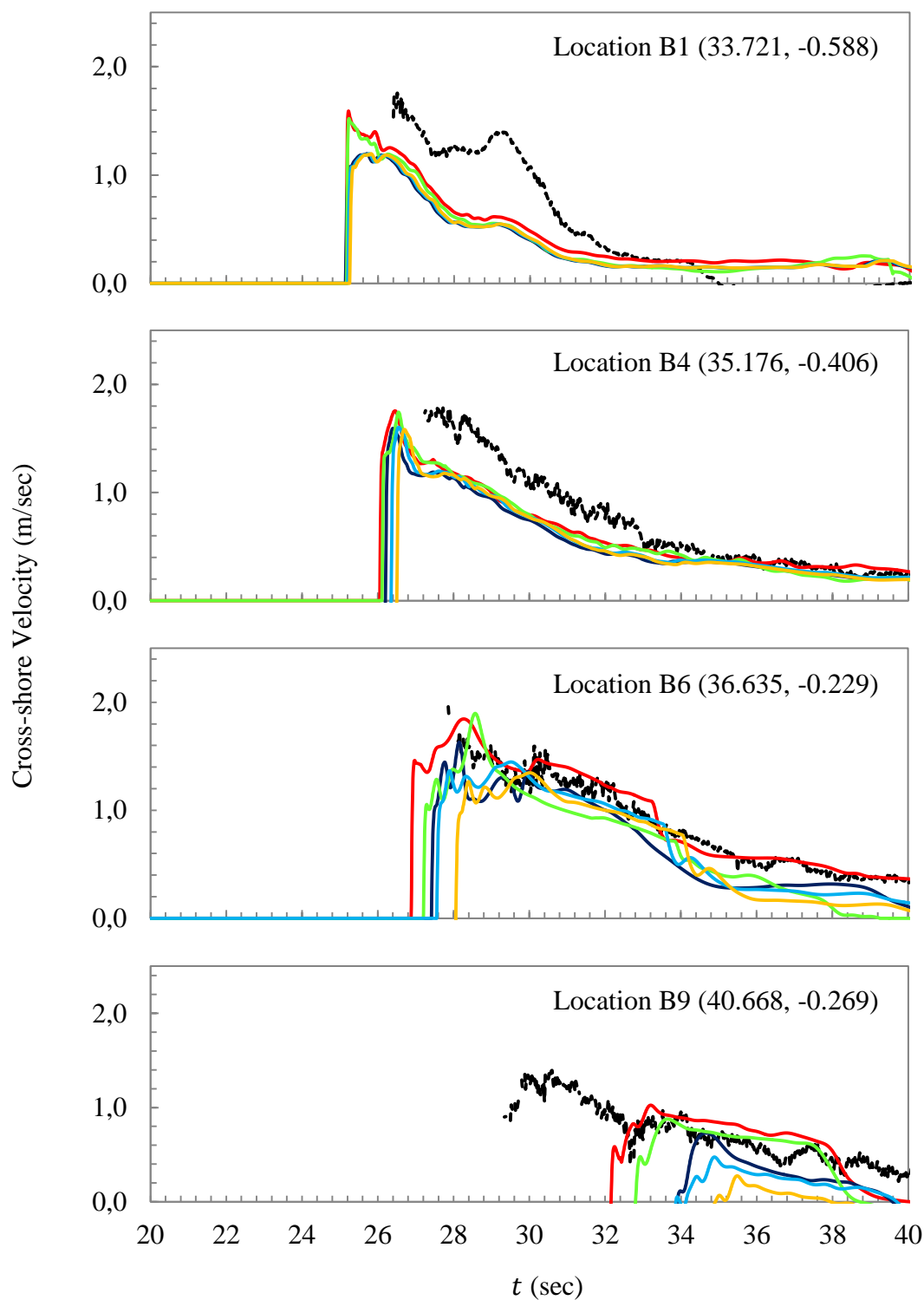


Figure 4.104 Comparison of predicted and measured cross-shore velocity for locations B1, B4, B6 and B9, respectively. The dashed black line represents the measured data; the red, green, purple, blue and orange lines represent the NAMI DANCE predictions when $n = 0$, $n = 0.005$, $n = 0.01$, $n = 0.02$ and $n = 0.03$, respectively.

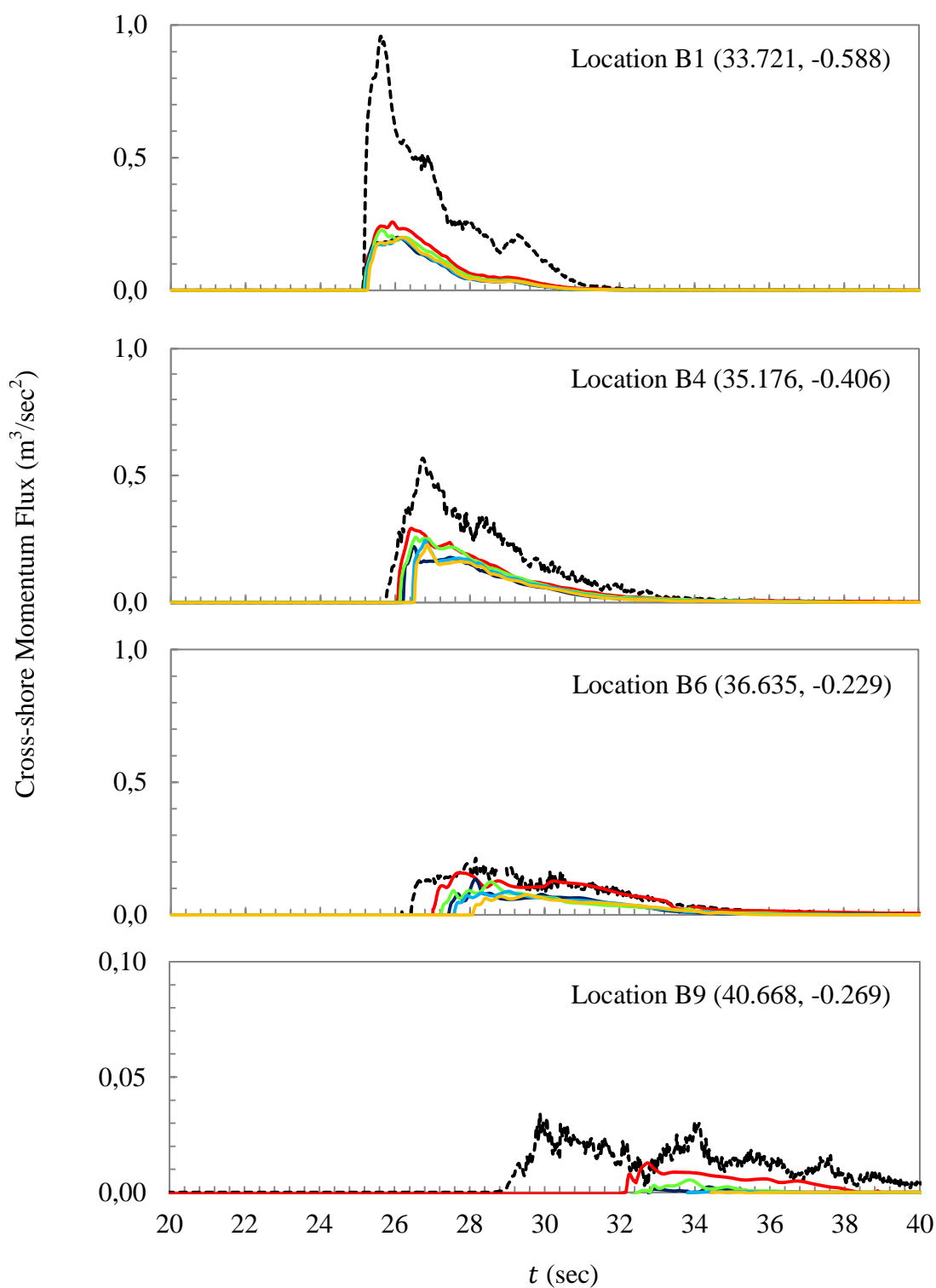


Figure 4.105 Comparison of predicted and measured cross-shore momentum flux for locations B1, B4, B6 and B9, respectively. The dashed black line represents the measured data; the red, green, purple, blue and orange lines represent the NAMI DANCE predictions when $n = 0$, $n = 0.005$, $n = 0.01$, $n = 0.02$ and $n = 0.03$, respectively.

The results reveal that the effect of varying friction is stronger in more inland areas. The overland flow depth and cross-shore velocity values decrease as friction factor is increased. In fact, the overland flow depth remains relatively unchanged for locations B1 and B4, after which the friction factor exhibits a greater influence. For more inland areas (i.e. locations B6 and B9), as the friction factor is increased by a factor of 6 (i.e. from 0.005 to 0.03), the maximum free surface elevation decreases by ~15%, but the cross-shore velocity and specific momentum flux decrease by 95 and 208%. This fact reveals that the predicted velocity and momentum flux terms are highly sensitive to the bottom friction factor further inland. Moreover, the arrival time of the inundation wave is earlier when less friction is applied. The effect of bottom friction on arrival times can be clearly seen in location B9. The results of friction analysis can not be verified by the physical model data as only one friction factor was tested in the experiments.

4.5.3.FLOW-3D[®] Model

The same physical experiment is reproduced using FLOW-3D[®] in a 3D domain, throughout which the fluid is inviscid, the flow is incompressible and the fluid density is constant. The effects of surface tension and air entrainment at the surface of the flow are neglected.

The numerical model is constructed using the Cartesian coordinate system, where the positive x direction is oriented along the fluid flow into the domain and the positive y direction is perpendicular to the direction of the flow, along the wavemaker. The gravitational acceleration, g , is in the downward direction (i.e. $-z$ direction) (Figure 4.106).

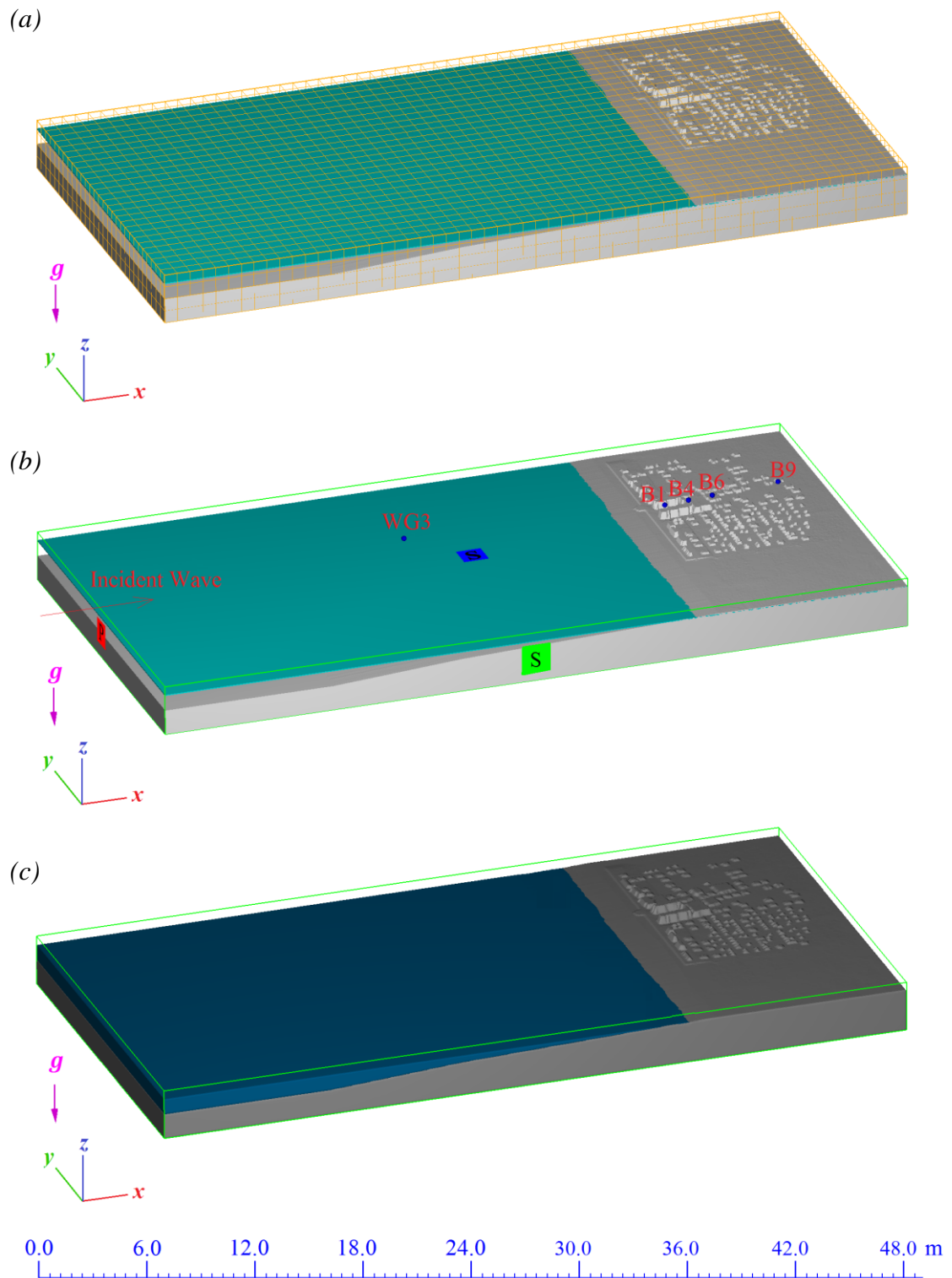


Figure 4.106 FLOW-3D® computational domain constructed for BMP 5: (a) meshing (enlarged for clarity); (b) boundary conditions and gauge locations; (c) after using FAVOR™

The incident wave is a synthetic time series recorded at a distance $x = 5$ m in the laboratory setting. As in the NAMI DANCE analysis, the initial section of the bathymetry up to $x = 5$ m is discarded. As a result, the incoming wave is introduced into the domain exactly at the location where it is recorded and consistency with the NAMI DANCE analysis is achieved (Figure 4.107). The predicted and recorded wave forms are in excellent agreement at the control point – WG3 for the first wave.

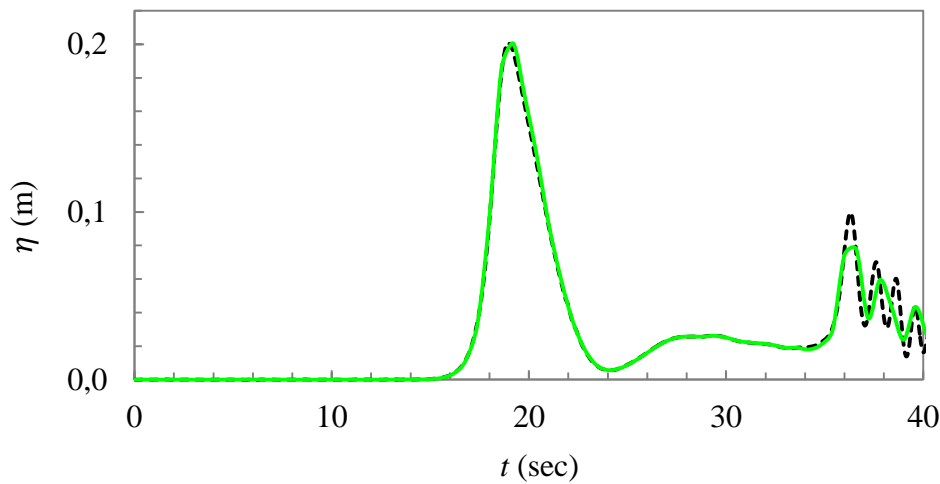


Figure 4.107 Comparison of computed and recorded free surface elevation at the control point, WG3. The green line represents the FLOW-3D[®] prediction; the black line represents the recorded free surface elevation at WG3.

At the minimum x boundary, the pressure boundary condition is applied. Thus, the input data, which is the free surface elevation time series recorded at $x = 5$ m, can be entered manually. The maximum x boundary has the wall boundary condition so as to define the end of the wave tank. The minimum and maximum y boundaries as well as the maximum z boundary feature the symmetrical boundary condition, where all the velocity derivatives and velocity components normal to the boundaries are set to zero. The wall boundary condition is valid for the minimum z boundary, where the bottom of the wave flume is defined.

4.5.3.1. Spatial Discretization

In order to simulate BMP 5 efficiently, it is necessary to model the macro-roughness elements properly. To achieve this, the FAVOR™ module of FLOW-3D® is used in order to decide whether the elements are modeled accurately enough. It is found that the grid size has to be selected smaller than 0.1 m, i.e. $\Delta x \leq 0.1$ m, since for larger grid resolutions, macro-roughness elements can not be modeled properly. For $\Delta x = 0.1$ m, the macro-roughness elements can be modeled properly but not accurately. Therefore, finer grid size of 0.05 m is preferred. For grid resolutions smaller than 0.05 m, (i.e. $\Delta x = 0.01$ m and $\Delta x = 0.025$ m), there is no visible change in the model accuracy of macro-roughness elements. The previous numerical model validations that used BMP 5 recommend the use of adaptive mesh refinement, the coarsest grid having a resolution of approximately 0.1 m and the finest grid, which only covered the town of Seaside model region, having a 0.01 m resolution (NTHMP, 2015). Even though it is possible to use adaptive meshing techniques via FLOW-3D®, uniform gridding, where Δx and Δy are 0.05 m, is preferred in order to attain consistency.

It is also necessary to analyse the effect of the vertical grid size, Δz , on the three-dimensional FLOW-3D® model. Coarser Δz values prevent accurate modeling of macro-roughness elements. Therefore, the use of uniform grids, i.e. $\Delta x = \Delta y = \Delta z = 0.05$ m, is preferred throughout the whole computational domain.

The time step, Δt , is selected as 0.001 second to be consistent with the simulations conducted using NAMI DANCE. When variable time stepping is employed in order to assess the effect of the time step size, no significant effect is observed.

4.5.3.2. Friction

In order to assess the effect of friction, different Manning's roughness coefficients are considered: (i) $n = 0$ (i.e. frictionless bottom), (ii) $n = 0.005$, (iii) $n = 0.01$, (iv) $n = 0.02$ and (v) $n = 0.03$ (Figure 4.107 – 4.109).

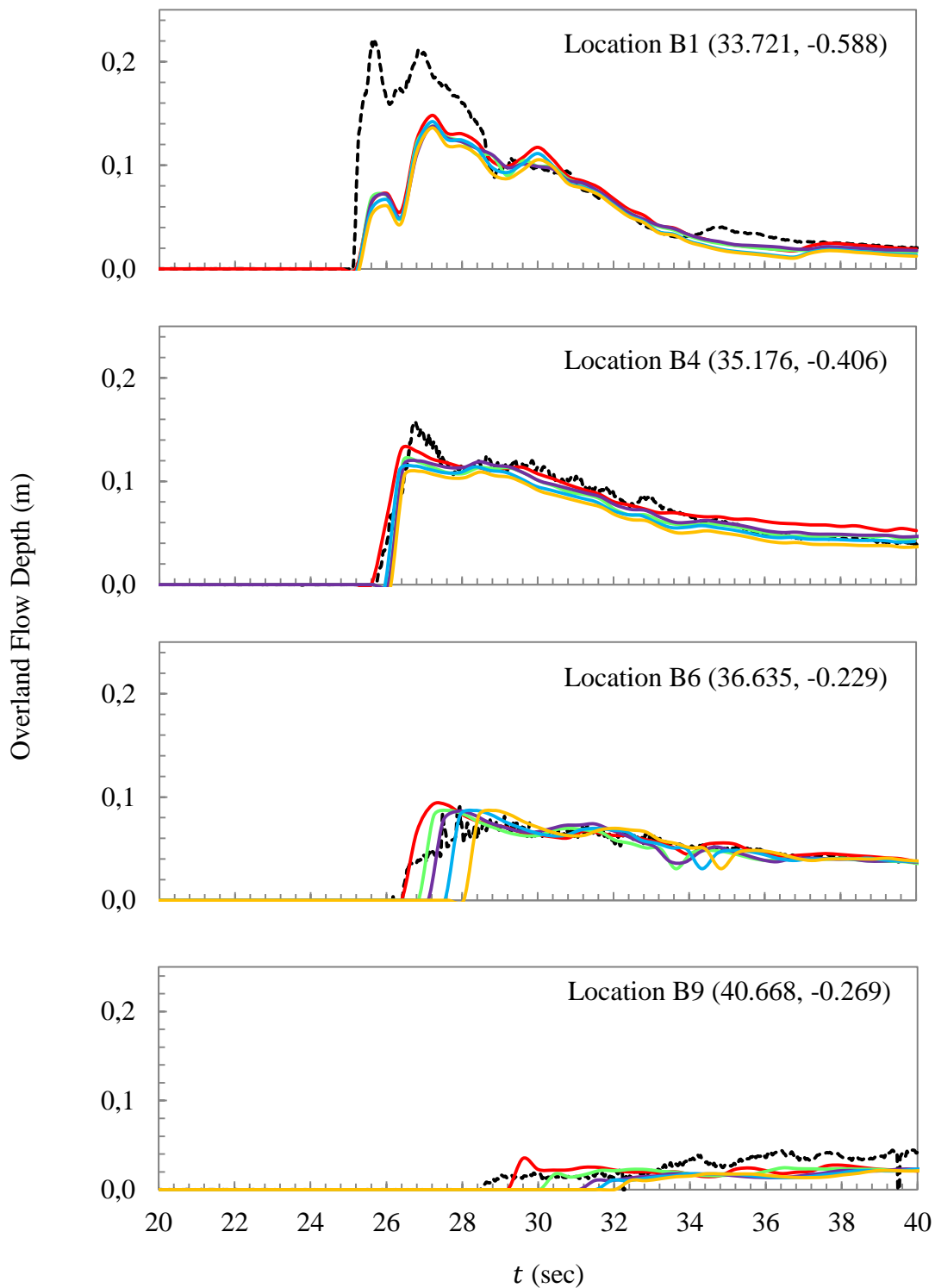


Figure 4.108 Comparison of predicted and measured overland flow depth for locations B1, B4, B6 and B9, respectively. The dashed black line represents the measured data; the red, green, purple, blue and orange lines represent the FLOW-3D[®] predictions when $n = 0$, $n = 0.005$, $n = 0.01$, $n = 0.02$ and $n = 0.03$, respectively.

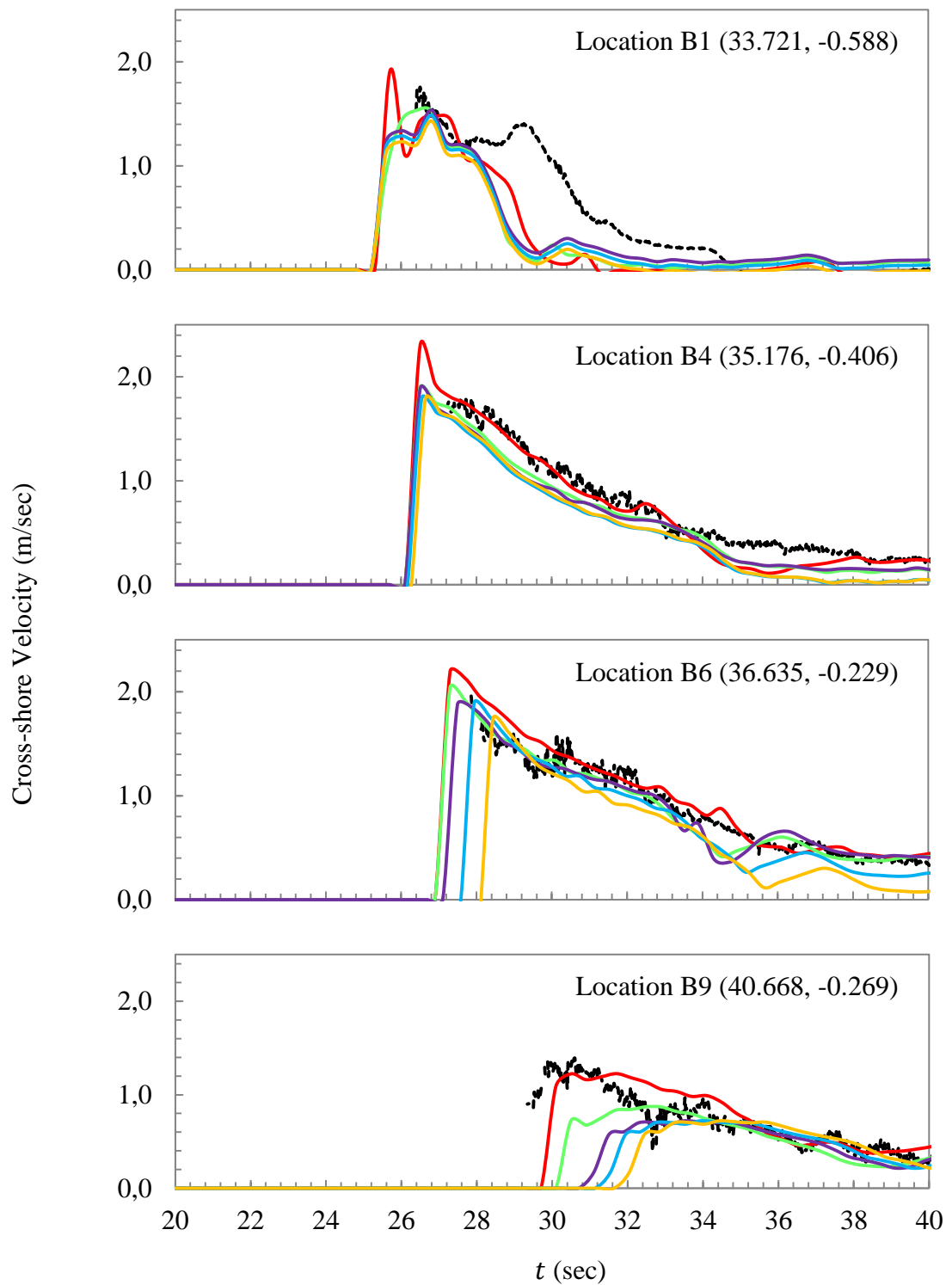


Figure 4.109 Comparison of predicted and measured cross-shore velocity for locations B1, B4, B6 and B9, respectively. The dashed black line represents the measured data; the red, green, purple, blue and orange lines represent the FLOW-3D[®] predictions when $n = 0$, $n = 0.005$, $n = 0.01$, $n = 0.02$ and $n = 0.03$, respectively.

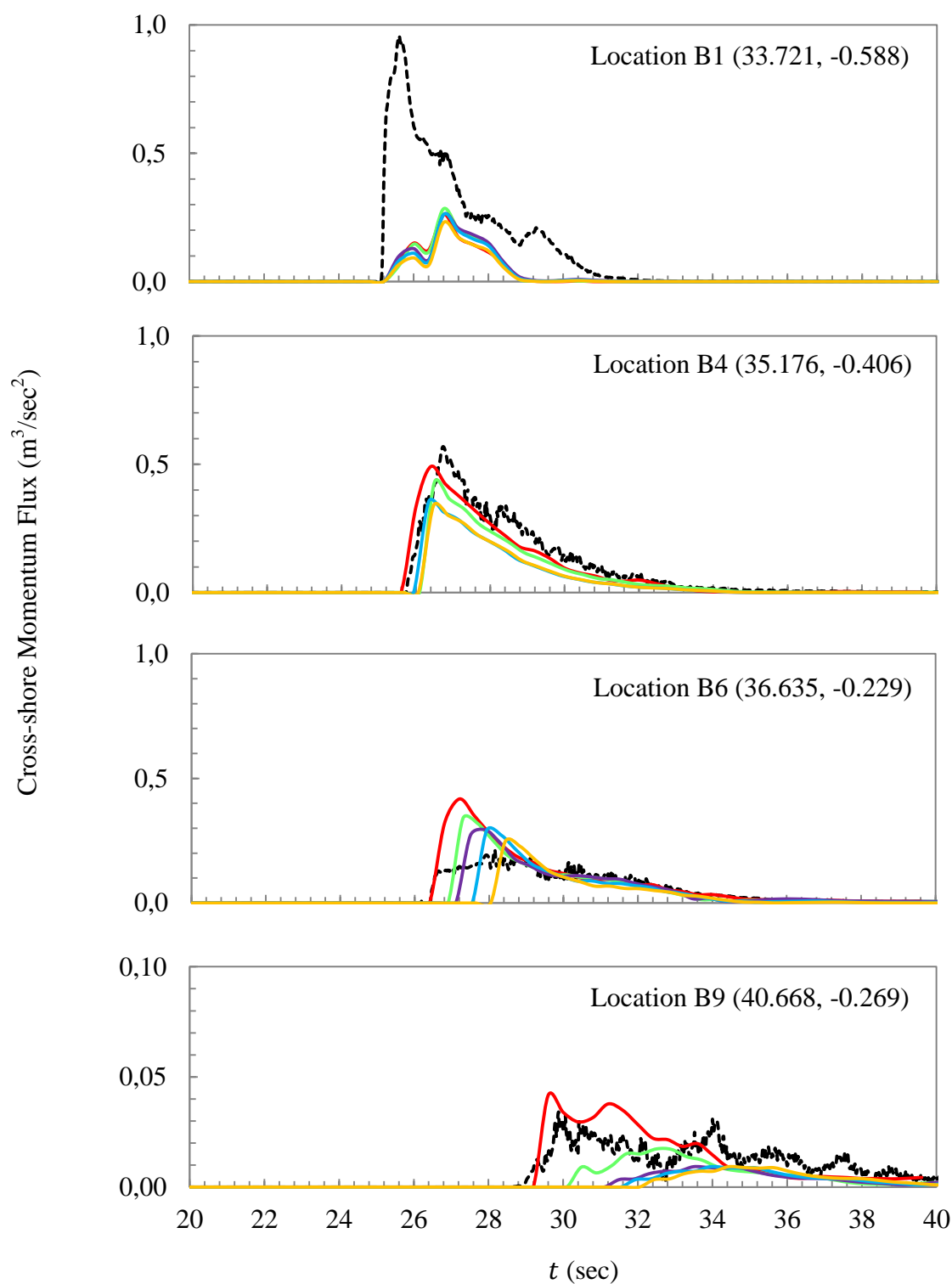


Figure 4.110 Comparison of predicted and measured cross-shore momentum flux for locations B1, B4, B6 and B9, respectively. The dashed black line represents the measured data; the red, green, purple, blue and orange lines represent the FLOW-3D[®] predictions when $n = 0$, $n = 0.005$, $n = 0.01$, $n = 0.02$ and $n = 0.03$, respectively.

The results indicate that the overland flow depth and cross-shore velocity values decrease as the friction factor is increased. However, in more inland areas (i.e. locations B6 and B9), the effect of varying friction is stronger as opposed to that in location B1, which is closest to the shoreline. When the bottom surface conditions are very rough, in the furthest areas inland, there is a decrease in the overland flow depth by 20%, in the cross-shore velocity by 60%, and in the specific momentum flux by 80%. These results support the findings of the NAMI DANCE simulations and reveal the sensitivity of velocity and momentum flux terms to bottom friction. The arrival time of the inundation wave is earliest when no friction is set in the model. The effect of bottom friction on arrival times can be clearly observed in the above figures. It is seen that in location B1, which is situated closest to the shoreline, the friction effect is almost negligible; however, dominance of friction on the arrival times is increased as the flow moves towards inland areas.

4.5.4. Simulation Results

Through the analysis of many disastrous tsunami incidents such as the 2004 Indian Ocean tsunami or the 2011 Great East Japan tsunami, the insight into and the understanding of tsunami deep water propagation and transformation in shallow waters have increased greatly in the last century. Yet, tsunami runup dynamics and coastal inundation mechanisms are still not sufficiently understood, especially in coastal urban agglomerations, where the tsunami induced on-land bore-like wave front patterns are strongly dominated by macro roughness elements such as houses and infrastructure (Goseberg and Schlurmann, 2010). This inundation process is difficult to model both physically and numerically (Cox et al. 2008).

Generally, the slope of the near coast region and the land cover characteristics, such as marshes or mangroves, and infrastructure and municipal developments, determine the maximum inundation distance in the coastal hinterland. BMP 5 focuses on the experimental study of the relationship between tsunami runup and macro-roughness elements and is used to test the abilities of 2D depth-averaged NSW and 3D-RANS models in predicting the flow conditions around macro-roughness elements.

The NAMI DANCE and FLOW-3D[®] model predictions regarding the overland flow depth, cross-shore velocity and cross-shore specific momentum flux are compared at four locations, B1, B4, B6 and B9 (Figures 4.111 – 4.113). It is a fact that inundation parameters are very sensitive to bottom friction for this specific case; therefore, it is important to calibrate the models according to the most appropriate roughness coefficient. The numerical simulations are conducted using a Manning's roughness coefficient of 0.01. After a careful friction analysis, it is found that the results most similar to the physical model are produced by this value, which is then used for all subsequent analyses with both models.

The results of the laboratory measurements reveal that, as the wave propagates around the macro-roughness, properties such as wave shape, the location of maximum free surface elevation, cross-shore velocity, and cross-shore momentum flux, change. The maximum overland flow depth, which is 0.22 m at location B1, decreases to 0.05 m at location B9. The cross-shore velocity is 2.0 m/sec at location B1 but falls to 1.4 m/sec at location B9. The maximum specific momentum flux, $0.96 \text{ m}^2/\text{sec}^3$ at location B1, becomes $0.03 \text{ m}^2/\text{sec}^3$ at location B9. The corresponding NAMI DANCE values are, for the maximum overland flow depth, 0.16 m at location B1 and 0.01 m at location B9. The maximum cross-shore velocity decreases from 1.2 m/sec to 0.7 m/sec and the maximum cross-shore momentum flux falls from $0.2 \text{ m}^2/\text{sec}^3$ at location B1 to $0.002 \text{ m}^2/\text{sec}^3$ at location B9. Similarly, the maximum overland flow depth computed via FLOW-3D[®] decreases from 0.14 m at location B1 to 0.03 m at location B9, the maximum cross-shore velocity decreases from 1.5 m/sec to 0.9 m/sec and the maximum cross-shore momentum flux decreases from $0.3 \text{ m}^2/\text{s}^3$ to $0.02 \text{ m}^2/\text{sec}^3$. Overall, it is found that the inundation depth decreases approximately by 80% as the wave propagates inland. There is a decrease of 30% in the cross-shore velocity and a fall of almost 97% in the cross-shore momentum flux. Note that the specific momentum flux is calculated by multiplying each time series of the overland flow depth by the square of the cross-shore velocity values. The momentum flux is an important parameter since it is directly related to the hydrodynamic force acting on the infrastructure (FEMA, 2008).

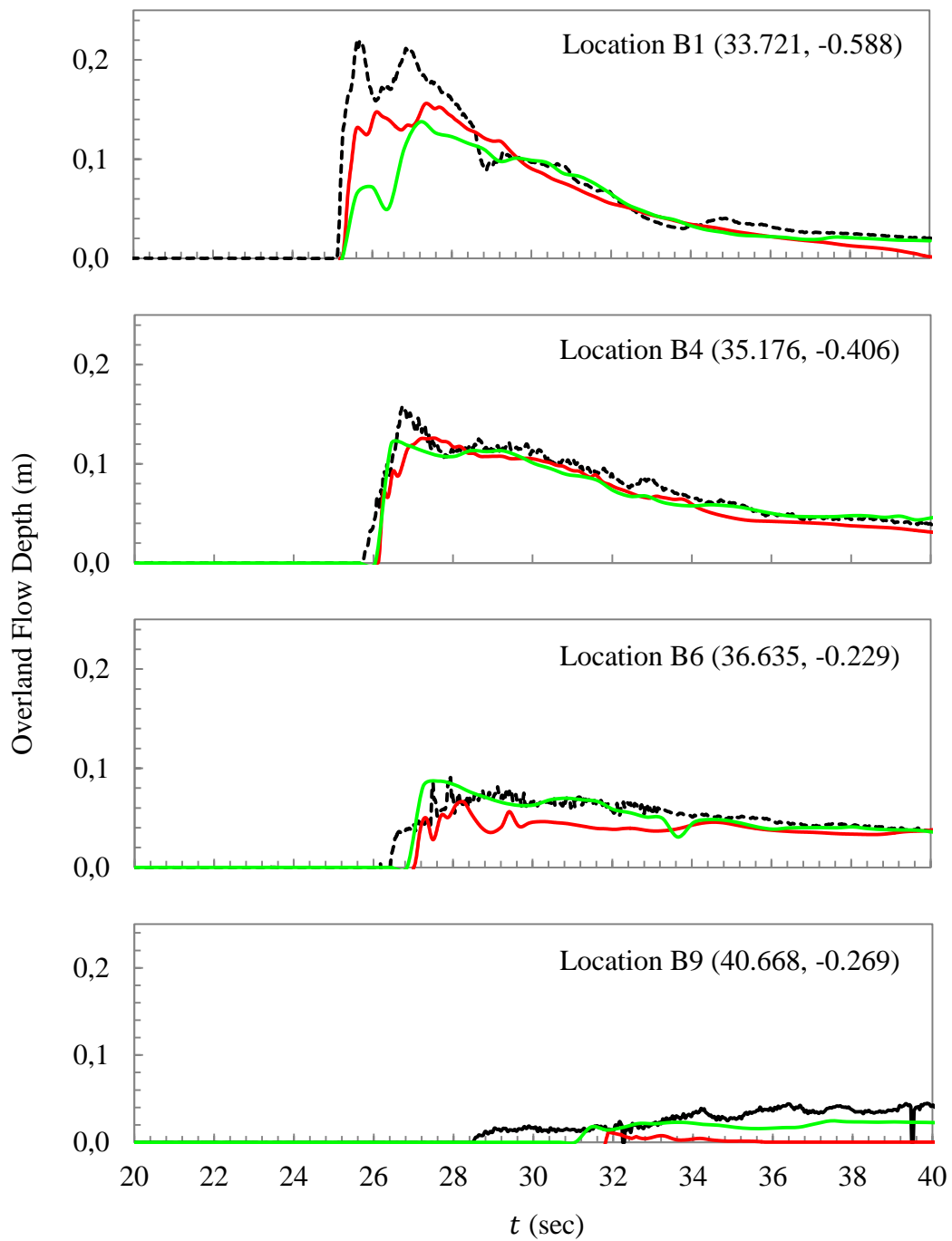


Figure 4.111 Comparison of predicted and measured overland flow depth for locations B1, B4, B6 and B9, respectively. The black line represents the laboratory measurements; the red line represents NAMI DANCE results; the green line represents the FLOW-3D® results.

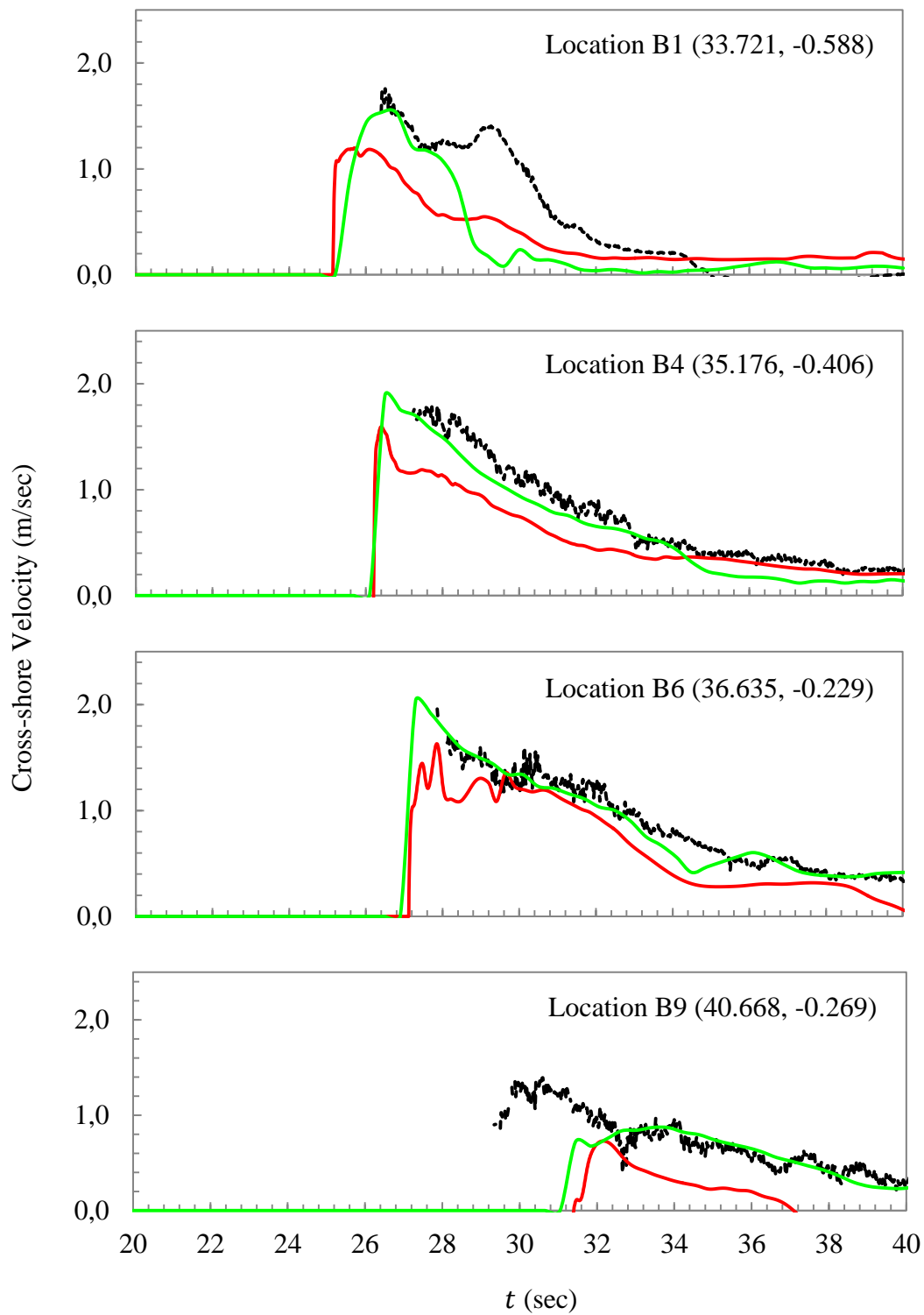


Figure 4.112 Comparison of predicted and measured cross-shore velocity for locations B1, B4, B6 and B9, respectively. The black line represents the laboratory measurements; the red line represents NAMI DANCE results; the green line represents the FLOW-3D[®] results

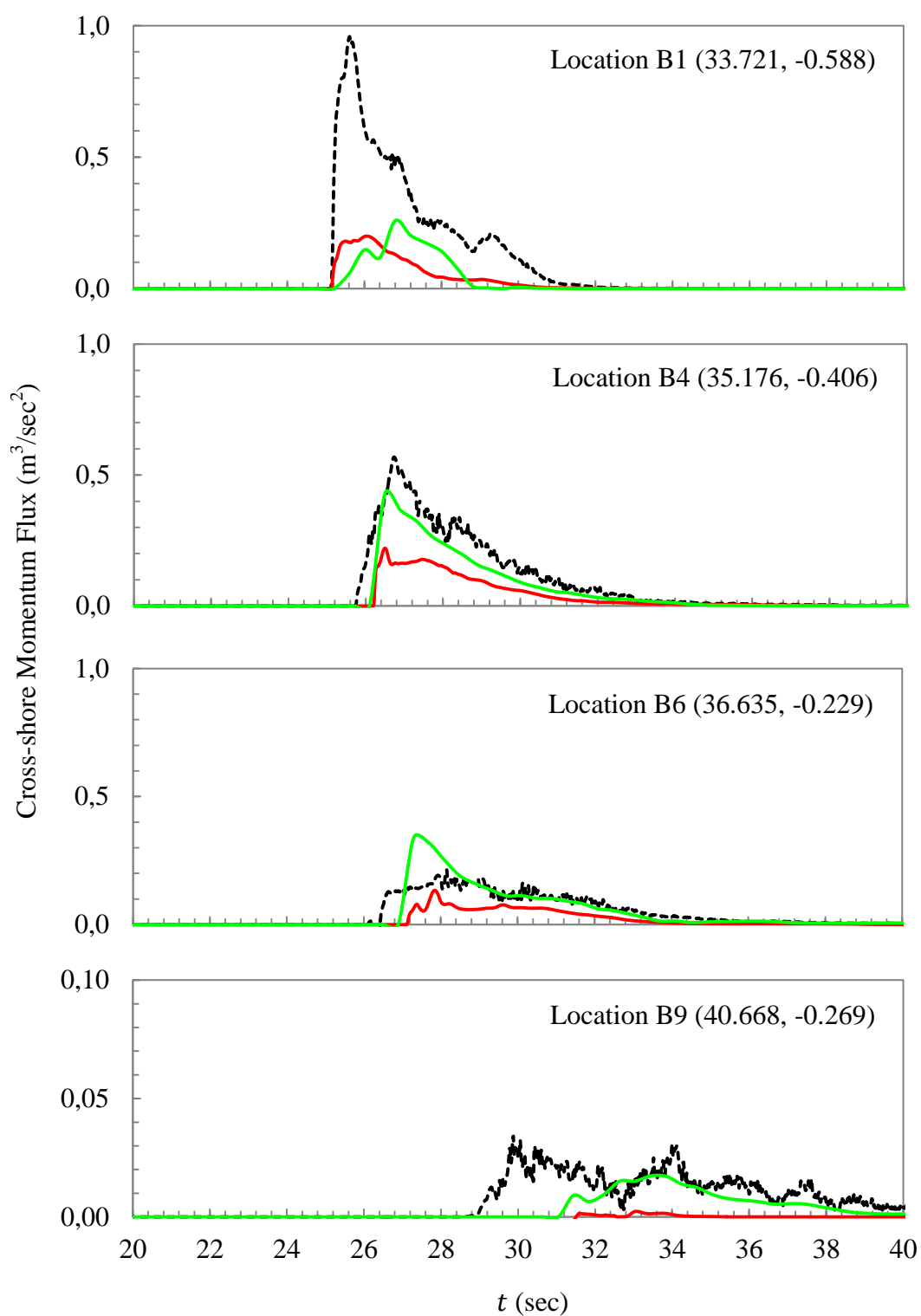


Figure 4.113 Comparison of predicted and measured cross-shore momentum flux for locations B1, B4, B6 and B9, respectively. The black line represents the laboratory measurements; the red line represents NAMI DANCE results; the green line represents the FLOW-3D[®] results.

The NRMSE of the NAMI DANCE and FLOW-3D[®] predictions for the overland flow depth, cross-shore velocity and cross-shore momentum flux at lines A, B, C and D are given in Figure 4.114.

The NRMSE of NAMI DANCE predictions for the overland flow depth at lines A and B is less than the threshold value, which is 10%. The NRMSE is around 15 % along line C, whereas it increases up to 30% along line D. FLOW-3D[®] predicts the overland flow depth along lines A, B and C with an NRMSE less than 10%. However, along line D, the numerical model overestimated the values with an NRMSE of approximately 25%.

The NRMSE of NAMI DANCE results regarding the cross-shore velocity ranges between 17% and 29%, with the largest at C9 location and along line D. FLOW-3D[®] predictions have the same trend as NAMI DANCE results, having an NRMSE range between 9% and 25%.

In the case of specific momentum flux, with the exception of line D which measured around 50% for both model results, most values are less than 20%. Overall, with the exception of line D, and line A for velocity, the NRMSE is less than 10%. The NRMSE for line D is relatively large. This anomaly may be attributed to the difference in the measurement locations. In the experimental model, the gauges along lines A, B, and C are located on the road, with no obstructions between the locations and the ocean, while along line D the gauges are situated mostly behind the buildings. The discrepancy between lines A, B and C and line D may be caused by the inherent difficulty of generating an energy dissipation process which includes turbulence in the numerical model, as the broken wave passes around the buildings. These results also coincide with the work of Park et al. (2013).

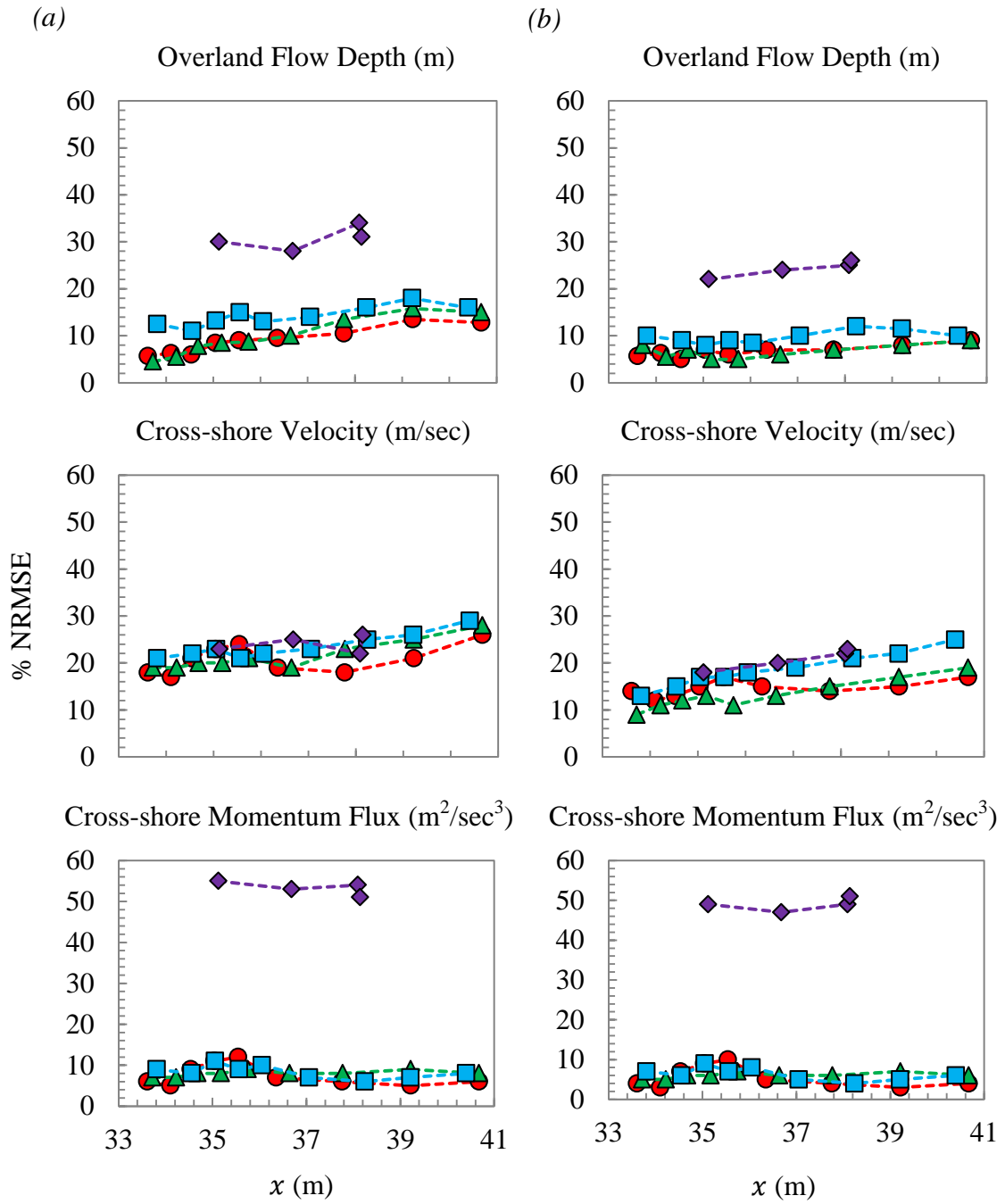


Figure 4.114 NRMSE of (a) NAMI DANCE; (b) FLOW-3D[®] predictions along lines A, B, C, and D. The circles, triangles, squares and diamonds represent the predictions along lines A, B, C and D, respectively.

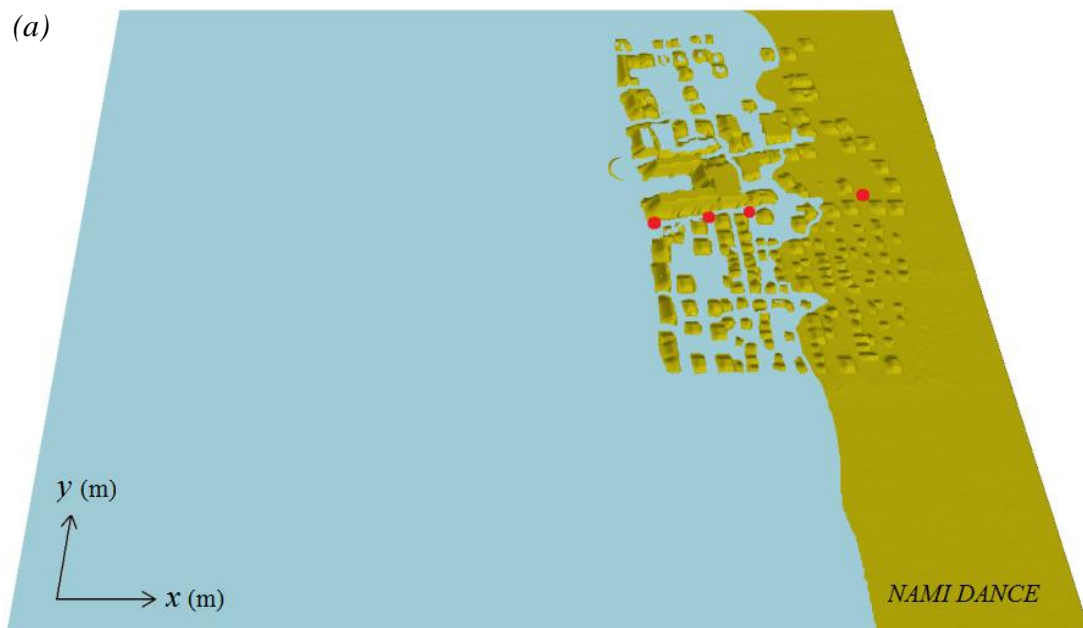


Figure 4.115 Snapshots of (a) NAMI DANCE; (b) FLOW-3D[®] simulations at time $t = 30$ sec. The red points correspond to gauges B1 through B9 where the model predictions are compared with the observations.

Figure 4.115 illustrates the snapshots of the NAMI DANCE and FLOW-3D[®] simulations at time $t = 30$ sec, which are performed to exhibit the inundation pattern, overtopping of some buildings, and the generation of many small waves within the flow.

To sum up, the majority of the previous benchmark tests for inundation models typically compare a time series of free surface elevation or maximum runup height. However, in BMP 5, the time series and maximum values of overland flow depth, cross-shore velocity and cross-shore momentum flux are extracted from the numerical models and directly compared with the physical model results for model verification.

It is found that the overland flow depth, cross-shore velocity and cross-shore momentum flux are very sensitive to bottom friction, as expected. The arrival time of the inundation wave is earlier and the leading velocity is larger as the friction factor is decreased. The maximum cross-shore momentum flux is considerably reduced as the friction factor is increased. This fact highlights the importance of comparing velocity terms in the validation and verification of tsunami inundation models as the flow velocity is directly related to the force exerted on the structures.

The results reveal that the general tendencies and magnitudes of predicted overland flow depth and cross-shore velocity are well matched with the physical model results for the locations that are close to the shoreline. In both models, it is observed that the maximum overland flow depth and cross-shore momentum flux rapidly decrease as the wave moves landward, while the cross-shore velocity slowly decreases. Specifically, from B1 to B9, the maximum overland flow depth decreases by 77%, the maximum cross-shore velocity decreases by 30% and the maximum momentum flux decreases by 97% in the physical model. Both numerical models succeed in catching the same trend.

The comparison of the predicted and recorded water level dynamics at the control point, i.e. $x = 18.618$ m, reveals that both models reproduce and transform the incident wave very well. The largest discrepancies between the numerical simulations and laboratory experiments occur during the inundation stage. Although both models manage to predict the maximum overland flow depth at locations B4 and B6, they underestimate the maximum water level at locations B1 and B9. In order to determine the reason for the mismatch between the simulations and measurements at the onland gauges along line B, an attempt is made to conduct an analysis of the free surface elevation time histories in the seaward direction from location B1. However, as the number of measurements near the coastline is not large enough to provide data about where/how the dynamics of the simulated wave diverged from that observed, the idea of this analysis is dropped.

According to the measurements of the cross-shore velocities at B1, B4, B6 and B9, the 2D depth-averaged model NAMI DANCE predicts the cross-shore velocity approximately 20% less than the 3D model FLOW-3D[®]. The FLOW-3D[®] results are in considerably good agreement with the laboratory measurements. The model is able to predict the maximum cross-shore velocity accurately and follows a similar trend with the laboratory data. This is where the importance of vertical velocity component steps in. It is reasonable to conclude that w is an important parameter in tsunami inundation calculations and should be considered in order to reflect real life data as well as possible.

4.6. BMP 6: 2011 Tōhoku Tsunami in Hilo Harbor, Hawaii

4.6.1. Problem Description

On 11 March 2011, the M_w 9.0 Tōhoku earthquake, also known as Great East Japan earthquake, generated a devastating nearfield tsunami across the northeastern Japan coasts with up to 39.75 m of runup (Mori et al., 2011), causing localized damage to coastal infrastructure across the Pacific (Figure 4.116).

A warning was issued by the Pacific Tsunami Warning Center for Hawaii and coastal residents and marine vessels were evacuated. The waves reached Hawaii 7 hours after the earthquake. The surges did not stop for another day, creating strong hazardous currents around the islands and causing harbors and marinas to be closed for up to 38 hours. Hilo Harbor, for instance, experienced a mix of 15 min and 30 min oscillations (Allan et al., 2012; Lynett et al., 2013).

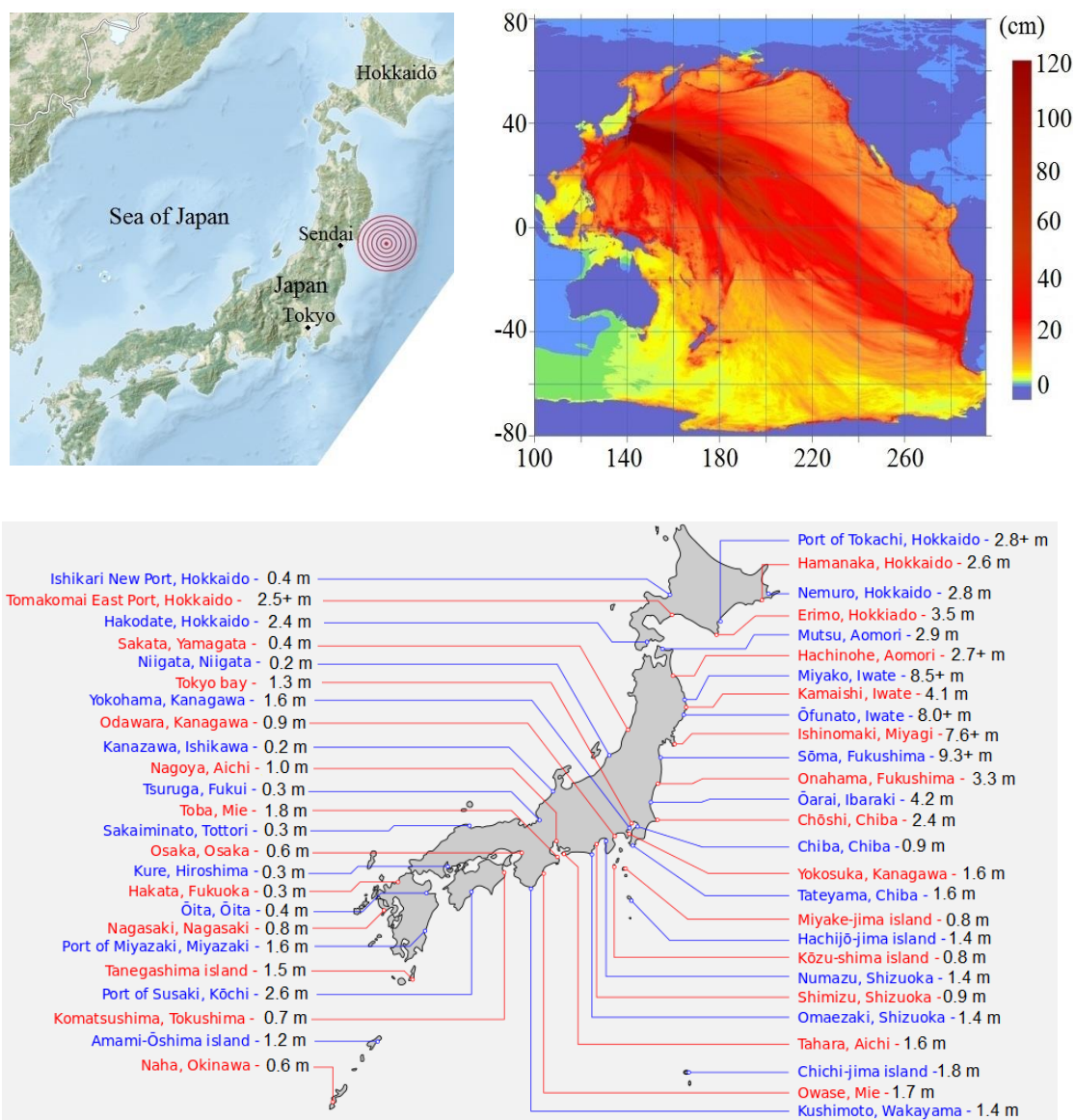


Figure 4.116 (a) The epicenter of 2011 Tōhoku earthquake; (b) contours of maximum wave amplitudes, detailing tsunami energy propagation (Credit: NOAA); (c) the maximum tsunami heights observed after 2011 Tōhoku earthquake (Credit: Wikipedia)

During the 11 March 2011 Tōhoku tsunami, the 328 current meters that had been placed around the islands of Hawaii recorded the time series of the fluid velocity at varying depths of water within the water column at 18 different locations (stations) (Lynett et al., 2014) (Figure 4.117 and Table 4.28).

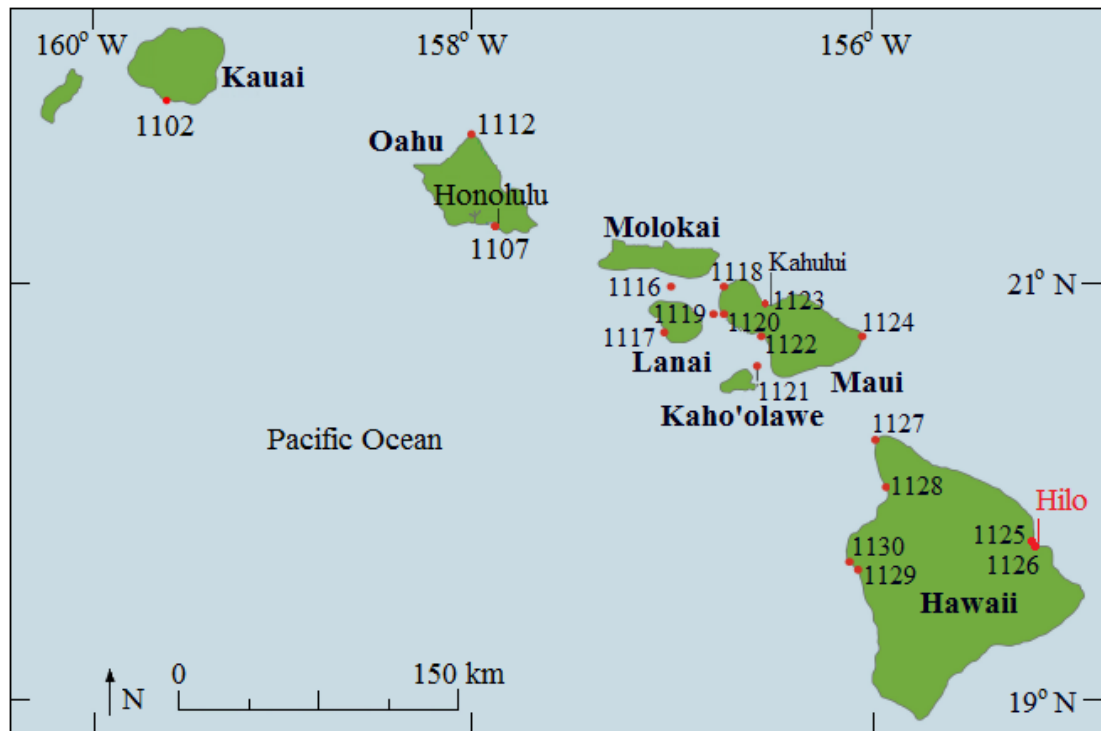


Figure 4.117 Location of current velocity meter stations deployed around Hawaii, including the two stations at Hilo Harbor, which are used in BMP 6 (Cheung et al., 2013; Arcos and LeVeque, 2014)

Table 4.28 The identifications and depths of current meters at observation stations
(Arcos and LeVeque, 2014)

Station ID	Station Name	Lat ($^{\circ}$)	Long ($^{\circ}$)	Number of Current Meters	Depth at Station (m)	Max. Observed Velocity (m/sec)
HA1102	Port Allen	21.896	200.408	6	12.56	1.62
HA1107	Approach to Honolulu Harbor	21.292	202.126	11	14.90	0.39
HA1112	Kahuku Point	21.730	202.010	26	67.37	0.81
HA1116	Kalohi Channel	21.003	203.041	22	105.60	Tsunami within background currents
HA1117	Kaumalapau Harbor	20.785	203.008	12	19.62	Tsunami within background currents
HA1118	Haweia Point	21.002	203.308	34	83.69	0.51
HA1119	Auau Channel East Side	20.867	203.253	29	73.51	0.43
HA1120	Lahaina	20.869	203.315	14	20.48	0.52
HA1121	Alalakeiki Channel	20.613	203.492	28	153.98	0.76
HA1122	Maalaea Bay	20.765	203.508	18	49.83	0.41
HA1123	Kahului Harbor	20.902	203.528	8	14.02	1.84
HA1124	Hana Bay	20.761	204.022	14	21.19	0.24
<i>HA1125</i>	<i>Approach to Hilo Harbor</i>	<i>19.745</i>	<i>204.918</i>	<i>15</i>	<i>19.29</i>	<i>0.70</i>
<i>HA1126</i>	<i>Hilo Harbor</i>	<i>19.742</i>	<i>204.930</i>	<i>9</i>	<i>12.46</i>	<i>1.04</i>
HA1127	Upolu Point	20.265	204.098	27	72.10	Tsunami within background currents
HA1128	Kawaihae Entrance	20.041	204.158	17	41.74	0.37
HA1129	Kailua Kona	19.635	204.000	17	20.48	0.35
HA1130	Honokohau	19.668	203.968	21	56.60	Tsunami within background currents

The data recorded in the velocity meters are direct measurements of the 2011 Tōhoku tsunami, which makes them very valuable in tsunami research. Moreover, compared to many previous studies, they provide information about a much wider range of bathymetric conditions including open coastline, deep channels and harbors. The effect of the 2011 Tōhoku tsunami on Hawaiian Islands was discussed in many studies. Yamazaki et al. (2012) made velocity comparisons at the Kilo Nalu Observatory near Honolulu Harbor, Cheung et al (2013) made comparisons for all the velocity meter stations around the island, and Arcos and LeVeque (2014) compared several velocity records around the Hawaiian Islands.

The instrumentally recorded data sets from the 2011 Tōhoku tsunami were of perfect quality and coverage so they contributed greatly to model validation and scientific research. BMP 6 introduces a part of this data set from the recordings at Hilo Harbor. The modern town of Hilo, which is the largest settlement in Hawaii County, overlooks the Hilo Bay (Figure 4.118).



Figure 4.118 Hilo Bay and the town of Hilo in 1929, the year when the breakwater was completed (Credit: Wikipedia)

Because of its topography, Hilo Bay has been hit by tsunamis resulting from the earthquakes in active areas such as Chile and the Aleutian Islands several times, making it known as the *the tsunami capital of the United States*. 96 people were killed when the tsunami from the 1946 Aleutian Islands earthquake struck Hilo Bay. A tsunami following the 1960 Valdivia earthquake hit Hilo Bay on May 20 and killed 61 people. After the February 27, 2010 Chile earthquake, tsunami warnings were made. Fortunately, no one was injured.

To provide a clear understanding of the location of Hilo Harbor, aerial views of the study area are provided in Figure 4.119.

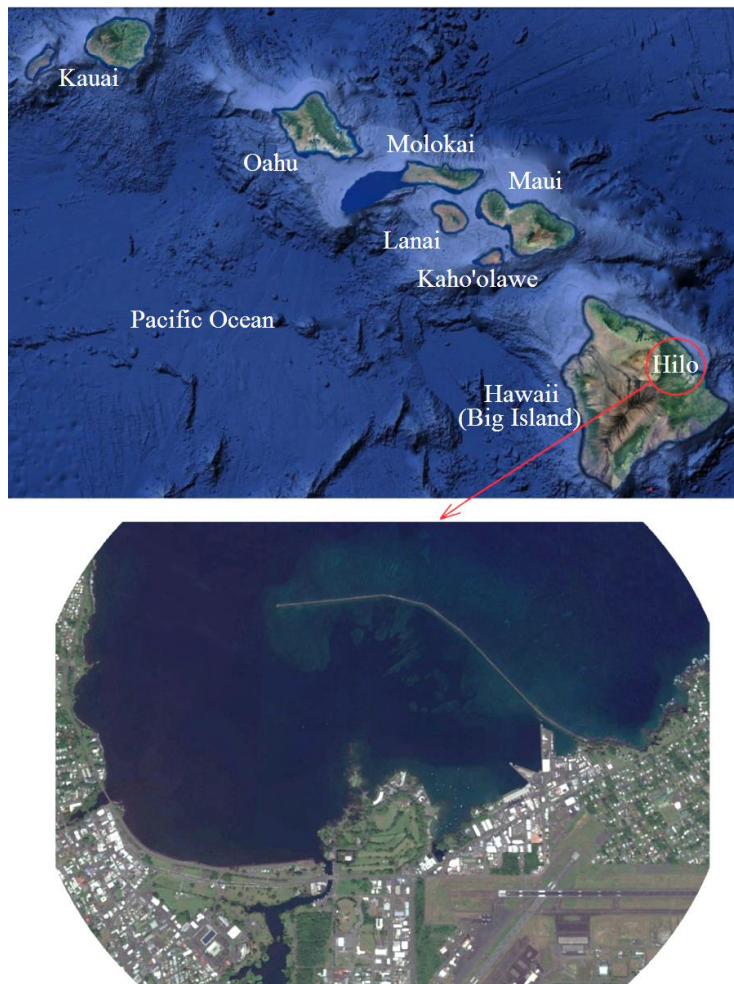


Figure 4.119 Google Earth images of Hawaiian Islands and Hilo Harbor

The 2011 Tōhoku tsunami caused no significant inundation as it propagated across the Hawaiian Islands yet, the surges it created over insular shelves, nearshore reefs and harbors were energetic and persistent (Cheung et al., 2013). Strong currents driven by the surges were recorded at the semi-enclosed Hilo Harbor by two NOAA Acoustic Doppler Current Profilers (ADCPs) at 6-min sampling intervals. The data from those two NOAA ADCPs and from the local tidal gauge provide the BMP 6 data set. BMP 6 is a field benchmark problem and is Benchmark Problem 2 of the 2015 National Tsunami Hazard Mitigation Program (NTHMP) workshop, which was held in Portland, U.S.

The case in BMP 6 is idealized to a certain extent to reduce its complexity by isolating the differences in the employed incident wave forcing so that the best modeling results are obtained. The *reduction* is realised as a flattening of the bathymetry at a depth of 30 meters. In other words, in the offshore portion of the bathymetry grid, there are no depths greater than 30 m. The bathymetry data is provided in (lat, long) on a 1/3 arcsec grid (Figure 4.120).

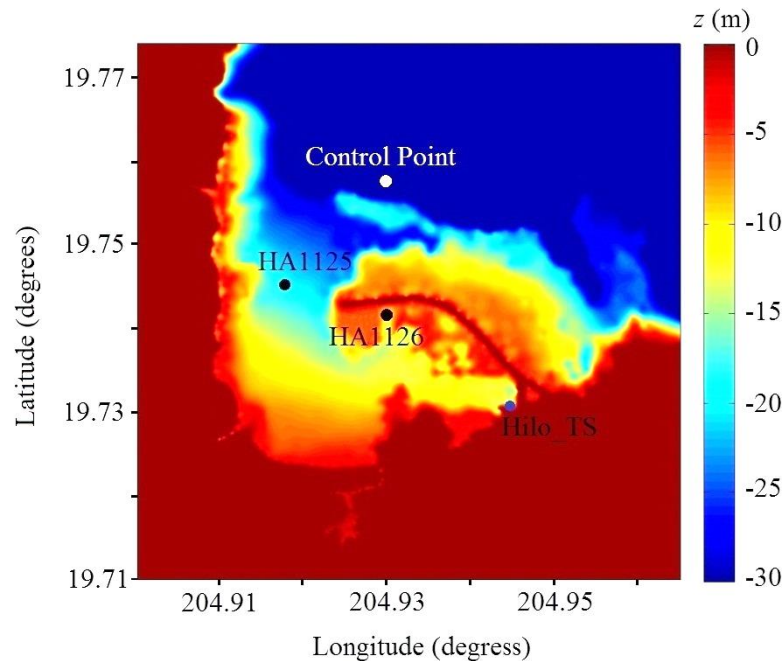


Figure 4.120 The bathymetry of Hilo Harbor. The white dot represents the control point, the black dots are the two ADCP locations and the blue dot is the Hilo tide station (NTHMP, 2015).

In BMP 6, the free surface elevation time series from the Hilo tide station and the velocity information from the two ADCPs, namely HA1125 and HA1126 are to be compared and reliable agreements with the measured data are to be achieved. However, the primary goal is to understand the importance of model resolution and numerics on the prediction of currents.

The Hilo tide station (Hilo_TS) is located at (lat, long) = (19.731, 204.945). *The simulated data at the Hilo tide station is shifted to match the measured tide station data such that the leading numerical wave arrives at the proper time. This time shift is also used in the velocity comparisons.*

The first ADCP, HA1125, is located at the Hilo Harbor entrance, at (lat, long) = (19.745, 204.918). The second ADCP, HA1126, is located inside the Hilo Harbor, at (lat, long) = (19.742, 204.930). Here, it is important to note that *the data recorded at the ADCPs are averaged over depth and filtered to remove the long period tidal components.*

In BMP 6, the simulations are driven with an offshore simulated free surface elevation time series which is supposed to be located at (lat, long) = (19.758, 204.930) (i.e. Control Point) (Figure 4.121).

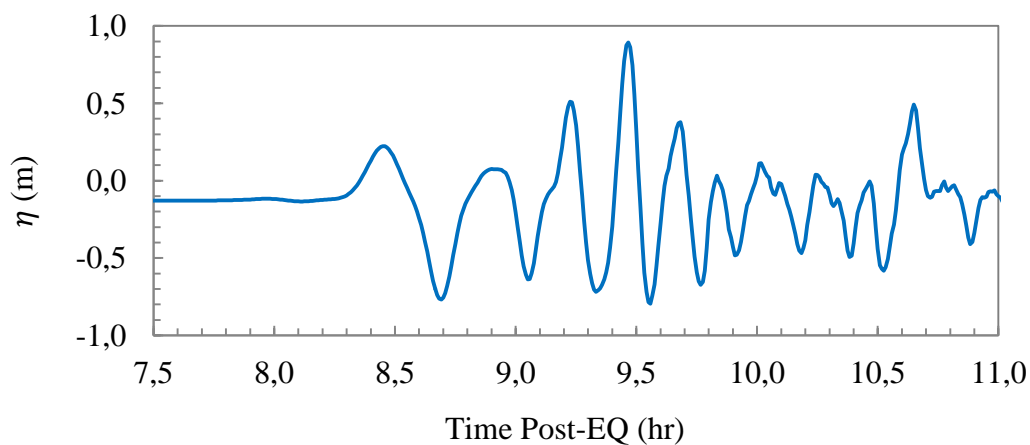


Figure 4.121 The incident wave of BMP 6: time series of ocean surface elevation at Control Point (NTHMP, 2015)

BMP 6 can be simulated in any of the following ways: *i*) through upper grid boundary, *ii*) with an internal source generator in the northern part of the domain or *iii*) from source to Hilo harbor with nesting (simulation of the complete problem). For all the conditions above, the modeled time series has to be checked at the control point to ensure that the proper offshore wave conditions are generated.

It is required that BMP 6 be simulated in three different numerical configurations: *i*) at ~20 m resolution (2/3 arcsec), using a Manning's roughness coefficient of 0.025 (or approximate equivalent if using a different bottom stress model), *ii*) at ~10 m (1/3 arcsec) resolution using a Manning's roughness coefficient of 0.025 (or approximate equivalent if using a different bottom stress model) and *iii*) at 5 m resolution (1/6 arcsec, or the lowest resolution possible), using a Manning's roughness coefficient of 0.025 (or approximate equivalent if using a different bottom stress model). The simulation results are to be compared locally and also the statistical measures of spatial variability should be examined. The simulation time is determined as 13.5 hours in order to capture the resonance oscillations around the Hawaiian Islands during the crucial initial hours of the event.

4.6.2. NAMI DANCE Model

The computational domain of NAMI DANCE is the full geographic footprint of the 1/3 arc second benchmark bathymetry at longitude $204.901^\circ \leq x \leq 204.965^\circ$ and latitude $19.710^\circ \leq y \leq 19.774^\circ$. The x axis of the Cartesian coordinate system is parallel to the Hilo breakwater and the y axis is perpendicular to the wave propagation direction (Figure 4.122). The gravitational force, g , is in the downward direction.

BMP 6 bathymetry is automatically converted from the geographic coordinate system to Universal Transverse Mercator coordinate system (UTM) by FLOW-3D[®]. When the NAMI DANCE model is run with the UTM coordinates to ensure consistency, the results are found to be exactly the same. The geographic coordinate system is favoured in the simulations performed via NAMI DANCE.

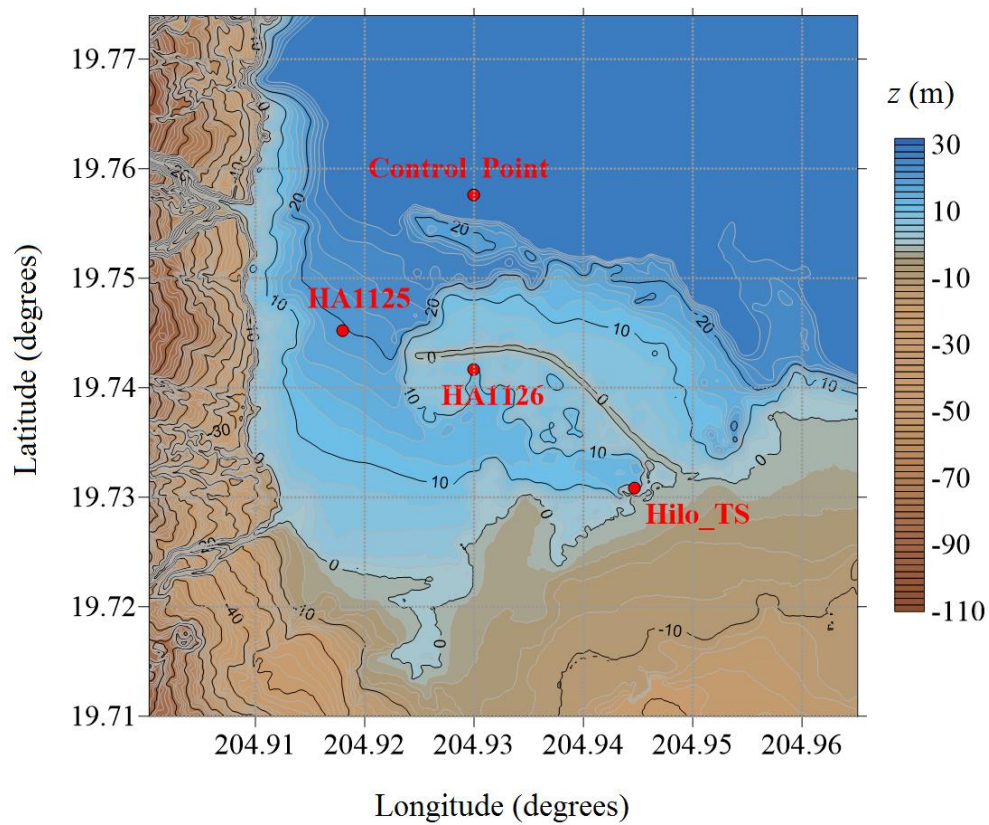


Figure 4.122 NAMI DANCE computational domain for BMP 6

Figure 4.123 illustrates the 3D view of NAMI DANCE computational domain.



Figure 4.123 3D top view of NAMI DANCE computational domain for BMP 6

The offshore simulated time series at the Control Point is inputted through the northern grid boundary, i.e. maximum y boundary. The simulation results are shifted by -17 min to match the measured tide station data.

4.6.2.1. Spatial Discretization

The results of the simulations with different spatial grid resolutions are compared to identify the grid resolution effect. The numerical modeling of BMP 6 is carried out at 5 m, 10 m and 20 m grid resolutions with a Manning's roughness coefficient of 0.025, which is the recommended value for the analysis of this benchmark problem. The computed and measured time series of the water surface elevation at the Hilo tide station are compared. The *average flow speeds* recorded at the two ADCP locations, HA1125 and HA1126, are also compared with the predictions.

The grid refinement study shows reasonable self-consistent overall convergence of the results, going down from a 20 m resolution to a 10 m one and then a 5 m one (Figure 4.124). The average flow distribution computed with the three different cell sizes consistently displays the same flow pattern. The maxima of the predicted average flow speed is 0.7 m/sec at 20 m resolution, 0.81 m/sec at 10 m resolution, and 0.85 m/sec at 5 m resolution at HA1125 and, at HA1126, 0.9 m/sec, 1.05 m/sec and 1.1 m/sec at 20, 10 and 5 m resolutions, respectively.

The time step, Δt , is selected as 0.25 second, which satisfies the stability condition for the NAMI DANCE solutions. Different time steps are also tested; however, no significant change is observed in the numerical predictions.

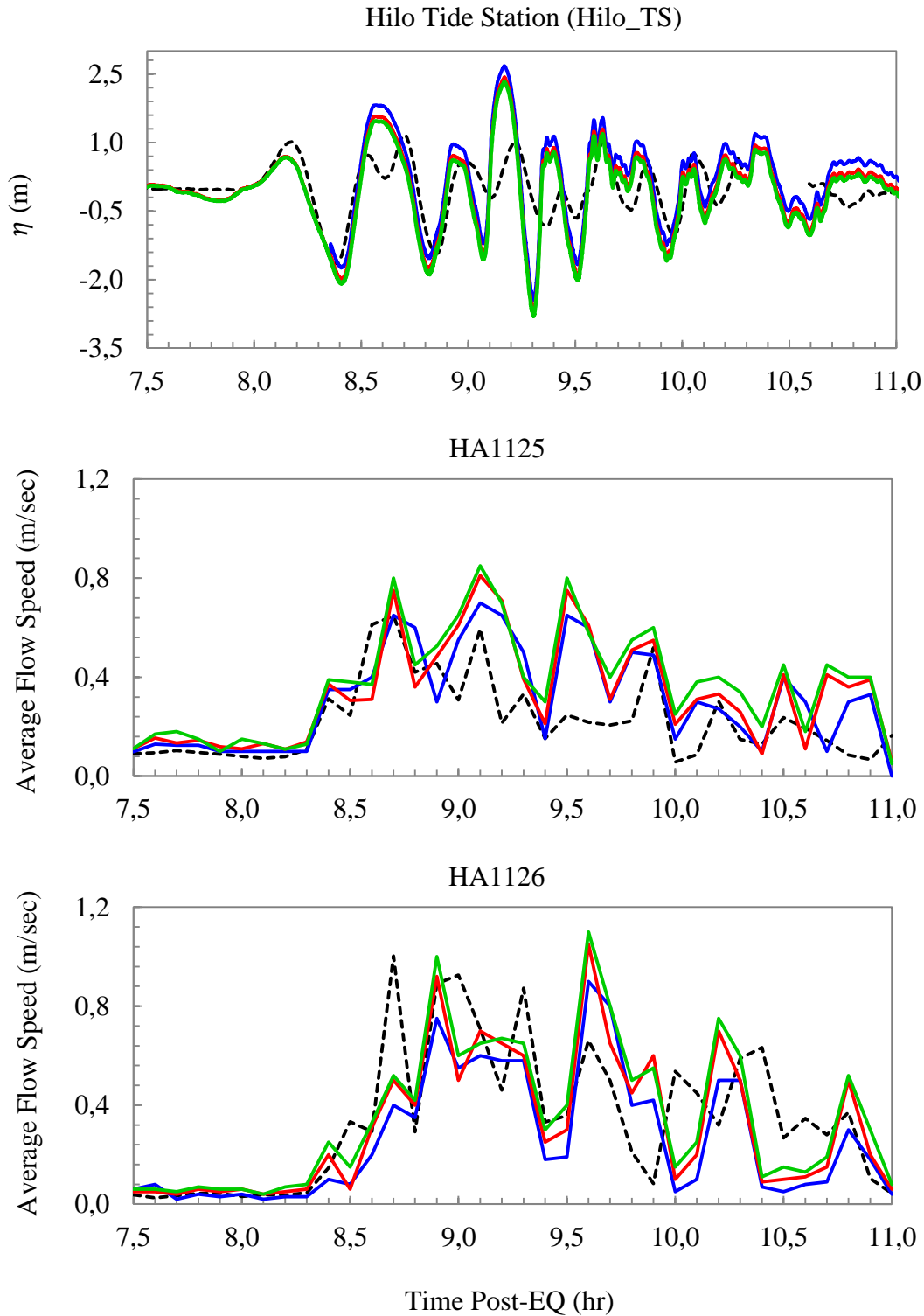


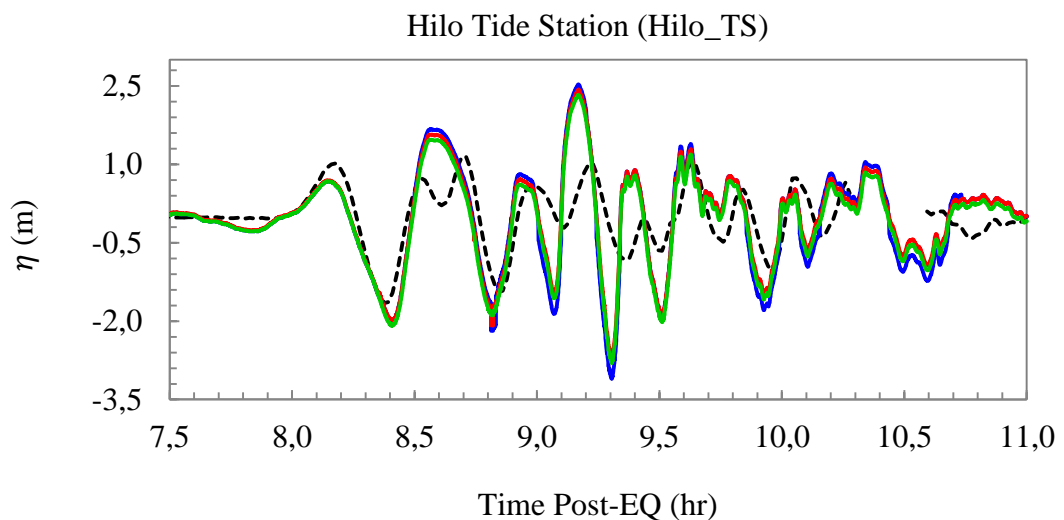
Figure 4.124 NAMI DANCE convergence test for BMP 6 at: (a) Hilo tide station; (b) HA1125; (c) HA1126. The dashed black line represents the field data; the solid blue, red and green lines represent the numerical predictions for $\Delta x = 20$ m, $\Delta x = 10$ m, and $\Delta x = 5$ m, respectively.

Evidently, the accuracy of the numerical predictions depends on the grid resolution in the areas with high vorticity concentration. As the grid resolution decreases, finer details of the flow pattern appear around the breakwater head in the form of small eddies. On the other hand, at the ADCPs, the sensitivity of the model predictions to the grid size is less due to either the ADCP locations away from the main vorticity sources or the low sampling intervals. Overall, the results reveal that 10 m grid resolution, i.e. $\Delta x = 10$ m, is sufficient for the convergence of the results and provides good fits to the measured data.

4.6.2.2. Friction

The results of simulations with different roughness coefficients are compared to identify the effect of friction. Figure 4.125 shows the comparisons of the computed free surface elevation at the Hilo tide station and the average flow speeds at the two ADCPs, HA1125 and HA1126, with the measured data, with Manning's roughness coefficients of: (i) $n = 0$ (i.e. frictionless bottom), (ii) $n = 0.015$ and (iii) $n = 0.025$ at 10 m grid resolution.

It is found that the effect of varying friction is very limited and only slightly felt in the maximum and minimum values of the time series in the current speed and surface elevation (Figure 4.126).



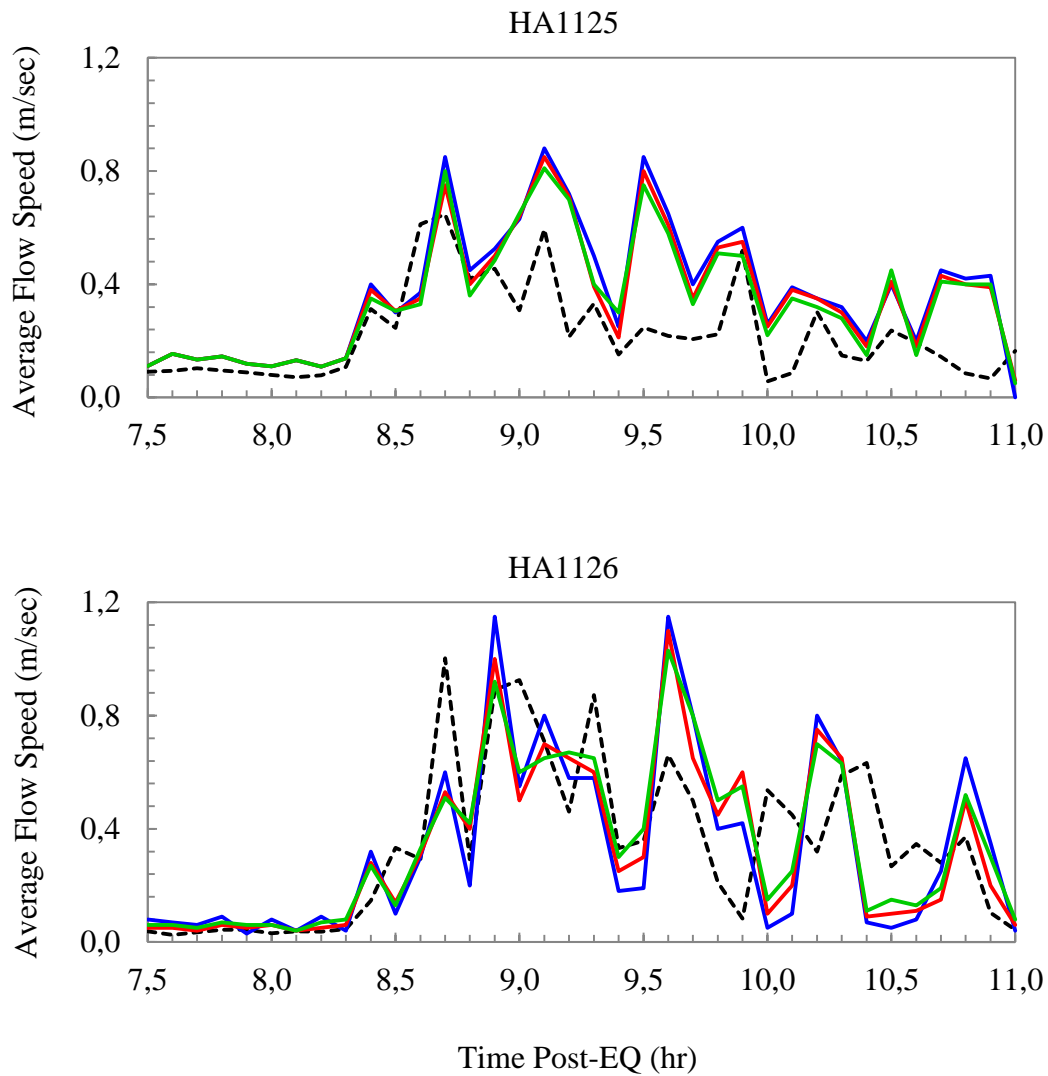


Figure 4.125 NAMI DANCE results according to different Manning's roughness coefficients at: (a) Hilo tide station; (b) HA1125; (c) HA1126. The dashed black line represents the measured data; the solid blue, red and green lines represent the NAMI DANCE predictions when $n = 0$, $n = 0.015$ and $n = 0.025$, respectively.

4.6.3.FLOW-3D[®] Model

The approximate dimension of the FLOW-3D[®] computational domain is 6770 m by 6680 m (Figure 4.126).

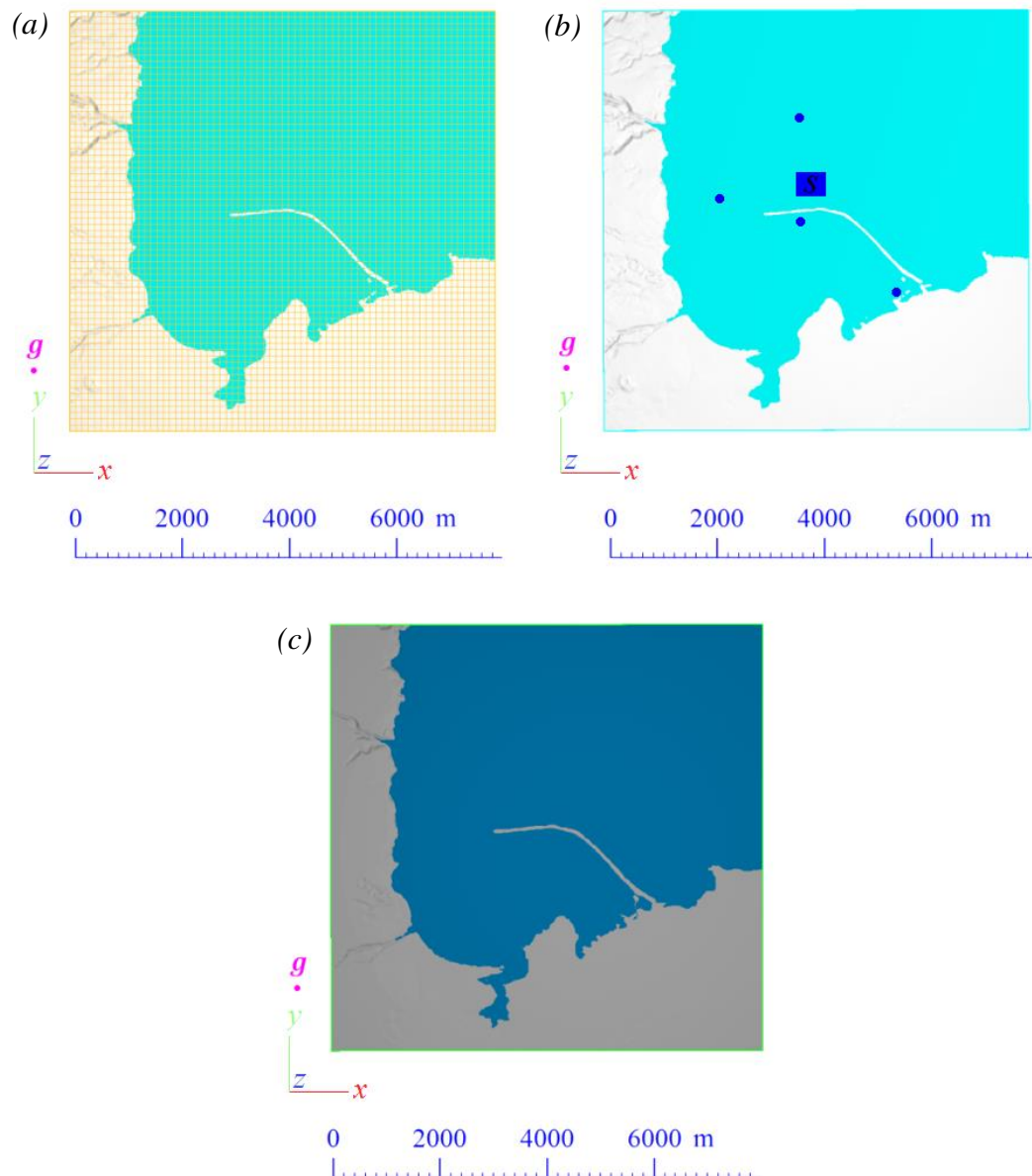


Figure 4.126 FLOW-3D[®] computational domain constructed for BMP 6: (a) meshing (enlarged for clarity); (b) boundary conditions and gauge locations; (c) after using FAVOR[™]

4.6.3.1. Spatial Discretization

In order to simulate BMP 6 efficiently, it is necessary to model the Hilo breakwater and cliffs around Hilo Harbor properly. To achieve this, the FAVOR™ module of FLOW-3D® is used in order to see whether the topography is modeled accurately enough. The numerical modeling of BMP 6 is carried out at 8 m, 10 m and 20 m grid resolutions with a Manning's roughness coefficient of 0.025. The computed and measured time series of the water surface elevation at the Hilo tide station are compared. The *average flow speeds* recorded at the two ADCP locations, HA1125 and HA1126, are also compared with the predictions.

The results show that a 20 m grid resolution is not adequate to accurately model the Hilo topography in FLOW-3D®. On the other hand, proper modeling of the study domain is possible with a 10 m resolution. Minimal difference is seen in the results using a high resolution grid, i.e. 8 m. It is important to note that employing a resolution higher than 8 m is not possible due to the computational constraints of the 3D model for this size of domain. There is not much difference between the predictions made with 8 m and 10 m resolutions; therefore, no significant difference is expected for a higher resolution simulation.

It is also necessary to analyse the effect of the vertical grid size, Δz , on the simulations in a three-dimensional model. When the grid size is decreased from 10 m to 8 m with constant Δx , the results are the same as those obtained when the horizontal grid size is changed. It is preferred to use a uniform grid size along the computational domain, i.e. $\Delta x = \Delta y = \Delta z = 10$ m.

The grid refinement study shows reasonable self-consistent overall convergence of the results, going from a 10 m to a 8 m resolution (Figure 4.127). The simulation which is carried out using a 20 m grid size does not provide accurate predictions of the average current speeds at HA1125 and HA1126 stations. For finer grid resolutions, however, a very well agreement is achieved.

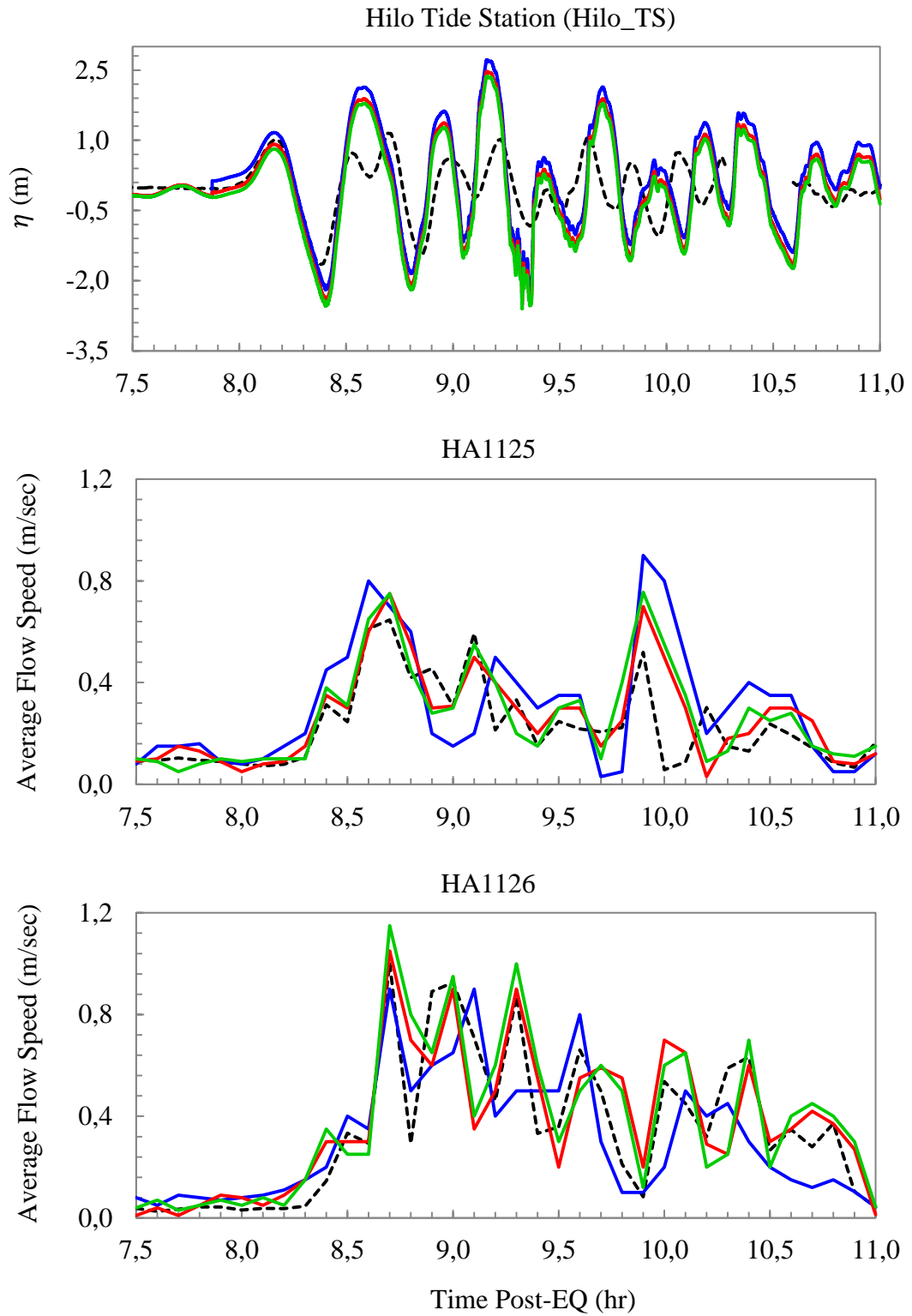


Figure 4.127 FLOW-3D[®] convergence test for BMP 6 at: (a) Hilo tide station; (b) HA1125; (c) HA1126. The dashed black line represents the field data; the solid blue, red and green lines represent the numerical predictions for $\Delta x = 20$ m, $\Delta x = 10$ m, and $\Delta x = 8$ m, respectively.

The average flow distribution computed with the 8 m and 10 m cell sizes consistently displays the same flow pattern. The maxima of the predicted average flow speed is 0.9 m/sec at 20 m resolution, 0.75 m/sec at 10 m resolution, and 0.76 m/sec at 8 m resolution at HA1125 and, at HA1126, 0.9 m/sec, 1.05 m/sec and 1.15 m/sec at 20, 10 and 8 m resolutions, respectively.

The results indicate that the grid size is effective in the areas with high vorticity concentration. Similar to the NAMI DANCE results, the FLOW-3D[®] results show that, with the decrease of the grid size, finer details of the flow pattern appear around the breakwater head in the form of small eddies. The model results at the ADCPs are less sensitive to the grid size due to either the ADCP locations away from the main vorticity sources or the low sampling intervals. Overall, the results are consistent with the NAMI DANCE simulations and reveal that a 10 m grid resolution, i.e. $\Delta x = 10$ m, is sufficient for the convergence of the results, which agree well with the measured data.

The time step, Δt , is selected as 0.25 second to be consistent with the simulations conducted using NAMI DANCE. When variable time stepping is employed in order to assess the effect of the time step size, no significant effect is observed.

4.6.3.2. Friction

The effect of friction is investigated through the application of different roughness coefficients to the BMP 6 numerical model. Figure 4.128 shows the comparisons of the computed free surface elevation at the Hilo tide station and the average flow speeds at the two ADCPs, HA1125 and HA1126, with the measured data, with Manning's roughness coefficients of: (i) $n = 0$ (i.e. frictionless bottom), (ii) $n = 0.015$ and (iii) $n = 0.025$ at 10 m grid resolution.

The results support the findings of NAMI DANCE simulations and indicate that the effect of varying friction is slightly felt in the surface elevation and in the maximum and minimum values of the time series in the current speed (Figure 4.128).

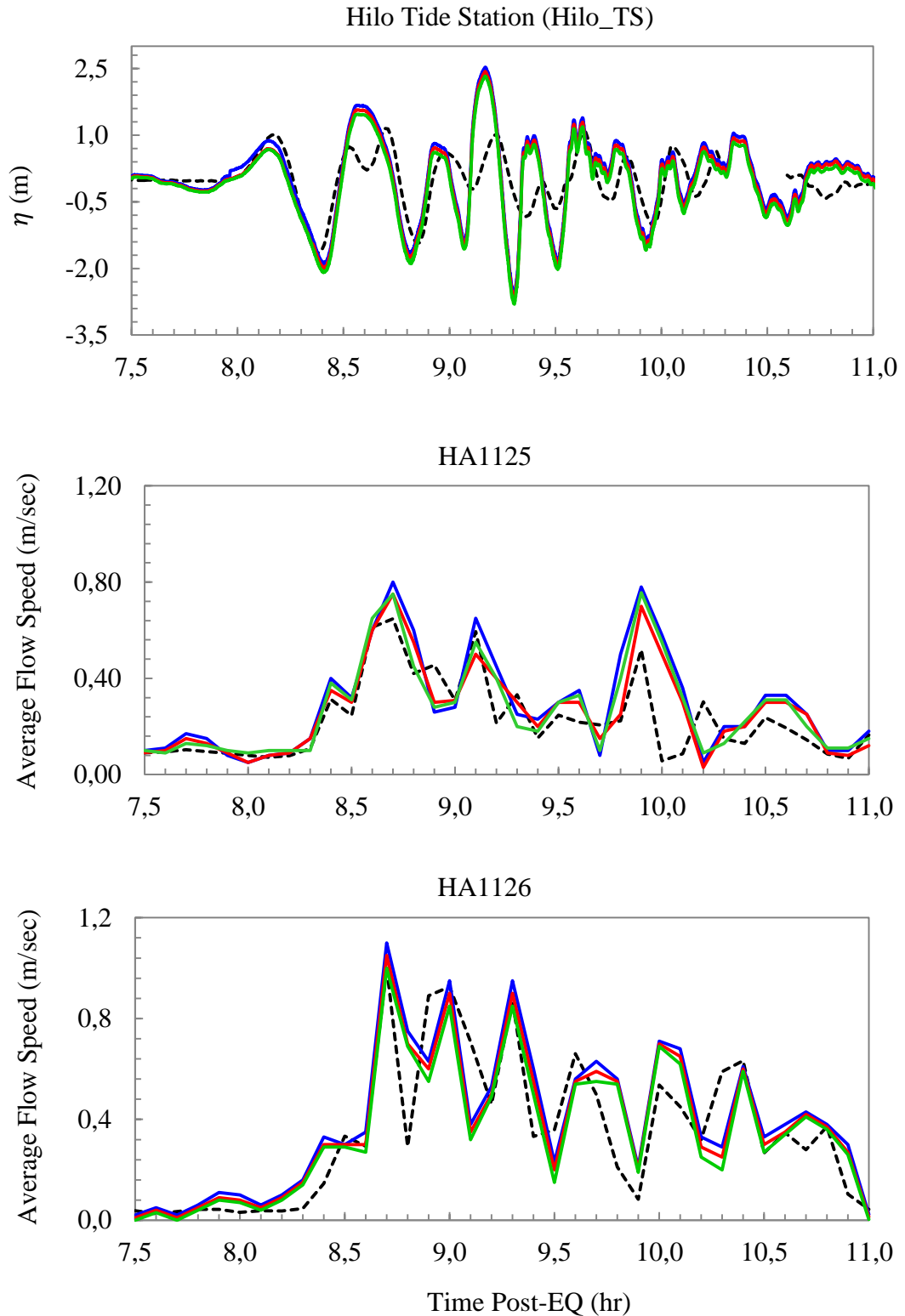


Figure 4.128 FLOW-3D[®] results according to different Manning's roughness coefficients at:
 (a) Hilo tide station; (b) HA1125; (c) HA1126. The dashed black line represents the measured data; the solid blue, red and green lines represent the FLOW-3D[®] predictions when $n = 0$, $n = 0.015$ and $n = 0.025$, respectively.

4.6.4. Simulation Results

The grid resolution is taken as 10 m and Manning's roughness coefficient, n , is set to 0.025 as recommended for the following inter-model analyses. In addition, the maximum tsunami current maps are constructed for each model for a 10 m grid resolution. It is important to note that strong vortex shedding creates vortices that can be quite different at different resolutions (Lynett et al., 2017). In fact, when high resolution simulations are performed, finer details of the flow pattern appear around the breakwater head in the form of small eddies.

The incident wave propagates southward and enters the harbor through a wide entrance, in the middle of which ADCP HA1125 is located. The waves refract and diffract around the breakwater before reaching HA1126 and the Hilo tide station. The reflected waves interact with the subsequent arrivals to produce a complex wave field in Hilo Bay. The three grid resolutions (i.e. 5 m, 10 m and 20 m) give nearly the same surface elevations at the tide gauge and very similar average current speeds at the two ADCPs.

Even though the results indicate that both models follow the same trend regarding the current velocity components, whether the flow spectral content is reproduced correctly can not be decided because of the relatively low sampling rate (6 min) of the velocity measurements. In the spatial discretization and friction analyses conducted previously, before the comparisons are made between the measured and computed free surface elevation time series at the Hilo tide station and the average current speeds at the two ADCPs, the simulated time histories were re-sampled to match the sampling method of the recorded data. No re-sampling is done in the following analyses.

Figure 4.129 illustrates the comparison of the modeled and observed 2011 Tōhoku tsunami dynamics at the Hilo tide station. For both models, the wave crests/troughs agree with each other till $t = 9$ hrs; however, the wave train between $t = 9$ hrs and $t = 9.5$ hrs is overestimated.

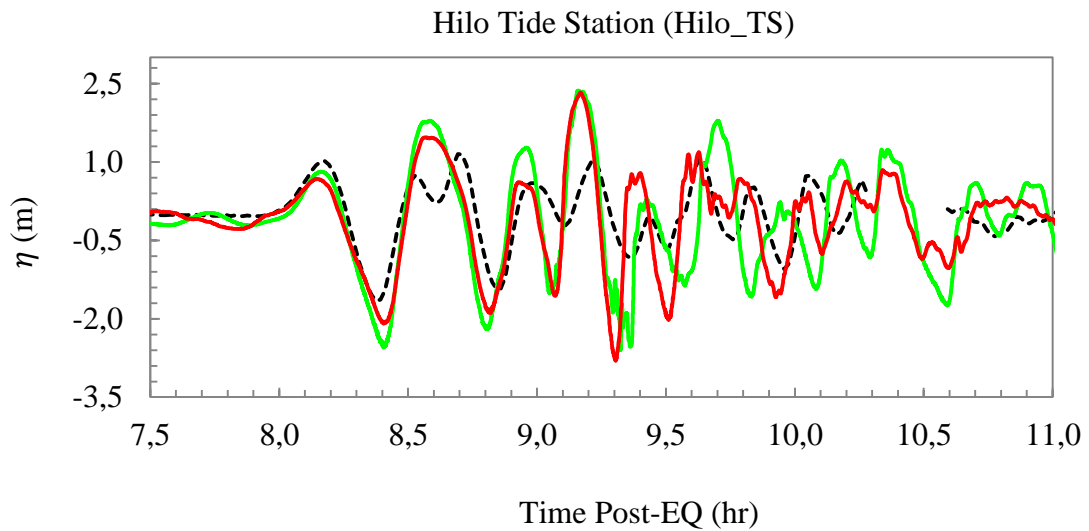


Figure 4.129 Comparison of the free surface elevation time series at Hilo tide station. The dashed black line represents the laboratory measurements; the red line represents the NAMI DANCE results; the green line represents the FLOW-3D[®] results.

The predicted u and v components of current velocities in N – S and E – W directions are favourably compared with their observed counterparts (Figure 4.129). It is seen that the predicted velocity components have lots of fluctuation and thus several maxima/minima after $t = 9$ hrs. These values are not observed in the recorded data. *Because of the coarse time sampling of the tsunami currents during the Tōhoku 2011 event, some peak velocities might be missing in the recorded data.* The sampling of the predicted current velocity components is 3 seconds for both models, while the sampling interval of the recorded velocity data is 6 minutes. This may be the main reason why there is a mismatch between the predicted and recorded velocity values after $t = 9$ hrs.

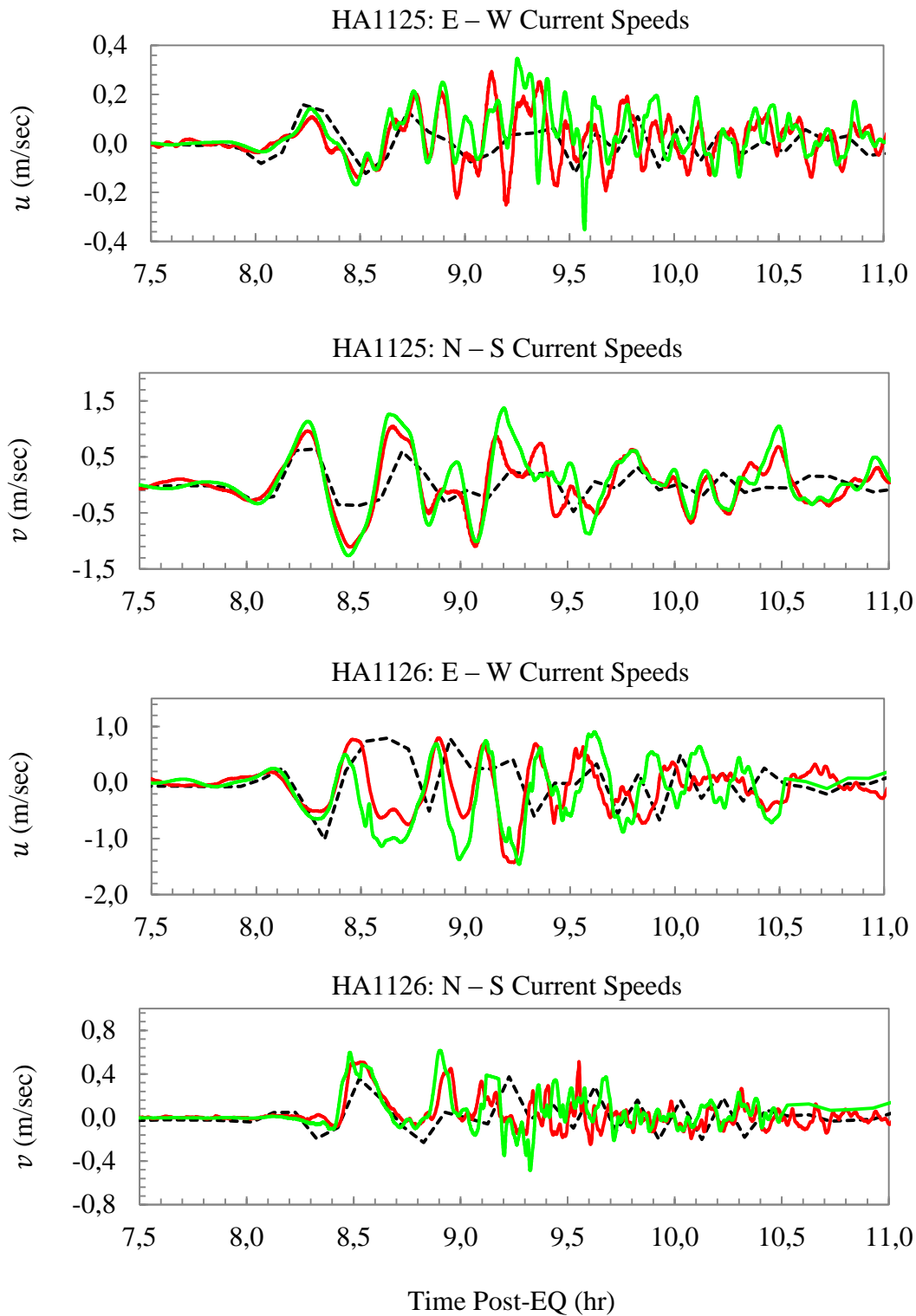


Figure 4.130 Comparison of velocity components in E – W and N – S directions at HA1125, located at the entrance of the Hilo Harbour and at HA1126, located inside the Hilo Harbour. The dashed black line represents the laboratory measurements; the red line represents NAMI DANCE results; the green line represents the FLOW-3D® results.

While time series comparisons are useful for understanding how errors and variations evolve temporally, they do not help to understand how quickly flow properties change spatially. To examine spatial variability, maps for the predicted maximum current distribution are constructed for both models (Figures 4.131 and 4.132). The greatest speeds are found in the area around breakwater head and along the coast where the depths are shallow. In these areas the predicted current speeds are in an excess of 4 m/s. These results are consistent with the findings of the previous studies (Cheung et al., 2013, NTHMP, 2015; Lynett et al., 2017).

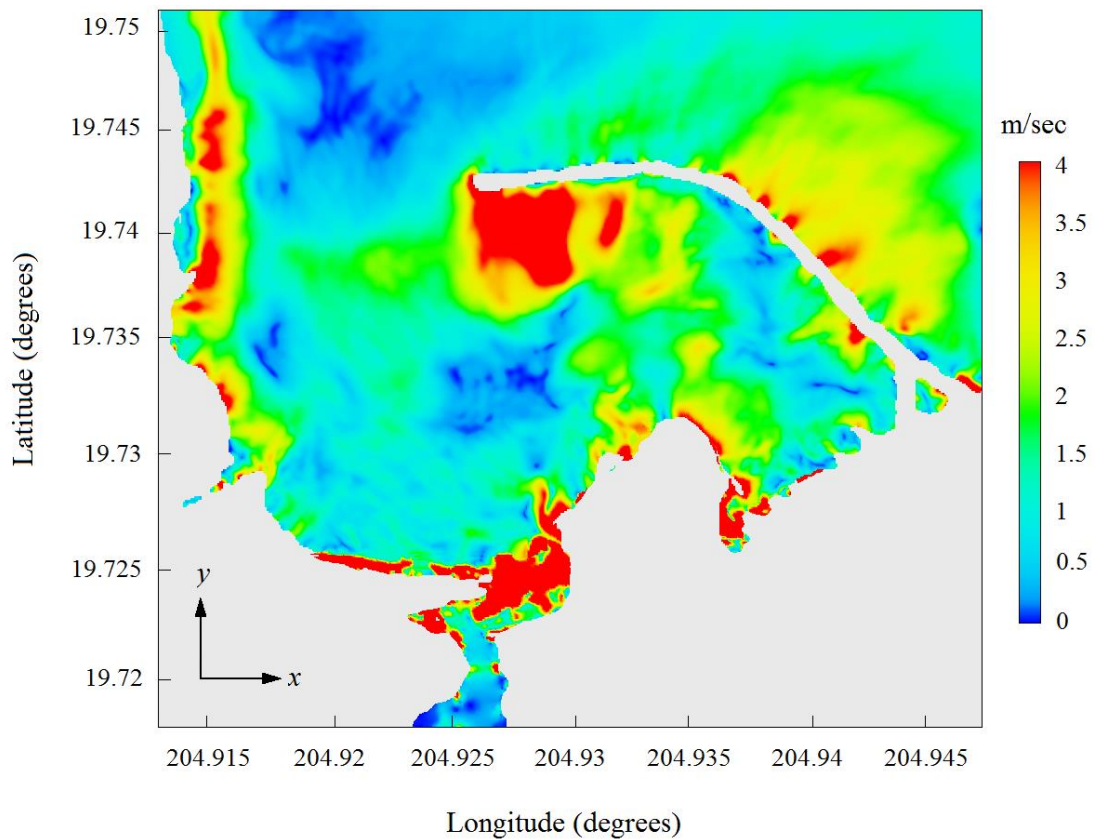


Figure 4.131 The distribution of the computed maximum current speed during the entire duration of the NAMI DANCE simulation. The resolution of computational domain is 10 m.

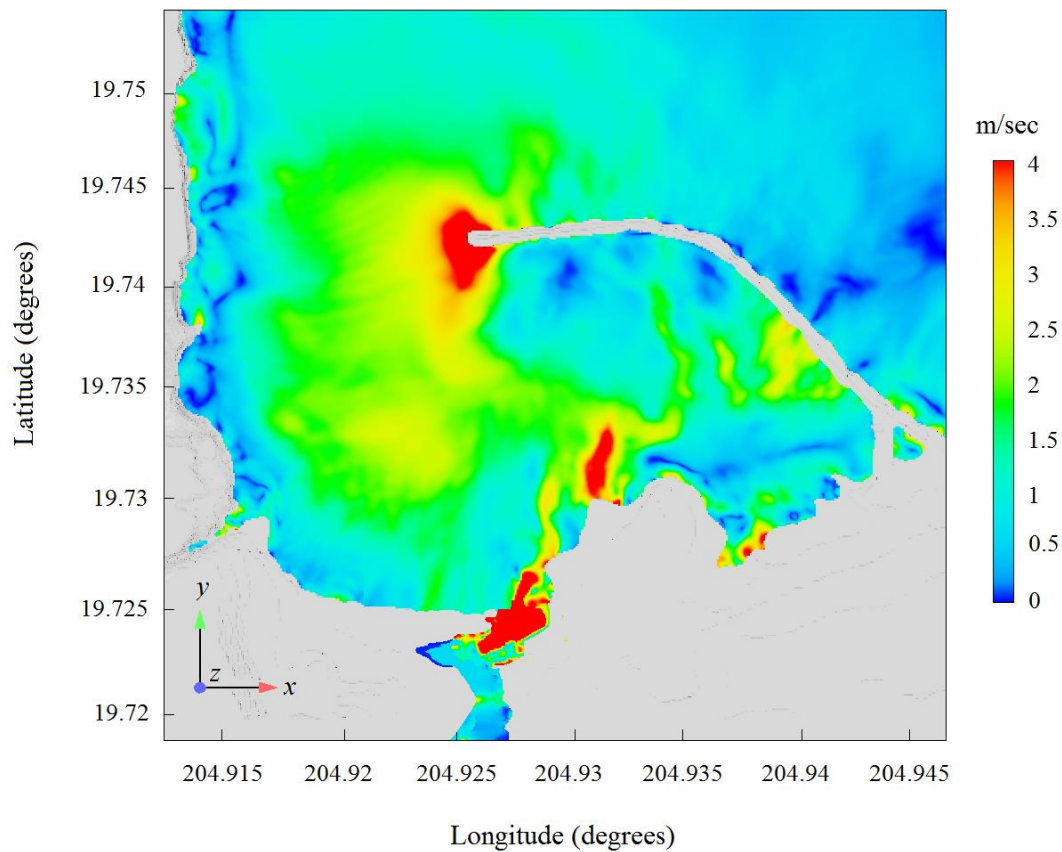


Figure 4.132 The distribution of the computed maximum current speed during the entire duration of the FLOW-3D[®] simulation. The resolution of computational domain is 10 m.

As stated in Chapter 4, Table 4.1, the allowable error thresholds vary according to the reference data types. BMP 6 provides field data, for which the allowable NRMSE and MAX limits are 25% and 20%, respectively, for free surface elevation time series according to the OAR PMEL-135 standard. At present, no allowable error threshold is provided for the recorded velocity values in the field. Here, it is important to note that, for the sake of consistency with the previous BMPs, the statistical error analysis is conducted only to include the first maxima/minima of the wave train and current velocities. When whole time segment (i.e. from $t=7.5$ hrs to $t=11$ hrs) is considered, the errors increase considerably. In fact, the NRMSE of the NAMI DANCE and FLOW-3D results for the free surface dynamics recorded at the Hilo tide station are calculated as 24% and 21% respectively, and the MAX errors are calculated as 33% and 27% for the NAMI DANCE and FLOW-3D results, respectively.

When the method proposed and employed for the previous BMPs is applied, the NRMSE of the NAMI DANCE and FLOW-3D results for the free surface dynamics recorded at the Hilo tide station are calculated as 13% and 11% respectively, and the MAX errors are calculated as 19% and 20% for the NAMI DANCE and FLOW-3D results, respectively.

The NRMSE and MAX error of the model results for the current velocities recorded at HA1125 and HA1126 are given in Table 4.29 and Figure 4.133.

Table 4.29 NRMSE and MAX errors for BMP 6

Gauge	NAMI DANCE		FLOW-3D [®]	
	% NRMSE	% MAX	% NRMSE	% MAX
HA1125 - u	33	39	21	29
HA1125 - v	30	35	27	23
HA1126 - u	34	17	19	5
HA1126 - v	28	35	23	27

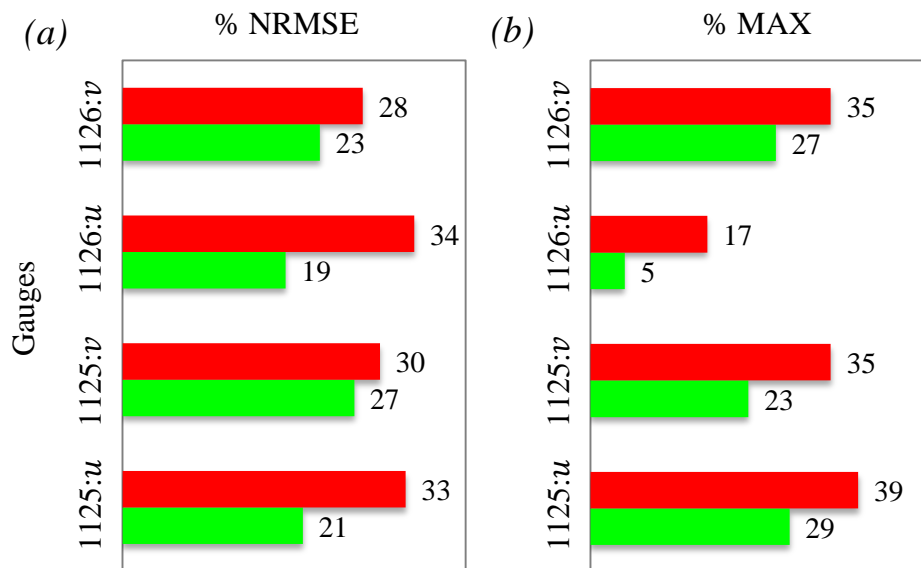


Figure 4.133 Error bars for BMP 6: (a) % NRMSE; (b) % MAX error. The red and green bars represent the errors of the NAMI DANCE and FLOW-3D[®] results, respectively.

The NRMSE of the NAMI DANCE results is around 30% while the MAX error ranges from 17% to 39%. The FLOW-3D[®] results have an NRMSE of around 20% and a MAX error range between 5% and 29%. The effects of grid refinement are crucial for the current velocities. At the ADCP 1125, the NRMSE difference in the velocity magnitude between the 20 and 10 m grids is about 4% for the NAMI DANCE results and 8% for the FLOW-3D results, whereas it is about 1% between the 10 and 5 m grids for both models. At the ADCP 1126, similar values are observed. Note that, at both locations, the maximum velocity is on the order of 1 m/s.

To sum up, the damage caused by tsunamis far from their sources amounts to millions of dollars. This damage is usually done by the strong currents that are generated in harbors and along coastlines, rather than by high flow depth or long inundation distances. In the U.S., the damage that has been done by tsunamis in the last ten years costs over \$170 million. The 2011 Tōhoku tsunami, for instance, probably caused \$90 million in damages in the U.S., despite the fact that the highest waves arrived near low tide and there was little on-shore inundation (Arcos and LeVeque, 2014). It is obvious that understanding and predicting the velocities of currents generated by tsunamis in harbors and channels better is essential and further research into this issue should be carried out.

A recent study by Lynett et al. (2014) illustrates that moderate damage can be done by tsunami current velocities between 1.5 m/sec to 3 m/sec while velocities above 3 m/sec can cause major damage. Tsunami science is primarily involved in the ability to measure and compute tsunami velocities. Depth-averaged water velocity is calculated by tsunami models, but not enough data sets have been available to validate the model results until recently. The comparison of tsunami velocity simulations with laboratory results, post-tsunami survey data and analysis of survivor videos, or direct measurement from current meters is a relatively new area of research. It should be noted that directly measured tsunami currents yield limited data.

As stated earlier, substantial damage and lengthy closure of harbors and marinas resulted from the incessant oscillations and dangerous currents around Hawaii triggered by the 2011 Tōhoku tsunami. The data collected from this tsunami is valuable because of Hilo Harbor's location. BMP 6 provides probably the most comprehensive current data set for a tsunami since the collected data is from the most interesting and challenging locations due to the Hilo Harbor's location. The point measurements for the validation and assessment of the model results in Hawaii were obtained from a number of tide gauges, bottom pressure sensors and ADCPs. Spectral analysis of the computed surface elevation and currents reveals complex flow patterns due to multiscale resonance. Thus, the recorded tsunami current data of BMP 6 has great importance since the differences between two- and three-dimensional models can be assessed based on this data.

The depth-averaged velocity, which is most relevant to the primary flow caused by tsunamis, is calculated from the arithmetic mean of the recorded components over the water column in the N – S and E – W directions in BMP 6. Being a depth-averaged model, NAMI DANCE gives the direct solutions for the depth-averaged velocities at HA1125 and HA116 locations. With FLOW-3D[®] there are two options. The depth-averaged velocities at the given gauge points are automatically calculated or, if desired, calculated from the arithmetic mean of the predicted velocity components over the water columns. For this study, the first option is chosen in order to save time.

The computed free surface elevation time series at the Control Point and the Hilo tide gauge are compared with the previously recorded data. Starting about $t = 10.3$ hrs after the earthquake, there is a gap in the data because the gauge did not function properly. The two velocity components at the two ADCP locations, HA1125 and HA1126, are compared with the recorded values. Moreover, the average current speed values at both ADCPs are also compared at all three resolutions. The results show good agreement between the computed and recorded time series at the Control Point, the Hilo tide station and the two ADCPs for both models.

The grid converge test results indicate there is almost negligible variability in the free surface elevation time series at the Hilo tide station at different resolutions. In the average current speed analysis a small, but slightly larger variability is observed at all three resolutions. These results suggest that, both the free surface elevation and current velocity solutions are well-resolved for this particular benchmark problem. However, further inspection of the maximum current speed variability in the areas with strong vorticity concentration may require higher resolution. The variability of field-scale currents due to the existence of eddies is still a matter of controversy in the field of numerical modeling. Previous studies suggest that as grid size increases, the vortex strengthens and expands (NTHMP, 2015). This creates some difficulty: in eddy areas, many models will increasingly diverge with decreasing resolution (i.e. increasing grid size). Therefore, it is recommended a single model be accompanied by careful and conservative expert interpretation and identification of where potential eddies could form and move in the nearshore region (NTHMP, 2015).

It is known that there is complex nearshore circulation driven by winds, waves, eddies, and tides in the strongly stratified water around Hawaii (Eich et al., 2004; Lowe et al., 2009; Johnson et al., 2013). The ADCP measurements showed variations of the flow velocity over the water column before the tsunami arrived, which indicated the existence of three-dimensional background currents. The predicted current velocity components at HA1125 are slightly higher, but the predictions are in phase with the measurements. The flow field around HA1126 is subject to vortices generated around the breakwater head. Thus, velocity measurements with a higher sampling rate and numerical models with proper turbulence closure are required for a meaningful comparison. Particularly, at the ADCP HA1126, there is good agreement between the FLOW-3D[®] results and the recorded data for the first and second peaks of the current velocities in N – S and E – W directions. This shows the importance of the 3D numerical model structure in the reproduction of tsunami-induced coastal currents in harbors.

As a large number of closely located measurements were made in Hilo Harbor during the 2011 tsunami, it remains a unique location in terms of instrumentation observations. Yet, demonstrating model accuracy is still problematic. There are mainly two reasons for this. First, the ADCP time series data are sampled every six minutes. The velocity field under a tsunami, particularly inside a harbor, can change quickly. There are studies suggesting that a sample rate of a minute is necessary to resolve nearshore currents (Lynett et al., 2012). If the flow is affected by eddies, the sample rate may decrease. Secondly, BMP 6 is a field-data case that is subject to uncertainty and error due to initial condition and propagation of the tsunami wave over half of the Pacific, as well as the fact that the ADCP measurements may be imprecise. It is a fact that Hilo Harbor is possibly the best location for instrumented measurements of tsunami-induced currents, and it has highlighted the necessity of higher resolution sampling of nearshore tsunami-induced currents.

CHAPTER 5

SUMMARY AND CONCLUSIONS

The assessment of coastal environment is a major issue in coastal engineering. Surface water waves that interact with structures or that propagate over varying topographies should be predicted accurately, which poses a challenge. Over the past several decades, many numerical models have been developed to compute wave transformation from deep water to shallow water (Liu, 1994; Wu, 2001). As waves propagate over varying topographies and interact with submerged structures, wave reflection, shoaling, refraction and diffraction can all have a combination of effects. Energy transfers can become more complicated due to nonlinear effects during these interactions. Therefore, the computation needed for the accurate prediction of the variation of free surface elevation and velocity field over structures can be too costly. As a consequence, when nonlinear and dispersive waves over irregular, steep topography are simulated, it is vital that the efficiency and accuracy of models be ensured (Wu and Yuan, 2005).

There are mainly three approaches to the modeling of surface water waves. The first one is Laplace's equation, which is based on the potential flow theory with the assumption of irrotational motion and incompressible fluid. Numerical techniques such as Boundary Element Methods (Longuet-Higgins and Cokelet, 1976; Isaacson, 1982; Grilli et al., 2001) and spectral methods (Dommermuth and Yue, 1987; Bateman et al., 2001) have been employed to solve the Laplace's equation. In general, the application of this type of technique to three-dimensional waves is difficult (Tsai and Yue, 1996). Moreover, when modeling the flows that involve shear, vortex and turbulence generation during their interaction with structures, the potential flow theory is not recommended (Wu and Yuan, 2005).

The second approach to model wave transformation is a so-called depth-integrated model (Liu, 1994). It is based on the idea of integrating the vertical dimension to minimize computational cost. For example, Peregrine (1967) derived the conventional Boussinesq model under the constraint of the equal importance of weak nonlinearity and dispersion. A great deal of progress has been made to remove this constraint by accounting for higher-order effects (Madsen et al., 1991; Nwogu, 1993; Wei et al., 1995; Madsen et al., 2002). The improvement of depth-integrated models also demands higher-order numerical schemes and computation, thus motivating the development of multi-layer Boussinesq models (Lynett and Liu, 2004b; Hsiao et al., 2005).

The third approach is the non-hydrostatic model. Recently, the development of non-hydrostatic models has gained importance because they are able to resolve the variations of surface displacement and velocity field over complicated bottom topographies. Essentially, these types of models are based on the Navier–Stokes equations. To track the moving air–water interface, several methods such as the Lagrangian–Eulerian method (Hodges and Street, 1999; Zhou and Stansby, 1999), the Marker-and-Cell method (Harlow and Welch, 1965), the Volume-of-Fluid method (Hirt and Nichols, 1981) and the Level set method (Iafrati et al., 2001) have been incorporated. The practical applications of these models are limited due to the high cost of computation and strict requirements for stability even though they can handle complicated free surfaces (i.e. breaking waves).

The computational cost of 3D numerical models, which require the numerical solution of the full Navier-Stokes equations, is higher than that of 2D numerical models, which are based on the shallow water approximation. Determining which model would be suitable for a particular problem requires knowledge and experience. The selection of a proper model also depends on the nature of the problem (Wang and Chu, 2012).

This study investigates the sufficiency of nonlinear forms of two-dimensional depth-averaged shallow water equations in tsunami wave evolution, propagation, amplification and inundation and focuses on two numerical tools; NAMI DANCE and FLOW-3D[®]. NAMI DANCE solves nonlinear forms of two-dimensional depth-averaged shallow water (2D-NSW) equations in long wave problems. FLOW-3D[®] simulates linear and nonlinear propagating surface waves as well as long waves by solving three-dimensional Reynolds-averaged Navier-Stokes (3D-RANS) equations. The codes are applied to analytical, experimental and field benchmark problems and validated. A total of six benchmark problems are considered. This dissertation is the first in-depth study to employ such a large number of benchmark problems in order to validate the commercial numerical model FLOW-3D[®] in tsunami wave evolution, propagation and inundation.

The first benchmark problem (BMP 1) covers both analytical and experimental investigations of evolution, propagation and runup of a single solitary wave climbing up a plane beach. Benchmark problem 2 (BMP 2) is composed of physical model studies which focus on wave transformation and overtopping around a conical island. Benchmark problem 3 (BMP 3) describes a series of experiments that analyze the transformation of a single solitary wave as it propagates up a shallow triangular-shaped shelf. Benchmark problem 4 (BMP 4) focuses on the laboratory experiments investigating the propagation and inundation of a tsunami wave over a complex 3D beach and the extreme runup observed at the very narrow valley with very steep slopes leading to the beach. Benchmark problem 5 (BMP 5) investigates the interaction between the macro-roughness elements and tsunami inundation characteristics. The last benchmark problem, Benchmark problem 6 (BMP 6), provides a comprehensive current data set for the Japan 2011 tsunami recorded in Hilo Harbor, Hawaii. It is also possible to regard BMP 6 as a *case study* as it is a field benchmark presenting real data. NAMI DANCE and FLOW-3D[®] are both tested and validated via BMPs 1 – 5 and then applied to a case study, namely BMP 6.

BMP 1 analyses reveal that NAMI DANCE can not accurately describe the wave form of the *large amplitude* solitary wave in *very shallow areas* (i.e. $H = 5.9$ cm and $d \cong 20$ cm). The wave crest steepens, which is typical of any hydrostatic model, and the predicted wave heights are approximately 30% smaller than the laboratory measurements and FLOW-3D[®] results. This leads to the underestimation of the runup height of large amplitude solitary waves, by approximately 20% – 25% by the depth-averaged model.

When the results of BMP 2 are assessed, it is seen that NAMI DANCE predicts the simulated runup 20% less than the measured one on the lee side of the island for the *large amplitude* solitary wave case (i.e. $H = 5.8$ cm and $d = 32$ cm). The reason for this is that the simulated waves steepen more rapidly than those measured in the laboratory experiments for large amplitude waves, which is a well-known effect of the shallow water approximation (NTHMP, 2011). For BMP 2 case, it is obvious that 3D-RANS equations show an appreciable improvement over the 2D depth-averaged NSW equations. The vertical velocity component, w , is fairly effective on the back side of the island for the large amplitude case. It rapidly increases and becomes nearly as large as the horizontal velocity component the moment the two splitting waves converge behind the island.

BMP 3 involves energetic breaking waves with overtopping, vortex formation and runup. There is no delay in the arrival times at the proposed gauges for the three-dimensional model predictions. However, NAMI DANCE shows small time delays at the gauges located in the wake of the island. Moreover, NAMI DANCE underestimates the propagation speed of the wave and somewhat misrepresents the waveform at the gauge located behind the obstacle, on the centerline, where strong turbulence and nonlinearities occur. At this gauge, NAMI DANCE predicts the wave amplitude nearly 10% less just prior to wave breaking. Moreover, the cross-shore velocity component is predicted 20% less than the measured one and the FLOW-3D[®] results. On the other hand, FLOW-3D[®] predicts the cross-shore and longshore velocity components reasonably well with no mismatch in the phase at all gauges.

This shows that the 2D depth-averaged NSW equations are not capable of reflecting strong nonlinearities in the flow. Therefore, 3D-RANS equations are required to adequately resolve the initial wavelength and to prevent the wave front from steepening prior to island impact.

In BMP 4, it is seen that both models are able to reproduce the rapid sequence of runup and rundown as well as the maximum runup in the narrow gully near the village of Monai. However, NAMI DANCE predicts the amplitude of the waves reflected from the coast 20% – 30% less than the values measured in the laboratory and FLOW-3D[®] results. The reason for this is that the flow conditions are not fully hydrostatic after the wave is reflected from the coast. It is important to note that the vertical velocity component gets extremely large on the steep slopes of the narrow valley and ignoring it may lead to unreliable results. Thus, depth-averaged models seem insufficient for runup on steep slopes since NSW equations do not include the vertical velocity component.

The majority of the previous benchmark tests for inundation models engage in time series of free surface elevation or maximum runup height. However, in BMP 5, the time series and maximum values of *overland* flow depth, cross-shore velocity and cross-shore momentum flux are considered. Both models reproduce and transform the incident wave very well, as expected. The largest discrepancies between the numerical simulations and laboratory experiments occur during the inundation stage. Both models manage to reproduce the maximum overland flow depth at the gauges situated close to the shore, however, they underestimate the maximum overland flow depth at landward locations. Compared to the measurements along line B, NAMI DANCE computes the cross-shore velocity ~20% and cross-shore momentum flux ~50% less than FLOW-3D[®] at the farthest landward locations. This is a huge deviation in terms of force calculations. On the other hand, FLOW-3D[®] is able to predict the maximum cross-shore velocity accurately and follows a similar trend with the laboratory data.

As stated earlier, BMP 6 can also be considered as a *case study*, providing a comprehensive tsunami current data set recorded after the 2011 Tōhoku tsunami at Hilo Harbor, Hawaii. The depth-averaged velocity, which is most relevant to the primary flow caused by tsunamis, is calculated from the arithmetic mean of the recorded components over the water column in the N – S and E – W directions and the data is filtered to remove the long period tidal components. It is important to note that the flow field inside the Hilo Harbor is subject to vortices; therefore, the data recorded at HA1126 requires a higher sampling rate for a meaningful comparison. Particularly, at both ADCPs, there is good agreement between the FLOW-3D® results and the recorded data for the first and second peaks of the current velocities in N – S and E – W directions. This shows the importance of the 3D model structure in the reproduction of tsunami-induced coastal currents in harbors.

As stated previously, numerical models solve the nonlinear partial-differential equations (PDE's) describing fluid flow with numerical methods. Numerical methods are the process of discretizing the PDE's into algebraic equations and solving those algebraic equations to obtain the solutions. This is where grid size and time step size are involved. There are several types of errors associated with numerical solutions. The first type is called truncation error, which is caused by a truncated Taylor series expansion replacing the spatial derivative and time derivative. The order of truncation error is proportional to Δx (grid size) and Δt (time step size). This implies that as Δx and Δt decrease, the truncation error decreases. However, decreased grid size and time step size result in an increased number of computational operations, which introduces an additional error called computational round-off error. Moreover, decreasing grid size does not necessarily always provide stability. Therefore, the determination of grid and time step size is an important issue in numerical modeling. In this study, spatial discretization analysis is done for all benchmark problems. The most prominent result obtained is that grid size is a key parameter for the wave – macro-roughness interaction analyses as well as for real case tsunami inundation studies, where analysis of the areas with strong vorticity concentration may require higher resolution.

Friction is another important parameter in the assessment of inundation heights and distances. While friction is negligible offshore, its effects start to be felt in the shallower regions and along the shoreline. For laboratory conditions, several friction parameters are proposed for several materials; however, the determination of the friction factor is relatively difficult for field studies since it is not uniform in real life. Especially for regions with dense settlements along the shorelines, variations in the bottom friction are considerably large, making the friction factor very crucial in the estimation of inundation parameters. BMP 5 is quite a good example illustrating this. Thus, calibration of the friction parameter is essential for all tsunami numerical models.

The limited consideration of bottom friction and the neglect of coastal structures like seawalls or revetments, which may attenuate wave impact, usually results in unreliable runup height and inundation distance predictions. In fact, previous tsunami inundation case studies suggest that there may be a considerably high overestimation of 150% – 200% in predicted maximum water levels, which is probably caused by inaccuracies in the topography/bathymetry and friction factors and the disregard of coastal structures (Løvholt et al., 2012b). Thus, the importance of friction is realised by many researchers in tsunami inundation studies. Different friction coefficients are tested in numerical models to account for land cover roughness such as forests or human-made structures, which are supposed to influence inundation characteristics. In the analysis of large-scale tsunamis, most case studies show that Manning's roughness coefficients of $0.025 \leq n \leq 0.035$ give relatively reliable results in the validation of tsunami models against runup height and inundation distance measurements obtained from field surveys (Løvholt et al., 2012b).

Even though 2D depth-averaged models are very satisfactory in predicting wave evolution, transformation and propagation along both simple and complex bathymetries, they have some shortcomings when the bottom topography becomes too shallow, when there are obstacles in the propagation direction of the wave or when nonlinear effects develop and/or are dominant, raising the need for non-

hydrostatic solutions. Due to the assumptions in the derivation of 2D depth-averaged NSW equations (i.e. hydrostatic pressure distribution along depth), these equations can not produce accurate results when non-hydrostatic effects are present such as wave breaking and turbulence. To illustrate, in the extreme wave cases of BMP 1 and BMP 2 (i.e. large amplitude waves), NAMI DANCE predicts a steeper wave front and, therefore, its predictions of a wave height are 20% less than the laboratory measurements and FLOW-3D[®] results since it neglects wave breaking.

Numerical simulations conducted in order to forecast possible tsunami damage to the settlements have started to play a crucial role in tsunami hazard mitigation in recent years. In other words, the analysis of the interaction of tsunami waves with both coastal defense structures and settlements along the coastline is very important in tsunami mitigation. The results of this study suggest that three-dimensional models, capable of solving non-hydrostatic effects, should be favoured when very shallow areas are studied and/or complex flows such as vortices, turbulence mixing, etc. are dominant. BMP 5 is a very good example illustrating this phenomenon. The force exerted on structures due to inundation flow is directly related to the momentum flux, which is the multiplication of the overland flow depth by the square of cross-shore velocity. Therefore, it is very important to calculate these parameters as accurately as possible. Even though the resolution of the bathymetry is crucial in detailed inundation calculations including settlements, it is seen that three-dimensional models give better results regarding tsunami wave arrival times, overland flow depths and velocities.

Overall, it is seen that both models are capable of predicting the evolution, transformation and inundation of small amplitude waves perfectly, when nonlinear effects are negligible. In the case of large amplitude waves and/or when nonlinear effects are dominant, NAMI DANCE predicts the wave height (i.e. BMP 1, BMP 2 and BMP 4) approximately 20% lower than the measurements and FLOW-3D[®] predictions when the wave reaches very shallow areas (before breaking).

Accordingly, the runup heights are predicted by the depth-averaged NSW equations 15% – 20% lower than the laboratory measurements and FLOW-3D[®] results.

As a result, it is concluded that 2D depth-averaged NSW equations are more than sufficient for the modeling of a tsunami from its source to the shore. However, when the wave reaches shallower regions, i.e. $d \leq 30$ m, and when nonlinear effects develop, 3D-RANS equations should be favoured over the 2D depth-averaged NSW equations. In real life, the vertical velocity component plays an important role in tsunami inundation and wave-structure interaction; therefore, it should not be neglected in tsunami inundation simulations, which are carried out for tsunami hazard mitigation. Also, model predictions for overland flow depth and cross-shore velocity are being more commonly used for structural loading calculations; thus, further research is needed to quantify errors and variability in inundation velocities. As 3D numerical models consume too much computing power and time (Table 5.1), 2D depth-averaged NSW models are recommended for the transformation of tsunami waves from their source to nearshore regions.

In order to prepare for possible future events, it is important to hindcast past largest tsunamis such as the 2004 Indian Ocean tsunami and 2011 Tōhoku tsunami. Although they are often based on coarse data, rapid tsunami hazard assessments are indispensable in risk assessment and mitigation because fast and cost-effective hazard mapping can be done. For the rapid assessment of possible tsunami damage, 2D depth-averaged equations are the best option *for now* since they are fast, accurate and reliable. However, for high risk areas, such as nuclear power plant sites, military zones and heavily populated regions, 3D analyses should be preferred for mitigation strategies. At this point, it is important to note that, when modeling a global tsunami, it is not necessary to solve the whole domain, starting from the source to the shore, via 3D equations. It will be sufficient to model the transformation of tsunami waves from their source to nearshore regions via 2D depth-averaged NSW equations and use 3D models in the rest of the study domain, i.e. the nearshore region, where the shoaling effect starts to be significant, and on land.

Table 5.1 Mesh properties and process time for all BMPs

BM Test	Category	Tested Quantity	Grid Size (m)	Time Step (sec)	Simulation Time (sec)	NAMI DANCE	FLOW-3D®
						Process Time <i>Intel® Xeon® E5-1650 v3 3.5 GHz Processor</i>	Process Time <i>Intel® Xeon® E5-1650 v3 3.5 GHz Processor</i>
BMP 1	Analytical Solution and Laboratory Measurements	Runup/Amplitude	0.01	0.02	60	10 minutes	4 hours
BMP 2	Laboratory Measurements	Runup/Amplitude	0.05	0.02	40	40 minutes	6 hours
BMP 3	Laboratory Measurements	Amplitude/Velocity	0.05	0.001	20	15 hours	2 days
BMP 4	Laboratory Measurements	Runup/Amplitude	0.014	0.05	50	3 hours	3 days
BMP 5	Laboratory Measurements	Runup/Velocity	0.05	0.001	40	21 hours	3 days
BMP 6	Field Measurements	Amplitude/Velocity	10	0.25	48 600	2 days	15 days

It is necessary to validate numerical models incessantly via the newly developed benchmark problems. In the field of numerical modeling, the key parameter is uncompromised and reliable data. Therefore, obtaining measurements of real tsunami data is of utmost importance. The placement of new offshore DART buoys in the strategic areas most vulnerable to tsunamis would provide invaluable data for modelers. It is also crucial to conduct further research regarding the 3D tsunami modeling and be aware of the newly developed methods.

Most tsunami modelers base their studies on the shallow water equations for predictions of propagation and runup of tsunami waves, whereas others rely on dispersive wave models, sometimes even with enhanced nonlinear properties. The latter are in-house models or available as standard codes, free or commercial (Glimsdal et al., 2013). With the advances in computing technology and the development of new numerical methods, it is highly probable that there will be a significant decrease in the required computing power and time for the solutions of three-dimensional equations and that 3D numerical models will be overwhelmingly employed in numerical simulations regarding tsunami hazard mitigation strategies.

REFERENCES

- Abadie, S., Morichon, D., Grilli, S., and Glockner, S. . (2010). Numerical Simulation of Waves Generated By Landslides Using a Multiple-Fluid Navier-Stokes Model. *Coastal Engineering*, 57, 779–794.
- Abbott, M. B. and Ionescu, F. (1967). On the Numerical Computation of Nearly Horizontal Flows. *J. Hydraul. Res.*, 5(2), 97-117.
- AIAA. (1998). *Guide for the Verification and Validation of Computational Fluid Dynamics Simulations*. Am. Institute of Aeronautics and Astronautics.
- Airy, G. (1845). Tides and Waves. *Encyc. Metrop.*, 192, 241-396.
- Allan, J. C., Komar, P. D., Ruggiero, P. and Witter, R. (2012). The March 2011 Tōhoku Tsunami and Its Impacts Along the U.S. West Coast. *J. Coastal Res.*, 28(5), 1142–1153.
- Anderson, J. D. (2009). Governing Equations of Fluid Dynamics. (J. Wendt, Ed.) *Comp. Fluid Dynamics*, 15-51.
- Apotsos,A., Gelfenbaum,G., Jaffe,B., Watt,S., Peck,B., Buckley,M., and Stevens,A. (2011). Tsunami Inundation and Sediment Transport in a Sediment-Limited Embayment on American Samoa. *Earth-Science Reviews*, 107, 1-11.
- Arakawa, A. and Lamb, V. R. (1977). Computational Design of the Basic Dynamical Processes of the UCLA General Circulation Model. *Methods in Computational Physics*, 17, 173–265.
- Arcement, G.J. and Schneider, V. R. (1989). *Guide for Selecting Manning's Roughness Coefficients for Natural Channels and Flood Plains*. Federal Highway Administration. Also published as US Geological Survey Water Supply Paper 2339.
- Arcos, M. E. M. and LeVeque, R. J. (2014). Validating Velocities in the GeoClaw Tsunami Model using Observations Near Hawaii from the 2011 Tōhoku Tsunami. *Pure and Applied Geophysics*.
- Ayca, A. (2012). Development of a Web GIS-Based Tsunami Inundation Mapping Service; A Case Study For Marmara Sea Region. *M.Sc. Thesis*. Ankara, Turkey: Middle East Technical University.

- Aydin, B. and Kanoglu, U. (2012). Analytical Solution for Nonlinear Shallow-water Wave Equations. *Proceedings of 15th World Conference on Earthquake Engineering*. Lisboa, Portugal.
- Aytore, B. (2015). Assessment of Tsunami Resilience of Ports by High Resolution Numerical Modeling: A Case Study for Haydarpasa Port in the Sea of Marmara. *M.Sc. Thesis*. Ankara, Turkey: Middle East Technical University.
- Basu, D., Green, S., Das, K., Janetzke, R. and Stamatakis, J. (2009). Navier-Stokes Simulations of Surface Waves Generated by Submarine Landslides: Effect of Slide Geometry and Turbulence. *Proceedings of SPE Americas E&P Environmental & Safety Conference*. San Antonio, Texas, USA.
- Basu, D., Green, S., Das, K., Janetzke, R. and Stamatakis, J. (2009). Numerical Simulation of Surface Waves Generated by a Subaerial Landslide at Lituya Bay, Alaska. *Proceedings of 28th International Conference on Ocean, Offshore and Arctic Engineering*. Honolulu, Hawaii, USA.
- Bateman, W. J. D., Swan, C. and Taylor, P. H. (2001). On The Efficient Numerical Simulation of Directionally Spread Surface Water Waves. *J. Comp. Physics*, 174, 277–305.
- Bazin, H. (1865). Recherches Experimentales Sur La Propagation Des Ondes. *Mem. Presentes Par Divers Savants a L'Acad. Sci. Ins.*, 19, 495-644.
- Bernard, E. N., Mofjeld, H. O., Titov, V. V., Synolakis, C. E. and Gonzalez, F. I. (2006). 2006 Tsunami: Scientific Frontiers, Mitigation, Forecasting, and Policy Implications. *Phil. Trans. R. Soc. A* 364, 1989–2007.
- Bhinder, M. A., Mingham, C. G., Causon, D. M., Rahmati, M. T., Aggidis, G. A. and Chaplin, R. V. (2009). Numerical and Experimental Study of a Surging Point Absorber Wave Energy Converter. *Proceedings of the 8th European Wave and Tidal Energy Conference*. Upsala, Sweden.
- Biausser, B., Grilli, S.T. and Fraunié, P. (2003). Numerical Simulations of Three-Dimensional Wave Breaking by Coupling of a VOF Method and a Boundary Element Method. *Proceedings of 13th International Offshore and Polar Engineering Conference*. Honolulu Hawaii.
- Blottner, F. (1989). Accurate Navier-Stokes Results for the Hypersonic Flow Over a Spherical Nosetip. *AIAA Journal of Spacecraft and Rockets*, 27(2), 113-122.

- Borrero, J.C., Bu, J., Saiang, C., Uslu, B., Freckman, J., Gomer, B., Oka, E.A. and Synolakis, C.E. (2003). Field Survey and Preliminary Modeling of the Wewak, Papua New Guinea Earthquake and Tsunami of September 9, 2002. *Seismol. Res. Letts.*, 74, 393-405.
- Boussinesq, J. (1871). Theorie de l'intumescence liquide appelee onde solitaire ou de translation se propageant dans un canal rectangulaire. *Comptes Rendus Acad. Sci. Paris*, 72, 755-759.
- Boussinesq, J. (1872). Theorie Des Ondes Et Des Remous Qui Se Propagent Le Long D'un Canal Rectangulaire Horizontal, En Communiquant Au Liquide Contenu Dans Ce Canal Des Vitesses Sensiblement Pareilles De La Surface Au Fond. *J. Math. Pures Appl.*, 17, 55-108.
- Briggs, M. J., Synolakis, C. E., and Harkins, G. S. . (1994). Tsunami Runup on a Conical Island. *IAHR International Symposium on Waves - Physical and Numerical Modeling*. Vancouver, BC, Canada.
- Briggs, M. J., Synolakis, C. E., Harkins, G. S., Green, D. R. (1995). Laboratory Experiments of Tsunami Runup on a Circular Island. *PAGEOPH*, 144.
- Briggs, M. J., Synolakis, C.E., Harkins, G., and Green, D.R. . (1996). Benchmark Problem #2: Runup of Solitary Waves on a Circular Island, Long-Wave Runup Models. "International Workshop on Long Wave Modeling of Tsunami Runup. Friday Harbor, San Juan Island, WA.
- Bronisz, C. L. and Hirt, C. W. (1991). Flows with Density Stratification: An Illustration of Higher Order Scalar Transport. *Flow Science Technical Note*.
- Bryant, E. (2008). *Tsunami: The Underrated Hazard* (2nd ed.). Springer-Verlag Berlin Heidelberg.
- Cankaya, Z. C. (2016). High Resolution Tsunami Vulnerability Assessment by GIS-Based Multi-Criteria Decision Making Analysis at Yenikapi, Istanbul. *M.Sc. Thesis*. Ankara, Turkey: Middle East Technical University.
- Carrier, G. F. (1966). Gravity Waves on Water of Variable Depth. *J. Fluid Mech.*, 24, 641-659.
- Carrier, G. F. and Greenspan, H. P. (1958). Water waves of Finite Amplitude on a Sloping Beach. *J. Fluid Mech.*, 4, 97-109.
- Carrier, G. F., Wu, T. T. and Yeh, H. (2003). Tsunami Run-up and Draw-Down. *J. Fluid Mech.*, 475, 79-99.

- Celik, I. B., Ghia, U., Roache, P. J., Freitas, C. J., Coleman, H., and Raad, P. E. (2008). Procedure for Estimation and Reporting of Uncertainty Due to Discretization in CFD Applications. *J. Fluids Eng.*, 130(7).
- Chan, I.-C and Liu, P. L.-F. (2012). On the Runup of Long Waves on a Plane Beach. *J. Geophys. Res.*, 117.
- Chau, K. W. (2010). *Modelling for Coastal Hydraulics and Engineering*. Taylor and Francis Ltd.
- Chaudhry, M. H. (1993). *Open Channel Flow*. Prentice-Hall, Englewood Cliffs, N.J.
- Chen, C. H. (2012). Study on the Application of FLOW-3D for Wave Energy Dissipation by a Porous Structure. *M. Sc. Thesis*. National Sun Yat-sen University.
- Chen, Q., Kirby, J., Dalrymple, R., Kennedy, A., and Chawla, A. (2000). Boussinesq Modeling Of Wave Transformation, Breaking, and Runup. II: 2-D. *J. Waterw. Port C. Div.*, 126, 48-56.
- Cheung, K. F., Bai, Y. and Yamazaki, Y. (2013). Surges Around the Hawaiian Islands from the 2011 Tōhoku Tsunami. *J. Geophys. Res. Oceans*, 118, 5703–5719.
- Choi, B. H., Dong, C. K., Pelinovsky, E. and Woo, S. B. (2007). Three- dimensional Simulation of Tsunami Runup Around Conical Island. *Coastal Engineering*, 54, 618–629.
- Choi, B. H., Pelinovsky, E., Kim, D. C., Didenkulova, I. and Woo, S. B. (2008). Two- and Three-Dimensional Computation of Solitary Wave Runup on Non-plane Beach. *Nonlin. Processes Geophys.*, 15, 489–502.
- Choi, J., Kwon, K. K. and Yoon, S. B. (2012). Tsunami Inundation Simulation of a Built up Area using Equivalent Resistance Coefficient. *Coastal Engineering*, 2(2), 25 (pages).
- Chow, V. (1959). *Open-Channel Hydraulics*. New York: McGraw-Hill Book Company.
- Christensen, E. (2006). Large Eddy Simulation of Spilling and Plunging Breakers. *Coastal Engineering*, 50(4), 181-198.
- Cox, D., T. Tomita, P. Lynett, and R.A. Holman. (2008). Tsunami Inundation with Macroroughness in the Constructed Environment. *Proceedings of 31st International Conference on Coastal Engineering, ASCE*, (pp. 1421–1432).

- Dalrymple, R. (1992). Prediction of Storm/Normal Beach Profiles. *Journal of Waterway, Port, Coastal, and Ocean Engineering*, 118, 193-200.
- Dalrymple, R.A. and Kriebel, D.L. (2005). The Bridge — Linking Engineering and Society: Lessons in Engineering from the Tsunami in Thailand. *National Academy of Engineering*, 35(2), 4-14.
- Dao, M.H. and Tkalich, P. (2007). Tsunami Propagation Modelling – A Sensitivity Study. *Natural Hazards Earth System Sciences*, 7, 741–754.
- Das, K., Janetzke, R., Basu, D., Green, S. and Stamatakis, J. (2009). Numerical Simulations of Tsunami Wave Generation by Submarine and Aerial Landslides Using RANS and SPH Models. *Proceedings of 28th International Conference on Ocean, Offshore and Arctic Engineering*, (pp. 581-594). Honolulu, Hawaii, USA.
- Dean, R.G. and Dalrymple, R. A. (1984). *Water Wave Mechanics for Scientists and Engineers*. Englewood Cliffs: Prentice-Hall, Inc.
- Dilmen D. I., Kemec, S., Yalciner, A. C., Duzgun, S. and Zaytsev, A. (2014). Development of Tsunami Inundation Map in Detecting Tsunami Risk in Gulf of Fethiye, Turkey. *Pure Appl. Geophys.*
- Dilmen, D. (2009). GIS Based Tsunami Inundation Maps: Case Studies from Mediterranean. *M.Sc. Thesis*. Ankara, Turkey: Middle East Technical University.
- Dimakopoulos, A.S., Guercio, A. and Cuomo, G. (2014). Advanced Numerical Modelling of Tsunami Wave Propagation, Transformation and Run-up. *Proceedings of the Institution of Civil Engineers Engineering and Computational Mechanics*, 167,(3).
- Dingemans, M. (1994). *Comparison of Computations with Boussinesq-Like Models and Laboratory Measurements*, Technical Report H1684.12 . Delft Hydraulics, The Netherlands.
- Dold, J. W., Peregrine, D. H. (1986). Water-Wave Modulation. *Proceedings of 20th International Conference on Coastal Engineering*, 1, pp. 163–175.
- Dommermuth, D.G. and Yue, D.K.P. (1987). A High-Order Spectral Method for the Study of Nonlinear Gravity Waves. *J. Fluid Mech.*, 184, 267-288.

- Dutykh, D., Katsaounis, T. and Mitsotakis, D. (2011). Dispersive Wave Runup on Non-Uniform Shores. *The International Symposium on Finite Volumes for Complex Applications VI*.
- Eich, M. L., Merrifield, M. A. and Alford, M. H. (2004). Structure and Variability of Semidiurnal Internal Tides in Mamala Bay, Hawaii. *J. Geophys. Res.*, 109.
- Emmerson, G. (1977). *John Scott Russell: A Great Victorian Engineer and Naval Architect*. London: John Murray Publishers.
- ERCOTAC. (2002). Quality and Trust in Industrial CFD-a European Initiative. *Best Practice Guidelines, Verion 1.0, EROCFAC Special Iinterest Group*.
- Euler, L. (1768). *Institutionum Calculi Integralis*.
- FEMA (Federal Emergency Management Agency). (2008). *Guidelines for Design of Structures s for Vertical Evacuation from Tsunamis — FEMA P646 Report*. Redwood City, C.A.: Prepared by the Applied Technology Council for the Federal Emergency Management Agency.
- Fenton, J. D. (1972). A Ninth-order Solution for the Solitary Wave. *J. Fluid Mech.*, 53(2), 257-271.
- Fenton, J. D. (1985). A Fifth-Order Stokes Theory for Steady Waves. *J. Waterway, Port, Coastal and Ocean Eng.*, 111(2).
- Fenton, J. D. (1999). Numerical Methods for Nonlinear Waves. (P.-F. Liu, Ed.) *Advances in Coastal and Ocean Engineering*, 5, 241-324.
- Ferziger, J. and Peric, M. (1999). *Computational Methods for Fluid Dynamics*. Springer Berlin.
- Fisher, G. (1959). Ein numerisches Verfahrrens zur Errechnung von Windstau und Gezeiten in Randmeeren. *Tellus*, 9, 60-76.
- Flanders, H. (1973). Differentiation Under the Integral Sign. *The American Mathematical Monthly*, 80(6), 615-627.
- Flow Science. (2002). FLOW-3D User's Manual.
- Franchello, G. and Krausmann, E. (2008). *HyFlux2: A Numerical Model for The Impact Assessment of Severe Inundation Scenario to Chemical Facilities and Downstream Environment*. JRC Scientific and Technical Reports, EUR 23354 EN.

- Freilich, M. H. and Guza, R. T. (1984). Nonlinear Effects on Shoaling Surface Gravity Waves. *Philosophical Transactions of The Royal Society*, 311(1515).
- Freitas, C. J. (2002). The Issue of Numerical Uncertainty. *Applied Mathematical Modelling*, 26(2), 237- 248.
- French, R. H. (1985). *Open-Channel Hydraulics*. New York: McGraw-Hill.
- Fujima, K., Dozono, R. and Shigemura, T . (2000). Generation and Propagation of Tsunami Accompanying Edge Waves on a Uniform Sloping Shelf. *Coastal Engineering*, 42, 211 – 236.
- Glimsdal, S., Pedersen, G. K., Harbitz, C. B. and Løvholt, F. (2013). Dispersion of Tsunamis: Does It Really Matter? *Nat. Hazards Earth Syst. Sci.*, 13, 1507–1526.
- Glimsdal, S., Pedersen, G., Atakan, K., Harbitz, C. B., Langtangen, H. P., and Løvholt, F. (2006). Propagation of the December 26, 2004 Indian Ocean Tsunami: Effects of Dispersion and Source Characteristics. *Int. J. Fluid Mech. Res.*, 33, 15–43.
- Goda, Y. (2010). *Random Seas and Design Of Maritime Structures*. World Scientific.
- Goring, D. (1978). Tsunamis-The Propagation of Long Waves onto a Shelf. *Ph.D. Thesis*. California Institute of Technology, Pasadena, California.
- Goseberg, N. and Schlurmann, T. (2010). Numerical and Physical Study on Tsunami Run-Up and Inundation Influenced by Macro-Roughness Elements. *Proceedings of 32nd International Conference on Coastal Engineering*. American Society of Civil Engineers, ASCE.
- Goseberg, N., Wurpts, A. and Schlurmann, T. (2013). Laboratory-scale Generation of Tsunami and Long Waves. *Coastal Engineering*, 79, 57-74.
- Goseberg, N., Wurpts, A., Schlurmann, T. (2013). Laboratory-scale Generation of Tsunami and Long Waves. *Coastal Engineering* , 79, 57-74.
- Grilli, S. and Subramanya, R. (1996). Numerical Modeling of Wave Breaking Induced by Fixed or Moving Boundaries. *Computational Mech.*, 17, 374-391.
- Grilli, S. and Svendsen, I. A. (1989a). Computation of Nonlinear Wave Kinematics during Propagation and Runup on a Slope. In Water Wave Kinematics. In Torum, & Gudmestad (Ed.), (*Proc. NATO ARW, Molde, Norway*) NATO ASI Series E: Applied Sciences. 178, pp. 387-412. Kluwer Academic Publishers.

- Grilli, S. and Svendsen, L. A. (1990). Corner Problems and Global Accuracy in the Boundary Element Solution of Nonlinear Wave Flows. *Engineering Analysis with Boundary Elements*, 7(4), 178-195.
- Grilli, S., Guyenne, P., and Dias, F. (2001). A Fully Nonlinear Model for Three Dimensional Overturning Waves over Arbitrary Bottom. *Intl. J. Numer. Methods in Fluids*, 35(7), 829-867.
- Grilli, S., Harris, J., Tajalibakhsh, T., Kirby, J., Shi, F., Masterlark, T., and Kyriakopoulos, C. (2012). Numerical Simulation of the 2011 Tōhoku Tsunami: Comparison with Field Observations and Sensitivity to Model Parameters. *International Offshore and Polar Engineering Conference*. Intl. Society of Offshore and Polar Eng.
- Grilli, S., Skourup, J., and Svendsen, I. (1989). An Efficient Boundary Element Method for Nonlinear Water Waves. *Engng. Analysis with Boundary Elements*, 6(2), 97-107.
- Grilli, S., Svendsen, I. and Subramanya, R. (1997). Breaking Criterion and Characteristics For Solitary Waves on Slopes. *J. Waterway, Port, Coastal and Ocean Eng.*, 123(3), 102-112.
- Grilli, S.T., Subramanya, R., Svendsen, I.A., and Veeramony, J. (1994). Shoaling of Solitary Waves on Plane Beaches. *J. Waterway, Port, Coastal, and Ocean Eng.*, 120, 609-628.
- Guignard, S., Grilli, S. T., Marcer, R., and Rey, V. (1999). Computation of Shoaling and Breaking Waves in Nearshore Areas by the Coupling of BEM and VOF Methods. *Proceedings of 9th Offshore and Polar Engineering Conference*, (pp. 304–309). Vol. III, ISOPE99, Brest, France.
- Guignard, S., Marcer, R., Rey, V., Kharif, C. and Fraunié, P. (2001). Solitary Wave Breaking on Sloping Beaches : 2D Two Phase Flow Numerical Simulation by SL-VOF Method. *Eur. J. Mech. B, Fluids*, 20(2001), 57-74.
- Gusiakov, V. K. (1978). Static Displacement on the Surface of an Elastic Space. *III-posed Problems of Mathematical Physics and Interpretation of Geophysical Data*, 23-51.
- Hansen, W. (1956). Theorie zur Errechnung des Wasserstandes und der Stromungen in Randmeeren nebst Anwendungen. *Tellus*, 8, 287-300.

- Harig, S., Chaeroni, C., Pranowo, W. S., and Behrens, J. (2008). Tsunami Simulations on Several Scales: Comparison of Approaches With Unstructured Meshes and Nested Grids. *Ocean Dynam.*, 58, 429-440.
- Harlow, F. H. and Welch, J. E. (1965). Numerical Calculation of Time-Dependent Viscous Incompressible Flow of Fluid with Free Surface. *The Physics of Fluids*, 8.
- Hasselmann, K., Barnett, T. P., Bouws, E., Carlson, H., Cartwright, D. E., Enke, K., Ewing, J. A., Gienapp, H., Hasselmann, D. E., Kruseman, P., Meerburg, A., Muller, P., Olbers, D. J., Richter, K., Sell, W., and Walden, H.,. (1973). Measurement of Wind-Wave Growth and Swell Decay During the Joint North Sea Wave Project (JONSWAP). German Hydrographic Institute, Amburg.
- Hereman, W. (2013). Shallow Water Waves and Solitary Waves. (A. Robert , Ed.) *Encyclopedia of Complexity and Applied System Science*, 8112-8125.
- Hibbert, S. and Peregrine, D. H. (1979). Surf and Run-up on a Beach: a Uniform Bore. *J. Fluid Mech.*, 95, 323–345.
- Hirt, C. W. (1999). *Addition of Wave Transmitting Boundary Conditions to the FLOW-3D Program*. Flow Science, Inc.
- Hirt, C. W. and Nichols, B. D. (1981). Volume of Fluid (VOF) Method for the Dynamics of Free Boundaries. *J. Comp. Physics*, 39, 201-225.
- Hirt, C. W. and Sicilian, J. M. (1985). A Porosity Technique for the Definition of Obstacles in Rectangular Cell Meshes. *Proceedings of 4th International Conference of Ship Hydrodynamics*. Washington D. C.
- Hodges, B. R. and Street, R. L. (1999). On Simulation of Turbulent Nonlinear Free-Surface Flows. *J. Comp. Physics*, 151, 425–457.
- Hokkaidō Tsunami Survey Group. (1993). Tsunami Devastates Japanese Coastal Regions. *EOS, Trans. AGU*, 74(37), pp. 417-432.
- Horrillo J., Kowalik, Z. and Shigihara, Y. (2006). Wave Dispersion Study in the Indian Ocean-Tsunami of December 26, 2004. *Marine Geodesy*, 29, 149-166.
- Horrillo J., Wood A., Kim, G.-B. and Parambath A. (2013). A Simplified 3-D Navier-Stokes Numerical Model for Landslide-Tsunami: Application to the Gulf of Mexico. *J. Geophys. Res. Oceans*, 118, 6934-6950.

- Horrillo, J. J., Wood, A. L., Williams, C., Parambath, A. and Kim, G.-B. . (2010). *Construction of Tsunami Inundation Maps in the Gulf of Mexico*,. Tech. Rep. Award NA09NWS4670006), National Tsunami Hazard Mitigation Program (NTHMP), Natl. Weather Serv. Prog. Office NOAA.
- Horrillo, J., Grilli, S. T., Nicolsky, D., Roeber, V. and Zang, J. (2015). Performance Benchmarking Tsunami Models for NTHMP's Inundation Mapping Activities. *Pure Appl. Geophys.*, 172, 869–884.
- Hsiao, S.C., Hsu, T.W., Lin, T.C., and Chang, Y.H. (2008). On the Evolution and Run-Up of Breaking Solitary Waves on a Mild Sloping Beach. *Coastal Engineering*, 55, 975-988.
- Hsiao, S.-C., Lynett, P., Hwung, H.-H., Liu, P.L.-F. (2005). Numerical Simulations of Nonlinear Short Waves Using a Multilayer Model. *J. Eng. Mech.*, 131(3), 231–243.
- Hwang, L. S., Butler, H. L., and Divoky, D. J. (1972). Tsunami Model: Generation and Open-Sea Characteristics. *Bull. Seismol. Soc. Am.*, 62, 1579-1596.
- Iafrati, A., Mascio, A. D., and Campana, E. F. (2001). A Level Set Technique Applied to Unsteady Free Surface Flows. *Int. J. Num. Methods in Fluids*, 35, 281–297.
- Imamura, F. (1995). Review of Tsunami Simulation with a Finite Difference Method, Long-Wave Runup Models. *World Scientific*, 25-42.
- Imamura, F. and Goto, C. (1988). Truncation Error in Numerical Tsunami Simulation by the Finite Difference Method. *Coastal Engineering in Japan*, 31(2), 245-263.
- Imamura, F. and Imteaz, M. A. (1995). Long Waves in Two-Layers: Governing Equations and Numerical Model. *Sci. of Tsunami Hazards*, 13(1), 3-24.
- Imamura, F., Gica, E., Takahashi, T., and Shuto, N. (1995). Numerical Simulation of the 1992 Flores Tsunami: Interpretation of Tsunami Phenomena in Northeastern Flores Island and Damage at Babi Island. *Pure Appl. Geophys.*, 144, 555-568.
- Imamura, F., Yalciner, A. C. and Ozyurt, G. (2006). TUNAMI N2 Tsunami Modelling Manual.
- Imteaz, M. A. and Imamura, F. (2001). A Non-linear Numerical Model for Stratified Tsunami Waves and its Application. *Sci. of Tsunami Hazards*, 19, 150-159.

- Insel, I. (2009). The Effects of The Material Density and Dimensions of The Landslide on the Generated Tsunamis. *M.Sc. Thesis*. Ankara, Turkey: Middle East Technical University.
- Ioualalen, M., Asavanant, J., Kaewbanjak, N., Grilli, S. T., Kirby, J. T., and Watts, P. (2007). Modeling the 26 December 2004 Indian Ocean tsunami: Case Study of Impact in Thailand. *J. Geophys. Res.*, 112.
- Isaacson, M. d. (1982). Nonlinear-Wave Effects on Fixed and Floating Bodies. *J. Fluid Mech.*, 120, 267-281.
- ISEC. (2004). International Science and Education Conference.
- ISEC. (2009). International Science and Education Conference. National Institute of Education, Singapore.
- Johnson, A. E., Powell, B. S. and Steward, G. F. (2013). Characterizing the Effluence Near Waikiki, Hawaii with a Coupled Biophysical Model. *Cont.Shelf Res.*, 54, 1-13.
- Kaiser, G., Scheele, L., Kortenhaus, A., Løvholt, F., Römer, h., and Leschka, S. (2011). The Influence of Land Cover Roughness on the Results of High Resolution Tsunami Inundation Modeling. *Nat. Hazards Earth Syst. Sci.*, 11, 2521-2540.
- Kanoglu, U. (1998). The Runup of Long Waves Around Piecewise Linear Bathymetries. *Ph.D. Thesis*, 273 pp. Los Angeles, California: University of Southern California,.
- Kanoglu, U. (2004). Nonlinear Evolution and Runup–Rundown. *J. Fluid Mech.*, 513, 363–372.
- Kanoglu, U. and Synolakis, C. E. (1998). Long Wave Runup on Piecewise Linear Topographies. *J. Fluid Mech.*, 374, 1-28.
- Kian, R., Yalciner, A. C. and Zaytsev, A. and Aytore, B. (2015a). Wave Amplification And Resonance in Enclosed Basins; A Case Study in Haydarpasa Port of Istanbul. *Proceedings of Current, Waves and Turbulence Measurement*. 11. IEEE 2015.
- Kian, R., Yalciner, A. C. and Zaytsev, A. and Aytore, B. (2015b). Tsunami Induced Resonance in Enclosed Basins; Case Study Of Haydarpasa Port in Istanbul. *Proceedings of EGU General Assembly*, 17.

- Kim, C. Y. (2010). *Handbook of Coastal and Ocean Engineering*. LA, USA: World Scientific.
- Kim, D. C., Kim, K. O., Choi, B. H., Kim K. H. and Pelinovsky, E. (2013). Three-Dimensional Runup Simulation of the 2004 Indian Ocean Tsunami at the Lhok Nga Twin Peaks. (D. C. Conley, G. Masselink, P. Russell, & T. O'Hare, Eds.) *J. Coastal Res., Special Issue No. 65*, 272-277.
- Kim, D. C., Kim, K. O., Pelinovsky, E., Didenkulova, I. and Choi, B.H. (2013). Three-dimensional Tsunami Runup Simulation for the Port of Koborinai on the Sanriku coast of Japan. (D. Conley, G. Masselink, P. Russell, & T. O'Hare, Eds.) *J. Coastal Res., Special Issue No:65*, 266-271.
- Kim, G.-B. (2012). Numerical-Simulation-of-Three-Dimensional-Tsunami-Generation-by-Subaerial-Landslides. *M.Sc. Thesis*. Texas A&M University, Texas.
- Kim, K. O., Kim, D. C., Choi, B.-H., Jung, T. K., Yuk, J. H. and Pelinovsky, E. (2015). The Role of Diffraction Effects in Extreme Run-up Inundation at Okushiri Island due to 1993 Tsunami. *Nat. Hazards Earth Syst. Sci.*, 15, 747–755.
- Kim, S. K., Liu, P.L.-F. and Liggett, J. A. (1983). Boundary Integral Equation Solutions for Solitary Wave Generation, Propagation and Runup. *Coastal Engineering*, 7, 299-317.
- Kirby, J. T., Wei, G., Chen, Q., Kennedy, B., and Dalrymple, R. A. (1998). Fully Nonlinear Boussinesq Wave Model. *User Manual*. Rep. No. CACR-98-06, Univ. of Delaware.
- Ko, K.-O., Choi, J.-W., Yoon, S.-B. and Park, C.-B. (2011). Internal Wave Generation in FLOW 3D Model. *Proceedings of 21st International Offshore and Polar Engineering Conference*. Maui, Hawaii, USA.
- Kobayashi, N. , Otta, A. K. and Roy, I. (1987). Wave Reflection and Runup on Rough Slopes. *J. Waterway, Port, Coastal and Ocean Eng.*, 113(3), 282-298.
- Koh, H.L., Teh, S.Y. and Izani, A.M.I. (2005). Meso Scale Simulation of December 26 2004 Tsunami With Reference To Malaysia and Thailand. *Proceedings of 3rd International Symposium on Southeast Asian Water Environment* (pp. p 89–96). The University of Tokyo and Asian Institute of Technology (AIT), Bangkok, Thailand.

- Korteweg, D. J. and de Vries, G. (1895). On the Change of Form of Long Waves Advancing in a Rectangular Canal, and on a New Type of Long Stationary Waves. *Philos. Mag.*, 39, 422-443.
- Koshimura, S., Namegaya, Y. and Yanagisawa, H. (2009b). Tsunami Fragility: A New Measure to Identify Tsunami Damage. *J. Disaster Res.*, 4(6), 479–488.
- Koshimura, S., Oie, T., Yanagisawa, H. and Imamura, F. (2009a). Developing Fragility Functions for Tsunami Damage Estimation Using Numerical Model and Post-Tsunami Data from Banda Aceh, Indonesia. *Coastal Engineering*, 51(3), 243–273.
- Kurkin A. A., Kozelkov A. C., Zaitsev A. I., Zahibo N. and Yalciner A. C. (2003). Tsunami risk for the Caribbean Sea Coast. *Izvestiya, Russian Academy of Engineering Sciences*, 4, 126 – 149.
- Lai, J. W., Hsu, T. W. and Lan. Y. J. (2010). Experimental and Numerical Studies on Wave Propagation over Coarse-Grained Sloping Beach. *Coastal Engineering*, 1-15.
- Laitone, E. (1960). The Second Approximation to Cnoidal and Solitary Waves. *J. Fluid Mech.*, 9, 430-444.
- Langseth, J. O. and LeVeque, R. J. (2000). A Wave Propagation Method for Three-dimensional Hyperbolic Conservation Laws. *J.Comp. Physics*, 165, 126–166.
- Leendertse, J. (1967). Aspects of Computational Model for Long-Period Water-Wave Propagation. *Ph.D. Thesis*, 165. Technische Hogeschool Delft, Rand Corporation, R.M. 5294-PR.
- Leendertse, J. J., Alexander, R. C. and Liu, S.-K. (1973). *A Three-Dimensional Model for Estuaries and Coastal Seas: Volume I, Principles of Computation*. Rand Report R-1417-OWRR, California.
- Leendertse, J. J., and Liu, S. K. (1975). *A Three-Dimensional Model for Estuaries and Coastal Seas, II: Aspects of Computation*. Rand Report R-1764-0WRT.
- Leendertse, J.J. and Liu, S.K. (1978). A Three-Dimensional Turbulent Energy Model for Non-Homogeneous Estuaries and Coastal Systems, in Hydrodynamics of Estuaries and Fjords. (J. Nihoul, Ed.) *Elsevier Publ. Co.*, 387-405.
- LeVeque, R. (1994). CLAWPACK. *Proceedings of the Fifth International Conference on Hyperbolic Problems: Theory, Numerics, Applications*, J. Glimmet al. . 188. Singapore: World Scientific.

- LeVeque, R. J. (1998). Balancing Source Terms and Flux Gradients In High-Resolution Godunov Methods: The Quasi-Steady Wave-Propagation Algorithm. *J. Comp. Physics*, 146(1), 346-365.
- LeVeque, R. J. (2011). Proceedings and Results of the 2011 NTHMP. *National Tsunami Hazard Mitigation Program*.
- Li, Y. and Raichlen, F. (2001). Solitary Wave Runup on Plane Slopes. *J. Waterway, Port, Coastal and Ocean Eng.*, 127, 33-44.
- Lin, P. Z. and Liu, P. L.-F. (1999). Internal wave- maker for Navier–Stokes equations models. *J. Waterway, Port, Coastal and Ocean Eng.*, 125, 207–215.
- Lin, P. Z., Chang, K.-A., and Liu, P. L.-F. (1999). Runup and Rundown of Solitary Waves on Sloping Beaches. *J. Waterway, Port, Coastal and Ocean Eng.*, 125(5), 247-255.
- Liu, A. K., Chang, S. Y., Hsu, M.-K. and Liang, N. K. (1998). Evolution of Nonlinear Internal Waves in East and South China Seas. *J. Geophys. Res.*, 103(CC4), 7995 – 8008.
- Liu, P. L.-F, Cho, Y. S. and Fujima, K. (1994). Numerical Solution of Three-dimensional Run-up on a Circular Island. *Proceedings of International Sym.: Waves - Physical and Numerical Modelling*, (pp. 1031-1040). Canada.
- Liu, P. L.-F. (1994). Model Equations for Wave Propagations From Deep to Shallow Water. (P.-F. Liu, Ed.) *Advances in Coastal and Ocean Engineering*, 1, 125-158.
- Liu, P. L.-F., Cho, Y., Yoon, S., and Seo, S. (1995a). Numerical Simulations Of The 1960 Chilean Tsunami Propagation and Inundation at Hilo, Hawaii. (Y. Tsuchiya, & N. Shuto, Eds.) *Tsunami: Progress in Prediction, Disaster Prevention and Warning*, 4, 99-115.
- Liu, P.L.-F., Cho, Y.-S., Briggs, M. J., Kanoglu, U., Synolakis, C. E. (1995). Run-up of Solitary Wave on a Circular Island. *J. Fluid Mech*, 302, 259–285.
- Liu, P.L.-F., Wu, T. -R., Raichlen, F., Synolakis, C. E. and Borrero, J. (2005). Runup and Rundown Generated by Three-Dimensional Sliding Masses. *J. Fluid Mech.*, 536, 107-144.

- Liu, P.L.-F., Yeh, H., and Synolakis, C. E. (2008). Advanced Numerical Models for Simulating Tsunami Waves and Runup. *Advances in Coastal and Ocean Engineering*, 10.
- Longuet-Higgins, M.S. and Cokelet, E.D. (1976). The Deformation of Steep Surface Waves on Water. I. A Numerical Method of Computation. *Proceedings of the Royal Society of London. Series A, Mathematical and Physical Sciences*. 350, pp. 1-26. Royal Society.
- Løvholt, F., Kaiser, G., Glimsdal, S., Scheele, L., Harbitz, C. B., and Pedersen, G. (2012b). Modeling Propagation and Inundation of the 11 March 2011 Tōhoku Tsunami. *Natural Hazards Earth System Sciences*, 12, 1017–1028.
- Løvholt, F., Pedersen, G., and Glimsdal, S. (2010). Coupling of Dispersive Tsunami Propagation and Shallow Water Coastal Response. *Open Oceanography J.*, 4, 71–82.
- Lowe, R. J., Falter, J. L., Monismith, S. G. and Atkinson, M. J. (2009). Wave-Driven Circulation of a Coastal Reef-Lagoon System. *J. Phys. Oceanogr.*, 39(4), 873–893.
- Lynett P. J., Gately K., Wilson R., Montoya L., Arcas D., Aytore B., Bai Y., Bricker J. D., Castro M. J., Cheung K. F., David C. G., Dogan G. G., Escalante C., González-Vida J. M., Grilli S. T., Heitmann T. W., Horrillo J., Kânoğlu U., Kian R., Kirby J. T., Li W., Macías J., Nicolsky D. J., Ortega S., Pampell-Manis A., Park Y. S., Roeber V., Sharghivand N., Shelby M., Shi F., Tehranirad B., Tolkova E., Thio H. K., Velioglu D., Yalciner A. C., Yamazaki Y., Zaytsev A. and Zhang Y. J. (2017). Inter-Model Analysis of Tsunami-Induced Coastal Currents. *Ocean Modelling*, 114, 14-32.
- Lynett P., Borrero, J. C., Weiss, R. and Son, S. (2012). Observations and Modeling of Tsunami-Induced Currents in Ports and Harbors. *Earth and Planetary Science Letters*, 327-328, 68-74.
- Lynett, P. (2007). Effect of a Shallow Water Obstruction on Long Wave Runup and Overland Flow Velocity. *J. Waterway, Port, Coastal, and Ocean Eng.*, 133(6), 455–462.
- Lynett, P. (2015). *Solitary Wave Past a Conical Island*. Retrieved March 23, 2017, from <http://coastal.usc.edu/plynnett/research/exp/index.html>
- Lynett, P. and Liu, P. L. -F. (2004b). Linear Analysis of the Multi-Layer Model. *Coastal Engineering*, 51, 439-454.

- Lynett, P. J., Melby, J., and Kim, D.-H. (2010). An Application of Boussinesq Modeling to Hurricane Wave Overtopping and Inundation. *Ocean Engineering*, 37, 135–153.
- Lynett, P., Borrero, J., Son, S., Wilson, R., and Miller, K. (2014). Assessment of Current-Induced Tsunami Hazards for Maritime Planning. *Geophys. Res. Letts.*, 41.
- Lynett, P., Weiss, R., Renteria, W., Morales, G. D. L. T., Son, S., Arcos, M. E. M. A. and MacInnes, B. T. (2013). Coastal Impacts of the March 11th Tōhoku, Japan Tsunami in the Galapagos Islands. *Pure Appl. Geophys.*, 170, 1189–1206.
- Lynett, P., Wu, T.-R., and Liu, P. L.-F. (2002). Modeling Wave Runup with Depth-Integrated Equations. *Coastal Engineering*, 46(2), 89–107.
- Madsen, O. S. and Mei, C. C. (1969). The Transformation of a Solitary Wave Over and Uneven Bottom. *J. Fluid Mech.*, 39(4), 781-791.
- Madsen, P. A. and Sørensen, O. R. (1992). A New Form of the Boussinesq Equations with Improved Linear Dispersion Characteristics. Part 2. A Slowly-Varying Bathymetry. . *Coastal Engineering*, 18, 183 – 204.
- Madsen, P. A., Bingham, H. B. and Liu, H. (2002). A new Boussinesq Method for Fully Nonlinear Waves from Sshallow to Deep Water. *J. Fluid Mech.*, 462, 1–30.
- Madsen, P. A., Murray, R. and Sorensen, O. R. (1991). A New Form of the Boussinesq Equations with Improved Linear Dispersion Characteristics. Part 1. *Coastal Engineering*, 15, 371-388.
- Madsen, P.A., Fuhrman, D.R. and Schäffer, H.A. (2008). On The Solitary Wave Paradigm for Tsunamis. *J. Geophys. Res.*, 113.
- Maguire, A. E. (2011). Hydrodynamics Control and Numerical Modelling of Absorbing Wavemakers. *Ph.D. Thesis*. The University of Edinburgh.
- Mandli K.T., Ahmadia A.J., Berger M., Calhoun D., George D.L., Hadjimichael Y., Ketcheson D.I., Lemoine G.I., LeVeque R.J. (2016). Clawpack: Building an Open Source Ecosystem for Solving Hyperbolic PDEs. *PeerJ Computer Science*, 2:e, 68.

- MARNET. (2002). Best Practice Guidelines for Marine Applications of Computational UID Dynamics. *Technical report, WS Atkins Consultants and Members of the NSC, MARNET-CFD Thematic Network.*
- Matsuyama, M. and Tanaka, H. (2001). An Experimental Study of the Highest Run-Up Height in the 1993 Hokkaidō Nansei-Oki Earthquake Tsunami. *Proceedings of ITS 2001*, (pp. 879– 889).
- McCormick, M. E. (2010). *Ocean Engineering Mechanics with Applications*. New York: Cambridge University Press.
- McCowan, J. (1891). On the Solitary Wave. *Philos. Mag.*, 32, 45-58,533-555.
- Miles, J. (1980). Solitary Waves. *Ann. Reviews Fluid Mech.*, 12, 11-43.
- Mori, N., Takahashi, T., Yasuda, T., and Yanagisawa, H. (2011). Survey of 2011 Tōhoku Earthquake Tsunami Inundation and Run-Up. *Geophys. Res. Letts.*, 38.
- Munk, W. H. (1949). The Solitary Wave Theory and its Applications to Surf Problems. *Ocean Surface Waves*, 51, 376–424.
- Nandasena, N. A. K., Sasaki, Y. and Tanaka, N. (2012). Modeling Field Observations of The 2011 Great East Japan Tsunami: Efficacy of Artificial and Natural Structures on Tsunami Mitigation. *Coastal Engineering*, 67, 1-13.
- National Tsunami Hazard Mitigation Program. (2011). Annual NTHMP Meeting. Portland, Oregon.
- National Tsunami Hazard Mitigation Program. (2015). NTHMP Subcommittees & Annual Meeting. Portland, Oregon.
- Necmioglu, O. and Ozel, N. M. (2014). An Earthquake Source Sensitivity Analysis For Tsunami Propagation in the Eastern Mediterranean. *Oceanography*, 27(2), 76–85.
- Nichols, B.D. and Hirt, C.W. (1975). Methods for Calculating Multi-Dimensional, Transient Free Surface Flows Past Bodies. *Proceedings of 1st International Conference Num. Ship Hydrodynamics*. Gaithersburg.
- Nikuradse, J. (1933). Stromungsgesetze in rauhen Rohren. *Forschung auf dem Gebiete des Ingenieurwesens, Forschungsheft 361*.

- Nwogu, O. (1993). Alternative Form of the Boussinesq Equations for Nearshore Wave Propagation. *J. Waterway, Port, Coastal, and Ocean Eng.*, 119(6), 618-638.
- Oberkampf, W. and Roy, C. (2010). *Verification and Validation in Scientific Computing*. Cambridge Univ Pr.
- Okada, Y. (1985). Surface Deformation Due To Shear And Tensile Faults in a Halfspace. *Bull. Seismol. Soc. Am.*, 75, 1135–1154.
- Onat, Y. (2011). Database Development for Tsunami Warning System in Mediterranean Basin by Tsunami Modeling. *M.Sc. Thesis*. Ankara, Turkey: Middle East Technical University.
- Onat, Y. and Yalciner, A. C. (2013). Initial Stage of Database Development For Tsunami Warning System Along Turkish Coasts. *Ocean Engineering*, 74, 141–154.
- Orlanski, I. (1976). A Simple Boundary Condition for Unbounded Hyperbolic Flows. *J. Comp. Physics*, 21(3), 251 – 269.
- Osher, S. and Sethian, J.A. (1988). Fronts Propagating with Curvature Dependent Speed: Algorithms Based on Hamilton-Jacobi Formulations. *J. Comp. Physics*, 79, 12-49.
- Ozdemir, K. K. (2014). Database Development For Tsunami Information System. *M.Sc. Thesis*. Ankara, Turkey: Middle East Technical University.
- Ozel, N., Ocal, N., Yalciner, A. C., Kalafat, D. and Erdik, M. (2011). Tsunami Hazard in the Eastern Mediterranean and Its Connected Seas: Toward a Tsunami Warning Center in Turkey. *Soil Dynamics and Earthquake Engineering*, 31, 598–610.
- Ozer, C. (2012). Tsunami Hydrodynamics in Coastal Zones. *Ph.D. Thesis*. Middle East Technical University.
- Ozer, C. and Yalciner, A. C. (2011). Sensitivity Study of Hydrodynamic Parameters during Numerical Simulations of Tsunami Inundation. *Pure Appl. Geophys.*, 2083-2095.
- Pamuk, A. (2014). Assessment of Inland Tsunami Parameters and Their Effects on Morphology. *M.Sc. Thesis*. Middle East Technical University, Ankara.
- Parambath, A. L. (2010). Impact of Tsunamis on Near-Shore Wind Power Units. *M.Sc. Thesis*. Texas A&M University, Texas.

- Park, H., Cox, D. T., Lynett, P. J., Wiebe, D. M. and Shin, S. (2013). Tsunami Inundation Modeling in Constructed Environments: A Physical and Numerical Comparison of Free-Surface Elevation, Velocity, and Momentum Flux. *Coastal Engineering*, 79, 9–21.
- Patel, V. M., Dholakia, M. B. and Singh, A. P. (2016). Emergency Preparedness in the Case of Makran Tsunami: a Case Study on Tsunami Risk Visualization for the Western Parts of Gujarat, India. *Geomatics Natural Hazard and Risk*, 7(2), 826-842.
- Pedersen, G. and Gjevik, B. (1983). Run-up of Solitary Waves. *J. Fluid Mech.*, 135, 283-299.
- Pelinovsky, E., Kim, D.-C., Kim, K.-O and Choi, B.-H . (2013). Three-Dimensional Simulation of Extreme Runup Heights During the 2004 Indonesian and 2011 Japanese Tsunamis. *EGU General Assembly*. Vienna, Austria.
- Peregrine, D. H. (1967). Long Waves on a Beach. *J. Fluid Mech.*, 24(4), 815-827.
- Peregrine, D. H. (1972). Equations for Water Waves and the Approximations Behind Them. (R. Meyer, Ed.) *Waves on Beaches and Resulting Sediment Transport*, 95–121.
- Pierson, W.J. and Moskowitz, L. (1964). A Proposed Spectral Form for Fully Developed Wind Seas Based on the Similarity Theory of S. A. Kitaigorodskii. *J. Geophys. Res.*, 9, 5181–5190.
- Rayleigh, J. W. (1876). On Waves., . *Philos. Mag., Ser. 5,1, No. 4*, 257.
- Richtmyer, R. D. and Morton, K. W. (1967). *Difference Methods for Initial-Value Problems* (2nd ed.). Interscience Publishers.
- Roache, P. J. (1998). Verification and Validation in Computational Science and Engineering. *Hermosa Publishers Albuquerque, NM*.
- Roeber, V. and Cheung, K. F. (2012). Boussinesq-Type Model for Energetic Breaking Waves in Fringing Reef Environment. *Coastal Engineering*, 70(1), 1-20.
- Rueben, M., R. Holman, D. Cox, S. Shin, J. Killian, and J. Stanley. (2011). Optical Measurements of Tsunami Inundation Through an Urban Waterfront Modeled in a Large-Scale Laboratory Basin. *Coastal Engineering*, 58, 229 – 238.

- Russell, J. S. (1845). Report on waves, Tech. Rep. *Report of the 14th Meeting of the British Association for the Advancement of Science* (pp. 311-390). London: John Murray.
- Saint-Venant, B. (1871). Theorie Du Mouvement Non-Permanent Des Eaux Avec Application Aux Crues Des Rivières Et A L'introduction Des Marees Dans Leur Lit. *Comptes rendus Acad Sci Paris*, 73, 148-154, 237-240.
- Sato, S. (1996). Numerical simulation of 1993 southwest Hokkaidō Earthquake Tsunami around Okushiri Island. *J. Waterway, Port, Coastal and Ocean Eng.*, 122(5), 209–215.
- Shuto, N. (1991). Numerical Simulation of Tsunamis - Its Present and Near Future. *Natural Hazards*, 4, 171-191.
- Shuto, N. (1994). Building Damages due to the Hokkaidō Nansei-Oki Earthquake and Tsunami. *Tsunami Engineering Technical report no. 11*, 11 - 28, Tōhoku University (in Japanese).
- Shuto, N. and Matsutomi, H. (1995). Field Survey of the 1993 Hokkaidō Nansei-Oki Earthquake Tsunami. *PAGEOPH*, 144, 649-663.
- Sommerfeld, A. (1912). Die Greensche Funktion der Schwingungsgleichung. *Jahresbericht der Deutschen Mathematiker-Vereinigung*, 21, Reprinted in *Gesammelte Schriften*, 1, 272-316, 309-353.
- Sorensen, R. (1993). *Basic Wave Mechanics for Coastal and Ocean Engineers*. John Wiley, New York.
- Sozdinler, C. O., Yalciner, A. C. and Zaytsev, A. (2014). Investigation of Tsunami Hydrodynamic Parameters in Inundation Zones with Different Structural Layouts. *Pure Appl. Geophys.*, 1-22.
- Sozdinler, C. O., Yalciner, A. C., Zaytsev, A., Suppasri, A., and Imamura, F. (2015). Investigation of Hydrodynamic Parameters and the Effects of Breakwaters During the 2011 Great East Japan Tsunami in Kamaishi Bay. *Pure Appl. Geophys.*, 1-19.
- Spielvogel, L. (1976). Single Wave Run-up on Sloping Beaches. *J. Fluid Mech.*, 74, 685-694.
- Stelling, G. and Zijlema, M. (2003). An Accurate and Efficient Finite-Difference Algorithm For Nonhydrostatic Free-Surface Flow With Application to Wave Propagation. *Int. J. Numer. Meth. Fluids*, 43, 1-23.

- Stoker, J. (1957). *Water Waves The Mathematical Theory With Applications*. Interscience Publishers, Inc.
- Stokes, G. (1847). On the Theory of Oscillatory Waves. *Trans. Camb. Phil. Soc.*, 8, 441–455.
- Subramanya, R., and Grilli, S. T. (1994). Kinematics and Integral Properties of Fully Nonlinear Periodic Waves Shoaling Over a Gentle Slope. In Isaacson, & Quick (Ed.), *Proceedings of International Symposium on Waves-Physical and Numerical Modelling*, (pp. 1106-1115). Vancouver, Canada.
- Swigler, D. T. (2009). Laboratory Study Investigating the Three Dimensional Turbulence and Kinematic Properties Associated with a Breaking Solitary Wave. *M.Sc. Thesis*. Texas A&M University, USA.
- Switzer, A. D. (2005). Depositional Characteristics of Recent and Late Holocene Overwash Sand Sheets in Coastal Embayments from Southeast Australia. *Ph.D. Thesis*. University of Wollongong.
- Synolakis, C. E. (1986). The Runup of Long Waves. *Ph.D. Thesis*. California Institute of Technology, Pasadena, California.
- Synolakis, C. E. (1987). The Runup of Solitary Waves. *J. Fluid Mech.*, 185, 523–545.
- Synolakis, C. E. (1991). Tsunami Run-Up On Steep Slopes: How Good Linear Theory Really Is. *Natural Hazards*, 4, 221–234.
- Synolakis, C. E., Bernard, E. N., Titov, V. V., Kanoglu, U. and Gonzalez, F. (2007). *Standards, Criteria, and Procedures for NOAA Evaluation of Tsunami Numerical Models*. 55 p. Seattle, Washington,; NOAA OAR Special Report, Contribution No 3053, NOAA/OAR/PMEL,.
- Synolakis, C. E., Imamura, F., Tinti, S., Tsuji, Y., Matsutomi, H., Cooc, B., and Usman M. (1995). The East Java tsunami of the July 4 , 1994. *EOS Transactions AGU*, 76(26), 257,261-262.
- Synolakis, C. E., Okal, E. A. and Bernard, E. N. (2004). Tsunami Science Before and After Boxing Day. *Philosophical Transactions of the Royal Society*, A364.
- Synolakis, C. E., Bernard, E. N., Titov, V. V., Kanoglu, U. and Gonzalez, F. I. (2008). Validation and Verification of Tsunami Numerical Models. *Pure Appl. Geophys.*, 165, 2197–2228.

- Synolakis, C.E. and Bernard, E.N. (2006). Tsunami Science Before and After Boxing Day 2004. *Philosophical Transactions of the Royal Society*, A364.
- Tadepalli, S. and Synolakis C.E. (1996). Model for the Leading Waves of Tsunami. *Phys. Rev. Letts.*, 77, 2141-2144.
- Tadepalli, S. and Synolakis, C. E. (1994). The Run-up of N-Waves on Sloping Beaches. *Proceedings of R. Soc. London A*, 445, 99-112.
- Tadepalli, S. and Synolakis, C.E. (1995). The Run up of N-Waves on Sloping Beaches. *Proceedings of Roy. Soc A* , 445, 99.
- Takahashi, T. (1996). Benchmark Problem 4; the 1993 1495 Okushiri Tsunami—Data, Conditions and Phenomena. In 1496 Long-Wave Runup Models. *World Scientific*, 384–403.
- Takahashi, To., Takahashi, Ta., Shuto, N., Imamura, F. and Ortiz, M. (1995). Source Models for the 1993 Hokkaidō Nansei-Oki Earthquake Tsunami. *Pure Appl. Geophys.*, 144(3/4), 747-768.
- Thacker, W. C. (1981). Some Exact Solutions to the Nonlinear Shallow-Water Wave Equations. *J. Fluid Mech.*, 107, 499-508.
- Titov, V. V. (1997). Numerical Modeling of Long Wave Runup. *Ph.D. Thesis*, 141. University of Southern California, Los Angeles, California.
- Titov, V. V. and Gonzalez, F. I. (1997). *Implementation and Testing of the Method of Splitting Tsunami (MOST) Model*. NOAA Technical Memorandum ERL PMEL-112, Pacific Marine Environmental Laboratory, Seattle, WA.
- Titov, V. V. and Synolakis, C. E. (1995). Modeling of Breaking and Nonbreaking Long-Wave Evolution and Runup Using VTCS-2. *J. Waterway, Port, Coastal and Ocean Eng.*, 121(6), 308-316.
- Titov, V. V. and Synolakis, C. E. (1996). Numerical Modeling of Long Wave Runup Using VTCS-3. (Yeh H. et al, Ed.) *Long Wave Runup Models*, 242-248, World Scientific, Singapore.
- Titov, V. V. and Synolakis, C. E. (1998). Numerical Modeling of Tidal Wave Runup. *J. Waterway, Port, Coastal and Ocean Eng.*, 124(4), 157-171.
- Titov, V. V. and Synolakis, C. E. (1997). Extreme Inundation Flows During the Hokkaidō Nansei–Oki Tsunami. *Geophys. Res. Letts.*, 24(11), 1315–1318.

- Titov, V. V., Moore, C. W., Greenslade, D. J. M., Pattiaratchi, C., Badal, R., Synolakis, C. E., and Kanoglu, U. (2011). A new tool for inundation modeling: Community Modeling Interface for Tsunamis (ComMIT). *Pure Appl. Geophys.*
- Titov, V.V. and Synolakis, C.E. (1993). A Numerical Study of the 9/1/92 Nicaraguan Tsunami. *Proceedings of the IUGG/IOC International Tsunami Symposium* (pp. 627-636). Wakayama, Japan: Proceedings published by the Japan Society of Civil Engineers.
- Tomita, T., Honda, K. and Kakinuma, T. (2006). *Application of Storm Surge and Tsunami Simulator in Ocean and Coastal Areas (STOC) to Tsunami Analysis*. Technical Memorandum of Public Works Research Institute 4022.
- Tsai, W.-T. and Yue, D. K. (1996). Computation of Nonlinear Free-Surface Flows. *Annu. Rev. Fluid Mech.*, 28, 249–278.
- Tsunami Pilot Study Working Group. (2006). Seaside, Oregon Tsunami Pilot Study—Modernization of FEMA Flood Hazard Maps.
- Tuck, E. O. and Hwang, L. (1972). Long Wave Generation on a Sloping Beach. *J. Fluid Mech.*, 51(3), 449-461.
- U.S. Geological Survey. (2006). *Historic Earthquakes, Charleston, South Carolina, 1886 September 01 02:51 UTC (local August 31)*.
- Ursell, F. (1953). The Long-Wave Paradox in the Theory of Gravity Waves. *Mathematical Proceedings of the Cambridge Philosophical Society*, 49(4), 685-694.
- USACE (U.S. Army Corps of Engineers). (2006). Coastal Engineering Manual, EM 1110-2-1100. Washington, DC.
- Van Dorn, W. G. (1966). Boundary Dissipation of Oscillatory Waves. *J. Fluid Mech.*, 24, 769–779.
- Van Leer, B. (1977). Towards the Ultimate Conservative Difference Scheme. III. Upstream-Centered Finite-Difference Schemes for Ideal Compressible Flow. *J. Comp. Physics*, 23, 263–275.
- Van Leer, B. (1977). Towards The Ultimate Conservative Difference Scheme. IV. A New Approach to Numerical Convection. *J. Comp. Physics*, 23, 276–299.

- Velioglu, D., Kian, R., Yalciner, A.C. and Zaytsev, A. (2016). Performance Assessment of NAMI DANCE in Tsunami Evolution and Currents Using a Benchmark Problem. (R. Signell, Ed.) *J. Mar. Sci. Eng.*, 4(3), 49.
- Vinje, T. and Brevik, P. (1981). Numerical Simulation of Breaking Waves. *Advances Water Resources*, 4, 77-82.
- Vreugdenhil, C. (1994). *Numerical Methods for Shallow-Water Flow* (1 ed., Vol. 13). Springer Netherlands.
- Wang, T. and Chu, V.H. (2012). Manning Friction in Steep Open-Channel Flow. *Proceedings of the 7th International Conference on Computational Fluid Dynamics*. Big Island, Hawaii, USA. 2012.
- Watanabe, Y., Saeki, H. and Hosking, R. J. (2005). Three-dimensional Vortex Structures Under Breaking Waves. *J. Fluid Mech.*, 545, 291-328.
- Watts, P., Ioualalen, M., Grilli S., Shi, F. and Kirby, J.T. (2005). Numerical Simulation of the December 26, 2004 Indian Ocean Tsunami using a Higher-order Boussinesq Model. *Ocean Waves Measurement and Analysis, 5th International Symposium Waves*. Madrid, Spain.
- Wei, G., Kirby, J. T., Grilli, S. T. and Subramanya, R. (1995). A Fully Nonlinear Boussinesq Model for Surface Waves. Part 1. Highly Nonlinear Unsteady Waves. *J. Fluid Mech.*, 294, 71-92.
- Wei, Y., Bernard, E., Tang, L., Weiss, R., Titov, V.V., Moore, C., Spillane, M., Hopkins, M., and Kanoglu, U. (2008). Real-Time Experimental Forecast Of The Peruvian Tsunami of August 2007 for U.S. Coastlines. *Geophys. Res. Letts.*, 35.
- Wei, Y., Mao, X. Z. and Cheung, K. F. (2006). Well-Balanced Finite Volume Model for Long-Wave Runup. *J. Waterway, Port, Coastal and Ocean Eng.*, 132(2), 114 – 124.
- Wiegel, R. L. (1964). *Oceanographical Engineering*. Prentice-Hall.
- Wu, C. H. and Yuan, H. (2005). Efficient Non-Hydrostatic Modelling of Surface Waves Interacting With Structures. *Applied Mathematical Modelling*, 31, 687–699.
- Wu, N.-J., Hsiao, S.-C., Chen, H.-H. and Yang, R.-Y. (2016). The Study on Solitary Waves Generated by a Piston-Type Wave Maker. *Ocean Engineering*, 117, 114–129.

- Wu, T. (2001). A Unified Theory for Modeling Water Waves. *Advances in Applied Mechanics*, 37, 1-88.
- Yalciner, A. C. , Gülkan, P, Dilmen I., Aytore, B., Ayca, A., Insel I. and Zaytsev A. (2014b). Evaluation of Tsunami Scenarios For Western Peloponnese, Greece. *Bollettino di Geofisica Teorica ed Applicata*, 55, 485-500.
- Yalciner, A. C., Ozer, C., Karakus, H., Zaytsev, A. and Guler, I. (2010). Evaluation of Coastal Risk at Selected Sites against Eastern Mediterranean Tsunamis. *Proceedings of 32nd International Conference on Coastal Engineering*. Shanghai, China.
- Yalciner, A. C., Pelinovsky, E., Synolakis, C. E. and Okal, E. (2003). Submarine Landslides and Tsunamis. *Kluwer Academic Publishers*, 329 pp.
- Yalciner, A. C., Pelinovsky, E., Zaytsev, A., Kurkin, A., Ozer, C., and Karakus, H. (2007a). Modeling and Visualization of Tsunamis: Mediterranean Examples from Tsunami and Nonlinear Waves. (A. Kundu, Ed.) *Springer*, 2731-2839.
- Yalciner, A. C., Zaytsev, A., Aytore, B., Insel, I., Heidarzadeh, M., Kian, R. and Imamura. F. (2014a). A Possible Submarine Landslide and Associated Tsunami at the Northwest Nile Delta", Mediterranean Sea. *Oceanography*, 27(2), 68–75.
- Yalciner, A., Pelinovsky, E., Talipova, T., Kurkin, A., Kozelkov, A. and Zaitsev, A. (2004). Tsunamis in the Black Sea: Comparison of the Historical, Instrumental, and Numerical Data. *J. Geophys. Res.*, 109.
- Yalciner, A.C. and Pelinovsky, E. (2007). A Short Cut Numerical Method for Determination of Resonance Periods of Free Oscillations in Irregular Shaped Basins. *Ocean Engineering*, 34(5-6), 747-757.
- Yalciner, A.C., Alpar,B., Altinok,Y., Ozbay,I. and Imamura,F. (2002). Tsunamis in the Sea of Marmara: Historical Documents for the Past, Models for Future. *Marine Geology*, 190, 445-463.
- Yalciner, A.C., Dogan, P. and Sukru. E. (2005). December 26 2004, Indian Ocean Tsunami Field Survey, North of Sumatra Island. UNESCO.
- Yalciner, A.C., Suppasri, A., Mas, E., Kalligeris, N., Necmioglu, O., Imamura, F., Ozer, C., Zaitsev, A., Ozel, N.M. and Synolakis, C. (2012). Field Survey on the Coastal Impacts of March 11, 2011 Great East Japan Tsunami. *Pure Appl. Geophys.*

- Yalciner, A.C., Synolakis, C.E., Alpar, B., Borrero, J., Altinok, Y. and Imamura, F. (2001). Field Surveys and Modeling 1999 Izmit Tsunami. *International Tsunami Symposium ITS 2001*, 557-563. Seattle, Washington.
- Yamazaki, Y., Cheung, K. F., Pawlak, G. and Lay, T. (2012). Surges Along the Honolulu Coast from the 2011 Tōhoku Tsunami. *Geophys. Res. Letts.*, 39.
- Yamazaki, Y., Kowalik, Z. and Cheung, K. F. (2009). Depth-Integrated, Non-Hydrostatic Model for Wave Breaking and Run-Up. *Int. J. Numer. Methods Fluids*, 61(5), 473–497.
- Yamazaki, Y., Lay T., Cheung, K. F. , Yue, H. and Kanamori, H. (2011a). Modeling Near-Field Tsunami Observations to Improve Finite-Fault Slip Models for The 11 March 2011 Tōhoku Earthquake. *Geophys. Res. Letts.*, 38.
- Yeh, H. (2006). Maximum Fluid Forces in the Tsunami Runup Zone. *J. Waterway, Port, Coastal, and Ocean Eng.*, 132(6), 496-500.
- Yeh, H., Liu, P.-F., Briggs, M., and Synolakis, C. E. (1994). ‘Tsunami Catastrophe in Babi Island. *Nature*, 372, 6503–6508.
- Yeh, H., Synolakis, C. E. and Liu, P. L.-F. (1996). *Long Wave Runup Models*. World Scientific Publishing Co.
- Yen, B. (1991). *Hydraulic Resistance in Open Channels,: Channel Flow Resistance: Centennial of Manning’s Formula*. Littleton, Colo: Water Resources Publications.
- Yoon, S. B. (2002). Propagation of Distant Tsunamis over Slowly Varying Topography. *J. Geophys. Res.*, 107, 2002.
- Zahibo, N., Pelinovsky, E., Yalciner, A. C., Kurkin, A., Koselkov, A. and Zaitsev, A. (2003). The 1867 Virgin Island Tsunami. *Natural Hazards and Earth System Sciences*, 3, 367–376.
- Zaitsev, A. I. and Pelinovsky, E. N. (2011). Forecasting of Tsunami Wave Heights at the Russian Coast of the Black Sea. *Oceanology*, 51(6), 907–915.
- Zaitsev, A. I., Kovalev, D. P., Kurkin, A. A., Levin, B. V., Pelinovskii, E. N., Chernov, A. G. and Yalciner, A. C. (2009). The Tsunami on Sakhalin on August 2, 2007: Mareograph Evidence and Numerical Simulation. *Tikhookeanskaya Geologiya*, 28, 30-35.

- Zaitsev, A. I., Kozelkov, A. C., Kurkin, A. A., Pelinovsky, E. N., Talipova, T.G. and Yalciner, A. C. (2002). Tsunami Modeling in Black Sea. *Applied Mathematics and Mechanics*, 3, 27-45.
- Zaitsev, A., Yalciner, A. C., Pelinovsky, E., Kurkin, A., Ozer, C. and Insel, I. (2008). Tsunamis in Eastern Mediterranean Histories, Possibilities and Realities. *Proceedings of 7th International Conference on Coastal and Port Engineering in Developing Countries*. Dubai, USA.
- Zelt, J. (1991). The Run-up of Non-breaking and Breaking Solitary Waves. *Coastal Engineering*, 15, 205–246.
- Zelt, J. A. and Raichlen, F. (1990). A Lagrangian Model for Wave-induced Harbor Oscillations. *J. Fluid Mech.*, 213, 203-225.
- Zhang, J. (1996). I. Run-on of Ocean Waves on Beaches. II. Non-linear Waves in a Fluid-Filled Elastic Tube. *Ph.D. Thesis*. California Institute of Technology, Pasadena, CA.
- Zhang, Y. and Baptista, A. M. (2008). SELFE: A Semi-Implicit Eulerian-Lagrangian Finite-Element Model for Cross-Scale Ocean Circulation. *Ocean Modelling*, 21, 71–96.
- Zhou, H., Wei, Y., and Titov, V. V. (2012). Dispersive Modeling of the 2009 Samoa Tsunami. *Geophys. Res. Letts.*, 39.
- Zhou, J. G. and Stansby, P. K. (1999). An Arbitrary Lagrangian-Eulerian σ (ALES) model with Non-Hydrostatic Pressure For Shallow Water Flows. *Computer Methods in Applied Mechanics and Engineering*, 178(1-2), 199-214.

APPENDICES

APPENDIX A

GOVERNING EQUATIONS OF FLUID DYNAMICS

The cornerstone of computational fluid dynamics (CFD) is the governing equations of fluid dynamics, which are the equations of continuity, momentum and energy. These equations are the mathematical statements of the three fundamental physical principles upon which all of fluid dynamics is based (Anderson, 2009): *(i)* mass is conserved; *(ii)* acceleration is produced when a force acts on a mass (Newton's second law); *(iii)* energy is conserved.

The governing equations can be obtained in different forms (i.e. conservative or non-conservative forms). In CFD, the use of the equations in one form may lead to success, whereas the use of an alternate form may result in oscillations in the numerical results, or even instability. Therefore, the forms of the equations are of vital interest for all CFD models. In fact, the nomenclature which is used to distinguish these two forms (conservative versus non-conservative) has arisen primarily in the CFD literature.

It is important to apply the physical principles to a suitable model of the flow. A solid body is rather easy to see and define, whereas a fluid is a substance that is hard to grab and does not have a shape unless a container is used. If a solid body is in translational motion, the velocity of each part of the body is the same; on the other hand, if a fluid is in motion, the velocity may be different at every point of the fluid. Therefore, it is important to visualize a moving fluid so as to apply to it the fundamental physical principles (Anderson, 2009).

There are two approaches that can be applied for a continuum fluid (Figure A.1):

- (i) Finite control volume approach
- (ii) Infinitesimal fluid element approach

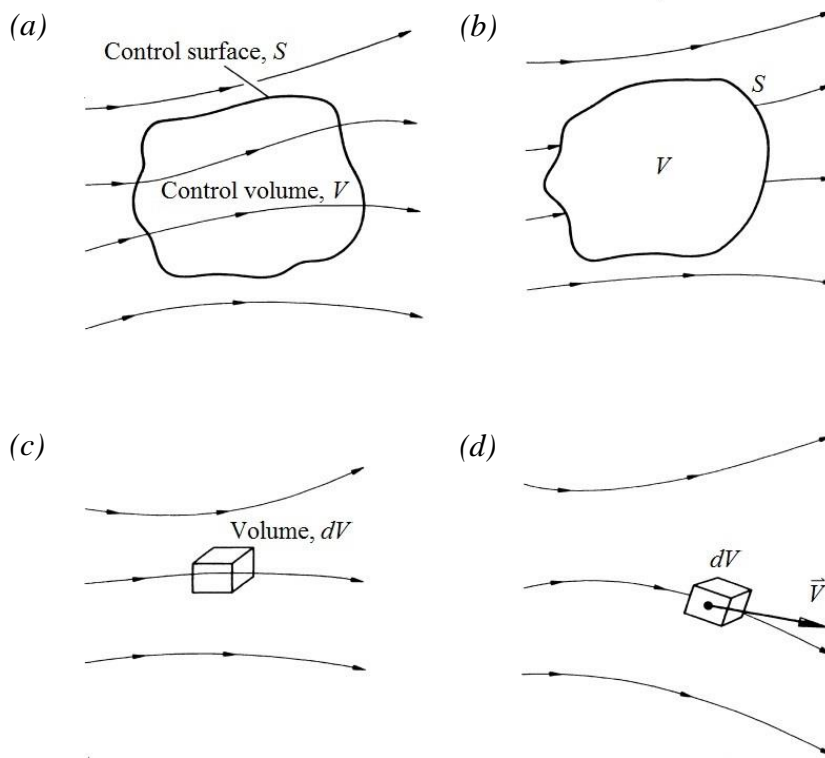


Figure A.1 Approaches for the continuum fluid: (a) fluid passing through a finite control volume fixed in space; (b) finite control volume moving with the fluid; (c) fluid passing through an infinitesimal cubical element fixed in space; (d) an infinitesimal cubical element moving with the fluid (Anderson, 2009)

Finite Control Volume

A closed volume is defined within a finite region of a general flow field, which is represented by the streamlines shown in Figure A.1 (a – b). This volume defines a control volume, V , and a control surface, S , which is referred to as the closed surface bounding the volume. The control volume may be fixed in space with the fluid moving through it, or may be moving with the fluid such that the same fluid particles always remain inside (Figure A.1 (a – b)). In either case, the control volume is a reasonably large, finite region of the flow.

The fundamental physical principles are applied to the fluid inside the control volume, and to the fluid crossing the control surface if the control volume is fixed in space. The control volume model enables focusing on the fluid in the finite region of the volume itself, instead of the whole flow field. The fluid flow equations that are directly obtained by applying the fundamental physical principles to a finite control volume are in *integral form*. These integral forms of the governing equations can be manipulated to *indirectly* obtain partial differential equations.

The equations obtained from the finite control volume fixed in space are called the *conservative form* of the governing equations (Figure A.1 (a)). The equations obtained from the finite control volume moving with the fluid, in either integral or partial differential form, are called the *non-conservative form* of the governing equations (Figure A.1 (b)) (Anderson, 2009).

Infinitesimal Fluid Element

An infinitesimally small fluid element in the flow with a differential volume, dV , is defined along a general flow field represented by the streamlines shown in Figure A.1 (c – d). The fluid element is infinitesimal in the same sense as differential calculus; however, it is large enough to contain a huge number of molecules so that it can be viewed as a continuous medium. The fluid element may be fixed in space with the fluid moving through it, or may be moving along a streamline with a vector velocity, \vec{V} , equal to the flow velocity at each point.

The fundamental physical principles are applied to just the fluid element itself. This application leads *directly* to the fundamental equations in *partial differential equation form*. The particular partial differential equations obtained directly from the fluid element fixed in space (Figure A.1(c)) are the *conservative form* of the equations. The partial differential equations obtained directly from the moving fluid element (Figure A.1 (d)) are called the *non-conservative form* of the equations (Anderson, 2009).

A.1. Derivation of Flow Equations

The differential equations of flow are derived by considering a differential volume element of fluid and describing mathematically:

(i) the conservation of mass of fluid entering and leaving the control volume;
equation of continuity.

(ii) the conservation of momentum entering and leaving the control volume;
equations of motion or Navier-Stokes equations.

A.1.1 Equation of Continuity

The mass conservation of fluid passing through an infinitesimal cubical element $\Delta V = \Delta x \Delta y \Delta z$ (Figure A.1) is stated as follows:

$$\text{rate of change of mass} = \text{transport rate of mass in} - \text{transport rate of mass out} \quad [\text{A. 1}]$$

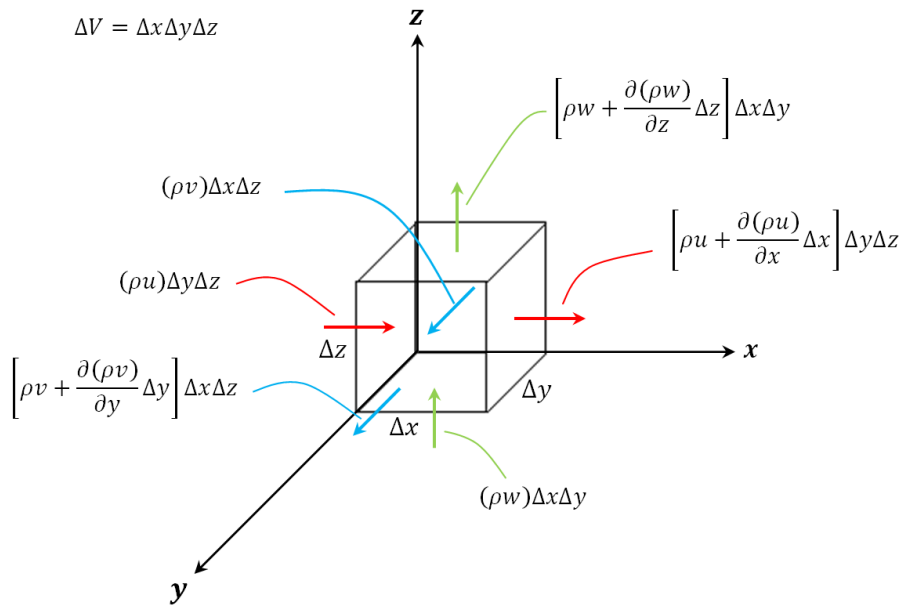


Figure A.2 Fluid passing through an infinitesimal cubical element

The transport rate of mass into the element at location x and through the face $\Delta y \Delta z$ is the product of *mass flux of fluid in x direction* and *surface area of face $\Delta y \Delta z$* :

$$\text{transport rate of mass in} = (\rho u)_x \Delta y \Delta z \quad [\text{A. 2}]$$

The transport rate of mass out of the element at location $x + \Delta x$ and through the face $\Delta y \Delta z$ is expressed by Equation [A.3]:

$$(\rho u)_{x+\Delta x} (\Delta y \Delta z) = \left[(\rho u)_x + \frac{\partial(\rho u)}{\partial x} \Delta x \right] (\Delta y \Delta z) \quad [\text{A. 3}]$$

The change in the fluid density is the only way that mass can be accumulated/depleted within the control volume.

$$\text{rate of change of mass} = \frac{\partial \rho}{\partial t} (\Delta x \Delta y \Delta z) \quad [\text{A. 4}]$$

By substituting Equations [A.2] – [A.4] in the conservation equation [A.1]:

$$\frac{\partial \rho}{\partial t} (\Delta x \Delta y \Delta z) = (\rho u)_x \Delta y \Delta z - \left[(\rho u)_x + \frac{\partial(\rho u)}{\partial x} \Delta x \right] (\Delta y \Delta z) \quad [\text{A. 5}]$$

$$\frac{\partial \rho}{\partial t} = - \frac{\partial \rho u}{\partial x} \quad [\text{A. 6}]$$

When the same considerations are applied to y and z directions, the *general equation of continuity* in three-dimensional flow is given by:

$$\frac{\partial \rho}{\partial t} = - \left[\frac{\partial(\rho u)}{\partial x} + \frac{\partial(\rho v)}{\partial y} + \frac{\partial(\rho w)}{\partial z} \right] \quad [\text{A. 7}]$$

By differentiating the product terms on the right hand side of Equation [A.7] and then collecting all derivatives of density on the left hand side:

$$\frac{\partial \rho}{\partial t} + u \frac{\partial \rho}{\partial x} + v \frac{\partial \rho}{\partial y} + w \frac{\partial \rho}{\partial z} = -\rho \left(\frac{\partial u}{\partial x} + \frac{\partial v}{\partial y} + \frac{\partial w}{\partial z} \right) \quad [\text{A. 8}]$$

Using:

$$\frac{D\rho}{Dt} = \frac{\partial \rho}{\partial t} + u \frac{\partial \rho}{\partial x} + v \frac{\partial \rho}{\partial y} + w \frac{\partial \rho}{\partial z} \quad [\text{A. 9}]$$

The general equation of continuity in three-dimensional flow becomes:

$$\frac{D\rho}{Dt} + \rho \left(\frac{\partial u}{\partial x} + \frac{\partial v}{\partial y} + \frac{\partial w}{\partial z} \right) = 0 \quad [\text{A. 10}]$$

For incompressible fluids (i.e. negligible variation in density of fluid), the general equation of continuity in three-dimensional flow is:

$$\frac{\partial u}{\partial x} + \frac{\partial v}{\partial y} + \frac{\partial w}{\partial z} = 0 \quad [\text{A. 11}]$$

A.1.2 Equations of Motion

Newton's second law of motion states that the net force on a fluid element equals to the product of its mass and its acceleration. It is a vector relation, and hence can be split into three scalar relations along x , y and z axes. The x -component is:

$$F_x = ma_x \quad [\text{A. 12}]$$

where F_x and a_x are the scalar components of the force and acceleration, respectively and m is mass.

The forces acting on the fluid element are:

- (i) *Body forces*, which act directly on the volumetric mass of the fluid element, i.e. gravitational, electromagnetic, centrifugal and coriolis forces.
- (ii) *Surface forces*, which act directly on the surface of the fluid element. These forces are: (a) pressure force acting on the surface and (b) viscous forces, which lead to the formation of shear and normal stresses acting on the surface.

If the *body force* per unit mass acting on the fluid element due to gravity is denoted by \vec{g} , with g_x as its x -component and the volume of the fluid element is $\Delta V = \Delta x \Delta y \Delta z$:

$$\text{Body force on the fluid element acting in } x \text{ direction} = \rho g_x \Delta x \Delta y \Delta z \quad [\text{A. 13}]$$

The net pressure force acting on the surface of the element in x direction is given as:

$$\text{Net pressure force in } x \text{ direction} = P \Delta y \Delta z - \left(P + \frac{\partial P}{\partial x} \Delta x \right) \Delta y \Delta z \quad [\text{A. 14}]$$

The shear and normal stresses in a fluid are related to the time rate of change of deformation of the fluid element (Figure A.2)

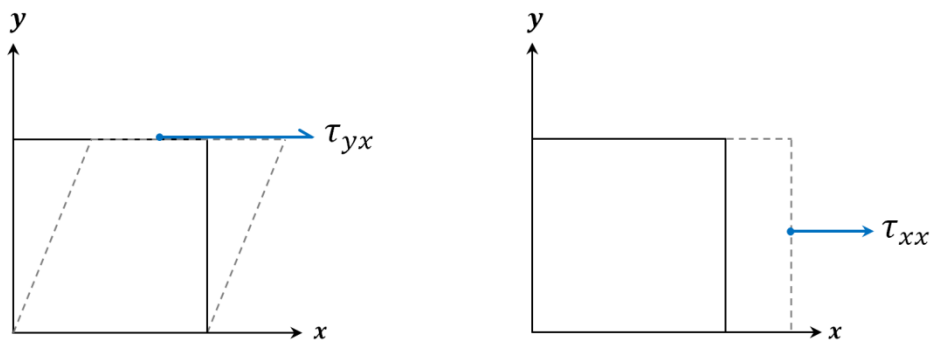


Figure A.3 Stress components acting on the surface of the fluid element: (a) shear stress; (b) normal stress on xy plane

The net shear and normal stresses acting on the surface of the element in x direction is given as:

Net shear and normal stresses in x direction =

$$\left[\left(\tau_{xx} + \frac{\partial \tau_{xx}}{\partial x} \Delta x \right) - \tau_{xx} \right] \Delta y \Delta z + \left[\left(\tau_{yx} + \frac{\partial \tau_{yx}}{\partial y} \Delta y \right) - \tau_{yx} \right] \Delta x \Delta z + \left[\left(\tau_{zx} + \frac{\partial \tau_{zx}}{\partial z} \Delta z \right) - \tau_{zx} \right] \Delta x \Delta y \quad [\text{A. 15}]$$

The surface forces exerted on the fluid element in x direction are shown in Figure A.3. τ_{ij} denotes a stress in j direction exerted on a plane perpendicular to the i axis.

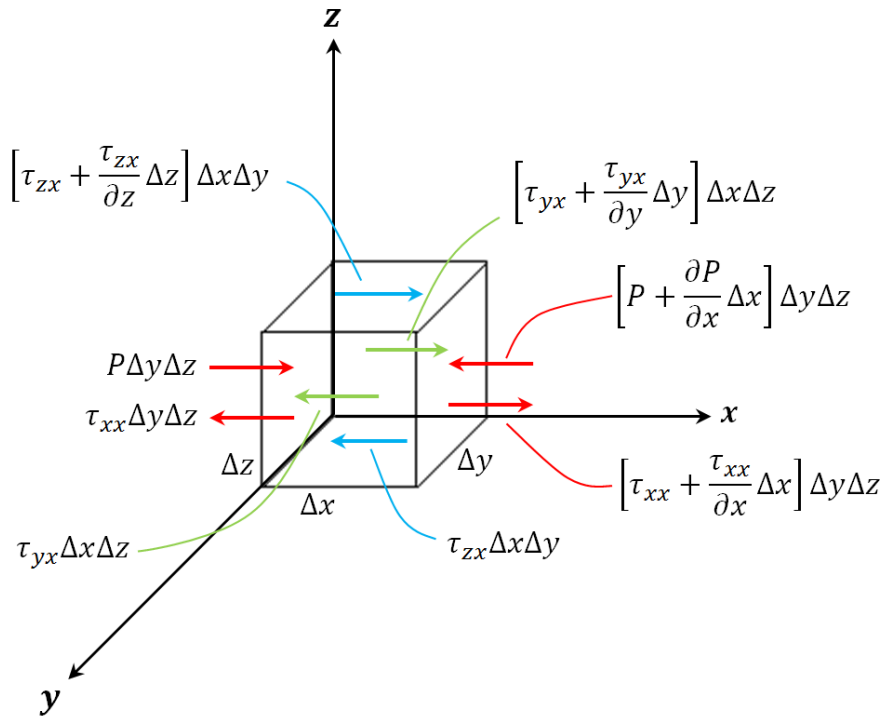


Figure A.4 Surface forces in x direction exerted on the fluid element

The total force in x direction, F_x , is the sum of Equations [A.13] - [A.15]:

$$F_x = \left(-\frac{\partial P}{\partial x} + \frac{\partial \tau_{xx}}{\partial x} + \frac{\partial \tau_{yx}}{\partial y} + \frac{\partial \tau_{zx}}{\partial z} \right) \Delta x \Delta y \Delta z + \rho g_x \Delta x \Delta y \Delta z \quad [\text{A. 16}]$$

The mass of the fluid element is fixed and is equal to:

$$m = \rho \Delta x \Delta y \Delta z \quad [\text{A. 17}]$$

The acceleration of the fluid element is the time rate of change of its velocity. Hence, the component of acceleration in x direction, a_x , is the time rate of change of u :

$$a_x = \frac{Du}{Dt} \quad [\text{A. 18}]$$

Combining Equations [A.12], [A.16], [A.17] and [A.18]:

$$\rho \frac{Du}{Dt} = -\frac{\partial P}{\partial x} + \frac{\partial \tau_{xx}}{\partial x} + \frac{\partial \tau_{yx}}{\partial y} + \frac{\partial \tau_{zx}}{\partial z} + \rho g_x \quad [\text{A. 19}]$$

Similarly,

$$\rho \frac{Dv}{Dt} = -\frac{\partial P}{\partial y} + \frac{\partial \tau_{xy}}{\partial x} + \frac{\partial \tau_{yy}}{\partial y} + \frac{\partial \tau_{zy}}{\partial z} + \rho g_y \quad [\text{A. 20}]$$

$$\rho \frac{Dw}{Dt} = -\frac{\partial P}{\partial z} + \frac{\partial \tau_{xz}}{\partial x} + \frac{\partial \tau_{yz}}{\partial y} + \frac{\partial \tau_{zz}}{\partial z} + \rho g_z \quad [\text{A. 21}]$$

Equations [A.19] – [A.21] are the x -, y - and z -components of the momentum equation in non-conservative form. These equations are also referred to as the Navier-Stokes equations. These equations describe how the velocity, pressure, temperature, and density of a moving fluid are related. The equations were derived independently by George Gabriel Stokes, in England, and Claude Louis Marie Henri Navier, in France, in the early 1800's. The equations are extensions of the Euler Equations and include the effects of viscosity on the flow.

The Navier-Stokes equations can be obtained in conservative form as follows:

$$\rho \frac{Du}{Dt} = \frac{\partial(\rho u)}{\partial t} + \frac{\partial(\rho u^2)}{\partial x} + \frac{\partial(\rho uv)}{\partial y} + \frac{\partial(\rho uw)}{\partial z} \quad [\text{A. 22}]$$

Substituting Equation [A.22] into [A.19], the equations of motion in x direction are obtained as:

$$\frac{\partial \rho u}{\partial t} = - \left(\frac{\partial(\rho u^2)}{\partial x} + \frac{\partial(\rho uv)}{\partial y} + \frac{\partial(\rho uw)}{\partial z} \right) - \frac{\partial P}{\partial x} + \frac{\partial \tau_{xx}}{\partial x} + \frac{\partial \tau_{yx}}{\partial y} + \frac{\partial \tau_{zx}}{\partial z} + \rho g_x \quad [\text{A. 23}]$$

Similarly,

$$\frac{\partial \rho v}{\partial t} = - \left(\frac{\partial(\rho vu)}{\partial x} + \frac{\partial(\rho v^2)}{\partial y} + \frac{\partial(\rho vw)}{\partial z} \right) - \frac{\partial P}{\partial y} + \frac{\partial \tau_{xy}}{\partial x} + \frac{\partial \tau_{yy}}{\partial y} + \frac{\partial \tau_{zy}}{\partial z} + \rho g_y \quad [\text{A. 24}]$$

$$\frac{\partial \rho w}{\partial t} = - \left(\frac{\partial(\rho wu)}{\partial x} + \frac{\partial(\rho wv)}{\partial y} + \frac{\partial(\rho w^2)}{\partial z} \right) - \frac{\partial P}{\partial z} + \frac{\partial \tau_{xz}}{\partial x} + \frac{\partial \tau_{yz}}{\partial y} + \frac{\partial \tau_{zz}}{\partial z} + \rho g_z \quad [\text{A. 25}]$$

For incompressible fluids (i.e. negligible variation in density of fluid), the simplified, three-dimensional unsteady forms of Navier-Stokes Equations are:

$$\rho \left(\frac{\partial u}{\partial t} + u \frac{\partial u}{\partial x} + v \frac{\partial u}{\partial y} + w \frac{\partial u}{\partial z} \right) = - \frac{\partial P}{\partial x} + \left(\frac{\partial \tau_{xx}}{\partial x} + \frac{\partial \tau_{yx}}{\partial y} + \frac{\partial \tau_{zx}}{\partial z} \right) + \rho g_x \quad [\text{A. 26}]$$

$$\rho \left(\frac{\partial v}{\partial t} + u \frac{\partial v}{\partial x} + v \frac{\partial v}{\partial y} + w \frac{\partial v}{\partial z} \right) = - \frac{\partial P}{\partial y} + \left(\frac{\partial \tau_{xy}}{\partial x} + \frac{\partial \tau_{yy}}{\partial y} + \frac{\partial \tau_{zy}}{\partial z} \right) + \rho g_y \quad [\text{A. 27}]$$

$$\rho \left(\frac{\partial w}{\partial t} + u \frac{\partial w}{\partial x} + v \frac{\partial w}{\partial y} + w \frac{\partial w}{\partial z} \right) = - \frac{\partial P}{\partial z} + \left(\frac{\partial \tau_{xz}}{\partial x} + \frac{\partial \tau_{yz}}{\partial y} + \frac{\partial \tau_{zz}}{\partial z} \right) + \rho g_z \quad [\text{A. 28}]$$

A.2. Leibniz Integral Rule

Let $f(x, t)$ be a function such that both $f(x, t)$ and its partial derivative $f_x(x, t)$ are continuous in t and x in some region of the (x, t) plane, including $a(x) \leq t \leq b(x)$, $x_0 \leq x \leq x_1$. Also suppose that the functions $a(x)$ and $b(x)$ are both continuous and both have continuous derivatives for $x_0 \leq x \leq x_1$. Then for $x_0 \leq x \leq x_1$:

$$\frac{\partial}{\partial x} \int_{a(x)}^{b(x)} f(x, t) dt = \int_{a(x)}^{b(x)} \frac{\partial}{\partial x} f(x, t) dt + f(x, b(x)) \frac{\partial b}{\partial x} - f(x, a(x)) \frac{\partial a}{\partial x} \quad [\text{A. 29}]$$

Equation [A.29] is the general form of the Leibniz integral rule, which is also known as differentiation under the integral sign. The rule is derived using the fundamental theorem of calculus (Flanders, 1973).

In order to provide a clear understanding how the Leibniz integral rule is applied to obtain the nonlinear shallow water equations, the expansion of the first term of the momentum equation in x direction, Equation [3.5], is given as an illustrative example:

$$\int_{-d}^{\eta} \frac{\partial u}{\partial t} dz = \frac{\partial}{\partial t} \int_{-d}^{\eta} u dz - u \frac{\partial \eta}{\partial t} \Big|_{z=-d} - u \frac{\partial (-d)}{\partial t} \Big|_{z=-d} \quad [\text{A. 30}]$$

CURRICULUM VITAE

PERSONAL DETAILS

Name and Surname : Deniz Velioğlu
Gender : Female
Birthdate : 20 November 1986
Nationality : Turkish

CONTACT INFORMATION

Address:

Ocean Engineering Research Center, Civil Engineering Department, Middle East Technical University, Universiteler Quarter, Dumlupinar Boulevard No:1, 06800 Cankaya, Ankara, TURKEY

Cell Phone:

+90 (541) 211 10 49

E-mail:

denizcivil@gmail.com, vdeniz@metu.edu.tr

Google Scholar profile:

<https://scholar.google.com.tr/citations?hl=en&user=V5vb5PEAAAAJ>

ResearchGate profile:

https://www.researchgate.net/profile/Deniz_Velioglu_Sogut

EDUCATION

Doctor of Philosophy, Civil Engineering, June 2017, GPA 3.86

Middle East Technical University – Ankara, TURKEY

Master of Science, Civil Engineering, February 2012, GPA 3.57

Middle East Technical University – Ankara, TURKEY

Bachelor of Science, Civil Engineering, June 2009, GPA 3.38

Middle East Technical University – Ankara, TURKEY

WORK EXPERIENCE

October 2012 – Present

Teaching and Research Assistant

Water Resources Laboratory,

Middle East Technical University,

Universiteler Quarter, Dumlupinar Boulevard No:1, 06800 Cankaya, Ankara,
TURKEY

October 2009 - October 2012

Teaching and Research Assistant

Hydromechanics Laboratory,

Middle East Technical University,

Universiteler Quarter, Dumlupinar Boulevard No:1, 06800 Cankaya, Ankara,
TURKEY

ACADEMIC EXPERIENCE

PUBLICATIONS

Peer Reviewed Journal Articles:

Lynett P. J., Gately K., Wilson R., Montoya L., Arcas D., Aytore B., Bai Y., Bricker J. D., Castro M. J., Cheung K. F., David C. G., Dogan G. G., Escalante C., González-Vida J. M., Grilli S. T., Heitmann T. W., Horrillo J., Kânoğlu U., Kian R., Kirby J. T., Li W., Macías J., Nicolsky D. J., Ortega S., Pampell-Manis A., Park Y. S., Roeber V., Sharghivand N., Shelby M., Shi F., Tehranirad B., Tolkova E., Thio H. K., **Velioglu D.**, Yalciner A. C., Yamazaki Y., Zaytsev A. and Zhang Y. J. (2017). Inter-Model Analysis of Tsunami-Induced Coastal Currents. *Ocean Modelling*, 114, 14-32, doi: 10.1016/j.ocemod.2017.04.003 – published June 2017

Kian R, **Velioglu D**, Yalciner A. C, Zaytsev A. (2016). Effects of Harbor Shape on the Tsunami Induced Sedimentation; L-Type Basin. *Journal of Marine Science and Engineering*, 4(3), 55, doi: 10.3390/jmse4030055 – published 02 September 2016

Velioglu D, Kian R, Yalciner A. C, Zaytsev A. (2016). Performance Assessment of NAMI DANCE in Tsunami Evolution and Currents Using a Benchmark Problem. *Journal of Marine Science and Engineering*, 4(3), 49, doi: 10.3390/jmse4030049 – published 18 August 2016

Manuscripts Submitted, In Revision or In Preparation:

Velioglu D. and Sogut E. (2017). Oran Highway Revetment Design. (*in preparation*)

Sogut E., **Velioglu D.**, Baykal C., Guler, I. (2017). Long-term beach evolution around groins using XBeach: A case study in Bafra, Turkey (*in preparation*)

Conference proceedings:

Velioglu D., Sogut E. and Guler I. (2017). Determination of Optimum Cross-section for Oran Highway Revetment. *European Geosciences Union (EGU) 2017*, Vienna, Austria, April 23-28.

Velioglu D., Yalciner A. C. and Zaytsev A. (2016). Performance and Comparison of Numerical Codes for Tsunami Inundation Using Benchmark Problems. *35th International Conference on Coastal Engineering (ICCE 2016)*, Antalya, Turkey, November 17-20.

Guler I., Sogut E., **Velioglu D.**, Cihan H. K., Esen M., Ergin A. and Yalciner A. C. (2016). Oran Highway Revetment Design. *9th International Conference on Coastal and Port Engineering in Developing Countries (IX PIANC-COPEDEC 2016)*, Rio de Janeiro, Brazil, October 16-21.

Kian R., **Velioglu D.**, Yalciner A. C. and Zaytsev A. (2016). Effects of Harbor Shape on the Tsunami Induced Sedimentation. *14th Estuarine and Coastal Modeling Conference (ECM14)*, Rhode Island, U.S., June 13-15.

Kian R., **Velioglu D.**, Yalciner A. C. and Zaytsev A. (2016). Change of Sediment inside Harbors due to Long Waves and Tsunami Motion; Case Study of Haydarpasa Harbor in Istanbul. *14th Estuarine and Coastal Modeling Conference (ECM14)*, Rhode Island, U.S., June 13-15.

Velioglu D., Kian R., Yalciner A. C. and Zaytsev A. (2016). Performance and Validation of a Numerical Code for Tsunami Inundation. *14th Estuarine and Coastal Modeling Conference (ECM14)*, Rhode Island, U.S., June 13-15.

Velioglu D., Yalciner A. C. and Zaytsev A. (2016). Validation and Comparison of 2D and 3D Codes for Nearshore Motion of Long Waves Using Benchmark Problems. *European Geosciences Union (EGU) 2016*, Vienna, Austria, April 17-22.

Velioglu D., Kian R., Yalciner A. C. and Zaytsev A. (2015). Validation and Performance Comparison of Numerical Codes for Tsunami Inundation. *2015 American Geophysical Union (AGU) Fall Meeting*, San Francisco, U.S., December 14-18.

Yalciner A. C., Kian R., **Velioglu D.** and Zaytsev A. (2015). Tsunami Induced Sedimentation in Ports; A Case Study in Haydarpasa Harbor, Marmara Sea. *2015 American Geophysical Union (AGU) Fall Meeting*, San Francisco, U.S., December 14-18.

Kian R., Pamuk A., **Velioglu D.**, Yalciner A. C., Zaytsev A. (2015). Tsunami Parametrelerinin Morfolojik Değişimlere Etkileri. *II. Kıyı ve Deniz Jeolojisi Sempozyumu (KDJS) ve IODP-ECORD Toplantısı*, İstanbul, Türkiye, Ekim 15-16.

Velioglu D., Tokyay N. and Dincer A. E. (2015). A Numerical and Experimental Study on the Characteristics of Hydraulic Jumps on Rough Beds. *36th International Association for Hydro-Environment Engineering and Research (IAHR) World Congress*, The Hague, the Netherlands, 28 June-3 July.

Velioglu D., Kian R., Yalciner A. C. and Zaytsev A. (2015). Validation of Numerical Codes to Compute Tsunami Runup and Inundation. *European Geosciences Union (EGU) 2015*, Vienna, Austria, April 12-17.

Yalciner A. C., Zaytsev A., Kanoglu U., Dogan G. G., **Velioglu D.**, Shargivand N., Kian R. and Aytöre B. (2015). NTHMP - *Mapping & Modelling Benchmarking Workshop* – Tsunami Currents, Portland, Oregon, U.S., February 09-10.

Kian R., **Velioglu D.**, Yalciner A. C. (2014). NAMI DANCE ve Funwave Modellerinin Performanslarının Karşılaştırılması. *IMO 8. Kıyı Mühendisliği Sempozyumu*, İstanbul,Türkiye, Kasım 06-09.

Velioglu D. and Tokyay N. (2012). Effects of Bed Roughness on the Characteristics of Hydraulic Jumps. *10th International Congress on Advances in Civil Engineering (ASCE)*, Ankara, Turkey, October 17-19.

AWARDS AND SCHOLARSHIPS

External:

2015: General Student Travel Grant, American Geophysical Union (AGU), \$1,000.

Internal:

2009-2011: Masters Scholarship, MSc in Hydropower Engineering, METU Development Foundation, \$3,000.

PROFESSIONAL MEMBERSHIPS

American Geophysical Union (AGU)

American Society of Civil Engineers (ASCE)

Turkish Chamber of Civil Engineers (TCCE)

International Association of Civil Engineering Students (IACES)

COMPUTER SKILLS

<i>Microsoft Office</i>	: Word, Excel, Power Point
<i>Programming Languages</i>	: MATLAB, Visual Basic
<i>Optimization Packages</i>	: LINDO
<i>Simulation Packages</i>	: AutoCAD, WaterCAD, MapInfo, SMS, ADCIRC, SWAN, NAMI DANCE, Flow3D
<i>Other</i>	: R, Surfer, Grapher, GEBCO, Adobe Photoshop

LANGUAGES

Turkish	: Mother Tongue
English	: Advanced Level
German	: Basic Knowledge
Japanese	: Basic Knowledge
Korean	: Basic Knowledge

PARTICIPATED WORKSHOPS AND FIELD TRIPS

- Maeslantkering, Sand Engine and Port of Rotterdam, Technical Tour, Den Haag, The Netherlands (July, 2015)
- IACES'09 Meeting, ITU, Istanbul, Turkey (June, 2009)
- IACES'08 Meeting, METU, Ankara, Turkey (June, 2008)
- DERINER Dam, Technical Trip, Artvin, Turkey (September, 2008)
- METU Career Days Seminars, Ankara, Turkey (April, 2008)
- OBRUK Dam, Technical Trip, Çorum, Turkey (December, 2007)
- Ankara-Bolu Tunnel Project, Technical Trip, Bolu, Turkey (January, 2006)
- TPAO Silivri Natural Gas Storage Project, In-situ Observation, Istanbul, Turkey (July, 2005)

REFERENCES

Professor Ahmet Cevdet Yalciner

Head of North-Eastern Atlantic and Mediterranean Tsunami Information Center of
UNESCO

Civil Engineering Department,

Ocean Engineering Research Center,

Middle East Technical University,

Universiteler Quarter, Dumlupinar Boulevard No:1, 06800 Cankaya, Ankara,
TURKEY

Phone: +90 (210) 210 54 38

yalciner@metu.edu.tr

Professor Aysen Ergin

Civil Engineering Department,

Ocean Engineering Research Center,

Middle East Technical University,

Universiteler Quarter, Dumlupinar Boulevard No:1, 06800 Cankaya, Ankara,
TURKEY

Phone: +90 (210) 210 54 41

ergin@metu.edu.tr

Professor Melih Yanmaz

Civil Engineering Department,

Water Resources Laboratory,

Middle East Technical University,

Universiteler Quarter, Dumlupinar Boulevard No:1, 06800 Cankaya, Ankara,
TURKEY

Phone: +90 (210) 210 54 45

myanz@metu.edu.tr